Solvothermal Synthesis of
Novel Inorganic Materials and Frameworks

By John Daniel Lampkin

A Thesis Submitted for the Degree of Doctor of Philosophy

September 2017

School of Chemistry, Food and Pharmacy

University of Reading

Abstract

Solvothermal synthesis has been used to prepare a number of main-group sulfides, oxysulfides, sulfates and an iron-selenide material. New phases were characterised using single-crystal X-ray diffraction to determine their structures followed by elemental analysis, powder X-ray diffraction, infra-red spectroscopy, Uv/*vis* diffuse reflectance spectroscopy, energy dispersive X-ray analysis, and, where appropriate, solid-state NMR and SQUID magnetometry.

The reactions conducted with main-group metals resulted in the formation of antimony sulfide, indium sulfide and indium-antimony sulfide frameworks. $(H_{1.33}tren)[In_{2.67}Sb_{1.33}S_8] \cdot tren$ is the first example of a structure containing mixed In(III)/Sb(V) T2 supertetrahedal units that link through sulfur vertices to generate an open, 3-D framework containing pores in which the organic amine molecules reside. Other sulfides produced include: the discrete bicyclic unit $[Co(tren)]_2[\mu\text{-}Ge_2S_6]$, 1-D structures $[Co(tren)]_2[Sb_2In_2S_8]$ and $[Fe(tren)][Sb_2S_4]$, 2-D structures $[Co(tren)(H_3tren)][In_4SbS_{10}].3H_2O$ and $[Co(tren)(H_3tren)][In_3Sb_2S_9].H_2O$, and 3-D structure $(Hdap)_6[In_{10}S_{18}]$.

The first examples of germanium oxysulfide (oxothiogermanate) compounds have been produced. A series of six materials incorporating discrete T2 supertetrahedral clusters of general formula $[Ge_4O_{6-x}S_{4+x}]^{4-}$ (x = 0, 2, 4) has been prepared, synthesised using a variety of tetra- and poly-amines. In $[Co(dap)_3)]_2[Ge_4O_2S_8]$, the T2 units are bridged by a GeO_4^{4-} unit to form a new discrete germanate unit, $[Ge_9S_8O_{14}]^{8-}$, while in $[Co(deta)_2]_4[Ge_9O_{14}S_8]$, the new $[Ge_9S_8O_{14}]^{8-}$ unit is manipulated to form a new 1-D chain, $[Ge_5O_9(OH)_2S_2]^{4-}$. With increasing sulfur -to-metal ratios, the optical band gap and thermal stability decrease.

Transition-metal sulfates were prepared solvothermally in the presence of an amine, water and concentrated sulfuric acid. The magnetic properties of the discrete complex, $[Co(Hdeta)_2(SO_4)_2]$, and the chain-based structure $(H_24,4'\text{-}bipy)[Co(H_2O)_2(4,4'\text{-}bipy)(SO_4)_2].H_2O$, were investigated using SQUID magnetometry. Both exhibit antiferromagnetic behaviour but the discrete complex also shows weak ferromagnetic contributions at low temperature. Further chain-based compounds were also prepared: $[Mn(SO_4)(tepa)]$, $[Co(SO_4)(dap)_2]$, $[Co(SO_4)(deta)]$ and the 3-D framework, $[Co(SO_4)(dab)]$.

A new iron-selenide compound, $[Fe(en)_3][FeSe_2]$ was also discovered, adding to a small list of chain-based iron-selenide compounds that have been prepared solvothermally.

Declaration Statement

I confirm that this is my own work and the use of all material from other sources have been properly and fully acknowledged.

John Lampkin.

Acknowledgements

Table of Contents

Table of Abbreviations

Amine	Abbreviation	Structure
Methylamine CNH_5	ma	
Ethylamine C_2NH_7	ea	
Diethylammonium C_4NH_{12}	dea	
Ethylenediamine $C_2N_2H_8$	en	
Diethylenetriamine $C_4N_3H_{13}$	deta	
Triethylenetetramine $C_6N_4H_{18}$	teta	
Tetraethylenepentamine $C_8N_5H_{23}$	tepa	
1,4-Diaminobutane $C_4N_2H_{12}$	dab	
1,2 Diaminopropane $C_3N_2H_{10}$	dap	
Tris(2-aminoethyl)amine $C_6N_4H_{18}$	tren	
4,4'-Bipyridine 2,2'-Bipyridine $C_{10}N_2H_8$	4,4'-bipy 2,2-bipy	
1,2-Diamino-cyclohexane $C_6N_2H_{14}$	1,2-chx	
Piperazine $C_4N_2H_{10}$	pip	

1,10-Phenanthroline $C_{12}N_2H_8$	phen	

x

Chapter 1: Introduction

1.1 Introduction to Microporous and Functional Materials

Zeolites are microporous aluminosilicate materials that are most frequently used in commercial absorbents, for example, in water and wastewater purification [1, 2, 3]. They are also used in the preparation of advanced materials [4] and catalysts [5] and in nuclear reprocessing [6]. There are currently over 40 naturally occurring zeolite structures known, with over 323 unique framework types (including synthetically made structures) discovered [7]. Zeolites can also be synthetically produced using solvothermal synthesis [8, 9] with the first investigations by Barrer [10] and Milton [11].

While these materials are incredibly useful, zeolites are electrically insulating materials and cannot be used in electronic-based products. Therefore, producing porous materials with semi-conducting properties (by reducing the band gap) may allow new technological applications to be pursued. Materials with optical and ion-exchange capabilities could be used, for example, as chemical sensors [12]. These are materials that can selectively absorb a molecule or ion from a solution, which can then be detected electronically.

Chemists over the past few decades have been replacing the lighter elements (such as Al, Si etc.) with heavier main-group metal elements (such as Sb, Ge, In etc.) whilst also replacing the anion component (replacing the oxygen with sulfur) [13]. These methodologies can be used to prepare materials with varying physical and optical properties, typically with a band gap smaller than that of a conventional zeolite material. Many different main-group, lanthanide and transition-metal based sulfide frameworks have been produced in this way.

1.2 Background to Chalcogenide Containing Functional Materials

1.2.1 Main-Group Sulfides

Antimony-sulfide open-framework materials are generally yellow in appearance when prepared without impurities. When the density of the number of atoms in the framework increases, the band gap between the valence and the conduction band decreases, resulting in the colour of the material darkening and eventually turning red. This was an observation from Parise and Ko [14] in 1992. A variety of literature [15, 16, 17, 18] has since shown trends and

variations within the band gap values of antimony-sulfide materials as a function of framework density.

The band gap can be measured through a number of experimental methods. One method is X-ray emission spectroscopy. This technique determines the energy of an electron moving from the conduction band back into the valence band, as an electron is removed from the inner core of electrons by the X-ray beam. The energy re-emitted from the transition depends on the detail of the density of states for the conduction and valence band. Understanding which orbitals produce the conduction and valence bands can allow some understanding of where to proceed experimentally to produce materials with reduced band gaps.

The valence and conduction bands in antimony sulfides are primarily composed of *s/p* orbitals of the sulfur atoms (sulfur being a -2 charge within the structure and antimony adopting either a +3 or +5 charge). One study [19], used XPS (X-ray photoelectron spectroscopy) to investigate the valence bands within Sb_2S_3 (from Sb_2S_3-Tl_2S). This showed that S *3p* orbitals dominate the valence band below the Fermi level (-4 to 0 eV), with other interactions seen between S *3p* and Sb *5p* orbitals, along with the lone pair in the Sb *5s* orbital. Another study [20] focused on $CsAgSb_4S_7$, also confirmed that the Sb *5s* lone pair interactions lie just below the Fermi level and that there are some amount of S *5p* orbital states present within the unoccupied states of the conduction band. Both studies indicate that there is a mix of Sb *5s*, *5p* and S *3p* orbitals within the valence band close to the Fermi level with a reliance on sulfur. As discussed in *R.J. Lees'* thesis [16], antimony-sulfide materials display a reduction in band gap on the increase of overlapping Sb 5s orbitals (lone pair) with the empty sulfur ligand orbitals; the more densely populated the material is with Sb atoms (per 1000 $Å^3$), the more chance of orbital overlap between these orbitals. This result has prompted the preparation of a number of antimony sulfides.

Open-framework sulfides have a variety of technological applications in, for example, optical and chemical sensing [12], ion exchange [21] and have a place in catalysis [22] and nuclear reprocessing [23, 24]. Recent research has sought to create semiconducting chalcogenide-based materials in which the band gap is tuned to enable them to be used as optical sensors [25] and photocatalysts [26].

1.2.2 Main-Group Oxysulfides

While the formation of pure sulfide-based frameworks has been investigated extensively due to the reasons already stated, very little research has been conducted on mixed anion (sulfur/oxygen) based frameworks, known as oxochalcogenides or oxysulfides. These materials combine the thermal stability of oxide-based structures with the conductive properties of sulfides. The layered structure of $(N_2H_2)_2Mn_3Sb_4S_8(\mu_3\text{-OH})_2$ is a good example of such a material [27] (Figure 1.1a). This material demonstrated good photocatalytic properties with a band gap of ~1.91 eV. The valence band in this material is predominantly made up of O $2p$, S $3p$ and Mn $3d$ contributions, while the conduction band is made of Sb $4p$, Mn $3d$ and S $3p$ contributions. The orbitals of oxygen contribute very little to the conduction band and again the S $3p$ orbitals play an important role in influencing the band gap.

Another more recent study on oxysulfides containing supertetrahedra has also shown promise [28]. In $[H_3O]_3[Heta]_{4.2}[H_2dpp]_{0.3}[In_4Sn_{16}O_{10}S_{32}]$ (eta = athanolamine, dpp =1,3-di(4-pyridyl)propane), the T4 supertetrahedra (Figure 1.1b) share sulfur vertices to form a 3-D structure with large cavities which, under ion exchange conditions, can remove heavy metal atoms quickly and with high selectivity with respect to which elements are removed from solution. It is thought that oxygen aids stability of the structure while sulfur acts as the driving force for the ion-exchange reaction (acting as binding sites for heavy elements during ion exchange). Both studies demonstrate that these mixed anion materials show promise for new families of semiconducting framework materials with ion exchange properties.
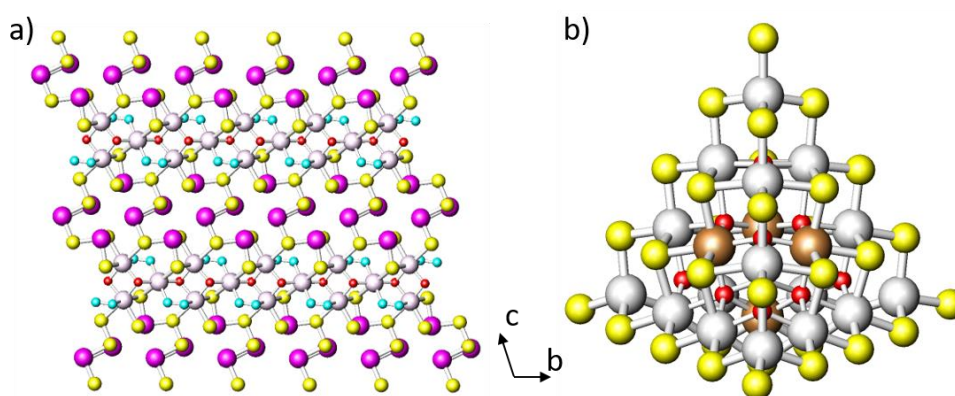
Figure 1.1: (a) A layer in the structure $(N_2H_2)_2Mn_3Sb_4S_8(\mu_3\text{-OH})_2$ and (b) the supertetrahedral units present in $[H_3O]_3[Heta]_{4.2}[H_2dpp]_{0.3}[In_4Sn_{16}O_{10}S_{32}]$ Key: light grey: Sn atoms, light pink: Mn atoms, brown: In atoms, pink: Sb atoms, yellow: S atoms, red: O atoms, light blue: N atoms. H atoms omitted for clarity.

1.2.3 Sulfate Containing Materials

Open-framework sulfate containing materials are also another area of interest, although these are not as abundant as those containing phosphate ions [29]. There has been a growth in the number of sulfate materials since the introduction of organic templating reagents in the presence of transition metal cations [30]. In 2004, the first nickel sulfate 3-D framework was formed $[H_2pip][Ni_2F_4(SO_4)H_2O]$ (pip = piperazine) [31]. Transition-metal sulfate materials have the potential to exhibit magnetic properties, for example $[H_3N(CH_2)_6NH_3][Fe_{1.5}F_3(SO_4)].0.5H_2O$ which is a kagome layered structure and shows a ferromagnetic transition below 19K [32].

Extending the sulfate materials to include lanthanide ions introduces photophysical properties into the materials [33]. This is because lanthanide ions exhibit luminescence behaviours [34-35] and can be useful as probes in biochemistry or for use in lasers. By incorporating them into sulfate frameworks, it is possible to induce these properties into the materials, in the same way that using paramagnetic transition metals may produce structures that exhibit magnetic behaviour.

1.2.4 Iron based Superconducting Materials

Initially, most superconducting materials discovered were oxides, as seen in $La_{2-x}Ba_xCuO_4$ [36], and were usually perovskites and layered structures [37]. A few iron containing oxides were also discovered to have superconducting properties, for example the compound $La[O_{1-x}F_x]FeAs$ (x = 0.05-0.12) [38] exhibits a superconducting transition temp, T_c, of 26 K.

Only a small number of studies have been performed on layered iron-selenide materials [39]. For example, one such layered material, $K_xFe_2Se_2$ ($0 \leq x \leq 1.0$) displays a T_c of 30 K [40], a small improvement over previous iron-selenide materials. More recently, the discovery of the chain-like iron selenides; $Fe_3Se_4(en)_2$ [41], $[Fe(deta)_2][FeSe_2]_2$ and $[Fe(tren)][FeSe_2]_2$ [42] (Figure 1.2) has demonstrated that solvothermal synthesis may be used to prepare a variety of new iron selenide materials. The magnetic characteristics of these chain-like structures can be tuned by using different amine ligands. Switching from deta to tren ligands for example, changes the nearest neighbour magnetic interactions from ferromagnetic to antiferromagnetic. Investigating FeSe compounds further using other amines and different experimental parameters may result in other novel structures.
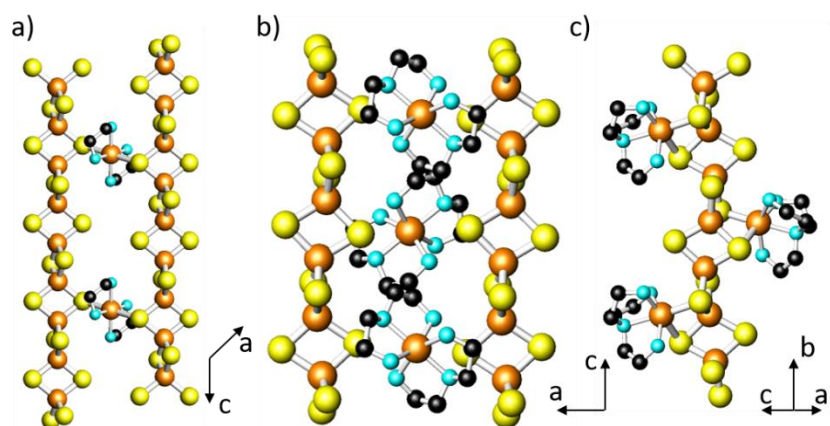
Figure 1.2: The FeSe$_2$ chains found in the compounds (a) Fe$_3$Se$_4$(en)$_2$ (b) [Fe(deta)$_2$][FeSe$_2$]$_2$ and (c) [Fe(tren)][FeSe$_2$]$_2$. Key: orange: Fe atoms, yellow: S atoms, light blue: N atoms. H atoms omitted for clarity.

1.3 Synthesis Routes to Functional Materials

The production of new functional materials is paramount to the continuation of developing new or improving existing technologies. Numerous synthesis routes have been employed in the past to prepare new materials and each has its own pros and cons.

1.3.1 High-Temperature Solid-State Synthesis

High-temperature solid-state synthesis has been used to produce numerous compounds, two examples being thermoelectric materials [43, 44] or mixed-anion chalcogenide semiconductors [45, 46, 47] which can be used in applications such as solar energy [48], ionic conduction [49] and infrared optics [50]. High-temperature solid-state methods are particularly suited for doping studies [51] or phase studies at different annealing temperatures [52]. Materials produced in this synthesis route tend to be condensed phases with high density, not suited to preparing open-framework materials.

1.3.2 Mechanochemical Synthesis

This synthesis route has picked up in recent years particularly in the preparation of thermoelectric materials [53] and chalcogenide glasses [54, 55]. The resultant powder from synthesis can be treated further to produce thin film solar cells [56] or materials with fast ionic conductor properties [57]. The process of ball-milling reagents usually gives the products directly but rarely produces inorganic open-framework materials.

1.3.3 Electrochemical Synthesis

Electrochemical methods are another option for the synthesis of functional materials, as they can produce materials at low temperature, are cost-effective and can be used to dope materials [58, 59]. The types of materials that these methods can produce include photovoltaic ZnTe/CdS/CdTe materials [60, 61, 62], chalcogenide nanostructures [63], oxide nanostructures [64, 65] and graphene oxides [66]. The draw-back of this synthesis route is that it requires specialist equipment and often involves complex synthetic mechanisms.

1.3.4 Flux Synthesis

Much like solvo/hydro and ionothermal synthesis, flux-based synthesis is a "soft" synthesis technique relying on lower temperatures compared to solid-state synthesis. This synthesis route can prepare a variety of chalcogenide compounds including both lanthanides and actinides [67] as well as main-group and transition metals [68, 69, 70]. It is usually difficult to predict the outcomes of these reactions as they cannot be structurally directed.

1.3.5 Ionothermal Synthesis

While solvothermal and hydrothermal synthesis are used widely, the need for further control led to the incorporation of ionic liquids into reactions to promote crystallisation [71]. Various chalcogenide main-group/transition metal structures have been prepared [72, 73, 74] as well as nanomaterials [75], zeolite analogues (Al/P) [76] and metal-organic frameworks (MOF) [77]. However, due to the low vapour pressure of ionic liquids, an additional solvent is usually required to generate the autogenous pressure. Additionally, some common ionic liquids are unstable in ionothermal conditions [78] and some of the organic components rearrange or breakdown [79].

1.3.5 Solvothermal Synthesis

Solvothermal synthesis was the chosen route for the projects conducted within this work. The route is simple, requires few steps and has a history of producing a wide variety of structures (see Section 1.4.2 to 1.5.4). While the method is simple, there are a large array of experimental parameters which may produce variations in structural motifs. Further discussion on solvothermal synthesis can be found in Chapter 2.

1.4 Solvothermal Synthesis of Sulfur Containing Materials

1.4.1 Choice of Main-Group Metal

When conducting experiments to form novel sulfide materials, the choice of metal cation is important, as maximising the amount of cation geometries available will lead to more diversity in structures produced. Throughout this work three main-group metals were investigated; antimony, indium and germanium.

Antimony: Antimony was chosen due to its oxidation states (+3, +5) and the lone pair (if Sb(III)) which introduces structural diversity leading to multiple coordination geometries. If this is paired with another main-group metal then even more diverse structural units are possible. The lone pair also aids the semiconducting nature of these materials as discussed in Section 1.2.1.

Indium: Indium is a well-known cation in chalcogenide materials, typically forming supertetrahedral structures due to the tetrahedral geometry of indium(III). Indium(III) sulfide units, InS_4^{5-}, have also been incorporated into frameworks which are not exclusively supertetrahedral units, but still have a tetrahedral geometry (section 1.4.2.3).

Germanium: This cation is also used frequently to produce chalcogenide materials as germanium is easy to dissolve under solvothermal conditions. Germanium has previously been reported to produce structures in +2 and +4 oxidation states (see Section 1.4.3) which has the potential to add further diversity to chalcogenide structures. Ge(IV) is the most common oxidation state observed in solvothermal chemistry and usually found in a tetrahedral geometry.

There are also mixed main-group metal structures which combine characteristics of each element.

1.4.2 Indium Sulfides

1.4.2.1 Primary Building Units and Supertetrahedral Clusters

The usual coordination geometry of indium is tetrahedral involving InS_4^{5-} units and indium shows a marked tendency to form supertetrahedral clusters. Supertetrahedra are denoted 'Tn', where the n term relates to the number of tetrahedral units down a given edge of the cluster. For example, $[In_4S_{10}]^{8-}$ has two tetrahedral units along an edge and is therefore denoted T2.

The formation of a supertetrahedron Tn indium-sulfide cluster can occur for a range of sizes n = 2 [80, 81], 3 [82], 4 [83], 5 [83], existing either as anions, *e.g.* in the case of the T2 units as [In$_4$S$_{10}$]$^{8-}$ ions [80], or terminated by S-H groups, as in [C$_6$H$_{16}$N][In$_4$S$_6$(SH)$_4$] [81] (Figure 1.3a). Supertetrahedral clusters larger than T3 are not known due to the oxidation state of indium. In T2 clusters, all the anion sites are either 2-coordinate (bridging) or 1-coordinate (terminal) and when the anions are chalcogenides (X^{2-}), charge balance can readily be achieved by using highly charged cations i.e. In (3+). The charge on the indium (+3) is too high, however, for charge balance to be achievable in higher order clusters, where some of the X^{2-} ions are found in high-coordinate sites *e.g.* 3-coordinate X^{2-} ions in T3 and T4 units and 4-coordinate in T4 and T5. This is rationalised using Pauling's electrostatic valence sum principle [84]. The larger indium-sulfide based T4 and T5 supertetrahedra are usually stabilised by incorporation of a divalent metal cation, as is found in the T4 unit [Cu$_4$In$_{16}$S$_{35}$]$^{14-}$ [85]. [Cd$_4$In$_{16}$S$_{31}$]$^{6-}$ and [Cd$_{13}$In$_{22}$S$_{52}$]$^{12-}$ [83] are also T4 and T5 units respectively, but with the additional feature of vertex sulfur atoms being replaced by an amine (Figure 1.3b).
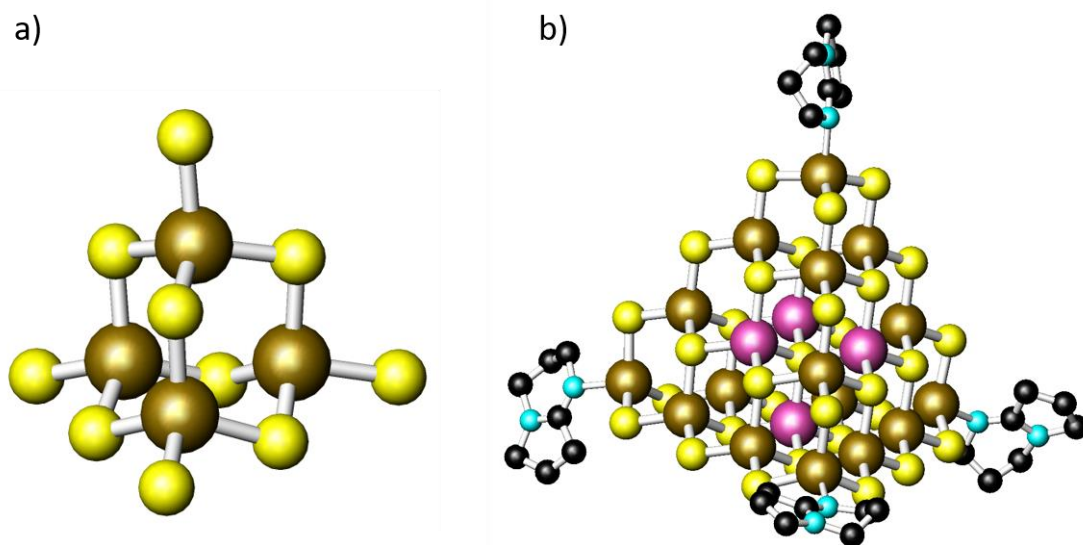
Figure 1.3: a) [In$_4$S$_{10}$]$^{8-}$ T2 unit in [C$_6$H$_{16}$N][In$_4$S$_6$(SH)$_4$] and b) T4 unit of [Cd$_4$In$_{16}$S$_{31}$]$^{6-}$. Key: brown: In atoms, scarlet: Cd atoms, yellow: S atoms, light blue: N atoms, black: C atoms. Hydrogen atoms omitted for clarity.

1.4.2.2 1-D Chain Motifs

Indium sulfides are not observed frequently outside of supertetrahedral structures. The linking of InS$_4$ tetrahedra to form infinite [InS$_2$]$^-$ chains has been reported in [M(en)$_3$]$_{0.5}$[InS$_2$] (M^{2+} =

Co, Ni) (en = ethylenediamine) [86] and [Ni(deta)$_2$]$_{0.5}$[InS$_2$] (deta = diethylenetriamine), [Ni(dap)$_3$]$_{0.5}$[InS$_2$] (dap = 1,2-diaminopropane), [C$_{10}$N$_4$H$_{26}$]$_{0.5}$[InS$_2$] [87] (Figure 1.4a) and the more complex chain of [Ni(tepa)]$_2$[In$_4$S$_7$(SH)$_2$]·H$_2$O (tepa = tetraethylenepentamine) [88] (Figure 1.4b).
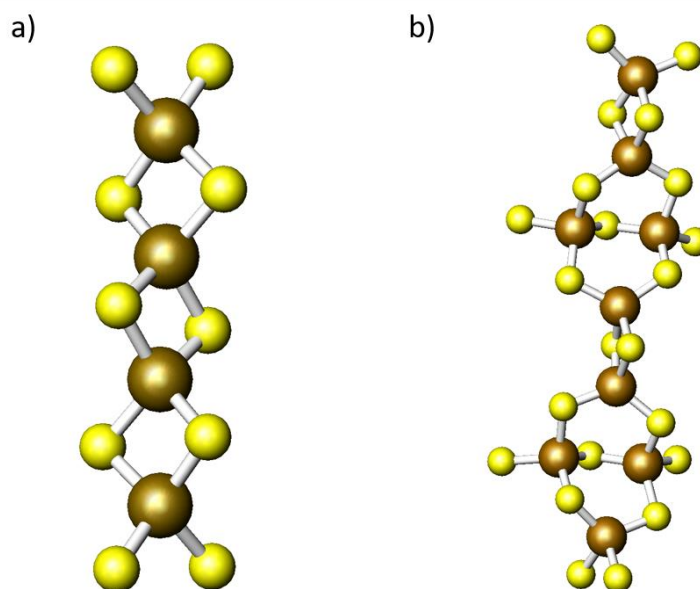
Figure 1.4: a) InS$_2$ infinite chain in [Ni(dap)$_3$]$_{0.5}$[InS$_2$] and b) the inorganic chain of [Ni(tepa)]$_2$[In$_4$S$_7$(SH)$_2$]·H$_2$O. Key: brown: In atoms, yellow: S atoms. Complexes omitted for clarity.

The only T2 observed supertetrahedral based chain (generated by sharing sulfur vertices) is found in the compound, {[Eu(tepa)]$_2$[μ_2-SbS$_3$](μ_2-H$_2$O)}[Eu(tepa)In$_4$S$_9$]·0.25tepa (tepa = tetraethylenepentamine) [89]. Here, T2 indium sulfide units share a common vertex to create a chain and each T2 is capped with an [Eu(tepa)]$^{3+}$ complex which bonds to the three bridging sulfur atoms at the base of the chains. This is the first example of such a structural motif (Figure 1.5). Two T3 based chains have also been reported in [Fe(phen)$_3$]$_4$[H$_4$In$_{20}$S$_{38}$]·Hphen·3Hdma·8H$_2$O and [Ni(phen)$_3$]$_4$[H$_4$In$_{20}$S$_{38}$]·2Hphen·2Hdma·3H$_2$O (DMA = dimethylamine, phen = phenanthroline) [90]. The two structures consist of T3 units sharing two common vertices which results in straight or zig-zag chains, respectively.
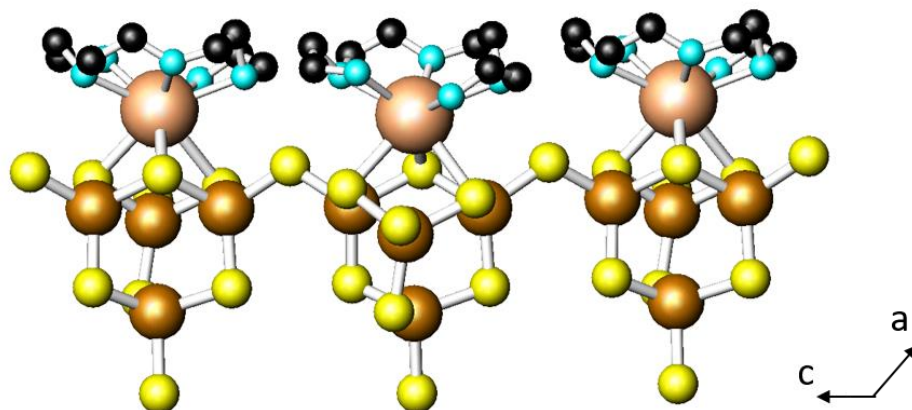
Figure 1.5: The chain $[Eu(tepa)In_4S_9]_n^{3n-}$ present in the compound $\{[Eu(tepa)]_2[\mu_2\text{-}SbS_3](\mu_2\text{-}H_2O)\}[Eu(tepa)In_4S_9]\cdot 0.25tepa$. Key: brown: In atoms, cream: Eu atoms, yellow: S atoms, light blue: N atoms, black: C atoms. Hydrogen atoms omitted for clarity.

1.4.2.2 2-D Layered Motifs

2-D indium sulfide layered motifs that are not based on supertetrahedra are relatively uncommon. One such layered compound $[(C_3H_7)_2NH_2]_3[In_6S_{11}H]$ [91] is composed of vertex and edge sharing InS_4^{5-} tetrahedra to form chains which are then linked by an edge sharing tetrahedron creating a pore space of 6.9 x 12.8 Å within the layers. With regard to supertetrahedral structures, one structure, $KInS_2$ [92], contains T2 units linked through 3 sulfur vertices to form a layered structure with K atoms in between, balancing the charge of the framework.

Aside from directly connecting supertetrahedral units through vertices, additional metal centres can be used to link supertetrahedral units. For example, $(dea\text{-}H)^+_7[In_{11}S_{21}H_2]$ (dea = diethylammonium) [93] contains T3 $[In_{10}S_{20}]^{10-}$ units linked by sharing sulfur vertices with an additional In atom located between the T3 units (Figure 1.6a). These layers pair with a second layer to form a double layer and the resulting layered system has a 6.5 Å inter-layer space between double layers (Figure 1.6b).
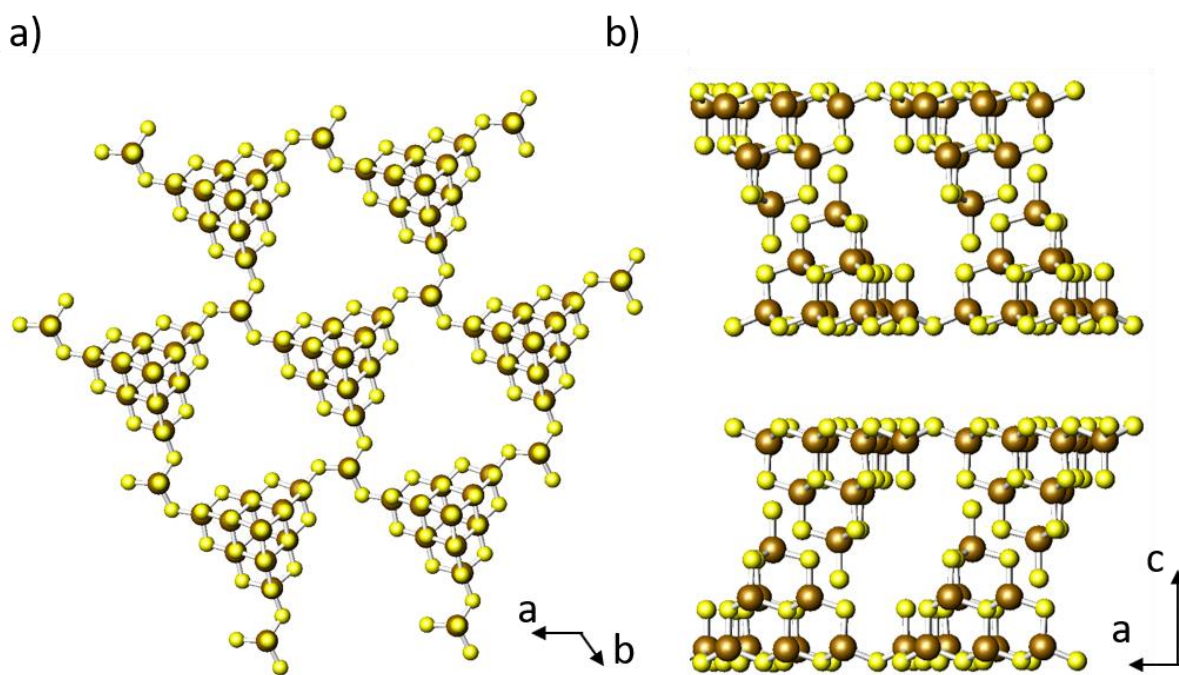
Figure 1.6: a) A single layer of $In_{11}S_{21}H_2$ and b) the double layers present within the crystal structure of $(dea-H)^+_7In_{11}S_{21}H_2$. Key: brown: In atoms, yellow: S atoms. Organic counterions omitted for clarity.

Only one known indium containing T5 2-D structure is known. This contains Cd^{2+} metal centres to compensate for the highly coordinated sulfur atoms. The compound $[In_{28}Cd_6S_{54}]\cdot[(CH_3)_4N]_{12}[(HSCH_2COOH)_2]_{3.5}$ [94] shares three sulfur vertices with other T5 units to form layers, between which the amine molecules reside.

1.4.2.3 3-D Frameworks

Supertetrahedral 3-D frameworks are more likely to form under solvothermal conditions and numerous variations of T3 open frameworks exist including $[(CH_3)_2NH_2]_6[In_{10}S_{18}]$ [95], $[In_{10}S_{18}]\cdot(hpp)_6(H_2O)_{15}$ (hpp = 1,3,4,6,7,8-hexahydro-2H-pyrimido[1,2-a]pyrimidine), $[In_{10}S_{18}]\cdot(dpm)_3(H_2O)_7$ (dpm = dipiperidinomethane) [96] and $[In_{10}S_{18}]\cdot(C_6H_{12}NH_2)_6(C_6H_{12}NH)(H_2O)_5$, $(C_6H_{12}NH$ = hexamethyleneimine) [97]. 3-D structures using T4 clusters have also been reported, for example the framework $[Cu_5In_{30}S_{54}]^{13-}$ [98] produces a zinc-blende like lattice and the T5 containing framework $[Cu_7In_{28}S_{53}]^{15-}$ [99], in which the T5 units are arranged into an array of infinite "super-supertetrahedra" by sharing a vertex point with three other T5 units, Figure 1.7.
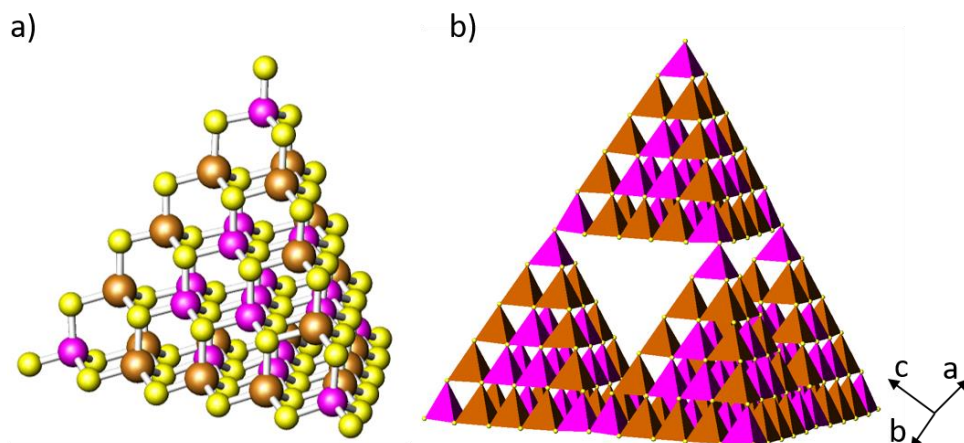
Figure 1.7: (a) The T5 $[Cu_7In_{28}S_{53}]^{15-}$ unit which forms the (b) super-supertetrahedron (polyhedral representation). Key: brown: In atoms, pink: Cu atoms, yellow: S atoms. Polyhedra Key: pink: Cu tetrahedra, brown: In tetrahedra. Organic counterions omitted for clarity.

3-D indium sulfide frameworks beyond supertetrahedral cluster configurations are also uncommon. One such compound, UCR-2InS-TMDP (TMDP = 4,4''-trimethylenedipiperidine) [100] creates a framework $[In_{33}S_{56}]^{13-}$ which consists of corner and edge sharing InS_4 tetrahedra. When the same reaction mixture is in the presence of transition-metal cations, T4 supertetrahedra $[M_4In_{16}S_{33}]^{10-}$ (M^{2+} = Mn, Co, Fe, Zn, Cd) are formed instead. This study produced a series of polymorphs and concluded that supertetrahedral units are less likely to form when using Te or Se as anion sources.

1.4.3 Germanium Sulfides

1.4.3.1 Primary Building Units and Supertetrahedral Clusters

As with indium(III), the most common germanium(IV) sulfide primary building unit is the tetrahedral unit, GeS_4^{4-}. Isolated GeS_4^{4-} units have not yet been reported, but the unit has been observed acting as a bridge between transition-metal complexes in $[Na(H_2O)_4][Cr(en)_3]_2[GeS_3OH]_2[Cr(en)_2(GeS_4)]$ [101] and $[VO(deta)]_2GeS_4$ [102]. Isolated dimeric $Ge_2S_6^{4-}$ units consisting of pairs of edge sharing GeS_4^{4-} tetrahedra have been also been observed in $(trenH_2)_2[Ge_2S_6]$ (tren = tris(2-aminoethyl)amine), $[Eu(deta)_3]_2[Ge_2S_6]Cl_2$ [103], $[Ni(deta)_2]_2(Ge_2S_6)$ (deta = diethylenetriamine) (Figure 1.8a) and

[Ni(deta)$_2$](H$_2$pipe)(Ge$_2$S$_6$) (pipe = piperazine) [104]. Ge$_2$S$_6^{4-}$ units have also been observed as bridging units in [{Ni(tepa)}$_2$(μ-Ge$_2$S$_6$)] (tepa = tetraethylenepentamine) [105] bridging two Ni(tepa) complexes (Figure 1.8b).
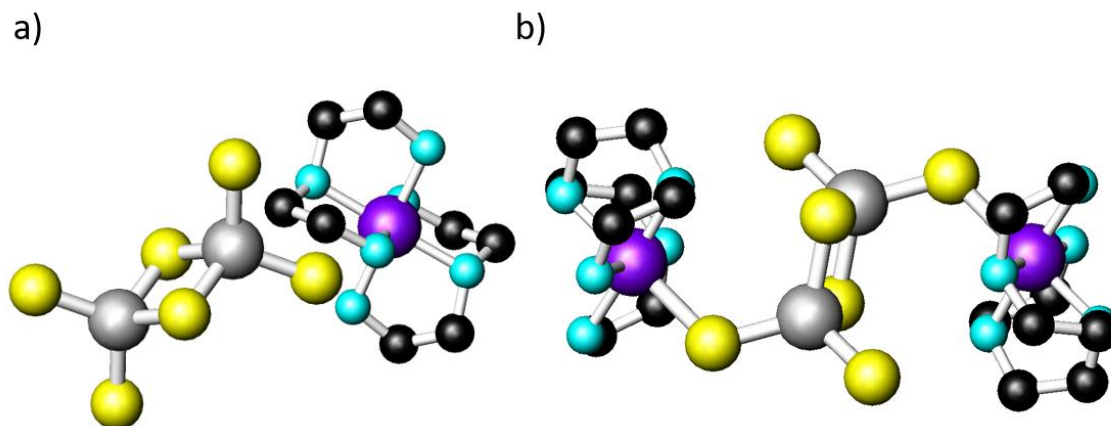
Figure 1.8: (a) A [Ni(deta)$_2$]$_2$ complex and Ge$_2$S$_6^{4-}$ unit present in [Ni(deta)$_2$]$_2$(Ge$_2$S$_6$) and (b) The bridging of complexes present in [{Ni(tepa)}$_2$(μ-Ge$_2$S$_6$)]. Key: silver: Ge atoms, dark purple: Ni atoms, yellow: S atoms, light blue: N atoms, grey: C atoms. H atoms omitted for clarity.

Unlike indium (III), however, germanium is not capable of producing supertetrahedral clusters larger than a T2 unit. This is due to the same reason that In cannot produce T4 or T5 units: germanium in a 4+ oxidation state cannot support the reduced bond contributions of sulfur at higher coordination.

Thiogermanate(IV) T2 anions [Ge$_4$S$_{10}$]$^{4-}$ are found, for example, in [M(dap)$_3$]$_4$[Ge$_4$S$_{10}$Cl$_4$] (dap = 1,2-diaminopropane) [106], [(CH$_3$)$_4$N]$_4$[Ge$_4$S$_{10}$] [107], (H$_2$bipy)$_2$Ge$_4$S$_{10}$.(bipy)·7H$_2$O (bipy = 4,4'-bipyridine) [108], [Ni(teta)$_2$]$_2$[Ge$_4$S$_{10}$] (teta = triethylenetetramine) [109] and [Ni(phen)$_3$]$_2$[Ge$_4$S$_{10}$]·xSol (Sol = 4MeOH·12H$_2$O or 24H$_2$O) [110]. A discrete T2 cluster, [H$_4$Ge$_4$S$_{10}$], in which protons balance the charge through S-H bonds to the terminal sulfur atoms, can be prepared at room temperature [111]. Alkali-metal ions have also been used as charge balancing cations, as seen in the compound Cs$_4$Ge$_4$S$_{10}$ [112].

Only one 1-D chain structure containing [Ge$_4$S$_{10}$]$^{4-}$ T2 units is known to exist: [Ge$_4$S$_9$](C$_3$H$_7$)$_2$NH$_2$(C$_3$H$_7$)NH$_2$(C$_2$H$_5$) [113]. This structure contains chains of T2 units directed along [010] with amine molecules located between chains within hydrogen bonding distance of the sulfur vertices. The only other 1-D Ge-S structure currently known that does

not contain supertetrahedra is [Mn(deta)$_2$][Ge$_2$S$_4$] [114] in which chains contain both Ge(IV) and Ge(II) centres. It is constructed from edge sharing GeS$_4^{4-}$ units which create an infinite [Ge$_2$S$_4$]$^{2-}$ anionic chain where the negative charge is balanced by the complex [Mn(deta)$_2$]$^{2+}$. The formal charge of the germanium centres was determined by bond distances and valence sums. The lower oxidation states of Ge are not normally observed in solvothermal chemistry and the only other occasion of their observation in a 1-D structure is the tellurium containing compound [(en)$_3$Mn][Ge$_5$Te$_{10}$] [115], which contains Ge(II), Ge(III) and Ge(IV) states. These oxidation states are more typically seen in structures produced in high-temperature solid-state chemistry. 2-D thiogermanates are not currently known. The presence of all three states was confirmed through bond valence calculations (3.78, 2.95, and 1.71 v.u.) and XPS analysis using binding energies and atomic ratios for each oxidation state.

Although supertetrahedral T2 selenidogermanate (IV) anions are reasonably common and have been found, for example, in Na$_4$[Ge$_4$Se$_{10}$] [116] or K$_4$[Ge$_4$Se$_{10}$] [117], only one example of a telluride analogue, (Et$_4$N)$_4$[Ge$_4$Te$_{10}$], has been reported to date [118]. Extended 3-D frameworks have also been produced by linking the thiogermanate(IV) T2 units *via* additional transition-metal centres bonding to the terminal sulfur atoms, for example, [(CH$_3$)$_4$N]$_2$MGe$_4$S$_{10}$ (M^{2+} = Fe, Cd, Mn) [119]. This same framework can also be found in the selenidogermanate compound [(CH$_3$)$_3$NH]$_2$[MnGe$_4$Se$_{10}$] [120]. Alternatively, low-temperature sol-gel approaches have also been reported to produce a 3-D framework containing T2 [Ge$_4$S$_{10}$]$^{4-}$ units, [(CH3)$_4$N]$_4$[Ge$_4$S$_{10}$] [121].

1.4.4 Antimony Sulfides

1.4.4.1 Antimony Sulfide Building Units and Discrete Clusters

Antimony-sulfide materials exhibit a wide range of structural motifs due to the varying geometries of antimony-sulfide units. Due to the lone pair of electrons on the antimony atom, it can adopt 3-fold, 4-fold and 5-fold coordination. SbS$_3^{3-}$ is a trigonal pyramid unit and is found in most antimony (III) chalcogenide-based structures. [M(en)$_3$][Sb$_2$S$_4$] (M^{2+} = Co, Ni) [122] is such an example where SbS$_3^{3-}$ trigonal pyramid units share two sulfur vertices to form infinite SbS$_2^-$ chains. SbS$_4^{5-}$ is another building unit for antimony (III) sulfides, this particular building block forming four bonds instead of three in a seesaw geometry. Both of

these antimony (III) chalcogenide building units can be seen below (Figure 1.9). Antimony (V) chalcogenide building units are less common [123]. One such unit is $Sb^{(V)}S_4^{3-}$, a tetrahedral primary building unit capable of forming Sb_2S_2 heterorings to form 1-D chains. The antimony (V) and antimony (III) cations may co-exist within the same framework, as seen in the $[Sb_4S_9]^{2-}$ repeating unit [124].

Any of these primary building units can share vertices or edges to form larger secondary units.
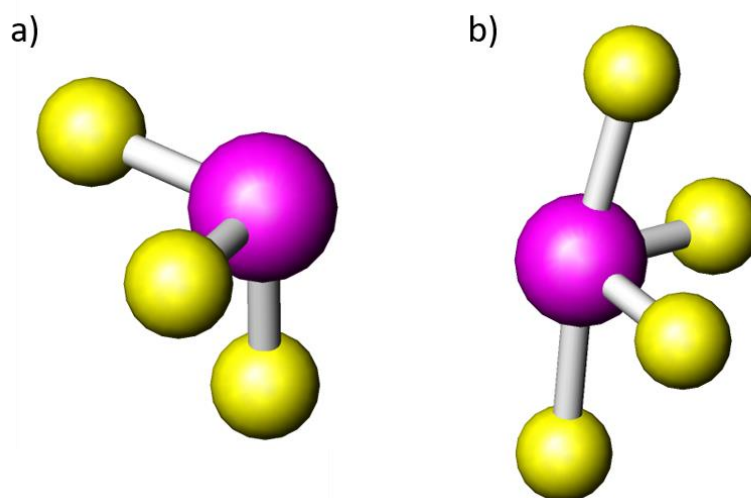
Figure 1.9: Primary building units of antimony(III) chalcogenides. a) SbS_3^{3-} and b) SbS_4^{5-} Key: Pink: Sb atoms, yellow: S atoms.

Typically, in an SbS_3^{3-} trigonal pyramid unit, the bond lengths are < 2.5 Å. These are known as the primary Sb-S bonds but longer secondary interactions can also occur up to and over 3 Å in length. The Sb-S bond lengths in SbS_4^{5-} seesaw units have two different sets of lengths: two bonds will be longer (2.6-2.8 Å) and two bonds will be shorter (< 2.5 Å). It is rare in materials chemistry for these longer bonding interactions to occur, especially since the distance can be equal to the sum of the van der Waals' radii for S and Sb (which is 3.8 Å), but it is nonetheless a distinctive feature of some structures. Each Sb-S bond contributes to the total valence of the central antimony atom which can be used to confirm the oxidation state. Equation 1.1 [125] can be used to show individual valence contributions (v_{ij}) of the bond using a valence parameter (R_{ij}) (where R_{ij} is a pre-determined bond length based on assumed oxidation states of the atoms involved [126]), with the observed bond length (d_{ij}) and where b is a constant equal to 0.37 Å.

$$v_{ij} = \exp[(R_{ij} - d_{ij})/b] \qquad \text{Equation 1.1}$$

All bond-valence contributions are then added together to produce the overall contribution, Equation 1.2.

$$\sum_v v_{ij} = V_i \qquad \text{Equation 1.2}$$

A plot of bond length against the bond-valence contributions can be used to demonstrate the ideal area for Sb-S bond lengths [15] (Figure 1.10). Bond lengths of 2.45 Å produce a bond valence contribution of 1 (v.u.) but a bond length of over 3 Å can produce a bond valence contribution below 0.2 (v.u.). This means that bonds over 3 Å are of little significance. Therefore, bond lengths under 3 Å are considered in this work.
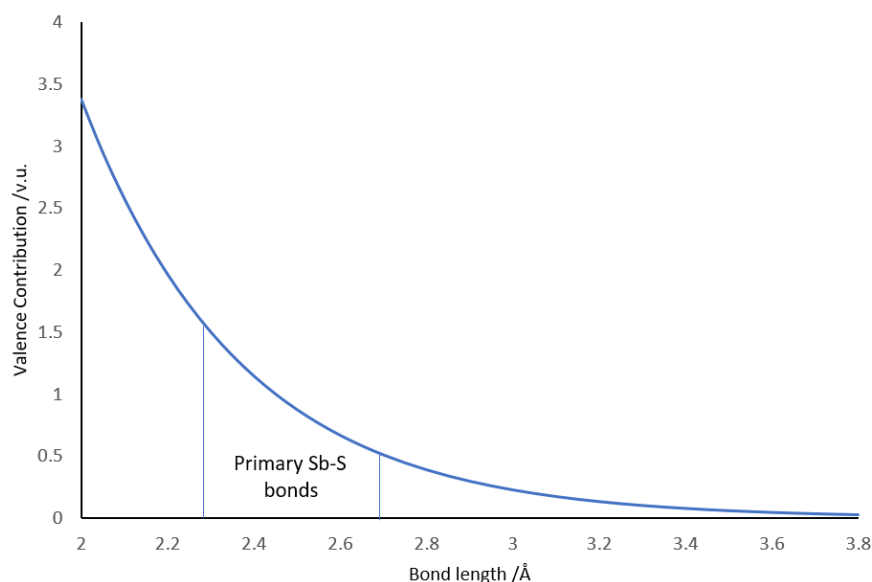
Figure 1.10: Bond-valence versus bond length within Sb-S bonds [16].

The simplest primary building unit to be isolated is SbS_4^{3-} which can exist as a discrete unit in $[Cr(en)_3][SbS_4]$ [127] (en = ethylenediamine), $[Ni(en)_3]_2[SbS_4][NO_3]$ [128] and $[Ni(deta)_2]_3[SbS_4]_2$ [129] (deta = diethylenetriamine). In each case the negative charge of the antimony sulfide unit is balanced by the transition-metal complex; here, the Sb(V) centre adopts a tetrahedral geometry typical of this oxidation state. The discrete SbS_3^{3-} unit has also been observed [127], in the compound $[Cr(en)_2]SbS_3$. Structures containing complexes bonding to sulfide units have been studied and observed both within small units (like SbS_3, see below) and frameworks, such as the discrete structures of $[Cr(teta)(SbS_3)]$ [130] (teta = triethylenetetramine), $[Mn(tren)(trenH)][SbS_4]$ (tren = tris(2-aminoehtyl)amine) and [Mn(1,2-

16

chx)$_3$]$_2$[Mn(1,2-chx)$_2$(SbS$_4$)$_2$]·6H$_2$O (1,2-chx = 1,2-diaminocyclohexane) [131] for example. These structures illustrate SbS$_3^{3-}$ or SbS$_4^{3-}$ acting as bidentate or monodentate ligands by sharing a sulfur edge or a vertex respectively (Figure 1.11). The use of different amines in these cases can affect the crystal packing, particularly the larger molecules with multiple donor atoms, like tren. For example, [Mn(tren)(trenH)][SbS$_4$] contains an unusual monodentate tren molecule leaving the other two ethylamine moieties of the tren molecule free to interact with each other *via* hydrogen bonding. While [Mn(1,2-chx)$_3$]$_2$[Mn(1,2-chx)$_2$(SbS$_4$)$_2$]·6H$_2$O (1,2-chx = 1,2-diaminocyclohexane) contains complexes of both [Mn(1,2-chx)$_3$] and [Mn(1,2-chx)$_2$(SbS$_4$)$_2$], the latter contains the SbS$_4^{3-}$ units in trans positions to each other which weakly interact with one another through hydrogen bonding. All these discrete complexes contain some amount of hydrogen bonding, providing stabilisation of the compounds.
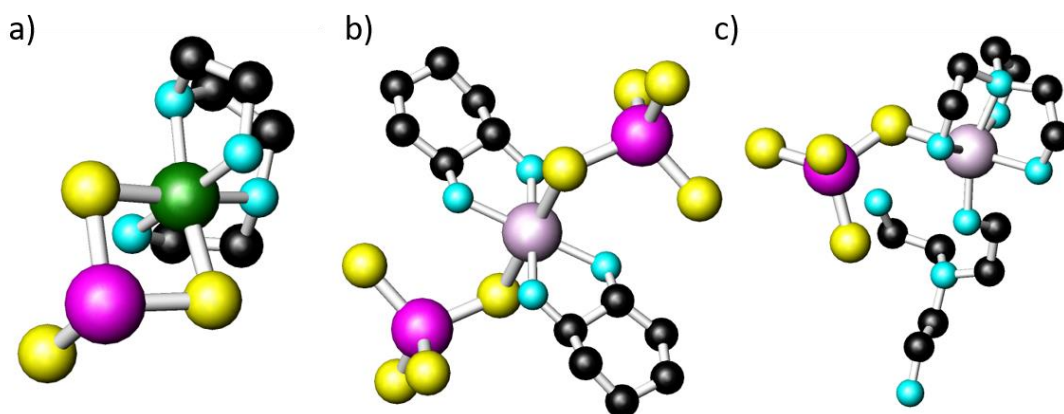
Figure 1.11: The Sb-S containing discrete units within the compounds of a) [Cr(teta)(SbS$_3$)], b) [Mn(1,2-chx)$_3$]$_2$[Mn(1,2-chx)$_2$(SbS$_4$)$_2$]·6H$_2$O and c) [Mn(tren)(trenH)][SbS$_4$] (right). Key: pink: Sb atoms, yellow: S atoms, dark green: Cr atoms, light pink: Mn atoms, light blue: N atoms, black: C atoms. Hydrogens are omitted for clarity.

Along with SbS$_3^{3-}$ and SbS$_4^{3-}$ units bonding to complexes, other small units such as dimeric [Sb$_2$S$_5$]$^{4-}$ or [Sb$_4$S$_8$]$^{4-}$ units acting as ligands have been observed within [Co(tren)]$_2$[Sb$_2$S$_5$] and [Co(tren)]$_2$[Sb$_4$S$_8$] respectively [132]. [Co(tren)]$_2$[Sb$_2$S$_5$] contains two vertex sharing SbS$_3^{3-}$ units to form a dimeric [Sb$_2$S$_5$]$^{4-}$ unit, which then bonds either end to the [Co(tren)] complex through a sulfur atom. Conversely, compound [Co(tren)]$_2$[Sb$_4$S$_8$] contains both SbS$_3^{3-}$ and SbS$_4^{5-}$ units, where two SbS$_4^{5-}$ units share a common edge and each of the two SbS$_3^{3-}$ units shares an edge with the Sb$_2$S$_6$ dimer, forming a chain-like unit consisting of three Sb$_2$S$_2$

heterorings. The remaining sulfur atom bonds to a $[Co(tren)]^{2+}$ complex completing the discrete unit.

Examples of secondary building units (common combinations of primary building units) include $[Sb_3S_6]^{3-}$ semicubes or $[Sb_4S_8]^{4-}$ heterorings (Figure 1.12a) [133, 134]. Both are constructed from SbS_3^{3-} primary units through shared vertices. The $[Sb_3S_6]^{3-}$ semicube can be in a boat (Figure 1.12b) or chair (Figure 1.12c) conformation but is most often seen in a chair conformation. Structures containing both the boat and the chair conformation are rare but has been seen in the compound $[(CH_3NH_2)_{1.03}K_{2.97}][Sb_{12}S_{20}]\cdot1.34H_2O$ [135]. The boat conformation has been isolated previously within the compound $[Ni(deta)_2]_3[Sb_3S_6]_2$ [136].
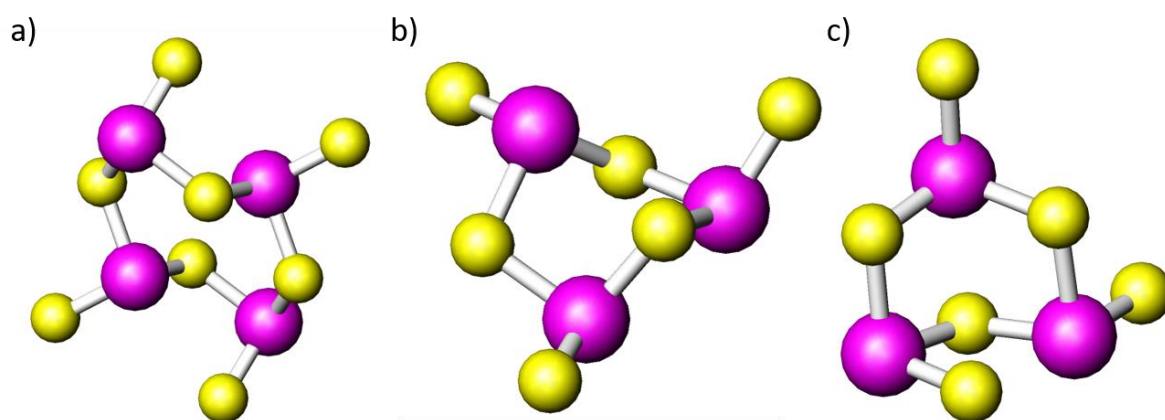
Figure 1.12: Examples of Secondary building units (a) $Sb_4S_8^{4-}$ heteroring from $[Mn(1,2-dap)_3]_2[Sb_4S_8]$ and (b) the $Sb_3S_6^{3-}$ semicube (boat) from $[Ni(deta)_2]_3[Sb_3S_6]_2$ and (c) (b) the $Sb_3S_6^{3-}$ semicube (chair) from $[(CH_3NH_2)_{1.03}K_{2.97}][Sb_{12}S_{20}]\cdot1.34H_2O$. Key: pink: Sb atoms, yellow: S atoms.

1.4.4.2 1-D Chain Motifs

There are many variations of chains that can be prepared but not all of them are straight and can contain different types of repeating units. The simplest 1-D antimony sulfide chain is likely to be $[M(en)_3][Sb_2S_4]$ (M^{2+} = Co, Ni) [122] consisting of SbS_3^{3-} trigonal pyramid units sharing two sulfur vertexes which form infinite SbS_2^- chains (Figure 1.13a). In $(CH_3NH_3)_2[Sb_2S_4]$ [137], a simple chain is constructed by two edge-sharing SbS_3^{3-} forming infinite chains of Sb_2S_2 rings. The structure of $[M(en)_3][Sb_4S_7]$ (M^{2+} = Fe, Ni) [122] is built from SbS_3^{5-} corner sharing units to form $[Sb_3S_6]^{3-}$ semicubes (chair conformation). These then link together through sharing two exocyclic sulfur atoms with SbS_3^{5-} units to form an infinite

18

chain. Another chain motif is seen in $[C_6H_{20}N_4][Sb_4S_7]$ [138], in which two $[Sb_4S_7]^{2-}$ chains are linked through an Sb_2S_2 ring, producing a double chain (Figure 1.13b).
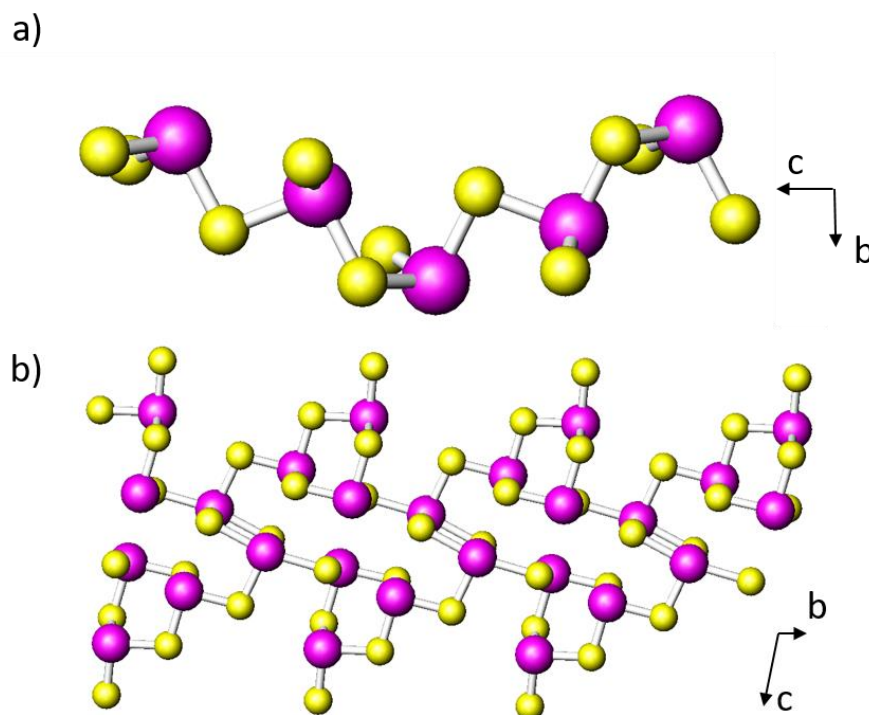
Figure 1.13: (a) The SbS_2^- chain in $[M(en)_3][Sb_2S_4]$ (M^{2+} = Co, Ni) and (b) the double chain present in $[C_6H_{20}N_4][Sb_4S_7]$. Key: pink: Sb atoms, yellow: S atoms.

In general, 1-D structures that use semicube motifs make up a substantial proportion of antimony sulfide chains [133, 136, 139, 140]. In $[Co(en)_3][Sb_4S_7]$ for example [138], $[Sb_3S_6]^{3-}$ semicubes in the chair conformation are bonded into chains *via* bridging SbS_3^{3-} units. The same motif is also found in $[pipH_2][Sb_4S_7]$ (pip = piperazine) [141]. An alternative motif is found in $(aepH_2)[Sb_6S_{10}]$ (aep = aminoethylpiperazine) [139], semicubes being linked directly to each other through a shared sulfur atom.

All of the antimony atoms in the previous examples contain antimony(III). The various geometries it can take offer a high degree of structural diversity, exemplified by $[Mn(deta)_2]_2[Sb_4S_9]$ [142], which contains three different antimony sulfide primary building units. Units $Sb^{III}S_3^{3-}$, $Sb^{III}S_4^{5-}$ and $Sb^VS_4^{3-}$ can be seen throughout the chain of the structure, built up into repeating $[Sb_4S_9]^{4-}$ units (Figure 1.14). The negative charge of the framework is balanced by two $[Mn(deta)_2]^{2+}$ complexes in which weak hydrogen bonding interactions occur between the N-H$^{...}$S atoms. The bond-valence sums are consistent with the presence of different formal oxidation states.
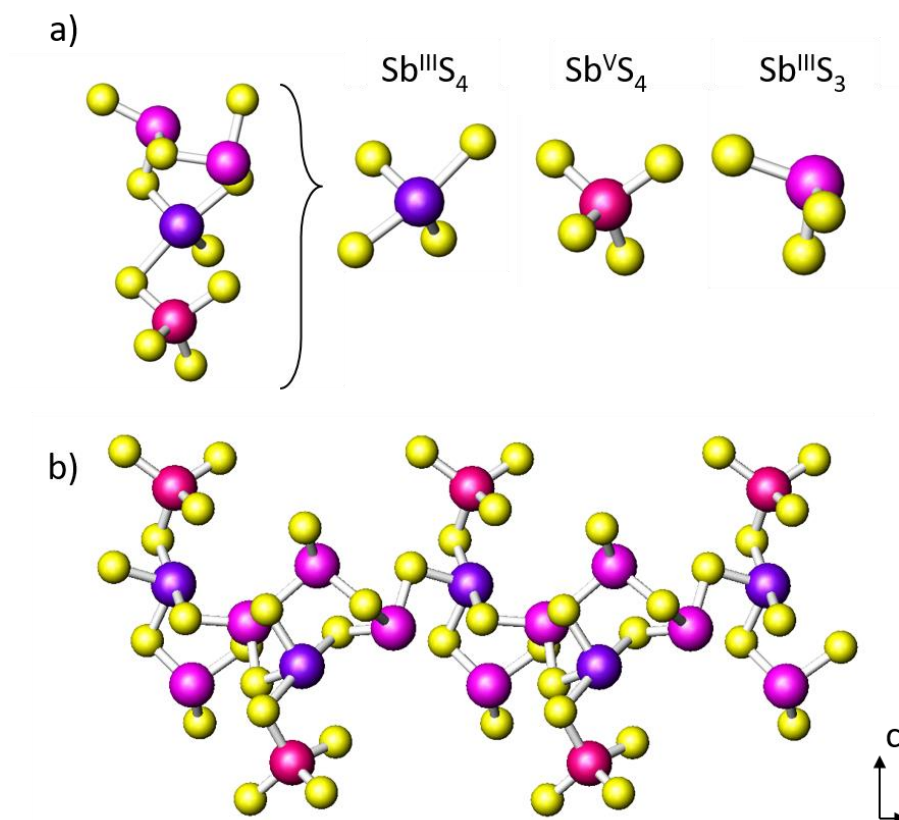
Figure 1.14: (a) Shows the three primary units present in the repeating unit of $[Sb_4S_9]^{4-}$ (b) displays the full 1-D repeating chain of $[Mn(deta)_2]_2[Sb_4S_9]$ Key: crimson, pink, purple: Sb atoms, yellow: S atoms.

Lastly, pendant transition-metal complexes can also be attached to chains as observed in $[Ni(tren)][Sb_2S_4]$ [143] (Figure 1.15). Here, the tren ligands leave the Ni complex coordinatively unsaturated, which allows the sulfur of the antimony sulfide atoms within the chain to act as ligands.
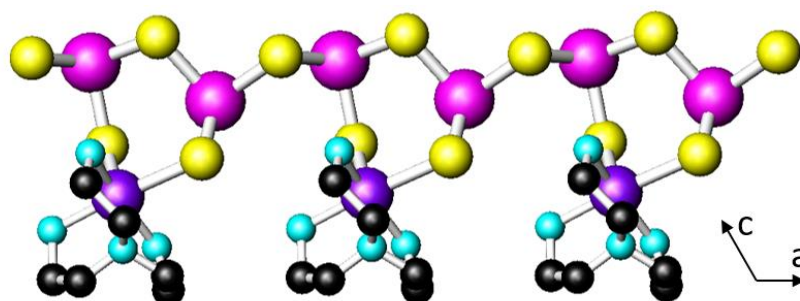
Figure 1.15: A chain present in $[Ni(tren)][Sb_2S_4]$ where a complex acts as a pendant. Key: dark purple: Ni atoms, pink: Sb atoms, yellow: S atoms, light blue: N atoms; black: C atoms. Hydrogen atoms are omitted for clarity.

1.4.4.3 2-D Layered Motifs

Single layer or double layer antimony-sulfide sheets can also be prepared. One example of a single layer can be seen in [Co(tren)][Sb_2S_4] [15] (Figure 1.16a). This structure contains cobalt complexes as pendants attached to the inorganic layer. These complexes also act as charge balancing cations against the negative charge of antimony-sulfide layer. Other single layered antimony sulfide structures include [maH_2]$_2Sb_8S_{13}$ [144] (maH = protonated methylamine), [Ni(deta)$_2$]$_3$[Sb_4S_7].H_2O [145] and [$C_8N_4S_{26}$]$_{0.5}$[Sb_7S_{11}] [146] ($C_8N_4S_{26}$ = N,N'-bis(3-aminopropyl)ethylenediamine). Of particular note is [$C_8N_4S_{26}$]$_{0.5}$[Sb_7S_{11}], which is the only structure to contain an Sb-Sb bond (2.921(2) Å) which links [Sb_7S_{11}]$^{2-}$ double chains into a single layer. Additionally, [Ni(deta)$_2$]$_3$[$Sb_{12}S_{21}$]·H_2O [145] contains the largest heterorings, $Sb_{32}S_{32}$, observed in a layered compound, which are large enough to act as channels and allow the [Ni(deta)$_2$] complexes to sit within them.

Double layered sheets usually contain a primary bond between the two layers linking the sheets. One such example of a double layer can be seen in the compound [paH]$_2$[Sb_4S_7] [147] (pa = *n*-propylamine), where single sheets (Figure 1.16b) are bonded through an Sb-S bond to produce a dual layer (Figure 1.16c). Sheets can contain heterorings and in this case $Sb_{10}S_{10}$ rings are observed within single layers. There are also pairs of protonated *n*-propylamine molecules separating the neighbouring sheets on each side. It is also seen that the distance between the protonated amine molecules and the sulfur atoms indicates the presence of hydrogen bonding (3.29 – 3.34 Å), linking the sheets in one plane. A similar double layer motif is found within the compound [eah]$_2$[Sb_4S_7] (eah = protonated ethylamine) [148].
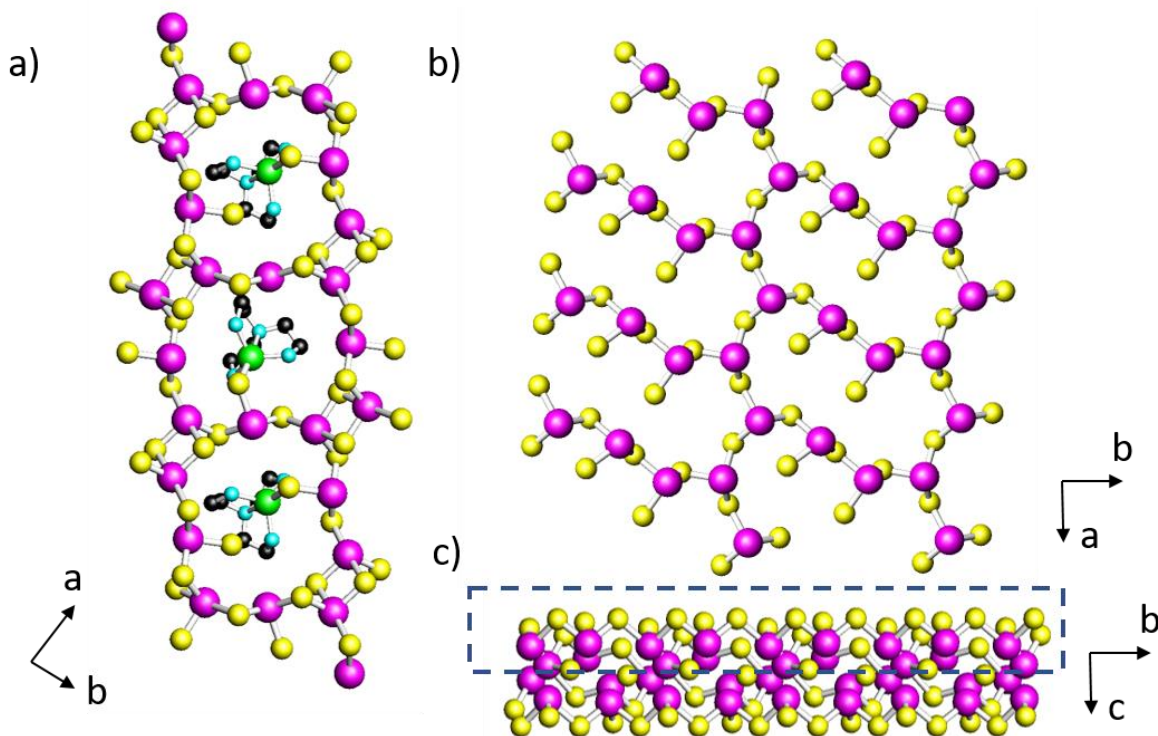
Figure 1.16: (a) A single layer of [Co(tren)][Sb_2S_4] with pendant complexes. (b) A single layer of [paH]$_2$[Sb_4S_7] which was extracted (blue box) from the double layer in (c). Key: pink: Sb atoms, yellow: S atoms, green: Co atoms, black: C atoms, light blue: N atoms. Hydrogen atoms are omitted for clarity.

1.4.4.3 3-D Frameworks

3-D antimony-sulfide structures are less common than other dimensionalities. 3-D frameworks usually include infinite pores within their structures, which is ideal for chemical sensor applications due to freedom of ion mobility [12]. [Co(en)$_3$][$Sb_{12}S_{19}$] is a rare example of a 3-D architecture [149]. The structure is built up from Sb_2S_2 rings, three of which share edges to form [Sb_6S_{12}]$^{6-}$ clusters (Figure 1.17a). These clusters are then cross linked to form ribbons and chains to generate the overall structure, Figure 1.17b. The [Co(en)$_3$]$^{2+}$ transition-metal complex within the pores act as charge balancing counter ions for the negative charge of the framework.
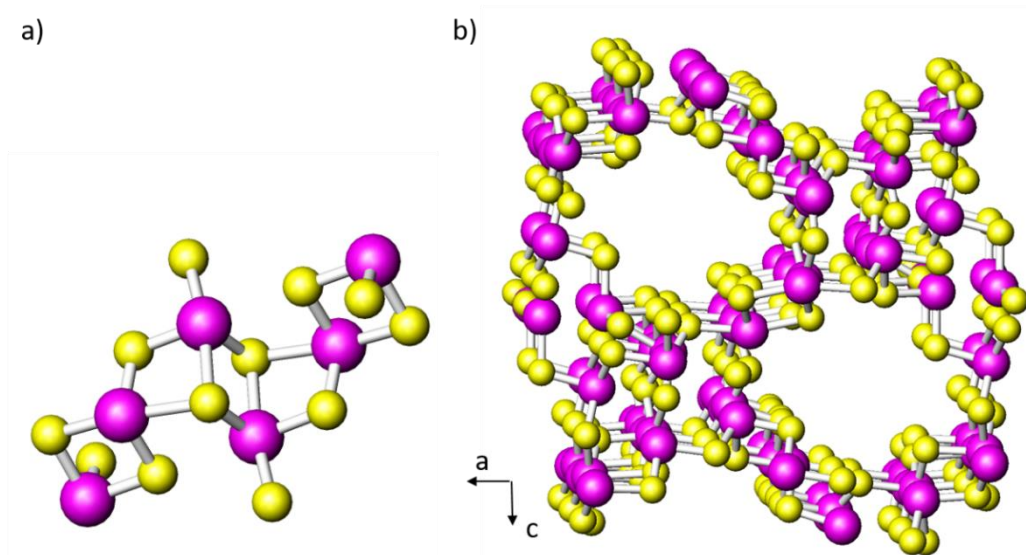
Figure 1.17: (a) $Sb_6S_{12}^{6-}$ cluster present within the structure of (b) $[Co(en)_3][Sb_{12}S_{19}]$ showing large pores. Key: pink: Sb atoms, yellow: S atoms. Complexes are omitted for clarity.

The compound $[Ni(phen)_3]_2[Sb_{18}S_{29}]$ [150] also adopts a 3-D framework, containing a porous double layer (using two ribbons of $[Sb_{10}S_{18}]_n^{6n-}$ linked by a $[Sb_2S_6]^{6-}$ dimer) and an interconnecting $[Sb_6S_{11}]^{4-}$ chain unit consisting of 2 semicubes (Figure 1.18).
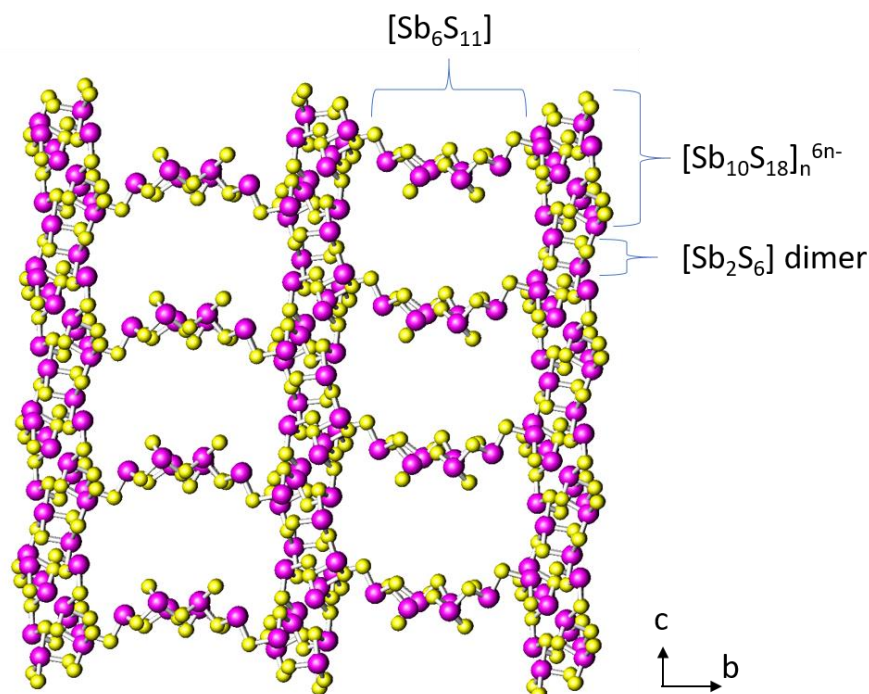
Figure 1.18: the inorganic framework of $[Ni(phen)_3]_2[Sb_{18}S_{29}]$ annotated with the various components that create the 3-D structure. Key: pink: Sb atoms, yellow: S atoms. Complexes are omitted for clarity.

A series of structures incorporating the reagent 1,4,8,11-tetraazacyclotetradecane (cyclam) has been synthesised, including $[C_{10}N_4H_{26}][Sb_4S_7]$, $[Ni(C_{10}N_4H_{24})][Sb_4S_7]$ and $[Co(C_{10}N_4H_{24})]_x[C_{10}N_4H_{26}]_{1-x}[Sb_4S_7]$ ($0.08 \leq x \leq 0.74$) [151]. All three contain the same 3-D $[Sb_4S_7]$ framework. SbS_3^{3-} and SbS_4^{5-} units share vertices to form $[Sb_4S_{10}]^{8-}$ clusters, these then forming $[Sb_4S_8]^{4-}$ chains by linking to other $[Sb_4S_{10}]^{8-}$ clusters through two common sulfur atoms. The chains are linked perpendicularly to each other to produce the 3-D framework.

1.4.5 Mixed Main-Group Metal Sulfides

Aside from binary or "pure" antimony/germanium/indium sulfide materials (with the exceptions of complex pendants), there are only a finite number of ways (albeit a substantial number) to prepare new structures using the same units each time. This can be seen with the germanium compounds in particular, where the most common structures seen are discrete T2 supertetrahedral units. By incorporating two main-group metals into a reaction, there is more potential for new structures by combining the different coordination geometry preferences of each element.

1.4.5.1 1-D Chain Motifs

Two examples of 1-D chain based compounds are $[M(deta)_2]_2[In_2Sb_4S_{11}]$ (M^{2+} = Co [152], Ni [153]) and $[Ni(en)_3][InSbS_4]$ [154], which both contain antimony and indium. The infinite $[In_2Sb_4S_{11}]_n^{4n-}$ ribbons (Figure 1.19a) and the infinite $[InSbS_4]_n^{2n-}$ chain in (Figure 1.19b) both contain a similar $[In_2SbS_8]^{7-}$ building unit. This unit is conformationally different in both chains; the position of the sulfur on the antimony atom in $[In_2Sb_4S_{11}]_n^{4n-}$ faces inward and bonds to the indium, the other faces away from the chain. The ribbon also contains an antimony sulfide backbone built from $[Sb_3S_7]^{5-}$ units. The mixed germanium-antimony sulfide $[(Me)_2NH_2][DabcoH]_2[Ge_2Sb_3S_{10}]$ (Dabco = 1,4-diazabicyclo[2.2.2]octane) contains a 1-D anionic ribbon, $[Ge_2Sb_3S_{10}]_n^{3n-}$ [155]. The ribbon found in this structure uses bridging Sb atoms and $[GeSbS_5]_n^{3n-}$ units (Figure 1.19c). The antimony and germanium atoms are in a +3 and +4 oxidation states respectively with the germanium in a tetrahedral geometry and the antimony in trigonal pyramid and seesaw geometries. The organic components present are weakly attracted to the sulfide ions of the chain, as weak van der Waals' forces are seen.

The only other Ge-Sb chain based material reported $[aepH_2][GeSb_2S_6]\cdot CH_3OH$ (aep = *N*-(2-aminoethyl)piperazine) [156] contains $[GeSb_2S_6]_n^{2n-}$ double ribbons. These are composed of two $[GeSb_3S_9]^{5-}$ ribbons which share an infinite SbS chain, acting like a backbone.
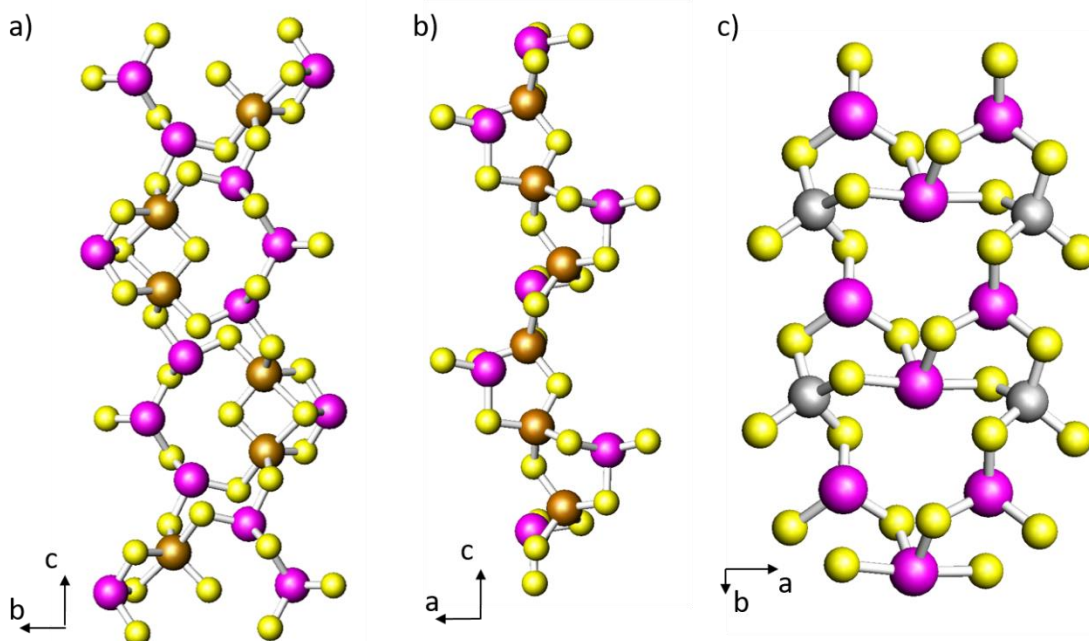
Figure 1.19: (a) The $[In_2Sb_4S_{11}]_n^{4n-}$ ribbon within $[M(deta)_2]_2[In_2Sb_4S_{11}]$, (b) $[InSbS_4]_n^{2n-}$ chain present within $[Ni(en)_3][InSbS_4]$ and (c) $[Ge_2Sb_3S_{10}]_n^{3n-}$ ribbon in $[(Me)_2NH_2][DabcoH]_2[Ge_2Sb_3S_{10}]$. Key: pink: Sb atoms, silver: Ge atoms, brown: In atoms, yellow: S atoms.

1.4.5.2 2-D Layered Motifs

The structure of $[Ni(en)_3][GeSb_2S_6]$ [155] is built up from 1-D chains of $[GeSbS_5]_n^{3n-}$ formed of GeS_4^{4-} tetrahedra sharing vertices with trigonal pyramidal SbS_3^{3-} units, the chains then interconnect with $[GeSb_2S_6]_n^{2n-}$ units to create a 2-D layered sheet. The structure $[Co(deta)_2]_2[GeSb_4S_{10}]$ [157] is composed of pseudo-semicubes, $[GeSb_2S_7]^{4-}$, formed from one tetrahedral GeS_4^{4-} and two trigonal pyramidal SbS_3^{3-} units. They resemble the shape of the $[Sb_3S_6]^{3-}$ semicube but have had a single SbS_3^{3-} unit replaced by a tetrahedral GeS_4^{4-} unit. The pseudo-semicubes $[GeSb_2S_7]^{4-}$ link together into chains and interconnect to create layers which contain large 10-membered $Sb_{10}S_{10}$ helical channels (both left and right chirality)

repeating unit within the layers (Figure 1.20a). [Mn(en)$_3$][GeSb$_2$S$_6$] contains [GeSb$_2$S$_8$]$^{6-}$ clusters which arrange into a 12-membered Ge$_4$Sb$_8$S$_{12}$ ring system in a single layer (Figure 1.20b).
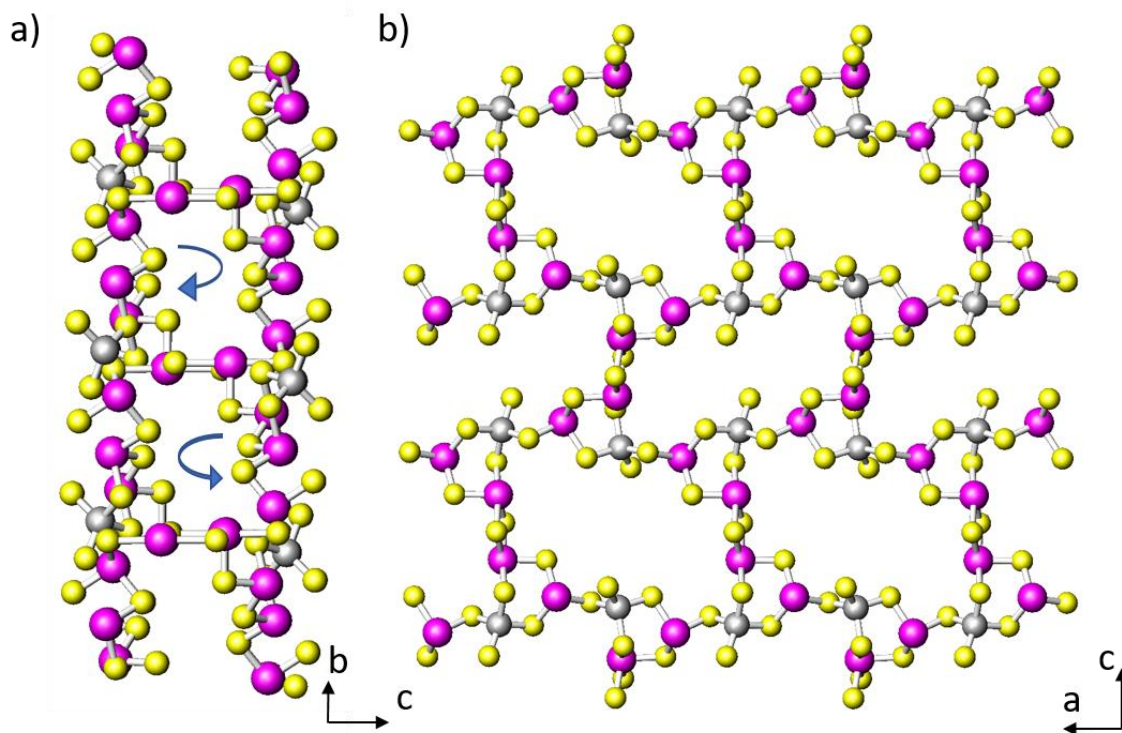
Figure 1.20: (a) A layer in [Co(deta)$_2$]$_2$[GeSb$_4$S$_{10}$] which contain 10-membered Sb$_{10}$S$_{10}$ helical channels that run parallel with [100]. (b) A single layer of [Mn(en)$_3$][GeSb$_2$S$_6$] contains repeating 12-membered Ge$_4$Sb$_8$S$_{12}$ rings. Key: silver: Ge atoms, pink: Sb atoms yellow: S atoms.

Other 2-D Ge-Sb materials include [Hdpa]$_3$[Ge$_3$Sb$_5$S$_{15}$]·0.5(C$_2$H$_5$OH) (dpa = dipropylamine) and [maH]$_{20}$[Ge$_{10}$Sb$_{28}$S$_{72}$]·7H$_2$O (ma = methylammonium) [158]. The first features a simple [Ge$_3$Sb$_5$S$_{15}$]$_n^{3n-}$ slab which contains elliptical windows within the layer. The second features a very complex structure which is built from two [Ge$_8$Sb$_{28}$S$_{72}$]$_n^{28n-}$ layers. The [Ge$_8$Sb$_{28}$S$_{72}$]$_n^{28n-}$ layer is formed from two parts; single chains of [GeSb$_3$S$_8$]$_n^{3n-}$ forming along [110] as the top section (Figure 1.21a) and the second section formed of a [GeSb$_4$S$_{11}$]$_n^{6n-}$ layer, which is built from four interconnected [Sb$_4$S$_{11}$]$_n^{10n-}$ units with GeS$_4^{4-}$ units linking together the sheet (Figure 1.21b). Both the top and bottom sections are linked through a Ge-S primary bond. Pairs of [Ge$_8$Sb$_{28}$S$_{72}$]$_n^{28n-}$ layers are then connected through a single germanium atom to produce a double layered 2-D structure (Figure 1.21c). The ion-

exchange ability of $[maH]_{20}[Ge_{10}Sb_{28}S_{72}]\cdot 7H_2O$ shows good selectivity for Cs^+ ions from solutions containing multiple cations.
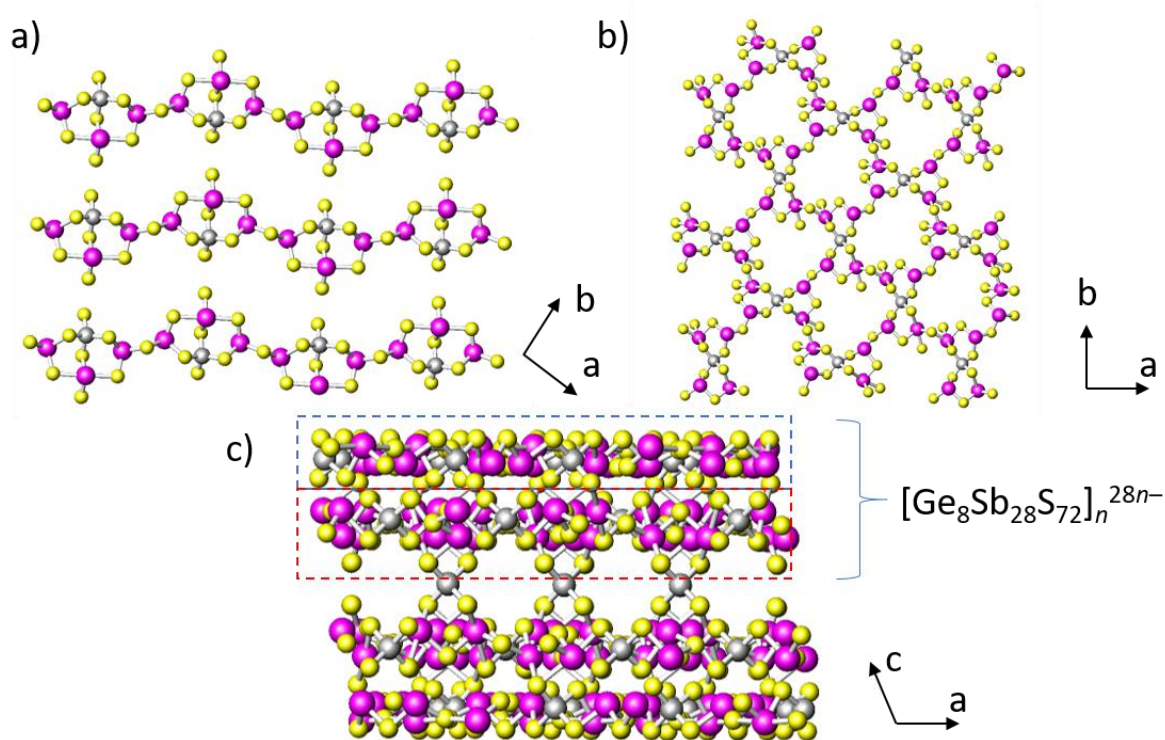
Figure 1.21: (a) The top section of the $[Ge_8Sb_{28}S_{72}]_n^{28n-}$ unit (blue box in c). (b) The bottom section of the $[Ge_8Sb_{28}S_{72}]_n^{28n-}$ unit (red box in c). (c) The inorganic double layer present in $[maH]_{20}[Ge_{10}Sb_{28}S_{72}]\cdot 7H_2O$. Key: silver: Ge atoms, pink: Sb atoms, yellow: S atoms.

A further example of a heterometallic sulfide is $[Ge(C_2N_2H_8)_3][GeSb_2S_6]$ [17] in which, interestingly, the charge balancing complexes contain Ge(II), meaning that this structure contains both Ge(IV) and Ge(II) metal centres. The layer is built up of cross linking $[GeSb_2S_8]^{6-}$ ring systems using Sb_2S_2 rings to generate the $[GeSb_2S_6]^{2-}$ layer.

A recent study [159] into indium-antimony sulfides uncovered three new layered materials, each prepared using a different amine: $[paH]_3[In_3Sb_2S_9]$ (pa = n-propylamine), $[Fe(en)_3][In_2Sb_2S_7]$ and $[Mg(deta)_2][In_2Sb_2S_7]\cdot 0.5H_2O$, Figure 1.22a, b and c respectively. The structure of $[paH]_3[In_3Sb_2S_9]$ consists of a $[In_3Sb_2S_9]_n^{3n-}$ layer built from single $[In_2Sb_2S_8]_n$ and double ribbons $[In_4Sb_2S_{12}]_n$. The other two structures contain the same layer stoichiometry $[In_2Sb_2S_7]_n^{2n-}$ but $[Mg(deta)_2][In_2Sb_2S_7]\cdot 0.5H_2O$ contains a secondary cluster of $[In_2Sb_2S_9]^{6-}$ which shares external common sulfur atoms with other $[In_2Sb_2S_9]^{6-}$ units.

[Fe(en)$_3$][In$_2$Sb$_2$S$_7$] however, does not contain such a secondary unit and simply shares sulfur vertices between [In$_2$S$_7$]$^{8-}$ groups and trigonal pyramidal SbS$_3$$^{3-}$ units to create its layer motif.

Figure 1.22: The layers found in the structures of (a) [paH]$_3$[In$_3$Sb$_2$S$_9$], (b) [Fe(en)$_3$][In$_2$Sb$_2$S$_7$], (c) [Mg(deta)$_2$][In$_2$Sb$_2$S$_7$]·0.5H$_2$O. Key: brown: In atoms, pink: Sb atoms, yellow: S atoms.

[Ni(deta)$_2$]$_3$(In$_3$Sb$_2$S$_9$)$_2$·2H$_2$O [153] contains chain-like [In$_6$S$_{18}$]$^{18-}$ units and SbS$_3$$^{3-}$ units; these are then interconnected to give the [In$_3$Sb$_2$S$_9$]$_n$$^{6-}$ layer which contains a 12-membered ring system delimited by eight InS$_4$$^{5-}$ tetrahedra and four SbS$_3$$^{3-}$ trigonal pyramids. Moreover, [dpaH]$_5$In$_5$Sb$_6$S$_{19}$·1.45H$_2$O (dpa = dipropylamine) [160] is built up from two bicyclic fragments, each composed of fused 5- and 3-membered ring systems (In$_2$Sb$_3$S$_5$ and In$_2$SbS$_3$ respectively) of corner sharing InS$_4$ and SbS$_3$ units. The two units then bond together through sharing a central In atom belonging to the 3-membered rings, forming [In$_5$Sb$_6$S$_{19}$]$^{5-}$ units (Figure 1.23a). These units then share sulfur vertices to form the layered structure, in which there are 12-membered In$_6$Sb$_6$S$_{12}$ rings throughout (Figure 1.23b).

The compound [Me$_2$NH$_2$]$_2$[In$_2$Sb$_2$S$_{7-x}$Se$_x$] (x = 0, 2.20, 4.20, 7) [161] is an interesting example of a layered indium-antimony material as it contains two chalcogenides, sulfur and selenium. The material is prepared solvothermally and, depending on the chalcogenide ratios, it exhibits a different band gap. As the Se concentration increases, the band gap reduces and expands the photocatalytic activity from the UV to the visible region, as seen with photodegradation experiments with methyl orange. The layers (in x = 7) are constructed from [In$_2$Sb$_2$Se$_{10}$] clusters which share common selenium vertices to form the [In$_2$Sb$_2$Se$_7$]$_n$$^{2n-}$ layer.
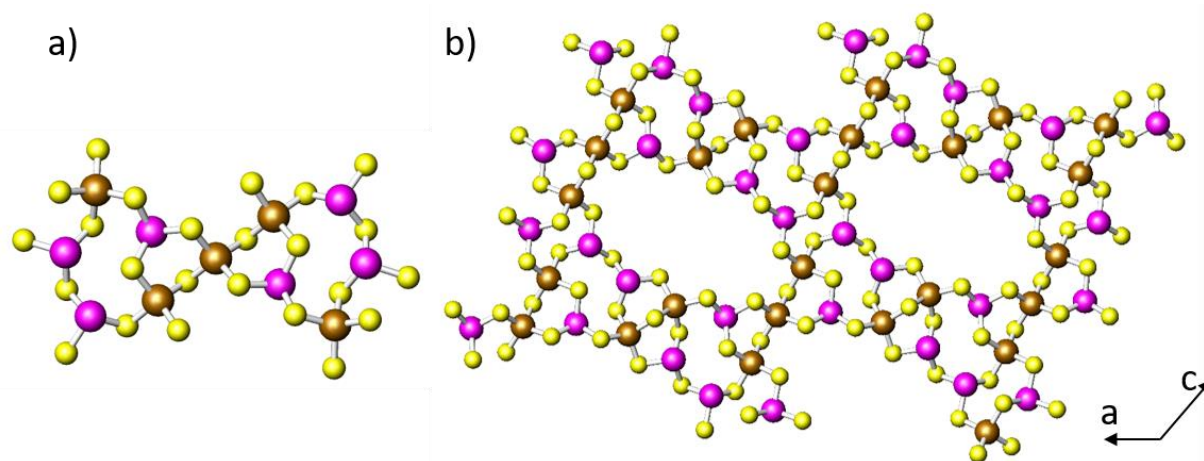
Figure 1.23: (a) The building unit $[In_5Sb_6S_{19}]^{12+}$ which forms the layer (b) in $[dpaH]_5In_5Sb_6S_{19} \cdot 1.45\ H_2O$. Key: brown: In atoms, pink: Sb, yellow: S atoms.

1.4.5.3 3-D Frameworks

As with the binary main-group sulfides, 3-D structures are less common, although a few mixed-metal Ge-Sb-S and In-Sb-S frameworks have been discovered.

$[(CH_3)_4N]_2[MGe_4S_{10}]$ (M = Fe, Cd, Mn) [119] and $[dmaH]_2[GeSb_2S_6]$ [162] provide examples of 3-D frameworks utilising either supertetrahedral-based units or combinations of InS_4 tetrahedra and SbS_3^{3-} trigonal bipyramids leading to a complicated framework. In $[(CH_3)_4N]_2[MGe_4S_{10}]$, thiogermanate(IV) T2 units are linked into 3-D frameworks *via* additional transition-metal centres bonding to each terminal sulfur atom (Figure 1.24a). By comparison, $[dmaH]_2[GeSb_2S_6]$ is formed from alternating GeS_4^{4-} and SbS_4^{5-} units producing helical chains directed along the *c*-axis, with intersecting channels along the *b*-axis built from alternating GeS_4^{4-} units and larger $[Sb_3S_{10}]^{11-}$ units (Figure 1.24b). The connecting helical chains result in a channel in which the dimethylammonium molecules reside, forming N-H…S hydrogen bonding interactions.

Two 3-D In-Sb-S frameworks have been reported, namely $[(Co(en)_3)]_3(en)[In_6Sb_6S_{21}] \cdot H_2O$ [163] and $[M(dap)_3][InSb_3S_7]$ (M = Co, Ni) [164]. The structure of $[In_6Sb_6S_{21}]$ is created from $[In_2Sb_2S_9]$ clusters and 1-D $[InSb_2S_8^{4-}]_n$ chains to form a porous framework. The pores are bounded by a 20-membered ring channels delimited by eight SbS_3^{3-} units and twelve InS_4^{5-} units, inside which the cationic complexes are located (Figure 1.25a). The framework $[InSb_3S_7]^{2-}$ was regarded as the first In-Sb-S 3-D framework, built from antiparallel 1-D $[InSb_2S_8^{4-}]_n$ chains in the (010) plane and cross linked through SbS_4^{5-} units to give the 3-D dimensionality (Figure 1.25b). The resulting porous framework contains 16-membered ring

channel delimited by twelve SbS_3^{3-} units and four InS_4^{5-} units with dimensions 7.90×16.45 Å. Again, the cationic complexes reside within the pore space and balance the negative charge of the framework.
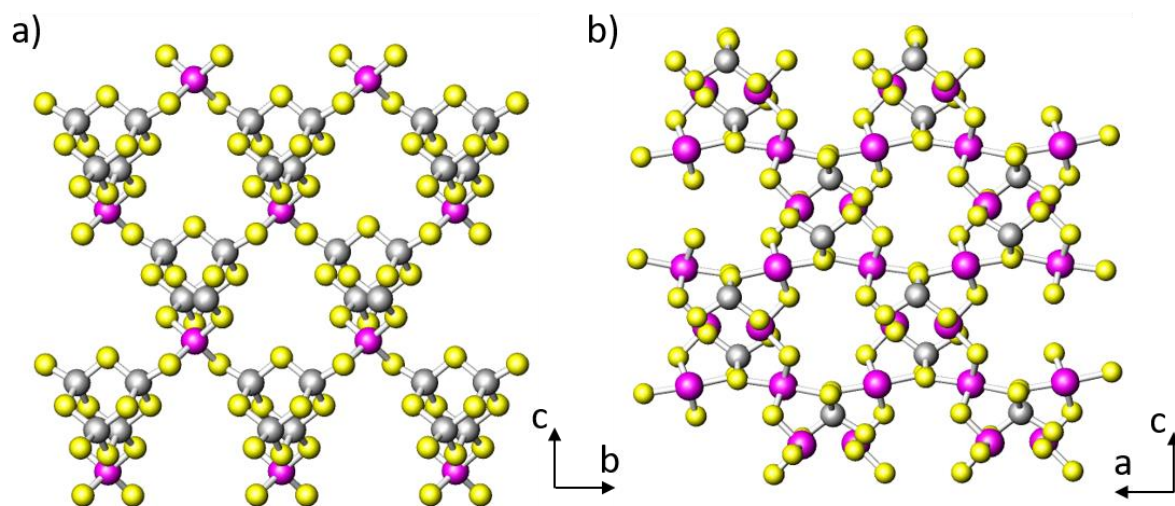
Figure 1.24: The 3-D structures of (a) $[(CH_3)_4N]_2[MGe_4S_{10}]$ (M = Fe, Cd, Mn) and (b) $[dmaH]_2[GeSb_2S_6]$. Key: silver: Ge atoms, pink: Sb atoms, yellow: S atoms.
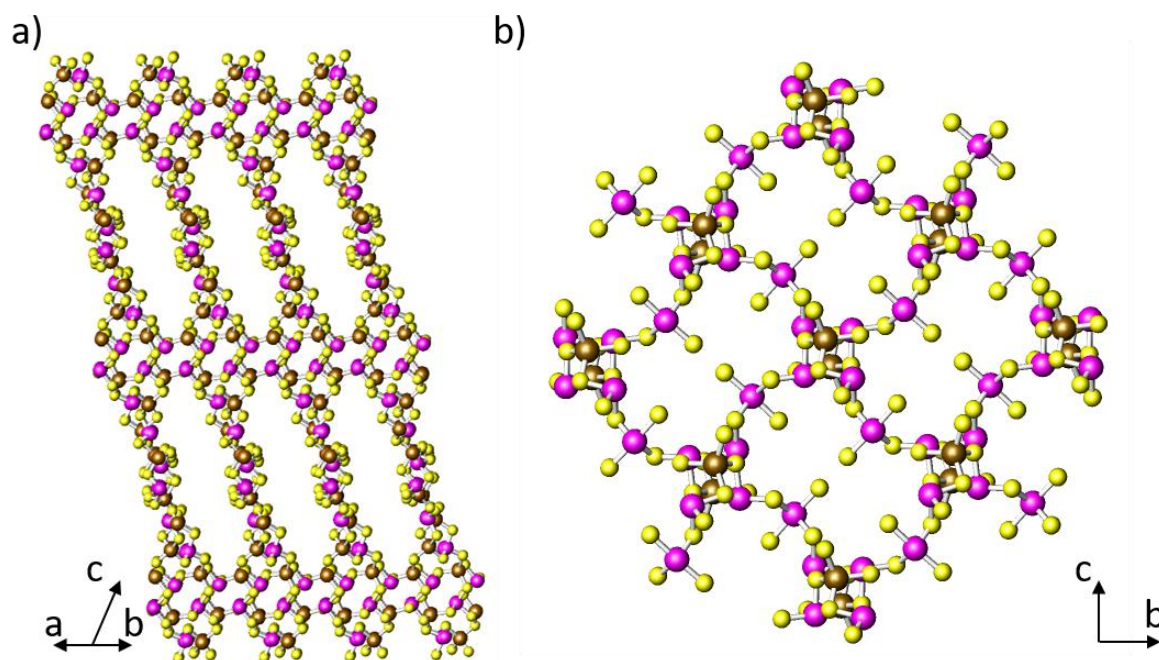
Figure 1.25: The 3-D structures of (a) $[(Co(en)_3)]_3(en)[In_6Sb_6S_{21}]\cdot H_2O$ and (b) $[M(dap)_3][InSb_3S_7]$ (M = Co, Ni). Key: brown: In atoms, pink: Sb, yellow: S atoms.

T2 [In$_4$S$_{10}$]$^{8-}$ units have also been linked together to produce a 3-D framework using the same strategy employed in the formation of [(CH$_3$)$_4$N]$_2$[MGe$_4$S$_{10}$] [119]. The inorganic structure in [NH$_3$CH$_3$]$_4$[In$_4$SbS$_9$SH] [21] is built from SbS$_3$$^{3-}$ units that share a common sulfur atom of the T2 supertetrahedral units (Figure 1.26). It is important to note that in this structure, Sb bonds to only three of the four vertices of the T2 supertetrahedron; the fourth sulfur position is protonated, aiding the charge balancing of the framework. This compound has good ion-exchange properties with high selectivity for Rb$^+$ ions. The unit-cell volume of the structure increases as the concentration of ions increases.
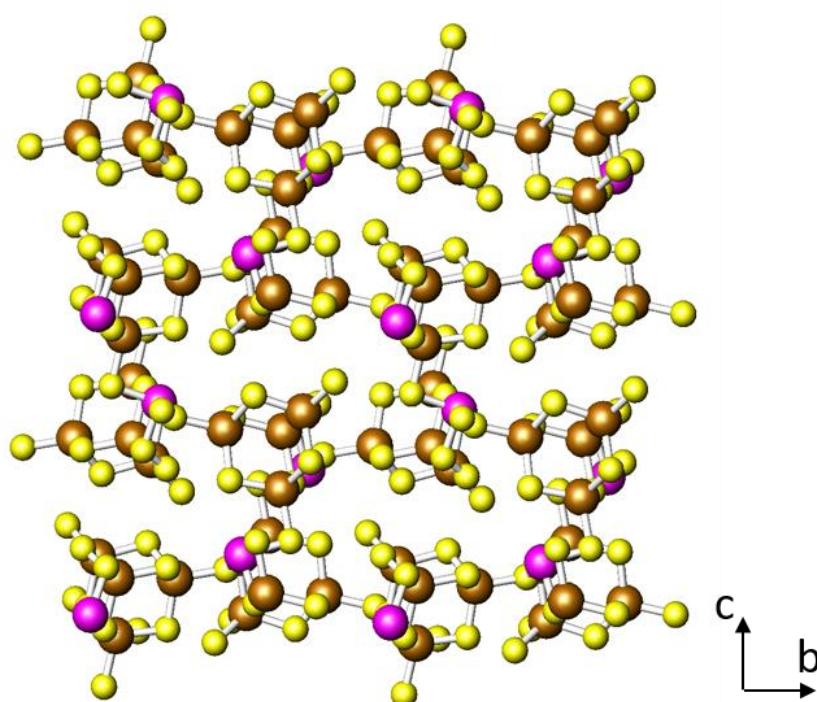
Figure 1.26: The 3-D structure of [NH$_3$CH$_3$]$_4$[In$_4$SbS$_9$SH]. Key: brown: In atoms, pink: Sb atoms, yellow: S atoms.

1.5 Solvothermal Synthesis of Transition-Metal Sulfates

1.5.1 0-D Discrete Sulfate Anions and Complexes Containing Sulfate Ions

The sulfate anion is typically found isolated in salt structures, in particular often paired with amines, for example in [H$_2$dap][SO$_4$] [165] or in protonated form in [H$_2$4,4'-bipy](HSO$_4$)$_2$ [166]. Alternatively, sulfate anions can also exist as ligands in discrete transition-metal complexes, for example in [CuSO$_4$(L)(H$_2$O)$_2$].nH$_2$O (L = acetophenone acylhydrazones)

[167], [Co(phen)(H$_2$O)$_4$](SO$_4$)·2(H$_2$O) (phen = 1,10-phenanthroline) [168] and [Ni((*L*-Rha)$_3$-tren)(SO$_4$)]·H$_2$O·3CH$_3$OH (Rha = rhamnose) [169], or as a charge balancing anion for the cationic complex [Co(N$_3$)$_2$(dpa)$_2$]$_2$SO$_4$·2H$_2$O (dpa = di-2-pyridylamine) [170]. It is also possible for compounds to contain multiple sulfate ions, to act simultaneously as both a ligand and as a free ion, e.g. in [VOSO$_4$(H$_2$O)$_4$]·SO$_4$·[deta] [171] or [(**L**Cu(H$_2$O)(μ-SO$_4$)(**L**Cu(H$_2$O)]SO$_4$ (L = bis(2-picolyl)amine) [172]. The latter dimeric structure contains a sulfate anion as a bridging ligand whilst containing a free sulfate anion to charge balance the cationic complexes. Discrete complexes that contain sulfate ligands are not known to have been produced solvothermally. Solvothermal synthesis is more likely to form structures of higher dimensionality.

1.5.2 1-D Chain Motifs

Organically templating sulfate materials to form 1-D structures has expanded since the work of *Rao et al* which reported the linarite-like materials [CdX$_2$SO$_4$]$^{2-}$ (X = Cl, Br) [30, 173] that contain infinite chains. Since then, different chains and topologies have been observed, many of which closely resemble known phosphate structures.

In the structures [Fe$_2$O(OH)(SO$_4$)](C$_5$H$_4$-NCOO) [174] and [Zn(SO$_4$)(H$_2$O)$_2$(2,2-bipy)] [175], infinite 1-D chains are observed. The iron-sulfate chain is created by distorted iron centered octahedra sharing vertices with oxygen, a hydroxyl oxygen and common sulfate anions. The chain alternates between the sulfate iron octahedra similar to the chain in [CdX$_2$SO$_4$]$^{2-}$ with amine molecules between layers of iron-sulfate chains. The infinite zinc-sulfate chain is created from alternating Zn centered octahedra and sulfate ions (Zn-O-S-O-Zn), with each Zn octahedron bonding to two monodentate sulfate ligands, a 2,2-bipy ligand and 2 water ligands (Figure 1.27a). This is analogous to the sulfate mineral chalcanthite [176]. A similar chain can also be seen in [Zn(phen)(SO$_4$)(H$_2$O)$_2$] [177] where the 2,2-bipy amines are replaced with 1,10-phenanthroline, Figure 1.27b.

A few vanadium sulfate chain based structures have been studied including [NH(CH$_2$)$_6$NH][(VO)$_2$(OH)$_2$(SO$_4$)$_2$]·H$_2$O, [H$_3$N(CH$_2$)$_2$NH$_3$][V(OH)(SO$_4$)$_2$]·H$_2$O, [H$_2$N(CH$_2$)$_4$NH$_2$][(VO)(H$_2$O)(SO$_4$)$_2$] [178] and [C$_2$H$_{10}$N$_2$]$_4$[GaV$_3$(SO$_4$)$_8$(OH)$_4$]·4H$_2$O [179]. The three chain-based structures reported by *Rao et al* [178] are presented in Figure 1.28 in the absence of amine ligands. The sulfate ions act as monodentate ligands (Figure 1.28a,b) or as bidentate ligands (Figure 1.28c). Additionally, the chain [(VO)$_2$(OH)$_2$(SO$_4$)$_2$] contains V$_2$O$_8$ dimers in place of vanadium octahedra. The structure of

[$C_2H_{10}N_2$]$_4$[$GaV_3(SO_4)_8(OH)_4$]·$4H_2O$ is analogous to the chain present in $H_3N(CH_2)_2NH_3$][$V(OH)(SO_4)_2$]·H_2O; the octahedra are either Ga or V centered in this case.
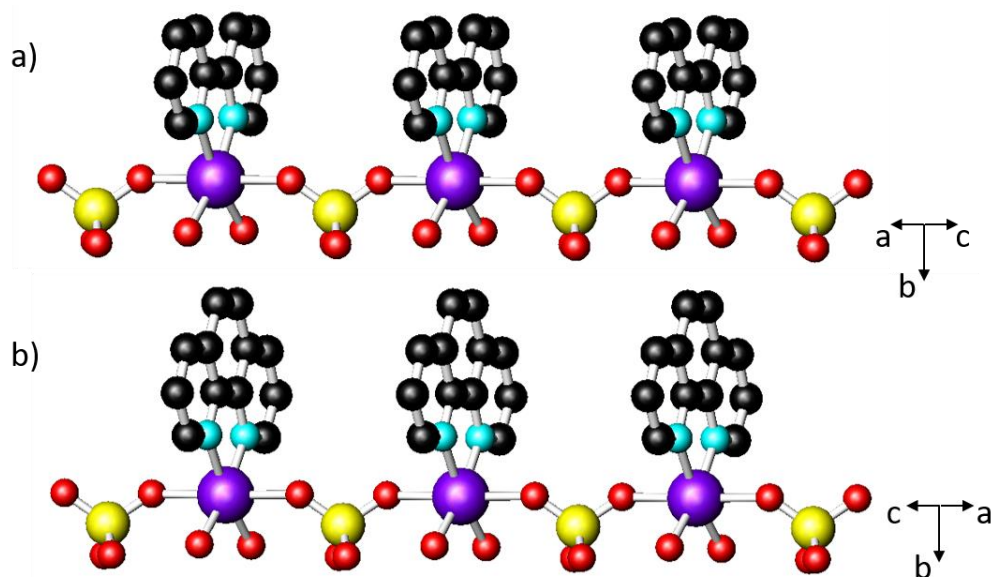
Figure 1.27: The chains present in the compounds (a) [$Zn(SO_4)(H_2O)_2(2,2\text{-bipy})$] and (b) [$Zn(phen)(SO_4)(H_2O)_2$]. Key: purple: Zn atoms, yellow: S atoms, red: O atoms, light blue: N atoms, black: C atoms. Hydrogen atoms omitted for clarity.
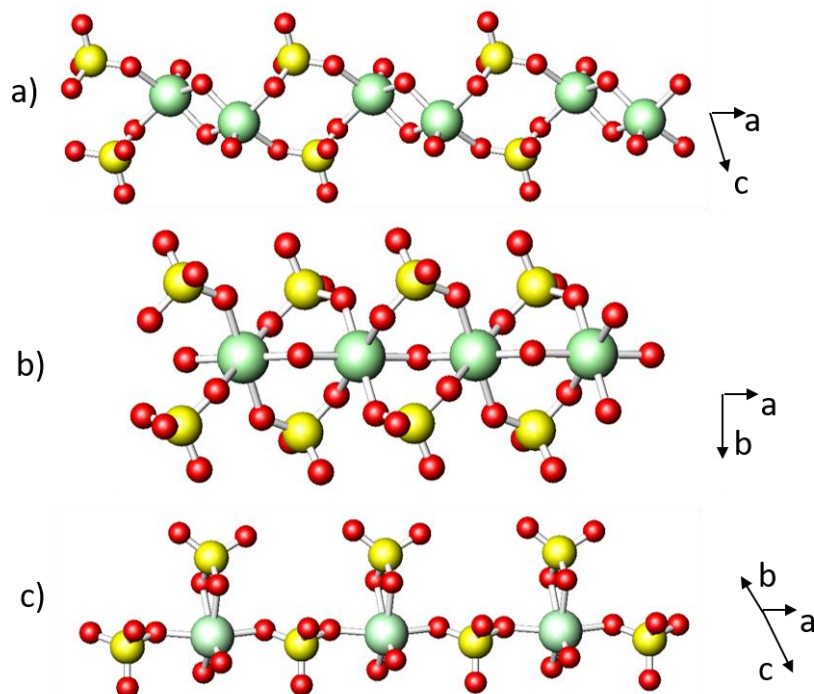
Figure 1.28: The chain-like sulfate structures found in (a) [$NH(CH_2)_6NH$][$(VO)_2(OH)_2(SO_4)_2$]·H_2O, (b) [$H_3N(CH_2)_2NH_3$][$V(OH)(SO_4)_2$]·H_2O and (c) [$H_2N(CH_2)_4NH_2$][$(VO)(H_2O)(SO_4)_2$]. Key: pale green: V atoms, yellow: S atoms, red: O atoms

Iron-sulfate chain-based structures have also been investigated [180] including; $[C_2H_{10}N_2]_{1.5}[Fe(SO_4)_3]\cdot 2H_2O$ (Figure 1.29a), $[C_2N_2H_{10}][Fe(SO_4)_2(OH)]\cdot H_2O$, $[C_6H_{18}N_2]_{0.5}[Fe(SO_4)_2(H_2O)_2]$ (Figure 1.29b) and $[C_6H_{18}N_2]_{0.5}[Fe_2(SO_4)(H_2O)_4(OH)]\cdot H_2O$ (Figure 1.29c). Each possesses a different structure resembling the ferrinarite, sideronatrite and kröhnkite minerals, respectively. Each infinite chain is built from either sharing oxygen vertices of the sulfate ions (monodentate) with iron centered octahedra only or by also including hydroxyl ions as bridges between iron octahedra (as seen in Figure 1.29c). Another series of 1-D iron sulfate materials [181] are the compounds $[H_3N(CH_2)_2NH_3][FeF_3(SO_4)]$, $[C(NH_2)_3]_2[FeF(SO_4)_2]$ and $[NH_2(CH_2)_4NH_2][FeF_3SO_4]$. Each of the chain-based structures incorporates fluorine into the infinite chain; $[FeF_3SO_4]^{2-}$ for example, is built from FeF_4O_2 octahedra by sharing vertices with F atoms and bridging SO_4^{2-} ions. The compound $[C(NH_2)_3]_2[FeF(SO_4)_2]$ exhibits antiferromagnetic interactions.
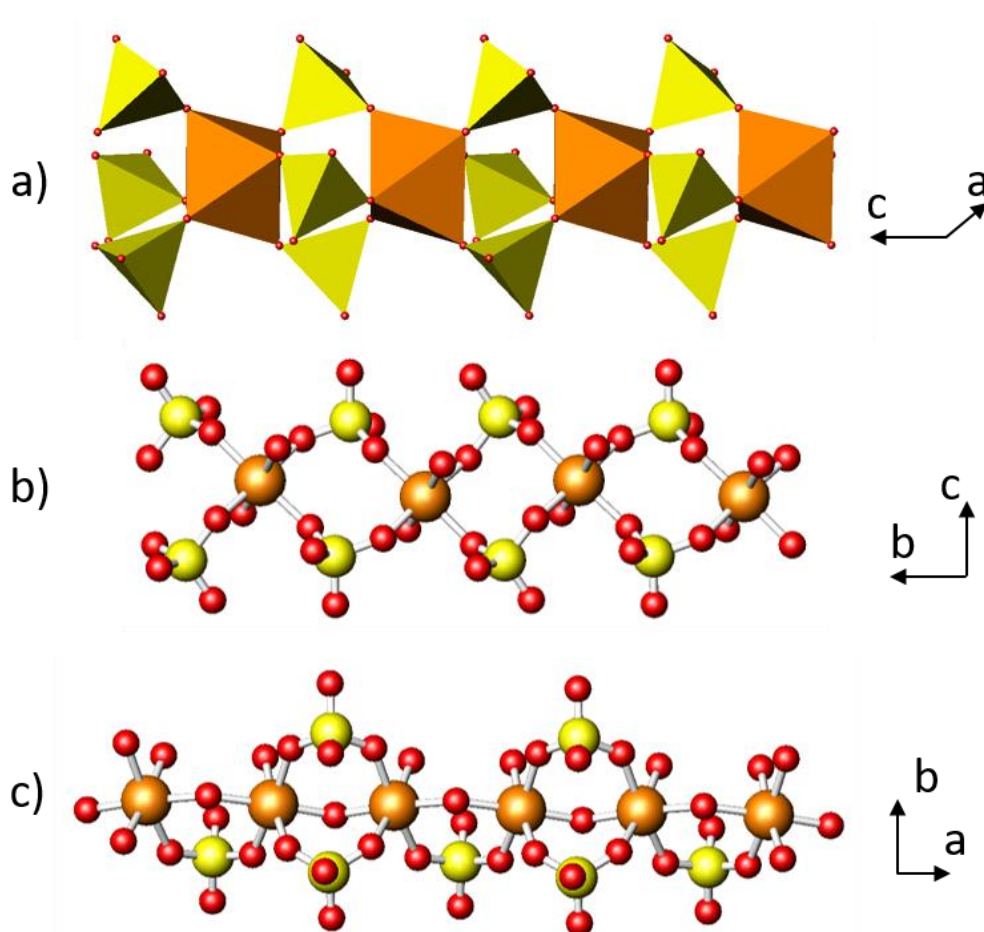
Figure 1.29: The sulfate structures of (a) $[C_2H_{10}N_2]_{1.5}[Fe(SO_4)_3]\cdot 2H_2O$, (b) $[C_6H_{18}N_2]_{0.5}[Fe(SO_4)_2(H_2O)_2]$ and (c) $[C_6H_{18}N_2]_{0.5}[Fe_2(SO_4)(H_2O)_4(OH)]\cdot H_2O$. Key: orange: Fe atoms, yellow: S atoms, red: O atoms. A polyhedral representation used in (a) for clarity, orange: Fe octahedra, yellow: SO_4 tetrahedra.

The sulfate chain-based structure [Fe(H$_2$bpdc)]SO$_4$ (H$_2$bpdc = 2,2'-bipyridyl-5,5'-dicarboxylic acid) [182] is built from a double chain structural motif. The chains contain five-coordinate Fe in a square pyramidal geometry that shares three vertices with three sulfate ions and two with a bidentate H$_2$bpdc ligand. This material exhibits antiferromagnetic interactions and has been found to be thermally stable up to 420 °C. [C$_2$NH$_8$]$_3$[Fe$_3$(μ$_3$-O)$_2$(SO$_4$)$_4$] [183] also exhibits antiferromagnetic interactions. The chain (directed along [010]) is assembled from four FeO$_6$ octahedra and two sulfate ions by sharing their vertices, producing six small ring systems. The other two sulfate tetrahedra then protrude away from the chains. Each iron atom is therefore connected to four equivalent sulfur atoms by four Fe-O-S linkages and two are bridged with an oxygen atom.

Chain-based manganese sulfates do not seem to be as common as iron sulfates but a few have been reported. [Mn(idp)(SO$_4$)(H$_2$O)$_2$] and [Mn(idp)(SO$_4$)(H2O)]·H$_2$O (idp = imidazo-[4,5-f]-1,10-phenanthroline) [184] are 1-D sulfate structures that contain large amine ligands that display π stacking between chains due to phenanthroline rings. Of these, [Mn(idp)(SO$_4$)(H$_2$O)$_2$] (Figure 1.30) consists of Mn centered octahedra sharing common vertices with two monodentate sulfate ions, two water molecules and two shared with the bidentate idp ligand. Additionally, [C$_4$N$_2$H$_{12}$][Mn(SO$_4$)$_2$(H$_2$O)] [185] is constructed from 4-membered rings consisting of two Mn centered octahedra, two water ligands and two sulfate tetrahedra, forming a ladder styled motif.
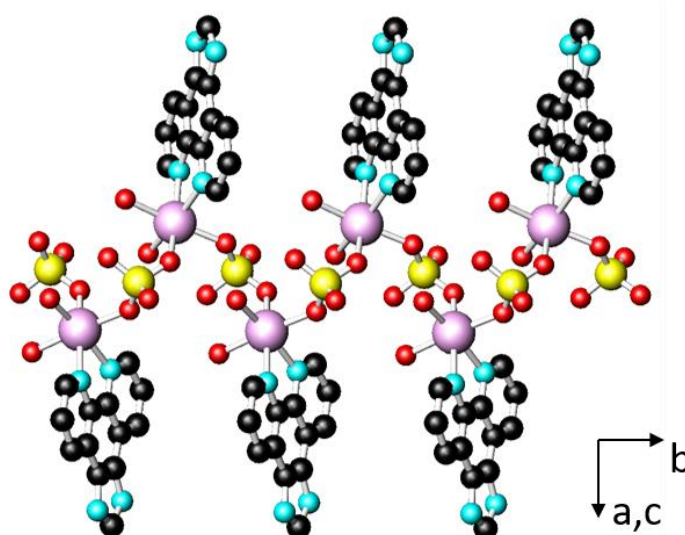
Figure 1.30: A single chain in the compound [Mn(idp)(SO$_4$)(H$_2$O)$_2$] Key: light pick: Mn atoms, yellow: S atoms, red: O atoms, light blue: N atoms, black: C atoms. Hydrogen atoms are omitted for clarity.

1-D cobalt sulfate structures have also been reported, such as $[Co(mbbz)(SO_4)] \cdot CH_3OH$ (mbbz = 1,1′-methylenebis-[1H-benzimidazole]) [186], $Co(SO_4)(H_2O)_3(4,4'$-bipy$) \cdot 2H_2O$ (4,4'-bipy = 4,4'-bipyridine) [187] and $[\{Co(\mu$-$SO_4)\mathbf{L}_3\}_n]$ ($\mathbf{L}$ = 3$\{5\}$-$tert$-butylpyrazole) [188]. $Co(SO_4)(H_2O)_3(4,4'$-bipy$) \cdot 2H_2O$ is created from linear Co-bipy-Co chains with one monodentate sulfate ion and three water ligands per Co octahedron (Figure 1.31a) and $[Co(\mu$-$SO_4)\mathbf{L}_3]_n$ consists of Co trigonal bipyramidal units linked through monodentate sulfate ions to produce the chain, with the remaining ligands being amine molecules (Figure 1.31b). A copper containing sulfate chain also uses bipy to create a chain, *via* Cu-bipy-Cu within the compound $Cu_2(4,4'$-bipy$)_2SO_4 \cdot 6(H_2O)$ [189]. It connects two sets of chains through the use of a sulfate ion, thereby creating a 1-D double chain.
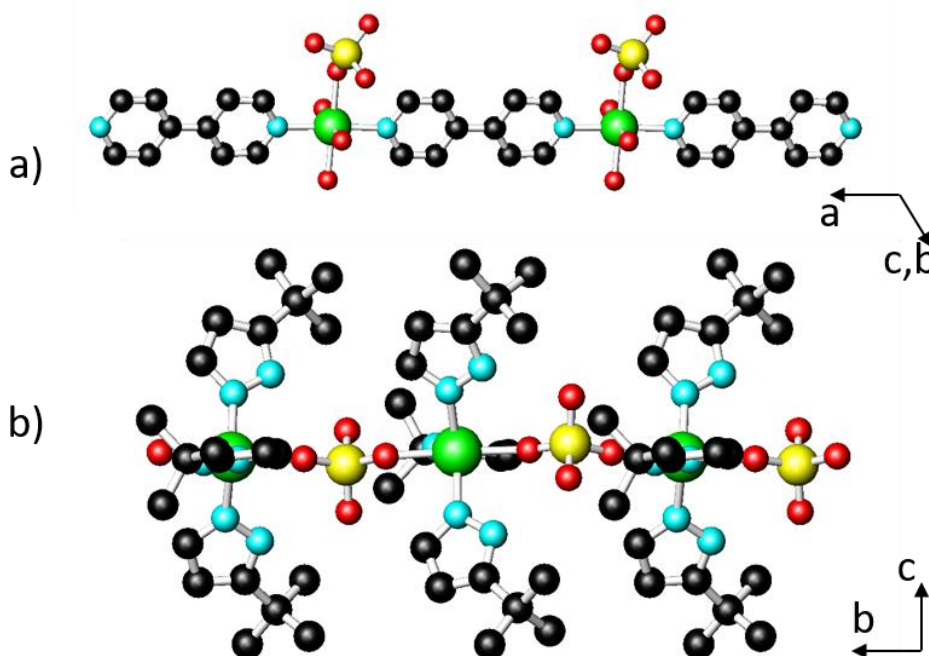
Figure 1.31: The sulfate structures found in (a) $Co(SO_4)(H_2O)_3(4,4'$-bipy$) \cdot 2H_2O$, and (b) $[\{Co(\mu$-$SO_4)\mathbf{L}_3\}_n]$. Key: green: Co atoms, yellow: S atoms, red: O atoms, light blue: N atoms, black: C atoms. Hydrogen atoms are omitted for clarity.

1.5.3 2-D Layer Motifs

A few 2-D layered iron sulfates have been produced using solvothermal techniques. $[H_3N(CH_2)_2NH_3][Fe_2F_2(SO_4)_2(H_2O)_2]$ [181] contains two sets of infinite chains built from corner sharing FeF_2O_4 and $FeF_2O_2(H_2O)_2$ octahedra, which are linked through sulfate to generate a layered structure in which there are pores, similar to the fluorophosphate ULM-10 [190]. Magnetic susceptibility measurements reveal a complex behaviour which suggests the

presence of metamagnetism within the structure. The diprotonated ethylenediamine cations reside between the layers of the structure. Other examples include $[H_3N(CH_2)_6NH_3]$ $[Fe^{II}_{1.5}F_3(SO_4)] \cdot 0.5H_2O$ [32] and $H_3N(CH_2)_2NH_2(CH_2)_2(NH_3)_4[Fe^{II}_9F_{18}(SO_4)_6] \cdot 9H_2O$ [191], both of which contain fluorine atoms and were synthesised with hexamethylenediamine and diethylenetriamine, respectively. Both exhibit a kagome lattice, a structural type that is known for interesting magnetic interactions when transition metals with unpaired electrons in the ground state [192] are present. The compound $[H_3N(CH_2)_6NH_3]$ $[Fe^{II}_{1.5}F_3(SO_4)] \cdot 0.5H_2O$ (Figure 1.32a) for example exhibits ferrimagnetic behaviour at 19 K, undergoing a change in magnetic structure below 15 K due to strong antiferromagnetic contributions. The slightly distorted lattice of $H_3N(CH_2)_2NH_2(CH_2)_2(NH_3)_4[Fe^{II}_9F_{18}(SO_4)_6] \cdot 9H_2O$ (Figure 1.32b) exhibits canted antiferromagnetism at low temperature.
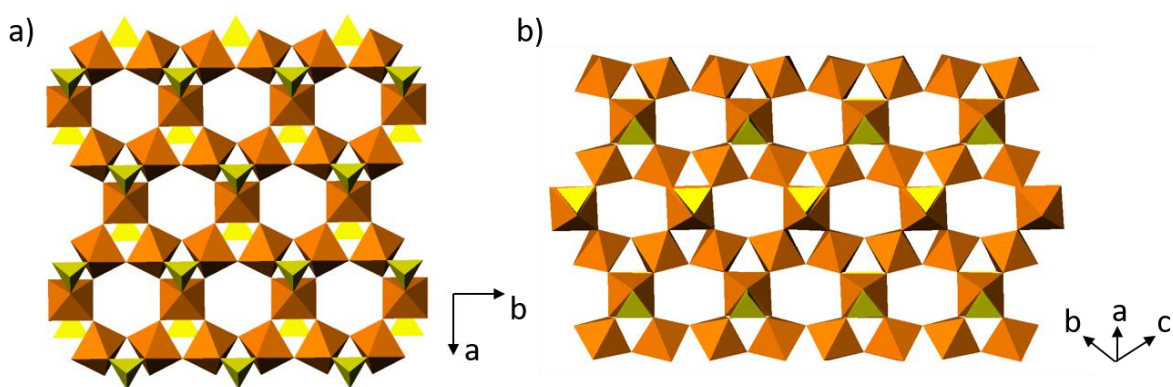
Figure 1.32: Polyhedral representations of (a) the kagome lattice present in $[H_3N(CH_2)_6NH_3]$ $[Fe^{II}_{1.5}F_3(SO_4)] \cdot 0.5H_2O$ and (b) the distorted kagome lattice present in $H_3N(CH_2)_2NH_2(CH_2)_2(NH_3)_4[Fe^{II}_9F_{18}(SO_4)_6] \cdot 9H_2O$. Key: orange: iron octahedra, yellow: SO_4 tetrahedra.

While not adopting a kagome lattice, the mixed valency of the compound $[NH_2(CH_2)_4NH_2][Fe_2^{III}Fe_3^{II}F_{12}(SO_4)_2(H_2O)_2]$ [193] is reported to contain a ferromagnetic transition and a further transition to a canted antiferromagnetic state at lower temperatures. The structure of $[Fe_2^{III}Fe_3^{II}F_{12}(SO_4)_2(H_2O)_2]$ consists of iron centered octahedra sharing vertices to form chains followed by a trimer of edge sharing octahedra to form the 1-D layer. The mixed valence compound $(C_2H_{10}N_2)_2[Fe^{III}_2Fe^{II}(SO_4)_6(H_2O)_4] \cdot 2H_2O$ [194] (Figure 1.33) can also be prepared with Cd(II) and Ni(II) replacing the Fe(II) cation. The divalent cation acts as a linker between $Fe_2(SO_4)_3$ chains, forming the 2-D layers. The magnetic data of the mixed valency iron analogue revealed the presence of ferromagnetism at low temperature.
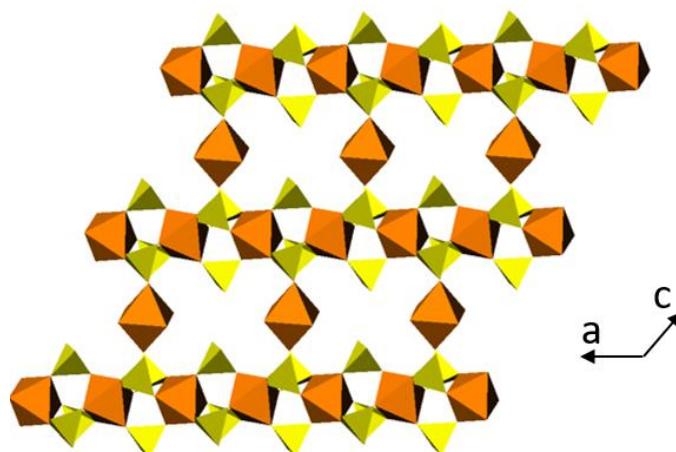
Figure 1.33: Polyhedral representations of $(C_2H_{10}N_2)_2[Fe^{III}_2Fe^{II}(SO_4)_6(H_2O)_4] \cdot 2H_2O$. Key: orange: iron octahedra, yellow: SO_4 tetrahedra.

Other transition-metal sulfates have also been shown to generate structures with layered sheets, for example, $[Mn(H_2O)_2(bpe)(SO_4)] \cdot H_2O$ (bpe = *trans*-1,2-bis(4-pyridyl)ethene) [195], $[C_4N_2H_{12}][Ni_3F_2(SO_4)_3(H_2O)_2]$ [196] and $(C_2NO_2H_5)MnSO_4$ [197]. The organically templated $[Mn(H_2O)_2(bpe)(SO_4)] \cdot H_2O$ is produced by cross linking Mn-sulfate-Mn chains using bpe molecules. The Mn centered octahedra are bound to two monodentate sulfate ions and two water molecules, with the remaining coordination sites occupied by amine linkers (Figure 1.34a). The structure of $[C_4N_2H_{12}][Ni_3F_2(SO_4)_3(H_2O)_2]$ consists of NiF_2O_4 octahedra and SO_4 tetrahedra. The NiF_2O_4 octahedra dimerise through sharing an edge with two fluorine atoms and an additional NiF_2O_4 octahedron links to this dimer at one end of the shared edges to form a trimer $Ni_3F_3O_{12}$. Lastly, the $Ni_3F_3O_{12}$ trimeric units share oxygen vertices of sulfate ions to produce a repeating hexameric unit forming a chain in a sinusoidal motif (Figure 1.34b). The structure is similar to that of sulfoborite [198].

Both cobalt and copper layered sulfates have been reported in $Co_3(SO_4)_3(OH)_2[enH_2]$ [199], $(NH_4)_3[Cu_2(OH)(SO_4)_3]$ and $(NH_4)_{1.5}[Cu_{1.25}(SO_4)_2]$ [200]. The cobalt sulfate contains a kagome-like lattice, consisting of corner sharing CoO_6 octahedra linked to form large triangular $[Co_9O_{36}]^{54-}$ units that link to six neighbouring triangles through bridging OH^- ions. Sulfate ions then bond at vertices above and below each hydroxyl group to form a $[Co_3(SO_4)_3(OH)_2]^{2-}$ layer (Figure 1.35). Magnetic data suggest that there is antiferromagnetic order below 7 K. The compounds $(NH_4)_3[Cu_2(OH)(SO_4)_3]$ and $(NH_4)_{1.5}[Cu_{1.25}(SO_4)_2]$ are good example of the differences in structure when using different geometries of the transition-metal cation. $[Cu_2(OH)(SO_4)_3]$ is constructed from square-pyramid CuO_5 units and two sulfate ions per Cu metal centre. Two sulfate ions bond to two separate CuO_5 units while

the third bonds to three separate units. The remaining coordination sites per Cu atom are OH⁻ bridging ligands which form $[Cu_4(OH)_2(SO_4)_2]^{2+}$ and are then interconnected by a sulfate ion to produce the layer. The structure in $(NH_4)_{1.5}[Cu_{1.25}(SO_4)_2]$ contains CuO_5 square-pyramids and CuO_4 tetrahedra sharing vertices to form $[Cu_3O_{12}]^{18-}$ units. These units connect with a pair of sulfate tetrahedra to produce chains directed along [110]. These chains then link into a sheet using sulfate ions adjacent to CuO_5 and CuO_4 units parallel with [010].
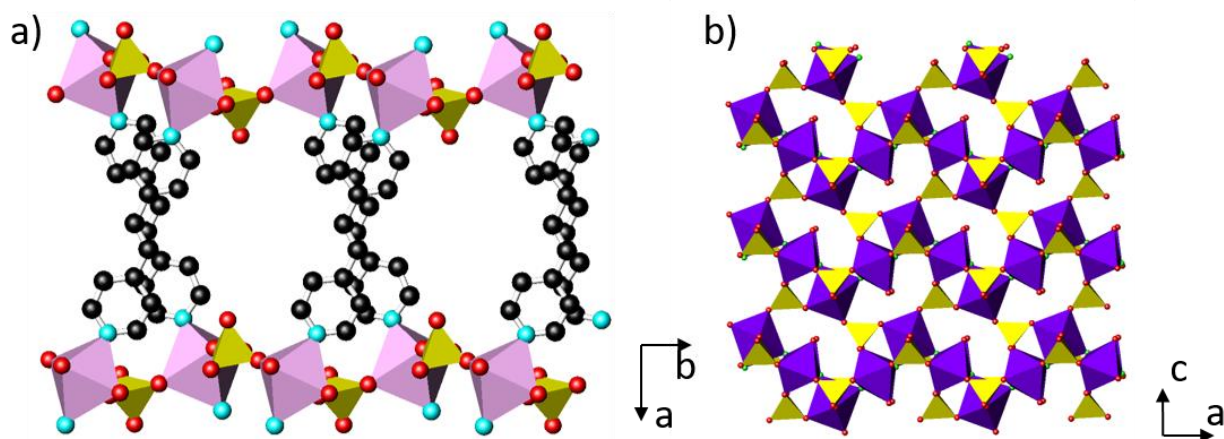
Figure 1.34: Layers within the structures (a) $[Mn(H_2O)_2(bpe)(SO_4)]\cdot H_2O$ (b) $[C_4N_2H_{12}][Ni_3F_2(SO_4)_3(H_2O)_2]$. Polyhedra Key: light pink: Mn octahedra, purple: Ni octahedra, yellow: SO_4 tetrahedra. Atom Key: red: O atoms, green: F atoms, light blue: N atoms, black: C atoms. Hydrogen atoms are omitted for clarity.
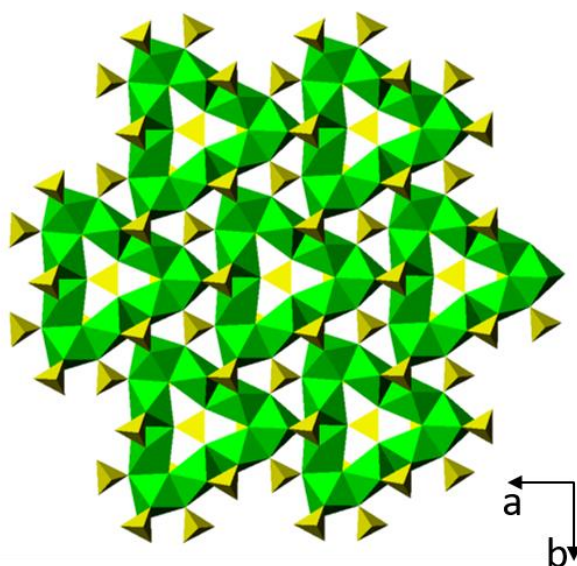
Figure 1.35: Polyhedral representation of the layer motif in $Co_3(SO_4)_3(OH)_2[enH_2]$. Key: green: cobalt octahedra, yellow: SO_4 tetrahedra.

1.5.4 3-D Frameworks

The formation of 3-D sulfate frameworks is more common for transition metals than for the main-group sulfides and many structures have been prepared and investigated. Co(en)SO$_4$ [201] contains sheets of alternating CoO$_4$N$_2$ octahedra and sulfate tetrahedra, with ethylenediamine connecting the sheets together (Figure 1.36). The structure [Co(H$_2$-bbim)(SO$_4$)(dmso)$_{0.5}$] (H$_2$-bbim = benzobisimidazole; dmso = dimethyl sulfoxide) [202] contains both 4- and 5-coordinate Co(II) ions which are found in CoN$_2$O$_2$ tetrahedra and CoN$_2$O$_3$ square-pyramidal units linked *via* monodentate sulfate ions to form chains. The organic bbim molecules link the chains together into a framework and dmso molecules bond to the CoN$_2$O$_3$ unit. The 3-D structure of [Zn(H$_2$-bbim)(SO$_4$)]·dmso [202] is similar to the Co variant. ZnN$_2$O$_2$ tetrahedra link *via* sulfate ions to form chains which are linked through bbim protonated cations for the 3-D structure.
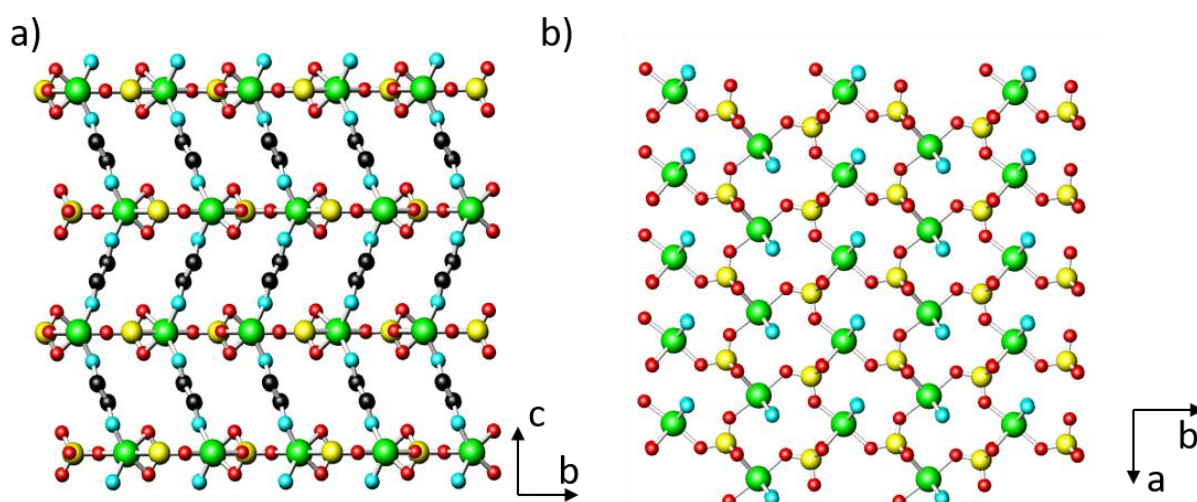
Figure 1.36: (a) The structure of Co(en)SO$_4$ along [100] showing organic amine pillars between layers and (b) the inorganic cobalt-sulfate layer viewed along [001]. Key: green: Co atoms, yellow: S atoms, red: O atoms, light blue: N atoms, black: C atoms. Hydrogen atoms are omitted for clarity.

The Ni(II) compound [C$_4$N$_2$H$_{12}$][Ni$_2$F$_4$(SO$_4$)H$_2$O] [196] (Figure 1.37) has also been prepared in the presence of piperazine. The structure is formed from NiO$_2$F$_4$ octahedra and two octahedra share edges through fluorine to form dimeric [Ni$_2$F$_6$O$_4$]$^{8-}$ units. The dimers share edges to form chains and crosslink with corner sharing sulfate ions to form layers. The layers contain 11-membered ring systems which form channels in which the diprotonated piperazine molecules reside and interact with the framework through hydrogen bonding. The layers are

linked together through a sulfate ion to produce the overall 3-D framework. The isostructural compound $M_3(OH)_2(SO_4)_2(H_2O)_2$ (M = Mn [203], Ni [204]) may be prepared with either Ni or Mn. The framework is built from bridging NiO_6 octahedra, which produces zigzag chains; these are cross linked to produce corrugated layers which are cross linked through sulfate ions. Magnetic data showed that these materials exhibited canted antiferromagnetism.
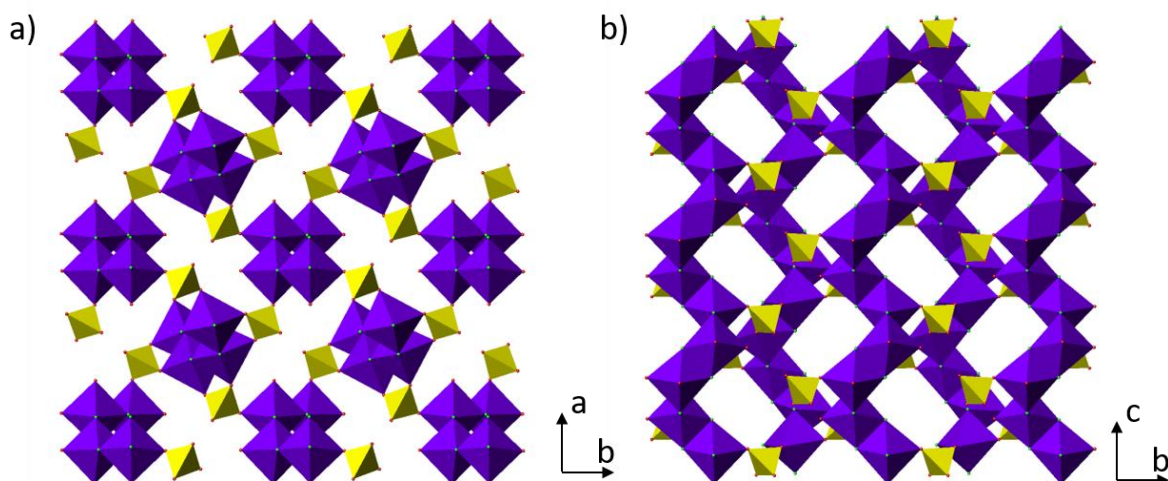
Figure 1.37: Polyhedral representation of $[C_4N_2H_{12}][Ni_2F_4(SO_4)H_2O]$ (a) directed along [011] which contains channels (b) directed along [100]. Key: purple: Ni octahedra, yellow: SO_4 tetrahedra.

A number of other manganese structures have been prepared through hydro/solvothermal synthesis including $[C_2H_6O_2][MnSO_4]$ [185], $[Mn_5(OH)_8SO_4]$ [205] and $[Mn_2(SO_4)_2(\mathbf{L})_2 \cdot (H_2O)_2]$ (L = 1,4-bis([1,10]phenanthroline-[5,6-d]imidazol-2-yl)benzene) [206]. The framework of $[C_2H_6O_2][MnSO_4]$ is built from alternating MnO_6 octahedra and sulfate ions, each Mn octahedron connecting to four monodentate SO_4^{2-} ions and *vice-versa*, resulting in two sets of zigzag chains containing 4-membered $Mn_2(SO_4)_2$ rings. The chains are connected through vertices to form the 3-D structure (Figure 1.38). This is the first transition-metal sulfate framework to resemble a zeolitic structure, in this case, gismondine (GIS). The structure of $[Mn_5(OH)_8SO_4]$ consists of distorted MnO_x pentahedral ($x = 5$) and octahedra ($x = 6$) interconnected through OH^- groups to form layers. These further connect with other manganese centres and sulfate ions to create a complete framework. This material exhibits weak antiferromagnetic interactions. $[Mn_2(SO_4)_2(\mathbf{L})_2 \cdot (H_2O)_2]$ forms a diamond-like interpenetrating network, when treating the $[Mn_2(SO_4)_2]^{2-}$ units as nodes and L ligands as linkers. This structure is made of dimeric Mn centered octahedra linked together through

organic linkers. This material was studied for its luminescence properties and found to emit at 464 nm (blue).
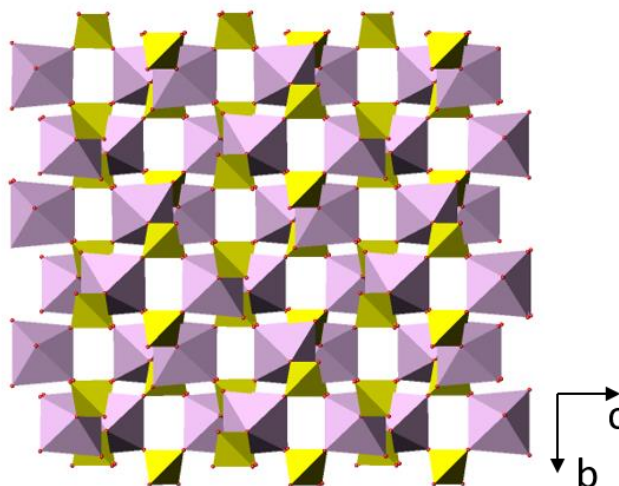
Figure 1.38: Polyhedral representation of $[C_2H_6O_2][MnSO_4]$. Key: light pink: Mn octahedra, yellow: SO_4 tetrahedra.

Copper sulfate 3-D frameworks include $[Cu_{0.5}(NH_4)][Cu(SO_4)_2]$ and $(NH_4)[Cu_{1.5}(SO_4)_2]$ [200] which contain 12-membered ring and 10-membered ring channels, respectively. $[Cu_{0.5}(NH_4)][Cu(SO_4)_2]$ is created from $[Cu_5(SO_4)_8]^{6-}$ secondary building units consisting of one tetragonally coordinated and four square-pyramidal Cu cations. These units produce infinite chains that share common sulfate vertices to produce a 3-D structure. $(NH_4)[Cu_{1.5}(SO_4)_2]$ instead uses $[Cu_6(SO_4)_8]^{4-}$ as a secondary unit that contains two tetragonal and four square-pyramid Cu atoms. These link up in the same way as the previous structure to produce the 3-D architecture. The compound $[Cu^ICu^{II}_2(mal)(SO_4)(bipy)_2 \cdot H_2O]_n$ [207] (mal = malic acid $C_4H_6O_5$, bipy = 4,4'-bipridine) is another example of a mixed-valence sulfate material. The Cu(II) centres form a dimer, which is bridged by the malate ligands and sulfate ions. Both Cu(II) cations share the remaining vertex with bipy linkers. The same sulfate ion that bridges the dimers together also bridges to a three coordinate Cu(I) cation that shares vertices with to bipy linkers. This forms an alternating double layer configuration as seen in Figure 1.39a; this links further through sulfate ions to produce the 3-D structure. Small channels form parallel with [010] in which water molecules reside (Figure 1.39b), with H atoms within hydrogen bonding distance of the oxygen atoms in the malate groups.
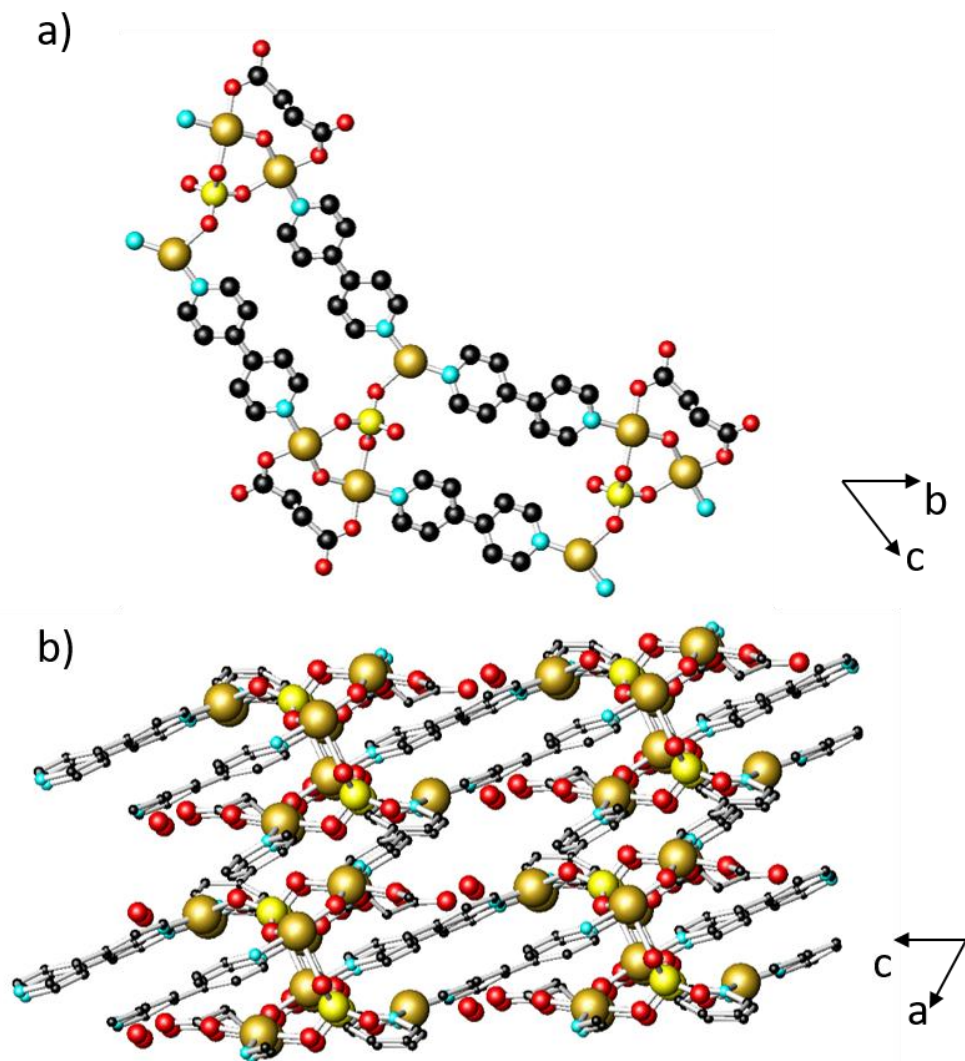
Figure 1.39: The double chains found in (a) the structure of $[Cu^ICu^{II}_2(mal)(SO_4)(bipy)_2 \cdot H_2O]_n$ which contains channels aligned with [010] *(b)*. Key: gold: Cu atoms, yellow: S atoms, red: O atoms, light blue: N atoms, black: C atoms. Hydrogen atoms are omitted for clarity.

Cd containing frameworks have also been investigated. The structure of $[Cd(SO_4)(4\text{-}abpt)(H_2O)]_n \cdot 3nH_2O$ (4-abpt = 4-amino-3,5-bis(4-pyridyl)-1,2,4-triazole) [208], Figure 1.40a, consists of an inorganic layer $[Cd(SO_4)(H_2O)]_n$ which is crosslinked through (abpt) amine linkers, similar to the [Co(en)SO_4] [201] framework discussed at the beginning of this section. $[Cd(bimb)_{0.5}(SO_4)(H_2O)]_n \cdot nH_2O$ (bimb = 1,4-bis(imidazol-1-ylmethy)benzene) [209] is another structure that exhibits this feature: a $[Cd(SO_4)(H_2O)]_n$ layer with (bimb) amine linkers to produce the 3-D framework, Figure 1.40b. Both structures contain water molecules located within the pore space.
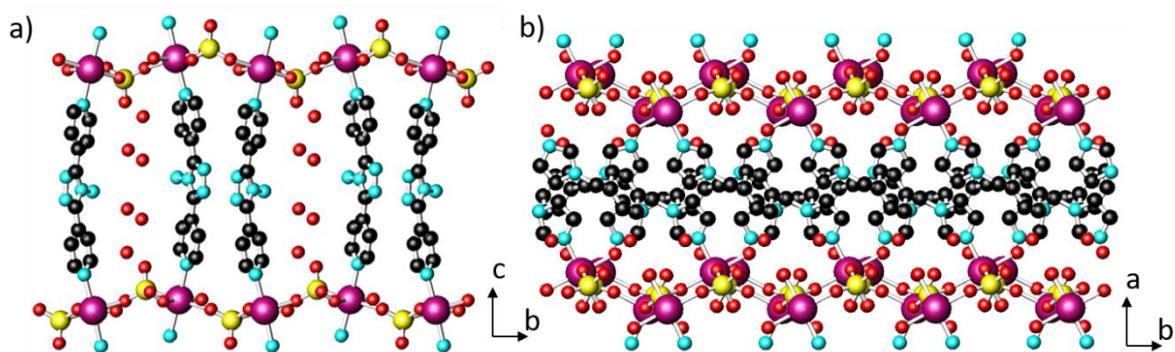
Figure 1.40: The structure of (a) $[Cd(SO_4)(4\text{-}abpt)(H_2O)]_n \cdot 3nH_2O$ viewed along [100] and (b) $[Cd(bimb)_{0.5}(SO_4)(H_2O)]_n \cdot nH_2O$ viewed along [001]. Key: scarlet: Cd atoms, yellow: S atoms, red: O atoms, light blue: N atoms, black: C atoms. Hydrogen atoms omitted for clarity.

Mixing lanthanides with transition metals further extends the building blocks used in sulfate materials and introduces photophysical characteristics [34, 35, 210]. The first 3*d*-4*f* sulfate framework discovered was the compound $[enH_2][La_2M(SO_4)_6(H_2O)_2]$ (M=Ni, Co) [211] (Figure 1.41). The structure consists of MO_6 octahedra and LaO_{10} polyhedra interconnected through sulfate ions, resulting in 8-membered $La_4(SO)_4$ rings in which are located diprotonated ethylenediamine cations. An example of photophysical characteristics is seen in $[Ln_2Mn(Hbidc)_2(SO_4)_2 \cdot 8H_2O]_n$ (Ln = Sm, Eu, Tb, Dy) [212] which displays emissions in the visible region for all four compounds.
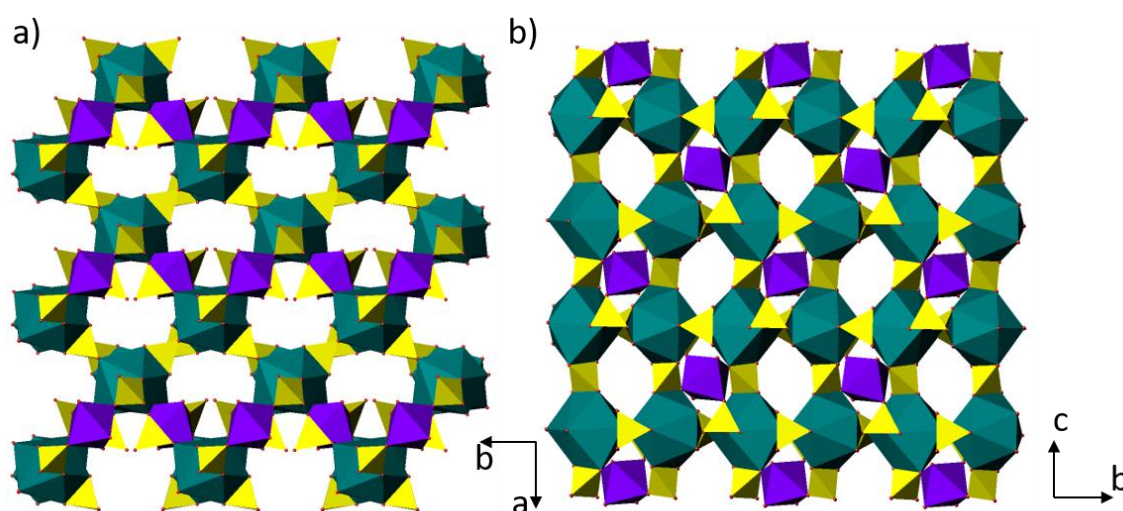
Figure 1.41: Polyhedral representation of the structure of $[enH_2][La_2Ni(SO_4)_6(H_2O)_2]$ (a) along [001] and (b) [100]. Key: dark green: La polyhedra, purple: Ni octahedra, yellow: SO_4 tetrahedra.

1.6 Aims of the Present Work

The aim of this work is to produce new materials using solvothermal techniques and to characterise the products using X-ray diffraction, elemental analysis, infra-red spectroscopy, Uv/*vis* diffuse reflectance spectroscopy, energy dispersive X-ray analysis, and, where appropriate, solid-state NMR and SQUID magnetometry. The materials that will be investigated are:

1) **Main-group sulfide compounds** (both mono and bimetallic in composition) - To further explore ways of connecting different primary building units to produce novel structures.

2) **Germanium oxysulfide compounds** – To prepare novel oxysulfide materials and characterise them. To determine whether the structures produced in this work are relatable to findings on oxysulfide materials published previously [27, 28] with regard to their effect on band gap and thermal stability.

3) **Sulfate containing compounds** - To further explore and characterise novel structures and investigate their magnetic properties.

4) **Iron selenide chain-based structures** – To prepare novel iron selenide structures using various amines, similar to the chain-based structures which have been recently reported [41, 42]. To investigate whether structures of higher dimensionality than those prepared previously, can be achieved using solvothermal chemistry.

Chapter 2: Preparation and Characterisation

2.1 Synthesis

Solvothermal synthesis is a standard procedure for producing a variety of materials including chalcogenides (see Section 1.4), sulfates (see Section 1.5), phosphates [213, 214], selenides [116, 117] and zeolites [215]. Such reactions in this study were conducted using a 23 ml Teflon-lined stainless-steel autoclave (Figure 2.1) in which the reagents were mixed directly within the cup of the Teflon liner. The mixture was stirred for ~10 minutes before being sealed and heated in an oven at a temperature ($403 \leq K \leq 473$) for the required time ($3 \leq$ days ≤ 10). A Teflon liner was used because it is chemically resistant but will warp under temperatures that exceed 473 K. The resultant solid product was then washed and filtered with ethanol, water and acetone, then left to dry in air. If it was known that a sample was water sensitive, through trial and error, then water was left out of the filtering stage. Depending on the severity of the sensitivity (if it degrades in minutes instead of hours), a glove bag filled with nitrogen was then used when filtering as well as the exclusion of water from the filtering process. Sensitive samples were only observed in sulfate samples, Chapter 5.

Figure 2.1: Teflon liners (left) and a stainless-steel autoclave (right)

It should be noted that the exact reaction routes of products from solvothermal synthesis are not known, but instead it is generally recognised as a conceptualised idea (a theory) that the construction occurs though a "building block" mechanism as described throughout Chapter 1 [15]. There is evidence for this mechanism as some simple building units have been isolated

previously [216], before their building up into larger structures. It is also believed that hydrogen bonding interactions between the protonated amines and the anionic frameworks stabilise the structures that form [137]. To summarise this, compound (1) $(H_{1.3}tren)[In_{2.67}Sb_{1.33}S_8]$.tren will be used as an example (Figure 2.2). The initial stages of a reaction form primary building units; in this case, tetrahedral MS_4 units are formed and the metal centres are either In(III) or Sb(V). As time progresses, these build up into secondary building units and in this step of the example it is suspected to be mixed-metal T2 supertetrahedral units, $In_{2.67}Sb_{1.33}S_{10}$. Occasionally, discrete clusters can be isolated from a reaction, particularly In_4S_{10} T2 supertetrahedral units which have been prepared and reported previously [106, 110, 217, 218, 219, 220]. Some secondary building units of solvothermal reactions can be isolated but most are too unstable and remain as intermediates (see Section 1.4.4.1). For a detailed breakdown of particular units within these types of materials see Chapter 1 and for more on compound (1) see Section 3.2.1. The final stage in this example is the 3-D framework which links the T2 units together through vertex sulfur atoms.
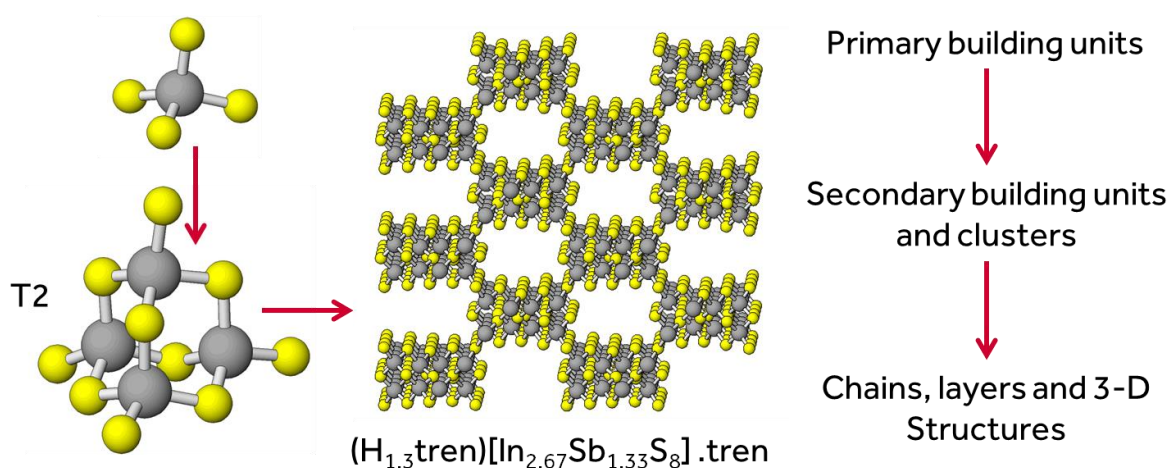
Figure 2.2: A schematic depicting the concepts behind structure formation *via* building block units. Key: silver: Sb/In disordered atom site, yellow: S atoms.

Solvothermal synthesis involves many variables, which can be adjusted to affect the outcome of an experiment. Such variables include: temperature, reaction time, rate of temperature changes, metal and chalcogen sources (*e.g.* $InCl_3$ in place of InO_2), reactant ratios, pH of solutions, quantity/type of amine, addition of water, overall quantity in a reaction and the composition of the reaction mixture. These can change the reaction and potentially promote or hinder the formation of crystals. Following identification of a new crystal structure, in-depth synthetic studies are conducted to optimise the reaction mixture to increase the yield of

crystals (or crystal size). The increase in size/yield of crystal formation then makes it easier to "crystal pick" (the manual removal of crystals from a mixed phase sample) and for characterisation to take place. Depending on which characterisation techniques are used; thermogravimetric analysis, infra-red analysis, elemental analysis and Uv-*vis* diffuse reflectance. A "basic" level of characterisation along with single-crystal X-ray diffraction requires ~20 mg of hand-picked crystals.

2.2 Characterisation
2.2.2 Powder X-ray Diffraction

Diffraction of X-rays occurs when an incoming (monochromated) X-ray beam hits a sample and only reflects when Braggs law is satisfied. The Bragg equation, equation 2.1, was devised in 1913 [221] during which time W. H. Bragg and W. L. Bragg were starting to determine many basic structures, such as those of NaCl and ZnS. They realised that the reflection of X-rays was not the same as the reflection of light from a mirror. Light reflects at an angle equal to the incident beam hitting the surface and any angle can reflect and be seen. Reflection of X-rays instead has rules by which reflections are "seen" only when conditions for constructive interference are allowed. The diagram in Figure 2.3 helps explain this principle.

$$2d_{hkl}sin\theta_{hkl} = \lambda \qquad \text{Equation 2.1}$$

X-ray waves (λ) fired onto a sample interact with the atom electron clouds and reflect at an angle (θ_{hkl}) identical to the angle of incidence. Neighbouring reflections will either be in-phase or out-of-phase creating constructive or destructive interference so that either the phases cancel each other out producing no signal or produce positive interference leading to a detectable signal. The in-phase/out-of-phase interactions of neighbouring X-rays is dependent on the *d*-spacing (d_{hkl}) within crystalline solids. Varying the *d*-spacing alters the phase sparation and therefore changes the angle at which constructive phases are observed. A full powder diffraction pattern only shows the reflections that satisfy the Bragg equation, the in-phase reflections. This however does not mean that the lost reflections are not important as they collectively give vital information about the type of centering a material has and the space group [222]. For example, the *100* (this is a hkl value or miller indice, which is a labelling system for planes in a crystal lattice) reflection in an *F* centered cubic material produces out of phase reflection and would not be seen in a powder diffraction pattern for that sample [223].
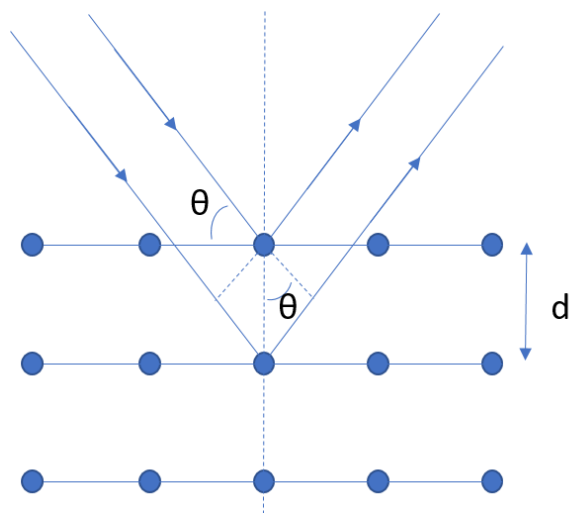
Figure 2.3: Diagram of the diffraction process in a crystalline solid sample

There is one consequence however, the diffraction pattern is a compressed one-dimensional image of the crystal and some structural information is lost. A powder sample contains a mixture of crystallites in various orientations and so when diffraction occurs it is averaging the 3-D representation of the pattern onto a 1-D plane (Figure 2.4). Indexing a powder pattern will allow the retrieval of unit cell details but nothing further. Therefore, powder X-ray analysis is a means to identify substances but not a means of obtaining atom positions in 3–D space, which is done through single-crystal X-ray analysis.
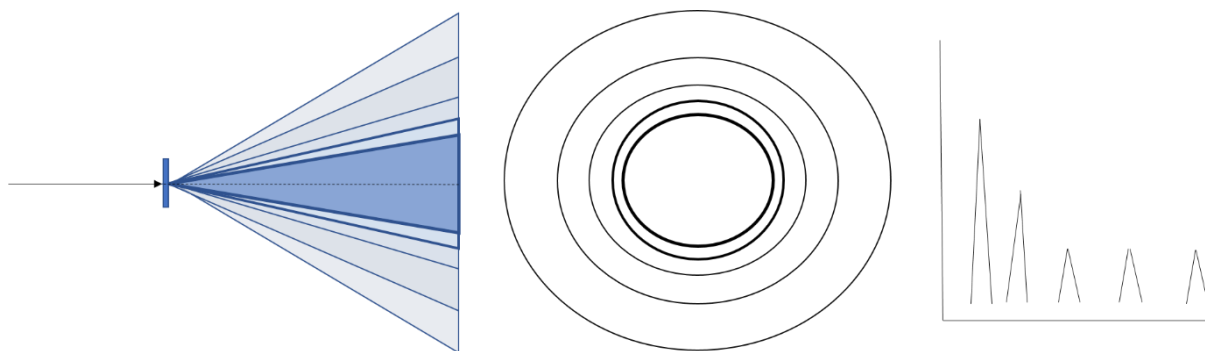
Figure 2.4: Diagrams of; initial Bragg diffraction of powder sample (left), direct powder pattern (middle) and subsequent X-ray powder pattern made from the diffracted ring position and intensities (right).

A Bruker D8 Discover diffractometer was used to obtain Powder X-ray diffraction (PXRD) patterns (Figure 2.5). A typical scan uses Cu radiation (K_α, λ = 1.5418 Å) which utilises Göbel mirrors instead of a monochromated beam and is equipped with a LynxEye detector. Göbel mirrors are an alternative to conventional monochromators in that they use stacked

crystal layers to reflect X-ray beams. The reflected beam from a Göbel mirror is a high energy Kα beam, useful for small quantities of sample. The direction of the diffracted beam is also more controlled than with conventional monochromaters due to the mirrors aligning in a bent parabolic fashion, allowing any beam hitting it to be diffracted into parallel beams onto a sample. Scans were carried out over the angular range $4 \leq 2\theta/° \leq 50$ counting for 0.25 seconds at each angular increment of $2\theta = 0.02019°$. The D8 Discover is designed to collect data on a large array of samples in a short timeframe, using an industry-standard 96-well sample holder. The holder uses a thin poly(methylmethacrylate) layer (PMMS) to suspend the sample within the well and this allows X-rays to pass through both the sample and the holder without interfering with the measurement. The measurement of samples is quick, with the shortest timeframe for a diffraction experiment being 10 minutes. For most samples this sampling time is adequate, but for wells that are inadequately filled (due to lack of product) some samples require longer measurements (40 minutes total) under standard conditions to improve noise to signal ratios. Bulk samples were ground using a pestle and mortar and the powder placed within one of the wells.
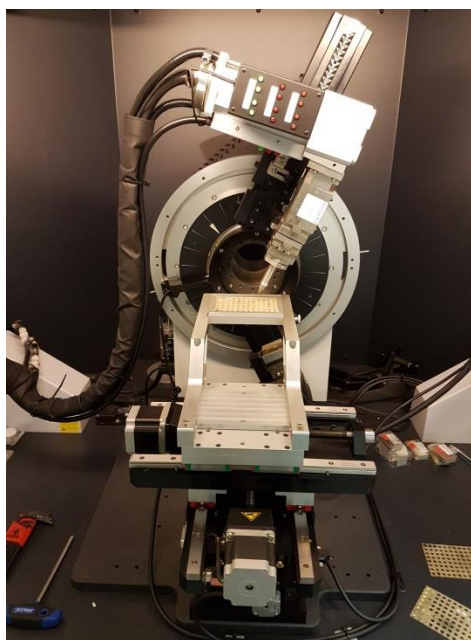
Figure 2.5: Bruker D8 Discover diffractometer

Powder X-ray diffraction data were also collected using a Bruker D8 Advance diffractometer. This operates with monochromatic Cu radiation ($K_{\alpha 1}$, $\lambda = 1.54056$ Å) and is also equipped with a Lynx Eye detector. Scans are between $5 \leq 2\theta/° \leq 64$ with a step count of 1.2 seconds per step at an angular increment of $2\theta = 0.02106°$. Each sample was finely ground and loaded

onto a zero-background holder made from a silicon single crystal. The holder was rotated at 30 rpm for the duration of the scan. Rotation of the sample is required so that all crystallites capable of diffracting can contribute to a diffraction pattern, increasing the overall intensities detected from the sample. The patterns were analysed using the add-on ICDD-PDF2 [224] database in the EVA software package [225], this is used to compare experimental patterns with known patterns on an external database.

2.2.1 Single-Crystal X-ray Diffraction

The choice of radiation source is an important factor in single-crystal X-ray diffraction studies and the decision is dependent on the sample being studied. Cu radiation (K_α, λ = 1.54184 Å) can produce a higher flux of incident photons compared to Mo (K_α, λ = 0.71073) but the disadvantage of Cu radiation is that it can be absorbed by the crystal if there are heavy elements present. This absorption arises from the larger electron clouds of heavier elements, which is directly seen in the mass absorption coefficients for each element (International Tables, Vol C, Table 4.2.4.3). Generally, intensity data for crystals containing elements heavier than silicon should be collected using Mo radiation. This is due to Mo radiation minimising absorption effects. As an added advantage, the shorter Mo wavelength allows higher resolution data to be collected due to the proportional relationship the Bragg equation gives; a smaller λ results in a smaller d spacing that can be collected which also translates to more data collected per frame (increasing efficiency over Cu sources). As a consequence, Mo radiation can increase the chance of peak overlap due to the dependence on the form factor, which adds complexity.

The diffraction of X-rays by the crystal can be explained either mathematically using Bragg's law or geometrically by the Ewald Sphere construction [226]. The Ewald Sphere construction extends Bragg's law to 3D space, all points crossing the Ewald Sphere that could possibly reflect are measured. Figure 2.6, is a 2-D interpretation of the 3-D sphere it represents with the crystal positioned in the middle, C. As the crystal rotates in the beam in the incident beam Q, most exit the sphere at O without diffracting. When Braggs law is satisfied, a reflection is seen and cuts the sphere at point P. Mathematically, angle theta is simply $(1/d)/(2/\lambda)$ (as OPQ is a right-angle triangle where OP is the scattering vector of $1/d$) or $\lambda/2d$, this is a rearrangement of the Bragg law (equation 1).
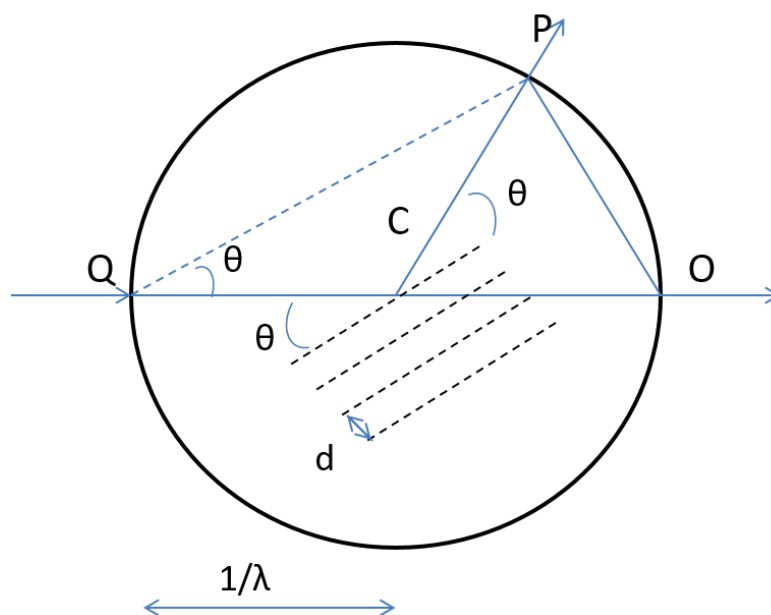
Figure 2.6: 2-D representation of the Ewald sphere construction.

Intensity data collections vary depending on the crystal quality; if a collection time was too high (in the order of many days) or the predicted total data collection percentage was below 60-70 %, another crystal was selected. The collection time is not determined exclusively by the collection percentage, it is also determined by the crystal symmetry. The symmetry determines how much data need to be collected; the lower the crystal symmetry, the more reflections are required to ensure a complete data set (all unique reflections), *i.e.* a crystal of monoclinic symmetry requires more reflections to be collected than for a crystal of cubic symmetry. If the total experiment time for collection is too long then lowering the collection time per frame is a viable option; however, this risks fewer data points being collected which results in a poorer refinement. The crystal symmetry is determined through indexing the pre-experimental data. This is a process that takes the smallest vectors between a set of reflections and attempts to build a unit cell. If the *hkl* values are integral, the symmetry elements are assigned by looking at which reflections are symmetrically equivalent or symmetrically absent. Symmetric absences are a result of reflections creating out-of-phase waves thereby creating a reflection that is not detectable, this aids in determining space groups by narrowing down possible symmetry relationships.

Upon collection of all reflections in an experiment, reduction of data is performed to produce the structure factors F_o from the intensity data collected $I(hkl)$. This reduction process also includes corrections to the data collection process from issues arising from; absorption,

crystal size, X-ray beam inhomogeneity and crystal decay. To use this collected and corrected data, a reverse Fourier function is used to translate the diffraction pattern into areas of electron density that the atoms in the structure have produced. The electron density ($\rho(xyz)$) in equation 2.2, is obtained through summation of the diffracted beams, their amplitudes (F_{hkl}) and phases ($\exp[i\phi(\text{hkl})]$) and ($\exp[-2\pi i(hx + ky + lz)]$).

$$\rho(xyz) = \frac{1}{V}\sum_{hkl} |F(hkl)|\exp[i\phi(\text{hkl})]\exp[-2\pi i(hx + ky + lz)] \quad \text{Equation 2.2}$$

Using this equation, the *xyz* positions to each *hkl* value can be determined but the phase of the reflections is not known. The phase is the angle of the wavelength from a chosen origin. This phase problem can be solved using direct methods or charge flipping.

- Direct methods (*i.e.* Sir92 [227]) calculate probable relationships between the most prevalent (highest intensity) reflections and mathematically generated phases to see if any such relationships can be found. This process continually generates phases that attempt to solve the structure. If it satisfies the probabilities then usually the heaviest atoms can be found, *i.e.* metal centres and sulfur atoms.

- Charge flipping [228], known as a dual space iterative method, is the alternative means of solving the phase problem. This uses an algorithm that alternates between direct and reciprocal space, between two sets of mathematical constraints based on amplitudes and electron density. Charge flipping can also be a means to confirm symmetry in a structure, as it analyses both the experimental amplitudes and reconstructed phases.

Once a trial structure has been found, refinement takes place. Structure refinement is a process that takes the atoms found in the solved structure and models the atomic positions and thermal parameters so that the calculated electron density fits the experimentally observed electron density. Thermal parameters model the atom for time-averaged temperature dependent movement and their distribution over unit cells. This is done either isotropically which uses only one parameter and models the atom as a sphere, or preferably, anisotropically which uses six parameters to model thermal motion of the atom. Lastly, weights are used to reflect errors in both the data and the model which improves the fit for the refinement.

The measure at which the solved structure is complete is calculated by evaluating the difference between the observed and calculated structure factors |*Fo*| and |*Fc*| respectively. This may be formulated according to Equation 2.3 where the term *R* is known as the *R*-factor

(Figure of merit). The *R*-factor is the summation of all differences and the structure should be modelled to reduce this number as much as possible (thereby reducing error). For example, materials that incorporate organic structure-directing agents often exhibit disorder when not modelled correctly, which raises the value. Other factors for bad *R*-factors include; twinning, bad data collection, absorption and incommensurate structures.

$$R = \frac{\sum ||F_o| - |F_c||}{\sum |F_o|} \qquad \text{Equation 2.3}$$

An Oxford Diffraction Gemini S Ultra (Figure 2.7) was used to obtain single-crystal X-ray diffraction data. This is a multi-source machine capable of producing either graphite-monochromated Cu (K$_\alpha$, λ = 1.54184 Å) or Mo (K$_\alpha$, λ = 0.71073 Å) radiation. An Oxford Cryosystems Cryostream cooling device was used to cool the crystals down to 150 K for each experiment. Crystals were mounted on a four-circle kappa geometry goniometer and a CCD (closed couple device) detector was used for reflection intensity measurement. Data collection was managed using Crysalis software [229] and all structure refinements were performed using the CRYSTALS suite of programs [230]. All refinements were processed in *F* and Chebychev polynomial weight schemes were applied [231]. Programs Mercury [232] and ATOMS [233] were used to view the structure using a CIF file created after the final cycles of refinement. Amendments to the CIF file itself were done so in enCIFer [234].

Figure 2.7: Oxford Diffraction Gemini S Ultra.

2.2.3 Infrared Spectroscopy

Infrared (IR) spectroscopy is used to investigate bond vibrations in each sample; a means of identifying functional groups present in a compound, *e.g.* water is characterised by features arising from ν(O-H) stretching vibrations around 3400 cm^{-1} and δ(H-O-H) bending vibrations at *ca.* 1600 cm^{-1}. IR spectroscopy can be used as a complementary analysis technique, for example by comparing it with thermogravimetric data. The temperature at which a weight loss due to water occurs indicates whether water identified by spectroscopy arises from water located in the pore space (relatively strongly bound, higher temperature weight loss) or from that absorbed on the surface of the material (weakly bound, lower temperature weight loss). Due to the large number of bonds present in the "fingerprint" region for framework structures, it is unlikely to give decisive data; instead the carbon, water, sulfate and amine stretching regions were more easily understood and analysed.

The samples were analysed on an ATI Mattson Genesis Series FT-IR, scanning through 440-4000cm^{-1} and collecting 16 scans in total. The samples were prepared by adding a small amount of finely ground sample (after having performed a background scan) onto the attenuated total reflectance (ATR) plate, and then screwing down the lid so that the material was flattened on the platinum plate. The measurement of the sample can then take place. All analyses of peak positions were carried out manually using Microsoft Excel.

2.2.4 UV-*Vis* Diffuse Reflectance and Band Gap Measurements

The theory of energy bands in a material (arising from linear combination of atomic orbitals, LCAO) explains that there is a separation between the filled valence bands and the conduction bands of a material, Figure 2.6. Optical excitation of an electron across the band gap produces an absorption energy at the wavelength of the band gap itself. This is an observable behaviour using diffuse reflectance spectroscopy and the absorption edge can be observed if it is between 0-4 eV [235]. Depending on the type of material this band gap can vary in size; for example, in antimony sulfide materials studies show [236-237] that valence bands contain *s/p* orbitals (sulfur 3*p* dominating) and the conduction band containing a mix of Sb 5*s*, 5*p* and S 3*p* orbitals within the conduction band with a reliance on sulfur. This produces a semiconducting property with respect to antimony sulfides due to the overlap available, Figure 8.
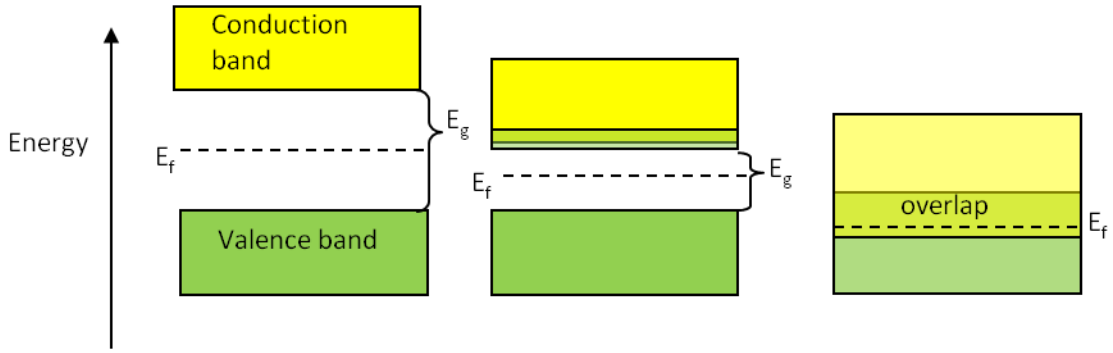
Figure 2.6: A diagram illustrating the energy bands in materials, insulator (left), semiconductor (middle) and conductor (right). E_f is the Fermi level and E_g is the band gap.

Uv-*vis* diffuse reflectance spectroscopy involves focusing a beam of light at a sample and the detection of the back-reflected light from the sample (some of which is absorbed). The Kubelka-Munk (K-M) function equation 2.4 [238], is applied to the collected data. This is a mathematical function used to convert the y-axis into absorptivity in which R_∞ is the reflectance of the sample layer, which is assumed to be an infinitely thick layer of powder (the sample), k is the molar absorption coefficient as defined by Lambert's law (A=εlc) and s is the scattering coefficient which is assumed to be independent of wavelength.

$$F(R_\infty) = \frac{(1-R_\infty)^2}{2R_\infty} = \frac{k}{s}$$ Equation 2.4

Once the K-M function is applied it is easy to determine the band gap value by drawing a straight line down the absorption edge and reading the value on the *x*-axis, when *y* = 0. An example of this can be seen in Figure 2.7 in which a dotted line is drawn down the absorption edge.
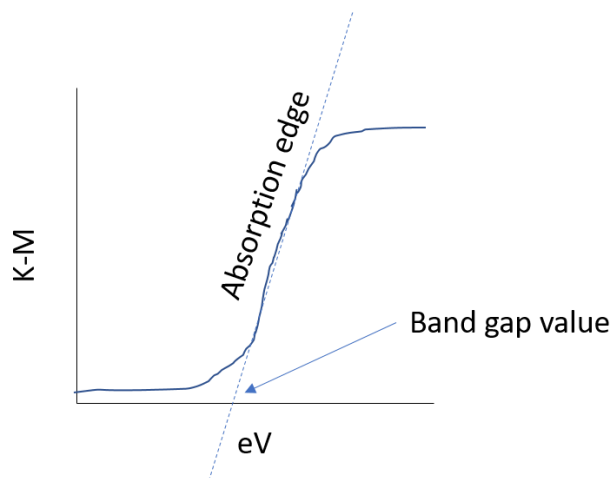
Figure 2.7: Diagram of a diffuse reflectance K-M plot.

56

Diffuse reflectance data were collected over the range of 9090-50,000 cm^{-1} (with a 2 nm slit at a speed of 120 nm s^{-1}) using a Perkin Elmer Uv-*vis* Lambda 35 Spectrometer, equipped with a Labsphere Reflectance Spectroscopy accessory. BaSO$_4$ was used as a reference, providing a 100% reflectance as a background scan. Approximately 6 mg of finely ground sample was used and placed atop the flattened BaSO$_4$ background disk.

2.2.5 Thermogravimetric Analysis

Thermal analysis was carried out using either a TA instruments Q50 or Q600 Thermogravimetric Analyser. In a typical experiment, approximately 6 mg of handpicked ground crystals were placed in a ceramic crucible and suspended in a platinum boat. The sample was heated from room-temperature to a target temperature ($673 \leq T/K \leq 1273$) at a rate of 5 K min^{-1} under a flow of N$_2$. The target temperature used was dependent on the sample; materials containing antimony sulfide components had the maximum temperature constrained to 673 K to reduce the formation of Sb$_2$O$_3$ (suspected carcinogen).

2.2.6 Scanning Electron Microscopy (SEM) and Energy Dispersive X-ray (EDX) Analysis

An electron gun with a tungsten filament is used to generate electrons which travel through a series of lenses which focus the beam onto the sample (Figure 2.8). There are a few interactions that can occur when the incident beam falls upon the sample. These interactions can be described as elastic scattering (back-scattering electrons), inelastic scattering (secondary electrons) and electromagnetic radiation (X-ray formation).
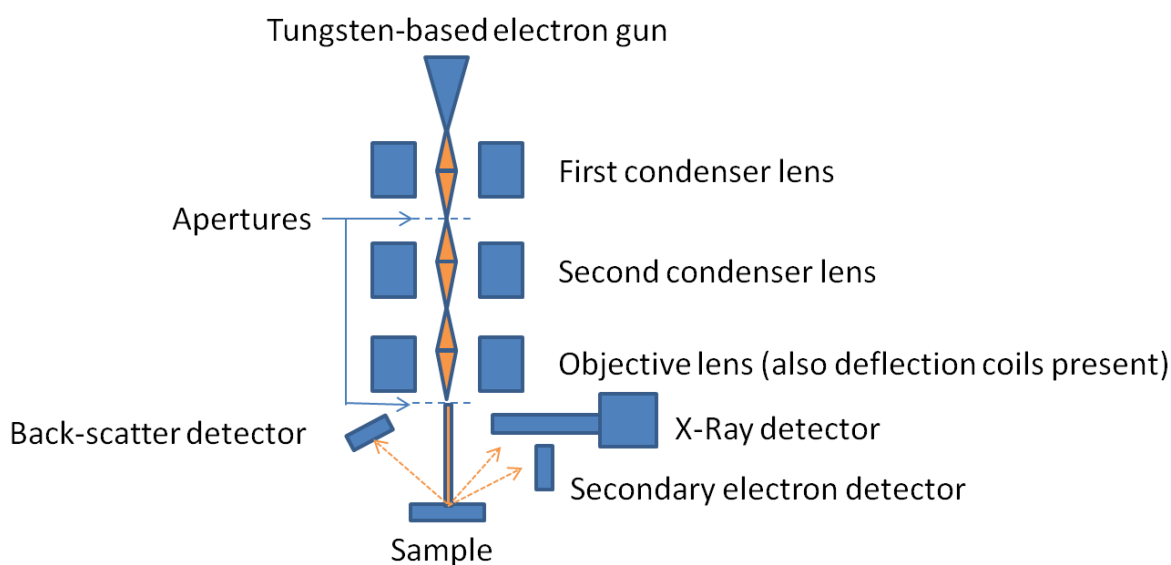
Figure 2.8: Diagram of an electron microscope.

In the case of inelastic scattering electrons, the incident beam removes electrons from the inner-shell atoms in the sample to produce "secondary electrons". It is these electrons that are detected to produce an image (once processed with amplified signals). This type of scattering is useful for topological investigations as the electrons are emitted on the surface of a material, typically when the energy exceeds the 2-6 eV required for secondary electron ejection. Back-scattered electrons are reflected from deeper within the sample and can provide some composition information. This technique is influenced by heavier elements due to the increase in scattering power caused by a higher Z value of the atom. This shows good contrast to the different regions of elements within a sample. Lastly, when the sample beam interacts with the atoms of the sample, the inner electrons (k-shell) can be removed and replaced by an electron from an outer shell, which produces X-rays. The wavelength of X-rays produced depends on which shell the electron is promoted from, *e.g.* in Figure 2.9 an electron falling from the m-shell to the k-shell produces K_β radiation. This results in a spectrum that is characteristic of a given element and can be analysed to identify elements in the sample. Furthermore, when the results of a scan for each element is standardised this can also be a means of generating a chemical composition [239-240]. Standards are either obtained experimentally if pure elemental materials are found, or premeasured standards are found with most energy dispersive X-ray software which is also acceptable, considering some standards are hard to obtain.
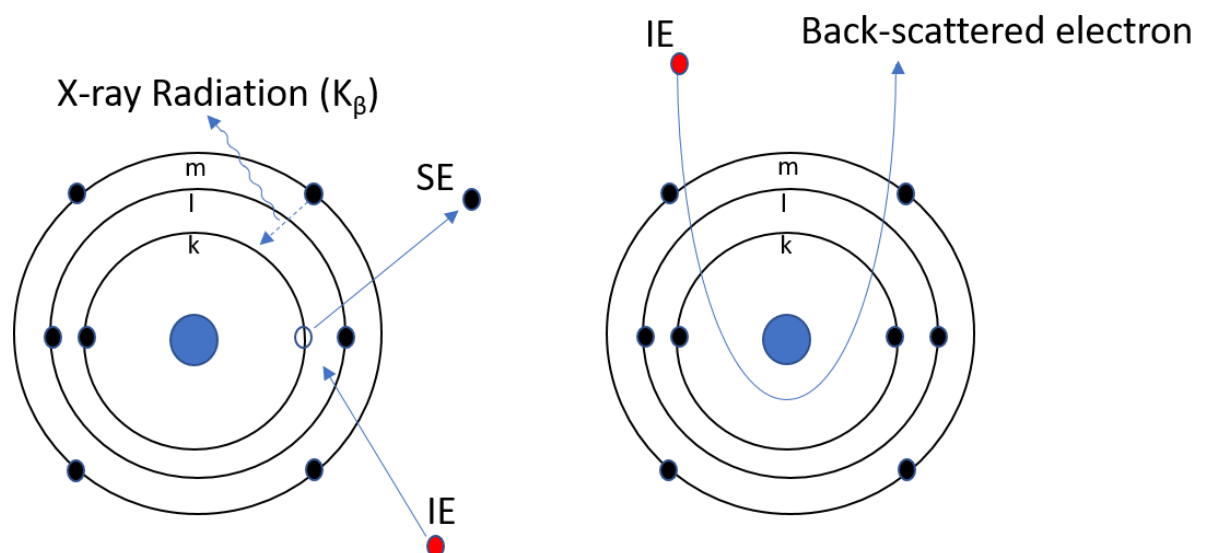
Figure 2.9: Types of scattering present when the incident electron (IE) beam interacts with atoms in a sample. Secondary electrons (SE) and X-ray radiation left, back-scattering electrons right.

Scanning electron micrograph images and energy dispersive X-ray data were collected on a Cambridge 360 Stereoscan electron microscope fitted with an Oxford Instruments Inca energy dispersive X-ray analysis system (Figure 2.10). This operates at 20 kV and 200 pA, with a stage distance of 25-30 mm for scanning electron microscope studies and 15-25 mm for energy dispersive X-ray collections. Samples were prepared by sticking crystals (or powder) onto an adhesive carbon stub and loaded into the main chamber. The stage was manually set to a safe working distance to avoid lens collisions during initial setup.

Figure 2.10: Cambridge 360 Stereoscan electron microscope.

2.2.7 Solid-State Nuclear Magnetic Resonance (NMR)

In NMR spectroscopy, the spin state value of an element is important and is dictated by the number of protons and neutrons within the nucleus, the spin state can range between $0 \leq I \leq 8$ in ½ increments. With regard to isotopes, the maximum integer spin is 7 for ^{176}Lu but a maximum half-integer spin of 9/2 for known for some isotopes (including ^{175}Lu). For example, hydrogen has a spin state $I = ½$ as it contains 1 proton and no neutrons, both of which are assigned a ½ spin value resulting the net value of ½. While ^{12}C is $I = 0$ and therefore not NMR active, the natural abundance of ^{13}C within all carbon results in a few percent of ^{12}C containing ^{13}C (^{13}C is $I = 1/2$). This is enough to allow measurements on ^{12}C within NMR.

In a typical cross-polarisation magic angle spinning (CPMAS) NMR measurement, the sample is placed in the centre of a superconducting magnet. The permanent magnetic field produced by the magnet interacts with the nuclear spin states present in all nuclei. By doing so, the magnetic field applied is either in the same direction of as magnetic moment arising from the nuclear spin or opposes it. This results in an energy difference between allowed spin

states. The direction of the spin state can be reversed by applying the electromagnetic radiation of the appropriate energy (matching the energy difference between the two orientations) and this change is detectable through spectroscopic methods.

The CPMAS NMR signals are also influenced by the environment of a given nucleus, allowing identification of potential structural fragments [241].

In solution NMR molecules move rapidly (tumbling motions etc.) and this produces sharp, well resolved resonances in the NMR spectrum. In the solid-state, the signals in NMR spectrum are far broader and is due to the fixed positions of the atoms throughout the material, causing shielding anisotropy and long relaxation times. Therefore, a correction is required to reduce line broadening in solid-state NMR which arises from anisotropic interactions between atoms present within solid crystal structures. While this anisotropy is also present in solution-based NMR, molecules in solution are more mobile compared to the atoms in a nearly-static solid. These fast motions result in an averaged intensity in solution NMR but not for solid-state NMR which produces line broadening. This is solved by rotating the sample quickly to average anisotropy present [242] (Figure 2.11). The spinning of the sample is rotated at a specific angle to the magnetic field, this is known as the magic angle, θ = 54.7356˚. This angle is a constant derived from an energy operator which reduces the anisotropy to 0. Relaxation times are corrected using cross-polarisation techniques which are a way of transferring polarisation from an abundant spin to a dilute spin, improving the signal to noise ratios.
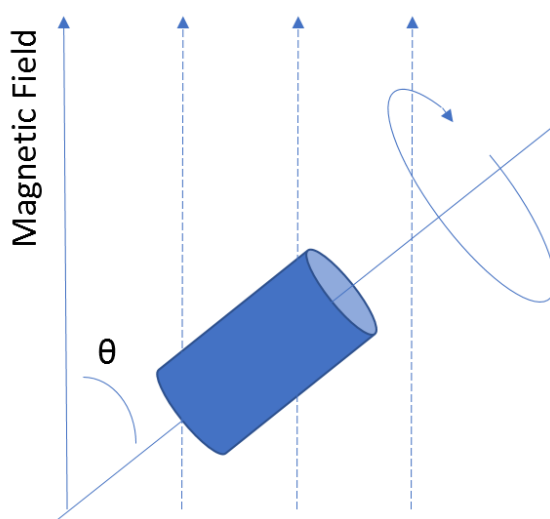
Figure 2.11: Schematic of magic angle spinning used in solid-state NMR. A sample (blue cylinder) is rotated about an axis at an angle θ to the magnetic field.

^{13}C solid-state cross-polarisation magic angle spinning NMR spectra were recorded on a Bruker Advance III spectrometer operating at Larmor frequency of 125.78 MHz (11.75 T). The standard bore 4 mm MAS probe was spun at 10 kHz rate. The CP contact time was 2.4 ms, and the 90° pulse width was 3.7 μs. A total of 24576 signal transients were accumulated with 2 s relaxation delay at ambient temperature. The spectrum was referenced to an external adamantane signal as a secondary reference (frequency peak at 38.5 ppm with respect to TMS). Samples were prepared by loading a rotor (a sample holder) with ~ 100 mg of finely grounded hand-picked crystals. The measurements were conducted by Dr Radoslaw Kowalczyk, CAF lab NMR technician, Department of Chemistry, University of Reading.

2.2.8 Analysis of Magnetic Properties

Any atom or ion that contains unpaired electrons is paramagnetic. This means that in the presence of a magnetic field there will be an alignment of moments (vectors representing permanent magnetic dipoles) which causes an induced magnetization parallel to the field. Whereas diamagnetic materials (fully paired electrons present in an atom or ion) oppose magnetic fields but is very weak. Therefore, paramagnetic materials exhibit a positive susceptibility and diamagnetic materials a negative susceptibility. If the force of attraction in paramagnetic materials can be measured then the number of unpaired electrons per atom can be determined. A SQUID detector however, measures voltage variation as a sample is moved through the detection coils and can provide an accurate measurement of a samples magnetic moment.

When a sample becomes magnetised by a magnetic field, the magnetisation (M) is defined as the magnetic dipole moment per unit volume. Therefore, magnetisation is proportional to the applied field (B) and is expressed by equation 2.5. Where χ_m is the magnetic susceptibility (volumetric), the magnetisation induced by unit applied magnetic field and μ_o is the vacuum permeability.

$$M = \mu_o{}^{-1}\chi_m B \qquad\qquad \text{Equation 2.5}$$

The use of χ_m (χ or κ as it is sometimes known) is not very suitable for chemists to work in, so it is more practical to use χ per mol (χ_{mol}) by incorporating the molar mass (Mr) and density (ρ) to give equation 2.6.

$$\chi_{mol} = \frac{\chi_m M_r}{10^3 \rho} \qquad\qquad \text{Equation 2.6}$$

If the equation above is broken down, the use of density produces χ per gram (as $\chi=\kappa/\rho$) which then needs to be multiplied by Mr, in g ($\chi_{mol} = \chi \times RMM$) to produce χ per mol.

As mentioned at the beginning of the section, external magnetic fields attempt to orientate moments in materials. It does so however, against the thermal energies that try to randomise the orientation of the moments. This can be described by Curie's law, $\chi = C/T$, where C is the Curie constant [243]. The value of C, gives us information of the magnetic moment μ of the atom or ion which does not vary with temperature like χ (if the law holds true). However, not many paramagnetic solids obey this law. The interactions between the moments themselves need to be considered, where all moments can take any orientation (the Langevin assumption), here, the Curie-Weiss law is used. Equation 2.7 depicts this law using a modification on the Curie law using the Weiss constant θ.

$$\chi_{mol} = \frac{C}{T - \theta} \qquad \text{Equation 2.7}$$

If a Curie-Weiss law holds true in a particular measurement, then a plot of the reciprocal susceptibility as a function of temperature should be a straight line with gradient of $1/C$ and intercept $-\theta/C$. The plot in Figure 12 demonstrates the various magnetic ordering of measured materials and which laws may apply. For example, a negative shift in the x-axis (-θ value) occurs when the susceptibility values are lower than in an ideal paramagnetic material and displaces the Curie-Weiss plot to lower temperatures, this then extrapolates over to the inverse plot seen below [244]. The θ value can be used as a rationale as to what type of ordering may be present, if any but is not always an indication of long-range ordering. Anti-ferromagnetism for example, is the alignment of spins pointing in opposite directions (when below the Néel temperature T_n) and ferromagnetism is the alignment of spins in the same direction (when below critical temperature T_c).
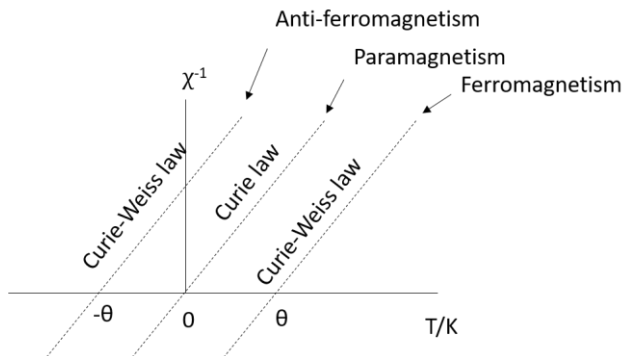
Figure 12: Reciprocal of susceptibility versus temperature for paramagnetic substances but may show magnetic ordering at low temperatures [244].

The properties of a paramagnetic material can be expressed with an effective magnetic moment μ which is related to the χ_{mol} using Equation 2.8. Where N_a is Avogadro's number, μ_β is a Bohr magneton, k is the Boltzmann's constant and T is the temperature in K [245].

$$\chi_{mol} = \frac{N_a\mu_\beta{}^2\mu^2}{3kT}$$
<div align="right">Equation 2.8</div>

With relation to the Curie law ($\chi = C/T$) then its constant C can be defined using Equation 2.9

$$C = \frac{N_a\beta^2\mu^2}{3k}$$
<div align="right">Equation 2.9</div>

The magnetic moment μ is the overall contribution of the unpaired spins in a material and the effect of the orbital motion of electrons. The magnetic moment is therefore calculated from the magnetic susceptibility of a measured compound. It is however, possible to use a spin-only formula to produce a theoretical value, Equation 2.10. Here the orbital contributions are regarded as zero, quenched. S is the sum of the spins of unpaired electrons in the atoms or ions of the sample being measured. Table 2.1 gives the value of the quantum spin numbers S and μ for possible numbers of spins present for different numbers of unpaired d electrons. When the experimental value differs from that of the theoretical value obtained using Equation 2.10, orbital contributions are likely to be increasing the value.

$$\mu = 2\sqrt{S(S+1)}$$
<div align="right">Equation 2.10</div>

Table 2.1: Values of S and μ for unpaired $3d$ electrons.

No. of Unpaired Spins	Spin Quantum number (S)	Magnetic Moment (μ) in Bohr Magneton
1	1/2	1.73
2	1	2.83
3	3/2	3.87
4	2	4.90
5	5/2	5.92

Magnetic susceptibility data were collected using a Superconducting Quantum Interference Device (SQUID). A SQUID magnetometer (Figure 13) measures samples in a superconducting loop with two parallel Josephson junctions, Figure 14. The sample moves

through an external field produced by the superconducting magnet. A magnetic flux change is produced by the samples magnetic moments moving through the pick-up coils which are inductively coupled to the SQUID sensor and thereby induce a current in the SQUID. This in turn causes a voltage to be detected across the loop which is detectable.
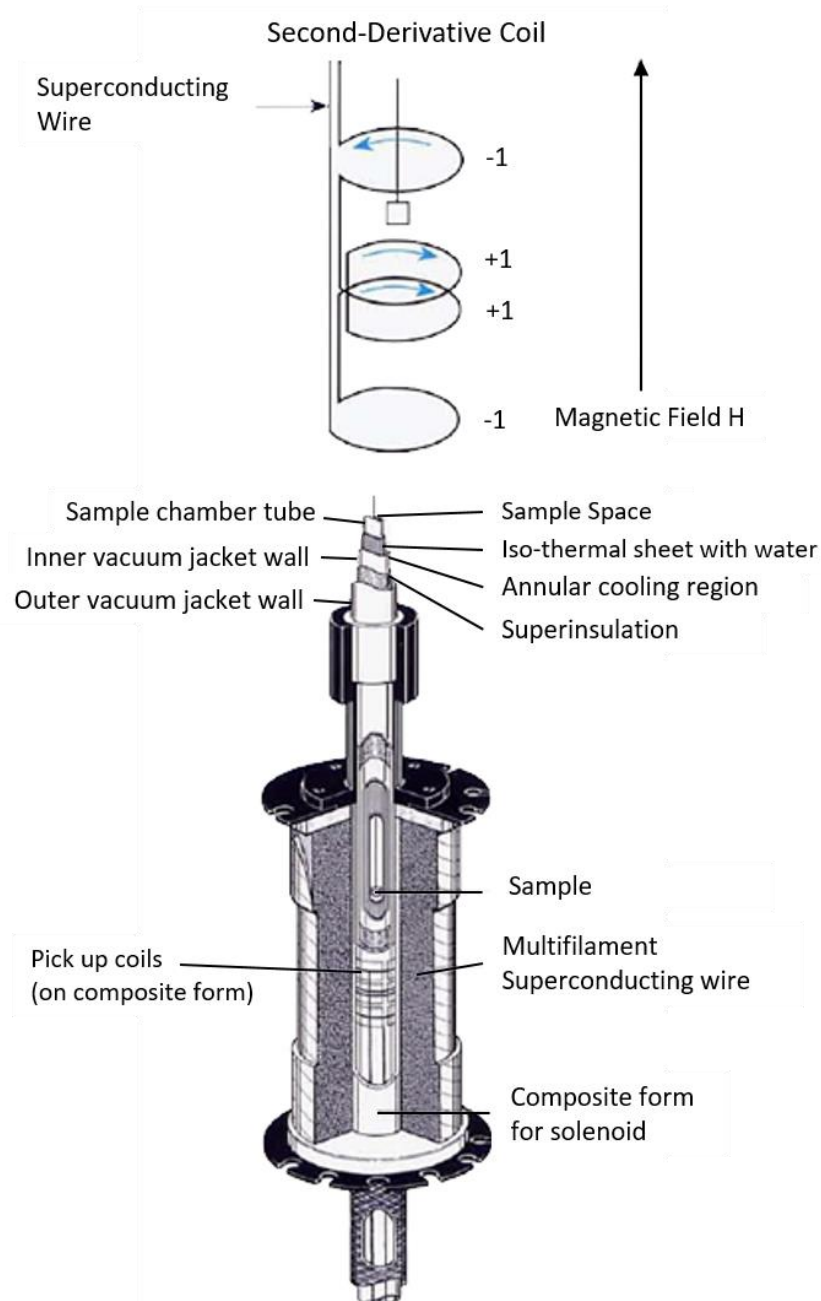
Figure 13: A Schematic of the SQUID magnetometer [246] and the second derivative coil which is at the centre of the magnet.
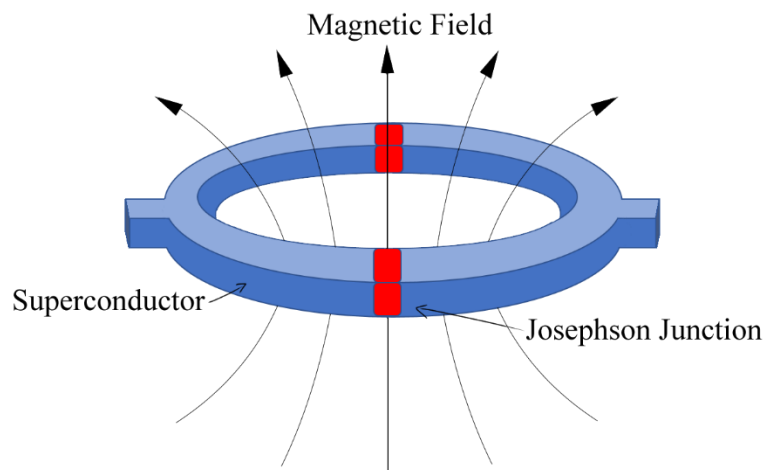
Figure 14: Diagram of a DC SQUID device

Magnetic property measurements were conducted at the University of Madrid (ICMM) by Dr Jesus Prado Gonjal (previously of the University of Reading) using a Quantum Design 5T MPMS-SQUID (Magnetic Properties Measurement System-Superconducting Quantum Interference Device). A commercial gelatin capsule with a 50 mg capacity was filled with the sample powder. This capsule minimizes the background signal due to having a magnetic susceptibility lower than 10^{-7} emu/Oe g. If the capsule is not completely full (due to only having few mg of sample), free space was filled with a small piece of cotton. This is to avoid powder movement because it may produce spatial offset problems, such as background-sample positioning. The capsule was inserted in a lightweight homogeneous tube sample holder (a straw, from Quantum Design), which is attached to the end of a rigid sample rod. This rod was introduced into the SQUID. The sample was then centered in the SQUID pickup coils to ensure that all coils sense the magnetic moment of the sample. During a centering measurement, the instrument scans the entire length of the straw and the position where the magnetic moment is stronger was chosen.

The temperature dependence of the magnetisation was measured following zero-field-cooling (ZFC) & field-cooling (FC) protocols:

- The samples were first cooled from room temperature (300 K) to 5 K with no applied field. A field of 1000 Oe was then applied at 5 K and the zero field cooled (ZFC) magnetisation data collected on warming to 300 K.

- Subsequently, the samples were cooled again in the applied magnetic field of 0.1 T and field cooled (FC) magnetisation data were recorded on warming top 300 K.

- Magnetisation data as a function of applied magnetic field measurements were then carried out over the range $-5 \leq H/\text{T} \leq 5$ at a constant temperature of 300 K and 5 K. The sample is saturated at 5 T first and then the measured cycles are conducted in zero field.

2.2.9 Elemental Analysis

All elemental analysis was performed by Medac Ltd. Typical analyses were conducted on ~2 mg of hand-picked crystals. The sample is burned in a stream of oxygen to produce H_2O and CO_2. Samples were combusted in a stream of O_2, thereby converting the hydrogen and carbon present in the organic component to H_2O and CO_2 respectively. Measurement of the amount produced allows the percentage by weight of the two elements present in the original sample to be determined. [247].

In the work reported in Chapters 3-5 the results in terms of the weight percentage of C, H and N are compared to the values calculated from the crystallographically-determined formula obtained by single-crystal X-ray diffraction to support the formulation so determined.

2.2.10 Atomic Absorption Analysis

Atomic absorption spectroscopy data were collected using an Analytik Jena, novAA 350 flame AAS spectrometer with an acetylene fuelled flame for atomisation. Solutions for analysis were prepared by gently heating *ca.* 10 mg of sample in a minimal amount (~ 5 ml) of 16 M HNO_3. On dissolution of the solid, the solution was diluted to 100 ml. Standards were created from a stock 1000 ppm potassium solution (Fisher Chemicals).

Chapter 3: Indium Containing Sulfide Materials

3.1 Introduction

As outlined in Chapter 1, one strategy for the creation of novel phases is to exploit the complementary coordination preferences of different main-group elements. This chapter focusses on indium and mixed indium-antimony sulfides. Indium(III) chalcogenides are constructed from tetrahedral InS_4^{5-} building blocks which can link together to form discrete supertetrahedra Tn (n = 2 [80, 81] 3 [82], 4 [83], 5 [83]), existing either as anions, *e.g.* in the case of the T2 units as $[In_4S_{10}]^{8-}$ ions [80], or terminated by S-H groups, as in $[C_6H_{16}N][In_4S_6(SH)_4]$ [81]. The larger indium-sulfide based T4 and T5 supertetrahedra are usually stabilised on incorporation of a divalent metal cation, as is found in $[Cd_4In_{16}S_{31}]^{6-}$ and $[Cd_{13}In_{22}S_{52}]^{12-}$ [83]. As well as existing as discrete units, the supertetrahedra can be connected *via* corner sharing to generate frameworks, as found in $KInS_2$ [92], which contains T2 units linked to form a layered structure and $[In_{10}S_{18}]^{6-}$ [248] and $[M_4In_{16}S_{33}]^{10-}$ (M = Mn, Co, Zn, Cd) [249], which consist of 3-D frameworks constructed from T3 and T4 supertetrahedra, respectively. Alternatively, indium-sulfide supertetrahedra may be joined through a variety of inorganic linkers, such as InS_4^{5-} tetrahedra, as in T3 containing (dea-H)$_7$In$_{11}$S$_{21}$H$_2$ (dea = 5 diethylammonium) [93], or SbS_3^{3-} trigonal pyramids, as in T2 containing $[NH_3CH_3]_4[In_4SbS_9(SH)]$ [21].

By contrast, antimony shows greater geometrical variety of primary building units. In the Sb(III) oxidation state, SbS_3^{3-} trigonal-pyramidal geometry is favoured, although an SbS_4^{5-} see-saw geometry is also known, Sb(V) however usually adopts a tetrahedral SbS_4^{3-} arrangement. Only a few mixed-metal Sb(III)-In(III) sulfides have been reported to date including $[Co(deta)_2]_2In_2Sb_4S_{11}$ (deta = diethylenetriamine) [152], which consists of chains constructed from InS_4^{5-}, SbS_3^{3-} and SbS_4^{5-} units, $[Co(dap)_3]InSb_3S_7]$ (dap = 1,2-diaminopropane) [164], a 3-D framework containing large channels constructed from InS_4^{5-} tetrahedra and SbS_3^{3-} trigonal pyramids and $[NH_3CH_3]_4[In_4SbS_9(SH)]$, in which indium-containing $In_4S_{10}^{8-}$ T2 adamantane units are linked through their terminal sulfur atoms by SbS_3^{3-} trigonal pyramids to create a 3-D framework [21].

By utilising the exclusively tetrahedral coordination of indium and the more geometrically diverse antimony, structures in this work were prepared and charge balanced with either

amine complexes or protonated amines. The results demonstrate that subtle changes in reaction conditions have a marked effect on the nature of the product, including whether single crystals or polycrystalline materials form. Using solvothermal synthesis, multiple reactions were conducted on attempting to optimise reaction conditions to promote crystal formation.

The new phases synthesised include three antimony-indium structures, one of which, $(H_{1.3}tren)[In_{2.67}Sb_{1.33}S_8] \cdot tren$ (**1**), has been published recently in the *Journal of Solid State Chemistry* [250] and contains adamantane-like T2 supertetrahedral units comprised of corner-sharing InS_4^{5-} and SbS_4^{3-} tetrahedra. Lastly, a 3-D T3 indium-sulfide framework was prepared using an alternative amine to what had been presented in the literature thus far.

3.2 Indium-Antimony Frameworks

3.2.1 $(H_{1.3}tren)[In_{2.67}Sb_{1.33}S_8] \cdot tren$ (1): A Mixed-Metal 3-D Framework
3.2.1.1 Synthesis

The compound $(H_{1.3}tren)[In_{2.67}Sb_{1.33}S_8] \cdot tren$ (**1**), was synthesised from a mixture of Sb_2S_3 (67 mg 0.20 mmol), $InCl_3$ (160 mg, 0.72 mmol), CoS (34 mg, 0.37 mmol), S (42 mg, 1.31 mmol) and tris(2-aminoethyl)amine (tren) (3.2 ml, 21 mmol). The reagent mixture, initially pH ~ 7, was stirred for 10 minutes in a 23 ml Teflon-lined stainless-steel autoclave before being heated at 433 K for 5 days at a heating rate of 1 K min^{-1}. The products were then cooled overnight at 1 K min^{-1} before being filtered and washed successively with ethanol, water and acetone. Single crystals in the form of yellow blocks were handpicked and corresponded to a yield of *ca.* 20 % by weight of solid product. Combustion analysis gave values of C: 13.98 %, H: 3.98 %, N: 10.37 %, respectively. These are in good agreement with the values calculated for the formula, $(H_{1.3}tren)[In_{2.67}Sb_{1.33}S_8] \cdot tren$, (C: 14.14 %, H: 3.69 %, N: 10.99 %) established from a combination of EDX, single-crystal X-ray diffraction, TGA and solid-state ^{13}C NMR results (*vide infra*). Powder X-ray diffraction data for the as-synthesised product demonstrated that in addition to compound (**1**), Sb and InSb were present as minor impurity phases, together with an as yet unidentified phase. Although cobalt ions were included in the reaction mixture, no cobalt was detected in the title compound. Repeating the synthesis in the absence of cobalt led to a considerably lower yield of (**1**) (~3 %) suggesting that the transition-metal ion aids crystallisation of the new indium-antimony sulfide. Such use of

transition metals as mineralisers has previously been reported in the solvothermal synthesis of antimony sulfides [138].

Single-crystal X-ray diffraction data were collected at 150 K using graphite monochromated MoK$_\alpha$ (λ = 0.71073 Å) radiation. The structure was solved using the program SIR92 [227] and the model refined in F using the CRYSTALS suite of programs [230]. The structure solution reveals the inorganic framework has a metal to sulfur ratio M:S of 4:8, where M represents a mixture of In and Sb . They were subsequently fixed in accordance with the EDX results (vide infra) corresponding to the composition $[In_{2.67}Sb_{1.33}S_8]^{1.33-}$. The organic counterions are highly disordered and could not be located in difference Fourier maps. Therefore, the metal and sulfur framework atoms were refined anisotropically and Platon SQUEEZE [251] applied to model the electron density within the pores. Crystallographic details are summarised in Table 3.1, bond lengths, angles, occupancies and thermal parameters are presented in Table A1.1.

Table 3.1: Crystallographic data for [(tren)(H$_{1.3}$tren)][In$_{2.67}$Sb$_{1.33}$S$_8$] **(1)**

Formula weight	1018.78
Crystal Habit	Yellow block
Crystal system	Tetragonal
Space group	$I\bar{4}2d$
Temp /K	150
a /Å	12.6248(5)
c /Å	19.4387(18)
V /Å³	3098.2(3)
Z	4
Wavelength /Å	0.71073
μ /mm^{-1}	3.645
Total reflections ($I > 3\sigma(I)$)	1044
R factor	0.0519
wR factor	0.0542

3.2.1.2 Structure Description and Analysis

Analytical electron microscopy EDX measurements (Table 3.2) confirmed the presence of sulfur, indium and antimony in crystals of compound **(1)**. The measured sulfur content was however lower than that expected for the crystallographically-determined framework composition, $[M_4S_8]$ (M = (In + Sb)). EDX measurements on a ground Sb$_2$S$_3$ reference sample

69

also resulted in a reduced sulfur content, suggesting that sulfur volatilisation occurs under the high vacuum conditions of the electron microscope. This phenomenon has been previously observed by other workers [252]. Therefore, only the In: Sb ratio could be determined reliably from the electron microscopy data, giving a value of 2.67(5):1.33(5) in the inorganic framework.

Table 3.2: EDX data for pristine $(H_{1.33}tren)[In_{2.67}Sb_{1.33}S_8]\cdot tren$ crystals with an accompanying SEM image.

Scan	S /wt %	In /wt %	Sb /wt %	In:Sb ratio
1	33.43	43.02	23.55	1.94
2	33.94	43.79	22.27	2.09
3	33.17	44.29	22.54	2.08
4	29.71	45.86	24.43	1.99
5	32.87	44.53	22.60	2.09
6	32.00	42.96	25.04	1.82
7	33.36	43.71	22.93	2.02
8	28.25	48.24	23.51	2.18
9	33.02	43.94	23.04	2.02
10	32.52	44.25	23.23	2.02
11	28.78	45.95	25.28	1.93
12	33.79	42.95	23.26	1.96
13	31.60	45.01	23.40	2.04
14	32.66	42.63	24.71	1.83
15	33.18	44.68	22.15	2.14
Average	32.15(1.90)	44.39(1.84)	23.46(2.47)	2.01(0.19)
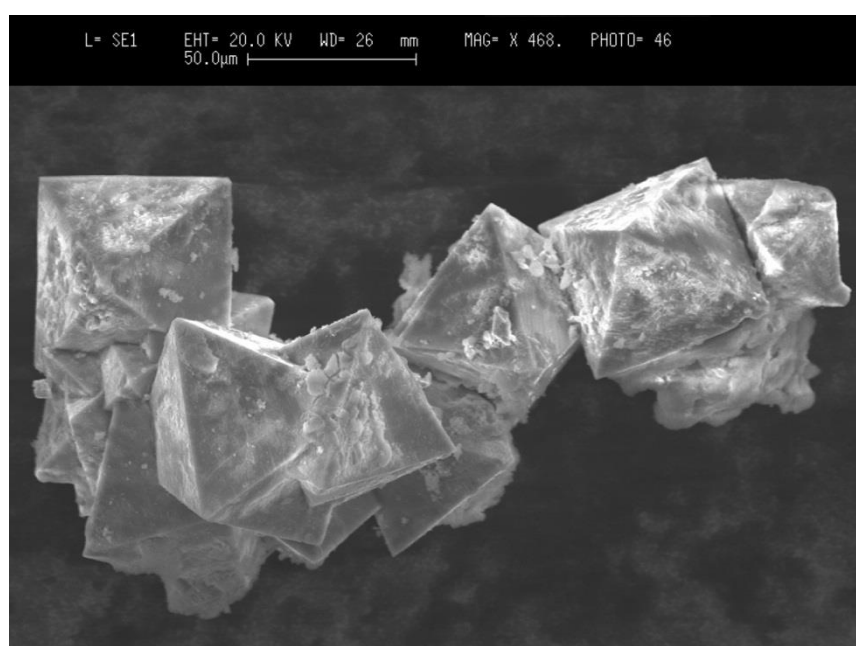
The crystal structure contains only one metal site, hereafter denoted M, which was assigned site occupancy factors of 0.6675 and 0.3325 for In and Sb respectively, on the basis of the EDX results. In the structure, the M atom is coordinated by 4 sulfur atoms and has a slightly distorted tetrahedral geometry with bond lengths of 2.382(3) Å (M–S2), 2.412(4) Å, and 2.451(4) Å (M–S1) and 2.427(2) Å (M–S3) with S–M–S bond angles in the range (99.22(11) $\leq \alpha/° \leq$ 117.03(4)). The location of antimony in a tetrahedral environment provides compelling evidence for it being present as Sb(V). The M–S bond lengths are comparable with Sb(V)–S distances of (2.399(7) $\leq d/$Å $\leq$ 2.435(6)) found in discrete SbS_4^{3-} tetrahedra [127] and In(III)–S distances reported previously for an $In_4S_{10}^{8-}$ T2 supertetrahedron [21] which lie in the range (2.444(2) $\leq d/$Å $\leq$ 2.476(4)). The presence of Sb(V) and In(III) gives rise to a negatively charged framework with composition $[In_{2.67}Sb_{1.33}S_8]^{1.33-}$.

The MS$_4$ tetrahedra are linked through shared vertices to form adamantane-like T2 supertetrahedral clusters (Figure 3.1). The supertetrahedra are linked through terminal (S3) atoms, reminiscent of the linkage of ZnS$_4$ tetrahedra in zinc blende, to form a 3-D metal-sulfur framework in which there are pores and channels (Figures 3.2 and 3.3). When van der Waals' radii are taken into consideration (Fig. A1.1), the pore dimensions are *ca.* 5×4 Å^2 parallel to [100] (Figure 2) and *ca.* 6×6 Å^2 parallel to [111] (Figure 3).
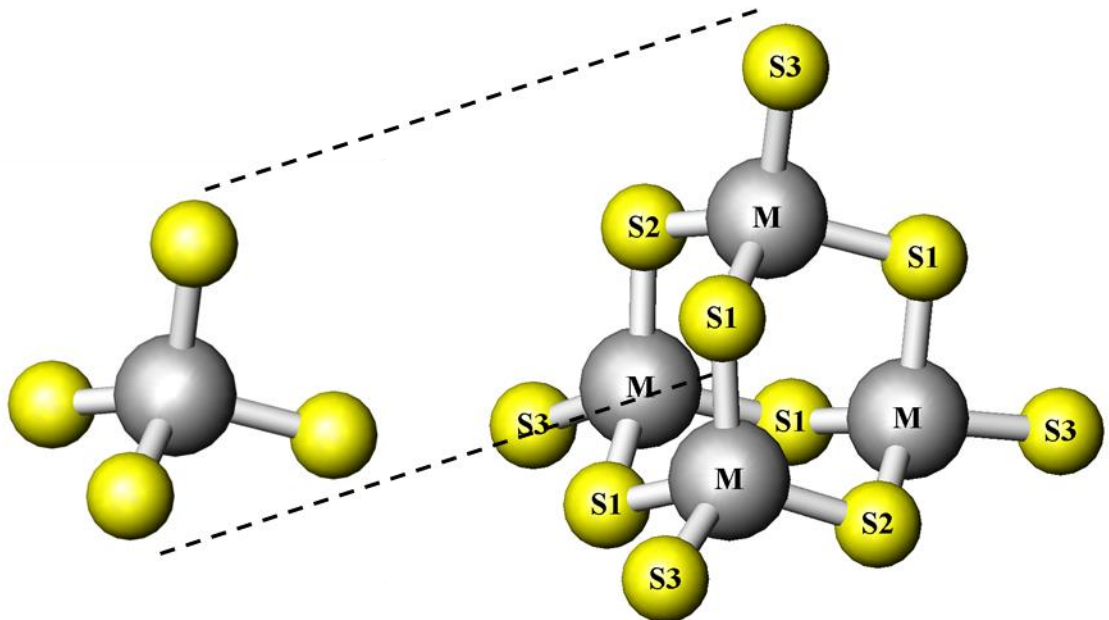
Figure 3.1: Linking of tetrahedral MS$_4$ primary building units to form M$_4$S$_{10}$ adamantane-like T2 clusters (M = (0.67 In+0.33 Sb)) in (H$_{1.33}$tren)[In$_{2.67}$Sb$_{1.33}$S$_8$]·tren. Key: grey: M atoms, yellow: S atoms.
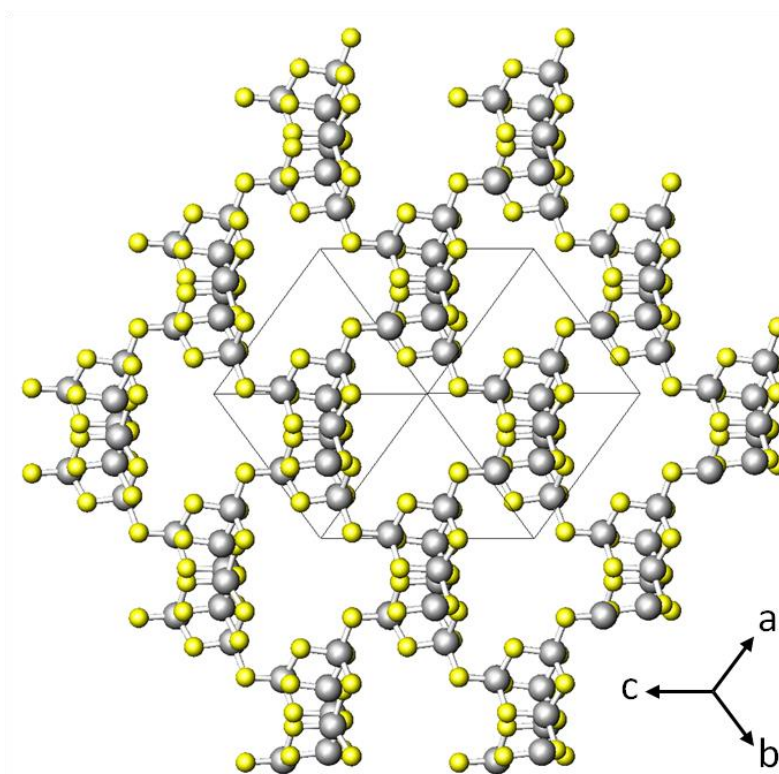
Figure 3.2: View of the pore space in the $[In_{2.67}Sb_{1.33}S_8]^{1.33-}$ framework viewed along the [111] direction. Key: grey: *M* atoms, yellow: S atoms.
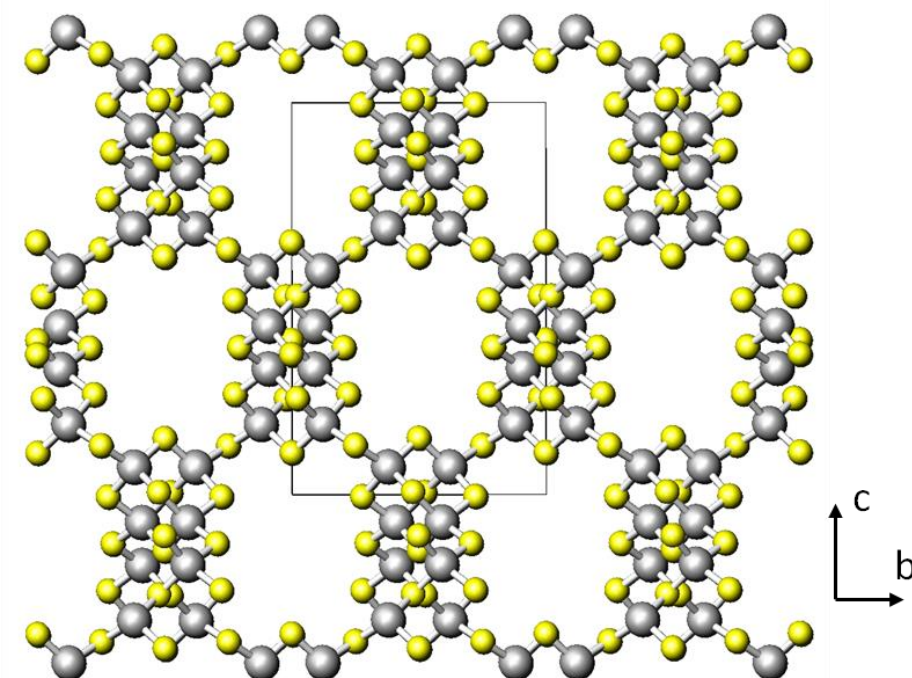
Figure 3.3: View of the pore space in the $[In_{2.67}Sb_{1.33}S_8]^{1.33-}$ framework viewed along the [100] direction. Key: grey: M atoms, yellow: S atoms.

The powder X-ray diffraction data for handpicked crystals of (1) show good agreement with the pattern calculated on the basis of the single-crystal diffraction study (Figure 3.4). Impurities are evident within the bulk sample which contains Sb, InSb and an unknown phase.
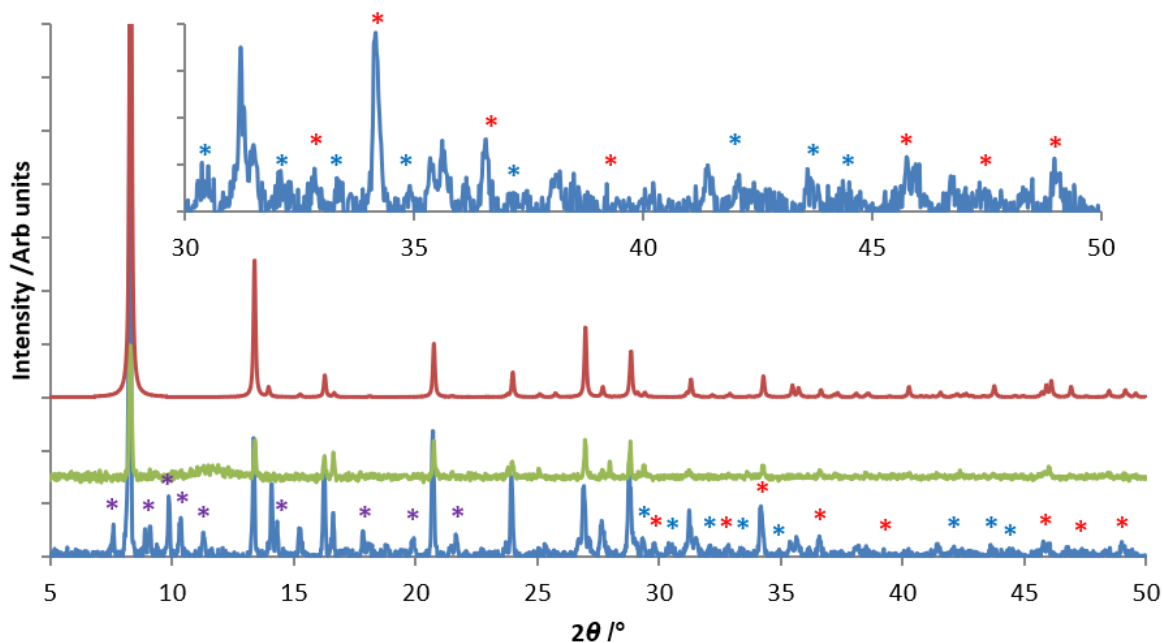
Figure 3.4: Powder X-ray diffraction patterns of the bulk as-synthesised product (blue), handpicked crystals (green) and the simulated pattern calculated from single-crystal diffraction data (red). Additional peaks in the as-synthesised product pattern corresponding to Sb (red asterisks), InSb (blue asterisks) and an as-yet unidentified phase (purple asterisks).

Although the tren molecules could not be located directly in the single-crystal X-ray diffraction study, their presence is supported by the infrared spectrum of (1) (Figure 3.5) with their peak assignments in Table 3.3. The ν(O-H) stretch is likely to be external water molecules, especially as the TGA data (discussed later) shows an initial but small weight loss below 100 °C. The IR compares well with the data from the NIST database on tris(2-aminoethyl)amine [253]. There is a shift in the ρ(N-H) bend however, but this is likely due to its protonation. Further evidence for the presence of tren in (1) is provided by the ^{13}C solid-state NMR spectrum (Figure 3.6). This reveals two peaks at 38.75 and 55.01 ppm of relative intensity 1:1, consistent with equal numbers of carbon atoms in two different environments, as is found in the tren molecule. The difference in the width of the two peaks may be associated with the greater degree of freedom of the outer carbon atoms, leading to

broadening of the peak at 55.01 ppm. Attempts to conduct ^{15}N based NMR were made but the signals produced were too weak to be identifiable.
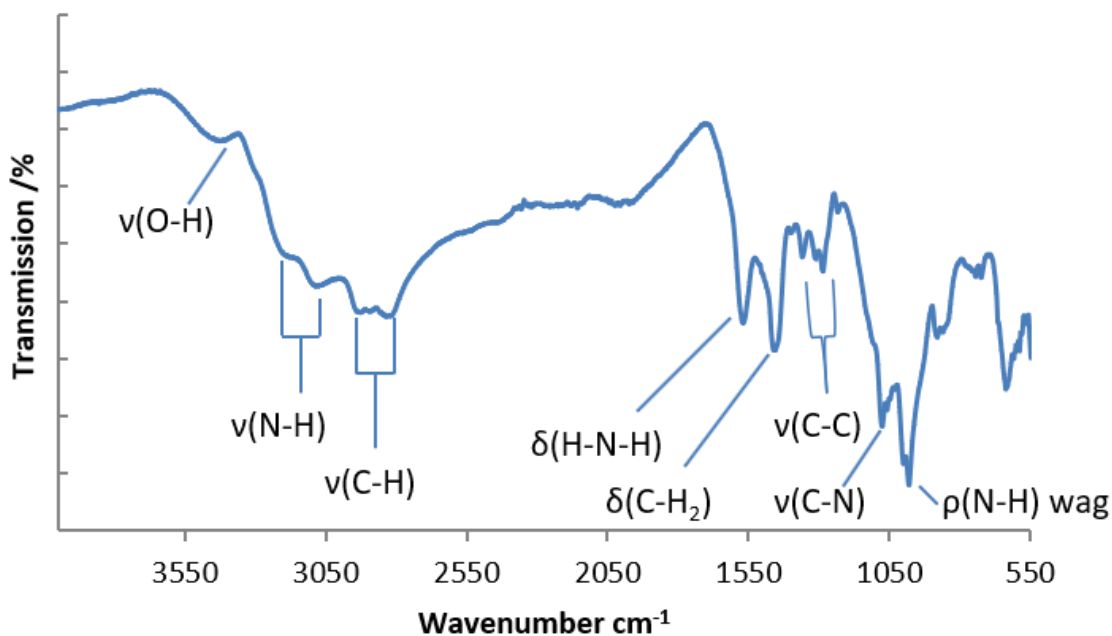
Figure 3.5: Infrared spectrum of $(H_{1.33}tren)[In_{2.67}Sb_{1.33}S_8]\cdot tren.$ **(1)**

Table 3.3: Infrared spectrum assignments of $(H_{1.33}tren)[In_{2.67}Sb_{1.33}S_8]\cdot tren$ **(1)**

Stretching mode	Wavenumber /cm^{-1}
v(O-H)	3485
v(N-H)	3109 (sym) and 3182 (asym)
v(C-H)	2868 (sym) and 2950 (asym)
δ(H-N-H)	1580
δ (C-H$_2$)	1466
v(C-C)	1293-1364 (multiple peaks)
v(C-N)	1078
ρ(N-H) wag	979
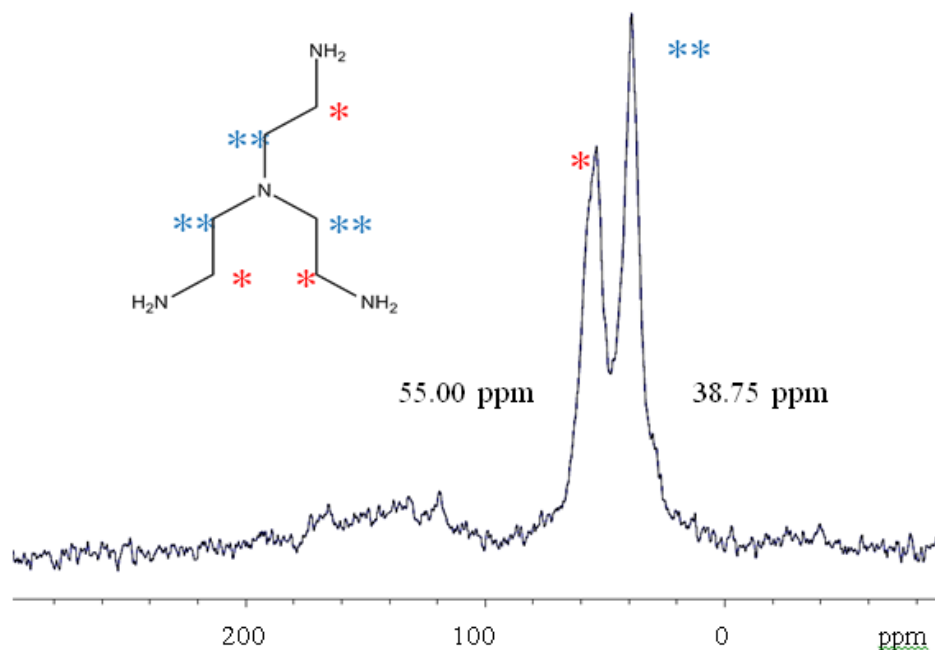
Figure 3.6: Solid-state ^{13}C NMR (10 kHz) of $(H_{1.33}tren)[In_{2.67}Sb_{1.33}S_8]\cdot tren$ **(1)** recorded under N_2. Key: (**) inner carbon, (*) outer carbon.

Thermogravimetric analysis of compound **(1)** (Figure 3.7) reveals a total weight loss of 28.92 % on heating the sample to 400 °C. This is in good agreement with a value of 28.88 % calculated for the loss of two tren molecules per formula unit, consistent with the formulation $(H_{1.33}tren)[In_{2.67}Sb_{1.33}S_8]\cdot tren$, when the degree of protonation necessary to balance the negative charge of the framework. The weight loss occurs in two stages of 9.62 % and 19.28 % at onset temperatures of 220 and 270 °C, respectively (with corresponding maxima in the DTG curve at 252 and 274 °C). The first weight loss of 9.62 % corresponds to the loss of an ethylenediamine molecule that would arise on cyclisation of tren to piperazine (Figure A1.2). Thermal degradation of larger amines to generate ethylenediamine [254] and the rearrangement of polyamines under solvothermal conditions [255] have been reported previously. Combustion analysis of the product obtained on stopping the thermal analysis after the first weight loss gave: C: 12.26 %, H: 2.82 % and N: 7.76 %, corresponding to $C_{10}N_{5.4}H_{28}$, which, within experimental error, is consistent with the presence of piperazine and tren in the pores ($C_{10}N_6H_{29.33}$ calculated). The second weight loss of 19.28 % is consistent with the loss of piperazine and tren on further heating to 260 °C. The powder X-ray diffraction pattern of the final solid product from thermogravimetric analysis was poorly crystalline and could not be indexed (Figure A1.3). However, as some of the peaks of **(1)** are

still visible in the powder X-ray diffraction data after partial removal of the organic component, experiments were later conducted to explore possible ion-exchange behaviour of **(1)** (Section 3.2.1.3.).
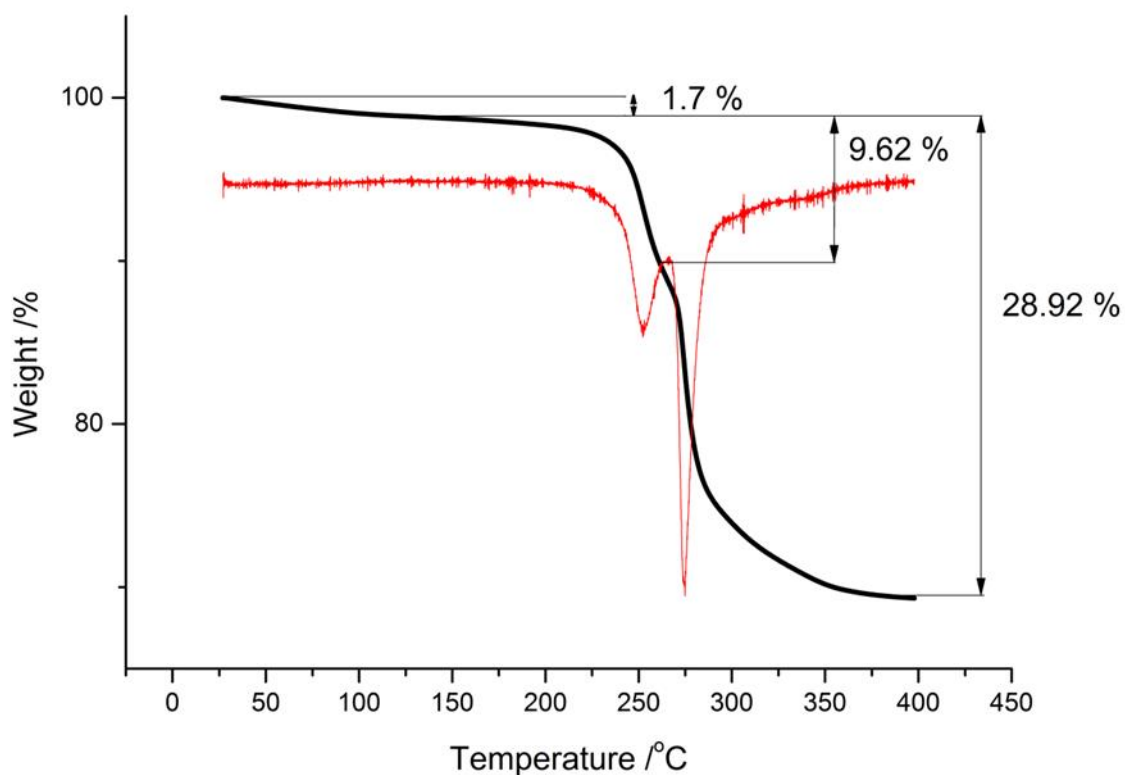
Figure 3.7: Thermogravimetric analysis curve of $(H_{1.33}tren)[In_{2.67}Sb_{1.33}S_8] \cdot tren$ heated under N_2 (black) and the corresponding derivative (DTG) curve (red).

The diffuse reflectance spectrum of **(1)** (Figure 3.8a) exhibits an optical band gap of 2.7(2) eV. This value is consistent with expectations from the variation of optical band gap with metal centre density established by Powell *et al.* (Figure 3.8b). The analysis initially demonstrated that the band gap of thioantimonates [18] decreases with increasing density of antimony atoms. This was later extended to bimetallic thiometallates [17] which contain antimony.
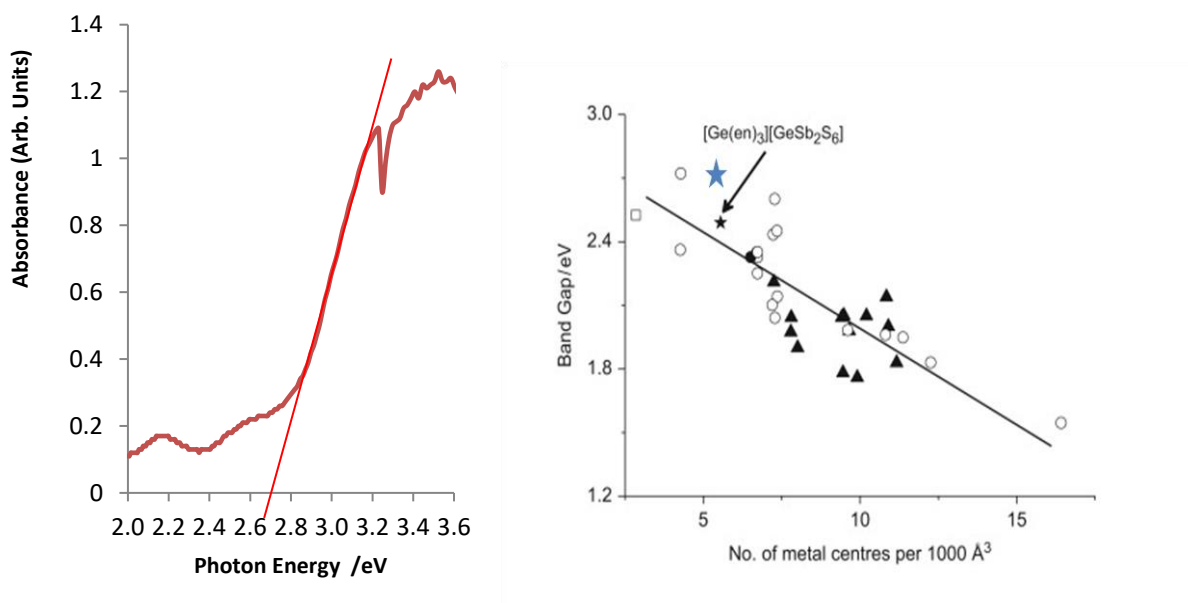
Figure 3.8: (a) Diffuse reflectance spectrum of $(H_{1.33}tren)[In_{2.67}Sb_{1.33}S_8] \cdot tren$ and (b) an optical band gap *versus* metal centre density plot [18, 17]. Key: open square, discrete unit; open circles, chain structures; solid triangles, layered structures; solid circle, three-dimensional structure; black star, two-dimensional germanium-antimony sulfide framework studied in [17]; blue star, compound (**1**).

3.2.1.3 Ion Exchange Capability in Alkali-salt Solution

In order to assess the potential ion-exchange capability of $(H_{1.33}tren)[In_{2.67}Sb_{1.33}S_8] \cdot tren$, crystals were immersed in aqueous solutions of potassium and lithium chloride (0.1 M, 2 M and 3 M) at pH ≈ 6. These solutions were heated at 343 K over periods ranging from 3 h to 5 d. Crystals were also immersed in deionised water for 3 h at 343 K and room temperature for comparison. All crystal samples were then washed with ethanol, water and acetone. In each case, the soaking in water or aqueous solution resulted in a change in the colour of the crystals from yellow to orange, Figure 3.9. The TGA (Figure A1.4) and combustion analysis data for the solid products after immersion in water and alkali-metal chloride solutions (summarised in Table A1.2) are broadly similar.

77

a)
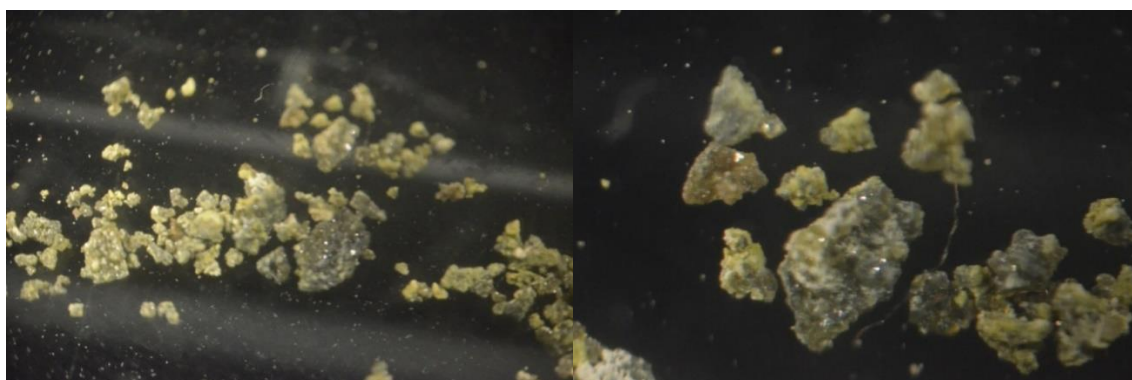
b)
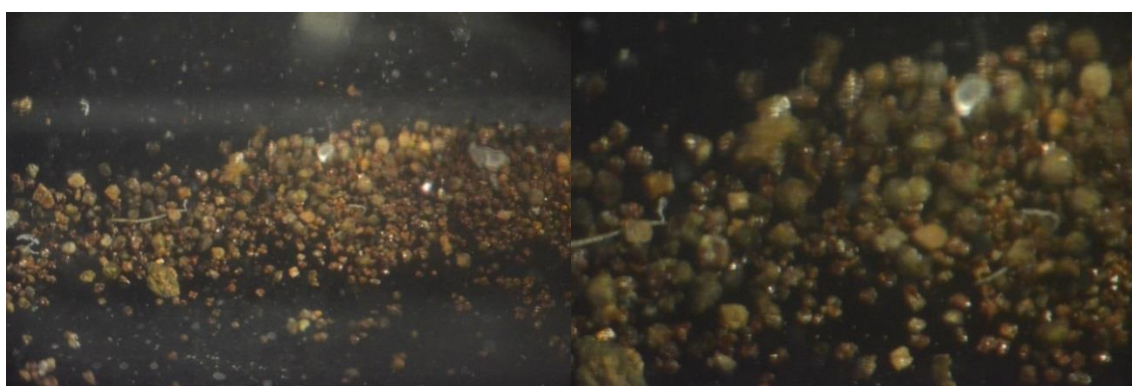
c)
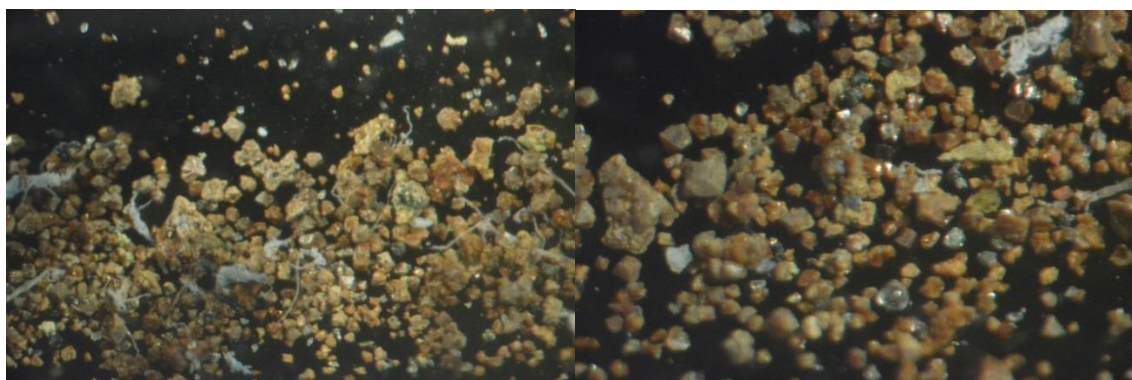
Figure 3.9: Photographic images of different magnifications a) Pristine handpicked crystals $(H_{1.33}tren)[In_{2.67}Sb_{1.33}S_8]\cdot tren$ b) 3M Potassium solution immersed sample c) 3M Lithium solution immersed sample. Images taken using an SLR attachment atop a microscope which is using a light polarised filter.

On immersion in both water and the aqueous alkali-metal chloride solutions, there is a significant reduction in the organic content of the crystals (up to 50 %), suggesting the partial removal of tren molecules from the pore space. This loss of organic component is

accompanied by an uptake of water into the crystals. Evidence for water incorporation is provided both by the weight losses observed in the products that were soaked in aqueous solutions *via* TGA curves at low temperature (~ 100 °C) (Figure A1.3) and by the infrared data (Figure 3.10) where, in each case for the infrared data, there is an increase in the intensities of the ν(O-H) and δ(H-O-H) bands at 3400 and 1640 cm^{-1}, respectively. This shows an increased activity of dipole moment changes caused by the presence of more water molecules.
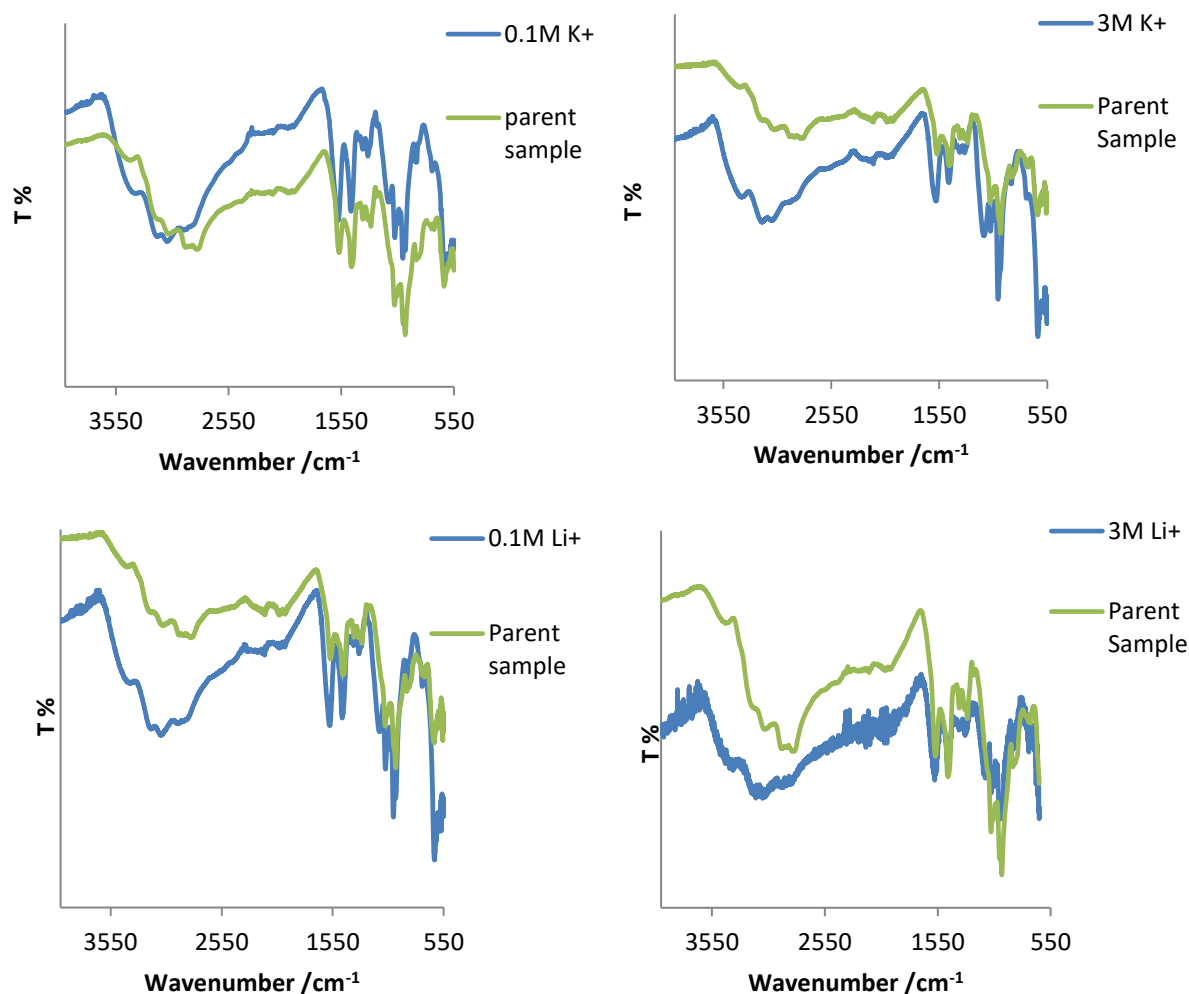
Figure 3.10: IR spectra of crystals after being soaked in 0.1 M (3 hours) and 3 M (5 days) in KCl and LiCl solutions.

The uptake of alkali-metal ions on soaking in salt solutions, determined from atomic absorption spectroscopy (Table 3.4), is extremely low (<2.4 wt% for K$^+$, for example). This is much lower than would be expected on charge-balancing grounds were the alkali-metal ions to replace protonated amine.

Table 3.4: Experimental results of atomic absorption for K^+ for after soaking crystals of $(H_{1.33}tren)[In_{2.67}Sb_{1.33}S_8]\cdot tren$ (1) in 0.1 M and 3 M KCl solutions.

Sample	Wt% of K+
0.1 M 3 hours	0.23
3 M 3 hours	2.35
3 M 5 days	1.22

This suggests that the alkali-metal ions are merely absorbed on the crystal surface and that immersion of compound (1) in alkali-metal solutions does not result in ion-exchange. Therefore, the immersion in both water and alkali-metal chloride solutions leads to the removal of only the non-protonated amine from the pores and the product can be formulated as $(H_{1.33}tren)[In_{2.67}Sb_{1.33}S_8]\cdot(tren)_{1-y}(H_2O)_x$. There is some variation in the x and y values for samples produced on stirring in different alkali-metal chloride solutions (Table A1.2), with x in the range 2.5–4.7 and y in the range 0.7–1.0, although the generally the removal of neutral tren increases with increase in concentration of the alkali-metal salt solution. On stirring in 2 M KCl for 3 h, the limiting value of 50 % reduction in organic component is achieved, and the product has the composition $(H_{1.33}tren)[In_{2.67}Sb_{1.33}S_8]\cdot(H_2O)_4$. For the samples immersed in water for 3 h at 343 K and room temperature, the TGA results show that in both cases, removal of all the neutral tren is not achieved. Tren removal is however greater at 343 K than at room temperature ($y = 0.67$ and $x = 3.96$ and $y = 0.22$ and $x = 2.34$, respectively).

The soaked samples exhibit a decrease in crystallinity compared to the pristine samples as the concentration of alkali-metal chloride solution and soaking time increases, as evidenced by peak broadening in the powder X-ray diffraction patterns (Figure 3.11). However, unit-cell parameters could be measured (using SXRD) for crystals soaked for 3 h in water, 0.1 M KCl, NaCl and LiCl and 2 M KCl (Table 3.5) as the single-crystal diffraction patterns were clear enough to obtain lattice parameter values, unlike the powder data. Table 3.6 includes a list of lattice parameters for two calculated formulas and the pristine crystals, displaying the maximum amount of water uptake as 4 water molecules and its effect on cell volume.

Table 3.5: Lattice parameters determined at 150 K for single crystals following immersion in water and alkali-metal chloride solutions at 343 K.

Salt solution	a /Å	c /Å	Cell Volume /Å³
Pristine crystals	12.6248 (5)	19.4387(18)	3098.2 (3)
KCl 0.1 M 3h	12.3435 (16)	18.639 (4)	2839.8 (8)
NaCl 0.1 M 3h	12.398 (3)	18.676 (9)	2870.7 (17)
LiCl 0.1 M 3h	12.4119 (10)	18.738 (7)	2886.7 (11)
Water only	12.4275 (13)	18.572 (3)	2868.3 (8)
KCl 2M 3h	12.348 (3)	18.574 (8)	2832.2 (15)
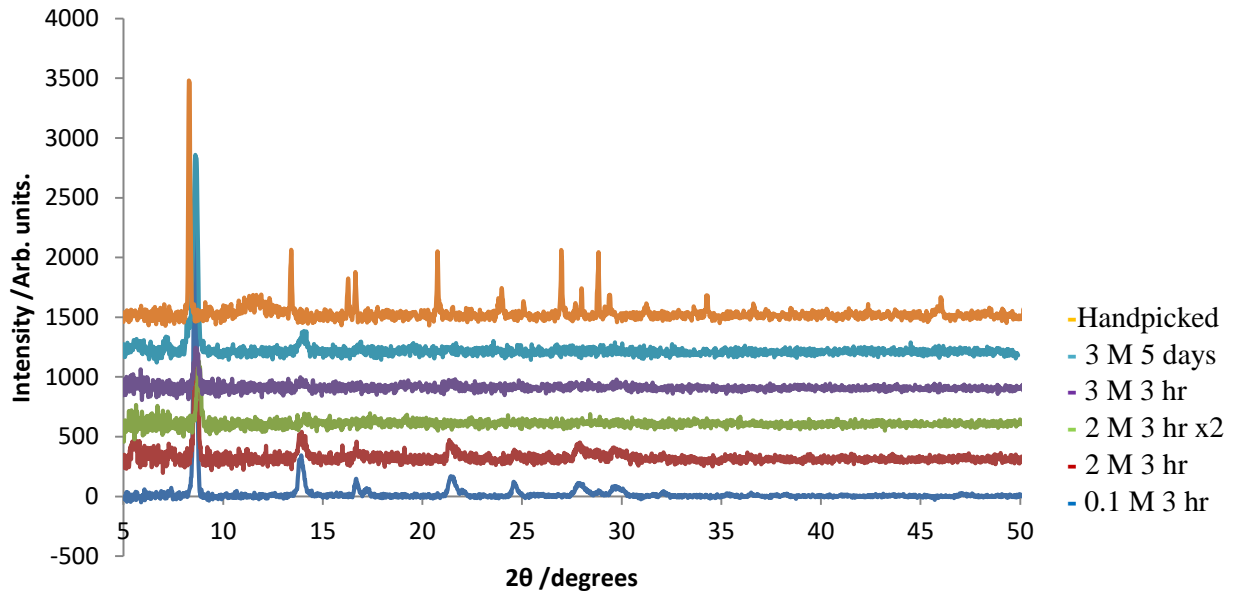
Figure 3.11: PXRD Patterns of Li^+ ion soaked samples.

Table 3.6: Lattice parameters determined at 150 K for single crystals produced following immersion for 3 h in water[§] and 2 M KCl solution[‡] for calculated chemical formulas.

	a/Å	c/Å	Cell Volume /Å³
$(H_{1.33}tren)[In_{2.67}Sb_{1.33}S_8] \cdot tren$	12.6248 (5)	19.4387 (18)	3098.2 (3)
$(H_{1.33}tren)[In_{2.67}Sb_{1.33}S_8] \cdot (tren)_{0.33} \cdot (H_2O)_4$[§]	12.4275 (13)	18.572 (3)	2868.3 (8)
$(H_{1.33}tren)[In_{2.67}Sb_{1.33}S_8] \cdot (H_2O)_4$[‡]	12.348 (3)	18.574 (8)	2832.2 (15)

Single-crystal X-ray data were indexed using the same tetragonal unit cell and space group as for the pristine material, and a reduction of up to ~9 % in the unit-cell volume was observed in the case of $(H_{1.33}tren)[In_{2.67}Sb_{1.33}S_8]\cdot(H_2O)_4$, obtained after immersion of compound (**1**) in 2 M KCl, Table 5. A medium-resolution structure solution for a crystal soaked in 0.1 M KCl solution (Table A1.3) confirmed that the In-Sb-S framework structure has been retained.

Diffuse reflectance data for products obtained after soaking in 0.1 M solutions for 3 h, show that the band gap is unaffected on replacing neutral tren molecules by water within the structure (Figure 3.12).
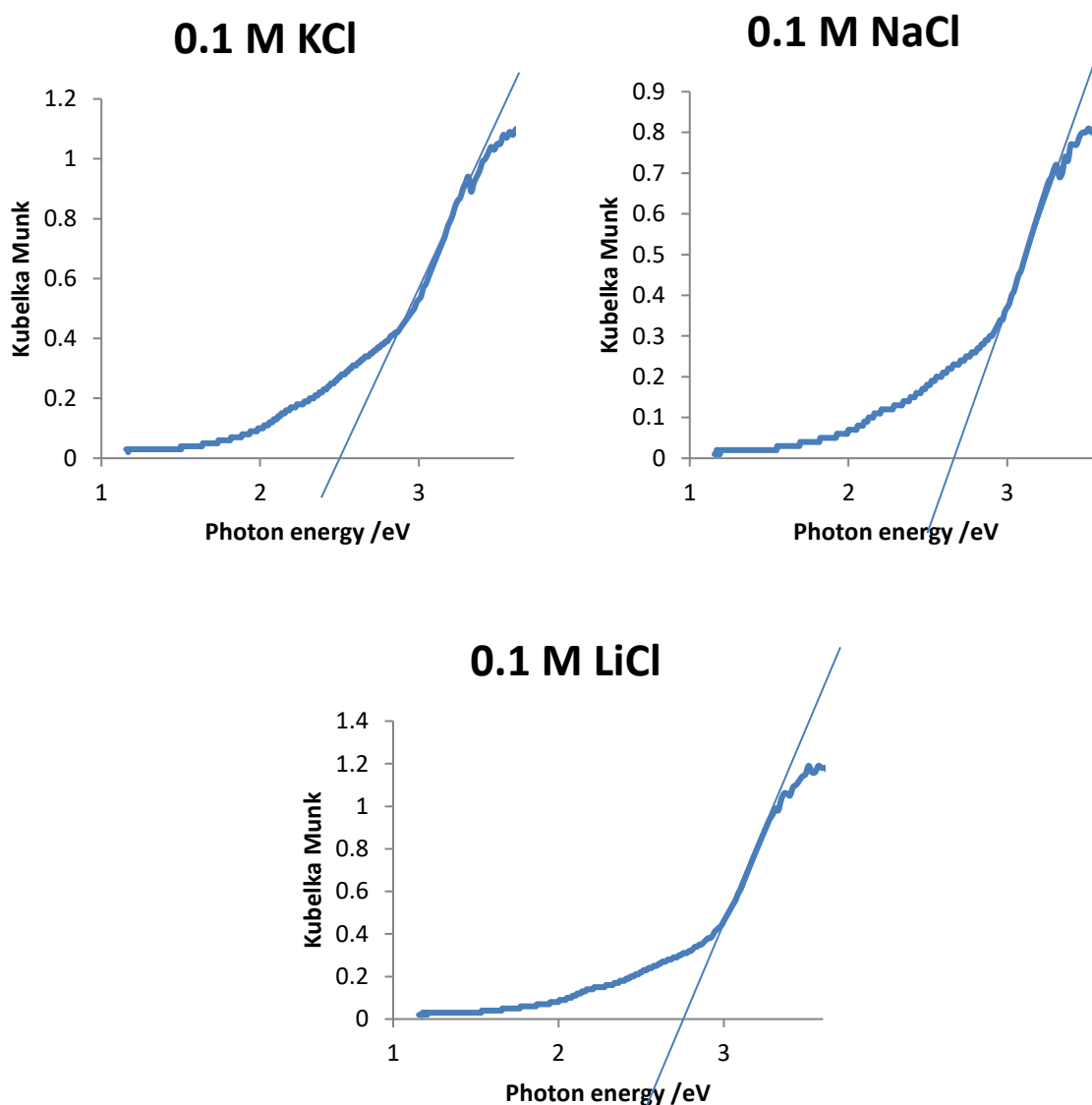
Figure 3.12: Diffuse reflectance data of samples of (**1**) immersed in 0.1M for 3 hours. Band gap values are 2.5(1) (K^+), 2.6(1) (Na^+), 2.7(1) (Li^+) eV, compared to the pristine phase (2.7(2) eV, Figure 3.8a).

3.2.2 [Co(tren)(H₃tren)][In₄SbS₁₀]·3H₂O (2) and [Co(tren)(H₃tren)][In₃Sb₂S₉]·H₂O (3): 2-D Layered frameworks

3.2.2.1 Synthesis

Compound [Co(tren)(H₃tren)][In₄SbS₁₀]·3H₂O (**2**) was synthesised from a mixture of Sb (46.4 mg, 0.38 mmol), InCl₃ (119 mg, 0.53 mmol), CoS (36 mg, 0.40), S (96 mg, 3 mmol), tris(2-aminoethyl)amine (tren) (3.2 ml, 21 mmol) and water (2 ml). The reagent mixture was stirred for 10 min in a Teflon-lined stainless-steel autoclave before being sealed and heated to 433 K for 8 days. The ramp rate for both heating and cooling was 1 K min⁻¹. The products were cooled overnight before being filtered and washed successively with ethanol, water and acetone. Single crystals of (**2**) in the form of yellow plates, were observed along with pale-yellow powder. Powder X-ray diffraction analysis (Figure 3.13) confirms the presence of (**2**) in the bulk sample, along with an unidentifiable powder, and Sb₂O₃ and Co₃S₄ impurities. Attempts were made to optimise the reaction to produce a higher yield of crystals but these were unsuccessful. All reactions gave products containing either powder only or very small quantities of crystals; this rendered crystal picking impractical and therefore no chemical analysis could be performed.
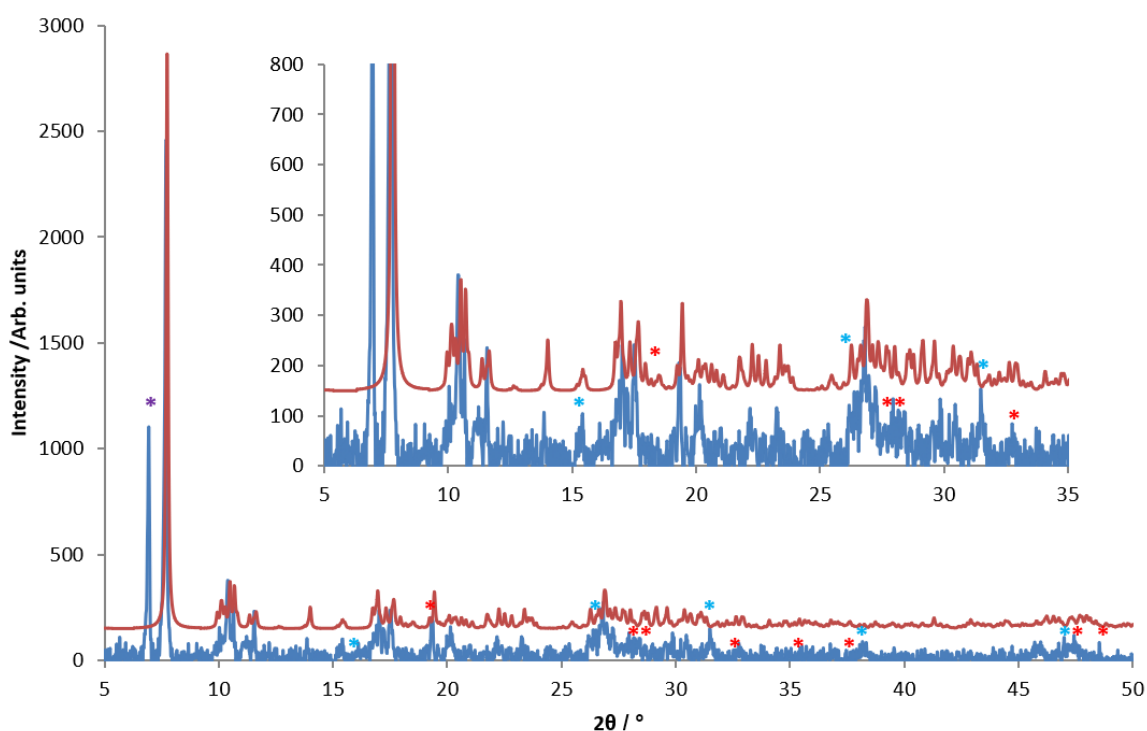
Figure 3.13: Powder X-ray diffraction patterns of the bulk as-synthesised product (blue) and the simulated pattern calculated from single-crystal diffraction data (red). Additional peaks in the as-synthesised product pattern annotated with asterisks correspond to Sb₂O₃ (red), Co₃S₄ (blue) and an as-yet unidentified phase (purple).

Compound [Co(tren)(H$_3$tren)][In$_3$Sb$_2$S$_9$]·H$_2$O (**3**) was synthesised from a mixture of Sb$_2$S$_3$ (66.8 mg 0.19 mmol), InCl$_3$ (80 mg, 0.36 mmol), CoS (35.3 mg 0.39mmol), S (25 mg, 0.78 mmol), tren (3.2 ml, 21 mmol) and water (2 ml). The reagent mixture was stirred for 10 min in a Teflon-lined stainless-steel autoclave before being sealed and heated to 433 K for 8 days. The ramp rate for both heating and cooling was at 1 K min^{-1}. The products were cooled overnight and before being filtered and washed successively with ethanol, water and acetone. Single crystals of (**3**) in the form of yellow plates were observed along with pale yellow powder. Powder X-ray diffraction analysis (Figure 3.14) confirms the presence of (**3**) in the bulk sample, along with an unidentifiable powder, and In$_2$O$_3$ and Co$_9$S$_8$ as impurities. As with (**2**), attempts to optimise the reaction to increase the yield of crystals were unsuccessful. Reactions produced samples containing either powder only or very small quantities of crystals, rendering crystal picking to provide material for chemical analysis impractical.
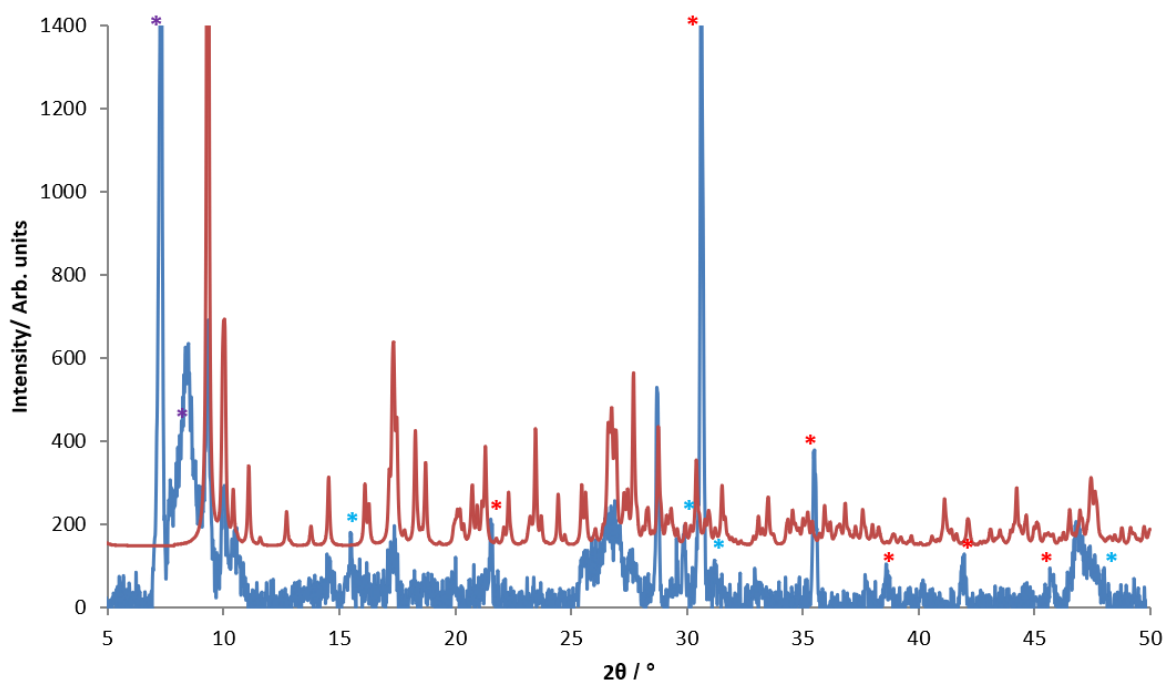
Figure 3.14: Powder X-ray diffraction patterns of the bulk as-synthesised product (blue) and the simulated pattern calculated from single-crystal diffraction data (red). Additional peaks in the as-synthesised product pattern annotated with asterisks correspond to In$_2$O$_3$ (red), Co$_9$S$_8$ (blue) and an as-yet unidentified phase (purple).

The optimisation of the synthesis of both compounds was unsuccessful. Hand-picking crystals that were both small in size and yield to produce sufficient material for complementary analysis techniques would have been too inefficient and time consuming. Reactions were

restricted to the temperature and timeframe described in earlier but reaction stoichiometry, reagent stock (e.g. switching Sb for SbS_3) and quantity used (thereby increasing or decreasing pressure in the Teflon liner through overall mass used) were changed. Ideally, some of the reactions listed in Table A1.4 could have been repeated at different temperatures but this was not possible due to time constraints and other experiments taking priority.

Samples of (2) and (3) were submitted to the National Crystallographic Service at the University of Southampton for the collection of single-crystal X-ray diffraction data. Data collections were conducted at 100 K on a Rigaku Saturn724+ X-ray diffractometer using graphite monochromatic MoK$_\alpha$ (λ = 0.71073 Å) radiation. Structure solving/refinements were conducted by the author.

Structure (2) was solved using SIR92 [227] while structure (3) was solved using Superflip [228]. Both refinements were conducted in *F* and a Chebychev polynomial weighting scheme was applied. Collections of (2) and (3) contained minor amounts of twinning (<5 % in each case). Structure (3) exhibits significant disorder (large ellipsoids) associated with the non-chelating ethylamine fragments of the tren molecule located between the layers, in particular, C(11), C(12), C(10), N(7) and N(8). This is likely due to the mobility present as they are not chelating fully to the Co metal centre. Restraints were used to keep the C-C and C-N bond distances at 1.54 Å and 1.45 Å respectively with a 0.01 Å variation for movement. Structure (2) exhibits a much lower level of disorder associated with C(2) and C(4) of the fully chelated tren but did not require restraints. The disorder can be viewed in the asymmetric units as large ellipsoids which is clearly seen in structure of (3), Figure 3.15. N(7) and C(11) had to be refined at half occupancy in order to stabilise the ethylamine "arm". Three oxygens were also discovered through the Fourier maps and these are associated with water in the structure of (2) while only one could be found in the structure of (3). Hydrogen atoms on the amine ligands were placed geometrically with a U[equiv] value 1.2 times the U[equiv] of the carbon to which they are attached. Crystallographic details are summarised for structures (2) and (3) in Table 3.7. Atomic coordinates of all non-hydrogen atoms can be found in Tables A1.5 and A1.6.

Table 3.7: Crystallographic data for structures [Co(tren)(H$_3$tren)][In$_4$SbS$_{10}$]·3H$_2$O (**2**) and [Co(tren)(H$_3$tren)][In$_3$Sb$_2$S$_9$]·H$_2$O (**3**).

Chemical formula	[Co(tren)(H$_3$tren)][In$_4$SbS$_{10}$]·3H$_2$O	[Co(tren)(H$_3$tren)][In$_3$Sb$_2$S$_9$]·H$_2$O
Formula mass	2554.12	1153.87
Crystal Habit	Yellow plate	Yellow plate
Crystal system	Monoclinic	Triclinic
Symmetry space group	$P2_1$	$P\bar{1}$
Temp /K	100	100
a /Å	10.08571(14)	10.1486 (7)
b /Å	45.6324(4)	10.2883 (7)
c /Å	10.30365(14)	19.1273 (13)
α /°	90	81.660 (10)
β /°	118.3639(18)	86.467 (11)
γ /°	90	60.370 (8)
V /Å³	4172.60(6)	1717.49 (12)
Z	2	1
μ /mm^{-1}	3.723	4.572
Total reflections ($I > 3\sigma(I)$)	18768	4811
R factor	0.0657	0.1280
wR factor	0.0642	0.1373
Goodness of fit ref	0.9397	1.0780
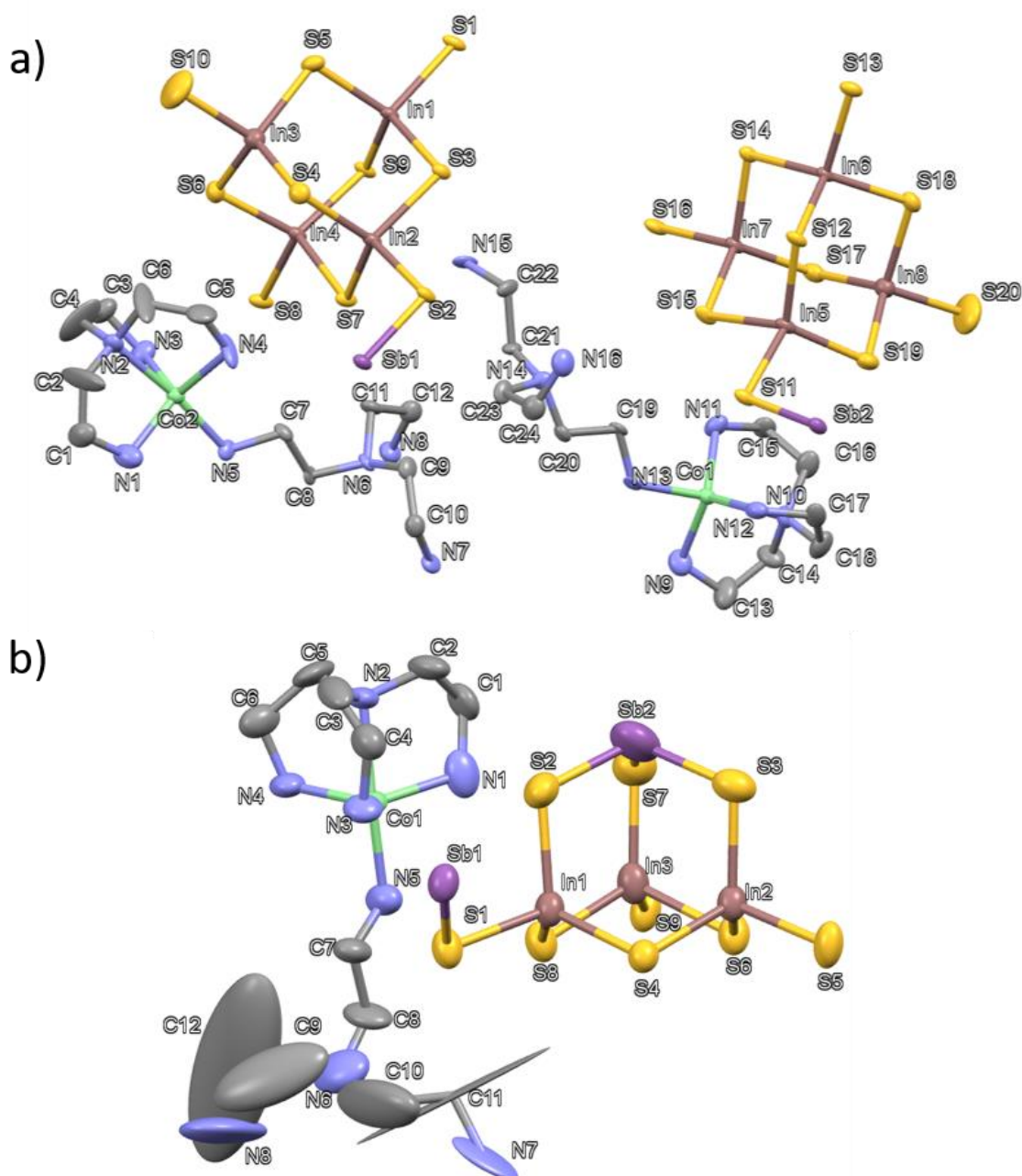
Figure 3.15: Asymmetric units of; (a) structure (**2**) and (b) structure (**3**) displaying thermal ellipsoids of each atom at 50 % probability. Key: brown: In atoms, purple: Sb atoms, green: Co atoms, yellow: S atoms, light blue: N atoms, grey: C atoms. Hydrogen and water oxygens are omitted for clarity.

3.2.2.2 Structure Description and Analysis

Structures (**2**) and (**3**) both contain similar structural motifs with accompanying $[Co(tren)(H_3tren)]^{5+}$ complexes and water within pore spaces. The difference between the two structures stems from the replacement of an indium atom by an antimony atom in

[Co(tren)(H$_3$tren)][In$_3$Sb$_2$S$_9$]·H$_2$O (**3**). Bond-valence calculations for each metal centre in the crystal structures of (**2**) and (**3**) indicate formal oxidation states +3 for both indium and antimony, Table 3.8 and Table 3.9 respectively. The oxidation state of cobalt was determined to be Co(II), this was based on bond lengths which is discussed later.

Table 3.8: Bond-valence calculation results for cation metal centres in [Co(tren)(H$_3$tren)][In$_4$SbS$_{10}$]·3H$_2$O (**2**).

	$\sum v_{ij}$		$\sum v_{ij}$		$\sum v_{ij}$
In(1)	3.04	In(5)	3.04	Sb(1)	3.22
In(2)	3.04	In(6)	3.04	Sb(2)	3.22
In(3)	3.10	In(7)	3.08		
In(4)	2.99	In(8)	3.06		

Table 3.9: Bond-valence calculation results for cation metal centres in [Co(tren)(H$_3$tren)][In$_3$Sb$_2$S$_9$]·H$_2$O (**3**).

	$\sum v_{ij}$		$\sum v_{ij}$
In(1)	3.15	Sb(1)	3.29
In(2)	3.15	Sb(2)	3.37
In(3)	3.27		

Structure (**2**) contains only trigonal pyramidal SbS$_3$$^{3-}$ and tetragonal InS$_4$$^{5-}$ moieties. The InS$_4$$^{5-}$ tetrahedra are linked through shared vertices to form adamantane like T2 supertetrahedral clusters, [In$_4$S$_{10}$]$^{6-}$. The T2 units are linked through three bridging S atoms (S 16, 11 and 13 on one adamantane, 8, 1 and 2 on the other) by bonding to Sb atoms. This creates a layer of T2 units linked together by Sb atoms. The fourth remaining sulfur atom of the adamantane units remains as a terminal atom, S(20) and S(10). The linking of the indium T2 clusters through Sb creates a 9-membered In$_6$Sb$_3$S$_9$ ring system that repeats throughout the layer, these 9-membered ring systems contain [Co(tren)(H$_3$tren)]$^{5+}$ cations (Figure 3.16a). One tren molecule acts as a tetradentate ligand to the cobalt cation while a second tren molecule acts as a monodentate ligand coordinating the cobalt centre through only one ethylamine moiety. This results in a trigonal bipyramidal cobalt(II) complex. The remaining two ethylamine "arms" of the second tren molecule extend into the free space between two layers (Figure 3.16b), interacting with free water molecules between double layers with donor-acceptor distances seen in Table 3.10, supporting the presence of hydrogen bonding. There are also weak hydrogen bonding interactions between the complexes and framework,

holding them in place. Overall this forms a double layered system which can be seen in Figure 3.17.

Table 3.10: Bond lengths found in [Co(tren)(H$_3$tren)][In$_4$SbS$_{10}$].3H$_2$O (2) between acceptor and donor atoms containing hydrogen bonding.

Symmetry operations: a = -x, -y-1, -z; b = -x+1, -y-1, -z; c = -x+1, -y-1, -z+1; d = -x+2, -y-1, -z+1

	Length /Å		Length /Å
N(16)…O(2)[a]	2.719(19)	N(8)…O(1)[d]	3.100(19)
N(16)…O(1)[b]	3.306(19)	N(8)…O(3)[d]	2.873(19)
N(15)…O(2)[b]	2.814(19)	N(6)…O(1)[d]	3.298(19)
N(14)…O(1)[b]	2.924(19)	N(5)…S(2)	3.345(8)
N(7)…O(2)[c]	2.923(19)	N(15)…S(7)	3.319(5)
N(7)…O(1)[d]	2.878(19)		
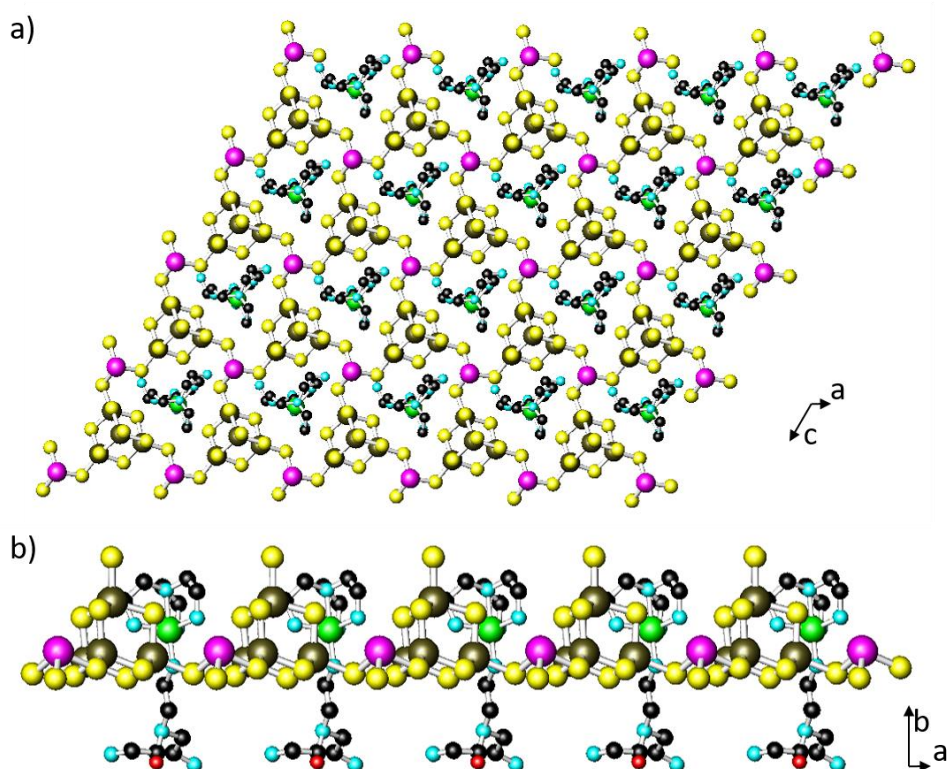
Figure 3.16: Views of a single layer within structure (2) showing (a) view perpendicular to the (010) plane with complexes seen within the 9-membered In$_6$Sb$_3$S$_9$ ring and (b) view along the [001] direction with the ethylamine moieties of the tren ligands extending into the inter-layer space. Key: brown: In atoms, purple: Sb atoms, green: Co, yellow: S atoms, light blue: N atoms, black: C atoms. Hydrogen atoms are omitted for clarity.
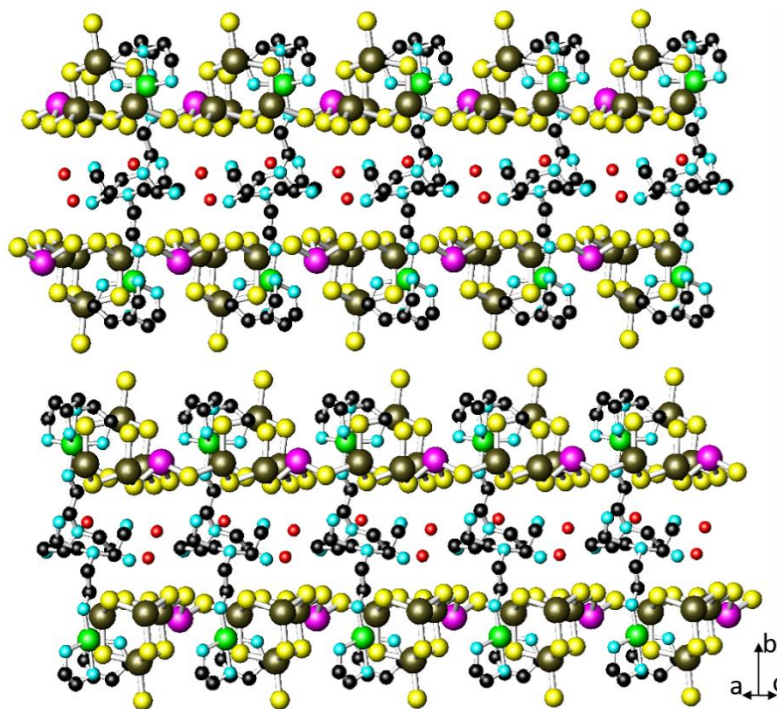
Figure 3.17: Double layer formation within structure (**2**) viewed along [101]. Key: brown: In atoms, purple: Sb atoms, green: Co, yellow: S atoms, light blue: N atoms, black: C atoms. Hydrogen atoms are omitted for clarity.

The structure of $[Co(tren)(H_3tren)][In_3Sb_2S_9]\cdot H_2O$ (**3**), contains a layer motif, similar to that of structure (**2**). The primary building units of this structure are also trigonal pyramidal SbS_3^{3-} and tetragonal InS_4^{5-} moieties. In structure (**2**), four InS_4^{5-} tetrahedra are linked through shared vertices to create T2 adamantane units, but in (**3**), one metal site is fully occupied with an antimony atom sitting atop the three InS_4^{5-} units. This antimony centre does not have a terminal sulfur atom (no electron density seen in Fourier maps) so remains as an SbS_3^{3-} unit. The three tetrahedral InS_4^{5-} moieties with one SbS_3^{3-} unit result in a T2-like structure, $[In_3Sb_1S_9]^{6-}$, but with a vertex removed. The three terminal sulfur atoms of this unit are shared with an SbS_3 unit that serves to link T2 units to form layers analogous to those seen in (**2**). As with structure (**2**), the 9-membered $In_6Sb_3S_9$ rings that form within the layer houses the five-coordinate cobalt(II) complexes which are coordinated by the two tren ligands in the same manner to that described above for (**2**) (Figure 3.18). Two of these layers form double layers by creating channels of the branched monodentate tren and water molecules; these contain donor-acceptor interaction which occur between the branched amine within the channel with the free water molecules (N(7)…O(1), 2.98(8) Å and N(8)…O(1) 2.62(6) Å and the adjacent framework layer (N(7)…S(4) 3.34(4) Å, Figure 3.19. This is an indication of hydrogen

bonding within the structure. Due to the disorder present within this structure, in particular that associated with the ethylamine moieties located between the layers, it is difficult to determine the exact number of water molecules present.
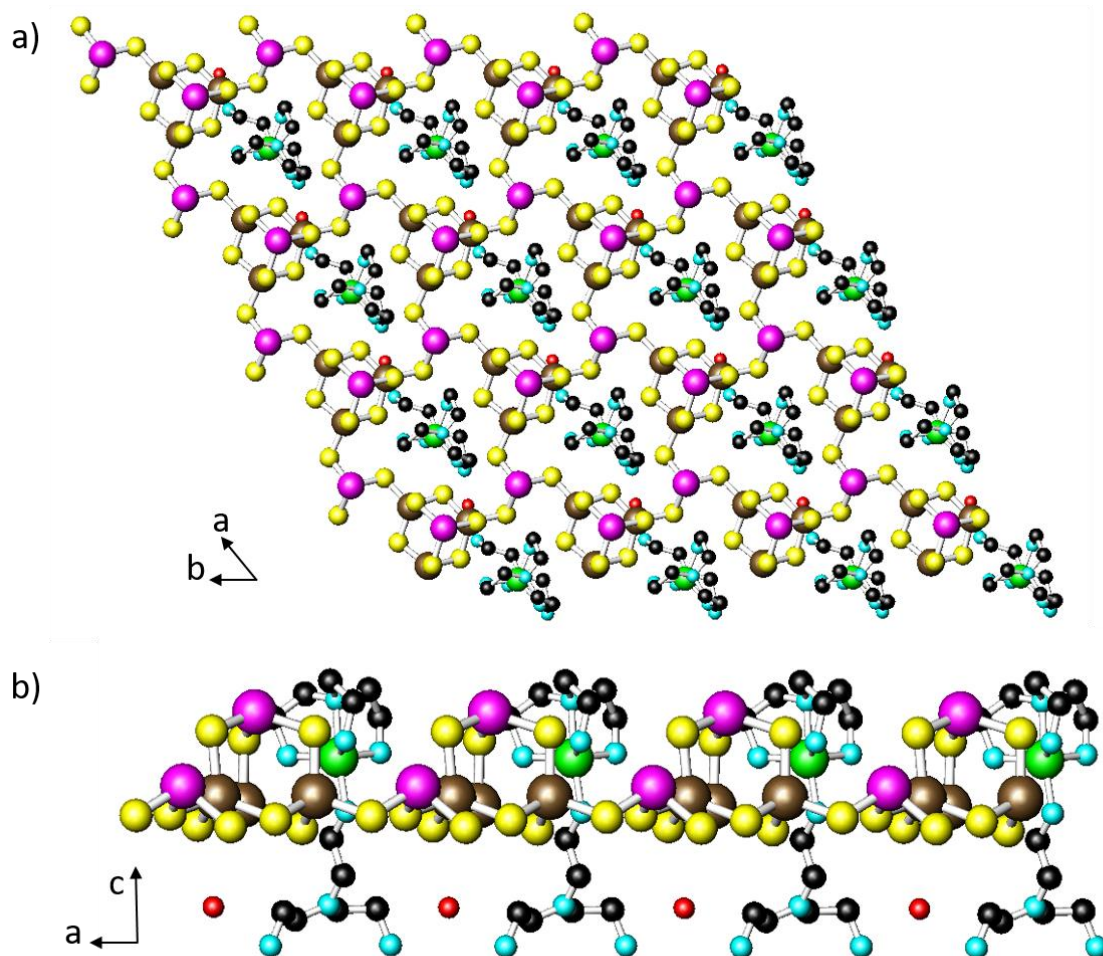
Figure 3.18: Views of a single layer within structure (3) (a) view along the [001] direction with complexes seen within the 9-membered $In_6Sb_3S_9$ rings and (b) view perpendicular to the (010) plane with the branching amines extending into the inter-layer space. Key: brown: In atoms, purple: Sb atoms, green: Co, yellow: S atoms, light blue: N atoms, black: C atoms. Hydrogen atoms are omitted for clarity.
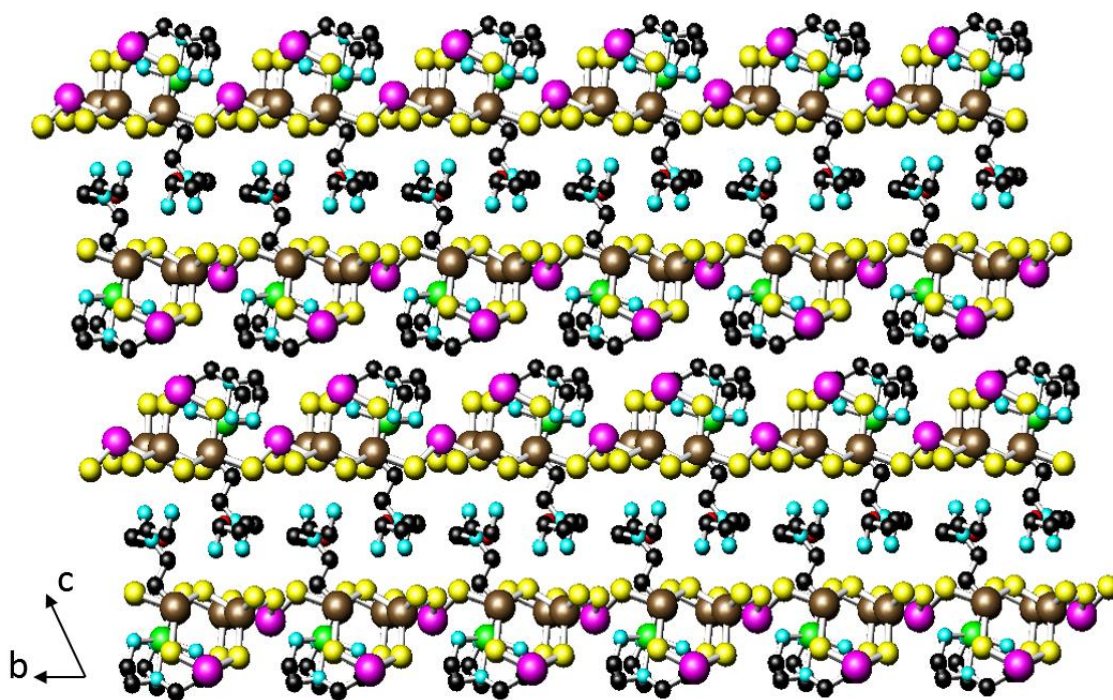
Figure 3.19: Double layer formation within structure (**3**) viewed along [100]. Key: brown: In atoms, purple: Sb atoms, green: Co, yellow: S atoms, light blue: N atoms, grey: C atoms. Hydrogen atoms are omitted for clarity.

The structures of (**2**) and (**3**) contain similar structural features and both form double layered frameworks with channels containing hydrogen bonding interactions between the amine, water and framework. However, (**2**) and (**3**) display different stacking arrangements of the double layers, Figure 3.20. Primary antimony-antimony bonds typically occur at distances under 3.5 Å [256]. The distance between the antimony atoms from neighbouring layers antimony atom in (**3**) is 3.707(4) Å. Calculations [257] and experimental studies [258] suggest this is consistent with the presence of a very weak Sb-Sb bond. In structure (**2**), the T2 units are located above the complexes of the adjacent layer due to the additional sulfur atom of the T2 units within layers. The replacement of indium with antimony from the T2 unit in (**3**) causes the double layers to draw closer together by introducing Sb-Sb interactions. This Sb-Sb bond also attempts to align the T2 units of opposing layers unlike (**2**) which aligns T2 units above the adjacent layers complexes. Charge balancing of the five negative charges on the frameworks of structures (**2**) and (**3**), requires, in addition to the double positive charge of the cobalt cation, protonation of the second amine between layers. Protonation of both free ethylamine "arms" and of the central nitrogen provides the additional positive charge required.
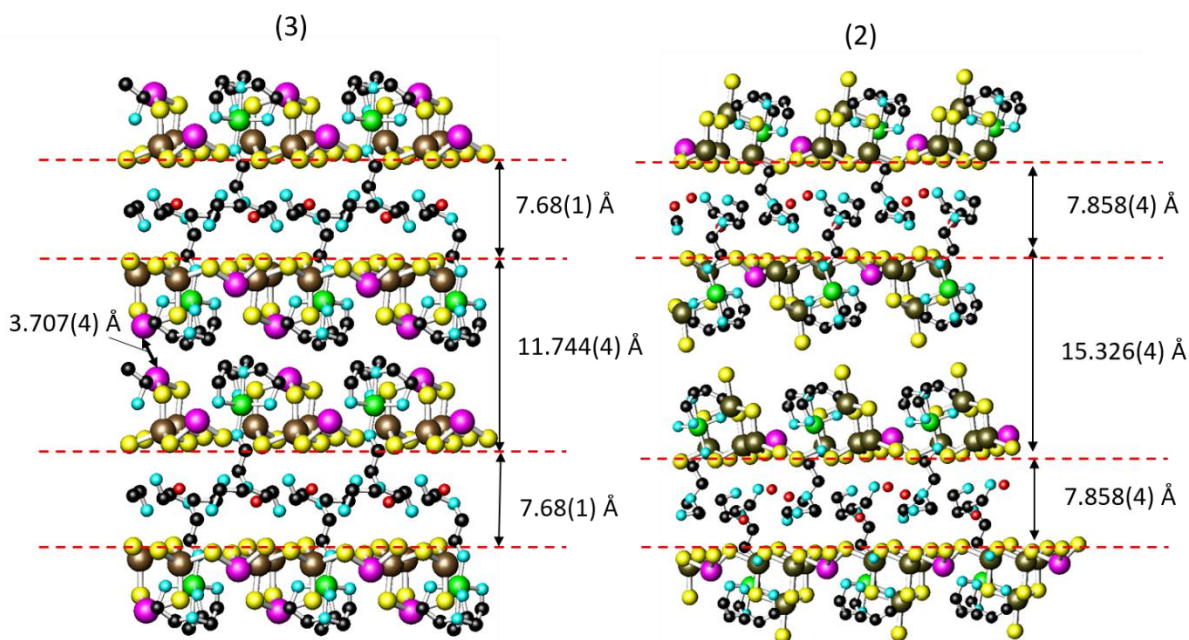
Figure 3.20: View of the layers in structures **(3)** (left) and **(2)** (right) with distances between planes of sulfur atoms at the base of each layer indicated. Key: brown: In atoms, purple: Sb atoms, green: Co, yellow: S atoms, light blue: N atoms, grey: C atoms. Hydrogen atoms are omitted for clarity.

In-S bond lengths within both **(2)** and **(3)** are similar ranging between $(2.436(2) \leq d/\text{Å} \leq 2.502(2))$ and $(2.407(8) \leq d/\text{Å} \leq 2.476(5))$ respectively (Table 3.11 and 3.12). The SbS_3^{3-} units linking the T2 units into a layer in each structure have Sb-S distances [259, 132] typical of those associated with Sb(III)-S systems, at an average distance of ~2.42 Å in both structures. The $[Co(tren)(H_3tren)]^{5+}$ complexes found in both **(2)** and **(3)** are slightly strained due to the rigidity of tren molecules when acting as a tetradentate ligand to the metal centre. The biting point (torsion angle between the metal centre and amine) is smaller on average than the preferred 120 ° that is usually seen in the equatorial plane of a trigonal bipyramidal complex. Bond angles in multidentate ligands around a metal centre are dependent on the metal-ligand bond lengths because of this rigidity [260]. The central bonding N atom from the fully coordinated tren molecules in each complex observe a Co-N bond length ~0.2 Å longer (2.232(9) Å, 2.233(9) Å in **(2)** and 2.199(15) Å in **(3)**), compared to all other Co-N lengths ranging from $(2.035(18) \leq d/\text{Å} \leq 2.098(10))$ for **(2)** and **(3)** combined. This has also affected the position of the other three nitrogen atoms by pulling the tren molecule away from its ideal geometric positions around Co, again due to rigidity. The bond lengths also support the presence of Co(II) metal centres, as ligand-Co distances have been observed previously

between $(2.036(4) \leq d/\text{Å} \leq 2.146(8))$ in five coordinate Co(II) complexes, for example in $[\text{Co}^{II}\text{S}_2^{Me2}\text{N}_3(\text{Pr,Pr})]\cdot\text{CH}_3\text{CN}$ [261]. The bonding angles between equatorial N-Co-N atoms are between $(113.1\,(4) \leq \alpha/° \leq 120.2(4))$ for **(2)** and $(116.8(8) \leq \alpha/° \leq 120.0(8))$ for **(3)** as they can no longer strictly stay in the equatorial plane in trigonal bipyramidal geometry. A selection of bond angles can be found in Table 3.13 and 3.14 for **(2)** and **(3)** respectively.

Table 3.11 A selection of bond lengths in $[\text{Co(tren)}(\text{H}_3\text{tren})][\text{In}_4\text{SbS}_{10}]\cdot 3\text{H}_2\text{O}$ **(2)**

symmetry codes: a = x, y, z+1; b = x-1, y, z

	Length /Å		Length /Å		Length /Å		Length /Å
Sb(1)-S(1)[a]	2.440(2)	In(2)-S(3)	2.477(2)	In(6)-S(12)	2.462(2)	In(8)-S(20)	2.477(4)
Sb(1)-S(8)[b]	2.420(2)	In(2)-S(4)	2.447(3)	In(6)-S(13)	2.494(2)	Co(1)-N(11)	2.055(9)
Sb(1)-S(2)	2.412(2)	In(2)-S(7)	2.439(2)	In(6)-S(14)	2.457(2)	Co(1)-N(12)	2.057(10)
Sb(2)-S(13)[a]	2.438(2)	In(3)-S(4)	2.441(3)	In(6)-S(15)	2.439(3)	Co(1)-N(13)	2.076(7)
Sb(2)-S(16)[b]	2.432(2)	In(3)-S(5)	2.445(3)	In(7)-S(14)	2.466(2)	Co(1)-N(9)	2.057(10)
Sb(2)-S(11)	2.401(2)	In(3)-S(6)	2.448(3)	In(7)-S(15)	2.437(2)	Co(1)-N(10)	2.231(9)
In(1)-S(1)	2.490(2)	In(3)-S(10)	2.481(4)	In(7)-S(16)	2.480(2)	Co(2)-N(1)	2.063(12)
In(1)-S(3)	2.461(2)	In(5)-S(11)	2.502(2)	In(7)-S(17)	2.441(3)	Co(2)-N(2)	2.234(9)
In(1)-S(5)	2.440(3)	In(5)-S(12)	2.454(2)	In(8)-S(17)	2.451(3)	Co(2)-N(3)	2.099(10)
In(1)-S(9)	2.459(2)	In(5)-S(15)	2.459(2)	In(8)-S(18)	2.456(3)	Co(2)-N(4)	2.048(9)
In(2)-S(2)	2.486(2)	In(5)-S(19)	2.436(3)	In(8)-S(19)	2.436(3)	Co(2)-N(5)	2.060(8)

Table 3.12 A selection of bond lengths in $[\text{Co(tren)}(\text{H}_3\text{tren})][\text{In}_3\text{Sb}_2\text{S}_9]\cdot\text{H}_2\text{O}$ **(3)**

symmetry codes: a = x+1, y-1, z; b = x, y-1, z

	Length /Å		Length /Å		Length /Å		Length /Å
Sb(1)-S(9)[a]	2.408(6)	In(1)-S(1)	2.475(5)	In(2)-S(5)	2.461(6)	Co(1)-N(1)	2.09(2)
Sb(1)-S(5)[b]	2.407(6)	In(1)-S(2)	2.454(7)	In(2)-S(6)	2.433(5)	Co(1)-N(2)	2.198(15)
Sb(1)-S(1)	2.432(6)	In(1)-S(4)	2.420(5)	In(3)-S(6)	2.454(6)	Co(1)-N(3)	2.036(18)
Sb(2)-S(2)	2.348(8)	In(1)-S(8)	2.445(5)	In(3)-S(7)	2.407(8)	Co(1)-N(4)	2.080(19)
Sb(2)-S(3)	2.427(8)	In(2)-S(3)	2.451(6)	In(3)-S(8)	2.423(5)	Co(1)-N(5)	2.081(19)
Sb(2)-S(7)	2.455(9)	In(2)-S(4)	2.448(5)	In(3)-S(9)	2.458(5)		

Table 3.13 A selection of bond angles in [Co(tren)(H₃tren)][In₄SbS₁₀]·3H₂O (**2**)

symmetry codes: a = x, y, z+1; b = x-1, y, z

	Angle / °		Angle / °		Angle / °		Angle / °
S(1)-In(1)-S(3)	107.05(8)	S(6)-In(4)-S(9)	115.85(9)	S(15)-In(7)-S(16)	108.14(8)	N(10)-Co(1)-N(13)	175.7(3)
S(1)-In(1)-S(5)	106.67(9)	S(7)-In(4)-S(9)	108.06(8)	S(14)-In(7)-S(17)	112.23(8)	N(11)-Co(1)-N(13)	103.3(3)
S(3)-In(1)-S(5)	113.32(8)	S(8)-In(4)-S(9)	113.08(8)	S(15)-In(7)-S(17)	113.53(9)	N(12)-Co(1)-N(13)	99.0(3)
S(1)-In(1)-S(9)	104.42(7)	S(11)-In(5)-S(12)	109.28(7)	S(16)-In(7)-S(17)	107.98(9)	N(1)-Co(2)-N(2)	80.0(4)
S(3)-In(1)-S(9)	108.83(7)	S(11)-In(5)-S(15)	97.47(7)	S(17)-In(8)-S(18)	112.57(9)	N(1)-Co(2)-N(3)	118.1(5)
S(5)-In(1)-S(9)	115.79(9)	S(12)-In(5)-S(15)	107.68(8)	S(17)-In(8)-S(19)	116.61(9)	N(2)-Co(2)-N(3)	80.6(3)
S(2)-In(2)-S(3)	101.29(7)	S(11)-In(5)-S(19)	110.76(8)	S(18)-In(8)-S(19)	110.73(9)	N(1)-Co(2)-N(4)	118.9(5)
S(2)-In(2)-S(4)	106.29(8)	S(12)-In(5)-S(19)	116.67(9)	S(17)-In(8)-S(20)	103.57(17)	N(2)-Co(2)-N(4)	81.9(4)
S(3)-In(2)-S(4)	109.40(8)	S(15)-In(5)-S(19)	113.24(9)	S(18)-In(8)-S(20)	104.64(16)	N(3)-Co(2)-N(4)	115.6(5)
S(2)-In(2)-S(7)	109.07(7)	S(12)-In(6)-S(13)	103.84(7)	S(19)-In(8)-S(20)	107.61(18)	N(1)-Co(2)-N(5)	94.4(4)
S(3)-In(2)-S(7)	109.96(8)	S(12)-In(6)-S(14)	110.67(7)	N(9)-Co(1)-N(10)	80.5(4)	N(2)-Co(2)-N(5)	173.8(3)
S(4)-In(2)-S(7)	119.26(9)	S(13)-In(6)-S(14)	109.74(8)	N(9)-Co(1)-N(11)	113.0(4)	N(3)-Co(2)-N(5)	99.9(3)
S(4)-In(3)-S(5)	112.38(9)	S(12)-In(6)-S(18)	112.57(8)	N(10)-Co(1)-N(11)	80.3(4)	N(4)-Co(2)-N(5)	103.3(4)
S(4)-In(3)-S(6)	115.42(9)	S(13)-In(6)-S(18)	103.51(8)	N(9)-Co(1)-N(12)	118.9(4)	S(1)ᵃ-Sb(1)-S(8)ᵇ	95.60(8)
S(6)-In(4)-S(7)	113.89(9)	S(14)-In(6)-S(18)	115.57(8)	N(10)-Co(1)-N(12)	81.0(3)	S(1)ᵃ-Sb(1)-S(2)	99.54(8)
S(6)-In(4)-S(8)	105.87(9)	S(14)-In(7)-S(15)	112.12(8)	N(11)-Co(1)-N(12)	120.3(4)	S(8)ᵇ-Sb(1)-S(2)	95.18(8)
S(7)-In(4)-S(8)	98.88(7)	S(14)-In(7)-S(16)	102.02(8)	N(9)-Co(1)-N(13)	95.8(3)		

Table 3.14 A selection of bond angles in [Co(tren)(H₃tren)][In₃Sb₂S₉]·H₂O (**3**)

symmetry codes: *a = x+1, y-1, z; b = x, y-1, z*

	Angle / °		Angle / °		Angle / °		Angle/ °
S(9)ᵃ-Sb(1)-S(5)ᵇ	96.6(2)	S(2)-In(1)-S(4)	113.9(2)	S(4)-In(2)-S(6)	112.06(18)	N(1)-Co(1)-N(2)	81.5(8)
S(9)ᵃ-Sb(1)-S(1)	96.0(2)	S(1)-In(1)-S(8)	104.65(18)	S(5)-In(2)-S(6)	111.2(2)	N(1)-Co(1)-N(3)	117.0(7)
S(5)ᵇ-Sb(1)-S(1)	97.6(2)	S(2)-In(1)-S(8)	111.5(2)	S(6)-In(3)-S(7)	112.6(2)	N(2)-Co(1)-N(3)	82.9(7)
S(2)-Sb(2)-S(3)	111.7(2)	S(4)-In(1)-S(8)	112.39(19)	S(6)-In(3)-S(8)	108.5(2)	N(1)-Co(1)-N(4)	119.9(7)
S(2)-Sb(2)-S(7)	106.1(3)	S(3)-In(2)-S(4)	110.7(2)	S(7)-In(3)-S(8)	117.8(3)	N(2)-Co(1)-N(4)	80.9(6)
S(3)-Sb(2)-S(7)	108.8(3)	S(3)-In(2)-S(5)	103.6(3)	S(6)-In(3)-S(9)	97.62(18)	N(3)-Co(1)-N(4)	117.1(8)
S(1)-In(1)-S(2)	102.9(2)	S(4)-In(2)-S(5)	101.52(19)	S(7)-In(3)-S(9)	108.6(3)	N(1)-Co(1)-N(5)	93.8(9)
S(1)-In(1)-S(4)	110.73(19)	S(3)-In(2)-S(6)	116.4(2)	S(8)-In(3)-S(9)	109.8(2)	N(2)-Co(1)-N(5)	172.6(7)

3.2.3 [Co(tren)]$_2$[Sb$_2$In$_2$S$_8$] (4): 1-D Indium-Antimony Chain
3.2.3.1 Synthesis

The compound [Co(tren)]$_2$[Sb$_2$In$_2$S$_8$] **(4)**, was synthesised from a mixture of Sb$_2$S$_3$ (68 mg 0.20 mmol), InCl$_3$ (80 mg, 0.369 mmol), CoS (34 mg, 0.37 mmol), S (25 mg, 0.79 mmol) and tris(2-aminoethyl)amine (tren) (3.2 ml, 21 mmol). The reagent mixture was stirred for 10 minutes in a 23 ml Teflon-lined stainless-steel autoclave which was sealed then heated at 453 K for 5 days at a heating rate of 1 K min^{-1}. The products were cooled overnight at 1 K min^{-1} before being filtered and washed successively with ethanol, water and acetone. The product contained single crystals in the form of small dark purple crystal blocks of compound **(4)** and yellow blocks, subsequently identified as compound **(1)**. The powder X-ray diffraction pattern of the bulk sample containing **(4)** (Figure 3.21) does not show a good agreement with the generated pattern from the single-crystal data. This is the result of there being only a small amount of crystals of **(4)** present but more crystals of **(1)**, therefore making the bulk powder resemble **(1)** more than **(4)**. In addition to the single crystals within the bulk sample, polycrystalline material was identified as the starting reagent S together with small amounts of Co$_3$S$_4$ and CoSbS. Attempts to produce pure samples of **(4)** by varying reagent ratios and oven temp/time were unsuccessful. Numerous attempts were made and no correlation could be made between when this compound forms and what parameters are changed. Therefore, only single-crystal X-ray and powder X-ray diffraction data could be collected for **(4)**.

Single-crystal X-ray diffraction data were collected for **(4)** at 150 K using graphite monochromated MoK$_\alpha$ (λ = 0.71073 Å) radiation. The structure was solved using the program SIR92 [227] and the model refined using the CRYSTALS suite of programs [230]. The refinement was conducted in *F* and a polynomial weighting scheme was applied. The tetrahedral sites within the inorganic chain were chosen to be In due to valence sum calculations being more agreeable with In(III) (3.12 and 2.92 v.u.) than with Sb(V) (3.86 and 3.14 v.u.). Tetrahedral antimony has only been observed thus far as Sb(V) and are unlikely to be Sb(III). There was also a decrease in the *R* factor upon using In instead of Sb, showing a noticeable improvement in statistics. Hydrogen atoms on the amine ligands were placed geometrically with a U[equiv] value 1.2 times the U[equiv] of the carbon to which they are attached. Crystallographic details are summarised in Table 3.15, atomic coordinates of all non-hydrogen atoms are shown in Table A1.7.
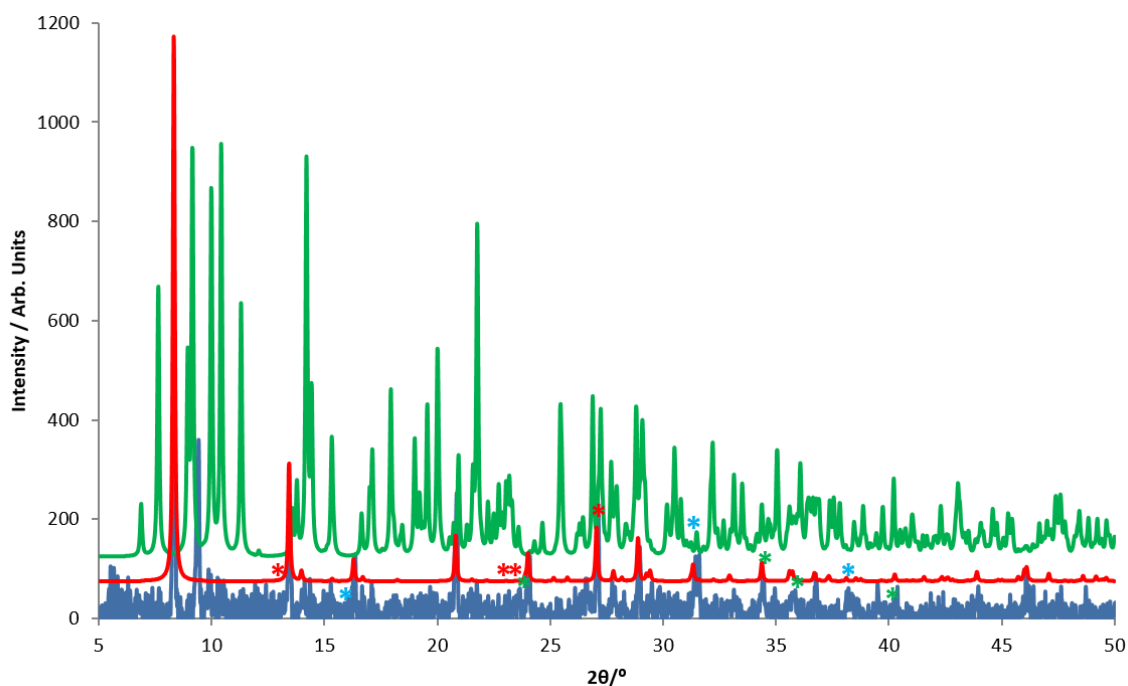
Figure 3.21: Powder X-ray diffraction patterns of the bulk as-synthesised product (blue) and the simulated pattern calculated from single-crystal diffraction data of (**4**) (green) and **(1)** (red). Peaks denoted with asterisks correspond to S (red), Co_3S_4 (blue) and CoSbS (green).

Table 3.15: Crystallographic data for $[Co(tren)]_2[Sb_2In_2S_8]$ **(4).**

Chemical formula	$[Co(tren)]_2[Sb_2In_2S_8]$
Formula mass	1139.99
Crystal Habit	Dark purple block
Crystal system	Triclinic
Symmetry space group	$P2_1$
Temp /K	100
a /Å	10.7885(6)
b /Å	12.7636(7)
c /Å	13.5289(7)
α /°	73.864(5)
β /°	76.142(4)
γ /°	67.928(5)
V /Å³	1639.19(9)
Z	2
μ /mm^{-1}	4.526
Total reflections ($I > 3\sigma(I)$)	7242
R factor	0.0484
wR factor	0.0470
Goodness of fit ref	1.0564

3.2.3.3 Structure Description and Analysis

The metal cations present in compound **(4)** were assigned oxidation states of +3 for In and Sb atoms and +2 for Co atoms on the basis of bond-valence sum calculations (Table 3.15). The structure of **(4)** is formed from InS_4^{5-} and SbS_3^{3-} units with two $[Co(tren)]^{2+}$ trigonal bipyramidal complexes (Figure 3.22). Edge sharing InS_4^{5-} tetrahedral units form a 2-membered In_2S_2 ring, the remaining sulfur atoms associated with each InS_4 tetrahedron share a vertex with SbS_3^{3-} and an InS_4^{5-} unit. The latter units also share a common vertex with each other thus forming 3-membered In_2SbS_3 rings each side of the 2-membered ring. Additionally, the InS_4^{5-} unit of each 3-membered ring belongs to an even larger 4 membered $Sb_2In_2S_4$ ring using two vertex atoms, thereby linking through indium, creating an infinite chain. The chain contains a repeating ring sequence of (-2-3-4-3-2-) shown in Figure 3.23. All SbS_3^{3-} atoms contain a sulfur atom which acts as a ligand and coordinates to the $[Co(tren)]^{2+}$ units. The In_2S_6 heteroring within the chain is a common unit in indium-antimony sulfide structures and has been observed in $[Co(tren)InSbS_4]$ [262] and $[Ni(deta)_2]_2In_2Sb_4S_{11}$ [153]. The heteroring is also present in the related 1-D chain-based structure of $[(Mn(tren))InAsS_4]$ [263].
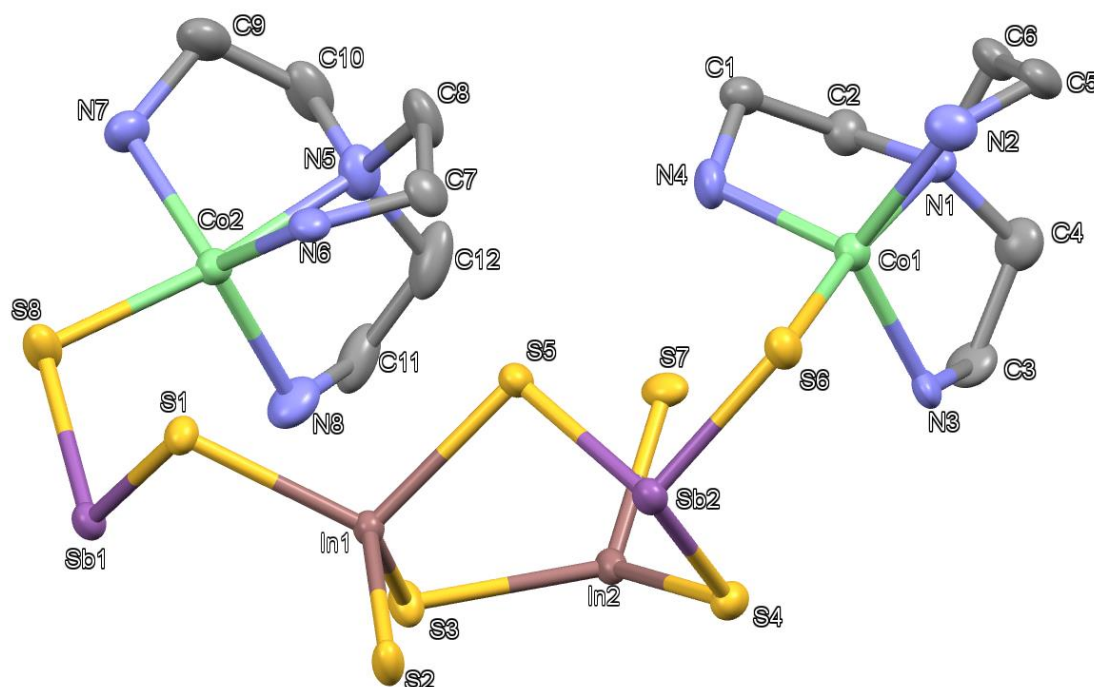
Figure 3.22: Asymmetric unit of $[Co(tren)]_2[Sb_2In_2S_8]$ **(4)** displaying thermal ellipsoids of each atom at 50 % probability. Key: brown: In atoms, purple: Sb atoms, green: Co, yellow: S atoms, light blue: N atoms, grey: C atoms. Hydrogen atoms are omitted for clarity.
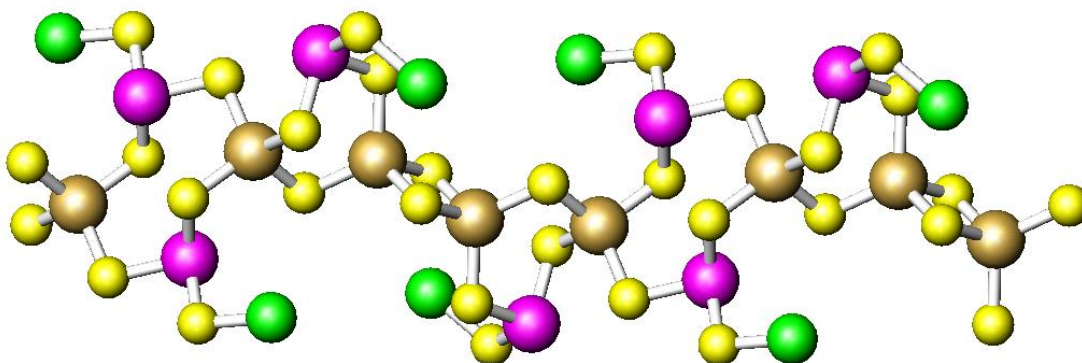
Figure 3.23: A section of a single chain within the structure of $[Co(tren)]_2[Sb_2In_2S_8]$ **(4)**, displaying the (-2-3-4-3-2-) ring system. Key: brown: In atoms, purple: Sb atoms, green spheres: Co, yellow: S atoms. H, C and N atoms are omitted for clarity.

Bond distances (Table 3.16) for compound **(4)** are typical of those observed for other indium-antimony sulfides in this chapter, with Sb-S and In-S distances lying in the range (2.3984(16) $\leq d/$Å $\leq$ 2.4455(16)) and (2.4132(15) $\leq$ d/Å $\leq$ 2.5191(16)) respectively. These bond distances are also similar to those found in $[(Co(en)_3)]_3(en)In_6Sb_6S_{21}.H_2O$ [163], $[Ni(en)_3][In_2Sb_2S_7]$ [262] and $[Ni(deta)_2]_{1.5}[In_3Sb_2S_9]\cdot H_2O$ [153]. The bond angles (Table 3.17) within $[Co(tren)]^{2+}$ are distorted compared to conventional trigonal bipyramidal geometries, this is due to the rigidity of the tren molecule on the biting angle between two nitrogen atoms, as seen with structures reported elsewhere in this chapter. The N-Co-N angles between the axial and equatorial ligands are between (78.2(2) $\leq \alpha/^\circ \leq$ 80.3(3)). The longer axial bond also affecting the position of the equatorial ligands as seen with structure **(2)** and **(3)**.

Table 3.16 A selection of bond lengths and bond valence sums in [Co(tren)]$_2$[Sb$_2$In$_2$S$_8$] **(4).**

symmetry codes: a = -x+1, -y, -z+1 b = -x, -y, -z+2

	length /Å	vij		length /Å	vij		length /Å	vij
Sb(1)-S(2)[a]	2.4302(15)	1.05	Sb(2)-S(4)	2.4455(16)	1.01	In(1)-S(1)	2.4616(15)	0.76
Sb(1)-S(1)	2.4439(15)	1.02	Sb(2)-S(5)	2.4304(15)	1.05	In(1)-S(2)	2.4521(15)	0.78
Sb(1)-S(8)	2.4028(17)	1.14	Sb(2)-S(6)	2.3984(16)	1.15	In(1)-S(3)	2.4132(15)	0.87
						In(1)-S(5)	2.4854(14)	0.71
∑vij		**3.21**			**3.21**			**3.12**
In(2)-S(7)[b]	2.4835(15)	0.72	Co(1)-S(6)	2.3788(17)	0.42	Co(2)-S(8)	2.3327(18)	0.48
In(2)-S(3)	2.4494(15)	0.79	Co(1)-N(1)	2.258(5)	0.32	Co(2)-N(5)	2.265(6)	0.32
In(2)-S(4)	2.5191(16)	0.65	Co(1)-N(2)	2.108(6)	0.48	Co(2)-N(6)	2.066(5)	0.54
In(2)-S(7)	2.4577(16)	0.77	Co(1)-N(3)	2.065(6)	0.54	Co(2)-N(7)	2.106(5)	0.49
			Co(1)-N(4)	2.087(6)	0.51	Co(2)-N(8)	2.100(6)	0.50
∑vij		**2.93**			**2.27**			**2.33**

Table 3.17 A selection of bond angles in [Co(tren)]$_2$[Sb$_2$In$_2$S$_8$] **(4).**

symmetry codes: *a = -x+1, -y, -z+1 b = -x, -y, -z+2*

	Angle / °		Angle / °		Angle / °
S(2)[a]-Sb(1)-S(1)	101.44(5)	S(2)-In(1)-S(5)	105.68(5)	N(1)-Co(1)-N(2)	78.2(2)
S(2)[a]-Sb(1)-S(8)	88.65(6)	S(3)-In(1)-S(5)	105.78(5)	S(6)-Co(1)-N(3)	98.42(17)
S(1)-Sb(1)-S(8)	97.48(6)	S(7)[b]-In(2)-S(3)	105.38(5)	N(1)-Co(1)-N(3)	79.6(2)
S(4)-Sb(2)-S(5)	97.61(5)	S(7)[b]-In(2)-S(4)	106.54(5)	N(2)-Co(1)-N(3)	121.5(2)
S(4)-Sb(2)-S(6)	106.08(5)	S(3)-In(2)-S(4)	118.27(5)	S(6)-Co(1)-N(4)	106.46(16)
S(5)-Sb(2)-S(6)	96.89(5)	S(7)[b]-In(2)-S(7)	95.88(5)	N(1)-Co(1)-N(4)	79.7(2)
S(1)-In(1)-S(2)	108.73(5)	S(3)-In(2)-S(7)	115.44(6)	N(2)-Co(1)-N(4)	112.9(2)
S(1)-In(1)-S(3)	112.61(5)	S(4)-In(2)-S(7)	112.07(6)	N(3)-Co(1)-N(4)	115.3(2)
S(2)-In(1)-S(3)	115.81(6)	S(6)-Co(1)-N(1)	173.72(15)		
S(1)-In(1)-S(5)	107.66(5)	S(6)-Co(1)-N(2)	98.00(16)		

The packing of the chains is presented in Figure 3.24. Rows of chains pack in a parallel alignment (Figure 3.24a) forming a layer, with complexes either side of the inorganic chain which gives each chain a zig-zag appearance. Layers of chains are then stacked along [101] with adjacent chains offset with respect to one another to minimise steric interactions between transition-metal complexes (Figure 3.24b). Distances between acceptor-donor atoms in **(4)** are in the range (3.354(6) $\leq d$/Å $\leq$ 3.747(9)) for N…S atoms, suggesting the presence of hydrogen bonding interactions, which may contribute to stabilization of the structure.
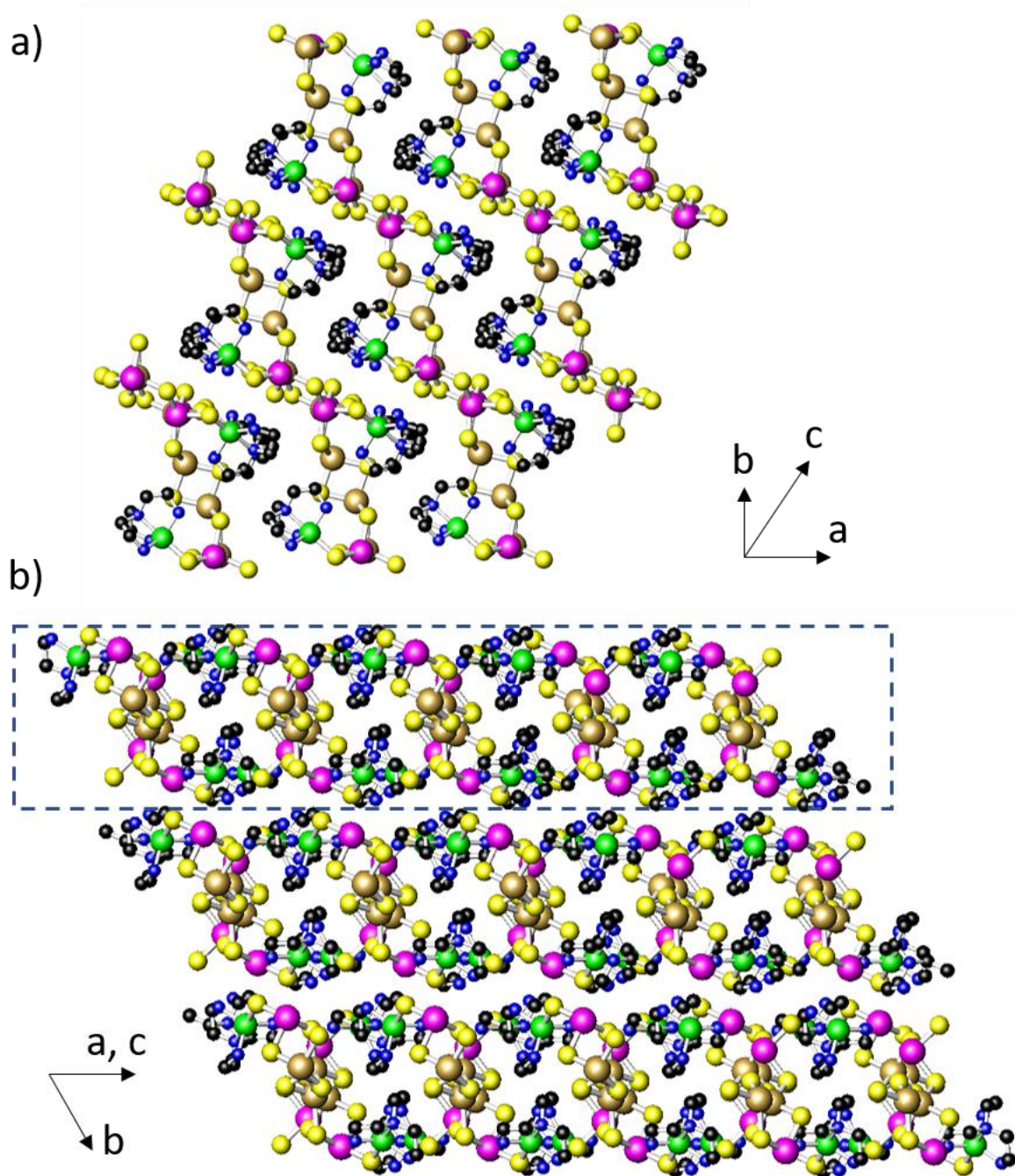
Figure 3.24: (a) View of a single layer of chains within the structure of **(4)**, this layer is represented by the blue box below in (b) which contains the stacked layers of chains which align down the [101] direction. Key: brown: In atoms, purple: Sb atoms, green: Co, yellow: S atoms, light blue: N atoms, black: C atoms. Hydrogen atoms are omitted for clarity.

3.2.3 (Hdap)$_6$[In$_{10}$S$_{18}$] (5): 3-D Supertetrahedral Framework
3.2.3.1 Synthesis

Compound (Hdap)$_6$[In$_{10}$S$_{18}$] (**5**) was synthesised from a mixture of In$_2$O$_3$ (200 mg, 1.36 mmol), CoS (173 mg, 1.90 mmol), S (113 mg, 3.52 mmol) and 1,2-diaminopropane (dap) (5 ml, 58.68 mmol). The reagent mixture was stirred for 10 min in a Teflon-lined stainless-steel autoclave, sealed then heated at 443 K for 8 days. The ramp rate for both heating and cooling was at 1 K min^{-1}. The reaction mixture was cooled overnight, before being filtered and washed with ethanol, water and acetone. Single crystals of (**5**) in the form of yellow blocks were observed within the bulk black powder along with unidentifiable teal coloured plates. The powder X-ray diffraction pattern of the bulk sample did not show good agreement with the calculated pattern (Figure 3.25). Due to the very small amount of (**5**) present in the sample, only the strongest peak is visible within the pattern. Other products were identified as S$_8$, Co$_9$S$_8$, In$_2$O$_3$, Co$_3$S$_4$ together with an unknown phase. The small quantity of single crystals of (**5**) was confirmed visually through an inspection under a microscope. The teal plates that formed in the reaction did not diffract sufficiently well enough during single-crystal X-ray diffraction experiments to be determined. Time constraints meant that experiments to optimise the reaction for further study could not be conducted.
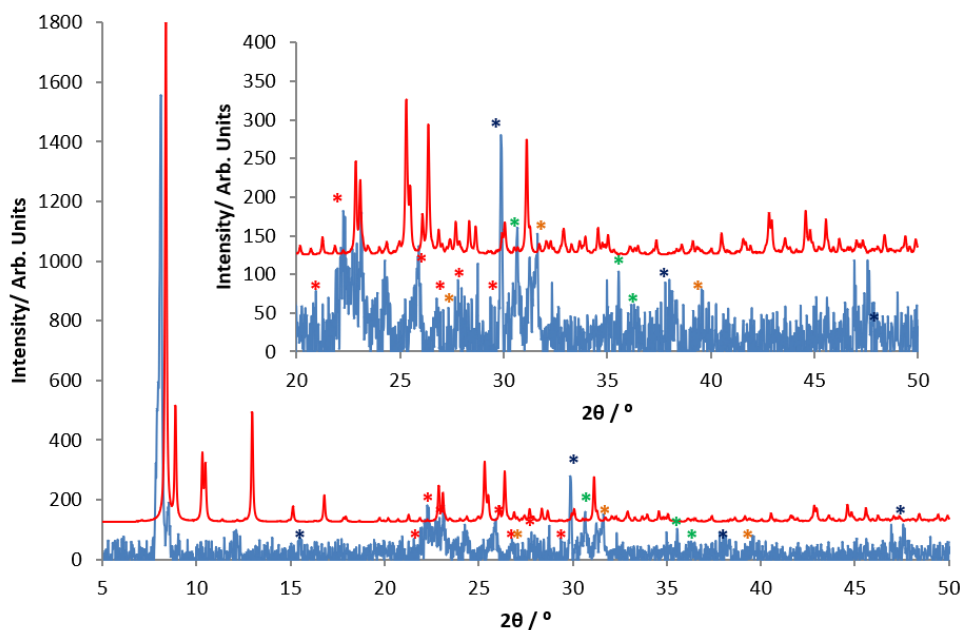
Figure 3.25: Powder X-ray diffraction patterns of the bulk as-synthesised product (blue) and the simulated pattern calculated of (**5**) from single-crystal diffraction data (red). Peaks in the bulk sample annotated with asterisks correspond to S$_8$ (red), Co$_9$S$_8$ (blue), In$_2$O$_3$ (green) and Co$_3$S$_4$ (orange).

Single-crystal X-ray diffraction experiments were conducted at 150 K using graphite monochromated MoK$_\alpha$ ($\lambda = 0.71073$ Å) radiation. The structure was solved using the program SUPERFLIP [228] and the model refined using the CRYSTALS suite of programs [230]. The model was refined in F and Chebychev polynomial weighting scheme was applied. Due to the large solvent-accessible void space, the organic counter ions were too disordered to model successfully. The electron density was modelled via platon SQUEEZE [251] therefore the final model contained only the inorganic framework. Crystallographic details are summarised in Table 3.18. Atomic coordinates of all non-hydrogen atoms can be found in Table A1.8.

Table 3.18: Crystallographic data for (Hdap)$_6$[In$_{10}$S$_{18}$] **(5).**

Formula weight	1725.28
Crystal Habit	Yellow block
Crystal system	Tetragonal
Space group	$P4_32_12$
Temp /K	150
a /Å	19.8889(4)
c /Å	31.9054(7)
V /Å³	12620.8(4)
Z	8
Wavelength /Å	0.71073
μ /mm^{-1}	4.176
Total reflections ($I > 3\sigma(I)$)	9523
R factor	0.0537
wR factor	0.0539

3.2.3.3 Structure Description and Analysis

Bond-valence calculations of In atoms within **(5)** ranged between 3.03-3.15 v.u. supporting that the oxidation state of In is +3 (Table 3.18). The structure of **(5)** is formed by vertex sharing InS$_4$$^{5-}$ units to form large T3 [In$_{10}$S$_{18}$]$^{6-}$ supertetrahedal units (Figure 3.26), these also share vertex sulfur atoms with other T3 clusters producing two arrays of interconnected networks that interpenetrate with each other. Each network consists of T3 clusters that are connected into repeating 6-membered ring systems (Figure 3.27). This structural unit has been documented previously as an analogue by Parise *et al*. [C$_2$H$_8$N]$_6$[In$_{10}$S$_{18}$] [81, 95] and an isostructural gallium sulfide version [C$_4$H$_{12}$N]$_6$[Ga$_{10}$S$_{18}$] [264], both are produced in the presence of dimethylamine (dma) or diethylamine (dea) respectively which form colourless

plates. The organic component in (**5**) could not be located through Fourier maps and there was not enough sample for further analysis. When applying SQUEEZE however, the program calculated that 3258 e$^-$ were present within the void space. This equates to a maximum of ten 1,2-diaminopropane molecules per asymmetric unit ((3258/43)/8 = 9.5). Taking the void volume into consideration, up to ten dap cations per asymmetric unit (18 Å^3 rule) could be accommodated in this space, a figure which is comparable to the twelve dma cations Parise *et al.* determined through the application of SQUEEZE to a material with the same $In_{10}S_{18}$ framework. Based on charge balancing and TGA data, their final formulation was $[C_2H_8N]_6[In_{10}S_{18}]$. In the present structure, the charge of the framework is -6 overall with no signs of transition-metal complexes (no regions of high electron density), only organic cations are available to provide charge balance. Therefore, the 1,2-diaminopropane molecules, whose presence is suggested by the output of the SQUEEZE program, need to be protonated. Based on available data and charge balances, this leads to the formulation of compound (**5**) as (Hdap)$_6$[In$_{10}$S$_{18}$], based on a minimum allowed dap count comparable to the previously published analogue and isostructural compounds [81, 95, 264].
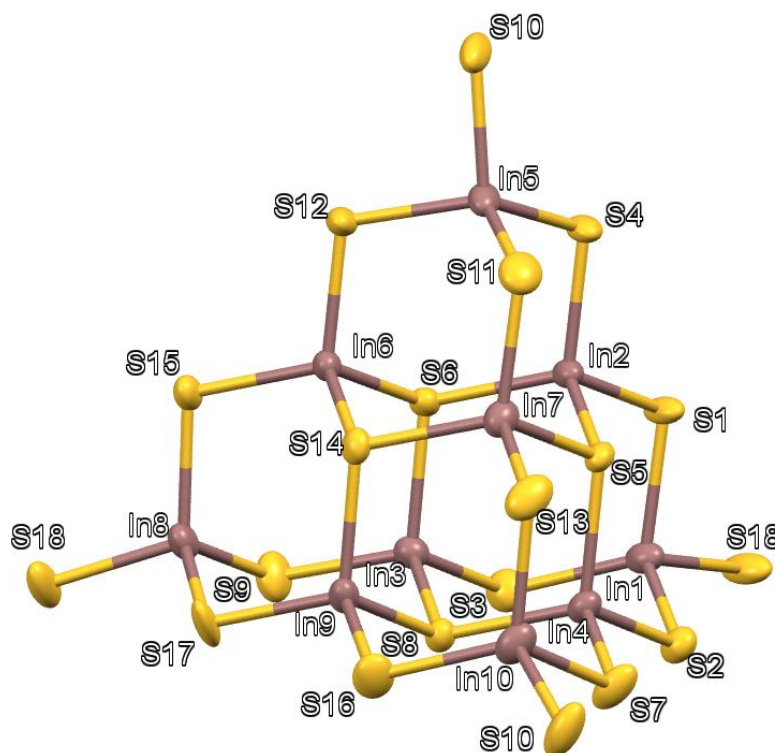
Figure 3.26: The T3 unit $[In_{10}S_{18}]^{6-}$ found in compound (**5**) represented with thermal ellipsoids at 50 % probability. Key: brown: In atoms, yellow: S atoms.
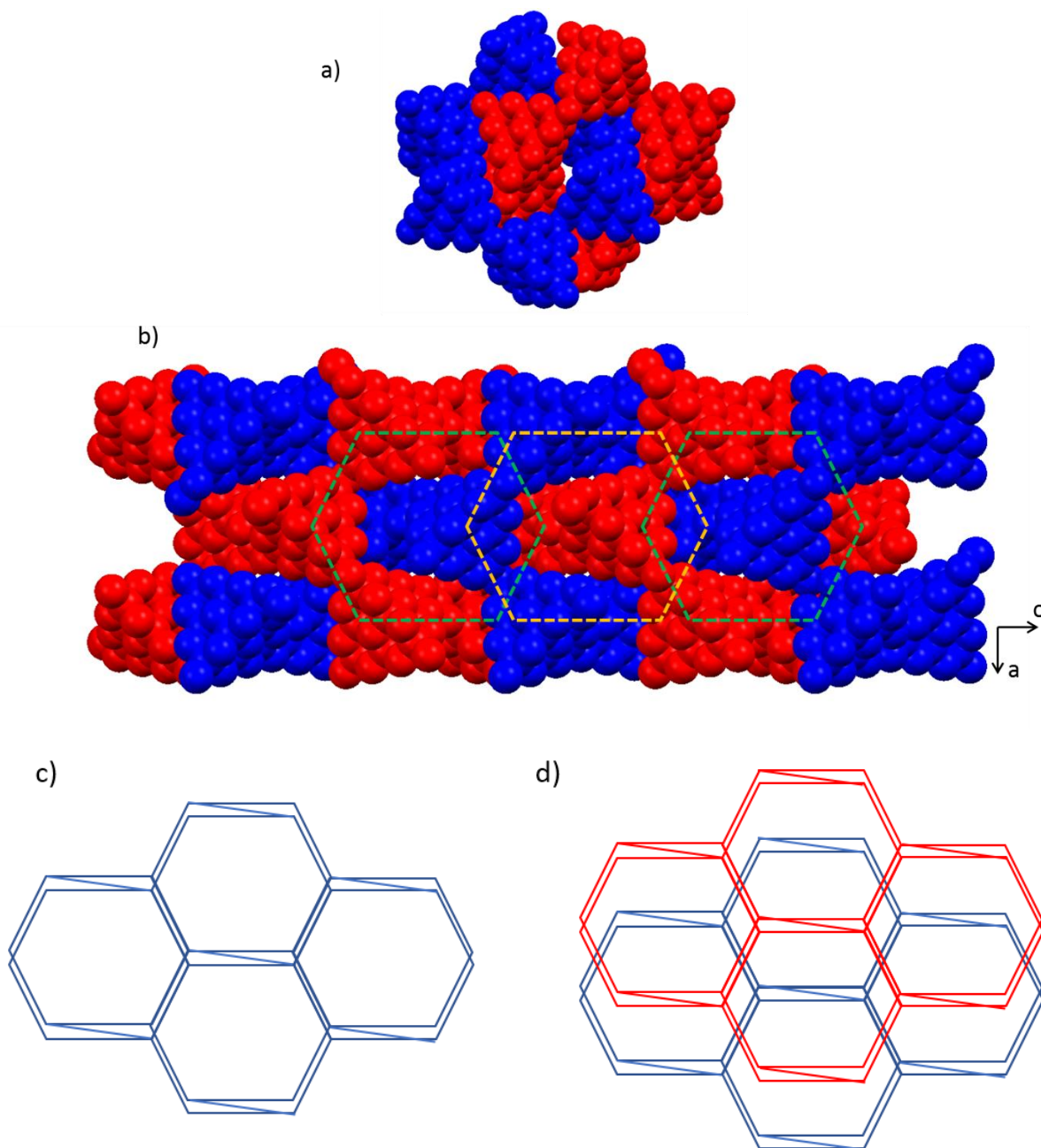
Figure 3.27: Space filling representations of structure **(5)** to demonstrate (a) two single interpenetrating 6-membered rings of opposite networks and (b) the interpenetrating sets of rings seen down [010]. Colour coded red and blue for the two interpenetrating 6-membered ring systems and using dashed hexagons to highlight the position of the rings. Diagrams (c) and (d) represent the topology of the rings systems where each vertex point is a supertetrahedral cluster. (c) contains one lattice of rings and (d) represents the secondary ring system interpenetrating the first.

In-S distances (Table 3.19) are observed to be between $(2.423(4) \leq d/\text{Å} \leq 2.425(4))$ for terminal sulfur atoms and $(2.399(4) \leq d/\text{Å} \leq 2.515(4))$ for all other bonding interactions, with tri-coordinated sulfur displaying the longest bond lengths. *Parise et al.* observed similar bond lengths including the shortened terminal positions caused by underbonding of sulfur atoms in $[C_2H_8N]_6[In_{10}S_{18}]$ [265] of 2.425 Å. Furthermore, the distances in (**5**) compare favourably with the vertex sharing indium sulfide T3 chain $[Fe(phen)_3]_4[H_4In_{20}S_{38}] \cdot Hphen \cdot 3Hdma \cdot 8H_2O$ (phen = 1,10-phenanthroline) or layered $[M(phen)_3]_4[In_{20}S_{37}]$ (M=Ni or Fe) [90], including the observation that the longest bond lengths within the T3 unit involve tri-coordinated sulfur atoms. Bond angles (Table 3.20) within each InS_4^{5-} tetrahedral unit including a terminal S atom distorted slight distortion with angles ranging between $(97.18(13) \leq \alpha/° \leq 114.78(16))$ compared to the internal InS_4^{5-} tetrahedra within the T3 unit, where corresponding angles are in the range $(107.84(14) \leq \alpha/° \leq 111.02(11))$. Displaying much more rigidity compared to In atoms containing terminal S atoms used in bonding to other T3 units, thus some bending.

Table 3.19 All bond lengths and valence sums in $(Hdap)_6[In_{10}S_{18}]$ (**5**).

symmetry codes: $a = -x+1/2; y+1/2; -z+3/4$ $b = x+1/2; -y+3/2; -z+5/4$

	length /Å	vij		length /Å	vij		length /Å	vij
In(1)-S(18)[a]	2.424(4)	0.84	In(2)-S(6)	2.502(3)	0.68	In(3)-S(6)	2.510(4)	0.67
In(1)-S(1)	2.468(4)	0.75	In(2)-S(1)	2.394(4)	0.91	In(3)-S(8)	2.503(4)	0.68
In(1)-S(2)	2.453(4)	0.78	In(2)-S(5)	2.501(4)	0.68	In(3)-S(9)	2.400(4)	0.90
In(1)-S(3)	2.467(4)	0.75	In(2)-S(4)	2.423(4)	0.84	In(3)-S(3)	2.399(4)	0.90
∑vij		**3.12**			**3.11**			**3.15**
In(4)-S(5)	2.508(3)	0.67	In(5)-S(11)	2.451(5)	0.78	In(6)-S(6)	2.495(4)	0.69
In(4)-S(7)	2.415(4)	0.86	In(5)-S(12)	2.462(4)	0.76	In(6)-S(15)	2.418(4)	0.85
In(4)-S(8)	2.503(4)	0.68	In(5)-S(10)	2.425(4)	0.84	In(6)-S(14)	2.507(4)	0.67
In(4)-S(2)	2.406(4)	0.88	In(5)-S(4)	2.452(4)	0.78	In(6)-S(12)	2.408(4)	0.88
∑vij		**3.09**			**3.16**			**3.09**
In(7)-S(5)	2.502(4)	0.68	In(8)-S(15)	2.470(4)	0.74	In(9)-S(16)	2.422(4)	0.85
In(7)-S(14)	2.515(4)	0.66	In(8)-S(18)	2.425(4)	0.84	In(9)-S(8)	2.501(4)	0.68
In(7)-S(13)	2.414(4)	0.86	In(8)-S(17)	2.466(4)	0.75	In(9)-S(17)	2.404(4)	0.89
In(7)-S(11)	2.431(4)	0.83	In(8)-S(9)	2.452(5)	0.78	In(9)-S(14)	2.499(4)	0.69
∑vij		**3.03**			**3.11**			**3.11**
In(10)-S(10)[b]	2.424(4)	0.84						
In(10)-S(7)	2.470(4)	0.74						
In(10)-S(16)	2.460(4)	0.76						
In(10)-S(13)	2.468(5)	0.75						
∑vij		**3.09**						

Table 3.20 A selection of bond angles in (Hdap)$_6$[In$_{10}$S$_{18}$] **(5)**

symmetry code: *a = -x+1/2; y+1/2; -z+3/4*

	Angle / °		Angle / °		Angle / °
S(6)-In(6)-S(15)	109.69(13)	S(18)-In(8)-S(9)	110.50(16)	S(1)-In(2)-S(5)	107.77(13)
S(6)-In(6)-S(14)	111.02(11)	S(17)-In(8)-S(9)	114.78(16)	S(6)-In(2)-S(4)	110.46(13)
S(15)-In(6)-S(14)	109.35(12)	S(18)^a-In(1)-S(9)	97.18(13)	S(1)-In(2)-S(4)	108.80(13)
S(6)-In(6)-S(12)	108.42(13)	S(18)^a-In(1)-S(2)	111.64(15)	S(5)-In(2)-S(4)	109.63(14)
S(6)-In(6)-S(12)	109.65(13)	S(1)-In(1)-S(2)	112.36(15)	S(5)-In(4)-S(7)	108.86(15)
S(14)-In(6)-S(12)	108.69(14)	S(18)^a-In(1)-S(3)	111.46(16)	S(5)-In(4)-S(8)	109.77(11)
S(15)-In(8)-S(18)	110.49(15)	S(1)-In(1)-S(3)	113.25(15)	S(7)-In(4)-S(8)	109.23(14)
S(15)-In(8)-S(17)	111.10(16)	S(2)-In(1)-S(3)	110.39(14)	S(5)-In(4)-S(2)	110.35(13)
S(18)-In(8)-S(17)	98.15(13)	S(6)-In(2)-S(1)	109.89(15)	S(7)-In(4)-S(2)	108.78(13)
S(15)-In(8)-S(9)	111.14(15)	S(6)-In(2)-S(5)	110.24(11)	S(8)-In(4)-S(2)	109.82(13)

3.4 Conclusion

The work in this chapter produced numerous structures including one which was published in the *Journal of Solid State Chemistry* [250]. The compound (H$_{1.3}$tren)[In$_{2.67}$Sb$_{1.33}$S$_8$].tren **(1),** contains adamantane-like [In$_{2.67}$Sb$_{1.33}$S$_8$]$^{1.33-}$ T2 supertetrahedral clusters, constructed from Sb(V)S$_4$ and In(III)S$_4$ tetrahedra, which are linked through their terminal sulfur atoms into a three-dimensional open-framework structure. Although it was not possible to locate the organic component, tren, directly using single-crystal X-ray diffraction data, its presence has been confirmed through ^{13}C solid-state NMR, infrared spectroscopy, combustion analysis and thermogravimetry. These data, together with the two-step weight loss observed in TGA, suggest that only one of the tren molecules is protonated in order to provide the required charge balancing for the anionic inorganic framework. Immersion of the material in a number of alkali-metal halide solutions leads to removal of approximately half of the organic component, consistent with removal of the non-protonated tren. This is accompanied by a reduction of *ca*. 8 % in unit cell volume, although at higher degrees of removal, there is a loss in crystallinity suggesting greater structural changes occur. Compounds [Co(tren)(H$_3$tren)][In$_4$SbS$_{10}$]·3H$_2$O **(2)** and [Co(tren)(H$_3$tren)][In$_3$Sb$_2$S$_9$]·H$_2$O **(3)** both display similar layered motifs but the structure of **(3)** contains an ordered antimony atom within the T2 unit which reduces the distance between double layers through a weak Sb-Sb interaction [257, 258]. Both structures contain layers in which 9-membered In$_6$Sb$_3$S$_9$ rings house complexes. The partially coordinated tren molecule descends into the space between layers

forming a channel with water molecules that interact with the adjacent layer forming the double layer. The structure of [Co(tren)]$_2$[Sb$_2$In$_2$S$_8$] **(4)** contains an interesting chain motif that is built from a (-2-3-4-3-2-) ring system. It also contains complexes that act as pendants to balance the charge of the inorganic chain. Lastly, the only pure indium sulfide to be produced from this work is (Hdap)$_6$[In$_{10}$S$_{18}$] **(5),** a large interlinking 3-D structure that is analogous to the compound produced by Parise *et al.* [C$_2$H$_8$N]$_6$[In$_{10}$S$_{18}$] [95] and isostructural to the compound [C$_4$H$_{12}$N]$_6$[Ga$_{10}$S$_{18}$] [264]. This compound was produced using dap molecules instead of dea or dma and six dap molecules were calculated to be within the pore space of the asymmetric unit through Platon SQUEEZE [251].

Chapter 4: Oxothiogermanate Materials

4.1 Introduction

The simplest supertetrahedral unit is the T2 cluster, illustrated in Figure 4.1 for the $[M_4X_{10}]$ adamantane-like $[Ge_4O_{6-x}S_{4+x}]$ ($x = 0, 2, 4$) clusters described in this project. In general, a supertetrahedral unit is described by the label, "Tn", where n corresponds to the number of tetrahedral units along a cluster edge. A number of main-group metals form chalcogenide compounds containing isolated M_4X_{10} (T2) and $M_{10}X_{20}$ (T3) clusters $e.g.$ gallium, T2 [266], T3 [267], indium, T2 [81], T3 [82] and tin, T2 [268, 269]. Extended frameworks of T3 clusters are also known for Ga [270] and In [95].

Pertinent to the work described in this chapter are the supertetrahedral-based chalcogenides of germanium(IV). Isolated T2 supertetrahedral $[Ge_4X_{10}]^{4-}$ clusters (X = S, Se, Te) have been formed under solvo- or hydrothermal conditions in the presence of amine cations or transition-metal-amine complexes which act as structure directing and/or charge-balancing agents.

Thiogermanate(IV) anions are found, for example, in $[M(dap)_3]_4Ge_4S_{10}Cl_4$ (dap = 1, 2-diaminopropane) (M= Co, Ni) [106], $[(CH_3)_4N]_4Ge_4S_{10}$ [107], $(H_2bipy)_2Ge_4S_{10}.(bipy)\cdot 7H_2O$ (bipy = 4,4'-bipyridine) [108], $[Ni(teta)_2]_2Ge_4S_{10}$ (teta = triethylenetetramine) [109] and $[Ni(phen)_3]_2Ge_4S_{10}\}\cdot x$Sol (Sol = 4MeOH·12H$_2$O or 24H$_2$O) [110]. A further discrete T2 cluster, $[H_4Ge_4S_{10}]$, prepared at room temperature, uses protons to balance the charge through S-H bonds to the terminal sulfur atoms [111]. The thiogermanate(IV) T2 units are also found linked into 3-D frameworks via additional transition-metal centres bonding on each terminal sulfur atom, for example, $[(CH_3)_4N]_2MGe_4S_{10}$ (M = Fe, Cd, Mn) [119].

To produce larger supertetrahedral units (T4, T5), a mixture of main group metals or transition metals are required to be present in the cluster. This arises from Pauling's electrostatic valence sum principle [84] which results in cation sites being too high in charge to support coordination sites such as Ge(IV) and tri-coordinate sulfur. Thus T3, $Ge_{10}S_{20}$ and higher clusters do not exist. To achieve larger clusters, two different metals are required, one with a high oxidation state and one with a low oxidation state. For example, indium containing T4 clusters $[In_{16}M_4S_{31}(DBN)_4]^{6-}$ (DBN = 1,5-diazobycyclo[4.3.0]non-5-ene) can be formed when coupled with M=Cd/Mo/Mn/Co/Fe [83] or indium containing T5 units can

form when coupled with Cu producing $[In_{30}Cu_5S_{56}]^{17-}$ clusters [99] or Cd producing $[In_{22}Cd_{13}S_{52}(1\text{-MIM})_4]^{12-}$ (1-MIM = 1-methylimidiazole) [83].

Two oxotelluridogermanate(IV) anions have been reported, $[Mn(en)_3]_2[Ge_4O_6Te_4]\cdot1.5en$ and $(enH)_3[Mn(en)_3][Ge_4O_6Te_4]\cdot4.7en$ [271], both of which contain the novel $[Ge_4O_6Te_4]^{4-}$ anion with a central adamantanoid Ge_4O_6 core and four terminal Te atoms. The only other Ge-O based structure containing the Ge_4O_6 cage is the compound $[\{Ge_4(\mu\text{-}O)_2(\mu\text{-}OH)_4\}\{W(CO)_5\}_4]\cdot4THF$ [272]. While this is not a chalcogenide containing compound, the germanium atoms bond to a complex at the positions where the sulfur atoms would be and the oxygen atoms in the core are protonated. A similar study produced germanium-oxide hexagonal-prism based clusters which also have complexes bonding to the germanium vertex positions; $[Ph_4P]_2[\{Ge_6(\mu_3\text{-}O)_6(\mu\text{-}OH)_2\}\{Cr(CO)_5\}_6]$, $[Ph_4P]_2[\{Ge_6(\mu\text{-}O)_2(\mu_3\text{-}O)_4(OH)_2\}\{W(CO)_5\}_6]$ and $[Ph_4P]_2[\{Ge_6(\mu\text{-}O)_2(\mu_3\text{-}O)_4(OEt)_2\}\{W(CO)_5\}_6]$ [273].

Currently, there are no known examples of oxothiogermanates in the literature. In this chapter, the synthesis and characterisation of the first series of oxothiogermanate(IV) compounds is reported. These materials contain discrete T2 supertetrahedral clusters of general formula $[Ge_4O_{6-x}S_{4+x}]^{4-}$ ($x = 0, 2, 4$) (**6-11**). The T2 units can be bridged by a GeO_4^{4-} unit to form a new discrete germanate unit, $[Ge_9S_8O_{14}]^{8-}$ (**12**), or can link to form a new 1-D chain $[Ge_5O_9(OH)_2S_2]^{4-}$ (**13**). In all the compounds, transition-metal-amine complexes are generated *in situ* during the solvothermal synthesis reactions and serve as charge balancing species to hold the structures together.

3.2 The Ge_4O_6 Cage and $[Ge_4O_6S_4]^{4-}$ Cluster

Structures (**6**)-(**9**) all contain the same inorganic components; a T2 supertetrahedral sulfur-capped adamantane unit, $[Ge_4O_6S_4]^{4-}$, constructed from linked GeO_3S^{4-} tetrahedra, Figure 4.1. Using the $[Ge_4O_6S_4]^{4-}$ cluster in (**6**) as an example, the Ge-S bond lengths lie between ($2.0990(11) \le d/\text{Å} \le 2.1006(11)$) and Ge-O between ($1.783(3) \le d/\text{Å} \le 1.810(3)$). The O-Ge-S angles are observed between ($112.51(10) \le \alpha/° \le 115.57(10)$) and O-Ge-O angles between ($103.12(13) \le \alpha/° \le 105.72(13)$) are observed. Compared to the literature values of $[Ge_4O_6Te_4]^{4-}$ [271] (the only other known T2 oxygen-chalcogenido germanate) the O-Ge-Te angles range between ($114.0(3) \le \alpha/° \le 116.0(2)$) and O-Ge-O between ($102.6(3) \le \alpha/° \le 105.4(4)$), showing similar distorted tetrahedral units. While the Ge-Te bond distances

average between $(2.439(1) \leq d/\text{Å} \leq 2.462(2))$ and Ge-O bond length lie between $(1.778(7) \leq d/\text{Å} \leq 1.802(7))$.

As mentioned previously, the only other Ge-O based structure containing the Ge_4O_6 cage is the compound $[\{Ge_4(\mu\text{-}O)_2(\mu\text{-}OH)_4\}\{W(CO)_5\}_4]\cdot4THF$ [272]. In $[\{Ge_4(\mu\text{-}O)_2(\mu\text{-}OH)_4\}\{W(CO)_5\}_4]\cdot4THF$, the O-Ge-O bond angles are marginally smaller compared to the clusters of **(6)-(9)**, in the range of $(92.38(12) \leq \alpha/° \leq 99.75(12))$ and the O-Ge-W angles are $(117.33(8) \leq \alpha/° \leq 126.46(9))$. The Ge-O bond lengths of $(1.76119(16) \leq d/\text{Å} \leq 1.895(3))$ are similar to the bond lengths reported in this chapter. This results in a similar sized adamantane unit, but with slightly distorted angles due to the large complexes bonding to the germanium atoms in the literature structures.
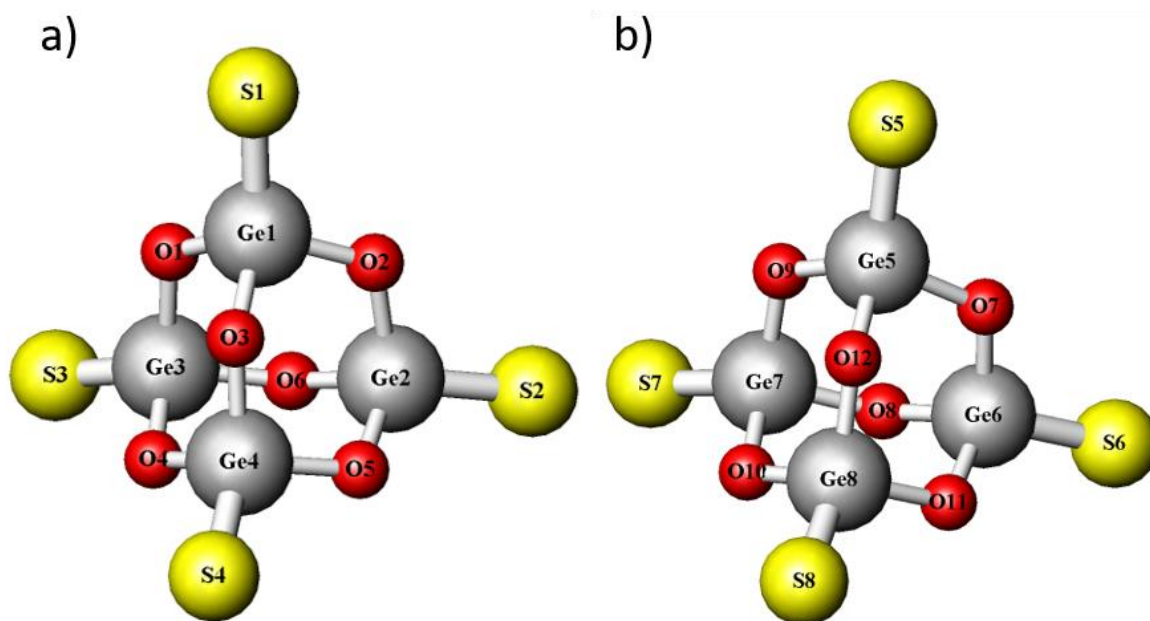
Figure 4.1: Labelling schemes for the T2 supertetrahedral sulphur-capped adamantane-like $[Ge_4O_6S_4]^{4-}$ units found (a) in **(6)** – **(9)** and (b) in **(8)**. Key: grey: Ge atoms, red, O atoms, yellow: S atoms.

4.3 Discrete Clusters
4.3.1 [Co(tren)$_2$]$_2$[Ge$_4$S$_4$O$_6$] (6)
4.3.1.1 Synthesis

[Co(tren)$_2$]$_2$[Ge$_4$S$_4$O$_6$] (**6**) was synthesised from a mixture of Sb$_2$S$_3$ (34 mg 0.1 mmol), GeO$_2$ (21 mg, 0.2 mmol), CoS (17 mg, 0.2 mmol), and tris(2-aminoethyl)amine (tren) (1.6 ml, 11 mmol). The reaction mixture was stirred for 10 minutes in a 23 ml Teflon-lined stainless-steel autoclave before being sealed and heated to 433 K at 1 K min^{-1} for 8 days. A few single crystals of (**6**) in the form of dark-red crystals were produced along with metallic black powder. Additional components were identified as unreacted Sb$_2$S$_3$, elemental Sb and crystals of compound (**7**). The bulk sample was analysed using powder X-ray diffraction (Figure 4.2) but the measured pattern, when compared with the pattern calculated from the single-crystal X-ray data, did not show the presence of (**6**) in the sample, confirming that the yield is very low. Compound (**6**) could not be prepared again, so only single-crystal X-ray data are reported here.
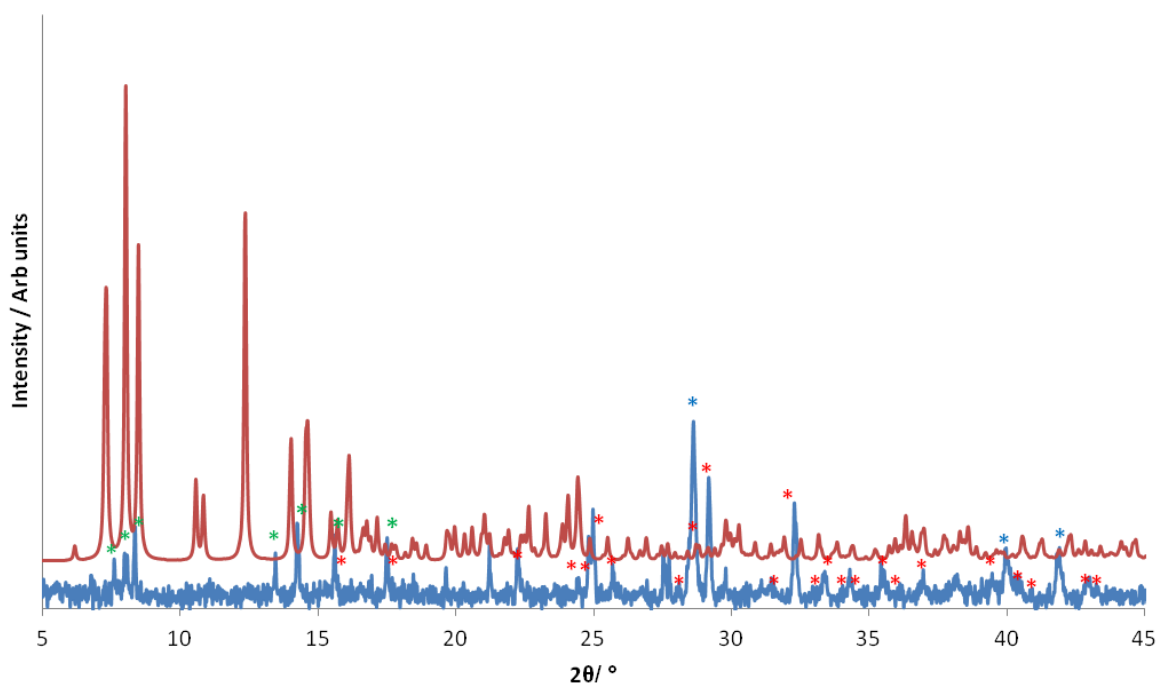
Figure 4.2: X-ray diffraction pattern of the bulk, as-synthesised product (blue) which contained only a few crystals of [Co(tren)$_2$]$_2$[Ge$_4$O$_6$S$_4$] (**6**). The simulated pattern calculated from single-crystal X-ray data for (**6**) is shown above (red). Peaks in the bulk sample annotated with asterisks correspond to Sb$_2$S$_3$ (red), Sb (blue) and compound (**7**) (green).

Single-crystal X-ray diffraction experiments were conducted at 150 K using graphite monochromated MoK$_\alpha$ (λ = 0.71073 Å) radiation. The structure was solved using SIR92 [227] and the model refined using the CRYSTALS suite of programs [230]. The model was refined against F and a Chebychev polynomial weighting scheme applied. Hydrogen atoms on the amine ligands were placed geometrically with a U[equiv] value 1.2 times the U[equiv] of the carbon to which they are attached. The crystal was twinned so the model was refined taking this into account with the two twin components being 59 % and 41 %. Crystallographic details are summarised in Table 4.1 and atomic coordinates of all non-hydrogen atoms can be found in Table A2.1.

Table 4.1: Crystallographic data for structures [Co(tren)$_2$]$_2$[Ge$_4$S$_4$O$_6$] **(6).**

Chemical formula	[Co(tren)$_2$]$_2$[Ge$_4$S$_4$O$_6$]
Formula mass	1217.52
Crystal Habit	Dark-red block
Crystal system	Triclinic
Symmetry space group	$P\bar{1}$
Temp /K	150
a /Å	12.3731 (5)
b /Å	12.7431 (5)
c /Å	15.3567 (9)
α /°	72.875 (4)
β /°	77.444 (4)
γ /°	88.387 (3)
V /Å³	2256.95 (19)
Z	2
μ /mm^{-1}	3.588
Total reflections ($I > 3\sigma(I)$)	8284
R factor	0.0882
wR factor	0.0467
Goodness of fit ref	0.9952

4.3.1.2 Structure Description and Analysis

The structure of (**6**) contains two [Co(tren)$_2$]$^{2+}$ complexes to balance the charge of the [Ge$_4$O$_6$S$_4$]$^{4-}$ clusters producing the compound [Co(tren)$_2$]$_2$[Ge$_4$S$_4$O$_6$] (Figure 4.3). Each cobalt complex in (**6**) contains two tren molecules in which two ethylamine moieties bond to the central cobalt atom as well as the tren central nitrogen. The third ethylamine moiety is excluded from coordination and is within hydrogen bonding distance to surrounding complexes within the crystal structure. The bond-valence calculations for the metal centres in the crystal structure of (**6**) indicate a formal oxidation state of +4 for germanium, Table 4.2. A

variation on the bonding of this complex has been seen once before in [Co(C$_6$H$_{18}$N$_4$)$_2$][Co(CO)$_4$]$_2$ [274]. In both compounds, the cobalt atoms are in strained octahedral environments due to the rigidity of the tren molecules. Bond lengths observed between Co-N atoms in (6) (Table 4.2) are within the range of (2.177(4) ≤ d/Å ≤ 2.303(3)), similar to the literature values (2.1800(13) ≤ d/Å ≤ 2.2206(12)) supporting the presence of +2 cobalt. As is found in [Co(C$_6$H$_{18}$N$_4$)$_2$][Co(CO)$_4$]$_2$, the two complexes in (6) contain longer axial positions with Co(2) containing the longest at 2.303(3) Å. A common feature of multidentate ligands is the influence of the biting points (N-Co-N angles) on bond length [260]. For example, in [Co(C$_6$H$_{18}$N$_4$)$_2$][Co(CO)$_4$]$_2$, the N-Co-N bond angles within single tren molecules (biting angles) to the metal centre are between (79.29(5) ≤ α/° ≤ 80.47(5)) and opposing tren N-Co-N bond angles vary between (85.53(5) ≤ α/° ≤ 100.71(5)). These compare relatively well to the angles found in (6) (Table 4.3) with N-Co-N biting angles observed between 78.46(13) ≤ α/° ≤ 81.98(14) and 82.62(13) ≤ α/° ≤ 107.14(14) for opposing tren N-Co-N angles. The complexes present in (6) and in the literature, are meridional conformations [275].
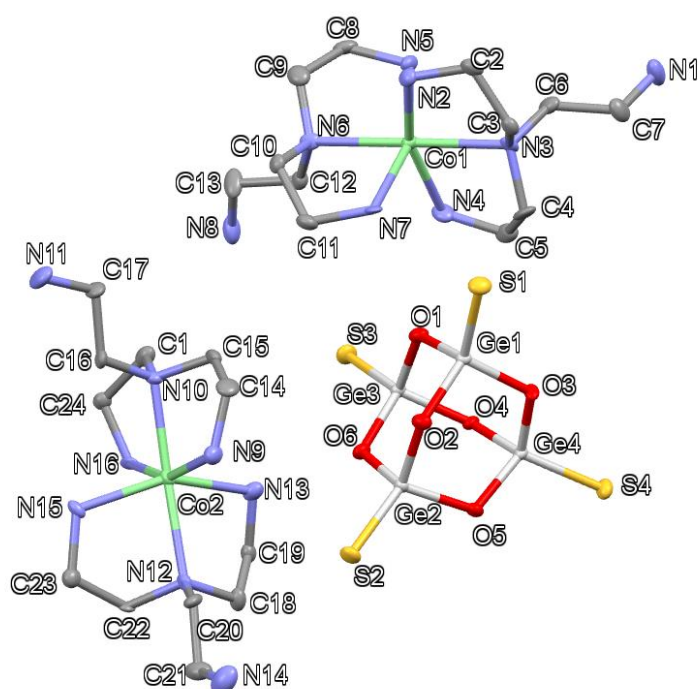
Figure 4.3: Asymmetric unit of (6) displaying thermal ellipsoids of each atom at 50 % probability. Key: light grey: Ge, green: Co atoms, yellow: S atoms, red: O atoms, light blue: N atoms, grey: C atoms. Hydrogen atoms are omitted for clarity.

Table 4.2 A selection of bond lengths and valence sums in [Co(tren)$_2$]$_2$[Ge$_4$S$_4$O$_6$] (**6**).

	Length /Å	v_{ij}		Length /Å	v_{ij}		Length /Å	v_{ij}
Ge(1)-S(1)	2.0922(11)	1.41	Ge(2)-S(2)	2.0990(11)	1.39	Ge(3)-S(3)	2.1006(11)	1.39
Ge(1)-O(2)	1.785(3)	0.90	Ge(2)-O(2)	1.792(3)	0.89	Ge(3)-O(6)	1.804(3)	0.89
Ge(1)-O(1)	1.796(3)	0.88	Ge(2)-O(6)	1.802(3)	0.86	Ge(3)-O(1)	1.802(3)	0.86
Ge(1)-O(3)	1.805(3)	0.86	Ge(2)-O(5)	1.810(3)	0.85	Ge(3)-O(4)	1.791(3)	0.85
∑vij		**4.05**			**3.99**			**3.99**
Ge(4)-S(4)	2.1003(11)	1.38	Co(1)-N(2)	2.189(4)		Co(2)-N(9)	2.178(4)	
Ge(4)-O(4)	1.794(3)	0.88	Co(1)-N(3)	2.219(4)		Co(2)-N(10)	2.190(4)	
Ge(4)-O(5)	1.799(3)	0.87	Co(1)-N(4)	2.217(4)		Co(2)-N(12)	2.303(4)	
Ge(4)-O(3)	1.783(3)	0.91	Co(1)-N(5)	2.151(4)		Co(2)-N(13)	2.170(4)	
			Co(1)-N(6)	2.225(4)		Co(2)-N(15)	2.136(3)	
			Co(1)-N(7)	2.173(4)		Co(2)-N(16)	2.255(4)	
∑vij		**4.05**						

Table 4.3 A selection of bond angles in [Co(tren)$_2$]$_2$[Ge$_4$S$_4$O$_6$] (**6**).

	Angle / °		Angle / °		Angle / °
S(1)-Ge(1)-O(2)	114.78(10)	O(6)-Ge(3)-O(4)	104.14(13)	N(4)-Co(1)-N(6)	99.31(14)
S(1)-Ge(1)-O(1)	112.71(10)	O(1)-Ge(3)-O(4)	103.86(13)	N(5)-Co(1)-N(6)	80.20(14)
O(2)-Ge(1)-O(1)	104.32(14)	S(4)-Ge(4)-O(4)	114.43(10)	N(2)-Co(1)-N(7)	85.88(14)
S(1)-Ge(1)-O(3)	115.53(9)	S(4)-Ge(4)-O(5)	113.13(10)	N(3)-Co(1)-N(7)	101.31(14)
O(2)-Ge(1)-O(3)	104.96(14)	O(4)-Ge(4)-O(5)	104.98(14)	N(4)-Co(1)-N(7)	94.44(15)
O(1)-Ge(1)-O(3)	103.25(13)	S(4)-Ge(4)-O(3)	112.51(10)	N(5)-Co(1)-N(7)	157.59(14)
S(2)-Ge(2)-O(2)	114.33(10)	O(4)-Ge(4)-O(3)	105.72(13)	N(6)-Co(1)-N(7)	80.11(14)
S(2)-Ge(2)-O(6)	113.85(10)	O(5)-Ge(4)-O(3)	105.24(13)	Ge(2)-O(2)-Ge(1)	119.83(16)
O(2)-Ge(2)-O(6)	104.49(14)	N(2)-Co(1)-N(3)	81.98(14)	Ge(3)-O(6)-Ge(2)	119.63(16)
S(2)-Ge(2)-O(5)	115.57(10)	N(2)-Co(1)-N(4)	160.28(15)	Ge(3)-O(1)-Ge(1)	120.22(16)
O(2)-Ge(2)-O(5)	103.12(13)	N(3)-Co(1)-N(4)	78.62(14)	Ge(4)-O(4)-Ge(3)	118.48(16)
O(6)-Ge(2)-O(5)	104.14(13)	N(2)-Co(1)-N(5)	87.18(14)	Ge(2)-O(5)-Ge(4)	118.27(16)
S(3)-Ge(3)-O(6)	115.56(10)	N(3)-Co(1)-N(5)	98.77(13)	Ge(1)-O(3)-Ge(4)	117.71(15)
S(3)-Ge(3)-O(1)	114.69(10)	N(4)-Co(1)-N(5)	99.19(16)		
O(6)-Ge(3)-O(1)	103.29(14)	N(2)-Co(1)-N(6)	100.16(13)		
S(3)-Ge(3)-O(4)	113.87(10)	N(3)-Co(1)-N(6)	177.54(13)		

The packing of the crystal structure in (**6**) is arranged so that all [Ge$_4$O$_6$S$_4$]$^{4-}$ units are surrounded by [Co(tren)$_2$]$^{2+}$ complexes. More specifically, the clusters and complexes arrange into columns (Figure 4.4a) and when a larger section of the structure is examined (Figure 4.4b), the columns align down the [001] direction and place complexes on adjacent columns near the clusters. Bond distances listed in Table 4.4 suggest that hydrogen bonding

interactions support the stability of the crystal structure, there are also two additional interactions between S(4)…N(5) and S(2)…N(15) at lengths of 3.243(4) and 3.264(3) Å, respectively. These hydrogen bonding interactions take place within and in-between the columns seen in Figure 4.4. Weak interactions are also seen between C…O atoms.

Table 4.4: Bond lengths found in (**6**) between acceptor and donor atoms containing hydrogen bonding.

Symmetry operations: a = -x+1, -y+2, -z+1; b = -x+1, -y+1, -z+2; c = x-1, y, z; d = -x+1, -y+1, -z+1; e = x, y-a, z

Donor-Acceptor	Bond length /Å	Donor-Acceptor	Bond length /Å
C(5)…O(4)[a]	3.472(7)	N(16)…N(8)[d]	3.236(7)
C(14)…O(2)[b]	3.325(7)	N(15)…O(3)[e]	3.070(7)
N(2)…N(14)[b]	3.138(7)	N(13)…O(6)	2.924(7)
N(2)…O(5)[c]	3.035(7)	N(14)…N(2)[b]	3.138(7)
N(7)…O(1)	2.946(7)		
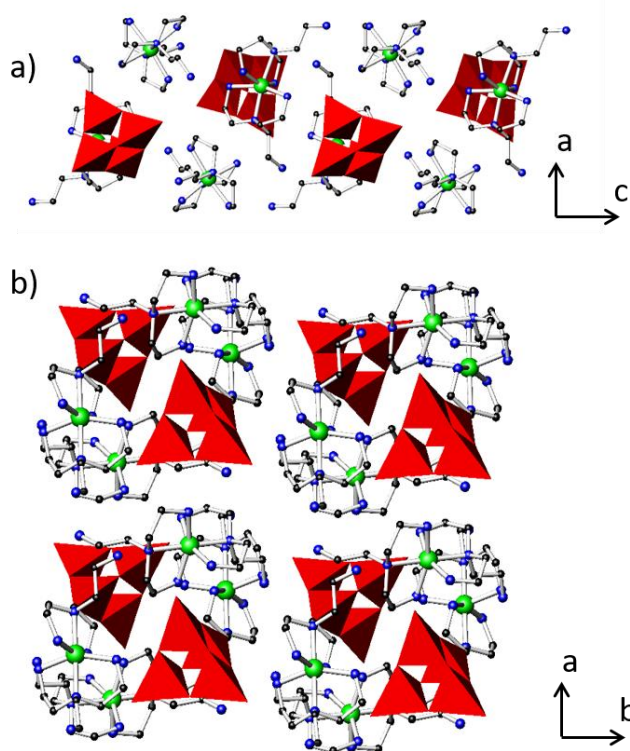
Figure 4.4: (a) A column of clusters and complexes of structure (**6**) found in the [001] direction, viewed in along [100] and (b) multiple columns in the crystal structure. Key: Red T2 polyhedra represent $[Ge_4O_6S_4]^{4-}$ units, green: Co atoms, blue: N atoms, black: C atoms. Hydrogen atoms are omitted for clarity.

4.3.2 [(Co(tren))$_2$μ-tren][Ge$_4$S$_4$O$_6$].2H$_2$O (7)

4.3.2.1 Synthesis

[(Co(tren))$_2$μ-tren][Ge$_4$S$_4$O$_6$].2H$_2$O (**7**) was synthesised from a mixture of GeO$_2$ (21 mg, 0.2 mmol), CoS (17 mg, 0.2 mmol), S (6 mg, 0.17 mmol) and tris(2-aminoethyl)amine (tren) (0.88 ml, 6 mmol). The reaction mixture was stirred for 10 minutes in a 23 ml Teflon-lined stainless-steel autoclave before being sealed and heated to 433 K at 1 K min^{-1} for 5 days. The same reaction mixture formed the same material on heating for up to 8 days. Dark-red block crystals of (**7**) were obtained along with black powder containing Co$_9$S$_8$, Co$_3$S$_4$, S and an unknown phase. The presence of (**7**) was confirmed by comparison of the powder X-ray diffraction patterns of the bulk sample with the calculated pattern generated from the single-crystal X-ray data, Figure 4.5. Combustion analysis of hand-picked crystals gave (C 18.36 %, H 4.38 %, N 14.01 %), which are close to the values from the crystallographically determined formula [(Co(tren))$_2$μ-tren][Ge$_4$S$_4$O$_6$].2H$_2$O (C 19.60 %, H 4.89 %, N 15.24 %). The reason for the discrepancy is due to the difficulty in crystal picking and possible contamination.
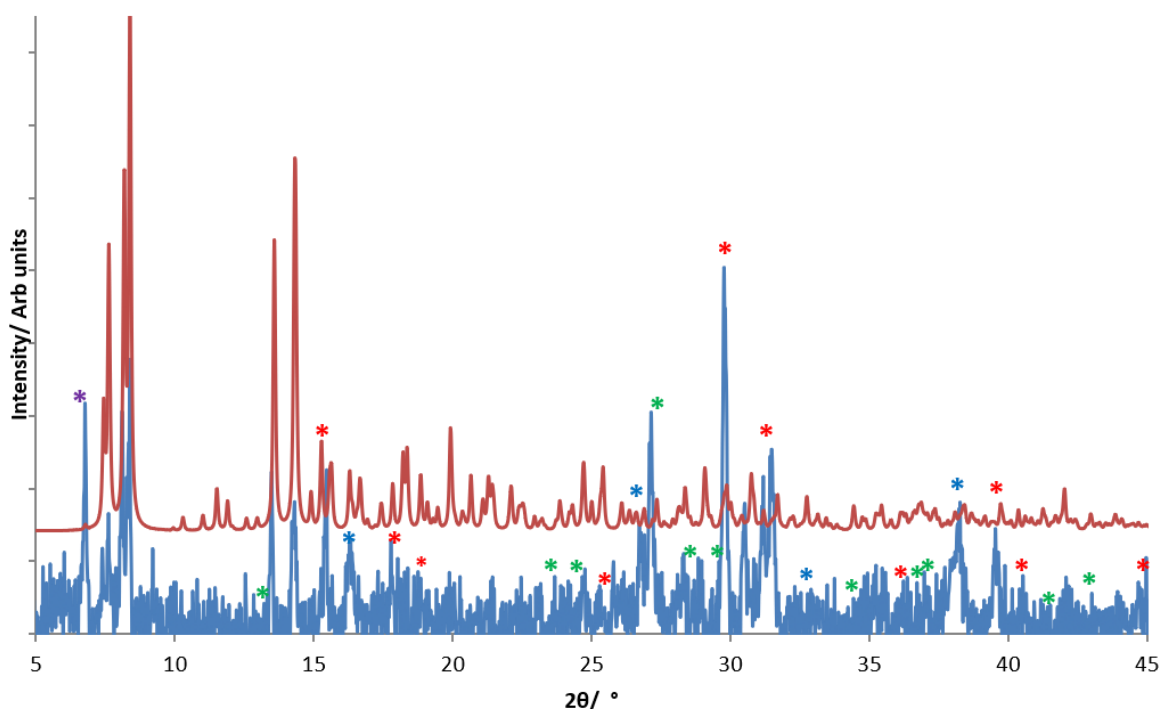
Figure 4.5: X-ray diffraction pattern of the bulk, as-synthesised product (blue) which contained crystals of [(Co(tren))$_2$μ-tren][Ge$_4$S$_4$O$_6$].2H$_2$O (**7**). The simulated pattern calculated from single-crystal X-ray data for (**7**) is shown above (red). Peaks in the bulk sample annotated with asterisks correspond to Co$_9$S$_8$ (red), Co$_3$S$_4$ (blue), S (green) and an unknown material (purple).

Single crystals were sent to Southampton University (National Crystallographic Service) for single-crystal X-ray experiments using a more intense source than that available in Reading. This experiment was conducted at 100 K using graphite monochromated MoKα (0.71073Å) radiation on a Rigaku Saturn724+ X-ray diffractometer. The refinement was conducted in F after being solved using Superflip [228] and polynomial weighting schemes were applied. Hydrogen atoms on the amine ligands were placed geometrically with a U[equiv] value 1.2 times the U[equiv] of the carbon to which they are attached. The model displayed disorder on nitrogen and carbon positions in the bridging tren molecule, these atoms were split to model this disorder, Figure 6 (with a total occupancy of 1 per pair). Restraints were also used with N-C bonds limited to 1.46 Å in length and C-C bonds 1.5 Å in length, both with a 0.01 Å variation for movement. Water molecules were present but one was split equally over two sites, O(8) and O(9). Crystallographic details are summarised for structure (**7**) in Table 4.5. Atomic coordinates of all non-hydrogen atoms are shown in Table A2.2. All images after Figure 4.6 will display only one of each of the split atoms pairs (highest occupancy) for simplicity.

Table 4.5 Crystallographic data for structures [(Co(tren))$_2$μ-tren][Ge$_4$S$_4$O$_6$]·2H$_2$O (**7**)

Chemical formula	[(Co(tren))$_2$μ-tren][Ge$_4$S$_4$O$_6$]·2H$_2$O
Formula mass	1099.77
Crystal Habit	Dark red block
Crystal system	Triclinic
Symmetry space group	P-1
Temp /K	100
a /Å	12.4290(9)
b /Å	12.4868(9)
c /Å	14.6553(10)
α /°	72.325(8)
β /°	68.989(8)
γ /°	87.202(10)
V /Å³	2018.4(3)
Z	2
μ /mm^{-1}	4.003
Total reflections (I >3σ(I))	4791
R factor	0.0732
wR factor	0.0800
Goodness of fit ref	1.0814
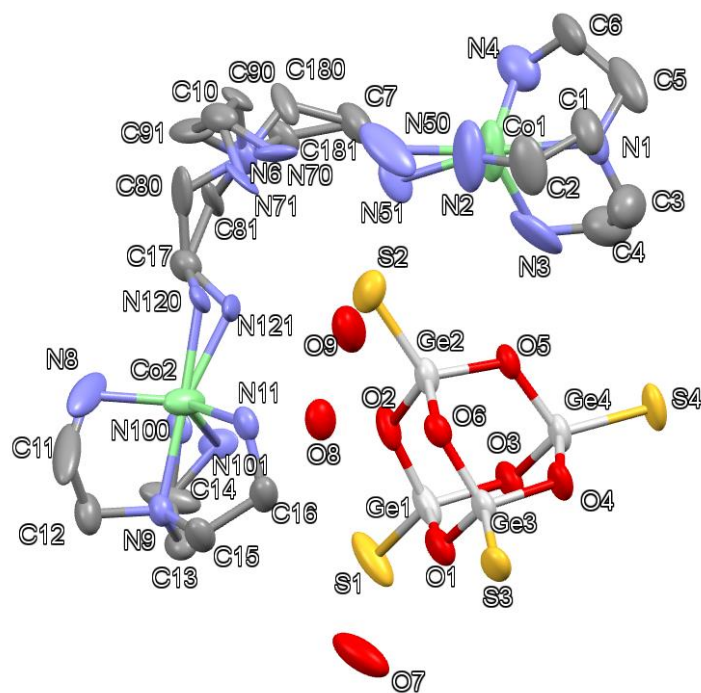
Figure 4.6: Asymmetric unit of (**7**) displaying thermal ellipsoids of each atom at 50 % probability. Key: light grey: Ge, green: Co atoms, yellow: S atoms, red: O atoms, light blue: N atoms, grey: C atoms. Hydrogen atoms are omitted for clarity.

4.3.2.2 Structure Description and Analysis

The T2 unit in compound (**7**) is identical to that in compound (**6**). The counter ion in compound (**7**) is unusual in that it consists of two trigonal bipyramidal Co(tren) complexes bridged *via* a third tren molecule. The bridging tren molecule has an uncoordinated $(CH_2)_2NH_2$ group which is within hydrogen bonding (N…S) distance of the T2 cluster, 3.49(2) Å. To the author's knowledge, this is the first time this complex bridging system has been observed. In addition, there are two water molecules in the asymmetric unit, as confirmed by the IR and TGA data. One water molecule is disordered over two sites (O(8) and O(9) at 0.5 occupancy).

The Co-N bond lengths in the cations in (**7**) (Table 4.6) show a stretched complex in which equatorial bonds are shorter ($1.948(17) \leq d/\text{Å} \leq 2.051(10)$) than axial bonds ($2.088(18) \leq d/\text{Å} \leq 2.266(12)$). This has been previously observed in the Co(II) trigonal bipyramidal complex Co(tren)Br [276], which demonstrated longer axial positions of 2.151(21) Å and 2.431(4) Å for N-Co and Co-Br bonds respectively. As with the complexes in structure (**6**), the bond angles (Table 4.7) are also distorted from the ideal 90 ° with internal N-Co-N biting angles in the range ($79.1(4) \leq \alpha/° \leq 83.4(5)$) due to rigidity of multidentate ligands.

119

The packing of the crystal structure is similar to (**6**), in which opposing T2 units and complexes align into rows down [100] (Figure 4.7a). The crystal packing is accumulation of the rows each side and is seen in Figure 4.7b. This arrangement prevents unfavourable interactions between the negatively charged clusters as they are surrounded by complexes. All interactions between acceptor and donor atoms within this compound can be seen in Table 4.8. These N…O interactions support the presence of weak hydrogen bonding throughout the structure. In addition, weak interactions are seen between C…O atoms.
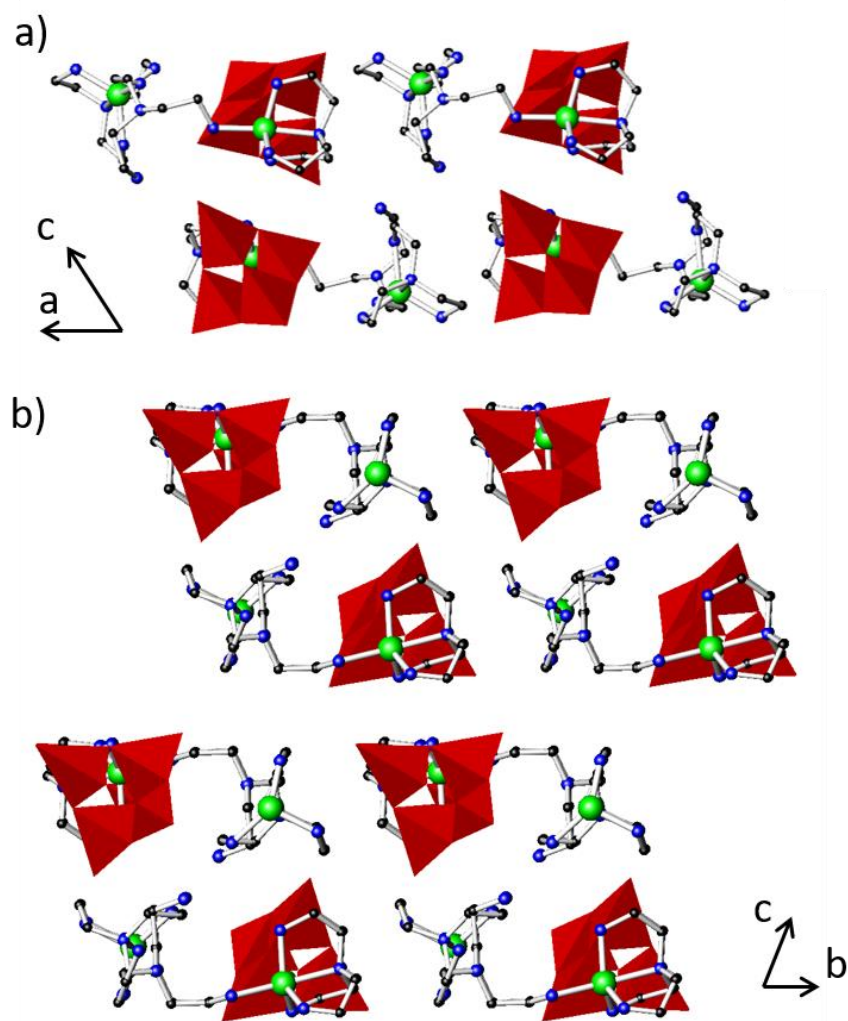
Figure 4.7: (a) A column of clusters and complexes of structure (**7**) aligned along the [100] direction, viewed in along [010] and (b) multiple columns in a fully packed crystal structure down [100]. Key: Red T2 polyhedra represent $[Ge_4O_6S_4]^{4-}$ units, green Co, blue N, black C. Hydrogen atoms and water are omitted for clarity.

Table 4.6: A selection of bond lengths and valence sums in [(Co(tren))$_2$μ-tren][Ge$_4$S$_4$O$_6$]·2H$_2$O (**7**).

	Length /Å	v_{ij}		Length /Å	v_{ij}		Length /Å	v_{ij}
Ge(1)-S(1)	2.085(3)	1.44	Ge(2)-S(2)	2.105(4)	1.36	Ge(3)-S(3)	2.097(3)	1.39
Ge(1)-O(2)	1.795(9)	0.88	Ge(2)-O(2)	1.789(7)	0.90	Ge(3)-O(6)	1.792(8)	0.89
Ge(1)-O(1)	1.788(9)	0.90	Ge(2)-O(6)	1.795(7)	0.88	Ge(3)-O(1)	1.801(8)	0.87
Ge(1)-O(3)	1.796(7)	0.88	Ge(2)-O(5)	1.788(6)	0.90	Ge(3)-O(4)	1.785(6)	0.90
∑vij		**4.10**			**4.04**			**4.05**
Ge(4)-S(4)	2.100(3)	1.38	Co(1)-N(1)	2.266(10)		Co(2)-N(8)	2.051(17)	
Ge(4)-O(4)	1.792(7)	0.89	Co(1)-N(2)	2.067(13)		Co(2)-N(9)	2.234(9)	
Ge(4)-O(5)	1.806(8)	0.85	Co(1)-N(3)	2.045(17)		Co(2)-N(11)	2.051(9)	
Ge(4)-O(3)	1.788(8)	0.90	Co(1)-N(4)	2.013(14)		Co(2)-N(100)	1.948(14)	
			Co(1)-N(50)	2.08(4)		Co(2)-N(101)	2.240(17)	
			Co(1)-N(51)	2.172(14)		Co(2)-N(120)	2.088(16)	
						Co(2)-N(121)	2.19(3)	
∑vij		**4.02**						

Table 4.7: A selection of bond angles in [(Co(tren))$_2$μ-tren][Ge$_4$S$_4$O$_6$]·2H$_2$O (**7**).

	Angle / °		Angle / °		Angle / °
S(1)-Ge(1)-O(2)	113.8(3)	S(3)-Ge(3)-O(1)	115.2(3)	N(2)-Co(1)-N(3)	117.0(7)
S(1)-Ge(1)-O(1)	115.2(3)	O(6)-Ge(3)-O(1)	102.8(4)	N(1)-Co(1)-N(4)	83.4(5)
O(2)-Ge(1)-O(1)	103.5(4)	S(3)-Ge(3)-O(4)	113.9(3)	N(2)-Co(1)-N(4)	125.9(7)
S(1)-Ge(1)-O(3)	116.4(3)	O(6)-Ge(3)-O(4)	104.4(3)	N(3)-Co(1)-N(4)	109.5(5)
O(2)-Ge(1)-O(3)	103.2(4)	O(1)-Ge(3)-O(4)	103.2(3)	N(1)-Co(1)-N(50)	156.3(8)
O(1)-Ge(1)-O(3)	103.0(4)	S(4)-Ge(4)-O(4)	114.6(2)	N(2)-Co(1)-N(50)	78.1(8)
S(2)-Ge(2)-O(2)	112.5(3)	S(4)-Ge(4)-O(5)	113.3(2)	N(3)-Co(1)-N(50)	116.5(11)
S(2)-Ge(2)-O(6)	113.0(3)	O(4)-Ge(4)-O(5)	104.1(3)	N(4)-Co(1)-N(50)	105.0(9)
O(2)-Ge(2)-O(6)	104.3(4)	S(4)-Ge(4)-O(3)	114.9(2)	N(1)-Co(1)-N(51)	168.5(5)
S(2)-Ge(2)-O(5)	116.5(3)	O(4)-Ge(4)-O(3)	104.4(4)	N(2)-Co(1)-N(51)	99.2(5)
O(2)-Ge(2)-O(5)	103.3(3)	O(5)-Ge(4)-O(3)	104.3(3)	N(3)-Co(1)-N(51)	91.0(6)
O(6)-Ge(2)-O(5)	106.0(3)	N(1)-Co(1)-N(2)	79.1(4)	N(4)-Co(1)-N(51)	106.4(5)
S(3)-Ge(3)-O(6)	115.7(2)	N(1)-Co(1)-N(3)	79.9(5)		

Table 4.8: Bond lengths found in (**7**) between acceptor and donor atoms containing hydrogen bonding.

Symmetry operations: a = x-1, y, z; b =-x+1, -y+1, -z; c = x, y-1, z; d =-x+1, -y+1, -z+1; e =-x+1, -y+2, -z

	Length /Å		Length /Å		Length /Å
C(90)…O(7)[a]	3.36(2)	N(8)…O(4)[c]	3.19(2)	N(2)…O(7)[a]	3.02(2)
C(6)…O(1)[a]	3.41(2)	N(11)…O(6)[d]	3.21(2)	N(4)…O(3)[e]	3.08(2)
C(80)…O(8)[b]	3.73(2)	N(101)…O(8)	2.26(2)	N(3)…O(5)	3.01(2)
C(81)…O(8)[b]	3.20(2)	N(100)…O(8)	2.98(2)	N(50)…O(7)[a]	2.94(2)
N(70)…O(7)[a]	3.24(2)	N(121)…O(9)	3.08(2)		

Thermogravimetric analysis (TGA) of compound (**7**) shows a total organic weight loss of 38.32 % in a two-step decomposition (Figure 4.8). The first, a 19.84 % weight loss, is attributed to loss of one tren and a piperazine molecule, the remaining organic components are then removed in the second step. The breakdown of amines under thermal conditions has been previously documented [254, 255] and a similar breakdown of the tren molecules in a crystal structure was seen in the compound $(H_{1.3}tren)[In_{2.67}Sb_{1.33}S_8] \cdot tren$ (**1**) from Chapter 3 [250] (Figure A1.2). A weight loss corresponding to the pore water is observable in the TGA but can be seen more clearly in the difference plot which shows a two-step weight loss. The first step represents external water and is removed until 43 ˚C, after which, the second weight loss begins and represents internal water within the crystal structure. This levels out at ~100 ˚C once the water has been removed. The second step equates to ~2.43 % which is slightly higher than the predicted 1.8 % of water. A reason for this could either be the margin of error when analysing such small mg quantities of sample or a molecule of water might still be present within the Fourier maps of the single crystal model, although this was not located.

The IR spectrum of (**7**) is shown in Figure 4.9. The vibrations have been tentatively assigned and provide evidence of amine presence as seen in Table 4.9 [253]. The multiple ν(C-N) vibrations between ~ 1000-1100 cm^{-1} are likely due to the presence of primary and secondary C-N sites because of the bridging tren molecule. The IR compares relatively well with the data from the NIST database on tris(2-aminoethyl)amine [253].The water ν(O-H) vibrations at 3387 cm^{-1} appear to be quite intense but the δ(H-O-H) usually at around 1640 cm^{-1} appears to be partially masked by the δ (H-N-H) bending, thus a shoulder is seen.
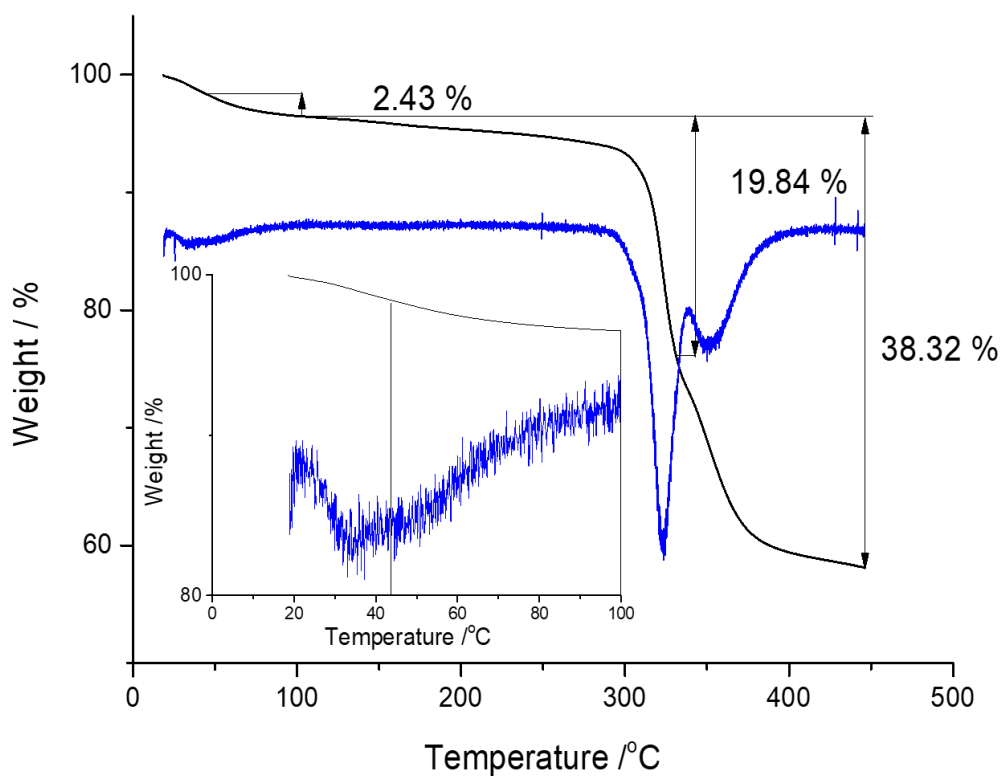
Figure 4.8: Thermogravimetric analysis curve of $[(Co(tren))_2\mu\text{-tren}][Ge_4S_4O_6]\cdot 2H_2O$ (**7**) heated under N_2 (black) and the corresponding derivative (DTG) curve (blue). An additional curve is represented to show the difference in peak position of internal water.
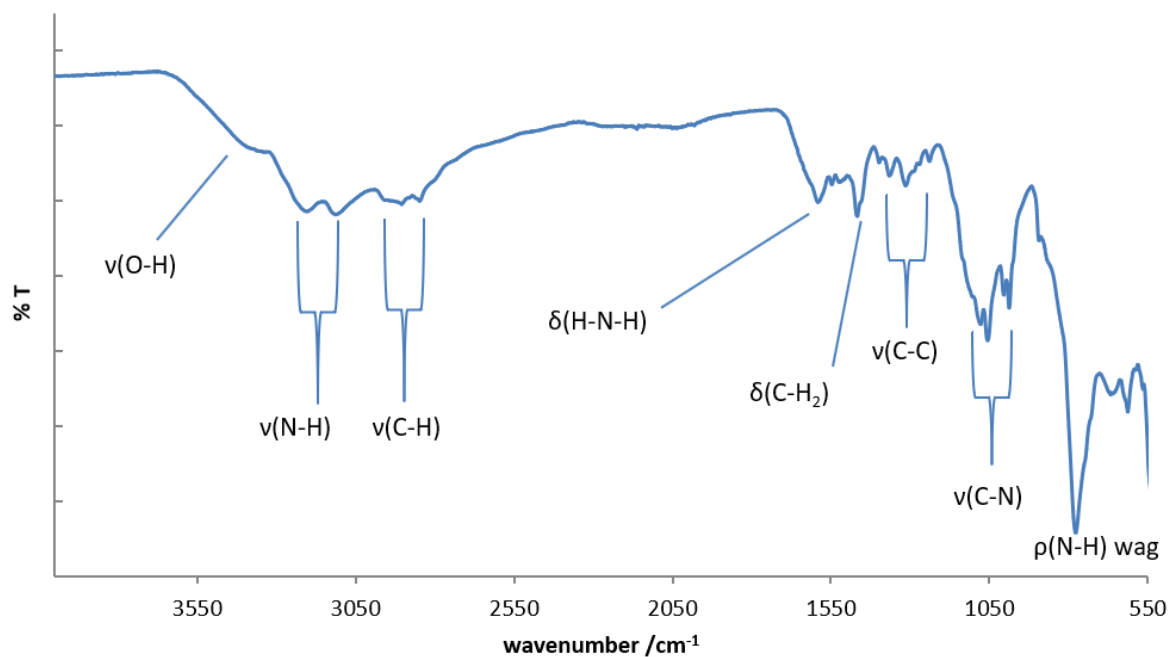
Figure 4.9: IR spectrum of $[(Co(tren))_2\mu\text{-tren}][Ge_4S_4O_6]\cdot 2H_2O$ (**7**) using hand-picked crystals

Table 4.9: Infrared spectrum assignments of $[(Co(tren))_2\mu\text{-tren}][Ge_4S_4O_6]\cdot 2H_2O$ **(7)**

Stretching mode	Wavenumber /cm^{-1}
ν(O-H)	3387
ν(N-H)	3097 (sym) and 3203 (asym)
ν(C-H)	2801 (sym) and 2962 (asym)
δ(H-N-H)	1589
δ (C-H$_2$)	1467
ν(C-C)	1238-1498 (multiple peaks)
ν(C-N)	1000-1100 (multiple peaks)
ρ(N-H) wag	979

The diffuse reflectance spectrum of compound (**7**) (Figure 4.10) contains an absorption edge at 4.1(3) eV and minor peaks between 2-3 eV. These are associated with *d-d* interactions of the cobalt centres [277]. As the state of the octahedral splitting is not known, specific transitions cannot be assigned. Other publications have observed the *d-d* transition metal peaks in the region ~1.5-3 eV, either in discrete templating complexes *e.g.* within $[M(deta)_2][AlB_6O_{11}(OH)]$ (M = Co, Ni, Cd, Zn)-[278], $[Ni(deta)_2]_{0.5}[InS_2]$ and $[Ni(dap)_3]_{0.5}[InS_2]$ [87] or as a complex pendant on a chain *e.g.* $[Ni(tepa)]_2[In_4S_7(SH)_2]\cdot H_2O$ [88].
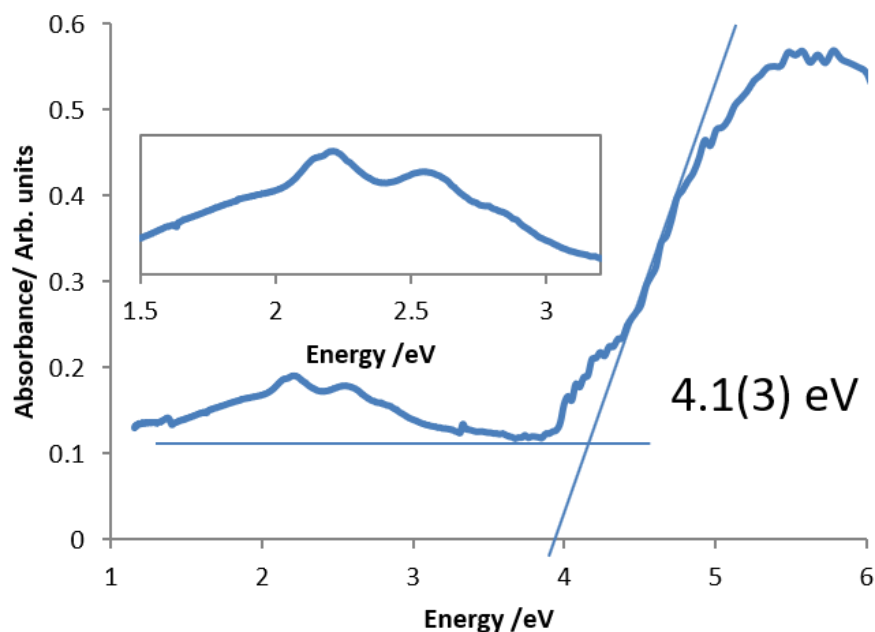
Figure 4.10: Diffuse reflectance spectrum of $[(Co(tren))_2\mu\text{-tren}][Ge_4S_4O_6].2H_2O$ (**7**) using hand-picked crystals showing a band gap of 4.1(3) eV.

4.3.3 [Co(deta)$_2$]$_2$[Ge$_4$O$_6$S$_4$]·H$_2$O (8) and (9)

4.3.3.1 Synthesis

[Co(deta)$_2$]$_2$[Ge$_4$O$_6$S$_4$]·H$_2$O (**8**) and (**9**) are polymorphs and both are synthesised from a mixture of GeO$_2$ (200 mg, 1.9 mmol), CoS (173 mg, 1.9 mmol), S (60 mg 1.7 mmol) and diethylenetriamine (5 ml, 46 mmol). The reaction mixture was stirred for 10 minutes in a 23 ml Teflon-lined stainless-steel autoclave before being sealed and heated to 413 K at 1 K min^{-1} for 5 days for (**8**) and 4 days for (**9**). Both reactions formed dark red/orange crystals along with black powder. X-ray diffraction patterns of the bulk samples in (**8**) and (**9**) both match the calculated patterns generated by single-crystal X-ray data, Figures 4.11 and 4.12, respectively. Other compounds were identified in the powder X-ray diffraction patterns of both (**8**) and (**9**) including, Co$_3$S$_4$, Co$_9$S$_8$ and unreacted CoS. The pattern of (**8**) also displayed a further peak which was not able to be identified. As the patterns are so similar, single-crystal X-ray analysis was used to identify which sample contained which crystals.

Figure 4.11: X-ray diffraction pattern of the bulk, as-synthesised product (blue) which contained crystals of [Co(deta)$_2$]$_2$[Ge$_4$O$_6$S$_4$]·H$_2$O (**8**). The simulated pattern calculated from single-crystal X-ray data for (**8**) is shown above (red). Peaks in the bulk sample annotated with asterisks correspond to Co$_3$S$_4$ (red), Co$_9$S$_8$ (blue), Co*S* (green) and an unknown material (purple).

Figure 4.12: X-ray diffraction pattern of the bulk, as-synthesised product (blue) which contained crystals of $[Co(deta)_2]_2[Ge_4O_6S_4]\cdot H_2O$ (**9**). The simulated pattern calculated from single-crystal X-ray data for (**9**) is shown above (red). Peaks in the bulk sample annotated with asterisks correspond to Co_9S_8 (red), CoS (blue) and Co_3S_4 (green).

The production of the two polymers is likely due to the reaction time of each material, where the shorter reaction time favours the formation of (**9**) and the longer (a day extra or longer) favours (**8**). While (**9**) is only observed during the shorter reaction time, the structure of (**8**) has been identified in a reaction that was intended to produce (**9**). This reaction was as repeat experiment using the ratios listed above for compound (**9**). This could indicate structure (**9**) as the potentially less thermodynamically stable form as attempting optimisation experiments failed to produce any substantial yields. Due to the small quantity of crystals that formed in reactions to produce (**9**), only (**8**) could be characterised fully.

Single crystals of both (**8**) and (**9**) were sent to Southampton University (National Crystallographic Service) for X-ray experiments. These measurements were conducted at 100 K using graphite monochromated MoKα (0.71073 Å) radiation on a Rigaku Saturn724+ X-ray diffractometer. The structure of (**8**) was solved with Superflip [228] while (**9**) was solved in SIR92 [227]. Both refinements were conducted against F and a Chebychev polynomial weighting schemes were applied. While there was no obvious twinning in the data set of (**8**), applying a twin law improved the statistics considerably, the two twin components were

0.3 % and 99.7 %. The data collection of (**9**) however was from a twinned crystal and required a twin law, with the two twin components being 51 % and 49 %. The oxygen water molecule O(7) was only found in (**9**) but could not be located in the model of (**8**) due to disorder, but electron density suspected to be water is seen within the pore space down [001] and can be observed in the TGA measurements. Atom O(5) in structure (**8**) was heavily disordered. Hydrogen atoms on the amine ligands were placed geometrically with a U[equiv] value 1.2 times the U[equiv] of the carbon to which they are attached. Crystallographic details are summarised for structures (**8**) and (**9**) in Table 4.10 with thermal ellipsoid representations of the asymmetric units of (**8**) and (**9**) in Figure 4.13 and 4.14 respectively. Atomic coordinates of all non-hydrogen atoms can be found in Tables A2.3 and A2.4.

Table 4.10 Crystallographic data for structures $[Co(deta)_2]_2[Ge_4O_6S_4]\cdot H_2O$ (**8**) and (**9**).

Chemical formula	(**8**) $[Co(deta)_2]_2[Ge_4O_6S_4]\cdot H_2O$	(**9**) $[Co(deta)_2]_2[Ge_4O_6S_4]\cdot H_2O$
Formula mass	1063.25	1063.25
Crystal Habit	Orange/red shard	Orange/red shard
Crystal system	Tetragonal	Tetragonal
Symmetry space group	$I4_1/a$	$P4_1$
Temp /K	100	100
a /Å	39.8141(4)	14.1817(10)
b /Å	39.8141(4)	14.1817(10)
c /Å	18.7098(3)	18.8966(10)
V /Å³	29658.0(4)	3800.5(2)
Z	16	4
μ /mm^{-1}	4.350	4.246
Total reflections ($I > 3\sigma(I)$)	10450	8256
R factor	0.1374	0.0237
wR factor	0.1179	0.0271
Goodness of fit ref	1.0479	1.0999

Figure 4.13: Asymmetric unit of (**8**) displaying thermal ellipsoids of each atom at 50 % probability. Key: light grey: Ge, green: Co atoms, yellow: S atoms, red: O atoms, light blue: N atoms, grey: C atoms. Hydrogen atoms are omitted for clarity.
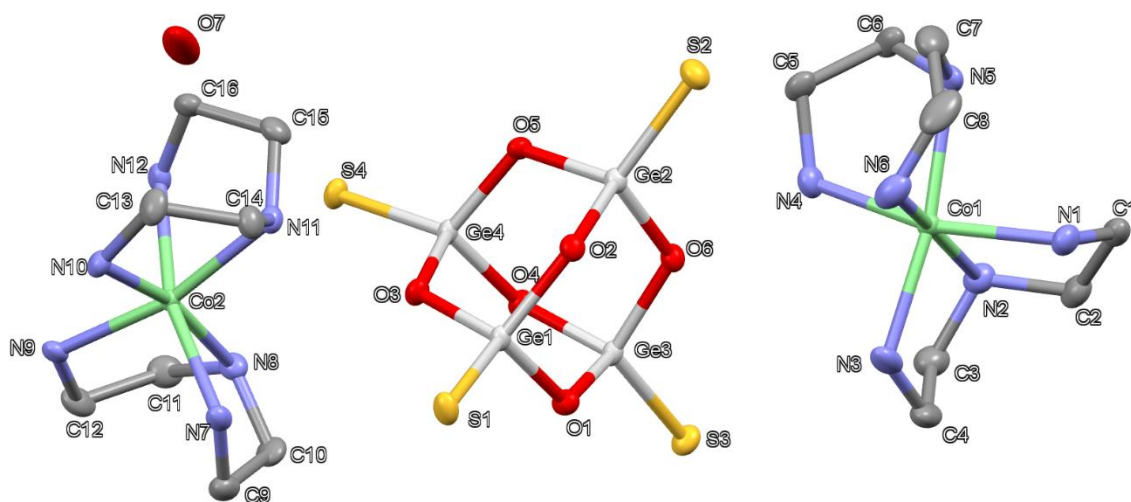
Figure 4.14: Asymmetric unit of (**9**) displaying thermal ellipsoids of each atom at 50 % probability. Key: light grey: Ge, green: Co atoms, yellow: S atoms, red: O atoms, light blue: N atoms, grey: C atoms. Hydrogen atoms are omitted for clarity.

4.3.3.2 Structure Description and Analysis

Compounds (**8**) and (**9**) are polymorphic with the formula $[Co(deta)_2]_2[Ge_4O_6S_4].H_2O$. As seen with the previous two structures, the $[Ge_4O_6S_4]^{4-}$ cluster is present in both. The counter ion in both polymorphs is a cobalt complex chelated by two deta molecules. Interestingly, the complexes present in (**8**) are both meridional and facial confomers in equal abundance.

128

The bond lengths and angles seen in (**8**) and (**9**) (Tables 4.11-4.14) are comparable to those seen in the previous structures. The presence of Co(II) is also evidenced in the bond lengths previously reported in the compound $[Co(deta)_2]_2In_2Sb_4S_{11}$ [152], N-Co distances here are between $(2.156(10) \leq d/\text{Å} \leq 2.239(7))$ similar to (**8**) $(2.107(14) \leq d/\text{Å} \leq 2.28(2))$ and (**9**) $(2.140(5) \leq d/\text{Å} \leq 2.245(4))$. There is no difference between the inorganic clusters seen here with the previous structures, but slight variations in N-Co-N angles are observed due to the use of deta molecules instead of tren. Angles vary between $(77.2(5) \leq \alpha/° \leq 81.8(5))$ for internal N-Co-N biting angles which are smaller compared to (**6**) and (**7**), while all other N-Co-N angles are between $(88.8(5) \leq \alpha/° \leq 105.7(5))$.

Table 4.11 A selection of bond lengths and valence sums in (**8**) $[Co(deta)_2]_2[Ge_4O_6S_4]\cdot H_2O$.

	Length /Å	v_{ij}		Length /Å	v_{ij}		Length /Å	v_{ij}
Ge(1)-S(1)	2.106(4)	1.36	Ge(2)-S(2)	2.099(4)	1.39	Ge(3)-S(3)	2.107(4)	1.36
Ge(1)-O(2)	1.79(1)	0.89	Ge(2)-O(2)	1.838(10)	0.78	Ge(3)-O(6)	1.832(10)	0.80
Ge(1)-O(1)	1.816(9)	0.83	Ge(2)-O(6)	1.747(12)	1.00	Ge(3)-O(1)	1.774(10)	0.93
Ge(1)-O(3)	1.795(8)	0.88	Ge(2)-O(5)	1.795(8)	0.88	Ge(3)-O(4)	1.827(11)	0.81
$\sum v_{ij}$		**3.96**			**4.02**			**3.90**
Ge(4)-S(4)	2.098(4)	1.39	Ge(5)-S(5)	2.098(4)	1.39	Ge(6)-S(6)	2.105(4)	1.36
Ge(4)-O(4)	1.763(10)	0.96	Ge(5)-O(7)	1.840(11)	0.78	Ge(6)-O(7)	1.722(10)	1.07
Ge(4)-O(5)	1.829(8)	0.80	Ge(5)-O(9)	1.835(11)	0.79	Ge(6)-O(8)	1.759(9)	0.97
Ge(4)-O(3)	1.788(8)	0.90	Ge(5)-O(12)	1.767(10)	0.95	Ge(6)-O(1)	1.817(9)	0.83
$\sum v_{ij}$		**4.05**			**3.91**			**4.23**
Ge(8)-S(8)	2.095(4)	1.40	Co(1)-N(1)	2.122(11)		Co(3)-N(13)	2.210(16)	
Ge(8)-O(10)	1.794(11)	0.88	Co(1)-N(2)	2.169(14)		Co(3)-N(14)	2.18(2)	
Ge(8)-O(11)	1.814(12)	0.84	Co(1)-N(3)	2.105(11)		Co(3)-N(15)	2.279(19)	
Ge(8)-O(12)	1.786(10)	0.90	Co(1)-N(4)	2.174(13)		Co(3)-N(16)	2.186(13)	
			Co(1)-N(5)	2.238(16)		Co(3)-N(17)	2.22(3)	
			Co(1)-N(6)	2.127(12)		Co(3)-N(18)	2.201(15)	
$\sum v_{ij}$		**4.02**						
Co(2)-N(7)	2.130(12)		Co(4)-N(19)	2.190(14)				
Co(2)-N(8)	2.121(14)		Co(4)-N(20)	2.185(17)				
Co(2)-N(9)	2.177(13)		Co(4)-N(21)	2.170(15)				
Co(2)-N(10)	2.201(14)		Co(4)-N(22)	2.210(17)				
Co(2)-N(11)	2.217(16)		Co(4)-N(23)	2.107(14)				
Co(2)-N(12)	2.126(13)		Co(4)-N(24)	2.28(2)				

Table 4.12 A selection of bond angles in $[Co(deta)_2]_2[Ge_4O_6S_4]\cdot H_2O$ (**8**).

	Angle / °		Angle / °		Angle / °
S(1)-Ge(1)-O(2)	114.7(4)	S(3)-Ge(3)-O(1)	115.7(3)	N(2)-Co(1)-N(3)	81.6(6)
S(1)-Ge(1)-O(1)	116.0(3)	O(6)-Ge(3)-O(1)	102.2(4)	N(1)-Co(1)-N(4)	91.6(5)
O(2)-Ge(1)-O(1)	102.9(5)	S(3)-Ge(3)-O(4)	114.8(3)	N(2)-Co(1)-N(4)	91.5(6)
S(1)-Ge(1)-O(3)	111.9(3)	O(6)-Ge(3)-O(4)	104.6(4)	N(2)-Co(1)-N(5)	162.3(5)
O(2)-Ge(1)-O(3)	104.5(5)	O(1)-Ge(3)-O(4)	105.1(5)	N(3)-Co(1)-N(5)	167.1(5)
O(1)-Ge(1)-O(3)	105.7(4)	S(4)-Ge(4)-O(4)	114.2(4)	N(4)-Co(1)-N(5)	105.8(5)
S(2)-Ge(2)-O(2)	113.8(3)	S(4)-Ge(4)-O(5)	116.4(3)	N(1)-Co(1)-N(6)	88.8(5)
S(2)-Ge(2)-O(6)	111.7(4)	O(4)-Ge(4)-O(5)	103.7(4)	N(3)-Co(1)-N(6)	77.3(5)
O(2)-Ge(2)-O(6)	103.7(4)	S(4)-Ge(4)-O(3)	112.2(3)	N(4)-Co(1)-N(6)	95.4(5)
S(2)-Ge(2)-O(5)	116.3(3)	O(4)-Ge(4)-O(3)	105.6(5)	N(5)-Co(1)-N(6)	169.7(6)
O(2)-Ge(2)-O(5)	105.5(5)	O(5)-Ge(4)-O(3)	103.5(4)		
O(6)-Ge(2)-O(5)	104.6(4)	N(1)-Co(1)-N(2)	80.8(5)		
S(3)-Ge(3)-O(6)	113.1(4)	N(1)-Co(1)-N(3)	103.3(4)		

Table 4.13 A selection of bond lengths and valence sums in $[Co(deta)_2]_2[Ge_4O_6S_4]\cdot H_2O$ (**9**).

	Length /Å	v_{ij}		Length /Å	v_{ij}		Length /Å	v_{ij}
Ge(1)-S(1)	2.1046(11)	1.37	Ge(2)-S(2)	2.0999(12)	1.38	Ge(3)-S(3)	2.1011(11)	1.38
Ge(1)-O(2)	1.797(3)	0.88	Ge(2)-O(2)	1.807(3)	0.85	Ge(3)-O(6)	1.812(3)	0.84
Ge(1)-O(1)	1.796(3)	0.88	Ge(2)-O(6)	1.792(3)	0.89	Ge(3)-O(1)	1.780(3)	0.92
Ge(1)-O(3)	1.784(3)	0.91	Ge(2)-O(5)	1.803(3)	0.86	Ge(3)-O(4)	1.798(3)	0.87
$\sum v_{ij}$		**4.04**			**3.98**			**4.01**
Ge(4)-S(4)	2.1042(11)	1.37	Co(1)-N(1)	2.142(4)		Co(2)-N(7)	2.156(4)	
Ge(4)-O(4)	1.798(3)	0.87	Co(1)-N(2)	2.199(4)		Co(2)-N(8)	2.214(4)	
Ge(4)-O(5)	1.792(3)	0.89	Co(1)-N(3)	2.150(4)		Co(2)-N(9)	2.153(4)	
Ge(4)-O(3)	1.788(3)	0.90	Co(1)-N(4)	2.171(4)		Co(2)-N(10)	2.172(4)	
			Co(1)-N(5)	2.245(4)		Co(2)-N(11)	2.205(4)	
			Co(1)-N(6)	2.140(5)		Co(2)-N(12)	2.162(4)	
$\sum v_{ij}$		**4.03**						

Table 4.14 A selection of bond angles in $[Co(deta)_2]_2[Ge_4O_6S_4]\cdot H_2O$ (**9**).

	Angle / ˚		Angle / ˚		Angle / ˚
S(1)-Ge(1)-O(2)	116.82(10)	O(6)-Ge(3)-O(1)	105.06(14)	N(2)-Co(1)-N(4)	89.28(15)
S(1)-Ge(1)-O(1)	115.62(11)	S(3)-Ge(3)-O(4)	114.07(11)	N(3)-Co(1)-N(4)	94.83(15)
O(2)-Ge(1)-O(1)	102.68(13)	O(6)-Ge(3)-O(4)	102.48(14)	N(1)-Co(1)-N(5)	88.32(15)
S(1)-Ge(1)-O(3)	111.84(10)	O(1)-Ge(3)-O(4)	104.48(14)	N(2)-Co(1)-N(5)	107.21(15)
O(2)-Ge(1)-O(3)	105.07(14)	S(4)-Ge(4)-O(4)	113.12(10)	N(3)-Co(1)-N(5)	169.83(16)
O(1)-Ge(1)-O(3)	103.34(14)	S(4)-Ge(4)-O(5)	118.60(10)	N(4)-Co(1)-N(5)	78.68(15)
S(2)-Ge(2)-O(2)	115.16(10)	O(4)-Ge(4)-O(5)	103.65(14)	N(1)-Co(1)-N(6)	93.21(17)
S(2)-Ge(2)-O(6)	113.17(10)	S(4)-Ge(4)-O(3)	111.15(10)	N(2)-Co(1)-N(6)	170.28(15)
O(2)-Ge(2)-O(6)	104.02(14)	O(4)-Ge(4)-O(3)	106.24(14)	N(3)-Co(1)-N(6)	94.25(18)
S(2)-Ge(2)-O(5)	113.78(10)	O(5)-Ge(4)-O(3)	102.90(14)	N(4)-Co(1)-N(6)	99.24(16)
O(2)-Ge(2)-O(5)	104.30(14)	N(1)-Co(1)-N(2)	79.94(16)	N(5)-Co(1)-N(6)	79.25(17)
O(6)-Ge(2)-O(5)	105.31(14)	N(1)-Co(1)-N(3)	99.93(16)		
S(3)-Ge(3)-O(6)	115.08(9)	N(2)-Co(1)-N(3)	80.29(17)		
S(3)-Ge(3)-O(1)	114.34(11)	N(1)-Co(1)-N(4)	159.92(15)		

The crystal structures of (**8**) and (**9**) pack in a similar manner. When viewed down [001], both (**8**) and (**9**) contain columns of clusters and complexes which pack 90 degrees to each other and repeat (four-fold screw axis). The columns themselves are staggered so that the complexes are placed next to the clusters of the neighbouring column and can be viewed in Figure 4.15 and 4.16. The difference in packing between the polymorphs is observed best when aligning complexes in-between rows of clusters along the *c* axis, Figure 4.17. Structure (**9**) displays a minor zig zag motif compared to that of (**8**) which is straight.
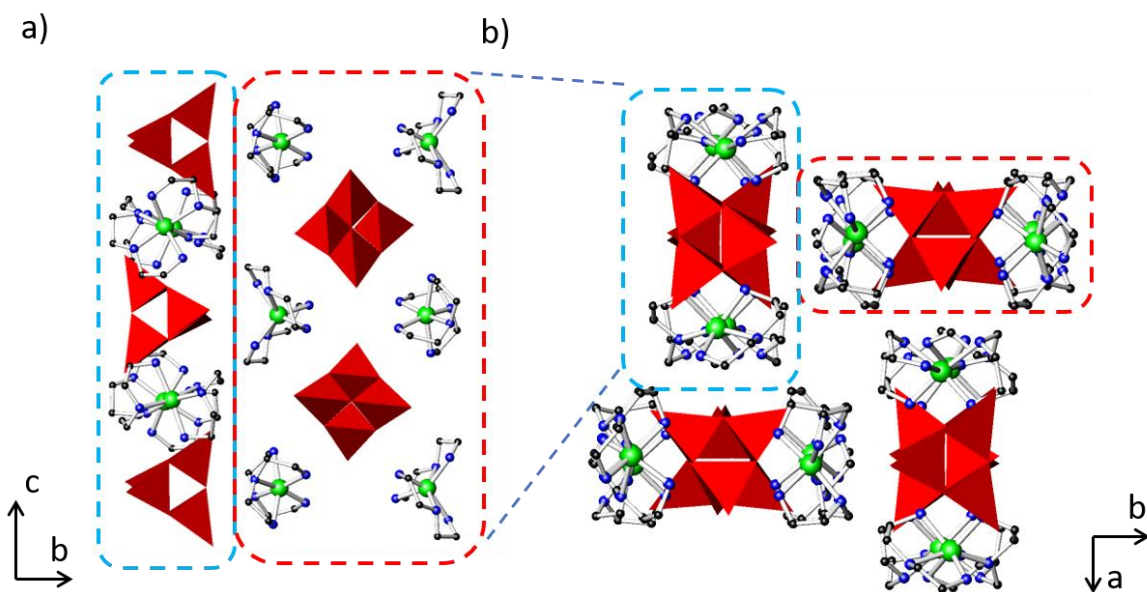
Figure 4.15: (a) Two columns of clusters and complexes in structure (**8**) aligned along the [001] direction, viewed in along [100] and (b) displays multiple columns in a fully packed crystal structure down [001]. Key: Red T2 polyhedra represent $[Ge_4O_6S_4]^{4-}$ units, green: Co atoms, blue: N atoms, black: C atoms. Hydrogen atoms are omitted for clarity.
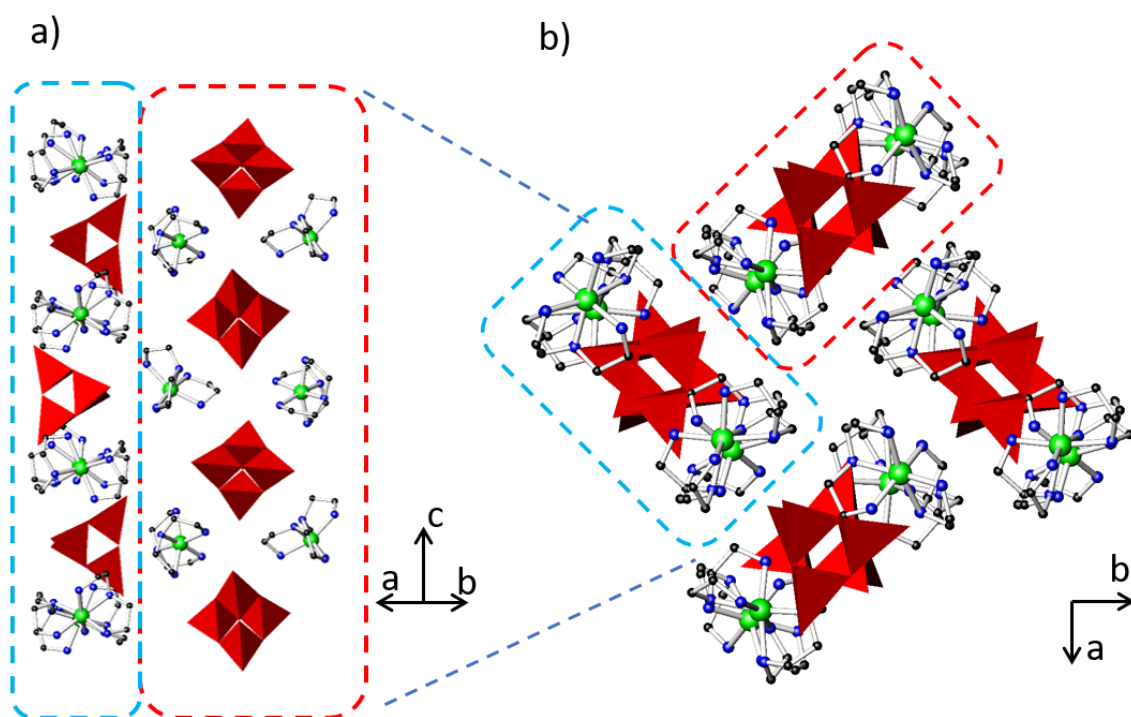
Figure 4.16: (a) Two columns of clusters and complexes in structure (**9**) aligned along the [001] direction, viewed in along [110] and (b) displays multiple columns in a fully packed crystal structure down [001]. Key: Red T2 polyhedra represent $[Ge_4O_6S_4]^{4-}$ units, green: Co atoms, blue: N atoms, black: C atoms. Hydrogen atoms are omitted for clarity.
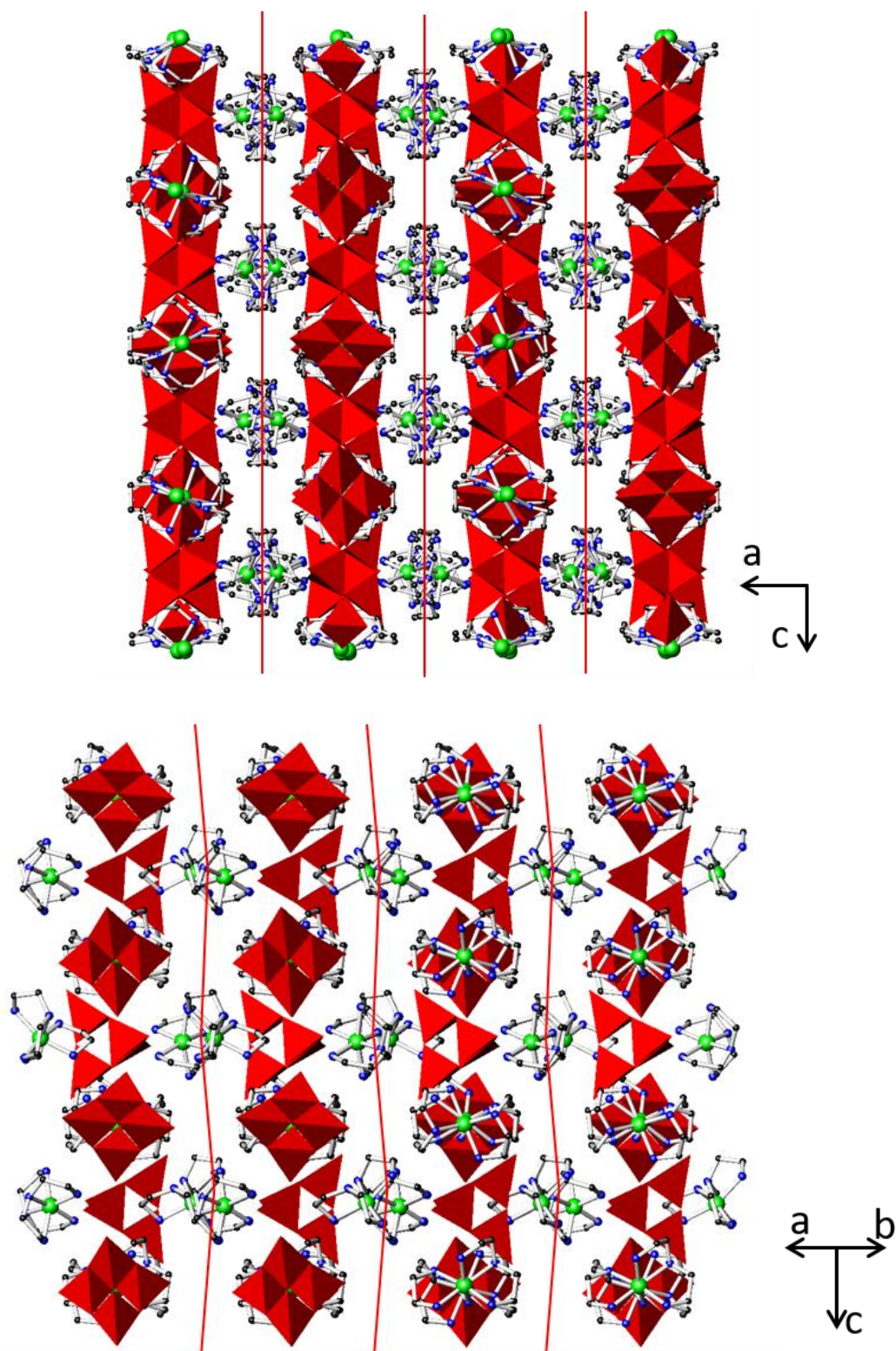
Figure 4.17: Crystal packing illustrating the differences between the polymorphs (**8**) (top) and (**9**) (bottom). Key: grey Ge, red O, yellow S, green Co, blue N, black C. Key: Red T2 polyhedra represent $[Ge_4O_6S_4]^{4-}$ units, green: Co atoms, blue: N atoms, black: C atoms. Hydrogen atoms are omitted for clarity.

Bond distances between donor and acceptor atoms are summarised in Table 4.15 and 4.16. These distances suggest hydrogen bonding is contained throughout the crystal structure. There are also minor interactions between S…N atoms $(3.33(1) \leq d/\text{Å} \leq 3.32(2))$ for (**8**) and only one interaction seen in (**9**), O(7)…S(1) 3.197(6) Å. In addition, weak C…N and C…O interactions are also observed for (**8**) and (**9**) respectively.

Table 4.15: Bond lengths found in (**8**) between acceptor and donor atoms containing hydrogen bonding.

Symmetry operations: a = y+7/4, -x+7/4, z+3/4; b = y-3/4, -x+5/4, -z+1/4; c = -y+5/4, x-5/4, -z+5/4; d = x-1, y-1/2, -z+1; e = -y+5/4, x-3/4, z-3/4

	Length /Å		Length /Å		Length /Å		Length /Å
N(1)…O(11)	3.16(3)	N(6)…O(5)[b]	3.07(3)	N(10)…O(9)[c]	3.11(3)	C(21)…N(15)	3.09(3)
N(2)…O(3)[a]	3.18(3)	N(7)…O(9)[c]	3.24(3)	N(11)…O(7)	3.16(3)	N(19)…O(8)	3.07(3)
N(3)…O(5)[b]	3.17(3)	C(9)…N(18)[c]	3.48(3)	N(12)…O(1)	3.09(3)	C(25)…N(24)	3.09(3)
N(4)…O(11)	3.12(3)	N(8)…O(7)	3.21(3)	N(13)…O(2)[d]	3.14(3)	N(22)…O(4)[b]	3.25(3)
N(5)…O(3)[a]	3.14(3)	N(9)…O(1)	3.15(3)	N(16)…O(12)[e]	3.09(3)		

Table 4.16: Bond lengths found in (**9**) between acceptor and donor atoms containing hydrogen bonding.

Symmetry operations: a = -y+2, x-1, z+1/4; b = y+1, -x+1, z-3/4; c = y, -x+2, z-3/4; d = -x+2,- y+1, z+1/2; e = -y+1, x, z+1/4

	Length /Å		Length /Å
N(1)…O(5)[a]	2.894(7)	N(7)…O(4)[e]	2.974(7)
C(1)…O(1)[b]	3.180(7)	N(8)…O(3)	3.146(7)
N(9)…O(2)[c]	3.239(7)	N(10)…O(4)[e]	3.309(7)
N(3)…O(7)[d]	2.970(7)	N(11)…O(3)	3.059(7)
N(4)…O(6)	3.080(7)	N(12)…O(2)[c]	3.035(7)

Thermogravimetric analysis of compound (**8**) displayed a four-step reduction in weight loss, Figure 4.18. The first weight loss was attributed to removal of water molecules within the structure, a 2.27 % weight loss. The onset temperature in the TGA was determined by the position of the peak in the DTG curve, as some part is external water on the sample. Much like with (**7**), loss of crystal water commenced at ~45 ˚C. The second and third step produces a 22.55 % weight change corresponding to just over half of the organic component present.

This is consistent with the breakdown of one of the [Co(deta)₂] complexes into two parts, one deta molecule with an ethylamine fragment (15.06 % total) first, followed by the remaining diethylamine molecule second. The remaining organic molecules and the inorganic cluster breakdown at the same time (36.24 % total). The TGA-DTG curve shows a small plateau at ~600 ˚C denoting a change in what is being removed from the structure, it is no longer the removal of the organic component and is likely to be the removal of sulfur. The powder X-ray diffraction pattern of the post-TGA product contains only Co_9S_8 and GeS_2 confirming the breakdown of the structure (Figure A2.1).
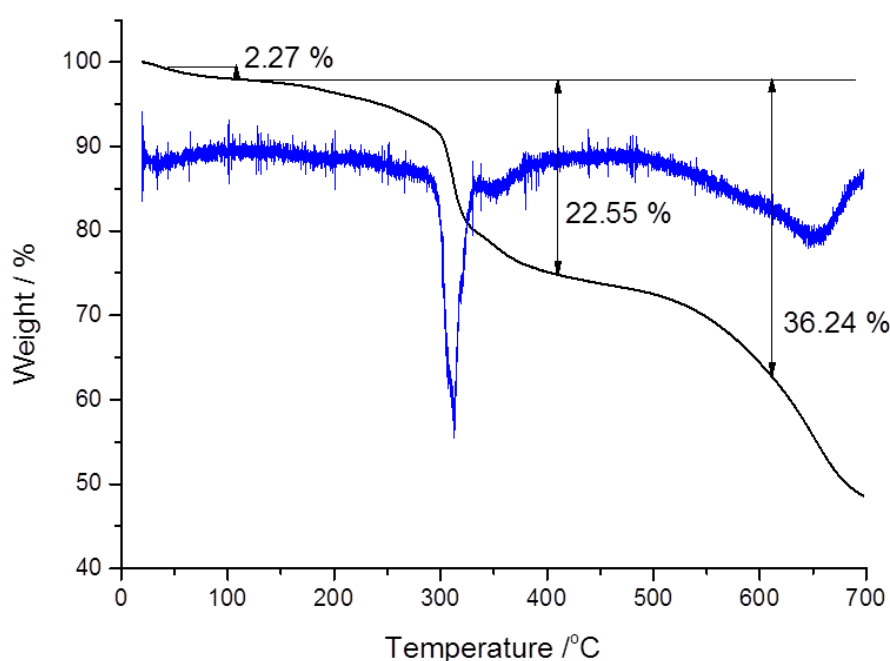
Figure 4.18: Thermogravimetric analysis curve of [Co(deta)₂]₂ [Ge₄O₆S₄]·H₂O (**8**) heated under N_2 (black) and the corresponding derivative (DTG) curve (blue).

The IR spectrum of (**8**) can be viewed in Figure 4.19 and the following vibrations have been tentatively assigned and provide evidence of amine presence as seen in Table 4.17. This compares relatively well to the IR present on the NUIST database [279].
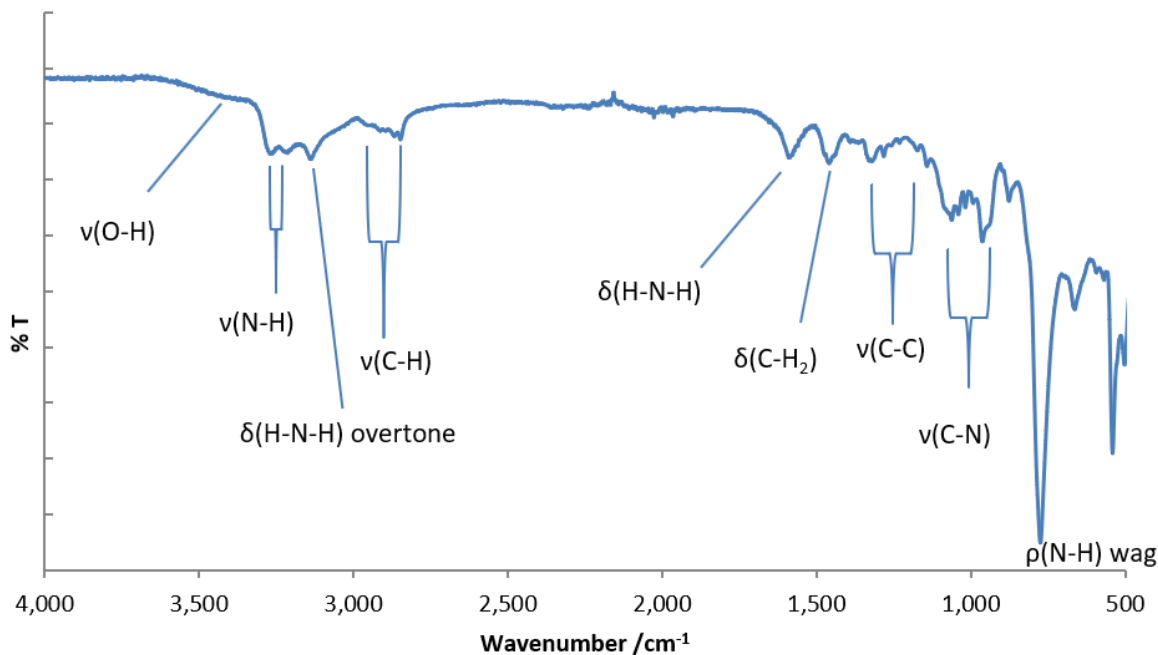
Figure 4.19: IR spectrum of [Co(deta)$_2$]$_2$ [Ge$_4$O$_6$S$_4$]·H$_2$O (**8**) using hand-picked crystals.

Table 4.17: Infrared spectrum assignments of [Co(deta)$_2$]$_2$ [Ge$_4$O$_6$S$_4$]·H$_2$O (**8**)

Stretching mode	Wavenumber /cm^{-1}
ν(O-H)	3407
ν(N-H)	3213 (sym) and 3263 (asym)
ν(C-H)	2846 (sym) and 2910 (asym)
δ(H-N-H)	1589 (3139 overtone)
δ (C-H$_2$)	1467
ν(C-C)	1173-1318 (multiple peaks)
ν(C-N)	963-1100 (multiple peaks)
ρ(N-H) wag	774

The diffuse reflectance spectrum of compound (**8**) produces an absorption edge of 4.1(3) eV (Figure 4.20). The peaks between 2-3 eV is thought to arise from *d-d* transitions from the Co(II) complexes [277]. The change from using tren ligands to deta ligands did not alter the position of the absorption edge and is likely driven by the sulfur content of the cluster as seen in previous oxothio structures [27, 28].
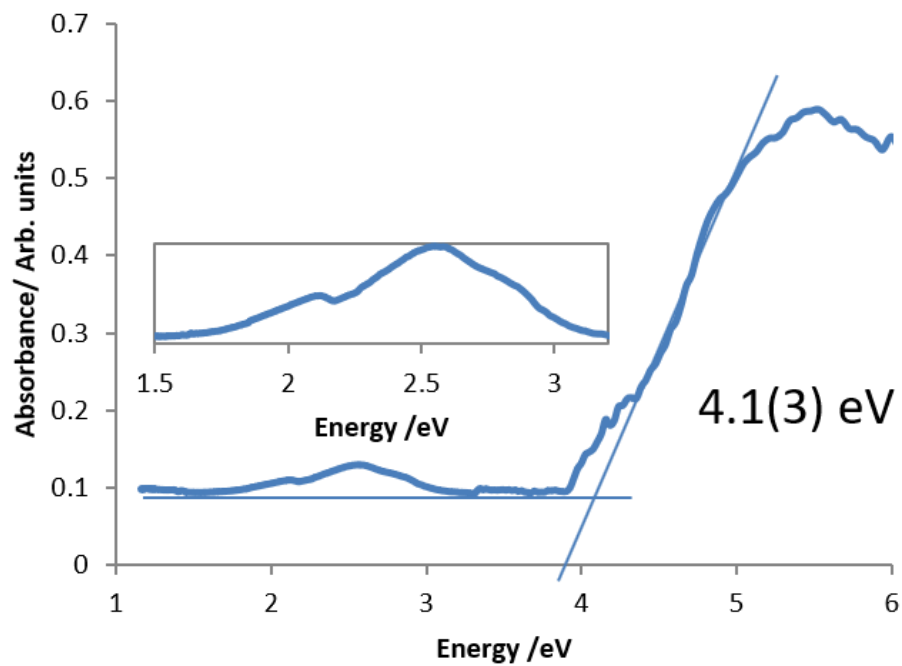
Figure 4.20: Diffuse reflectance spectrum of $[Co(deta)_2]_2 [Ge_4O_6S_4]\cdot H_2O$ (**8**) using hand-picked crystals showing a band gap of 4.1(3) eV.

4.3.5 [Co(deta)$_2$]$_2$ [Ge$_4$O$_4$S$_6$] (10)

4.3.5.1 Synthesis

[Co(deta)$_2$]$_2$ [Ge$_4$O$_4$S$_6$] (**10**) was synthesised using GeO$_2$ (200 mg, 1.9 mmol), CoS (173 mg, 1.9 mmol), S (80 mg 2.4 mmol) and diethylenetriamine (5 ml, 46 mmol). The reaction mixture was stirred for 10 minutes in a 23 ml Teflon-lined stainless-steel autoclave before being sealed and heated to 413 K at 1 °C min^{-1} for 6 days. The reaction formed red/orange crystals along with black powder. The presence of (**10**) was confirmed using powder X-ray diffraction measurements on the bulk product (Figure 4.21). The pattern matches well the calculated pattern generated by single-crystal X-ray data. The presence of Co$_9$S$_8$ and Co*S* were also observed. Combustion analysis, C 17.28 %, H 4.75 %, N 14.56 %, compares well with the crystallographically determined formula [Co(deta)$_2$]$_2$[Ge$_4$O$_4$S$_6$] (C 17.01 %, H 4.61 %, N 15.02 %).
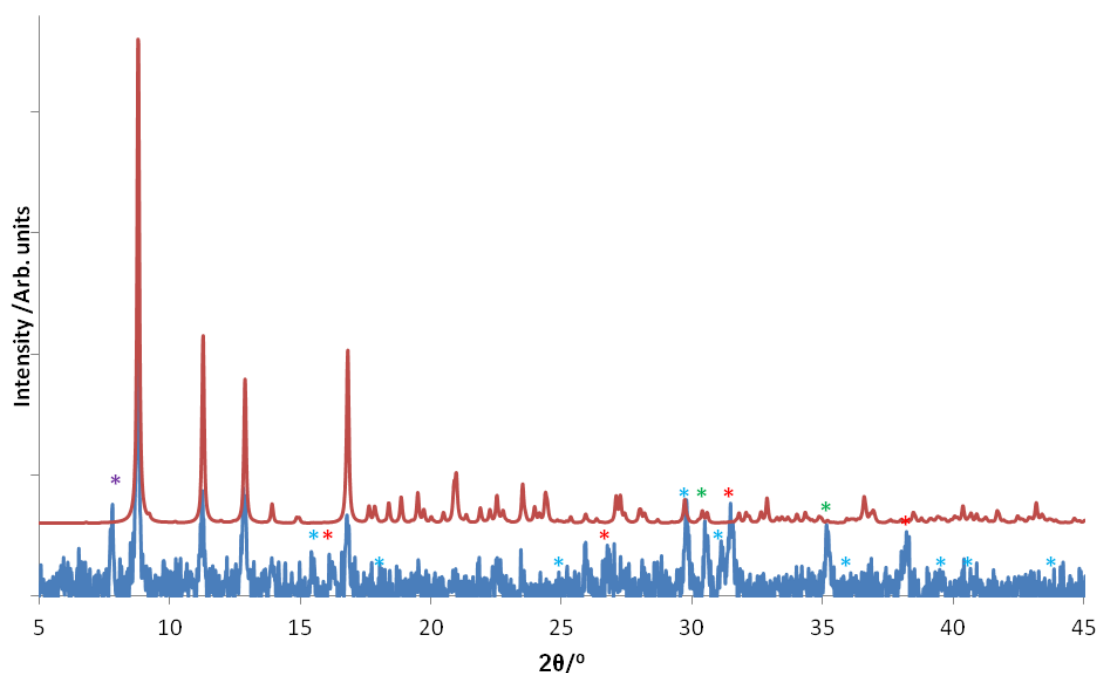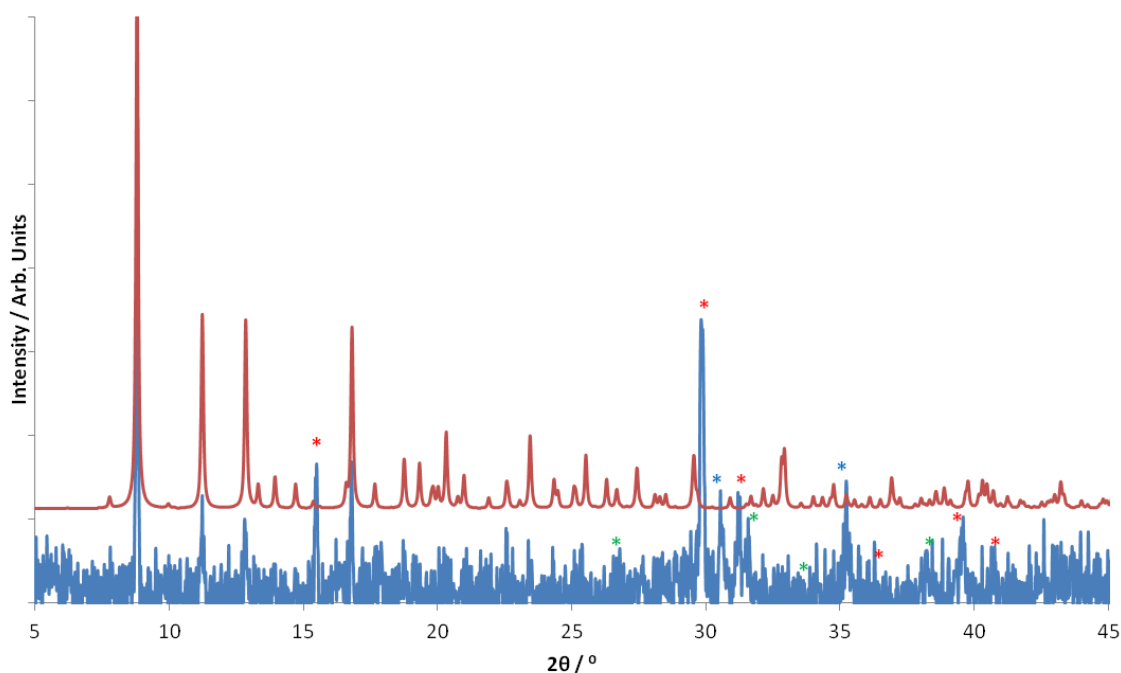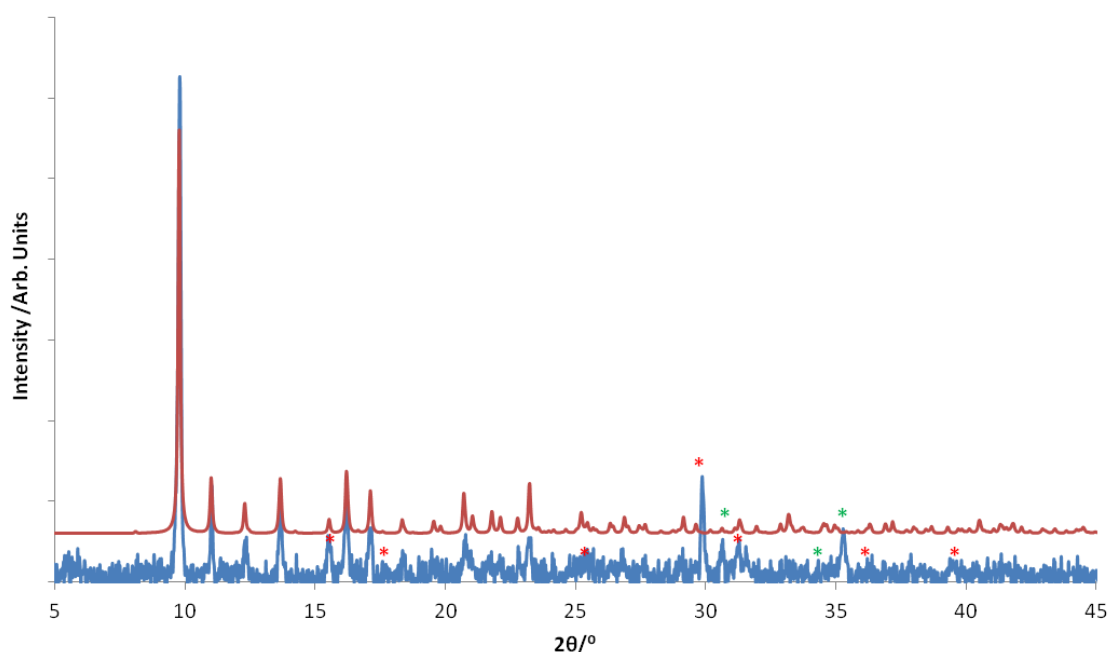

Figure 4.21: X-ray diffraction pattern of the bulk, as-synthesised product (blue) which contained crystals of [Co(deta)$_2$]$_2$ [Ge$_4$O$_4$S$_6$] (**10**). The simulated pattern calculated from single-crystal X-ray data for (**10**) is shown above (red). Peaks in the bulk sample annotated with asterisks correspond to Co$_9$S$_8$ (red) and Co*S* (green).

Alternatively, using GeO$_2$ (200 mg, 1.9 mmol), Co(oAc)$_2$4H$_2$O (338 mg, 1.35 mmol), S (120 mg, 3.42 mol) and diethylenetriamine (5 ml, 46 mmol) produces the same crystals with a

138

similar yield ~5 %. Increasing the sulfur content further results in the formation of [detaH$_2$][Co(deta)$_2$][Ge$_2$S$_6$] [280].

Single-crystal X-ray diffraction experiments were conducted at 150 K using graphite monochromated MoK$_\alpha$ (λ = 0.71073 Å) radiation. The structure was solved using SUPERFLIP [228] and the model refined using the CRYSTALS suite of programs [230]. The model was refined against F and a Chebychev polynomial weighting scheme was applied. Hydrogen atoms on the amine ligands were placed geometrically with a U[equiv] value 1.2 times the U[equiv] of the carbon to which they are attached. Crystallographic details are summarised in Table 4.18 and atomic coordinates of all non-hydrogen atoms can be found in Table A2.5.

Table 4.18 Crystallographic data for structures [Co(deta)$_2$]$_2$ [Ge$_4$O$_4$S$_6$] (**10**).

Chemical formula	[Co(deta)$_2$]$_2$ [Ge$_4$O$_4$S$_6$]
Formula mass	1077.99
Crystal Habit	Orange shard
Crystal system	Orthorhombic
Symmetry space group	*Pbcn*
Temp /K	150
a /Å	14.8360(5)
b /Å	16.0656(6)
c /Å	16.1761(6)
V /Å^3	3855.6(2)
Z	8
μ /mm^{-1}	4.286
Total reflections (I >3σ(I))	2821
R factor	0.0744
wR factor	0.0672
Goodness of fit ref	1.1058

4.3.5.1 Structure Description and Analysis

Upon increasing the sulfur content in reaction (**8**) and keeping all other variables the same, the reaction yields an oxo-thio germanate T2 unit that has two oxygen positions replaced with sulfur. Therefore, the new inorganic T2 unit is built up of vertex sharing GeO$_2$S$_2^{4-}$ units producing [Ge$_4$O$_4$S$_6$]$^{4-}$ clusters that also still contain sulfur atoms at the vertex positions, Figure 4.22. The accompanying charge balancing cation complex is a distorted pseudo-octahedral as seen previously.
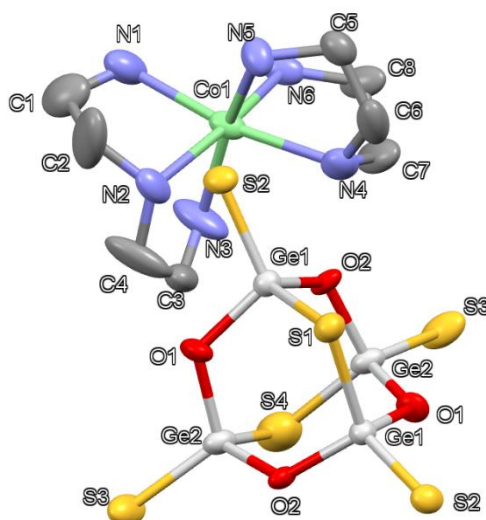
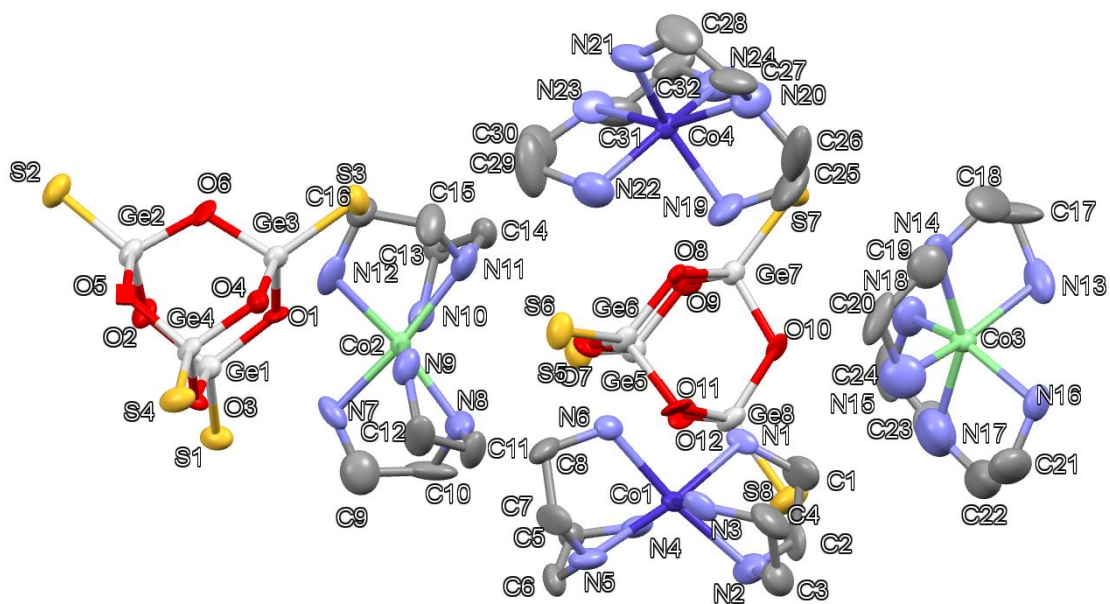Figure 4.22: Full T2 unit of (**10**) and accompanying complex displaying thermal ellipsoids of each atom at 50 % probability. Key: light grey: Ge, green: Co atoms, yellow: S atoms, red: O atoms, light blue: N atoms, grey: C atoms. Hydrogen atoms are omitted for clarity.

Bond-valence sums support the presence of Ge(IV) in the compound (Table 4.19). Due to the inclusion of sulfur in the core, the tetrahedral units have been affected; O-Ge-O angles were ($112.51(10) \leq \alpha/° \leq 115.57(10)$) and O-Ge-S angles were ($103.12(13) \leq \alpha/° \leq 105.72(13)$) as seen in (**6**) are now ($104.0(3) \leq \alpha/° \leq 105.4(3)$) and ($106.45(19) \leq \alpha/° \leq 112.45(9)$) respectively. The bond lengths O-Ge and S-Ge within the core pull and push the T2 unit into a distorted state, measuring ($1.787(5) \leq d/Å \leq 1.842(6)$) and ($2.233(4) \leq d/Å \leq 2.239(2)$) respectively. The Co-N bond lengths are similar to that of the complexes seen in (**8**) and (**9**), supporting the presence of +2 cobalt. As with all other complexes produced in this chapter so far, distortion of the octahedral shape arises due to the rigidity of the multidentate ligands. Internal biting angles of N-Co-N seen between ($78.0(3) \leq \alpha/° \leq 79.1(3)$) while N-Co-N angles between deta moieties are between ($90.3(3) \leq \alpha/° \leq 109.5(3)$). Selected bond lengths and bond angles can be seen in Table 4.19 and 4.20.

The packing of the crystal structure exhibits a "layered" system of clusters and complexes rather than using "chains" like in (**8**) and (**9**). Layers of clusters and complexes can be seen down [100] (Figure 4.23a) which stack up on top of one another in a staggered manner (Figure 4.23b). The staggering is necessary so that inorganic clusters are not sitting atop clusters of the adjacent layer, this is favourable as the cluster is then surrounded by complexes instead of repelling nearby clusters.

Table 4.19: A selection of bond lengths and valence sums in [Co(deta)$_2$]$_2$ [Ge$_4$O$_4$S$_6$] (**10**).

Symmetry operations: a = -x+2, y, -z+3/2

	Length /Å	v_{ij}		Length /Å	v_{ij}		Length /Å
Ge(1)-S(1)	2.239(2)	0.95	Ge(2)-O(2)^a	1.795(5)	0.88	Co(1)-N(1)	2.180(11)
Ge(1)-S(2)	2.115(2)	1.33	Ge(2)-S(3)	2.115(3)	1.33	Co(1)-N(2)	2.185(8)
Ge(1)-O(1)	1.823(6)	0.82	Ge(2)-S(4)	2.223(4)	0.99	Co(1)-N(3)	2.176(9)
Ge(1)-O(2)	1.787(5)	0.90	Ge(2)-O(1)	1.842(6)	0.78	Co(1)-N(4)	2.196(9)
						Co(1)-N(5)	2.129(8)
						Co(1)-N(6)	2.137(7)
$\sum v_{ij}$		**4.00**			**3.98**		

Table 4.20: A selection of bond angles in [Co(deta)$_2$]$_2$ [Ge$_4$O$_4$S$_6$] (**10**).

Symmetry operations: a = -x+2, y, -z+3/2

	Angle / °		Angle / °		Angle / °
S(1)-Ge(1)-S(2)	112.45(9)	S(3)-Ge(2)-O(1)	112.3(2)	N(1)-Co(1)-N(5)	93.4(3)
S(1)-Ge(1)-O(1)	106.45(19)	S(4)-Ge(2)-O(1)	109.40(19)	N(2)-Co(1)-N(5)	90.3(3)
S(2)-Ge(1)-O(1)	111.3(2)	Ge(1)-S(1)-Ge(2)^a	96.08(13)	N(3)-Co(1)-N(5)	163.5(4)
S(1)-Ge(1)-O(2)	108.47(18)	Ge(2)-S(4)-Ge(2)^a	95.6(2)	N(4)-Co(1)-N(5)	80.7(3)
S(2)-Ge(1)-O(2)	112.35(18)	N(1)-Co(1)-N(2)	79.1(3)	N(1)-Co(1)-N(6)	93.5(4)
O(1)-Ge(1)-O(2)	105.4(3)	N(1)-Co(1)-N(3)	95.8(4)	N(2)-Co(1)-N(6)	168.1(3)
O(2)^a-Ge(2)-S(3)	110.6(2)	N(2)-Co(1)-N(3)	78.0(3)	N(3)-Co(1)-N(6)	93.7(3)
O(2)^a-Ge(2)-S(4)	108.0(2)	N(1)-Co(1)-N(4)	169.5(3)	N(4)-Co(1)-N(6)	79.1(3)
S(3)-Ge(2)-S(4)	112.11(14)	N(2)-Co(1)-N(4)	109.5(3)	N(5)-Co(1)-N(6)	99.5(3)
O(2)^a-Ge(2)-O(1)	104.0(3)	N(3)-Co(1)-N(4)	92.1(4)	Ge(2)-O(1)-Ge(1)	121.9(3)
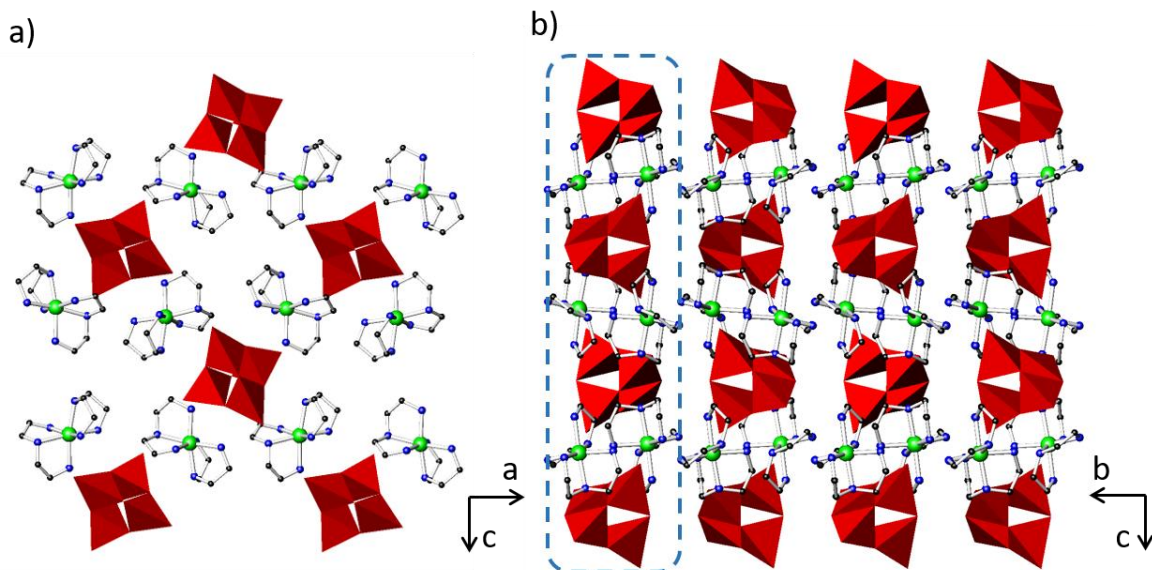
Figure 4.23: (a) One layer of clusters and complexes in structure (**10**) aligned in the [100] direction and viewed along [010] and (b) multiple columns of layers in a fully packed crystal structure down [100]. Key: Red T2 polyhedra represent $[Ge_4O_4S_6]^{4-}$ units, green: Co atoms, blue: N atoms, black: C atoms. Hydrogen atoms are omitted for clarity.

Intermolecular distances between donor and acceptor atoms can be viewed in Table 4.21, this supports the presence hydrogen bonding which holds the structure together. Furthermore, additional acceptor-donor interactions (sum of van der Waals' radii) can be seen throughout the structure ranging between 2.96(1)-3.59(2) Å including weak C…O interactions.

Table 4.21: Bond lengths found in (**10**) between acceptor and donor atoms containing hydrogen bonding.

Symmetry operations: a = x-1/2, -y+1/2, -z+1

Bond	length /Å
C(6)...O(2)	3.306(18)
N(5)…O(1)[a]	2.956(18)
N(4)…O(2)	3.214(18)

The TGA of compound (**10**) (Figure 4.24) shows multiple weight loss steps; the first step, an 18.45 % weight loss in total, is consistent with the removal of two deta molecules. Although the second step does not plateau, between 100 - 400 ˚C the difference is ~30.5% weight change. This is not a sufficient weight loss to account for the loss of the remaining two deta

142

molecules. Between 100-800 ˚C, a weight change of 58.20 % is observed. Powder X-ray analysis (Figure A2.2) of the resulting product shows only CoS and GeS_2 phases remain. This suggests that the thermal breakdown of the second complex (and thereby the removal of the last two deta molecules) happens simultaneously with the breakdown of the inorganic component.

The IR spectrum of (**10**) can be viewed in Figure 4.25 and the following vibrations have been tentatively assigned and provide evidence of amine presence as seen in Table 4.22. This compares relatively well to the IR present on the NUIST database [279]. An O-H stretch vibration at 3397 cm^{-1} and small water δ(H-O-H) vibration (shoulder) at 1620 cm^{-1} is expected to be external water based on the formula derived from the single-crystal model.

The diffuse reflectance spectrum of (**10**) Figure 4.26, produces a 4.1(2) eV absorption edge. On comparing the spectrum to that of (**7**) or (**8**), the absorption edge appears to be stronger in (**10**) due to the addition of more sulfur into the inorganic cluster. The small peaks at ~2.5 eV is suspected to be *d-d* cobalt(II) excitations [277] but due having no data on the octahedral splitting, specific transitions cannot be assigned.
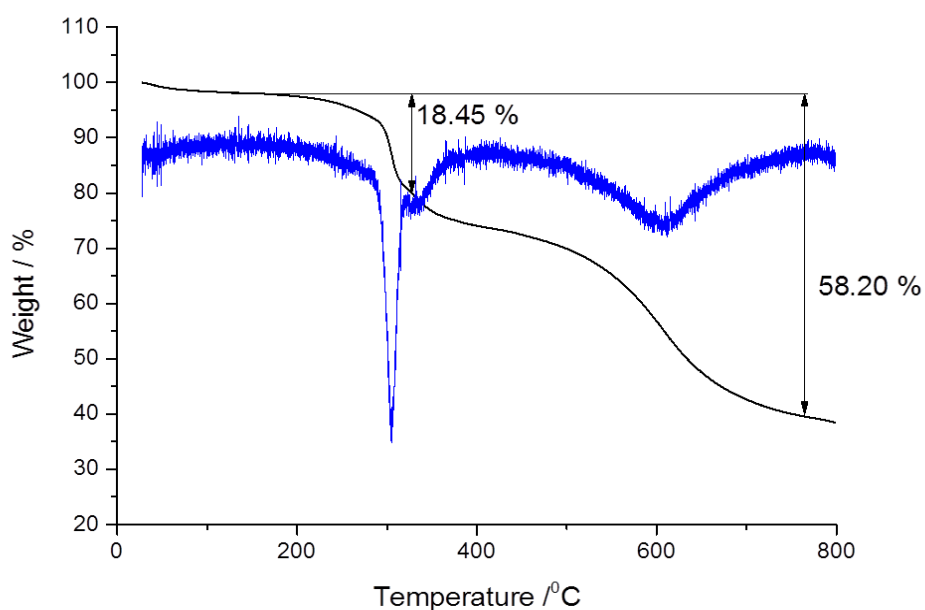
Figure 4.24: Thermogravimetric analysis curve of $[Co(deta)_2]_2 [Ge_4O_4S_6]$ (**10**) heated under N_2 (black) and the corresponding derivative (DTG) curve (blue).
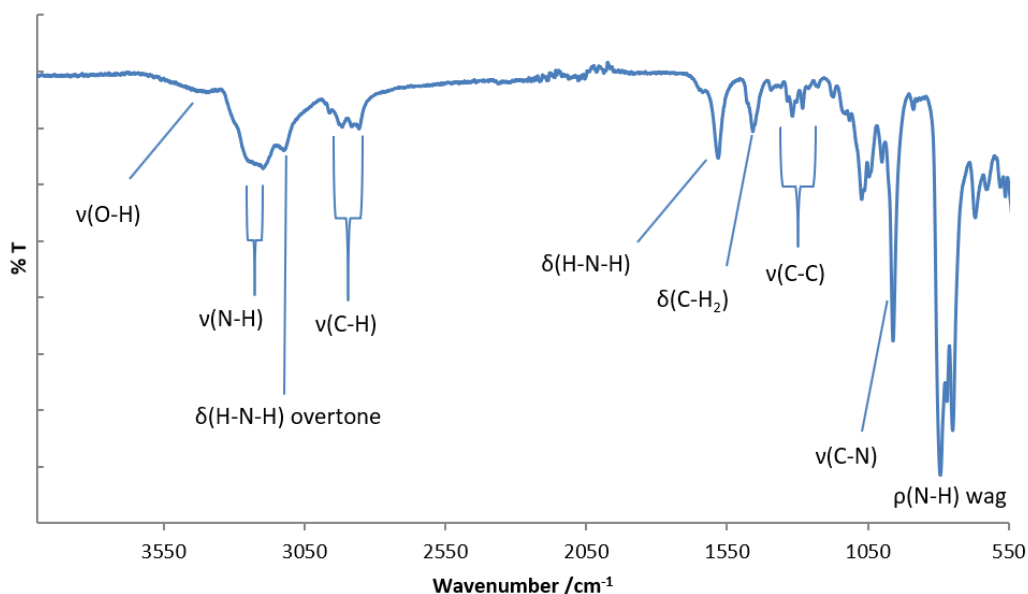
Figure 4.25: IR spectrum of [Co(deta)$_2$]$_2$ [Ge$_4$O$_4$S$_6$] (**10**) using hand-picked crystals.

Table 4.22: Infrared spectrum assignments of [Co(deta)$_2$]$_2$ [Ge$_4$O$_4$S$_6$] (**10**)

Stretching mode	Wavenumber /cm^{-1}
ν(O-H)	3397
ν(N-H)	3198 (sym) and 3270 (asym)
ν(C-H)	2845 (sym) and 2919 (asym)
δ(H-N-H)	1581 (3116 overtone)
δ (C-H$_2$)	1457
ν(C-C)	1224-1389 (multiple peaks)
ν(C-N)	960
ρ(N-H) wag	795
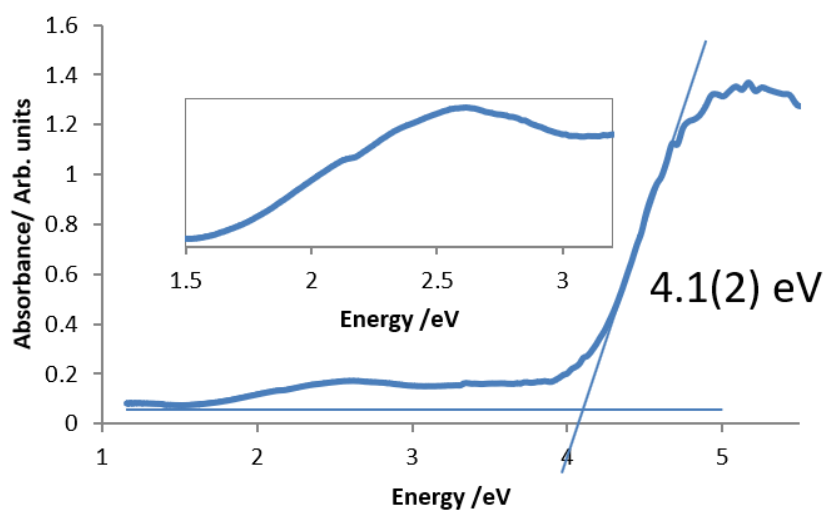
Figure 4.26: Diffuse reflectance spectrum of [Co(deta)$_2$]$_2$ [Ge$_4$O$_4$S$_6$] (**10**) using hand-picked crystals showing a band gap of 4.1(2) eV.

144

4.3.6 [Co(dap)₃)]₂[Ge₄O₂S₈] (11)

4.3.6.1 Synthesis

[Co(dap)₃)]₂[Ge₄O₂S₈] (**11**) was synthesised using GeO₂ (200 mg, 1.9 mmol), CoS (173 mg, 1.9 mmol), S (110 mg 3.5 mmol) and 1,2-diaminopropane (dap) (5 ml, 59 mmol). The reaction mixture was stirred for 10 minutes in a 23 ml Teflon-lined stainless-steel autoclave before being sealed and heated to 443 K at 1 K min⁻¹ for 8 days. The reaction formed semi-transparent yellow crystals along with black powder. The presence of (**11**) was also confirmed through powder X-ray diffraction of the bulk sample. The pattern generated (Figure 4.27) matched the calculated pattern generated from the single-crystal X-ray data. The presence of Co_9S_8 and Co_3S_4 was also observed. Combustion analysis, 19.01 %, H 5.14 %, N 13.60 %, is close to the crystallographically determined formula [Co(dap)₃)]₂[Ge₄O₂S₈] (C 18.40 %, H 5.10 %, N 14.30 %). The difference seen is due to the difficulty in picking out crystals from a powder whereby some of the other phases may have contaminated a few of the crystals by clinging to the surfaces.
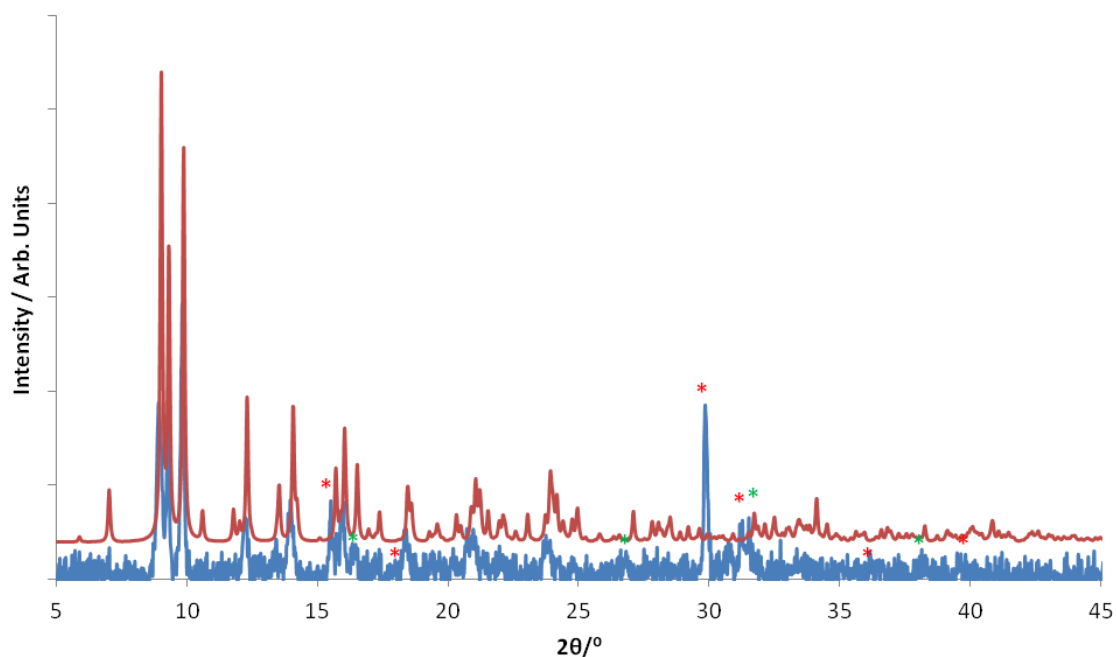
Figure 4.27: X-ray diffraction pattern of the bulk, as-synthesised product (blue) which contained crystals of [Co(dap)₃)]₂[Ge₄O₂S₈] (**11**). The simulated pattern calculated from single-crystal X-ray data for (**11**) is shown above (red). Peaks in the bulk sample annotated with asterisks correspond to Co_9S_8 (red) and Co_3S_4 (green).

This compound does not form if the sulfur content is increased significantly past the amount listed in the synthesis section. An attempt was made to try and synthesise a pure $[Ge_4S_{10}]^{4-}$ unit with 1,2-diaminopropane, but this did not yield any crystals. To the author's knowledge, this has not been produced without the inclusion of chlorine, $[Co(dap)_3][Ge_4S_{10}]Cl_4$ [106].

Single-crystals of (**11**) were sent to Southampton University (National Crystallographic Service) for single-crystal X-ray experiments. This collection was conducted at 100 K using graphite monochromated MoKα (0.71073 Å) radiation on a Rigaku Saturn724+ X-ray diffractometer. The structure of (**11**) was solved (by the author) with Superflip [228] and the model refined using the CRYSTALS suite of programs [230]. Two positions of methyl groups had to be split as the difference Fourier map appeared to show two possible positions of the methyl substituents on two dap molecules. Two bonds required restraints due to some disorder, C(8) - N(6) and C(15) - C(14). Splitting some of the other carbon atoms with large thermal elipsoids did not improve the model so they were left unsplit. The model was refined against *F* and a Chebychev polynomial weighting scheme was applied. Hydrogen atoms on the amine ligands were placed geometrically with a U[equiv] value 1.2 times the U[equiv] of the carbon to which they are attached. Crystallographic details are summarised in Table 4.23 and atomic coordinates of all non-hydrogen atoms can be found in Table A2.6.

Table 4.23 Crystallographic data for structures $[Co(dap)_3)]_2[Ge_4O_2S_8]$ (**11**).

Chemical formula	$[Co(dap)_3)]_2[Ge_4O_2S_8]$
Formula mass	1125.56
Crystal Habit	Yellow plate
Crystal system	Monoclinic
Symmetry space group	$P2_1/n$
Temp /K	100
a /Å	19.2991(5)
b /Å	11.1234(2)
c /Å	19.9249(6)
β /°	100.012(3)
V /Å³	4212.15(19)
Z	4
μ /mm^{-1}	4.021
Total reflections ($I > 3\sigma(I)$)	6799
R factor	0.0617
wR factor	0.0727
Goodness of fit ref	1.0873

4.3.6.2 Structure Description and Analysis

This compound was produced by further increasing the sulfur concentration over the previous structure of (**10**) and by using a different structure directing agent. This new reaction produced a T2 unit in which four of the six oxygen positions in the original Ge_4O_6 core were replaced by sulfur. The new cluster is thus formed from vertex sharing between two $GeOS_3^{4-}$ tetrahedra, one GeS_4^{4-} tetrahedron and one $GeO_2S_2^{4-}$ tetrahedron (Figure 4.28). The production of compound (**11**) uses 1,2-diaminopropane (dap) instead of deta as a structure directing agent and the charge-balancing complexes are now pseudo-octahedral $[Co(dap)_3]$.
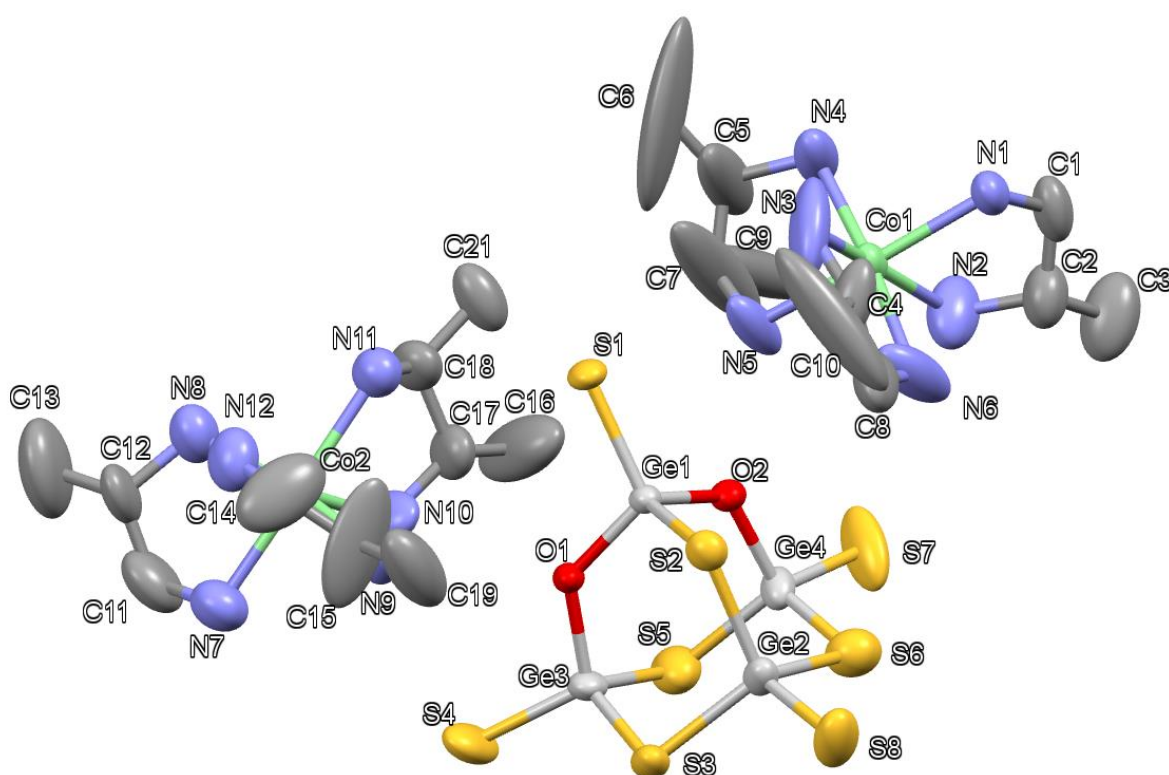
Figure 4.28: Asymmetric unit of (**11**) displaying thermal ellipsoids of each atom at 50 % probability. Key: light grey: Ge, green: Co atoms, yellow: S atoms, red: O atoms, light blue: N atoms, grey: C atoms. Hydrogen atoms are omitted for clarity.

The new $[Ge_4O_2S_8]^{4-}$ cluster distorts from the Ge_4O_6 core by introducing longer bond lengths due to the further increase in the number of sulfur atoms within the core. All angles around the last $GeO_2S_2^{4-}$ tetrahedron are just as distorted as the units seen in (**10**), but the bond lengths connecting it to the rest of the cluster have decreased, as seen in the cluster comparisons in Figure 4.29.

Bond-valence calculations seen in Table 4.24, support the oxidation state of Ge being +4. The N-Co bond lengths do not vary much $(2.121(9) \leq d/\text{Å} \leq 2.186(8))$ which perhaps reflect bidentate nature of dap compared to the tridentate nature of deta seen, for example, in (**9**), which contains longer Co-N bond lengths, $(2.142(4) \leq d/\text{Å} \leq 2.245(4))$. The Co-N bond lengths seen in (**10**) are comparable to the Co(II) complexes within the compound [Co(dap)₃][InSb₃S₇] [106], which has bond lengths in the range $(2.129(18) \leq d/\text{Å} \leq 2.178(19))$. The counterions present are distorted octahedral Co(II) complexes with internal dap N-Co-N biting angles of $(78.8(4) \leq \alpha/° \leq 82.1(7))$, which are similar to corresponding angles seen in (**5**) $(78.0(3) \leq \alpha/° \leq 79.1(3))$. The external N-Co-N angles of bonds of opposing dap moieties are between $(86.4(6) \leq \alpha/° \leq 97.1(4))$ are lower on average than those observed in (**10**), $(90.3(3) \leq \alpha/° \leq 109.5(3))$. The bidentate nature of dap perhaps distorts the angles less harshly than observed for the tridentate chain of deta. Selected bond angles can be viewed in Table 4.25.

S(2)-Ge(1)-O(3) 112.7(1)° S(3)-Ge(2)-O(2) 110.6(2)° S(1)-Ge(1)-O(2) 110.78(14)°

115.5(1)°   114.8(1)°   112.3(2)° 112.1(1)°   111.9(1)°   113.1(1)°

O(6)-Ge(4) 1.784(3) Å   O(1)-Ge(1) 1.824(6) Å   O(1)-Ge(3) 1.781(4) Å
O(3)-Ge(3) 1.802(3) Å   O(2)-Ge(1) 1.787(5) Å   O(2)-Ge(4) 1.779(4) Å
O(1)-Ge(2) 1.792(3) Å   S(4)-Ge(2) 2.223(4) Å   S(2)-Ge(2) 2.212(2) Å
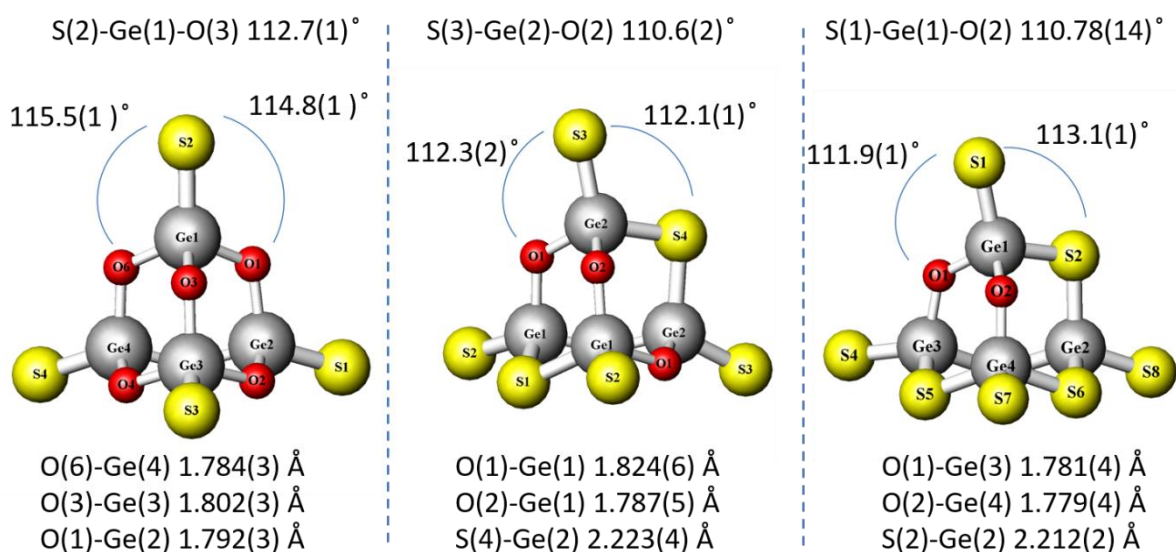
Figure 4.29: The inorganic clusters seen in [Ge₄O₆₋ₓS₄₊ₓ] $(x = 0, 2, 4)$ (**6**), (**10**) and (**11**) (left to right) labelled with selected bond lengths and angles to show distortion of the Ge₄O₆ core and that of the tetrahedra. Key: grey: Ge atoms, red: O atoms, yellow: S atoms.

Table 4.24: A selection of bond lengths and valence sums in [Co(dap)$_3$)]$_2$[Ge$_4$O$_2$S$_8$] (**11**).

	Length /Å	v_{ij}		Length /Å	v_{ij}		Length /Å	v_{ij}
Ge(1)-S(1)	2.1138(16)	1.33	Ge(2)-S(2)	2.212(2)	1.02	Ge(3)-S(3)	2.254(2)	0.91
Ge(1)-S(2)	2.2218(19)	1.00	Ge(2)-S(3)	2.233(2)	0.97	Ge(3)-S(4)	2.112(2)	1.34
Ge(1)-O(1)	1.775(4)	0.93	Ge(2)-S(6)	2.206(3)	1.04	Ge(3)-S(5)	2.163(3)	1.17
Ge(1)-O(2)	1.788(4)	0.90	Ge(2)-S(8)	2.128(2)	1.28	Ge(3)-O(1)	1.781(4)	0.91
∑vij		**4.16**			**4.31**			**4.33**
Ge(4)-S(5)	2.170(3)	1.14	Co(1)-N(1)	2.157(6)		Co(2)-N(7)	2.142(9)	
Ge(4)-S(6)	2.133(3)	1.27	Co(1)-N(2)	2.172(10)		Co(2)-N(8)	2.169(9)	
Ge(4)-S(7)	2.114(3)	1.33	Co(1)-N(3)	2.151(12)		Co(2)-N(9)	2.121(9)	
Ge(4)-O(2)	1.779(4)	0.92	Co(1)-N(4)	2.136(8)		Co(2)-N(10)	2.151(9)	
			Co(1)-N(5)	2.162(7)		Co(2)-N(11)	2.186(8)	
			Co(1)-N(6)	2.129(9)		Co(2)-N(12)	2.163(9)	
∑vij		**4.66**						

Table 4.25: A selection of bond angles in [Co(dap)$_3$)]$_2$[Ge$_4$O$_2$S$_8$] (**11**).

	Angle / °		Angle / °		Angle / °
S(1)-Ge(1)-S(2)	113.13(8)	S(3)-Ge(3)-S(5)	111.58(10)	N(2)-Co(1)-N(3)	166.9(5)
S(1)-Ge(1)-O(1)	111.94(14)	S(4)-Ge(3)-S(5)	108.91(13)	N(1)-Co(1)-N(4)	93.1(3)
S(2)-Ge(1)-O(1)	108.32(15)	S(3)-Ge(3)-O(1)	106.59(16)	N(2)-Co(1)-N(4)	96.1(5)
S(1)-Ge(1)-O(2)	110.78(14)	S(4)-Ge(3)-O(1)	111.25(15)	N(3)-Co(1)-N(4)	95.9(6)
S(2)-Ge(1)-O(2)	107.42(15)	S(5)-Ge(3)-O(1)	105.66(16)	N(1)-Co(1)-N(5)	169.9(3)
O(1)-Ge(1)-O(2)	104.8(2)	S(5)-Ge(4)-S(6)	113.50(12)	N(2)-Co(1)-N(5)	93.8(4)
S(2)-Ge(2)-S(3)	108.71(7)	S(5)-Ge(4)-S(7)	109.36(12)	N(3)-Co(1)-N(5)	93.4(4)
S(2)-Ge(2)-S(6)	110.10(9)	S(6)-Ge(4)-S(7)	107.51(14)	N(4)-Co(1)-N(5)	80.1(3)
S(3)-Ge(2)-S(6)	110.93(10)	S(5)-Ge(4)-O(2)	108.67(15)	N(1)-Co(1)-N(6)	91.7(3)
S(2)-Ge(2)-S(8)	110.43(11)	S(6)-Ge(4)-O(2)	107.13(16)	N(2)-Co(1)-N(6)	86.4(6)
S(3)-Ge(2)-S(8)	111.33(10)	S(7)-Ge(4)-O(2)	110.65(18)	N(3)-Co(1)-N(6)	82.1(7)
S(6)-Ge(2)-S(8)	105.32(11)	N(1)-Co(1)-N(2)	79.4(3)	N(4)-Co(1)-N(6)	174.9(4)
S(3)-Ge(3)-S(4)	112.63(9)	N(1)-Co(1)-N(3)	94.8(4)		

Crystal packing in the structure of (**11**) can be viewed in Figure 4.30. Here, alternating clusters and complexes pack into chains down [010] and group into sets of two. The two chains are staggered (Figure 4.30a) so that the adjacent complexes are near the clusters. These 2 chains then repeat throughout the crystal structure, resulting in clusters that are surrounded by complexes as seen with previous structures (Figure 4.30b).
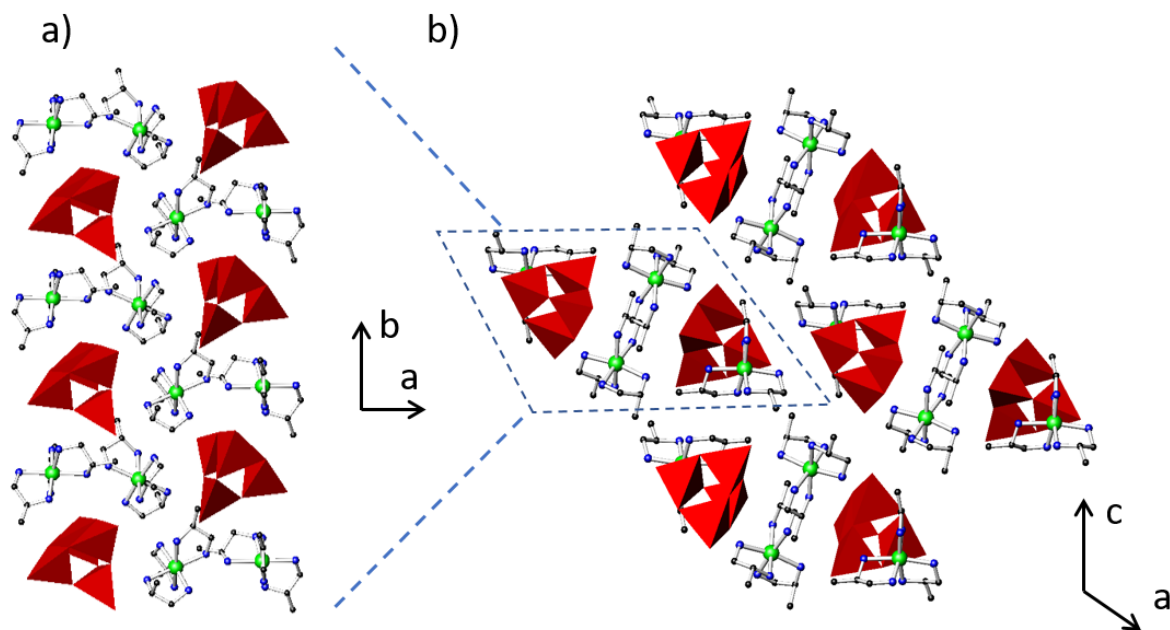
Figure 4.30: (a) two sets of clusters and complex chains in structure (**11**) aligned in the [010] direction, but viewed along [001] and (b) multiple columns of layers in a fully packed crystal structure down [010]. Key: Red T2 polyhedra represent $[Ge_4O_2S_8]^{4-}$ units, green: Co atoms, blue: N atoms, black: C atoms. Hydrogen atoms are omitted for clarity.

Distances between donor and acceptor atoms in (**11**) are mainly between C(8)…O(2) (as a weak interaction) and N(9)..O(1) which are 3.40(3) and 2.89(3) Å, respectively. If viewed with van der Waals' radii a few S…N and S…O interactions can occur, but at a longer range between ~3.33-3.87 Å. Both supporting the theory that the structure is held together through hydrogen bonding.

The TGA of compound (**11**) produces a loss of 34.95 % in a three-step reduction in weight, agreeing with the CHN values for this material (Figure 4.31). The first weight loss is 18.73 % which is consistent with approximately half of the organic component, so a breakdown of one complex. The second and third steps were assigned to the other half of the total organic weight, one dap molecule being removed first before the other two.

The IR spectrum of (**11**) can be viewed in Figure 4.32 and the tentative assignments are listed in Table 4.26. The vibrations observed provide evidence for the presence of amine.
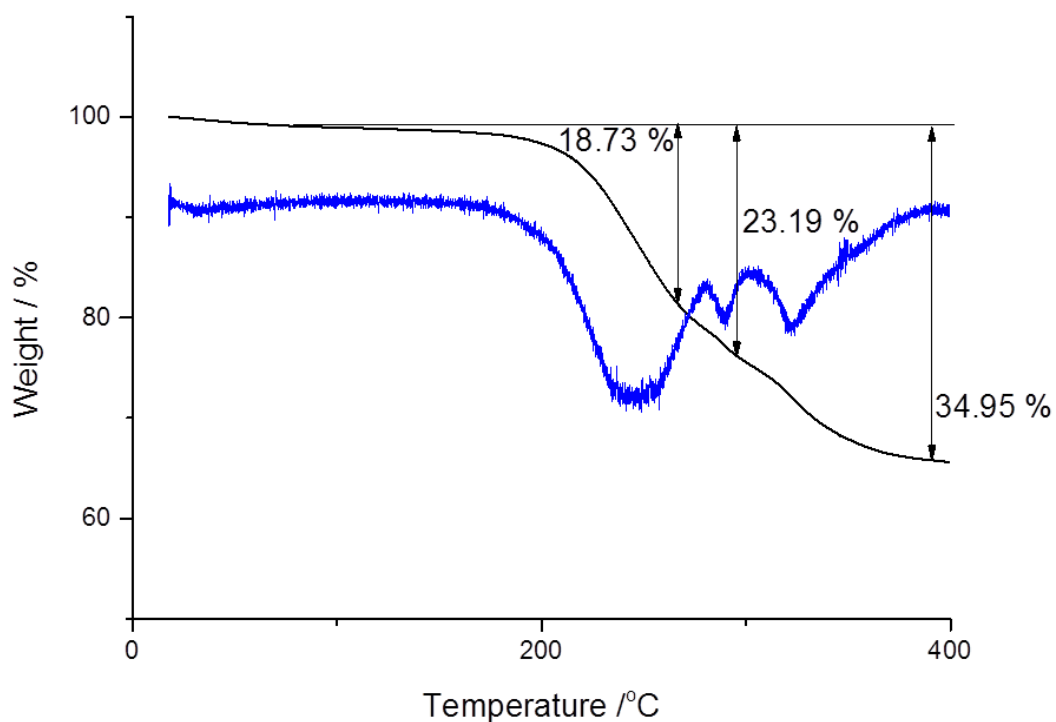
Figure 4.31: Thermogravimetric analysis curve of [Co(dap)₃)]₂[Ge₄O₂S₈] (**11**) heated under N₂ (black) and the corresponding derivative (DTG) curve (blue).
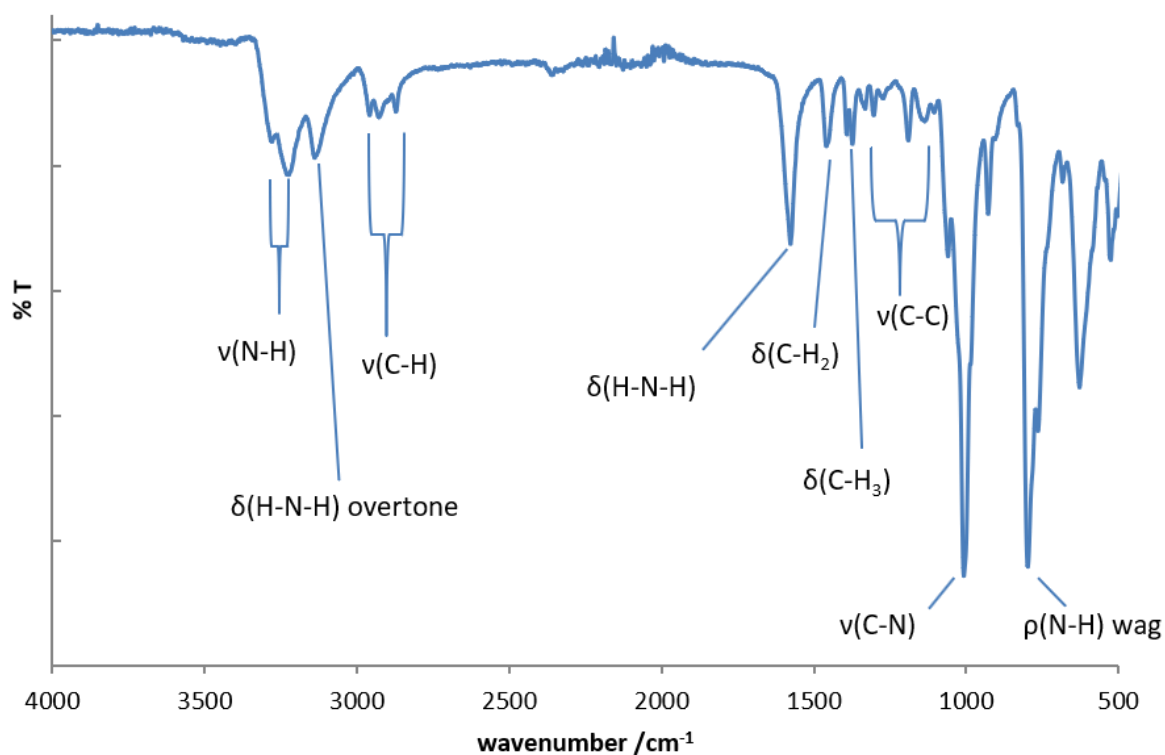
Figure 4.32: IR spectrum of [Co(dap)₃)]₂[Ge₄O₂S₈] (**11**) from hand-picked crystals.

Table 4.26: Infrared spectrum assignments of $[Co(dap)_3)]_2[Ge_4O_2S_8]$ (**11**)

Stretching mode	Wavenumber /cm^{-1}
ν(N-H)	3228 (sym) and 3278 (asym)
ν(C-H)	2871 (sym) and 2927 (asym)
δ(H-N-H)	1576 (3136 overtone)
δ (C-H$_2$)	1460
δ (C-H$_3$)	1373
ν(C-C)	1130-1302 (multiple peaks)
ν(C-N)	1006
ρ(N-H) wag	797

The diffuse reflectance spectrum of (**11**) Figure 4.33, shows a 3.4(2) eV absorption edge. The small peak at ~2.5 eV is suspected to be cobalt(II) d-d transitions [277], as seen for previous compounds in this chapter.
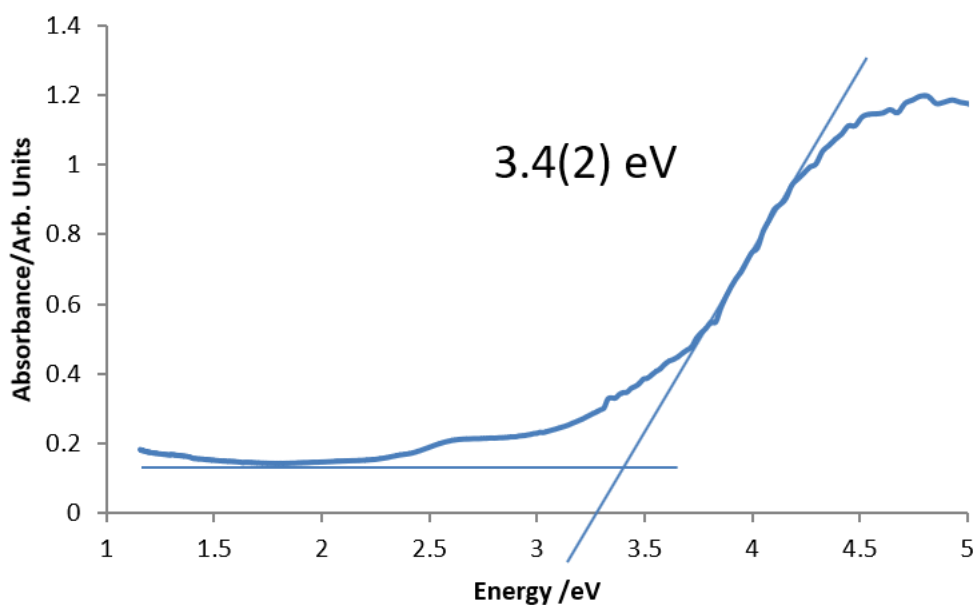
Figure 4.33: Diffuse reflectance spectrum of $[Co(dap)_3)]_2[Ge_4O_2S_8]$ (**11**) from hand-picked crystals.

4.3.7 [Co(deta)₂]₄[Ge₉O₁₄S₈] (12)

4.3.7.1 Synthesis

$[Co(deta)_2]_4[Ge_9O_{14}S_8]$ (**12**) was synthesised using the same mixture used in (**8**) and (**9**). The mixture contained GeO_2 (200 mg, 1.9 mmol), CoS (173 mg, 1.9 mmol), S (60 mg 1.7 mmol) and diethylenetriamine (5 ml, 46 mmol). The reaction mixture was stirred for 10 minutes in a 23 ml Teflon-lined stainless-steel autoclave before being sealed and heated to 453 K at 1 K min^{-1} for 5 days. The reaction formed orange crystals along with grey powder. The presence of (**12**) was confirmed through powder X-ray diffraction experiments on the bulk sample (Figure 4.34) and the pattern matched the calculated pattern generated by single-crystal X-ray data. The presence of unreacted GeO_2 and the presence of compound (**8**) were also observed. Combustion analysis, C 16.56 %, H 3.70 %, N 14.34 %, are close to the crystallographically determined formula $[Co(deta)_2]_4[Ge_9O_{14}S_8]$ (C 15.24 %, H 4.01%, N 14.56 %). The difference seen is due to the difficulty in picking out crystals from a powder whereby some of the other phases may have contaminated a few of the crystals by clinging to the surfaces.
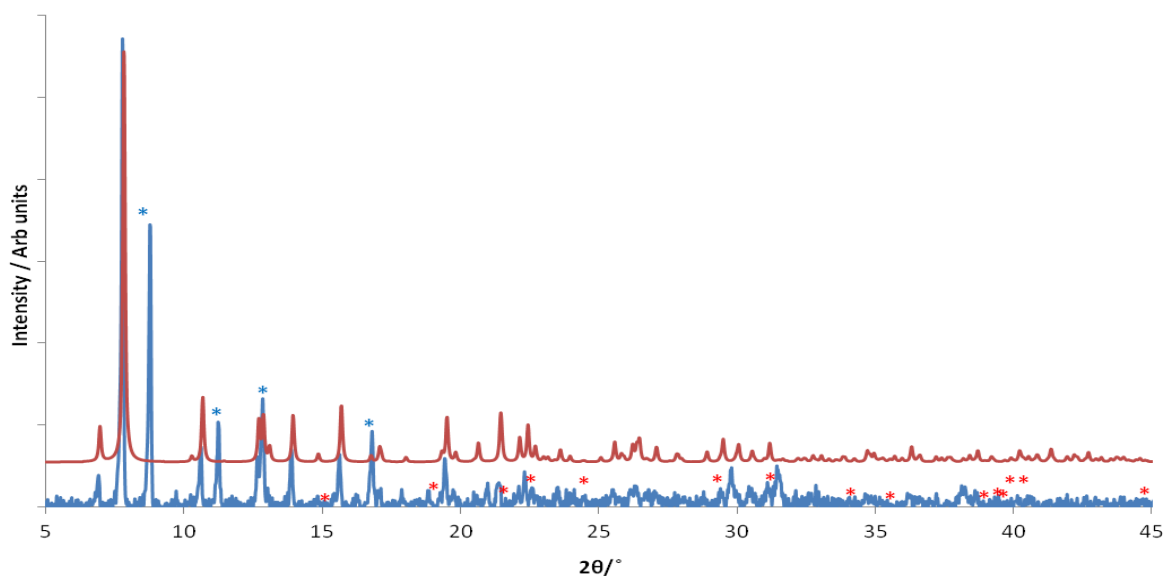
Figure 4.34: X-ray diffraction pattern of the bulk, as-synthesised product (blue) which contained crystals of $[Co(dap)_3)]_2[Ge_4O_2S_8]$ (**12**). The simulated pattern calculated from single-crystal X-ray data for (**12**) is shown above (red). Peaks in the bulk sample annotated with asterisks correspond to GeO_2 (red) and compound (**8**) (blue).

The reaction can also be performed at higher temperatures, up to 473 K, and still produce crystals in only marginally lower yield compared to that stated above.

Single-crystal X-ray diffraction experiments were conducted at 150 K using graphite monochromated MoK$_\alpha$ (λ = 0.71073 Å) radiation. The structure was solved using SUPERFLIP [228] and the model refined using the CRYSTALS suite of programs [230]. The model was refined against F and a Chebychev polynomial weighting scheme was applied. Hydrogen atoms on the amine ligands were placed geometrically with a U[equiv] value 1.2 times the U[equiv] of the carbon to which they are attached. Thermal U(ij) restraints were applied on atoms N(2), C(2), Ge(1) and O(1). Crystallographic details are summarised in Table 4.27, the asymmetric unit with thermal parameters can be seen in Figure 4.35 and atomic coordinates of all non-hydrogen atoms can be found in Table A2.7.

Table 4.27 Crystallographic data for structures [Co(deta)$_2$]$_4$[Ge$_9$O$_{14}$S$_8$] **(12).**

Chemical formula	[Co(deta)$_2$]$_4$[Ge$_9$O$_{14}$S$_8$]
Formula mass	2195.08
Crystal Habit	Orange block
Crystal system	Orthorhombic
Symmetry space group	*Fddd*
Temp /K	150
a /Å	15.347(3)
b /Å	30.896(5)
c /Å	33.052(4)
V /Å³	15672(4)
Z	8
μ /mm^{-1}	4.496
Total reflections ($I > 3\sigma(I)$)	1511
R factor	0.0580
wR factor	0.0594
Goodness of fit ref	1.1222
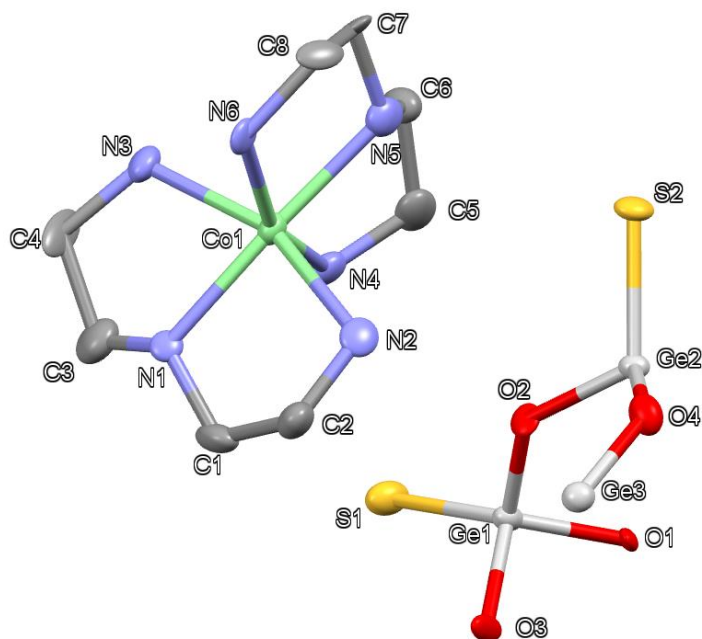
Figure 4.35: Asymmetric unit of **(12)** displaying thermal ellipsoids of each atom at 50 % probability. Key: light grey: Ge, green: Co atoms, yellow: S atoms, red: O atoms, light blue: N atoms, grey: C atoms. Hydrogen atoms are omitted for clarity.

4.3.7.2 Structure Description and Analysis

Compound **(12)**, is formed on increasing the heating temperature when using the same reaction mixtures used to produce compound (**8**) and (**9**) (section 4.3.3.1). Instead of producing structures that contain T2 $[Ge_4O_6S_4]^{4-}$ units, at the higher temperature two T2 units "fuse" together through a GeO_4^{4-} bridge, producing $[Ge_9O_{14}S_8]^{8-}$ (Figure 4.36). The inorganic unit is built from 8 GeO_3S^{4-} units and an additional germanium atom bridging the two sides. This is the first time this bonding motif has been observed in supertetrahedral structures.
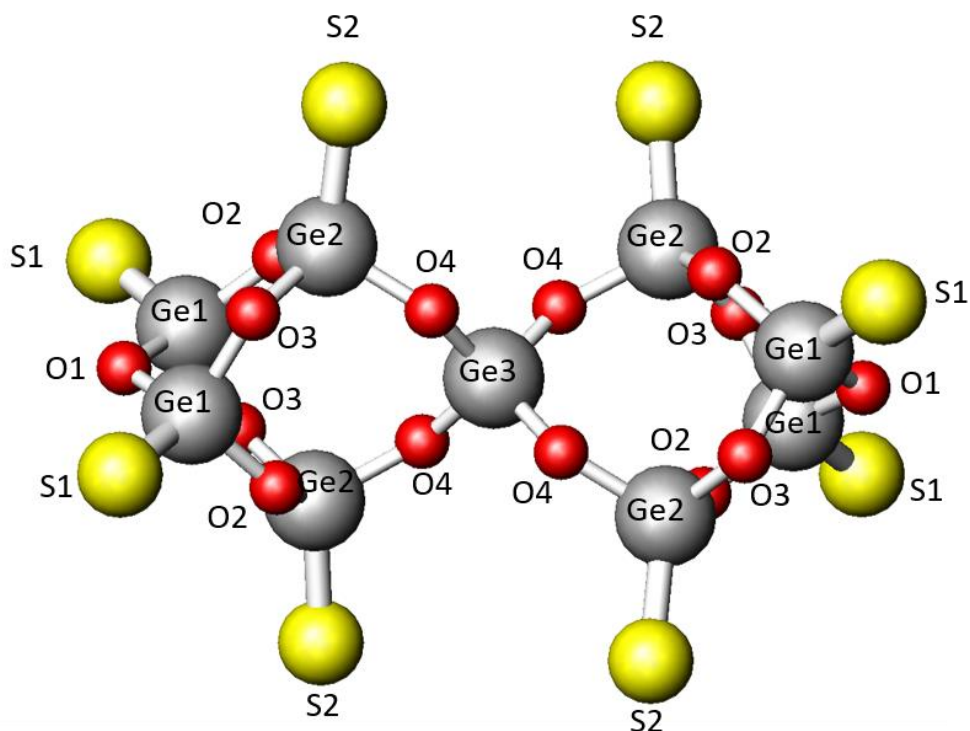
Figure 4.36: An annotated $[Ge_9O_{14}S_8]^{8-}$ unit from compound $[Co(deta)_2]_4[Ge_9O_{14}S_8]$ **(12)**. Key: grey: Ge atoms, red: O atoms, yellow: S atoms.

Bond-valence calculations (Table 4.28) indicate that germanium has a +4 oxidation state (Ge(1) 4.05, Ge(2) 4.05 and Ge(3) 4.17 v.u.). As in the previous compounds (**8**), (**9**) and (**10**), the charge balancing cation here is $[Co(deta)_2]^{2+}$. However, due to the much larger charge of the fused T2 doubling the contributions (-8 charge), four Co(II) complexes are required to balance a single inorganic unit. The spread of the Ge-O-Ge bond angles within the cluster have increased to between ($117.4(7) \leq \alpha/° \leq 135.0(6)$), when compared to (**6**) which was between ($117.71(15) \leq \alpha/° \leq 120.22(16)$), this allows space for the central $Ge(3)O_4^{4-}$ to be present, with minimal effect to the individual GeO_3S^{4-} tetrahedral units. The terminal Ge-S bond lengths have increased marginally, with Ge(1)-S(1) and Ge(2)-S(2) being 2.110(4) and 2.127(4) Å, respectively. The Co-N bond lengths in the $[Co(deta)_2]^{2+}$ complexes lie in the range ($2.149(12) \leq d/Å \leq 2.221(12)$), are similar to the bond lengths of complexes seen in (**8**) and (**9**). The N-Co-N biting angle of the ligands are between ($78.9(4) \leq \alpha/° \leq 80.1(4)$) and the N-Co-N angles between deta moieties are between ($84.4(4) \leq \alpha/° \leq 102.6(4)$). Selected bond lengths and bond angles can be seen in Table 4.28 and 4.29 respectively.

Table 4.28: A selection of bond lengths and valence sums in $[Co(deta)_2]_4[Ge_9O_{14}S_8]$ (**12**).

Symmetry operations: a = x, -y+5/4, -z+5/4; b = -x+9/4, y, -z+5/4; c = -x+9/4, -y+5/4, z

	Length /Å	v_{ij}		Length /Å	v_{ij}		Length /Å	v_{ij}
Ge(1)-S(1)	2.110(4)	1.35	Ge(2)-O(3)[a]	1.785(8)	0.90	Ge(3)-O(4)[b]	1.734(9)	1.04
Ge(1)-O(1)	1.791(7)	0.89	Ge(2)-S(2)	2.127(4)	1.29	Ge(3)-O(4)[c]	1.734(9)	1.04
Ge(1)-O(2)	1.784(8)	0.91	Ge(2)-O(2)	1.784(9)	0.91	Ge(3)-O(4)[a]	1.734(9)	1.04
Ge(1)-O(3)	1.786(9)	0.90	Ge(2)-O(4)	1.767(9)	0.95	Ge(3)-O(4)	1.734(9)	1.04
$\sum v_{ij}$		**4.05**			**4.05**			**4.16**
Co(1)-N(1)	2.134(11)							
Co(1)-N(2)	2.170(12)							
Co(1)-N(3)	2.216(11)							
Co(1)-N(4)	2.221(12)							
Co(1)-N(5)	2.149(12)							
Co(1)-N(6)	2.184(11)							
$\sum v_{ij}$								

Table 4.29: A selection of bond angles in $[Co(deta)_2]_4[Ge_9O_{14}S_8]$ (**12**).

Symmetry operations: a = x, -y+5/4, -z+5/4; b = -x+9/4, y, -z+5/4; c = -x+9/4, -y+5/4, z

	Angle / °		Angle / °		Angle / °
S(1)-Ge(1)-O(1)	118.1(4)	O(4)[b]-Ge(3)-O(4)[c]	113.2(6)	N(1)-Co(1)-N(5)	176.8(4)
S(1)-Ge(1)-O(2)	115.0(3)	O(4)[b]-Ge(3)-O(4)[a]	110.4(6)	N(2)-Co(1)-N(5)	99.4(4)
O(1)-Ge(1)-O(2)	104.9(4)	O(4)[a]-Ge(3)-O(4)[a]	104.9(6)	N(3)-Co(1)-N(5)	101.7(4)
S(1)-Ge(1)-O(3)	108.4(3)	O(4)[b]-Ge(3)-O(4)	104.9(6)	N(4)-Co(1)-N(5)	79.6(4)
O(1)-Ge(1)-O(3)	102.8(3)	O(4)[c]-Ge(3)-O(4)	110.4(6)	N(1)-Co(1)-N(6)	102.6(4)
O(2)-Ge(1)-O(3)	106.4(4)	O(4)[a]-Ge(3)-O(4)	113.2(6)	N(2)-Co(1)-N(6)	94.0(4)
O(3)[a]-Ge(2)-S(2)	114.4(3)	N(1)-Co(1)-N(2)	78.9(4)	N(3)-Co(1)-N(6)	91.9(4)
O(3)[a]-Ge(2)-O(2)	106.1(4)	N(1)-Co(1)-N(3)	79.9(4)	N(5)-Co(1)-N(6)	80.1(4)
S(2)-Ge(2)-O(2)	113.1(3)	N(2)-Co(1)-N(3)	158.8(4)	Ge(1)-O(1)-Ge(1)[a]	117.4(7)
O(3)[a]-Ge(2)-O(4)	101.7(4)	N(1)-Co(1)-N(4)	98.0(4)	Ge(2)-O(2)-Ge(1)	132.7(5)
S(2)-Ge(2)-O(4)	113.0(3)	N(2)-Co(1)-N(4)	97.3(4)	Ge(1)-O(3)-Ge(2)[a]	121.8(5)
O(2)-Ge(2)-O(4)	107.7(4)	N(3)-Co(1)-N(4)	84.3(4)	Ge(2)-O(4)-Ge(3)	135.0(6)

The packing of the crystal structure can be seen in Figure 4.37, showing the increased number of transition-metal complexes present compared to the previous compounds, particularly evident when viewed along the *a*-axis. The arrangement of the packing relies on a staggered complex-cluster system as seen with previous compounds, a single section representing the cluster and 4 complexes can be seen in Figure 4.37a which was removed from the larger

section in Figure 4.37b. The fused T2 units and transition-metal complexes form rows where the adjacent row are displaced by (0½0) along [001]. As seen with all other discrete units in this work, the clusters are surrounded by complexes and attempt to maximise the distance between cluster centres.

Distances between donor and acceptor atoms can be found in Table 4.30, supporting the presence of hydrogen bonding which is stabilising the structure.
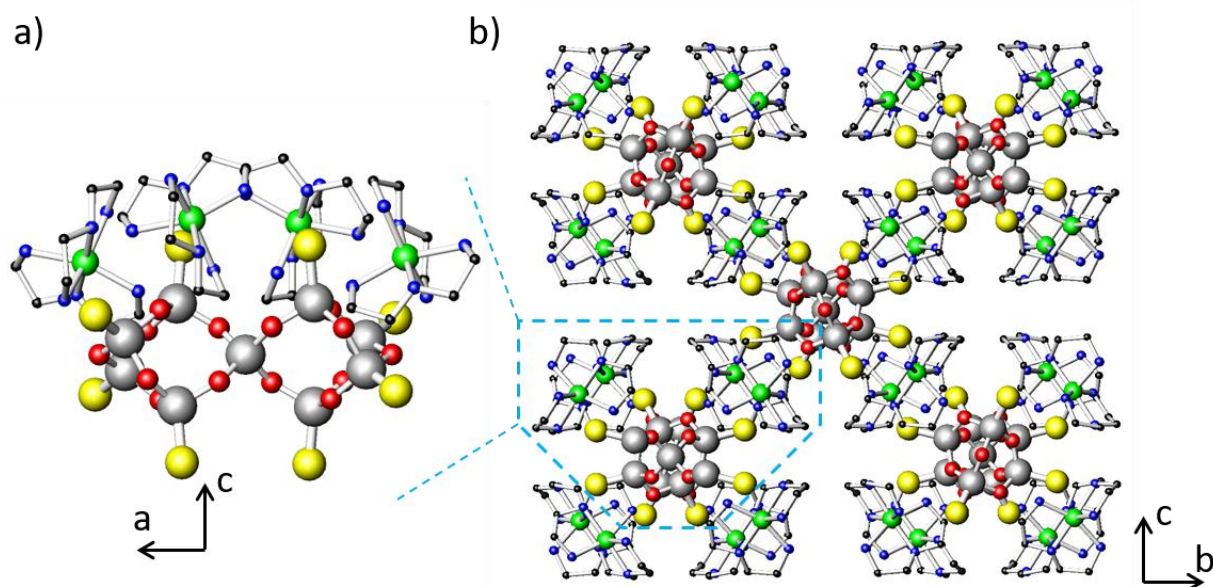
Figure 4.37: (a) A single section of (**12**) found in the [100] direction, but viewed along [010] and b) displays multiple rows of clusters and complexes in a fully packed crystal structure down [100]. Key: grey: Ge atoms, red: O atoms, yellow: S atoms, green: Co atoms, blue: N atoms, black: C atoms. Hydrogen atoms are omitted for clarity.

Table 4.30: Bond lengths found in (**12**) between acceptor and donor atoms containing hydrogen bonding.

Symmetry operations: a = x-5/4, -y+1, z-5/4

	length /Å
N(2…O(2)	2.94(1)
N(6)…O(3)[a]	2.91(1)
N(4)…S(1)	3.32(1)

Thermogravimetric analysis of compound (**12**) (Figure 4.39) indicates a total weight loss of 34.90 % in a two-step process. The first step, 8.94 % weight loss in total, was calculated to correspond to a loss of two molecules of deta. The rest of the organic component is removed in the second step. The overall total weight loss agrees well with the total loss seen in the CHN analysis.
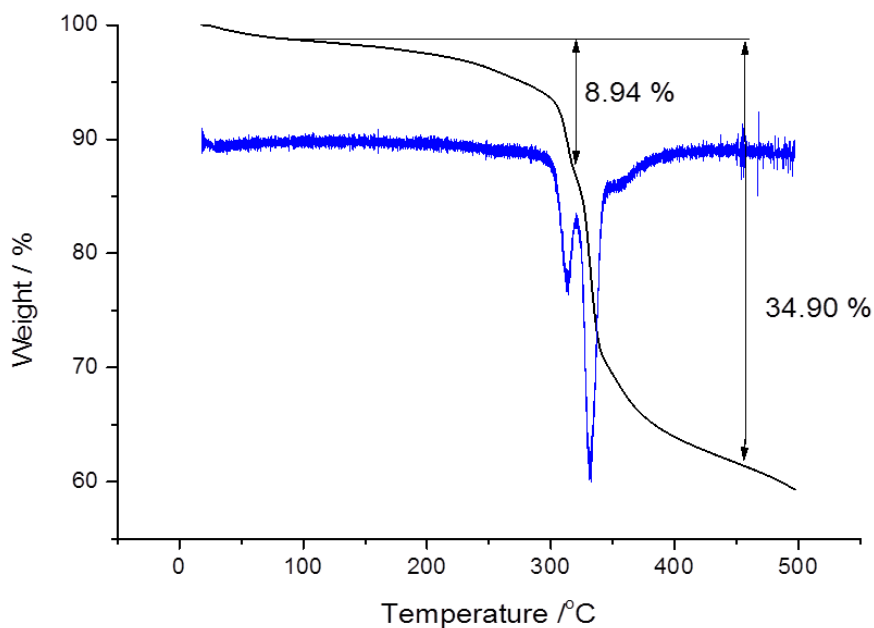
Figure 4.39: Thermogravimetric analysis curve of $[Co(deta)_2]_4[Ge_9O_{14}S_8]$ (**12**) heated under N_2 (black) and the corresponding derivative (DTG) curve (blue).

The IR spectrum of (**12**) can be viewed in Figure 4.40 and the tentative assignments are listed in Table 4.31. The vibrations observed provide evidence for the presence of amine and compares relatively well to the IR present on the NUIST database [279] apart from the C-N region, which here is more complicated.
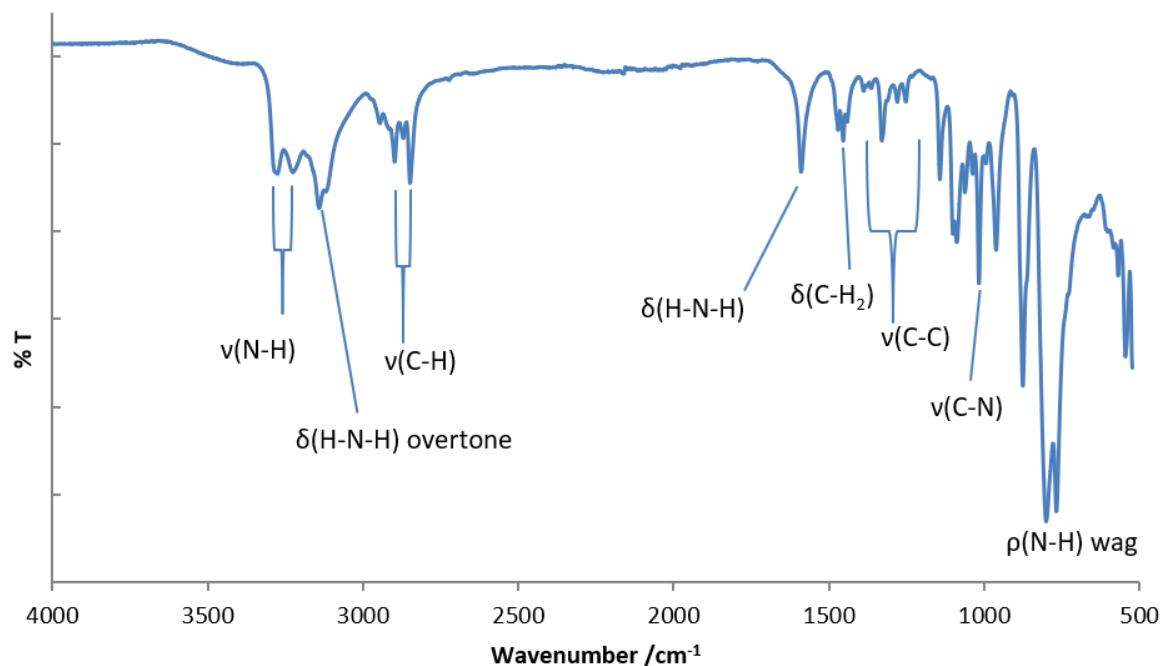
Figure 4.40: IR spectrum of [Co(deta)$_2$]$_4$[Ge$_9$O$_{14}$S$_8$] **(12)** from hand-picked crystals.

Table 4.31: Infrared spectrum assignments of [Co(deta)$_2$]$_4$[Ge$_9$O$_{14}$S$_8$] **(12)**

Stretching mode	Wavenumber /cm^{-1}
ν(N-H)	3226 (sym) and 3275 (asym)
ν(C-H)	2847 (sym) and 2903 (asym)
δ(H-N-H)	1591 (3133 overtone)
δ (C-H$_2$)	1455
ν(C-C)	1254-1366 (multiple peaks)
ν(C-N)	1009
ρ(N-H) wag	802

The diffuse reflectance spectrum for (**12**) (Figure 4.41) shows an absorption edge at 4.2(3) eV. The small peak at ~2.5 eV is suspected to arise from cobalt(II) *d-d* transitions [277], as seen in the previous data for **(6), (8)** and **(10)**.
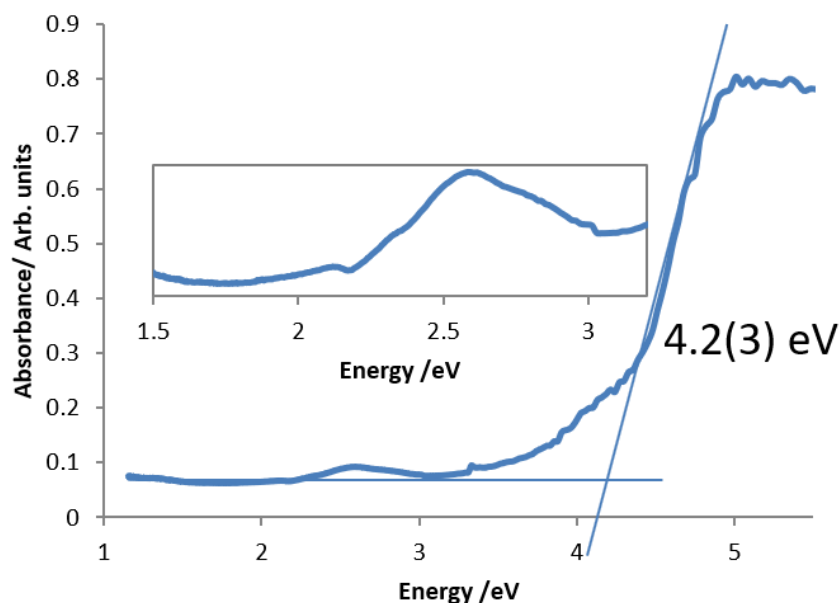
Figure 4.41: Diffuse reflectance spectrum of $[Co(deta)_2]_4[Ge_9O_{14}S_8]$ **(12)** from hand-picked crystals showing a band gap of 4.2(3) eV.

4.4 A 1-D Chain
4.4.1 $[Co(tren)]_2[Ge_5O_9(OH)_2S_2]$ **(13)**
4.4.1.1 Synthesis

$[Co(tren)]_2[Ge_5O_9(OH)_2S_2]$ **(13)** was synthesised using Sb (91.4 mg, 0.75 mmol) GeO_2 (118 mg, 1.6 mmol), CoS (34.4 mg, 3.8 mmol), S (96 mg 3 mmol), water (2 ml, 110 mmol) and tris(2-aminoethyl)amine (tren) (3.2 ml, 21 mmol). The reaction mixture was stirred for 10 minutes before being sealed and heated to 453 K at 1 K min^{-1} for 8 days. The reaction formed green crystal plates along with green and metallic black powder. The presence of (**13**) was confirmed through powder X-ray diffraction experiments on the bulk sample (Figure 4.42). The bulk powder pattern matched the calculated pattern generated by single-crystal X-ray data. The presence of unreacted Sb was also observed. Combustion analysis values of C 10.49 %, H 2.76 %, N 7.98% are too small compared to the crystallographically determined formula $[Co(tren)]_2[Ge_5O_{11}S_2]$ (C 13.86 %, H 3.40 %, N 10.78 %). The C/N ratio however is correct for the tren molecule to be present and the TGA analysis produces the full organic weight loss. The difference seen is due to the difficulty in picking out crystals from a powder

161

whereby some of the other phases may have contaminated a few of the crystals by clinging to the surfaces.
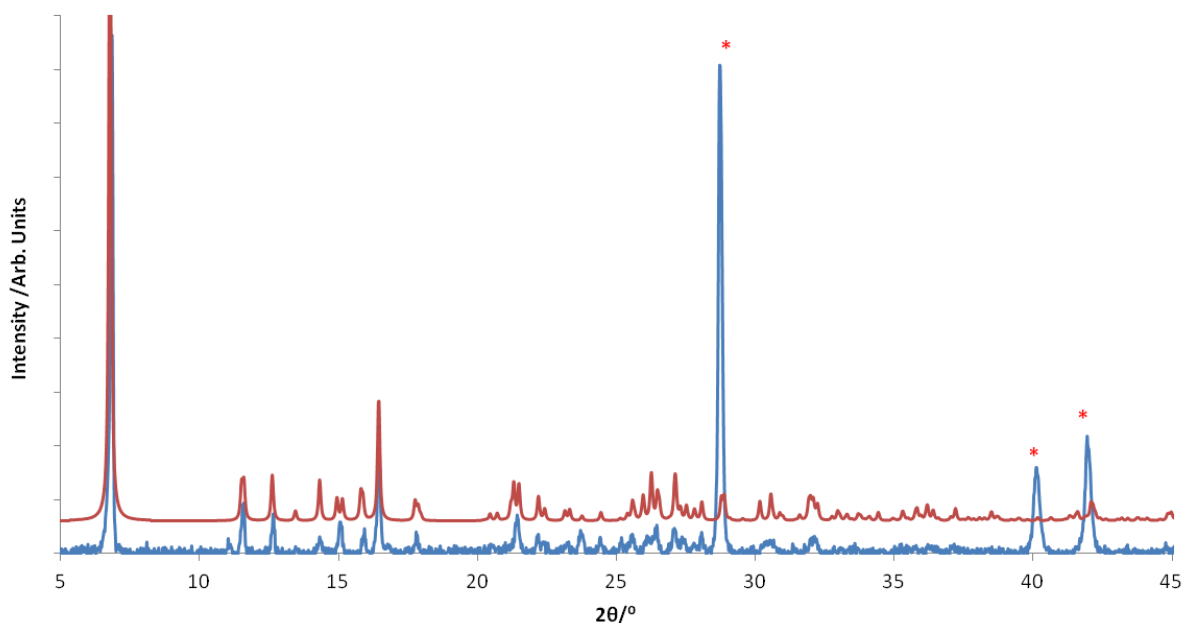
Figure 4.42: X-ray diffraction pattern of the bulk, as-synthesised product (blue) which contained crystals of $[Co(tren)]_2[Ge_5O_9(OH)_2S_2]$ (**13**). The simulated pattern calculated from single-crystal X-ray data for (**13**) is shown above (red). Peaks in the bulk sample annotated with asterisks correspond to Sb (red).

Reactions were conducted without the presence of antimony and the product (**13**) did not form. Instead, crystals of $[Co(tren)]_2[Ge_2S_6]$ (**21**) were formed in the reaction and this structure is discussed in Chapter 6.

Single-crystal X-ray diffraction data were collected at 150 K using graphite monochromated CuK$_\alpha$ (λ = 1.54184 Å) radiation. The structure was solved using SIR92 [227] and the model refined using the CRYSTALS suite of programs [230]. The model was refined against F and a Chebychev polynomial weighting scheme was applied. The crystal appeared to be twinned so a twin law was used and the two components were 69 % and 31 %. A bond-length restraint was applied between N(1) and C(1) to keep the bond lengths at 1.50(4) Å. In addition, a number of U(ij) restraints were used on various parts of the inorganic framework. Hydrogen atoms on the amine ligands were placed geometrically with a U[equiv] value 1.2 times the U[equiv] of the carbon to which they are attached. Crystallographic details are summarised in Table 4.32 and atomic coordinates of all non-hydrogen atoms can be found in Table A2.8.

Table 4.32: Crystallographic data for structures [Co(tren)]$_2$[Ge$_5$O$_9$(OH)$_2$S$_2$] (**13**).

Chemical formula	[Co(tren)]$_2$[Ge$_5$O$_9$(OH)$_2$S$_2$]
Formula mass	1015.52
Crystal Habit	Green plate
Crystal system	Monoclinic
Symmetry space group	*Ic*
Temp /K	150
a /Å	27.1391(13)
b /Å	7.2767(3)
c /Å	16.0090(7)
β /°	106.418(5)
V /Å³	3032.59(13)
Z	4
μ /mm^{-1}	15.765
Total reflections ($I > 3\sigma(I)$)	3031
R factor	0.0875
w*R* factor	0.0919
Goodness of fit ref	1.1225

4.4.1.2 Structure and analysis

Upon further synthetic studies, it was shown that the presence of water was necessary to produce compound (**13**). The addition of water into the reaction was initially intended to promote crystal formation, although it was found that OH groups were incorporated into the structure of [Co(tren)]$_2$[Ge$_5$O$_9$(OH)$_2$S$_2$] (**13**). Locally, the structure of (**13**) is formed from two GeO$_3$S^{4-} units connecting into a ring through sharing oxygen atoms with two GeO$_4$$^{4-}$ tetrahedra, producing a 4-membered Ge-O based ring with sulfur atoms pointing outwards either end. Atop this Ge$_4$O$_8$S$_2$ ring, a tetrahedral Ge(1)O$_4$ "crown" bonds to Ge(4) and Ge(3) through the remaining oxygen sites (Figure 4.43). The two GeO$_4$$^{4-}$ tetrahedra in this ring; Ge(5) and Ge(2), bridge through the third oxygen O(10) to create an infinite chain along axis *b* (Figure 4.44), whilst the fourth oxygen of this tetrahedron bonds to the charge balancing complexes, [Co(tren)]$_2$$^{2+}$.
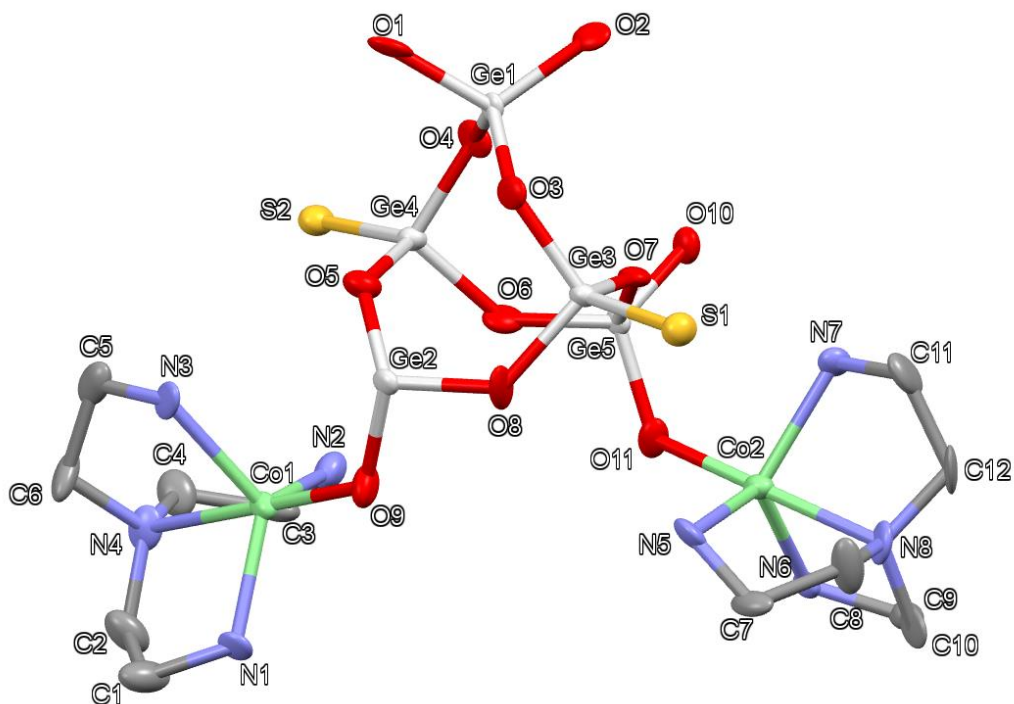
Figure 4.43: Asymmetric unit of (**13**) displaying thermal ellipsoids of each atom at 50 % probability. Key: light grey: Ge, green: Co atoms, yellow: S atoms, red: O atoms, light blue: N atoms, grey: C atoms. Hydrogen atoms are omitted for clarity.
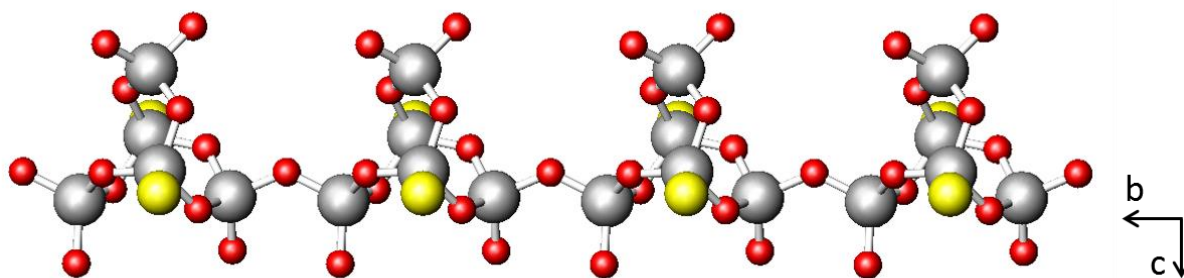
Figure 4.44: The chain of $[Ge_5O_9(OH)_2S_2]^{4-}$ units running parallel to the *b*-axis. Key: grey: Ge atoms, red: O atoms, yellow: S atoms. Pendants omitted for clarity.

This structure has the interesting feature of the charge balancing cation complexes bonding directly to the $[Ge_5O_9(OH)_2S_2]^{4-}$ chains as "pendants". While the use of transition-metal complexes is largely for charge balancing and structure directing, occasionally they are capable of bonding to the frameworks themselves. Currently however, there are no thiogermanates in the literature showing this type of framework-complex interaction. Discrete

clusters of Ge_2S_6 bonded to pendant units have been reported and include $[(Co(tepa)]_2[(\mu\text{-}Ge_2S_6)]$ (tepa = tetraethylenepentamine) [281] and $[Y_2(tepa)_2(\mu\text{-}OH)_2(\mu\text{-}Ge_2S_6)](tepa)_{0.5}.H_2O$ [103]. Both structures show complexes bonding to the anion cluster through a sulfur bond. In addition, complex pendant motifs are more common in other metal sulfides, especially in antimony-based sulfide frameworks *e.g.* $[Co(tren)]Sb_2S_4$ and $[Ni(tren)]Sb_2S_4$ [282] in which the complex bonds to one or two sulfur sites, respectively or in $[Fe(tren)]FeSbS_4$ [283] which contains a pendant iron complex as well as Fe-Sb-S chains.

The cluster generated on linking together the tetrahedral units (Figure 4.43) is structurally closely related to a fragment of the cluster observed in compound (**12**). Consider one of the $[Ge_4O_5S_4]^{2-}$ fragments linked to the tetrahedral $Ge(3)O_4^{4-}$ bridging unit (Figure A2.3). Breaking the Ge(1)-O(1)-Ge(1) bond generates a cluster with the same germanium-oxygen connectivity as that found in (**13**) and provides an oxygen atom available for bonding to an adjacent cluster to form a chain. Replacement of the S(1) atoms by (OCo(tren)] and protonation of the free completes the transformation.

The bond-valence calculations are summarised in Table 4.33, which support the oxidation assignments of +4 for Ge and +2 for Co. The structure of (**13**) is broken down into the $[Ge_5O_9(OH)_2S_2]$ cluster and the two $[Co(tren)]^{2+}$ pendant complexes. This however leaves a +2 charge missing. This is accounted for by taking the bond-valence calculations of oxygen into account for O(1) 1.03 and O(2) 1.06 v.u.. These values indicate a deficient valence contribution for the O^{2-} ions. Therefore the -2 charge is balanced by each oxygen atom bonding to a proton to form hydroxyl groups.

All Ge-O bonds (Table 4.33) lie between ($1.729(15) \leq d/Å \leq 1.805(15)$) and the two Ge-S bond lengths are 2.105(6) and 2.100(5) Å, both of which compare well to the other compounds produced in this chapter, for example the Ge-S bond lengths are between ($2.0990(11) \leq d/Å \leq 2.1006(11)$) and Ge-O between ($1.783(3) \leq d/Å \leq 1.810(3)$) in (**6**). The angles (Table 4.34) within GeO_3S tetrahedral units within this structure are similar as well, S-Ge(4)-O ($109.9(4) \leq \alpha/° \leq 118.5(6)$) and S-Ge(3)-O ($110.3(5) \leq \alpha/° \leq 119.4(5)$).

Table 4.33: A selection of bond lengths and valence sums in [Co(tren)]$_2$[Ge$_5$O$_9$(OH)$_2$S$_2$] (**13**).

Symmetry operations: a = x, y+1, z

	Length /Å	v_{ij}		Length /Å	v_{ij}		Length /Å	v_{ij}
Ge(1)-O(1)	1.726(15)	1.06	Ge(2)-O(10)[a]	1.739(12)	1.02	Ge(3)-S(1)	2.106(5)	1.36
Ge(1)-O(2)	1.743(13)	1.01	Ge(2)-O(5)	1.746(13)	1.01	Ge(3)-O(3)	1.797(13)	0.88
Ge(1)-O(3)	1.735(13)	1.04	Ge(2)-O(8)	1.753(12)	0.99	Ge(3)-O(7)	1.736(13)	1.03
Ge(1)-O(4)	1.728(14)	1.06	Ge(2)-O(9)	1.729(14)	1.05	Ge(3)-O(8)	1.782(14)	0.91
$\sum v_{ij}$		**4.17**			**4.07**			**4.18**
Ge(4)-S(2)	2.103(5)	1.37	Ge(5)-O(6)	1.741(14)	1.02	Co(1)-O(9)	1.922(13)	0.54
Ge(4)-O(4)	1.798(14)	0.87	Ge(5)-O(7)	1.752(13)	0.99	Co(1)-N(1)	2.078(16)	0.53
Ge(4)-O(5)	1.752(13)	0.99	Ge(5)-O(10)	1.744(12)	1.01	Co(1)-N(2)	2.110(19)	0.48
Ge(4)-O(6)	1.805(15)	0.86	Ge(5)-O(11)	1.735(14)	1.04	Co(1)-N(3)	2.145(17)	0.44
						Co(1)-N(4)	2.222(17)	0.36
$\sum v_{ij}$		**4.09**			**4.06**			**2.35**
Co(2)-O(11)	1.937(12)	0.52						
Co(2)-N(5)	2.113(18)	0.48						
Co(2)-N(6)	2.111(16)	0.48						
Co(2)-N(7)	2.108(17)	0.48						
Co(2)-N(8)	2.207(15)	0.37						
$\sum v_{ij}$		**2.33**						

Table 4.34: A selection of bond angles in [Co(tren)]$_2$[Ge$_5$O$_9$(OH)$_2$S$_2$] (**13**).

Symmetry operations: a = x, y+1, z

	Angle / °		Angle / °		Angle / °
O(1)-Ge(1)-O(2)	112.7(6)	O(3)-Ge(3)-O(7)	102.3(6)	O(7)-Ge(5)-O(11)	111.3(6)
O(1)-Ge(1)-O(3)	109.3(6)	S(1)-Ge(3)-O(8)	109.9(4)	O(10)-Ge(5)-O(11)	113.8(6)
O(2)-Ge(1)-O(3)	103.2(6)	O(3)-Ge(3)-O(8)	103.8(6)	O(9)-Co(1)-N(1)	99.8(6)
O(1)-Ge(1)-O(4)	102.5(6)	O(7)-Ge(3)-O(8)	106.5(6)	O(9)-Co(1)-N(2)	100.2(6)
O(2)-Ge(1)-O(4)	109.7(6)	S(2)-Ge(4)-O(4)	119.0(5)	N(1)-Co(1)-N(2)	118.6(7)
O(3)-Ge(1)-O(4)	119.8(7)	S(2)-Ge(4)-O(5)	114.2(5)	O(9)-Co(1)-N(3)	100.5(7)
O(10)[a]-Ge(2)-O(5)	99.4(6)	O(4)-Ge(4)-O(5)	102.1(6)	N(1)-Co(1)-N(3)	119.5(6)
O(10)[a]-Ge(2)-O(8)	109.8(7)	S(2)-Ge(4)-O(6)	110.5(5)	N(2)-Co(1)-N(3)	112.8(6)
O(5)-Ge(2)-O(8)	114.7(6)	O(4)-Ge(4)-O(6)	103.6(6)	O(9)-Co(1)-N(4)	179.5(6)
O(10)[a]-Ge(2)-O(9)	114.0(7)	O(5)-Ge(4)-O(6)	106.2(6)	N(1)-Co(1)-N(4)	80.3(7)
O(5)-Ge(2)-O(9)	112.1(6)	O(6)-Ge(5)-O(7)	115.6(6)	N(2)-Co(1)-N(4)	80.2(6)
O(8)-Ge(2)-O(9)	106.8(7)	O(6)-Ge(5)-O(10)	109.3(6)	N(3)-Co(1)-N(4)	79.0(7)
S(1)-Ge(3)-O(3)	118.7(5)	O(7)-Ge(5)-O(10)	101.1(6)		
S(1)-Ge(3)-O(7)	114.5(4)	O(6)-Ge(5)-O(11)	105.9(6)		

The crystal packing of structure (**13**) involves the pendant chains stacking on top of each other in the [001] direction. The pendants sit between the free space produced by the neighbouring chain, as seen in Figure 4.45a. Rows of chains then reside next to each other in a staggered formation promoted by S…N interactions, as seen in Figure 4.45b. Figure A2.4 displays the same figure as 4.45 but without carbon and nitrogen for clarity.

Distances between acceptor and donor atoms in (**13**) can be seen in Table 4.35, which suggests hydrogen bonding interactions are present within the crystal structure. There are also weaker S…N interactions between $(3.77(2) \leq d/Å \leq 3.85(2))$.
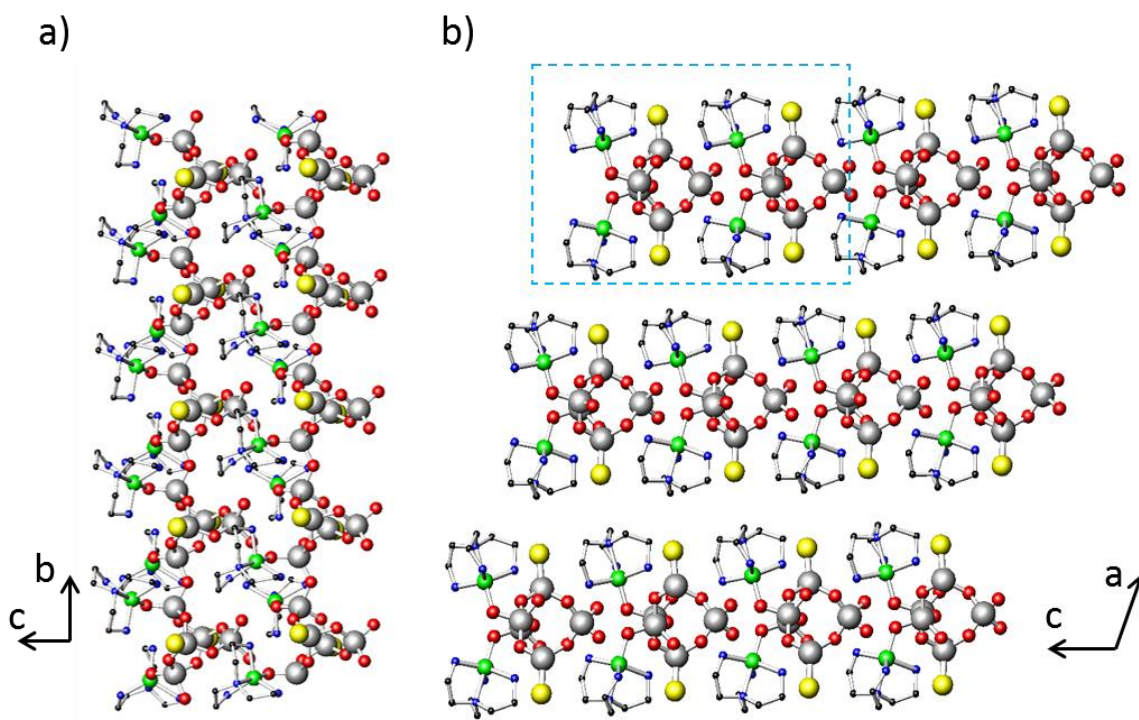
Figure 4.45: (a) Two chains of (**13**) (removed from the blue box in (b)) aligned in the [010] direction, but viewed along [100] and (b) multiple rows of chains in a fully packed crystal structure viewed along [010]. Key: grey: Ge atoms, red: O atoms, yellow: S atoms, green: Co atoms, blue: N atoms, black: C atoms. Hydrogen atoms are omitted for clarity.

167

Table 4.35: Bond lengths found in (**13**) between acceptor and donor atoms containing hydrogen bonding.

Symmetry operations: a = x, -y+2, z+1/2; b = x, -y+3, z+1/2; c = x, y+1, z; d = x, -y+1, z+1/2; e = x, y-1, z

	length /Å		length /Å
N(1)…O(4)^a	3.16(3)	N(5)…O(2)^a	3.19(3)
N(1)…O(1)^b	3.02(3)	N(6)…O(2)^d	2.97(3)
N(2)…O(1)^a	3.16(3)	N(6)…O(3)^a	3.15(3)
N(3)…O(5)	3.26(3)	N(7)…O(8)^e	3.19(3)
N(3)…O(6)^c	3.15(3)	N(7)…O(7)	3.12(3)

Compound (**13**) has a similar thermal behaviour to compound (**10**) in that the breakdown of the organic components leads quickly to the breakdown of the inorganic counterpart (Figure 4.46). The change in phase however at 700 ˚C gave an overall weight loss of 26.72 %, close to the calculated value for the loss of organic component (28.04 %). The difference, again, is due to the difficulty of crystal picking from a mixed phase sample which can produce small amount of contamination. The breakdown occurs in a three-step reduction in mass. The first step at 12.13 % equates to the loss of approximately one tren molecule and the second and third step correspond to the breaking down of the second tren molecule at 26.72 %.

The IR spectrum of (**13**) can be viewed in Figure 4.47 and the tentative assignments [253] are listed in Table 4.36. The vibrations observed provide evidence for the presence of amine. The ν (O-H) vibration at 3414 cm^{-1} is due to the OH groups present on the chain.
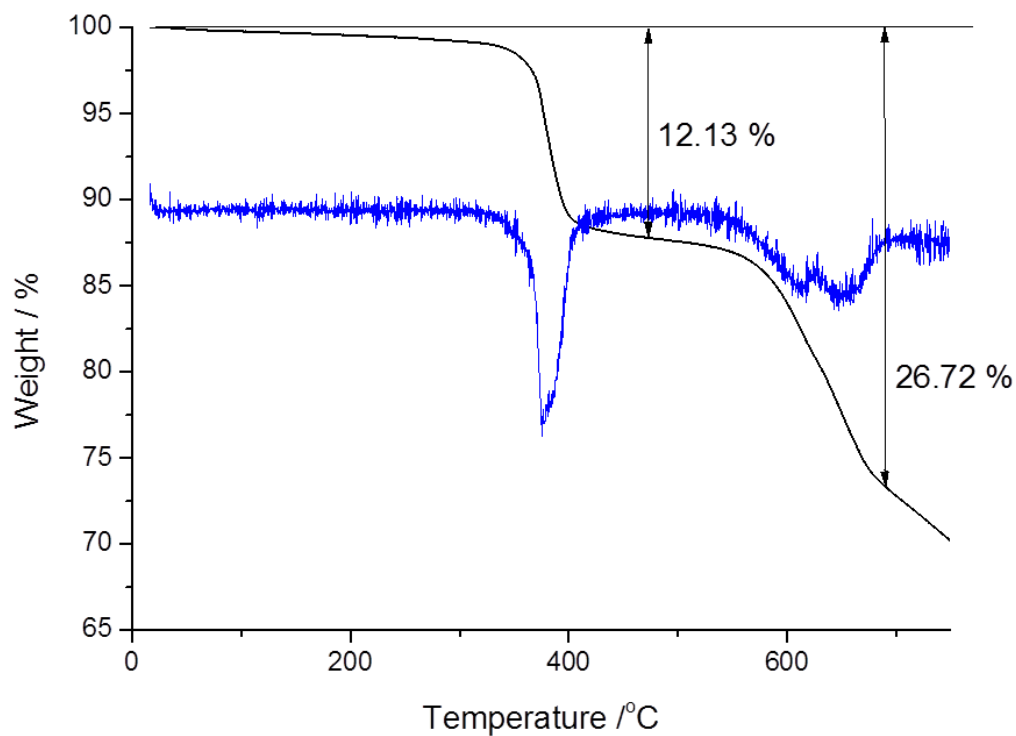
Figure 4.46: Thermogravimetric analysis curve of [Co(tren)]$_2$[Ge$_5$O$_9$(OH)$_2$S$_2$] (**13**) heated under N$_2$ (black) and the corresponding derivative (DTG) curve (blue).
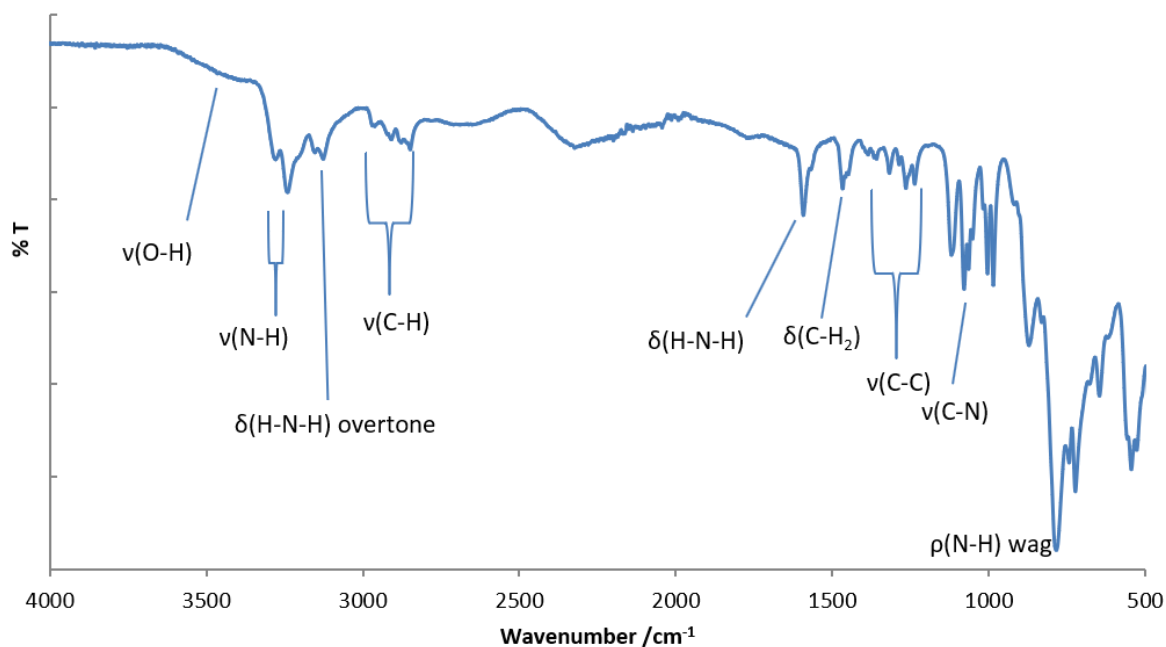
Figure 4.47: IR spectrum of [Co(tren)]$_2$[Ge$_5$O$_9$(OH)$_2$S$_2$] (**13**) from hand-picked crystals.

Table 4.36: Infrared spectrum assignments of $[Co(tren)]_2[Ge_5O_9(OH)_2S_2]$ (**13**)

Stretching mode	Wavenumber /cm^{-1}
ν(O-H)	3414
ν(N-H)	3236 (sym) and 3275 (asym)
ν(C-H)	2846-2961 (multiple peaks)
δ(H-N-H)	1592 (3133 overtone)
δ (C-H$_2$)	1467
ν(C-C)	1237-1366 (multiple peaks)
ν(C-N)	1079
ρ(N-H) wag	783

Finally, the diffuse reflectance spectrum of (**13**) (Figure 4.48) shows an absorption edge of 4.3(2) eV is present. All diffuse reflectance spectra in this chapter show minor cobalt *d-d* transitions between 2-3 eV, but spectrum (**13**) shows multiple peaks around this region. It is not understood how these interactions have arisen as there are currently no detailed optical studies available for transition-metal pendant styled sulfide frameworks containing germanium.
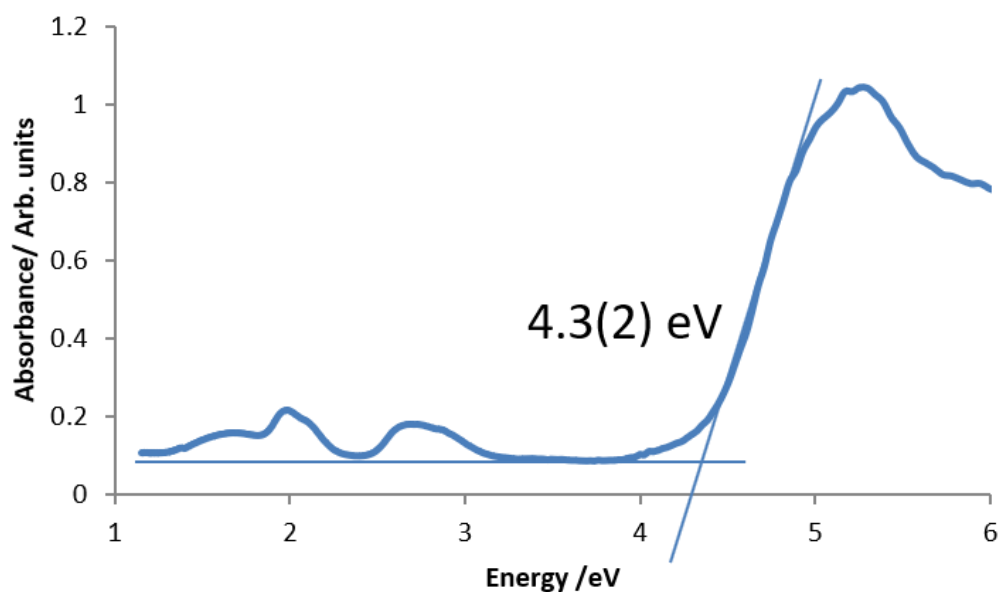
Figure 4.48: Diffuse reflectance spectrum of $[Co(tren)]_2[Ge_5O_9(OH)_2S_2]$ (**13**) from hand-picked crystals showing a band gap of 4.3(2) eV.

4.4 Conclusions

Eight novel oxothiogermanate materials based on T2 supertetrahedral units and fragments thereof have been produced and characterised. Compounds (**6**)-(**9**) all contain $[Ge_4O_6S_4]^{4-}$ T2 adamantane-like units. Compounds (**8**) and (**9**) have polymorphic crystal structures. The charge balancing complex, $[Co(tren)_2]_2$, seen in structure (**6**) has been seen previously in $[Co(C_6H_{18}N_4)_2][Co(CO)_4]_2$ [274]. Compound (**7**) contains the bridged tren complex $[(Co(tren))_2\mu\text{-tren}]$ which has not been observed previously. The difference between the optical measurements of (**7**) and (**8**) are minimal, despite the presence of different cobalt(II) complexes.

Upon the addition of sulfur to the reaction mixtures, anion substitution occurred with oxygen positions in the $[Ge_4O_6]$ core of the T2 unit being replaced by sulfur producing $[Ge_4O_4S_6]^{4-}$ (**10**) and $[Ge_4O_2S_8]^{4-}$ (**11**). The increase in sulfur concentration within the T2 core yields differences in thermal stability and optical properties. Studying the optical data of compounds $[Co(deta)_2]_2[Ge_4O_6S_4]\cdot H_2O$ (**8**), $[Co(deta)_2]_2 [Ge_4O_4S_6]$ (**10**) and $[Co(dap)_3)]_2[Ge_4O_2S_8]$ (**11**) reveals some interesting features (Figure 4.49). From the spectra of (**8**) to (**10**), it displays an initial increase in the absorbance of the peak positioned at ~5 eV (corresponding to the 4.1(2) eV absorption edge). This suggests the two additional sulfur atoms which replace two oxygen atoms affect this absorption edge. Upon increasing the sulfur concentration yet again in (**11**), the absorption band at ~5 eV move the absorption edge to lower energy. This may indicate a broadening of both conduction and valence bands thereby reducing the size of the band gap. It has been recorded previously that the sulfur in M_nS_x (M=main group metal) containing materials [19-20], including oxy-sulfide frameworks (see Section 1.2.2), contributes both to the conduction and valence bands.

171
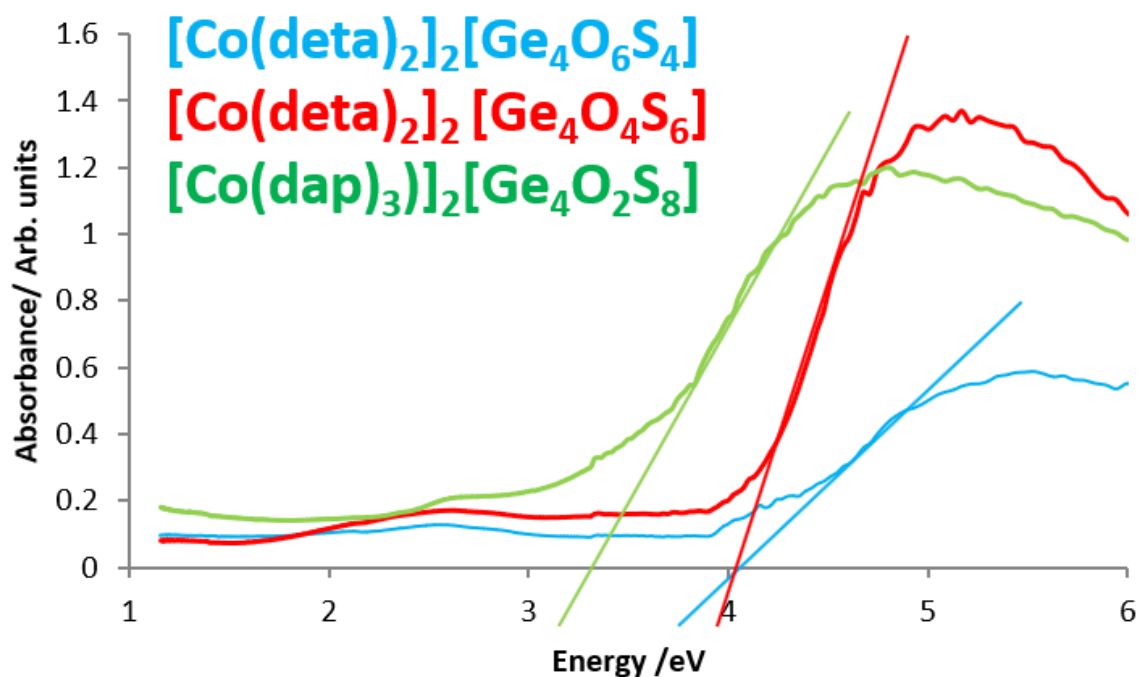
Figure 4.49: Diffuse reflectance spectra of; (**8**) blue, (**10**) red and (**11**) green.

Furthermore, the stability of the discrete clusters appears to reduce with increasing sulfur concentration, with the initial organic removal observed within the TGA-DTG curve maximas at ~320 °C, ~305 °C and ~250 °C for materials (**8**), (**10**) and (**11**) respectively. Compound (**11**) is also the only material to have completed its organic breakdown before 400 °C, which would then be followed by the breakdown of the discrete clusters themselves. More materials would need to be synthesised to be certain but the observations so far show that these materials appear more thermally stable with oxygen present.

Further synthetic manipulations allowed the production of $[Co(deta)_2]_4[Ge_9O_{14}S_8]$ (**12**) containing the unit $[Ge_9O_{14}S_8]^{8-}$, a 'fused' dimeric T2 system, which, as far as the author is aware is the first occurrence of such a supertetrahedral building unit. The analysis of the material showed the presence of a strong 4.2(3) eV absorption edge which is similar to the values of the $[Ge_4O_6S_4]$ clusters.

Finally, compound $[Co(tren)]_2[Ge_5O_9(OH)_2S_2]$ (**13**), demonstrates the use of the various building blocks produced so far to form a chain-based structure with pendant-like transition-metal complexes as charge balancing cations. The structural relationship between (**12**) and (**13**) can be seen in Figure A2.3. It should be noted that the thermal stability of the chain-

based structure is higher than those of the compounds containing discrete clusters as it only starts to break down at ~400 ˚C.

Taking all the band gap values obtained in this study, including the chain structure of (**13**) and comparing them to pure Ge_4S_{10} discrete clusters reveals a correlation between the Ge:S ratio (Figure 50) and the band-gap value. While Figure 4.49 demonstrates the effect of increasing sulfur within the T2 unit, Figure 4.50 demonstrates that pure thiogermanate materials (containing similar transition-metal complexes to those used here) have, on the whole, lower band gaps than those of the oxothiogermanate materials. The graph also demonstrates that on increasing the concentration of sulfur, within the T2 $[Ge_4O_{6-x}S_{4+x}]$ ($x = 0, 2, 4$) cluster, the band gap becomes smaller.
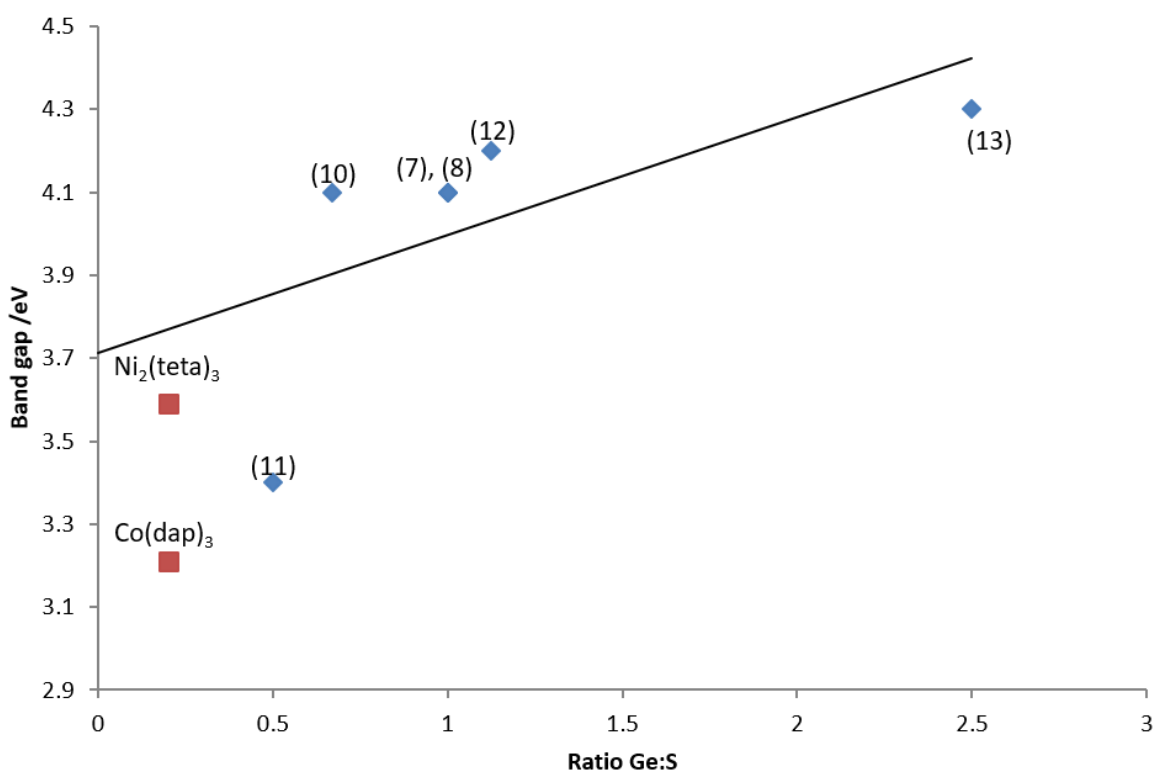
Figure 4.50: band gap energies for $[Ge_4O_{6-x}S_{4+x}]$ ($x = 0, 2, 4$) (**7**)-(**11**), $[Ge_9O_{14}S_8]$ (**12**) and $[Ge_5O_9(OH)_2S_2]$ (**13**) plotted against Ge:S ratios, comparing materials containing discrete Ge_4S_{10} clusters with similar complexes from literature values [106, 284] (red markers) versus the oxothiogermanate materials studied in this work (blue markers).

The work described in this chapter demonstrates that there are still ways of producing new interesting materials with novel building blocks. Solvothermal synthesis allows the use of a wide range of reagents, in different concentrations under different heating regimes which can

affect the outcome of a reaction. For example, compound **(13)** could only be prepared in the presence of water and antimony, even though the latter was not incorporated into the final crystalline product. In addition, the variation of sulfur concentration in the reaction mixture results in the formation of different discrete clusters. The increase in sulfur concentration within the cluster core also yields differences in thermal stability and optical properties. There is a decrease in optical band gap and thermal stability as the sulfur concentration increases, this is displayed both within the clusters (compounds **(8)**, **(10)** and **(11)**) and the oxothiogermanate materials as a whole. With further research, more oxothiogermanate materials could be produced and potentially be of higher dimensionality (2-D or 3-D structures) than those discovered so far.

Chapter 5: Transition-metal Sulfate Materials

5.1 Introduction

Solvothermal synthesis of sulfate containing transition-metal materials is a research area that holds great interest due to potential magnetic properties [285, 286], catalysts [287], medical use [288] and luminescent materials [289]. The initial organic templated sulfate structures were prepared at the turn of the century by Rao *et al.* [30] which quickly led to even more organically templated structures using sulfates and selenates [290]. Recently reported sulfate containing structures include those of new fluorine containing transition-metal sulfates [291], for example, the 2-D layered structure $[N_2C_6H_{16}]Mn_2F_2(SO_4)_2$ [292]. Other materials have been prepared by linking sulfate based units via organic units to form 3-D frameworks, *e.g.* $\{[M(thim_2)(SO_4)(H_2O)_2]_2 \cdot (thim_2) \cdot (H_2O)\}_n$ [M = Zn, Mn] (thim$_2$ = 2,5-bis(imidazol-1-yl)thiophene) [293]. These recent discoveries highlight that there is still much to uncover in this field, with considerable potential to generate new interesting structures.

This chapter describes structures produced using solvothermal reactions using transition-metal sulfates, organic templating reagents (amines), water and 18 M sulfuric acid acting as a secondary source of SO_4^{2-}. As described below many of the reaction products are moisture/air sensitive which made analysis and characterisation difficult. In many cases, analytical approaches were restricted by decomposition of the materials during crystal picking (the act of manually removing crystals from powder/mixed phases) while other materials could not be manipulated in air at all.

5.2 A Discrete Sulfate Cluster

5.2.1 $[Co(Hdeta)_2(SO_4)_2]$ (14)

5.2.1.1 Synthesis

Compound $[Co(Hdeta)_2(SO_4)_2]$ **(14)** was synthesised from a mixture of $CoSO_4.7H_2O$ (0.3449g 1.23 mmol), diethylenetriamine (deta) (0.22 ml, 2.04 mmol), 18 M H_2SO_4 (0.11 ml, 1.98 mmol) and H_2O (0.07 ml, 3.88 mmol). The reagent mixture was stirred for 10 min in a Teflon-lined stainless-steel autoclave before being sealed and heated to 453 K for 5 days using a heating rate of 1 K min $^{-1}$. The products were cooled overnight before being filtered and washed successively with ethanol and acetone inside an N_2 filled glove bag (suspected moisture sensitivity). Single crystals of **(14)** in the form of red blocks were the only solid products produced and their purity was confirmed from powder X-ray data (Figure 5.1).

Details of the powder X-ray experiment can be found in section 2.2.2. Combustion analysis gave values of C: 20.76 %, H: 6.75 %, N: 18.12 %, respectively which are in good agreement with the values calculated for the formula, $[Co(Hdeta)_2(SO_4)_2]$, (C: 21.00 %, H: 5.68 %, N: 18.37 %) established from the single-crystal X-ray diffraction data.
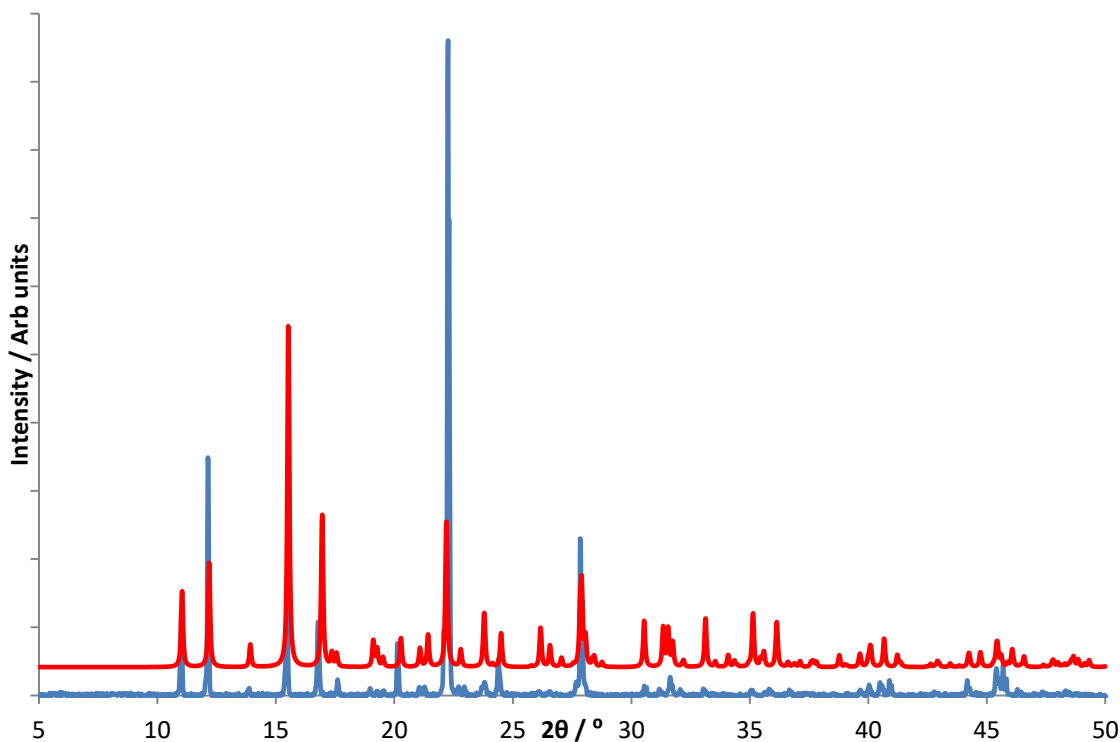
Figure 5.1: powder X-ray diffraction pattern of the bulk sample containing crystals of **(14)**, Key: blue, bulk sample: red, calculated pattern generated from single-crystal data.

Single-crystal X-ray diffraction experiments were conducted at 150 K using graphite monochromated MoK_α (λ = 0.71073 Å) radiation. The structure was solved using SIR92 [227] and the model refined using the CRYSTALS suite of programs [230]. The model was refined in *F* and a Chebychev polynomial weighting scheme was applied. Hydrogen atoms on the amine ligands were placed geometrically with a U[equiv] value 1.2 times the U[equiv] of the carbon to which they are attached. Crystallographic details are summarised in Table 5.1 and atomic coordinates of all non-hydrogen atoms can be found in Table A3.1.

Table 5.1: Crystallographic data for structure [Co(Hdeta)₂(SO₄)₂] **(14).**

Chemical formula	$[Co(Hdeta)_2(SO_4)_2]$
Formula mass	459.41
Crystal Habit	block
Crystal system	monoclinic
Symmetry space group	$P2_1/c$
Temp /K	150
a /Å	8.1118(3)
b /Å	10.4469(3)
c /Å	10.2073(4)
β /°	98.746(3)
V / Å³	854.94(5)
Z	2
μ /mm^{-1}	1.301
Total reflections ($I > 3\sigma(I)$)	2325
R factor	0.0292
wR factor	0.0375
Goodness of fit ref	1.0439

3.2.1.2 Structure Description and Analysis

The structure of compound **(14)** contains a crystallographically-distinct cobalt atom Co(1) which forms a pseudo-octahedral complex bonding to two bidentate deta molecules and two monodentate sulfate ions, Figure 5.2. The location of the two moieties around the complex have the deta molecules in the equatorial plane and sulfate ions in the axial positions trans to each other. The bond distances between the ligands and the cobalt metal centre are Co(1)-N(1) 2.1494(12) Å, Co(1)-N(2) 2.1496(11) Å and Co(1)-O(1) 2.2166(10) Å (Table 2), which are typical for amine based complexes [294, 295]. The octahedral geometry of the complex is slightly distorted, this is due to the rigidity of deta molecules in the equatorial plane, so the bite angle (torsion angle between the metal centre and amine) is smaller than the expected 90 ° angle. Consequently, the bite angles of bidentate ligands are therefore dependent on the metal-ligand bond lengths [260]. The internal bonding angle N(1)-Co(1)-N(2) is 81.98(4) ° while N(1)-Co(1)-N(2)* (* = symmetry equivalent site, -*x*+2; -*y*+1; -*z*+2) is 98.02(4) °, clearly displaying the strain associated with rigid multidentate ligands. An example of another cobalt complex that shows a similar feature due to multidentate ligands, is [Co(phen)(H₂O)₄](SO₄)·2(H₂O) [168], in which the phenanthroline N-Co-N angle is

177

77.20(8) ˚ instead of ~90 ˚. A selection of bond lengths and angles can be viewed in Table 5.2 and 5.3.
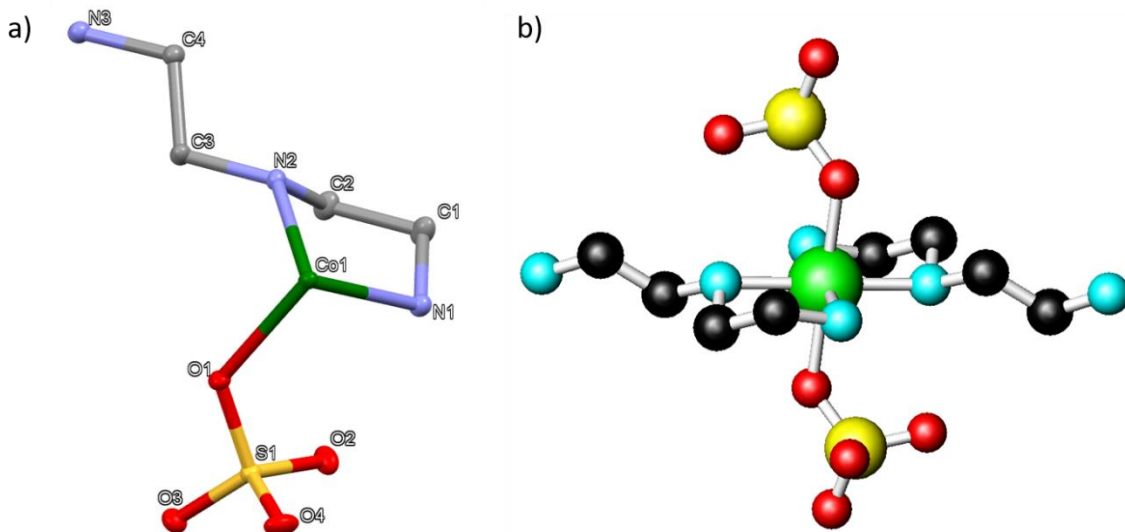
Figure 5.2: (a) Asymmetric unit of **(14)** displaying thermal ellipsoids of each atom at 50 % probability and (b) a full complex using a stick and ball model (right). Key: green: Co atoms, yellow: S atoms, red: O atoms, light blue: N atoms, grey/black: C atoms. Hydrogen atoms are omitted for clarity.

The bond valence sum for Co(1) produces a value of 2.18 (v.u.), thereby supporting the presence of a +2 oxidation state. The two SO_4^{2-} units produce a -4 charge but there is only one +2 charge from the cobalt, this leaves an imbalanced charge. This leads to the conclusion that the remaining (non-chelating) nitrogen of each deta molecule plays a charge balancing role and contains an additional proton supporting the formula $[Co(Hdeta)_2(SO_4)_2]$. The structure of **(14)** also contains acceptor-donor interactions confirming the presence of hydrogen bonding. Hydrogen bonding occurs (Table 5.4) between the sulfate oxygen atoms O(2, 3, 4) and the amine H-acceptor atoms, at distances in the range $(2.765(2) \leq d/\text{Å} \leq 3.340(2))$. In addition, a weak interaction is also observed between C(4)…O(3). The packing can be viewed in Figure 5.3, showing a constant preference for the branched amine to be near sulfate ions to reduce steric clashing of amine groups.

Table 5.2 Non-hydrogen bond lengths in $[Co(Hdeta)_2(SO_4)_2]$ **(14)** including bond valence sums.

symmetry codes: *a = -x+2; -y+1; -z+2*

	Length /Å	v_{ij}		Length /Å		Length /Å
Co(1)-O(1)[a]	2.2166(10)	0.24	O(1)-S(1)	1.5065(10)	C(2)-N(2)	1.4784(18)
Co(1)-N(2)[a]	2.1496(11)	0.43	S(1)-O(4)	1.4760(11)	C(3)-N(4)	1.5283(19)
Co(1)-N(1)[a]	2.1494(12)	0.43	S(1)-O(3)	1.4755(11)	C(4)-N(3)	1.4894(18)
Co(1)-O(1)	2.2166(10)	0.36	S(1)-O(2)	1.4796(11)		
Co(1)-N(1)	2.1494(12)	0.29	N(1)-C(1)	1.4832(18)		
Co(1)-N(2)	2.1496(11)	0.43	C(1)-C(2)	1.517(2)		
	$\sum v_{ij}=$	**2.18**				

Table 5.3 Selection of bond angles in $[Co(Hdeta)_2(SO_4)_2]$ **(14).**

symmetry codes: *a = -x+2; -y+1; -z+2*

	Angle / °		Angle / °		Angle / °
O(1)[a]-Co(1)-N(2)[a]	90.26(4)	N(1)[a]-Co(1)-N(1)	179.995	O(1)-S(1)-O(4)	108.65(6)
O(1)[a]-Co(1)-N(1)[a]	93.10(4)	O(1)-Co(1)-N(1)	93.10(4)	O(1)-S(1)-O(3)	109.09(6)
N(2)[a]-Co(1)-N(1)[a]	81.98(4)	O(1)[a]-Co(1)-N(2)	89.74(4)	O(4)-S(1)-O(3)	109.60(7)
O(1)[a]-Co(1)-O(1)	179.995	N(2)[a]-Co(1)-N(2)	179.995	O(1)-S(1)-O(2)	108.17(6)
N(2)[a]-Co(1)-O(1)	89.74(4)	N(1)[a]-Co(1)-N(2)	98.02(4)	O(4)-S(1)-O(2)	110.91(7)
N(1)[a]-Co(1)-O(1)	86.90(4)	O(1)-Co(1)-N(2)	90.26(4)	O(3)-S(1)-O(2)	110.38(6)
O(1)[a]-Co(1)-N(1)	86.90(4)	N(1)-Co(1)-N(2)	81.98(4)		
N(2)[a]-Co(1)-N(1)	98.02(4)	Co(1)-O(1)-S(1)	123.82(6)		

Table 5.4 Bond lengths found in **(14)** between acceptor and donor atoms containing hydrogen bonding .

symmetry codes: *a = -x+2, y+1/2, -z+3/2, b = -x+2, -y+1, -z+2, c = -x+1, -y+1, -z+2, d = x, y, z+1, e = x, -y+1/2, z+1/2*

	Length /Å		Length /Å
N(1)…O(4)[a]	3.340(2)	N(3)…O(4)[d]	3.122(2)
N(1)…O(2)	2.888(2)	N(3)…O(3)[d]	2.922(2)
N(2)…O(4)[b]	2.902(2)	N(3)…O(1)[e]	2.891(2)
C(4)…O(3)[c]	3.335(2)	N(3)…O(2)[c]	2.765(2)

Figure 5.3: (a) The crystal packing of **(14)** viewed along [100] and (b) [001]. Key: green: Co atoms, yellow: S atoms, red: O atoms, light blue: N atoms, black: C atoms. Hydrogen atoms are omitted for clarity.

Thermogravimetric analysis of **(14)** (Figure 5.4) displays a total weight loss of 46.93 % at 320 ˚C which occurs in a single step. This value is close to the combustion data (45.63 % total) and the calculated organic component using the formula generated from single-crystal data (45.05 % total). The discrepancy is suspected to be caused by the moisture sensitivity of the sample.
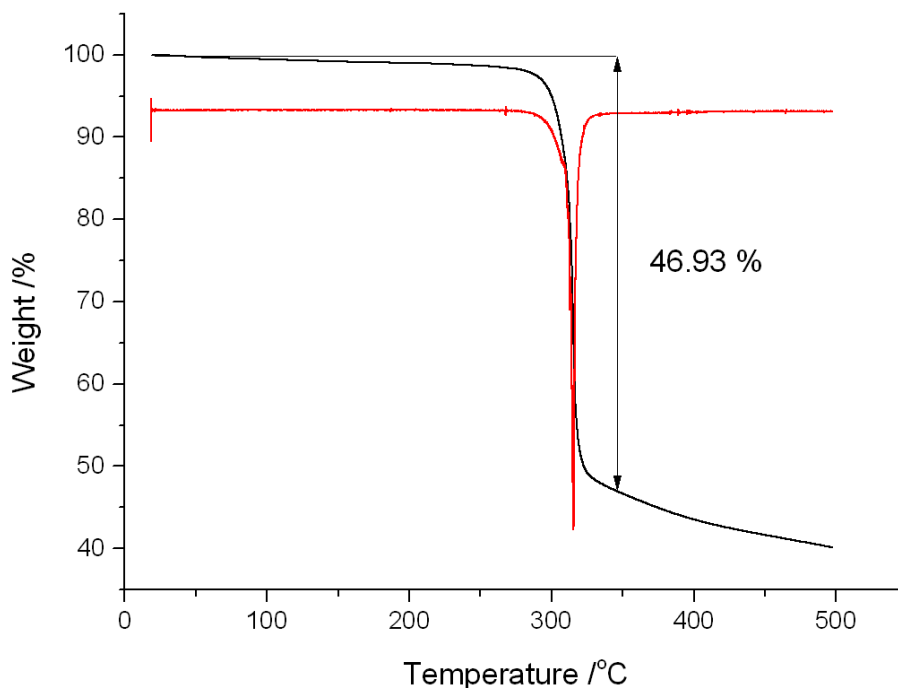
Figure 5.4: Thermogravimetric analysis curve of $[Co(Hdeta)_2(SO_4)_2]$ **(14)** heated under N_2 (black) and the corresponding derivative (DTG) curve (red).

180

The diffuse reflectance spectrum of **(14)** (Figure 5.5) leads to a measured band gap of 4.5(2) eV. The peak at 4 eV is likely to be a charge transfer peak and the two peaks below 3 eV were assigned Co(II) *d-d* interactions from ${}^4T_{1g}(F){\rightarrow}{}^4A_{2g}$ and ${}^4T_{1g}(F){\rightarrow}{}^4T_{2g}(P)$ transitions [296, 277]. The ${}^4T_{1g}(F){\rightarrow}{}^4T_{2g}$ transition is not visible at these energy levels and are beyond the range of the equipment used. Other publications have observed the *d-d* transition metal peaks around this ~1.5-3 eV energy level [297].

Infra-red (IR) data of **(14)** (Figure 5.6) shows the presence of monodentate SO_4^{2-} ligands, symmetric bending $\delta(S-O_4)$ and asymmetric stretching vibrational modes $\nu(S-O_4)$ are split into two bands at 580, 621 and 1043, 1099 cm^{-1} respectively. This splitting is due to lowering the symmetry of the SO_4^{2-} ion, from T_d to C_{3v}, if it were not bound to the complex, it would otherwise be observed as single peak absorption [298]. There is also an additional peak at 970 cm^{-1} which was assigned the $\nu(S-O_4)$ symmetric vibrational mode [299]. The presence of amine can also be seen in the spectrum and has been tentatively assigned [279], see Table 5.5.
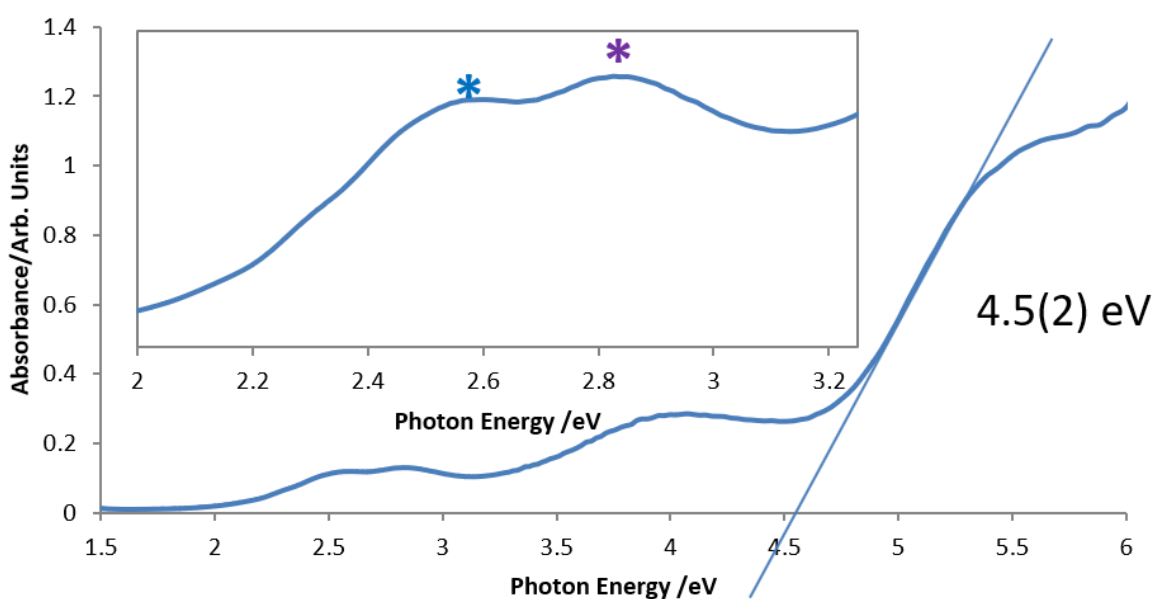
Figure 5.5: Diffuse reflectance spectrum of $[Co(Hdeta)_2(SO_4)_2]$ **(14)** showing a band gap of 4.5(2) eV. Asterisks denote *d-d* transitions ${}^4T_{1g}(F){\rightarrow}{}^4A_{2g}$ (blue) and ${}^4T_{1g}(F){\rightarrow}{}^4T_{2g}(P)$ (purple).
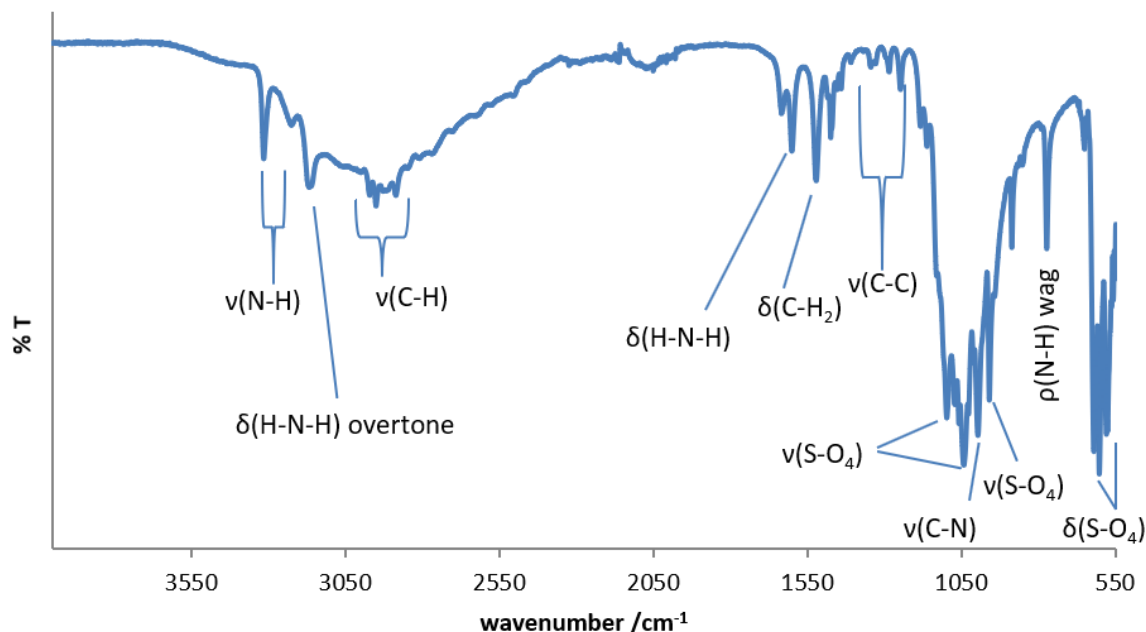
Figure 5.6: IR spectrum of [Co(Hdeta)$_2$(SO$_4$)$_2$] (**14**).

Table 5.5: Infrared spectrum assignments of [Co(Hdeta)$_2$(SO$_4$)$_2$] (**14**)

Stretching mode	Wavenumber /cm^{-1}
ν(N-H)	3226 (sym) and 3314 (asym)
ν(C-H)	2885-2968 (multiple peaks)
δ(H-N-H)	1600 (3167 overtone)
δ(C-H$_2$)	1523
ν(C-C)	1248-1343 (multiple peaks)
ν(S-O$_4$) (asym)	1043 and 1099
ν(C-N)	997
ν(S-O$_4$) (sym)	970
ρ(N-H) (wag)	774
δ(S-O$_4$)	580 and 621

While the oxidation state of Co(1) was assigned as +2 *via* valence calculations, there was still some ambiguity as to the spin state of the metal centre so magnetic susceptibility experiments were conducted (Table 5.6). The plot of reciprocal molar susceptibility as a function of temperature (Figure 5.7) exhibits a slight curvature below 80 K so the Curie-Weiss expression used in calculations was fitted to the section above 80 K. The inverse χ data of (**14**) produce a μ_{eff} of 4.4 μ_B. The spin-only moment for an octahedral high spin Co(II) d^7 cation is μ_{so} = 3.87 μ_B using the spin only equation (see section 2.2.8). If orbital contributions are also considered, this would raise the theoretical value which would then agree more favourably

182

with the experimentally obtained value of 4.4 μ_B. The Co(II) d_7 high spin ion contains one half filled orbital to allow orbital contributions to occur, this produces incomplete quenching and allows the electrons to have some orbital contribution that adds to the measured μ_{eff} value. Other such Co(II) high spin complexes have been reported with such orbital contributions, [CoCl$_2$(urotrop)$_2$] (urotrop = hexamethylenetetramine) and [Co(SCN)$_2$(pyCH$_2$OH)$_2$] (pyCH$_2$OH$_2$ = 2-hydroxypropylpyridine) [300], for example, have measured μ_{eff} values of 4.45 and 4.28 μ_B, respectively. Compound **(14)** also exhibits very minor antiferromagnetic contributions which can be seen in the inverse χ plot which has a negative theta value of -15 K. This value is not particularly large and implies weak near-neighbour interactions. The magnetisation as a function of magnetic field, Figure 5.8, shows a slight hysteresis and suggests the presence of a spontaneous magnetisation at low temperatures. This, coupled with the negative Weiss constant, suggests that a canted antiferomagnetic state may form at low temperatures. It also hints at a minor ferromagnetic behaviour through the presence of a hysteresis loop at 5 K. The saturated experimentally observed μ_{eff} value was extrapolated to give a μ_{sat} of 2.2 μ_B which is lower than what is expected if it were a ferromagnet. As this is only a weak component caused by the canting of the moments (thus appearing as if a net magnetic moment is present), this is to be expected for such a residual spontaneous magnetisation at low temperature. It is possible that **(14)** is an antiferromagnetic material with weak ferromagnetic contributions caused by canting of the moments.

Table 5.6: Magnetic data for structure [Co(Hdeta)$_2$(SO$_4$)$_2$] **(14).**

Range 80 $\leq$ T/K $\leq$ 300	C / emu mol^{-1} Oe^{-1}	Θ / K	μ_{eff} / μ_B
	2.43	-15	4.40
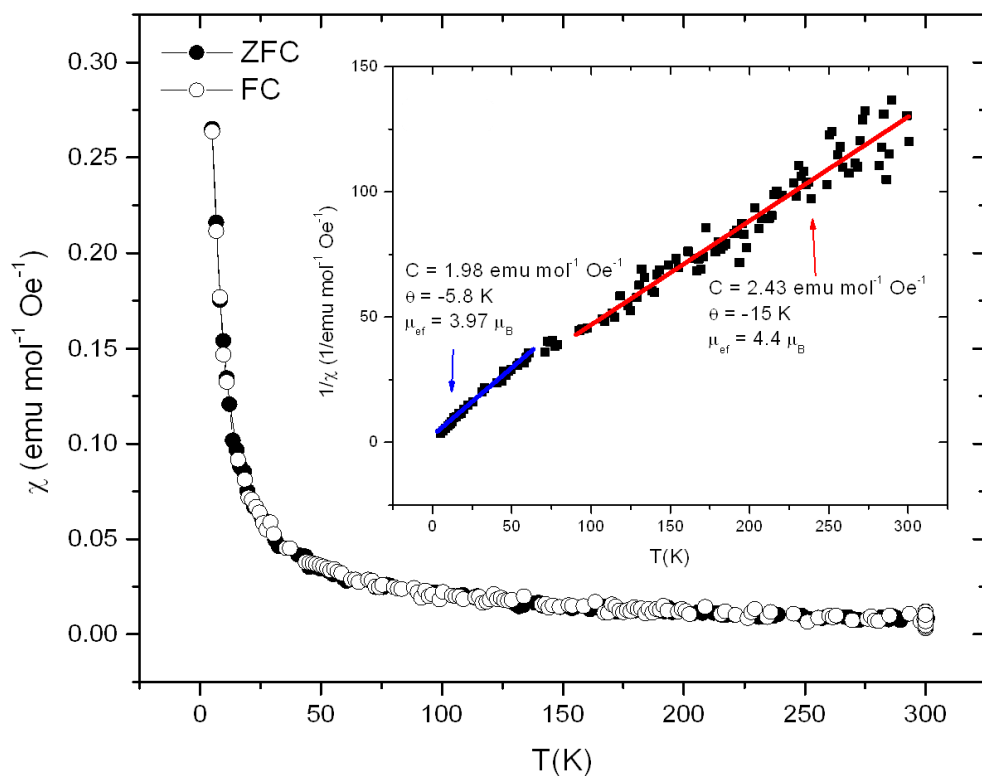
Figure 5.7: Field-cooled magnetic susceptibility and inverse magnetic susceptibility data for [Co(Hdeta)$_2$(SO$_4$)$_2$] **(14)**.
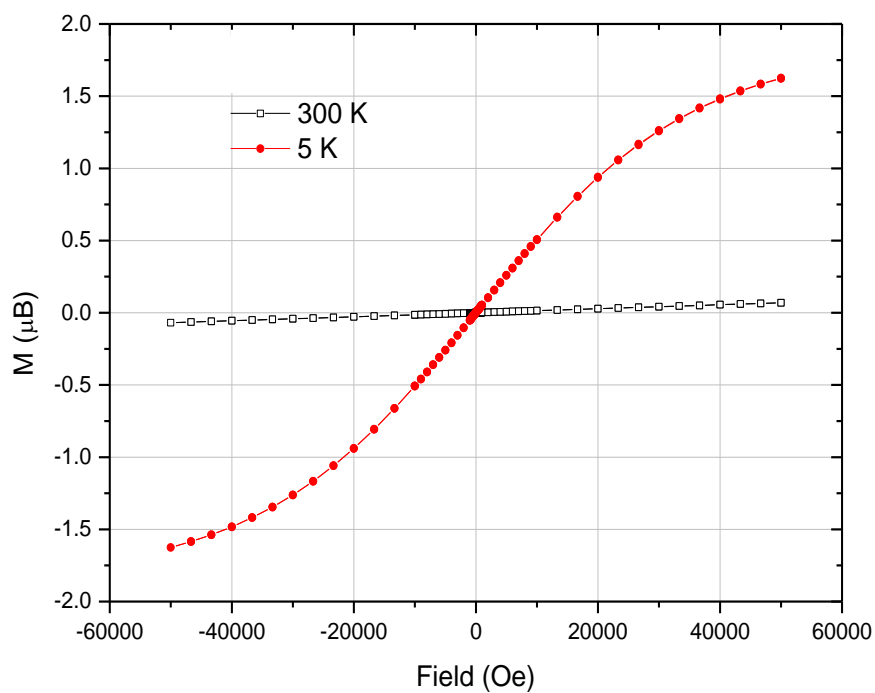
Figure 5.8: Magnetisation versus magnetic field plot of [Co(Hdeta)$_2$(SO$_4$)$_2$] **(14)**.

5.3 1-Dimensional Sulfate Structures
5.3.1 (H$_2$4,4'-bipy)[Co(H$_2$O)$_2$(4,4'-bipy)(SO$_4$)$_2$].H$_2$O (15)
5.3.1.1 Synthesis

Compound (H$_2$4,4'-bipy)[Co(H$_2$O)$_2$(4,4'-bipy)(SO$_4$)$_2$]·H$_2$O **(15)** was synthesised from a mixture of CoSO$_4$.7H$_2$O (0.350g 1.25 mmol), 4,4'-bipyridine (bipy) (0.204 g, 1.31 mmol), 18 M H$_2$SO$_4$ (0.2 ml, 3.6 mmol) and H$_2$O (0.05 ml, 2.77 mmol). The reagent mixture was stirred for 10 min in a Teflon-lined stainless-steel autoclave before being sealed and heated to 433 K for 8 days using a heating rate of 1 K min $^{-1}$. The products were cooled overnight before being filtered and washed successively with ethanol and acetone inside a nitrogen- filled glove bag. The bulk product of the reaction contained red blocks of **(15)**, colourless crystals and brown powder. Powder X-ray analysis of the bulk sample (Figure 5.9) confirms the presence of **(15)**, whilst also identifying the colourless crystals as [H$_2$4,4'-bipy](HSO$_4$)$_2$ [166] and the powder as Co$_3$S$_4$ along with an unidentified phase. Details of the powder X-ray experiment can be found in section 2.2.2. Combustion analysis gave values of C: 23.31 %, H: 4.47 %, N: 9.19 %, respectively. These are in poor agreement with the values calculated for the crystallographically-determined formula, (H$_2$4,4'-bipy)[Co(H$_2$O)$_2$(4,4'-bipy)(SO$_4$)$_2$].H$_2$O, (C: 38.74 %, H: 3.87 %, N: 9.03. %). This is likely to be due to difficulties encountered in cleanly picking crystals for analysis from the bulk product.

Single-crystal X-ray diffraction data were collected at 150 K using graphite monochromated MoK$_\alpha$ (λ = 0.71073 Å) radiation. The structure was solved using SIR92 [227] and the model refined using the CRYSTALS suite of programs [230]. The model was refined in *F* and a Chebychev polynomial weighting scheme were applied. The Platon Addsym routine [301] suggested that there was a missing translational symmetry element but it could not provide an alternative space group. Attempting to solve the structure in any other space group other than P-1 was unsuccessful. Hydrogen atoms on the amine ligands were placed geometrically with a U[equiv] value 1.2 times the U[equiv] of the carbon to which they are attached. Crystallographic details are summarised in Table 5.7 and Atomic coordinates of all non-hydrogen atoms can be found in Tables A3.2.
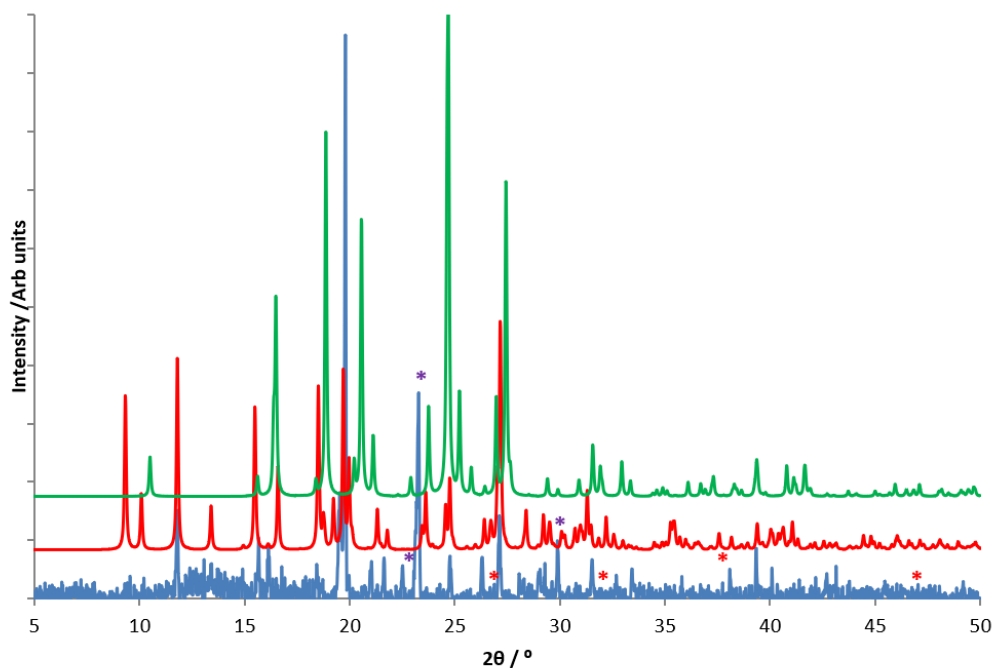
Figure 5.9: Powder X-ray diffraction pattern of **(15)**, Key: blue, bulk sample: red, calculated pattern generated from single-crystal data, green, [$H_2$4,4'-bipy](HSO_4)$_2$ [166], red asterisks, Co_3S_4, purple asterisks, unidentifiable phase.

Table 5.7: Crystallographic data for structure ($H_2$4,4'-bipy)[Co(H_2O)$_2$(4,4'-bipy)(SO_4)$_2$]·H_2O **(15)**.

Chemical formula	($H_2$4,4'-bipy)[Co(H_2O)$_2$(4,4'-bipy)(SO_4)$_2$]·H_2O
Formula mass	619.48
Crystal Habit	block
Crystal system	Triclinic
Symmetry space group	$P\bar{1}$
Temp /K	150
a /Å	9.3248(8)
b /Å	9.8459(9)
c /Å	13.5637(11)
α/ °	84.728(7)
β /°	76.496(7)
γ /°	73.880(7)
V /Å³	1162.78(10)
Z	2
μ /mm^{-1}	0.990
Total reflections (I >3σ(I))	5069
R factor	0.0597
wR factor	0.0121
Goodness of fit ref	1.1689

5.3.1.2 Structure Description and Analysis

The structure of **(15)** contains two crystallographically-distinct cobalt atoms, Co(1) and Co(2) (Figure 5.10). Each is coordinated by two water molecules, two monodentate SO_4^{2-} ligands and one nitrogen atom from each of two 4,4'-bipy ligands, producing a pseudo-octahedral geometry around each cobalt centre. The bipy ligands acts as linkers with the second nitrogen atom in each ligand being coordinated to a neighbouring cobalt atom. The nitrogen atoms from the two bipy ligands are trans to one another, leading to the formation of a linear one-dimensional chains directed along the [110] direction (Figure 5.11 bottom). Free 4,4'-bipy molecules and water molecules are located between the chains.
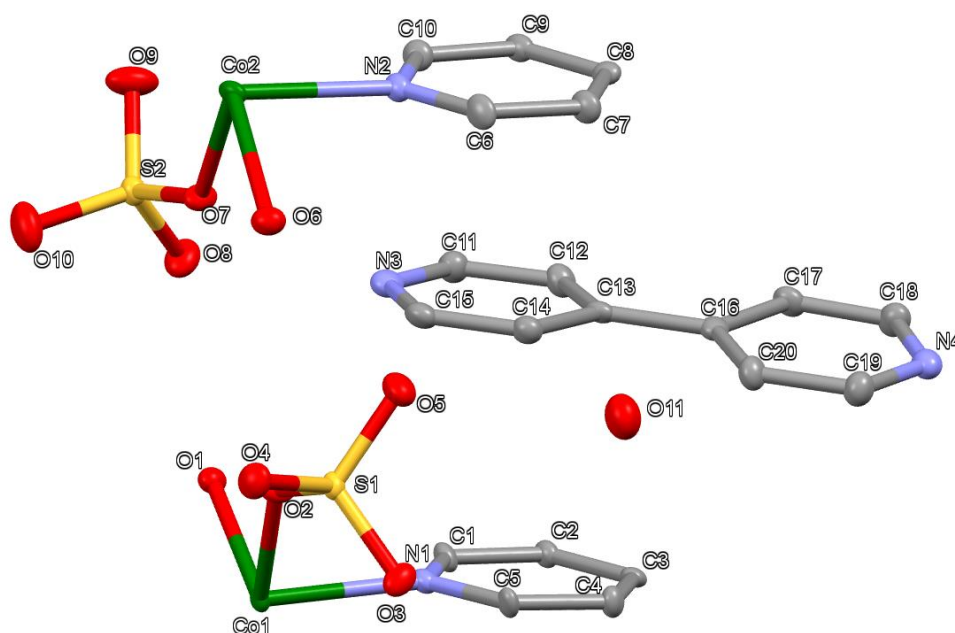
Figure 5.10: Asymmetric unit of **(15)** displaying thermal ellipsoids of each atom at 50 % probability. Key: green: Co atoms, yellow: S atoms, red: O atoms, light blue: N atoms, grey: C atoms. Hydrogen atoms are omitted for clarity.

The free 4,4'-bipy molecules however, are in positions between the 4,4'-bipy ligands, with distances (*d*) between free and coordinated 4,4'-bipy molecules lying in the range ($3.403(3) \leq d/\text{Å} \leq 3.977(3)$). These distances appear to within the range for π-π stacking interactions and are comparable to the π-π stacking distances seen in [Ag_2(N,N'-4,4'-bipy)$_2$(bpds)] (bpds = 4,4'-biphenyldisulfonate) [302].

Other bipy containing cobalt sulfate chains reported in the literature include; [Co(H$_2$O)$_4$(4,4'-bipy)](4,4'-bipyH$_2$)·2(SO$_4$)·2H$_2$O,   [Co(H$_2$O)$_3$(SO$_4$)(4,4'-bipy)$_2$]$_2$,

Co(H$_2$O)$_4$Co(H$_2$O)$_2$(SO$_4$)$_2$·8H$_2$O,

[Co(H$_2$O)$_6$][Co(SO$_4$)(C$_{10}$H$_8$N$_2$)(H$_2$O)$_3$][Co(SO$_4$)$_2$(C$_{10}$H$_8$N$_2$)(H$_2$O)$_2$] [303] and Co(SO$_4$)(H$_2$O)$_3$(4,4'-bipy)·2H$_2$O [187]. One structure, [Co(H$_2$O)$_4$(4,4'-bipy)](4,4'-bipyH$_2$)·2(SO$_4$)·2H$_2$O [303], contains 1-D chains of [Co(H$_2$O)$_4$(4,4'-bipy)] with free 4,4'-bipy molecules located between chains in a similar motif to (15). The free bipy molecules do not align with the chain itself and are slightly rotated within the plane towards [010], this is the same rotation seen in (15) (Figure 5.11 top). The nitrogen positions on the free 4,4'-bipy of the literature structure are protonated and interact with an oxygen site of a free sulfate anion.

The Co-N distances (Table 5.8) show a slight increase 2.1998(17) Å and 2.1966(18) Å compared to those in (14) to bonds, while the Co-O distances (average of 2.11 Å) are decreased. Overall, very little distortion of the octahedral geometry is seen, especially as the positions of symmetry equivalent N and O atoms bonding to the Co metal centres produce similar bond lengths, as seen in Table 5.8. The torsion angles, α, within each Co centre are a lot less strained when compared to the complex of structure (14). Here, angles vary between ($88.33 \leq \alpha/° \leq 91.67$) resulting in a closer approach to octahedral geometry as there are no bidentate ligands to distort bond angles, Table 5.9.

Bond-valence sums produce values of 2.04 and 2.08 for Co(1) and Co(2) respectively, which are consistent with the presence of cobalt in the +2 formal oxidation state. This leads to the conclusion that [Co(H$_2$O)$_2$(4,4'-bipy)(SO$_4$)$_2$] has a double negative charge. Charge-balancing requirements imply that the non-coordinated 4,4',-bipy molecule is therefore doubly protonated. The distances between the protonated nitrogen atoms of the free bipy and the oxygen atoms of neighbouring sulfate anions are N(3)…O(8) and N(4)…O(4), are 2.617(3) Å and 2.563(3) Å respectively, suggesting the presence of hydrogen-bonding interactions, which aid the packing of chains shown in Figure 5.12. The chains stack atop each other along [001] with the neighbouring chains being staggered in the [110] direction so neighbouring sulfate ions do not clash. Other donor-acceptor interactions within structure (15) show that the chains are linked via an interaction between water O(11) with O(10) and O(5) being 2.828(3) Å and 2.856(3) Å in length respectively, supporting the presence of hydrogen bonding. Additional donor-acceptor interactions can be found in Table 5.10.

Table 5.8 A selection of bond lengths in $(H_24,4'\text{-bipy})[Co(H_2O)_2(4,4'\text{-bipy})(SO_4)_2]\cdot H_2O$ **(15)** and bond valence sums.

symmetry codes: *a = -x+2; -y; -z+1, b = -x+2; -y; -z+2*

	Length /Å	v_{ij}		Length /Å	v_{ij}		Length /Å
Co(1)-N(1)[a]	2.1966(18)	0.38	Co(2)-N(2)[b]	2.1998(17)	0.38	S(1)-O(2)	1.4852(16)
Co(1)-O(1)[a]	2.1357(16)	0.30	Co(2)-O(6)[b]	2.0994(18)	0.33	S(1)-O(3)	1.4621(16)
Co(1)-O(2)[a]	2.0919(15)	0.34	Co(2)-O(7)[b]	2.0989(16)	0.33	S(1)-O(4)	1.4791(16)
Co(1)-O(1)	2.1357(16)	0.30	Co(2)-O(6)	2.0994(18)	0.33	S(1)-O(5)	1.4713(19)
Co(1)-O(2)	2.0919(15)	0.34	Co(2)-O(7)	2.0989(16)	0.33	S(2)-O(7)	1.4856(17)
Co(1)-N(1)	2.1966(18)	0.38	Co(2)-N(2)	2.1998(17)	0.38	S(2)-O(8)	1.4679(17)
	$\sum v_{ij}=$	**2.04**		$\sum v_{ij}=$	**2.08**		

Table 5.9 A selection of bond angles in $(H_24,4'\text{-bipy})[Co(H_2O)_2(4,4'\text{-bipy})(SO_4)_2]\cdot H_2O$ **(15).**

symmetry codes: a = -x+2; -y; -z+1, b = -x+2; -y; -z+2

	Angle / °		Angle / °		Angle / °
N(1)[a]-Co(1)-O(1)[a]	89.93(7)	N(1)[a]-Co(1)-N(1)	179.995	O(7)[b]-Co(2)-O(6)	90.09(7)
N(1)[a]-Co(1)-O(2)[a]	93.42(7)	O(1)[a]-Co(1)-N(1)	90.07(7)	N(2)[b]-Co(2)-O(7)	91.68(7)
O(1)[a]-Co(1)-O(2)[a]	92.61(6)	O(2)[a]-Co(1)-N(1)	86.58(7)	O(6)[b]-Co(2)-O(7)	90.09(7)
N(1)[a]-Co(1)-O(1)	90.07(7)	O(1)-Co(1)-N(1)	89.93(7)	O(7)[b]-Co(2)-O(7)	179.995
O(1)[a]-Co(1)-O(1)	179.995	O(2)-Co(1)-N(1)	93.42(7)	O(6)-Co(2)-O(7)	89.91(7)
O(2)[a]-Co(1)-O(1)	87.39(6)	N(2)[b]-Co(2)-O(6)[b]	90.20(7)	N(2)[b]-Co(2)-N(2)	179.995
N(1)[a]-Co(1)-O(2)	86.58(7)	N(2)[b]-Co(2)-O(7)[b]	88.32(7)	O(6)[b]-Co(2)-N(2)	89.80(7)
O(1)[a]-Co(1)-O(2)	87.39(6)	O(6)[b]-Co(2)-O(7)[b]	89.91(7)	O(7)[b]-Co(2)-N(2)	91.68(7)
O(2)[a]-Co(1)-O(2)	179.995	N(2)[b]-Co(2)-O(6)	89.80(7)	O(6)-Co(2)-N(2)	90.20(7)
O(1)-Co(1)-O(2)	92.61(6)	O(6)[b]-Co(2)-O(6)	179.995	O(7)-Co(2)-N(2)	88.32(7)

Table 5.10 Bond lengths found in **(15)** between acceptor and donor atoms containing hydrogen bonding. *symmetry codes: a = -x+2, -y, -z+1; b = x-1, y, z; c = -x+2, y+1, z+1; d = x-1, y+1, z; e = x, y+1, z; f = -x+1, y, z+2*

	length /Å		length /Å		length /Å
O(1)-O(3)[a]	2.669(3)	O(6)-O(5)	2.755(3)	C(17)-O(10)[d]	3.082(3)
C(2)-O(3)[b]	3.539(3)	C(7)-O(9)[e]	3.465(3)	C(19)-O(1)[e]	3.493(3)
N(3)-O(8)	2.617(3)	C(9)-O(9)[f]	3.237(3)	C(20)-O(11)	3.183(3)
C(4)-O(3)[c]	3.300(3)	O(11)-O(5)	2.856(3)	C(11)-O(6)[b]	3.416(3)
N(4)-O(4)[d]	2.563(3)	C(14)-O(11)	3.457(3)		
C(5)-O(3)	3.238(3)	C(15)-O(5)	3.248(3)		
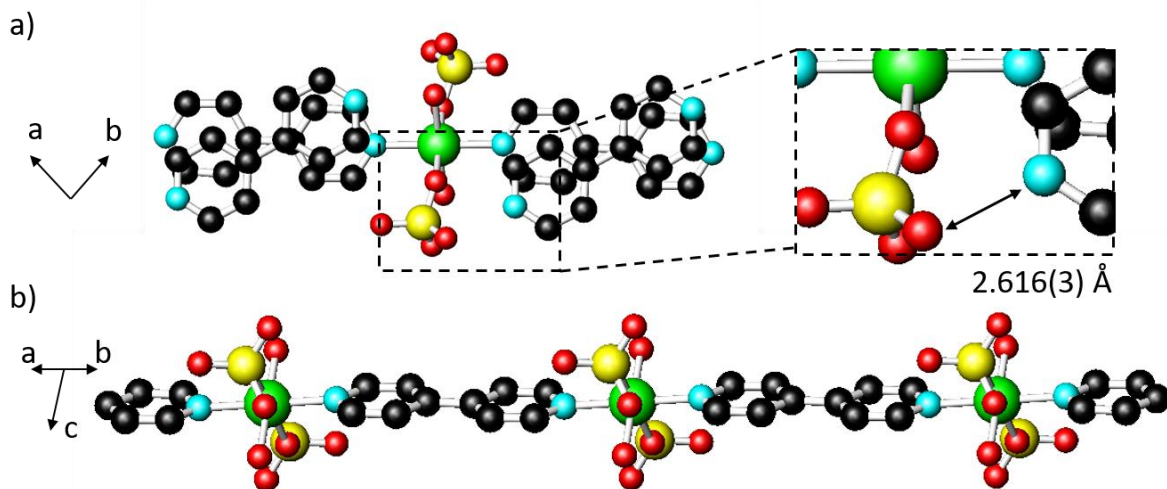
Figure 5.11: (a) Ball and stick diagrams of structure **(15)** highlighting the hydrogen bonding interactions between the free 4,4'-bipy and the sulfate oxygen atom. (b) A single chain of $[Co(H_2O)_2(4,4'-bipy)(SO_4)_2]^{2-}$ in **(15)**. Key: green: Co atoms, yellow: S atoms, red: O atoms, light blue: N atoms, grey: C atoms. Hydrogen atoms are omitted for clarity.
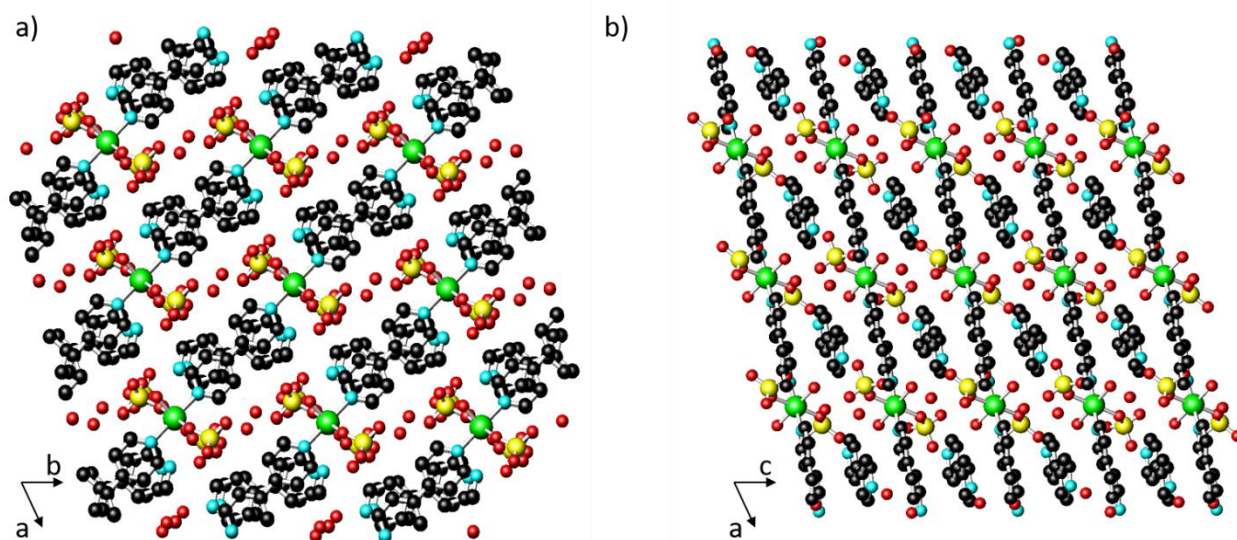
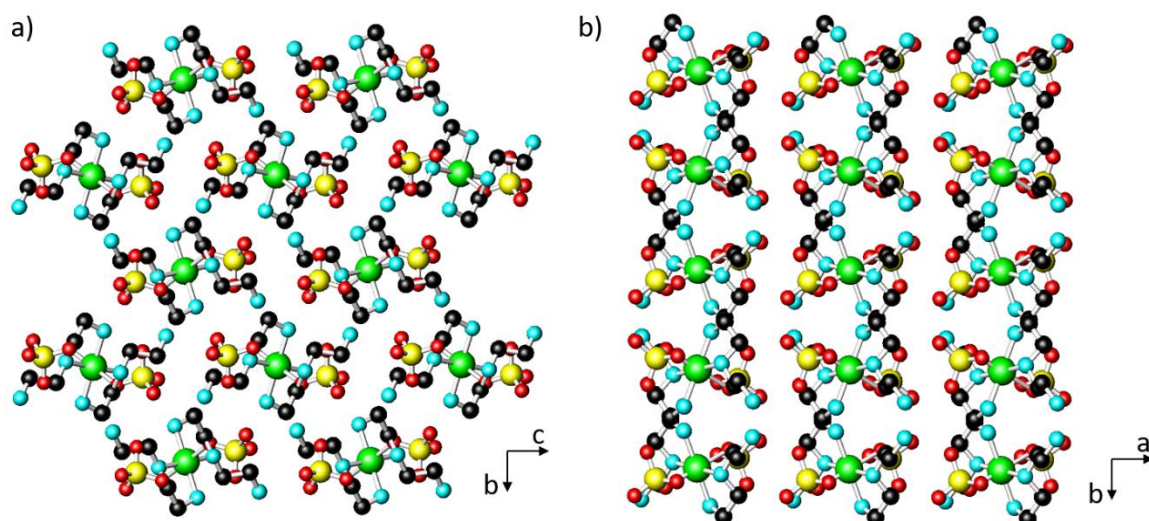Figure 5.12: (a) The crystal packing of **(15)** viewed along [001] and (b) [010]. Key: green: Co atoms, yellow: S atoms, red: O atoms, light blue: N atoms, black: C atoms. Hydrogen atoms are omitted for clarity.

Thermogravimetric analysis (TGA) of **(15)** indicates a complicated breakdown pathway of the material (Figure 5.13). There is an initial three-step weight loss which is assignable to loss of

water molecules. The first loss of 5.47 %, which occurs in the range 75 – 95 °C, is associated with absorbed water on the surface of the crystals. A second weight loss of 4.17 % follows and may be assigned to the free water in the pore space of (15). The third weight loss of 4.20 % (onset ~125 °C) may then be assigned to the water molecules coordinated to the cobalt-metal centres. The crystallographically-determined formula indicates that the pore and ligand water molecules should result in weight losses of 2.9 % and 5.8 % respectively. The experimental results appear to indicate one more pore water molecule than is suggested by the structure solution. The largest weight loss of 53.4 % (with an onset temperature of ~195 ° C), can then be assigned to the removal of the 4,4'-bipy molecules (51.1 % calculated). The final weight change step (onset ~400 °C) corresponds to the decomposition of sulfate anions. However, the weight loss suggests only ~ 2/3 of the sulfate ions originally present in (15) are removed. Although it was not possible to identify the nature of the final decomposition product by powder X-ray diffraction, due to the small amount of sample remaining, the product of TGA was analysed by infra-red spectroscopy.

IR data were recorded before and after the thermogravimetric measurement (Figure 5.14) and the assignments of vibrations can be found in Table 5.11. The crystals before TGA measurements contained: a large υ(O-H) stretch associated with H_2O at 3300 cm^{-1} (which may also be hiding a weak ν(N-H) stretch), (C-H) symmetric and asymmetric stretches between 3000-3100 cm^{-1}, δ(H-O-H) band at 1630 cm^{-1}, C=C arene stretching 1380-1530 cm^{-1}, ν(N-H) wag of the free protonated bipy molecule at 808 cm^{-1}, δ(S-O$_4$) bend and ν(S-O$_4$) asymmetric vibration modes are split into two bands at 603, 709 cm^{-1} and 970, 1064 cm^{-1} respectively (as seen with structure (14)). The only other observable ν(S-O$_4$) mode in a C_{3v} monodentate environment is the peak at 905 cm^{-1} for a symmetric stretch [299]. After the TGA measurement, all peaks associated with the amine and water disappeared, while SO_4^{2-} stretching modes were still evident, consistent with the TGA data which suggest that only 2/3 of the SO_4^{2-} is removed.

The Uv-vis diffuse reflectance data for (15) (Figure 5.15) yield a band gap of 3.8(3) eV, with a broad peak (potentially two peaks) at 2.5 eV similar to that of (14). This was assigned to two Co(II) d-d transitions $^4T_{1g}(F) \rightarrow {}^4A_{2g}$ and $^4T_{1g}(F) \rightarrow {}^4T_{2g}(P)$, as seen previously. Additional features seen can be compared to those seen in the chain structure [Co(H$_2$O)$_4$(4,4'-bipy)] [303], which shows peaks at 42,500 cm^{-1} (5.26 eV) and a shoulder at 37,200 cm^{-1} (4.61 eV). The first peak is in good agreement with the peak observed in the parent compound, (15), at

5.2 eV. The shoulder is not seen in the spectrum of **(15)**. In [303], These features were described as arising from π-π* interactions of the 4,4'-bipy molecules which is probably the same case here.
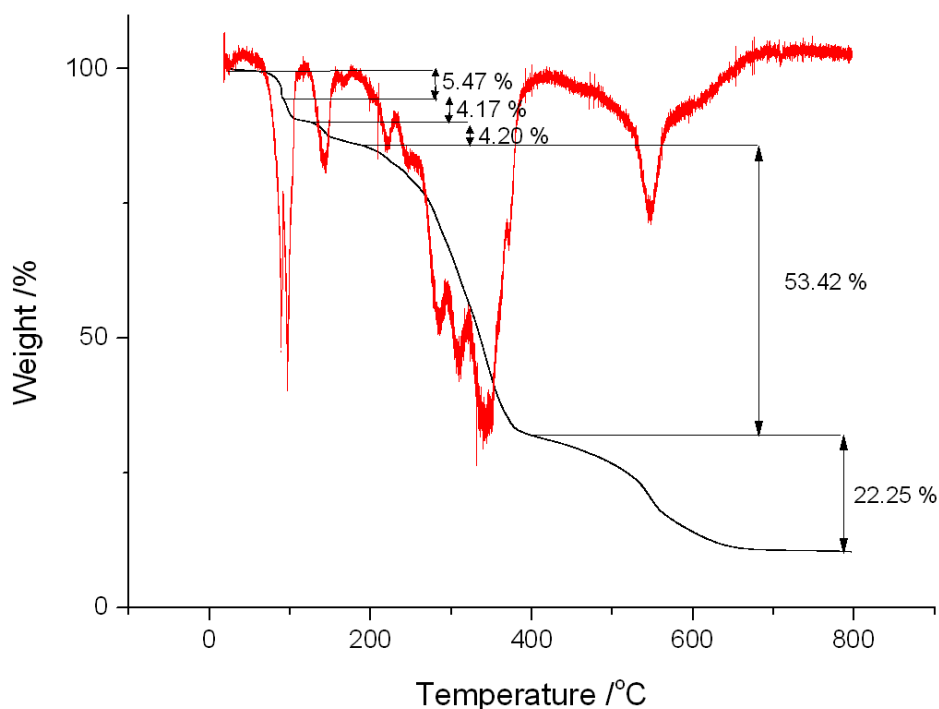
Figure 5.13: Thermogravimetric analysis curve of (H$_2$4,4'-bipy)[Co(H$_2$O)$_2$(4,4'-bipy)(SO$_4$)$_2$]·H$_2$O heated under N$_2$ (black) and the corresponding derivative (DTG) curve (red).
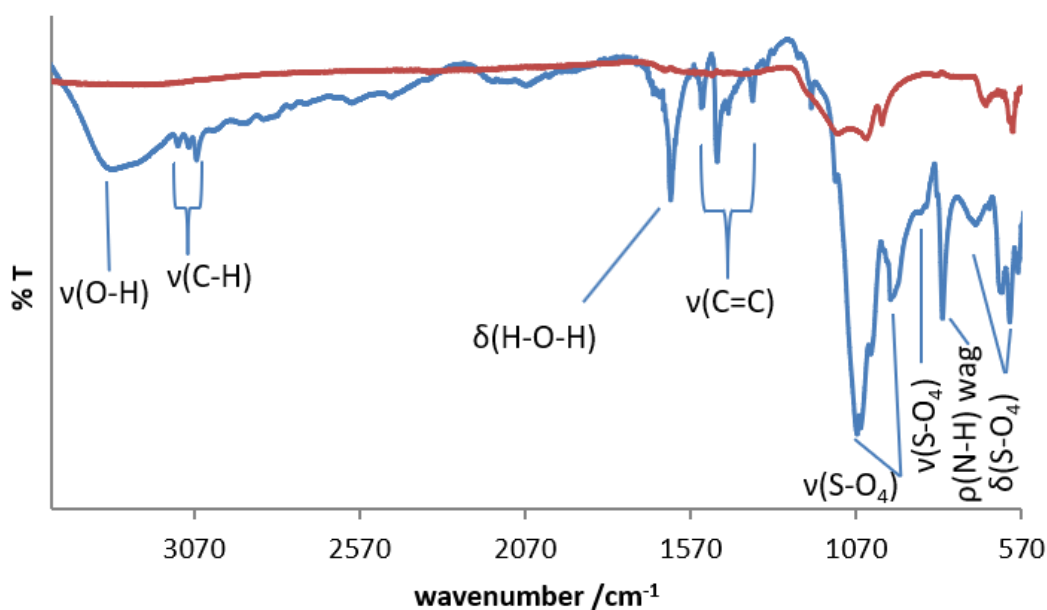
Figure 5.14: IR spectrum of (H$_2$4,4'-bipy)[Co(H$_2$O)$_2$(4,4'-bipy)(SO$_4$)$_2$]·H$_2$O before (blue) and after (red) TGA measurements.

192

Table 5.11: Infrared spectrum assignments of $(H_24,4'\text{-bipy})[Co(H_2O)_2(4,4'\text{-bipy})(SO_4)_2]\cdot H_2O$ (**15**)

Stretching mode	Wavenumber /cm^{-1}
ν(O-H)	3300
ν(C-H)	3000-3100 (multiple peaks)
δ(H-O-H)	1630
ν(C=C)	1380-1530 (multiple peaks)
ν(S-O$_4$) (asym)	970 and 1064
ν(S-O$_4$) (sym)	910
ρ(N-H) wag	808
δ(S-O$_4$)	603 and 709
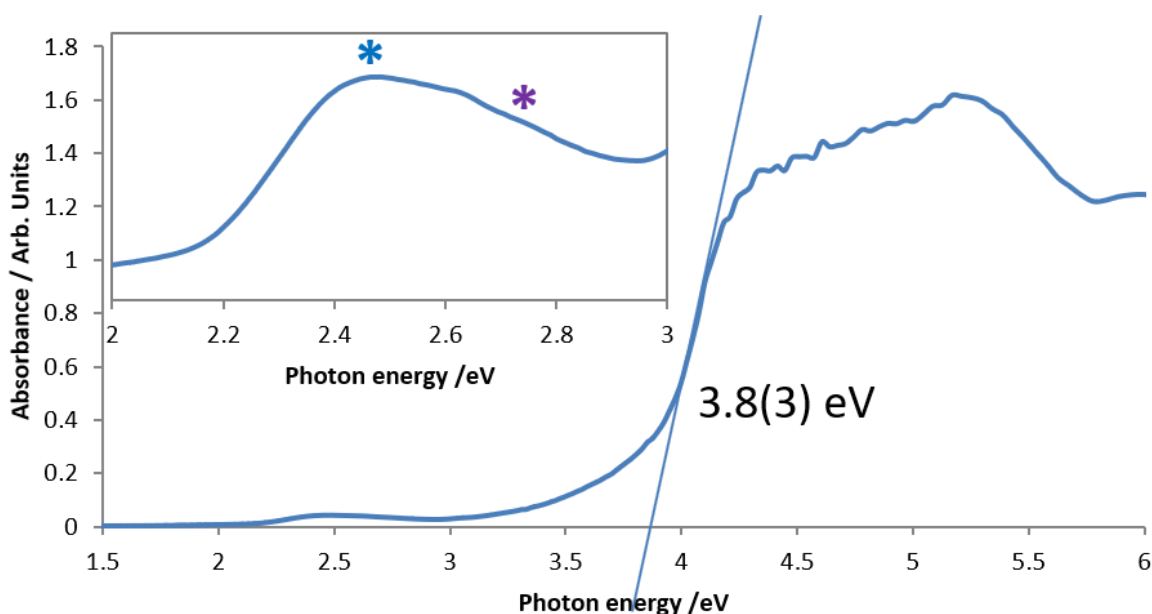
Figure 5.15: Diffuse reflectance spectrum of $(H_24,4'\text{-bipy})[Co(H_2O)_2(4,4\text{-bipy})(SO_4)_2]\cdot H_2O$ (**15**) showing a band gap of 3.8(3) eV. Asterisks denote *d-d* transitions $^4T_{1g}(F)\rightarrow{^4}A_{2g}$ (blue) and $^4T_{1g}(F)\rightarrow{^4}T_{2g}(P)$ (purple).

Magnetic susceptibility data for compound (**15**) can be viewed in Figure 5.16, the inverse χ plot displays a slight curve. The data are rather noisy as only a small amount of sample was available for the experiment. The curve does appear to follow a Curie-Weiss expression, but can only be fitted between $170 \leq T/K \leq 300$ due to the curvature present, Table 5.12. The measured Curie constant of 2.18 emu mol^{-1} Oe^{-1} leads to $\mu_{eff} = 4.1$, which compares with a

spin-only moment of $\mu_{so} = 3.87$ for an $S = 3/2$ ion. The effective magnetic moment is typical of octahedral Co(II) complexes with an orbital contribution to the spin-only value as seen previously [300]. The Weiss constant was determined as -50 K, indicating antiferromagnetic interactions between moments. Inspecting the magnetisation versus magnetic field plot (Figure 5.17), shows that a weak spontaneous magnetisation is present.

Table 5.12: Magnetic data for structure $(H_24,4\text{'-bipy})[Co(H_2O)_2(4,4\text{'-bipy})(SO_4)_2]\cdot H_2O$ (**15**).

Range $170 \leq$ T/K ≤ 300	C / emu mol^{-1} Oe^{-1}	Θ / K	μ_{eff} / μ_B
	2.18	-50	4.1
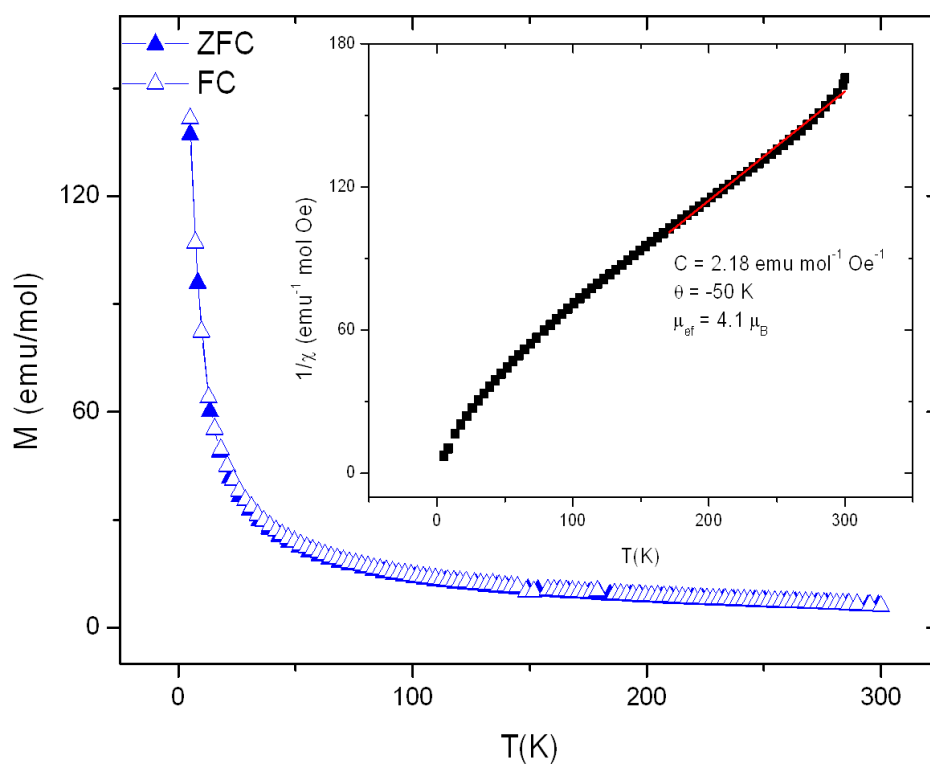
Figure 5.16: Field-cooled magnetic susceptibility and inverse magnetic susceptibility data for $(H_24,4\text{'-bipy})[Co(H_2O)_2(4,4\text{'-bipy})(SO_4)_2]\cdot H_2O$.
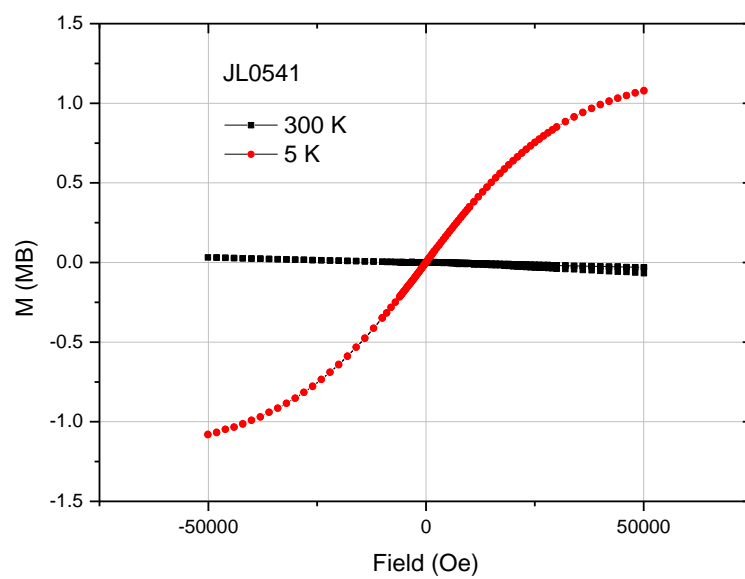
Figure 5.17: Magnetic moment versus magnetic field plot of $(H_24,4'\text{-bipy})[Co(H_2O)_2(4,4'\text{-bipy})(SO_4)_2]\cdot H_2O$.

5.4 Samples with Pronounced Air and Moisture Sensitivity

The following compounds were prepared but due to air or moisture sensitivity problems, only single-crystal X-ray experiments could be performed. Either the crystals themselves or the surrounding bulk sample became wet and liquified when outside a nitrogen atmosphere. Some cases showed extreme sensitivity and decayed in 10 seconds while some decayed over half an hour precluding further detailed analysis. Powder X-ray experimental parameters in this section are the same as those listed in Section 2.2.2, but not for compound (**18**). This had to be treated differently (details in Section 5.4.3.1) due to the severity of the sensitivity and would cause decay to occur inside a minute. Compound (**17**) and (**19**), while sensitive, could survive the standard procedure.

5.4.1 [Mn(tepa)(SO$_4$)] (16)
5.4.1.1 Synthesis

Compound [Mn(tepa)(SO$_4$)] (**16**) was synthesised from a mixture of MnSO$_4$.H$_2$O (0.3376g 1.99 mmol), tetraethylenepentamine (tepa) (0.5 ml, 2.64 mmol), 18 M H$_2$SO$_4$ (0.1 ml, 1.8 mmol) and H$_2$O (0.07 ml, 3.88 mmol). The reagent mixture was stirred for 10 min in a Teflon-lined stainless-steel autoclave before being sealed and heated to 453 K for 12 days using a heating rate of 1 K min^{-1}. The products were cooled overnight before being filtered and washed successively with ethanol and acetone inside an N$_2$ filled glove bag. Single crystals of (**16**) were produced in the form of clear blocks which were embedded within a thick viscous liquid or gel. This may be attributed to high sensitivity to moisture or to oxidation. If left in air, after a day or so, the viscous yellow liquid turns into a black liquid (Figure 5.18) including the crystals. It did however, shelter the crystals inside the bulk material for a brief time, when in oil, so characterisation by single-crystal X-ray could take place.

Figure 5.18: Photograph depicting the decomposition of the bulk sample on a glass slide which contains structure (**16**).

Single-crystal X-ray diffraction data were collected at 150 K using graphite monochromated MoK$_\alpha$ (λ = 0.71073 Å) radiation. The structure was solved using SIR92 [227] and the model refined using the CRYSTALS suite of programs [230]. The model was refined in F and modelled for twinning. Atoms of the inorganic component were located but anisotropic thermal parameters of only Mn and S atoms could be refined all other atoms were treated isotropically. The tepa molecules show a high degree of disorder and some oxygen positions are also disordered for example, N(14) and N(23) are disordered over symmetry sites. Not all atoms from the tepa molecules could be located so only a partial structure solution was found. Upon analysing the symmetry using Platon addsym routine [301], it was determined that the chosen space group was the best fit for the current data. Crystallographic details are summarised in Table 5.13 and Atomic coordinates of all non-hydrogen atoms can be found in Tables A3.3.

Table 5.13: Crystallographic data for structure [Mn(tepa)(SO$_4$)] **(16).**

Chemical formula	[Mn(tepa)(SO$_4$)]
Formula mass	2058.94
Crystal Habit	block
Crystal system	orthorhombic
Symmetry space group	*C2mm*
Temp /K	150
a /Å	13.1991(13)
b /Å	15.7717(16)
c /Å	20.0976(13)
V /Å³	4183.7(3)
Z	2
μ / mm^{-1}	1.1692
Total reflections ($I > 3\sigma(I)$)	2575
R factor	0.1331
w*R* factor	0.1392
Goodness of fit ref	5.5436

3.3.2.2 Structure Description and Analysis

The structure of **(16)** contains pseudo-pentagonal bipyramidal Mn complexes which coordinate to an entire tepa molecule in the equatorial plane, producing Mn(tepa) rings and bond with two monodentate SO$_4^{2-}$ ions in the remaining axial positions. Each sulfate ion

ligand bridges and bonds to another Mn(tepa) complex on the opposite side and this continues in an infinite chain producing [Mn(tepa)(SO$_4$)] (Figure 5.19).
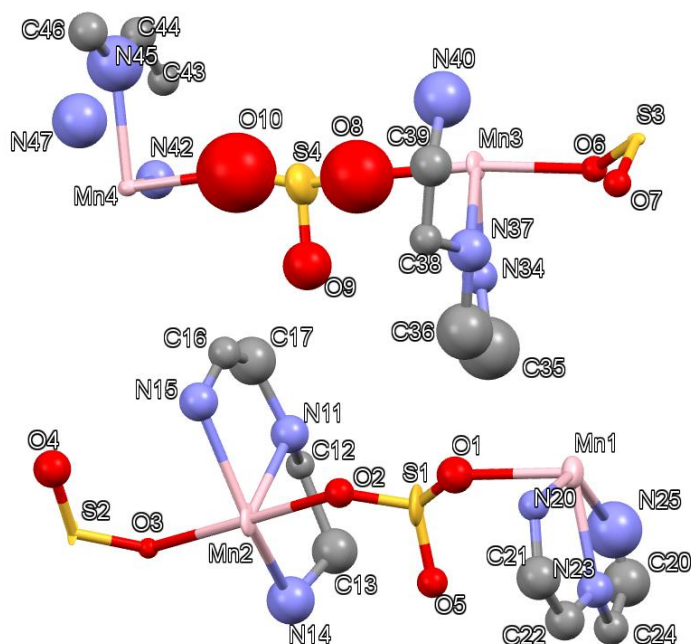
Figure 5.19: Asymmetric unit of **(16)** displaying thermal ellipsoids at 50 % probability or spheres (if isotropically refined) of each atom. Key: pink: Mn atoms, yellow: S atoms, red: O atoms, light blue: N atoms, grey: C atoms.

Bond-valence calculations for Mn(1), (2) and (3) were 2.11, 1.66 and 1.47 respectively, but Mn(4) could not be calculated. The reason for this is that not all of the tepa molecule around this particular centre was found, so was excluded from calculations. While these values are less consistent than with previous structures due to the severe disorder, they broadly indicate that Mn atoms should be in a +2 oxidation state. Including the SO$_4^{2-}$ ions, this results in a balanced charge for the structure. The coordination bond lengths (Table 5.14) around Mn centres varies between ($2.21(4) \leq d/\text{Å} \leq 2.53(7)$) for N-Mn bonds and between ($2.15(2) \leq d/\text{Å} \leq 2.31(2)$) for Mn-O bonds. This compares well to the Mn-O distances seen in the 2-D layered structure of (C$_2$NO$_2$H$_5$)MnSO$_4$ (C$_2$NO$_2$H$_5$ = glycerine) [197], with values between ($2.123(8) \leq d/\text{Å} \leq 2.353(6)$). As seen with previous structures utilising chain-based amine reagents (structure **(14)** and **(15)**), the tepa molecule is rigid and can only reach certain angles from the Mn centre. There are also the weakened valence contributions to consider as more bonds will reduce the ability for Mn(II) to satisfy bond contributions which results in longer weaker bonds. If compared with the complex [Mn(SO$_4$)$_2$(H$_2$O)$_4$] [304] the distances here are between

$(2.160(2) \leq d/\text{Å} \leq 2.189(2))$ due to only containing monodentate ligands which do not distort the octahedral geometry, unlike the previous example which uses glycerine. In structure **(16),** the angles (Table 5.15) around the N-Mn-N angles around the tepa molecules vary between $(58.6(11) \leq \alpha/° \leq 87.9(17))$ showing a much more distorted geometry (should be 72 ° in a pentadentate cyclic ring).

Table 5.14 A selection of bond lengths in [Mn(tepa)(SO$_4$)] **(16)** and valence sums.

symmetry codes: a = x, -y, z, b = x, -y, -z+1, c = x, y, -z+1

	Length /Å	vij		Length /Å	vij		Length /Å	vij
Mn(1)-N(23)[a]	2.21(4)	0.18	Mn(2)-N(11)[a]	2.32(3)	0.27	Mn(3)-O(8)[a]	2.23(8)	0.12
Mn(1)-N(23)[b]	2.21(4)	0.18	Mn(2)-N(15)[a]	2.40(3)	0.22	Mn(3)-N(34)[a]	2.26(2)	0.32
Mn(1)-N(23)[c]	2.21(4)	0.18	Mn(2)-N(14)[a]	2.43(4)	0.10	Mn(3)-N(37)[a]	2.45(3)	0.10
Mn(1)-O(1)[c]	2.23(3)	0.23	Mn(2)-O(2)	2.15(2)	0.29	Mn(3)-O(6)	2.22(2)	0.24
Mn(1)-N(20)[b]	2.32(3)	0.27	Mn(2)-O(3)	2.313(18)	0.19	Mn(3)-O(8)	2.23(8)	0.12
Mn(1)-O(1)	2.23(3)	0.23	Mn(2)-N(11)	2.32(3)	0.27	Mn(3)-N(34)	2.26(2)	0.32
Mn(1)-N(20)	2.32(3)	0.27	Mn(2)-N(14)	2.43(4)	0.10	Mn(3)-N(37)	2.45(3)	0.10
Mn(1)-N(23)	2.21(4)	0.18	Mn(2)-N(15)	2.40(3)	0.22	Mn(3)-N(40)	2.53(7)	0.15
Mn(1)-N(25)	2.22(11)	0.36						
	$\sum$vij=	**2.11**		$\sum$vij=	**1.66**		$\sum$vij=	**1.47**

Table 5.15 A selection of bond angles in [Mn(tepa)(SO$_4$)] **(16).**

symmetry codes: a = x, -y+1, z,

	Angle / °		Angle / °		Angle / °
O(8)[a]-Mn(3)-N(34)[a]	84.1(16)	N(34)[a]-Mn(3)-N(34)	72.3(13)	O(8)[a]-Mn(3)-N(40)	85(2)
O(8)[a]-Mn(3)-N(37)[a]	89.9(10)	N(37)[a]-Mn(3)-N(34)	146.8(10)	N(34)[a]-Mn(3)-N(40)	143.1(7)
N(34)[a]-Mn(3)-N(37)[a]	74.8(10)	O(6)-Mn(3)-N(34)	89.8(8)	N(37)[a]-Mn(3)-N(40)	70.0(8)
O(8)[a]-Mn(3)-O(6)	173.3(10)	O(8)-Mn(3)-N(34)	84.1(16)	O(6)-Mn(3)-N(40)	98.4(15)
N(34)[a]-Mn(3)-O(6)	89.8(8)	O(8)-Mn(3)-N(37)	100.7(10)	O(8)-Mn(3)-N(40)	85(2)
N(37)[a]-Mn(3)-O(6)	85.9(8)	N(34)-Mn(3)-N(37)	146.8(10)	N(34)-Mn(3)-N(37)	74.8(10)
N(34)[a]-Mn(3)-O(8)	90.9(16)	N(37)-Mn(3)-N(37)	137.4(15)	N(34)-Mn(3)-N(40)	143.1(7)
N(37)[a]-Mn(3)-O(8)	100.7(10)	O(6)-Mn(3)-N(37)	85.9(8)	N(37)-Mn(3)-N(40)	70.0(8)
O(6)-Mn(3)-O(8)	173.3(10)	O(8)-Mn(3)-N(37)	89.9(10)		

There are two crystallographically distinct chains present within the structure and these pack in a staggered manner within layers. The chains within a layer line up so the Mn(tepa) ring system sits alongside a sulfate of a neighbouring chain, thereby reducing steric clashes

between metal complexes (Figure 5.20 left). The layers of chains are then stacked on top of each other also in a staggered manner using the same method of tepa rings beside neighbouring sulfate. When fully packed it can also be seen that the chains are not straight but produce a slight sinusoidal wave (Figure 5.20 right).
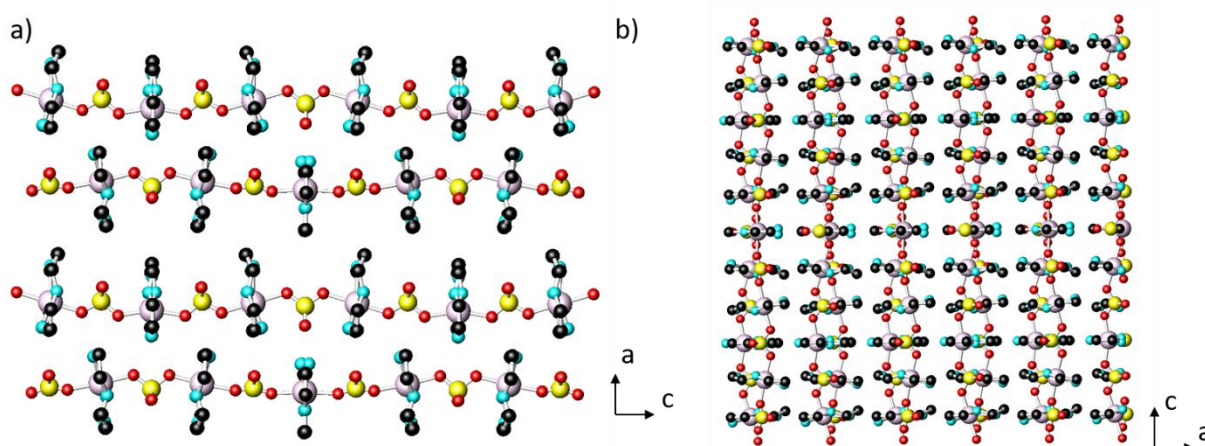
Figure 5.20: (a) Ball and stick diagrams of structure **(16)** highlighting the packing of single chains along the [001] and (b) the packing in all directions viewed down [010]. Key: green: Mn atoms, pink: S atoms, red: O atoms, light blue: N atoms, black: C atoms.

Structure **(16)** was produced as a result of investigating the nature of increasing the chain length of the amine molecules. A previous material, $[M(SO_4)(teta)]$ M = Mn, Fe (teta = triethylenetetramine), produced by Bailen [305], demonstrated the use of chain based amine reagents to create cross linking chains/layers. It was thought that increasing the chain with an extra ethylamine (from teta to tepa) would increase the size of the cross-linking section seen in Bailen's work, it instead formed new chain entirely. In general, the use of tepa molecules has also been used to increase the probability of bonding complexes onto frameworks by forming unsaturated octahedral complexes that contain a free coordination site *e.g.* $[Mn(tepa)Sb_2S_{10}]$ [306].

5.4.2 $[CoSO_4(dap)_2]$ (17)
5.4.2.1 Synthesis

Compound $[CoSO_4(dap)_2]$ **(17)** was synthesised from a mixture $CoSO_4.7H_2O$ (0.3498g 1.24 mmol), 1,2-diaminopropane (dap) (0.5 ml, 4.11 mmol), 18 M H_2SO_4 (0.1 ml, 1.8 mmol) and H_2O (0.07 ml, 3.88 mmol). The reagent mixture was stirred for 10 min in a Teflon-lined stainless-steel autoclave before being heated to 473 K for 10 days using a heating rate of 1 K

min $^{-1}$. The products were cooled overnight before being filtered and washed successively with ethanol and acetone inside an N_2 filled glove bag. Single crystals of (17) were produced in the form of orange blocks along with crystals of [H$_2$dap][SO$_4$] [165] as identified through powder X-ray analysis of the bulk product (Figure 5.21). An unidentified phase was also present.
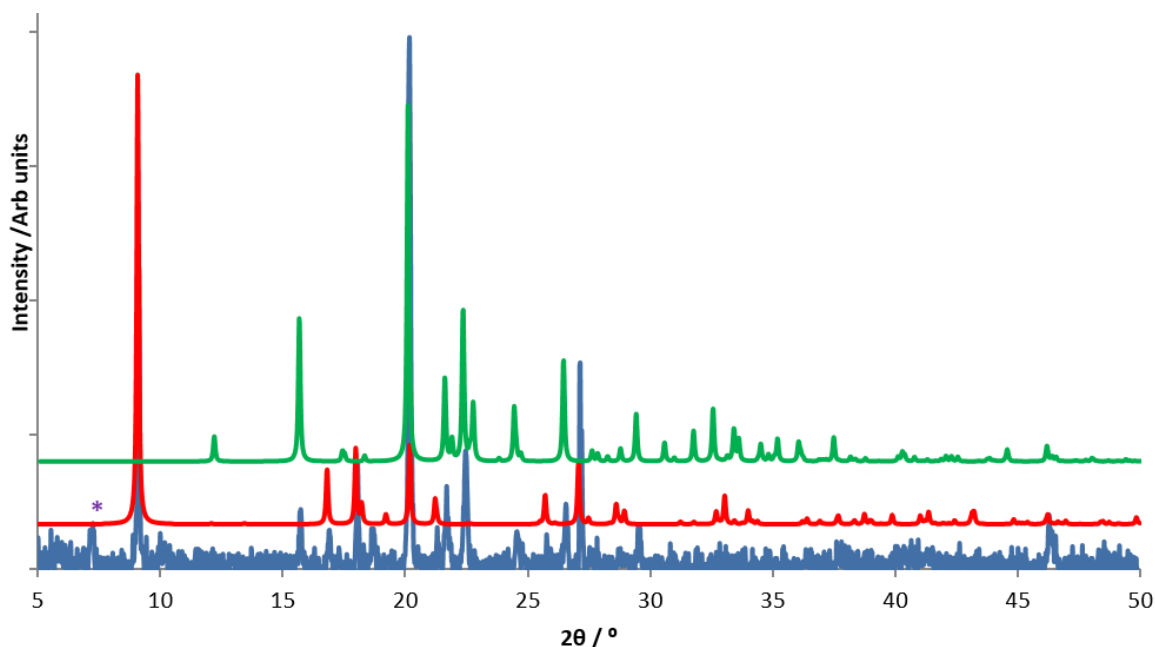
Figure 5.21: Powder X-ray diffraction pattern of (17), Key: blue, bulk sample: red, calculated pattern generated from single-crystal data, green, calculated pattern of (H$_2$dap)SO$_4$ [165] and purple asterisks mark an unidentifiable phase.

Single-crystals were sent to the National Crystallographic Service at Southampton University for single-crystal X-ray experiments. The data collection was conducted at 100 K using graphite monochromated MoKα (0.71075 Å) radiation on a Rigaku Saturn724+ X-ray diffractometer. The refinement was conducted in F after being solved by Superflip [228] and polynomial weight schemes were applied. The position of the methyl group could not be located so was modelled in the only two positions it can reside in, with an occupancy of 0.45 and 0.55 for C(4) and C(3) respectively (Figure 5.22). This appeared to produce the best results rather than having a 50/50 occupancy, perhaps suggesting some favourability in its position. Hydrogen atoms on the amine ligands were placed geometrically with a U[equiv] value 1.2 times the U[equiv] of the carbon to which they are attached. Crystallographic details are summarised for structure (17) in table 5.16. Atomic coordinates of all non-hydrogen atoms can be found in Tables A3.4.

Table 5.16: Crystallographic data for structure [CoSO$_4$(dap)$_2$] (**17**).

Chemical formula	[CoSO$_4$(dap)$_2$]
Formula mass	299.22
Crystal Habit	block
Crystal system	orthorhombic
Symmetry space group	*Cmca*
Temp /K	100
a /Å	19.4562(13)
b /Å	9.8571(5)
c /Å	13.1637(8)
V /Å^3	2524.55(15)
Z	8
μ /mm^{-1}	1.530
Total reflections ($I > 3\sigma(I)$)	1234
R factor	0.0579
wR factor	0.0658
Goodness of fit ref	1.0749

5.4.2.1 Structure Description and Analysis

The structure of (**17**) contains a crystallographically distinct Co atom (Figure 5.22) in a pseudo-octahedral geometry which coordinates to two monodentate sulfate ions and two bidentate dap molecules. The sulfate ion acts as a bridge and coordinates to another Co metal centre as a monodentate ligand, producing an infinite chain down [001].

Figure 5.22: (a) Asymmetric unit of (**17**) displaying thermal ellipsoids of each atom at 50 % probability and (b) the full coordination around Co(1) using a ball and stick model. Key: green: Co atoms, yellow: S atoms, red: O atoms, light blue: N atoms, grey/black: C atoms. Hydrogen atoms are omitted for clarity.

The bond-valence calculations for the Co metal atoms gave a value of 2.34 v.u. in total, therefore a +2 charge was assigned to Co. as the inorganic component already contains a -2 charge from the sulfate ions the overall charge of the chain is neutral. The distances (Table 5.17) between cobalt centres and ligands are 2.132(3) Å, 2.119(3) Å for Co-N bonds and 2.222(3) Å for Co-O bonds. This is comparable to the complex [Co(Hdeta)$_2$(SO$_4$)$_2$] structure **(14)** and similar to the literature, for example Co(Hdeta)$_2$(SO$_4$)$_2$ complexes contain Co-N and Co-O distances of between $(2.093(4) \leq d/\text{Å} \leq 2.160(5))$ and 2.268(4) Å respectively. Structure **(17)** also contains the same the distorted geometry of the octahedral bond angles in the amine plane similar to **(14)**. Bond angles (Table 5.18) between the bidentate amine and cobalt centre (biting angle) (N(1)-Co(1)-N(2)) are 81.51(11) ˚ while angles between opposing amine ligands N(1)-Co(1)-N(1*) and N(2)-Co(1)-N(2*) are 104.40(15) ˚ and 92.57(15) ˚ respectively.

Table 5.17 A selection of bond lengths in [CoSO$_4$(dap)$_2$] **(17)** and bond valence sums.

symmetry codes: $a = x, -y+3/2, z+1/2, b = -x+1, y, z$

	Length /Å	vij		Length /Å		Length /Å
Co(1)-O(2)^a	2.192(3)	0.26	O(1)-S(1)	1.501(3)	C(1)-C(4)	1.558(13)
Co(1)-N(2)^b	2.132(3)	0.45	S(1)-O(3)^b	1.484(3)	C(2)-N(1)	1.469(5)
Co(1)-N(1)^b	2.119(3)	0.47	S(1)-O(2)	1.472(3)	C(2)-C(3)	1.499(9)
Co(1)-O(1)	2.222(3)	0.24	S(1)-O(3)	1.484(3)		
Co(1)-N(2)	2.132(3)	0.45	N(2)-C(1)	1.466(5)		
Co(1)-N(1)	2.119(3)	0.47	C(1)-C(2)	1.529(6)		
	$\sum$vij=	**2.34**				

Table 5.18 A selection of bond angles in [CoSO$_4$(dap)$_2$] **(17).**

symmetry codes: $a = x, -y+3/2, z+1/2, b = -x+1, y, z$

	Angle / ˚		Angle / ˚		Angle / ˚
O(2)^a-Co(1)-N(2)^b	94.07(9)	N(2)^b-Co(1)-N(2)	92.57(15)	N(2)-Co(1)-N(1)	81.51(11)
O(2)^a-Co(1)-N(1)^b	85.76(9)	N(1)^b-Co(1)-N(2)	174.05(11)	O(1)-S(1)-O(3)^b	109.50(12)
N(2)^b-Co(1)-N(1)^b	81.51(11)	O(1)-Co(1)-N(2)	90.88(9)	O(1)-S(1)-O(2)	107.78(18)
O(2)^a-Co(1)-O(1)	172.83(12)	O(2)^a-Co(1)-N(1)	85.76(9)	O(3)^b-S(1)-O(2)	109.79(12)
N(2)^b-Co(1)-O(1)	90.88(9)	N(2)^b-Co(1)-N(1)	174.05(11)	O(1)-S(1)-O(3)	109.50(12)
N(1)^b-Co(1)-O(1)	89.86(8)	N(1)^b-Co(1)-N(1)	104.40(15)	O(3)^b-S(1)-O(3)	110.4(2)
O(2)^a-Co(1)-N(2)	94.07(9)	O(1)-Co(1)-N(1)	89.86(8)	O(2)-S(1)-O(3)	109.79(12)

As in the structure of **(16)**, the units pack by staggering the chains so the amine is in-between sets of adjacent amine ions, opposite a neighbouring chains sulfate ion. This also promotes intermolecular interactions by being near the sulfate linkers (Figure 5.23). Interactions between donor and acceptor atoms is seen throughout the structure and observed between sulfate-amine groups (Table 5.19), supporting the presence of hydrogen bonding.
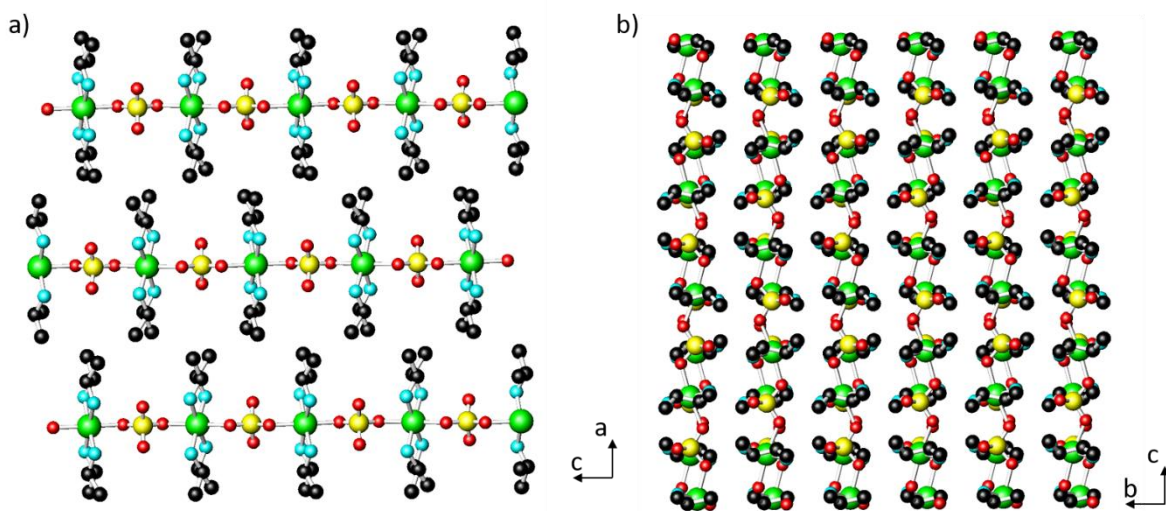
Figure 5.23: (a) 3 chains of **(17)** side by side within the crystal structure and (b) the crystal packing viewed down [100]. Key: green: Co atoms, yellow: S atoms, red: O atoms, light blue: N atoms, black: C atoms. Hydrogen atoms are omitted for clarity.

Table 5.19 Bond lengths found in **(17)** between acceptor and donor atoms containing hydrogen bonding.

symmetry codes: a = x, -y+2, -z+1, b = x, -y+3/2, z+1/2, c = -x+1, -y+1, -z+1

	Length /Å		Length /Å
N(1)…O(3)^a	2.977(11)	N(2)…O(3)^b	3.014(11)
N(1)…O(3)	2.944(11)	N(2)…O(1)^c	3.161(11)

Due to the Co(II) metal centres present in **(17)**, magnetic measurements were considered due to the unpaired electrons present in d^7 cobalt. The inverse χ plot (Figure 5.24) revealed that the molar magnetic susceptibility is negative. This demonstrates that the material is diamagnetic, which is not possible for a Co(II) ion. The current structure solution does not produce a high enough negative charge for the cobalt to be considered as Co(III), so further investigation is required. EDX analysis of hand-picked orange crystals (Table 5.20) showed a

range of cobalt concentrations in the crystallites examined (between 0-20 %) instead of the crystallographically determined 19.66 %. Upon reinspection of the crystals using single-crystal X-ray diffraction, it was noted that some of the orange crystals had the same unit cell as (H_2dap)SO_4 [165] (P2$_1$/n, a = 5.540(2), b = 15.667(3), c = 8.506(2) Å, β = 104.13(2) ˚) which were reported as colourless blocks. The orange colour of the second set of crystals could be the result of the incorporation of small amounts of cobalt ions on the surface of the crystals. Collectively, the results indicate that there is a presence of (H_2dap)SO_4, which would be diamagnetic (affecting magnetic measurements) and contains no cobalt (EDX would observe less than calculated cobalt presence). As the two phases could not be separated with any certainty, further analysis were not performed.

Table 5.20: Energy Dispersive X-ray (EDX) data for orange blocks handpicked from bulk sample of **(17)**.

Expected wt%: C = 14.06 %, N = 18.70%, O = 21.39 %, S = 10.71 %, Co = 19.66 %

C / wt%	N / wt%	O / wt%	S / wt%	Co / wt%
27.99	26.93	39.34	4.04	**1.70**
34.22	21.44	31.52	6.28	**6.53**
32.62	26.59	30.43	6.61	**3.75**
34.21	20.59	26.66	11.64	**6.90**
30.78	25.31	36.42	4.81	**2.68**
48.44	10.09	9.58	16.48	**15.41**
35.18	21.10	29.53	8.90	**5.28**
52.39	12.19	20.33	6.20	**8.88**
29.84	26.49	37.02	4.58	**2.08**
44.75	6.90	13.93	12.96	**20.74**
39.59	23.68	32.57	3.66	**0.50**
31.12	26.21	35.39	5.03	**2.25**
29.30	26.65	33.77	6.38	**3.90**
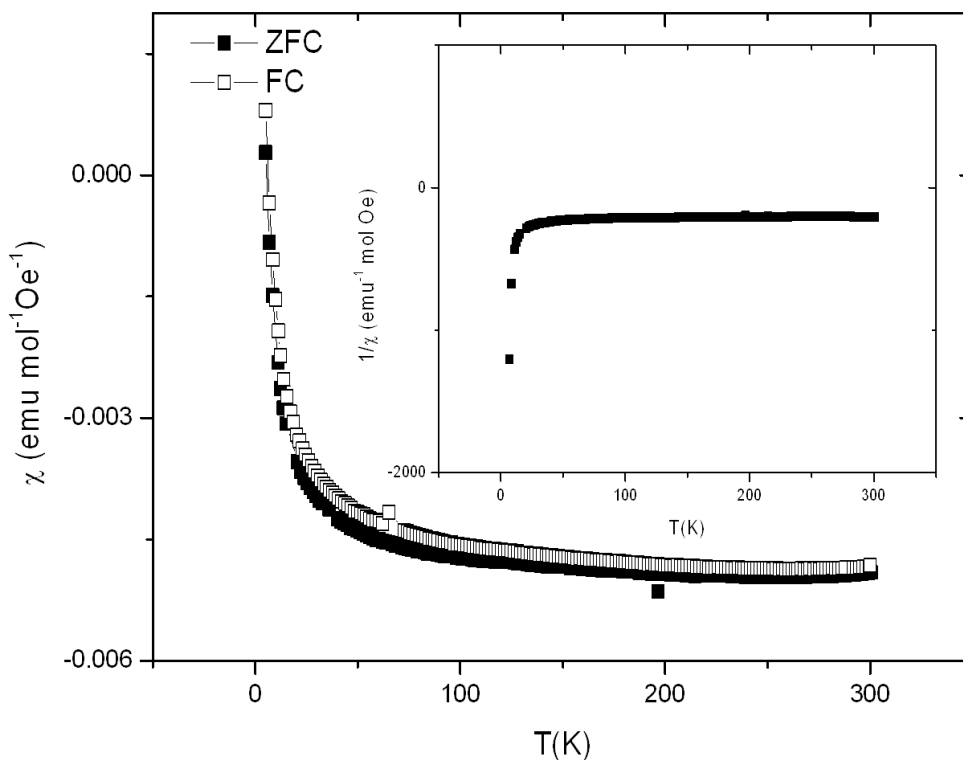
Figure 5.24: Field-cooled magnetic susceptibility data for [CoSO$_4$(dap)$_2$].

5.4.3 [Co(SO$_4$)(deta)] (18)

5.4.3.1 Synthesis

Compound [Co(SO$_4$)(deta)] **(18)** was synthesised from a mixture CoSO$_4$.7H$_2$O (0.3498g 1.24 mmol), 1,4-diaminobutane (dab) (0.4 ml, 3.98 mmol), 18 M H$_2$SO$_4$ (0.1 ml, 1.8 mmol) and H$_2$O (0.1 ml, 5.56 mmol). The reagent mixture was stirred for 10 min in a Teflon-lined stainless-steel autoclave before being heated to 473 K for 10 days using a heating rate of 1 K min^{-1}. The products were cooled overnight before being filtered and washed successively with ethanol and acetone inside an N$_2$ filled glove bag. Single crystals of **(18)** were produced in the form of purple plates along with clear crystals of (H$_2$dab)SO$_4$ [307] and small red crystallites of an unknown material. The red crystallites were too small for structure determination by single-crystal X-ray diffraction in the laboratory. The powder X-ray diffraction (Figure 5.25) also showed peaks from an unidentifiable phase as well as peaks from **(18)** and (H$_2$dab)SO$_4$. Due to the severity of the sensitivity, the powder X-ray diffraction experimental procedure had to be amended. The samples were prepared in a glove bag under an N$_2$ atmosphere, and

206

were ground in oil with a pestle and mortar. The paste was transferred to a zero-background disc and quickly loaded onto the machine. The scan was conducted at an increased speed to halve the usual hour collection time using the parameters 5-50 2θ/°, 0.021 step size, 0.6 s per step. Even in oil the crystals still degrade, (as seen with other sulfate samples) (Figure 5.26), but the degradation occurs over an hour instead of a few seconds, as is found in air. Crystal picking was attempted but the crystals and bulk sample degraded too quickly to be able to separate the phases without any other phases attaching itself to the crystals being removed.
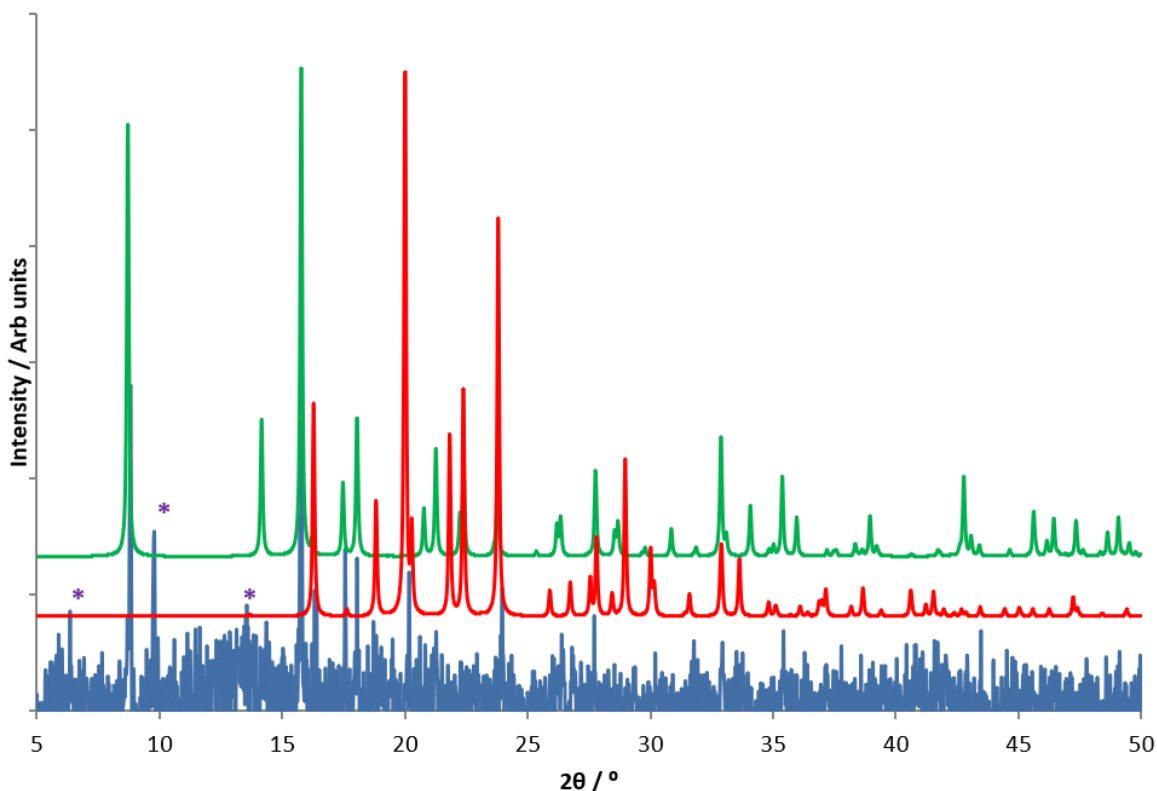
Figure 5.25: Powder X-ray diffraction pattern of (18), Key: blue, bulk sample: red, calculated pattern generated from single-crystal data, green, $(H_2dab)SO_4$ calculated through single crystal data [307] and purple asterisks are an unidentifiable phase.

Single-crystal X-ray diffraction experiments were conducted at 150 K using graphite monochromated MoK_α (λ = 0.71073 Å) radiation. The selection of the crystal was done quickly with the bulk sample in oil, a crystal located and then mounted. It is suspected that the low temperatures added to the crystals longevity otherwise this experiment would not have worked. The refinement was conducted in F after being solved by Superflip [228] and a polynomial weighting scheme was applied. Hydrogen atoms on the amine ligands were placed geometrically with a U[equiv] value 1.2 times the U[equiv] of the carbon to which

they are attached. Crystallographic details are summarised for structure **(18)** in Table 5.21. Atomic coordinates of all non-hydrogen atoms are presented in Tables A3.4.
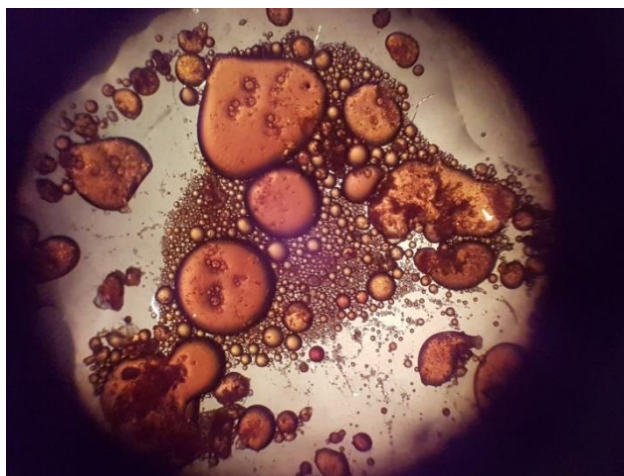
Figure 5.26: Photograph of a sulfate sample decomposing in oil into a liquid state on a glass slide.

Table 5.21: Crystallographic data for structure [Co(SO₄)(deta)] **(18).**

Chemical formula	[Co(SO$_4$)(deta)]
Formula mass	903.02
Crystal Habit	plate
Crystal system	orthorhombic
Symmetry space group	*Pcam*
Temp /K	150
a /Å	7.9338(3)
b /Å	10.1402(4)
c /Å	11.2246(5)
V /Å³	903.03(4)
Z	4
μ /mm^{-1}	2.120
Total reflections ($I > 3\sigma(I)$)	1298
R factor	0.0328
wR factor	0.0296
Goodness of fit ref	1.1045

5.4.3.2 Structure Description and Analysis

The structure of **(18)**, contains a crystallographically distinct Co (Figure 5.27) metal atom in a pseudo-octahedral geometry. This Co metal centre is bonded to one deta molecule and two sulfate ions in a facial geometric arrangement. One sulfate chelates as a bidentate ligand while

the other as a monodentate ligand. Each sulfate then bridges with another Co metal atom acting as either a monodentate or bidentate ligand. Therefore, each sulfate anion chelates to two metal centres as a bidentate ligand of one and a monodentate ligand of the other. This creates infinite chains down [100] producing a square wave arrangement of the chain, Figure 5.28. The Co metal centre produces a calculated total valence contribution value of 2.18 v.u. Therefore, Co was assigned an oxidation state of +2 and the counter charge is produced by one SO_4^{2-} unit, resulting in a neutral charge overall.

a)   b)
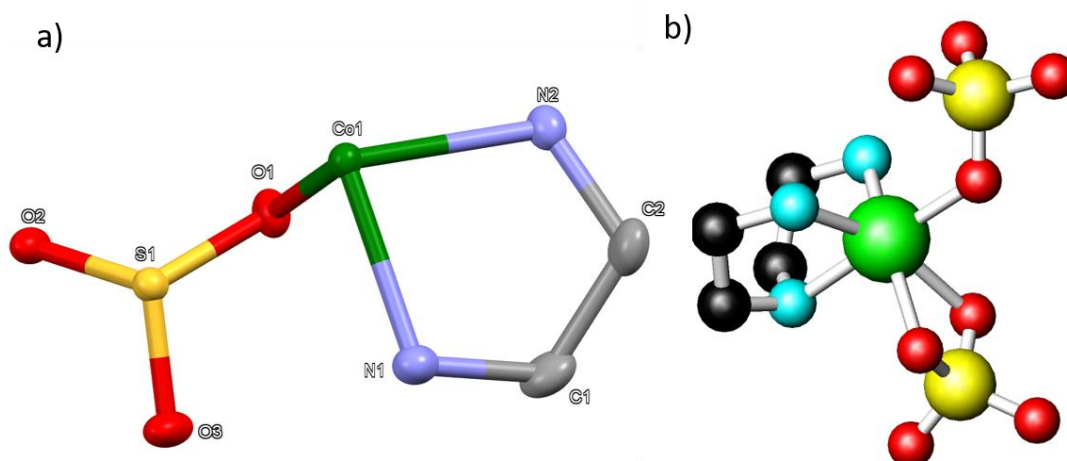
Figure 5.27: (a) Asymmetric unit of **(18)** displaying thermal ellipsoids of each atom at 50 % probability and (b) a fully coordinated Co centre. Key: green: Co atoms, yellow: S atoms, red: O atoms, light blue: N atoms, grey/black: C atoms. Hydrogen atoms are omitted for clarity.
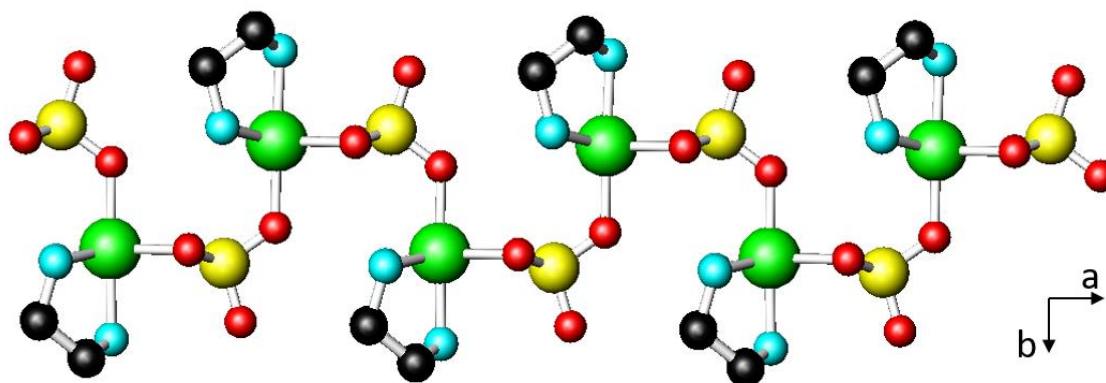
Figure 5.28: A single chain of [Co(SO₄)(deta)] seen down [001]. Key: green: Co atoms, yellow: S atoms, red: O atoms, light blue: N atoms, black: C atoms. Hydrogen atoms are omitted for clarity.

The geometry around the Co(II) centre shows a distorted octahedral geometry because of the presence of different ligands, namely bidentate sulfate and tridentate amine. Selected bond lengths and angles can be viewed in Tables 5.22 and 5.23. If the bidentate oxygens are viewed in the equatorial plane, the bond angles seen here are largely distorted. Angles of 63.98(5) °,

96.65(4) ° and 100.88(7) ° are seen between O(1a)-Co(1)-O(1), O(1)-Co(1)-N(2) and N(2a)-Co(1)-N(2) respectively. The position of the N(2) atoms has also been pulled upwards from the equatorial plane with an internal angle 82.19(5) ° between N(1)-Co(1)-N(2). While it is normal for multidentate ligands to distort the octahedral geometry which has been seen throughout this study, the incorporation of the bidentate sulfate ligand has shown it to be the most distorted metal centre observed in this work. This is likely to arise because the tetrahedral SO_4^{2-} unit is much more rigid than an ethyldiamine ligand resulting in a much narrower L-Co-L (L=ligand) biting angle.

Table 5.22 A selection of bond lengths in [Co(SO$_4$)(deta)] **(18)** and valence sums.

symmetry codes: *a = x, y, -z+3/2, b = x+1/2, -y+2, z*

	Length /Å	vij		Length /Å		Length /Å
Co(1)-O(1)ᵃ	2.2312(11)	0.23	S(1)-O(1)ᵃ	1.4948(11)	N(2)-C(2)	1.485(2)
Co(1)-N(2)ᵃ	2.1110(13)	0.48	S(1)-O(1)	1.4948(11)	C(1)-C(2)	1.515(3)
Co(1)-O(2)ᵇ	2.0782(15)	0.35	S(1)-O(2)	1.4910(15)		
Co(1)-O(1)	2.2312(11)	0.23	S(1)-O(3)	1.4589(16)		
Co(1)-N(1)	2.1704(18)	0.41	N(1)-C(1)ᵃ	1.470(2)		
Co(1)-N(2)	2.1110(13)	0.48	N(1)-C(1)	1.470(2)		
	∑vij=	**2.18**				

Table 5.23 A selection of bond angles in [Co(SO$_4$)(deta)] **(18).**

symmetry codes: *a = x, y, -z+3/2, b = x+1/2, -y+2, z*

	Angle / °		Angle / °		Angle / °
O(1)ᵃ-Co(1)-N(2)ᵃ	96.65(4)	N(2)ᵃ-Co(1)-N(1)	82.19(5)	N(1)-Co(1)-N(2)	82.19(5)
O(1)ᵃ-Co(1)-O(2)ᵇ	90.08(5)	O(2)ᵇ-Co(1)-N(1)	178.48(7)	O(1)ᵃ-S(1)-O(1)	104.52(9)
N(2)ᵃ-Co(1)-O(2)ᵇ	98.76(4)	O(1)-Co(1)-N(1)	88.63(5)	O(1)ᵃ-S(1)-O(2)	110.31(6)
O(1)ᵃ-Co(1)-O(1)	63.98(5)	O(1)ᵃ-Co(1)-N(2)	158.86(5)	O(1)-S(1)-O(2)	110.31(6)
N(2)ᵃ-Co(1)-O(1)	158.86(5)	N(2)ᵃ-Co(1)-N(2)	100.88(7)	O(1)ᵃ-S(1)-O(3)	111.12(6)
O(2)ᵇ-Co(1)-O(1)	90.08(5)	O(2)ᵇ-Co(1)-N(2)	98.76(4)	O(1)-S(1)-O(3)	111.12(6)
O(1)ᵃ-Co(1)-N(1)	88.63(5)	O(1)-Co(1)-N(2)	96.65(4)	O(2)-S(1)-O(3)	109.38(9)

Acceptor-donor interactions within and between the chains of **(18)**. For example, interactions can be observed between N(2)…O(1)d at 3.1018(2) Å in length linking all chains down the c-axis and a weak interaction between O(3)a…C(1) at 3.405 Å in length thereby cross linking

the chains. These support the presence of hydrogen bonding and further interactions can be found in Table 5.24.

Table 5.24 Bond lengths found in (18) between acceptor and donor atoms containing hydrogen bonding.

symmetry codes: $a = x+1/2, -y+1, z, b = x+1/2, -y+2, z, c = x+1, y, z, d = -x+1/2, y, -z+1$

	Length /Å		Length /Å
N(1)-O(3)	3.137(2)	N(2)-O(2)[c]	3.245(2)
C(1)-O(3)[a]	3.405(2)	N(2)-O(1)[d]	3.018(2)
N(2)-O(1)[b]	3.093(2)		

Studies on structures with bidentate sulfate ions have not been conducted extensively with transition-metal sulfates and how one bonding preference is favoured over another. Such studies have only been conducted using actinide metal complexes. For example, Extended X-ray Absorption Fine Structure analysis (EXAFS) [308] of Pu(IV)(η^2-O$_2$SO$_2$H)$^{3+}$/Pu(IV)(η^2-O$_2$SO$_2$)$^{2+}$ and An(IV)(SO$_4$)$_x$$^{(4-2x)}$ sulfate complexes demonstrates that sulfate ions act as both a monodentate and bidentate ligands. There is an increase in the presence of bidentate sulfate anions within actinide complexes, ongoing from Th to Pu because of increased Lewis acidity. Mulliken population calculations also showed the charge separation between the metal centre and the sulfate is at its greatest (with a large electronic interaction) with the more acidic actinides. The bidentate mode is rarely seen in transition-metal based compounds and therefore no analogous studies with transition metals and sulfate anions have been reported. There are however a two structures containing the bidentate sulfate mode within Bailen's [305] work; the 2-D structure of [Mn(SO$_4$)$_2$](enH$_2$) and the 3-D structure of [Mn$_2$(SO$_4$)$_2$(en)$_2$].

The synthesis of crystal (18) was carried out in the presence of 1,4-diaminobutane in the reaction mixture but the product contains deta molecules. This suggests that the decomposition of amine occurs during the synthesis of compound (18). The breakdown of tren molecules was observed in compounds (1) and (7) during analysis by TGA and it has been shown that under thermal treatment, larger amines can break down to ethylenediamine in a distillation column when left between ($503 \leq$ T/K ≤ 673) [254] and rearrangement of polyamines can occur in solvothermal reactions in the presence of metal ions [255]. The reaction to produce (18) was also investigated using deta in place of dab (CoSO$_4$.7H$_2$O (0.3438g 1.24 mmol), diethylenetriamine (deta) (0.4 ml, 3.70 mmol), 18 M H$_2$SO$_4$ (0.1 ml, 1.8

mmol) and H_2O (0.1 ml, 5.56 mmol)), to see if the same structure could be produced. Interestingly, compound **(14)** (see section 5.2.1) was produced. The reaction conditions were 5 days longer and at a higher temperature than the reactions that were initially conducted to form **(14)**. It appears that for the formation of structure **(18)** the use of dab is required which then breaks down under reaction conditions.

5.5 3-Dimensional Sulfate Structures

5.5.1 [Co(SO$_4$)(dab)] (19)

5.5.1.1 Synthesis

Compound [Co(SO$_4$)(dab)] **(19)** was synthesised from a mixture CoSO$_4$·7H$_2$O (0.3457g 1.23 mmol), 1,4-diaminobutane (dab) (0.4 ml, 3.98 mmol), 18 M H$_2$SO$_4$ (0.1 ml, 1.8 mmol) and H$_2$O (0.07 ml, 3.88 mmol). The reagent mixture was stirred for 10 min in a Teflon-lined stainless-steel autoclave before being heated to 473 K for 5 days using a heating rate of 1 K min $^{-1}$. The products were cooled overnight before being filtered and washed successively with ethanol and acetone inside an N$_2$ filled glove bag. Single crystals of **(19)** were produced in the form of dark pink plates along with (H$_2$dab)(SO$_4$) [307] crystalline material, only two phases appeared to be present which was confirmed though powder X-ray analysis (Figure 5.29). Moisture sensitivity was also seen in this sample, with crystals becoming partially liquified after extended time under the optical microscope.
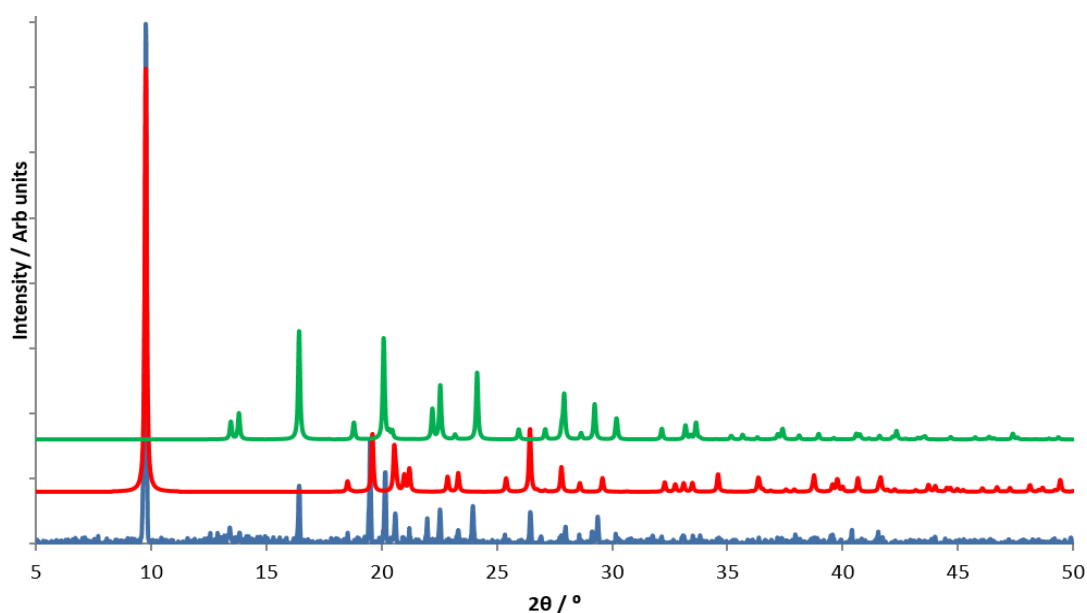
Figure 5.29: Powder X-ray diffraction pattern of **(19)**, Key: blue, bulk sample: red, calculated pattern generated from single-crystal data: green, (H$_2$dab)SO$_4$ calculated from single crystal data [307].

Single-crystal X-ray diffraction experiments were conducted at 150 K using graphite monochromated MoK$_\alpha$ (λ = 0.71073 Å) radiation. The refinement was conducted in F after being solved by Sir92 [227] and polynomial weight schemes were applied, Figure 5.30. Hydrogen atoms on the amine ligands were placed geometrically with a U[equiv] value 1.2 times the U[equiv] of the carbon to which they are attached. Crystallographic details are summarised for structure **(19)** in Table 5.25. Atomic coordinates of all non-hydrogen atoms can be found in Tables A3.6.

Table 5.25: Crystallographic data for structure [Co(SO$_4$)(dab)] **(19).**

Chemical formula	[Co(SO$_4$)(dab)]
Formula mass	243.15
Crystal Habit	plate
Crystal system	orthorhombic
Symmetry space group	*Pcam*
Temp /K	150
a /Å	9.8296(3)
b /Å	4.78679(12)
c /Å	18.1054(5)
V /Å³	851.90(4)
Z	4
μ /mm^{-1}	17.983
Total reflections ($I > 3\sigma(I)$)	788
R factor	0.0425
w*R* factor	0.0401
Goodness of fit ref	1.0434

5.5.1.2 Structure Description and Analysis

The structure of **(19)** contains one crystallographically distinct Co atom (Figure 5.30) which coordinates in a pseudo-octahedral geometry with one bidentate, two monodentate SO$_4^{2-}$ anions and two monodentate dab amine molecules. The sulfate ions bridge to other cobalt metal centres to form an inorganic layer in the (110) plane. The coordinated 1,4-diaminobutane is then used as a linker between sets of layers forming a 3-D structure (Figure 5.31).

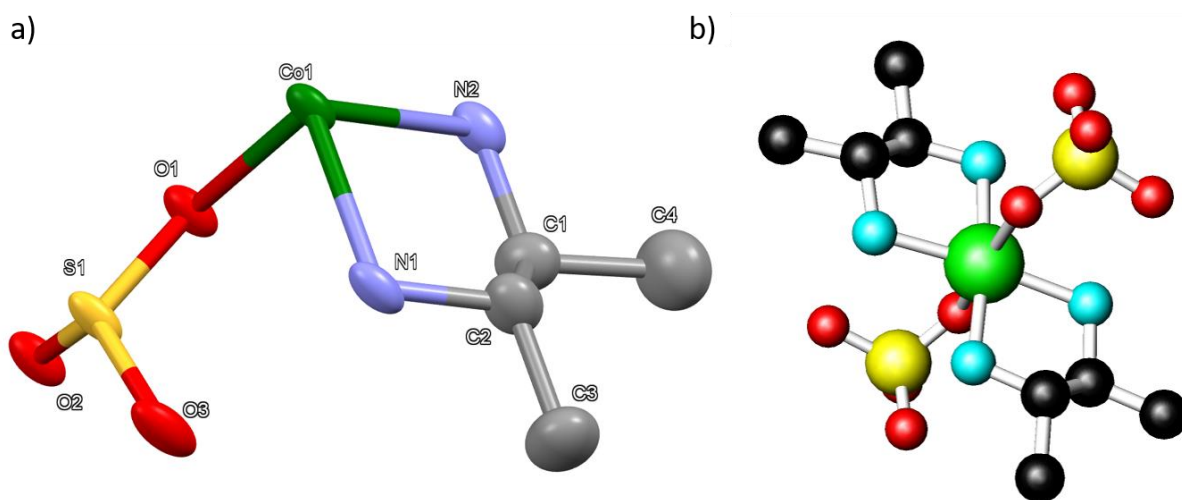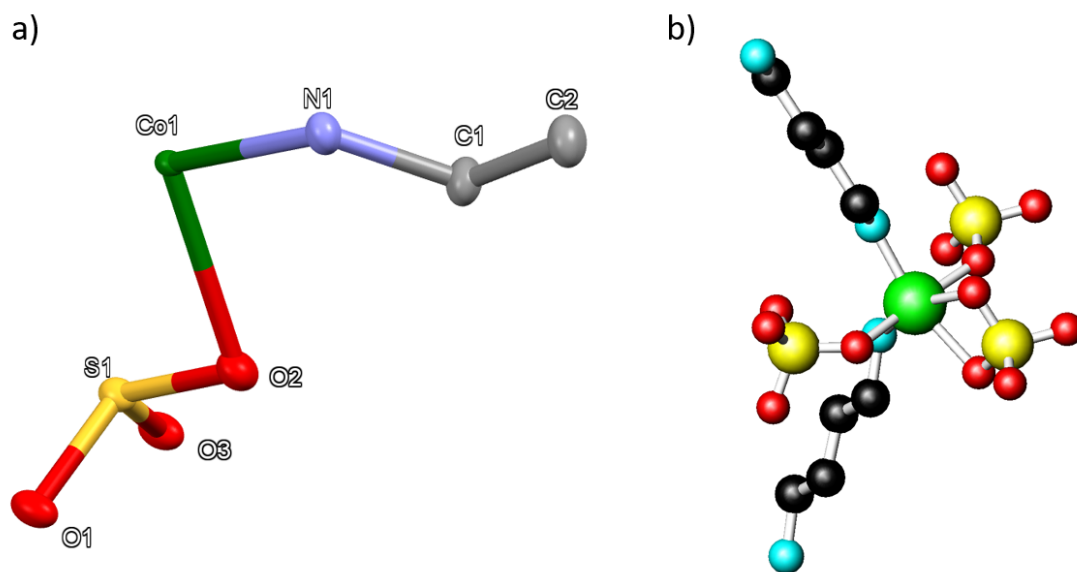Figure 5.30: (a) Asymmetric unit of **(19)** displaying thermal ellipsoids of each atom at 50 % probability and (b) the fully coordinated cobalt centre using a ball and stick model. Key: green: Co atoms, yellow: S atoms, red: O atoms, light blue: N atoms, grey: C atoms. Hydrogen atoms are omitted for clarity.
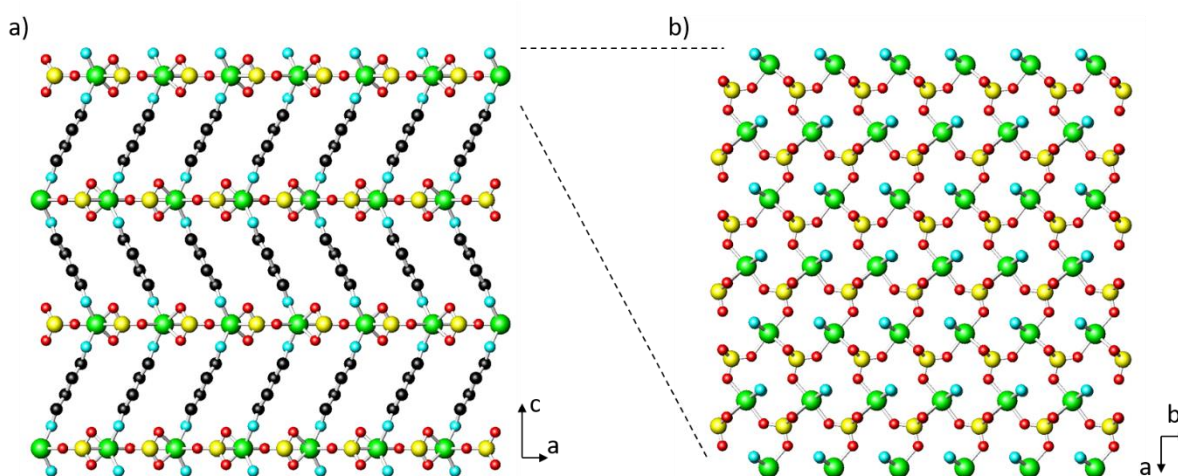
Figure 5.31: (a) The crystal packing of [Co(SO$_4$)(dab)] viewed down [010] and (b) the inorganic layer viewed down [001]. Key: green: Co atoms, yellow: S atoms, red: O atoms, light blue: N atoms, black: C atoms. Hydrogen atoms are omitted for clarity.

Bond-valence calculations produce a value of 2.12 v.u. for Co leading to the assignment of a +2 oxidation state of Co(1) within the structure. The SO$_4^{2-}$ anions produce the -2 counter balancing charge in the framework resulting in a neutral charge overall. As seen with the previous structure, [Co(SO$_4$)(deta)] the presence of bidentate sulfate leads to a distortion of

the octahedral structure which is again observed here. Bond distances here are similar to the structures investigated so far, Table 5.26. Bond angles around Co(1) in the plane of the bidentate are 64.57(9) ˚, 96.16(7) ˚ and 102.79(12) ˚ between O(2)-Co(1)-O(2*), O(2*)-Co(1)-N(1) and N(1*)-Co(1)-N(1) respectively, Table 5.27. These compare well to structure **(18)** which also contains bidentate sulfate ligands with similar bond-length and angle values.

Table 5.26 A selection of bond lengths in [Co(SO$_4$)(dab)] **(19)** and valence sums.

symmetry codes: $a = x, y, -z+3/2$; $b = x, y+1, z$; $c = x-1/2, -y+1, z$; $d = -x+1, -y+2, -z+1$

	Length /Å	vij		Length /Å
Co(1)-O2^a	2.2189(19)	0.24	O(2)-S(1)	1.4824(18)
Co(1)-O(3)^b	2.131(3)	0.31	S(1)-O(3)	1.479(2)
Co(1)-O(1)^c	2.103(3)	0.33	S(1)-O(1)	1.482(3)
Co(1)-N(1)^a	2.097(2)	0.50	N(1)-C(1)	1.479(3)
Co(1)-O(2)	2.2189(19)	0.24	C(1)-C(2)	1.523(4)
Co(1)-N(1)	2.097(2)	0.50	C(2)-C(2)^d	1.523(5)
	∑vij=	**2.12**		

Table 5.27 A selection of bond angles in [Co(SO$_4$)(dab)] **(19).**

symmetry codes: $a = x, y, -z+3/2$; $b = x, y+1, z$; $c = x-1/2, -y+1, z$

Atoms	Angle / ˚	Atoms	Angle / ˚	Atoms	Angle / ˚
O(2)^a-Co(1)-O(3)^b	86.48(8)	O(1)^c-Co(1)-O(2)	90.22(8)	O(2)-S(1)-O(2)^a	106.17(15)
O(2)^a-Co(1)-O(1)^c	90.22(8)	N(1)^a-Co(1)-O(2)	160.43(8)	O(2)-S(1)-O(3)	111.52(10)
O(3)^b-Co(1)-O(1)^c	176.10(10)	O(2)^a-Co(1)-N(1)	160.43(8)	O(2)^a-S(1)-O(3)	111.52(10)
O(2)^a-Co(1)-N(1)^a	96.16(7)	O(3)^b-Co(1)-N(1)	88.98(7)	O(2)-S(1)-O(1)	109.85(9)
O(3)^b-Co(1)-N(1)^a	88.98(7)	O(1)^c-Co(1)-N(1)	93.45(8)	O(2)^a-S(1)-O(1)	109.85(9)
O(1)^c-Co(1)-N(1)^a	93.45(8)	N(1)^a-Co(1)-N(1)	102.79(12)	O(3)-S(1)-O(1)	107.94(15)
O(2)^a-Co(1)-O(2)	64.57(9)	O(2)-Co(1)-N(1)	96.16(7)	Co(1)^b-O(3)-S(1)	133.76(16)
O(3)^b-Co(1)-O(2)	86.48(8)	Co(1)-O(2)-S(1)	94.54(9)	Co(1)^c-O(1)-S(1)	127.79(15)

Two weight losses associated with organic components were observed in the TGA of both hand-picked single crystals and the bulk sample (Figure 5.32). The second weight loss (~320 ˚C onset temperature) was assumed to be the organic amine from crystal **(19)**, as it increased upon being picked out of the bulk sample and is close to the calculated 36.25 % weight loss suggested by the crystallographically-determined formula. It still however, showed the weight loss at the 270 ˚C onset temperature (the first step) and was concluded to be contaminated. Dab has a boiling point of 300 ˚C and it is possible that either the crystals were breaking

down before the TGA forming free dab (which would be more easily removed) or, dab is present from the compound $(H_2dab)SO_4$. Due to the size of the crystals and contamination issues, no further characterisation was conducted.
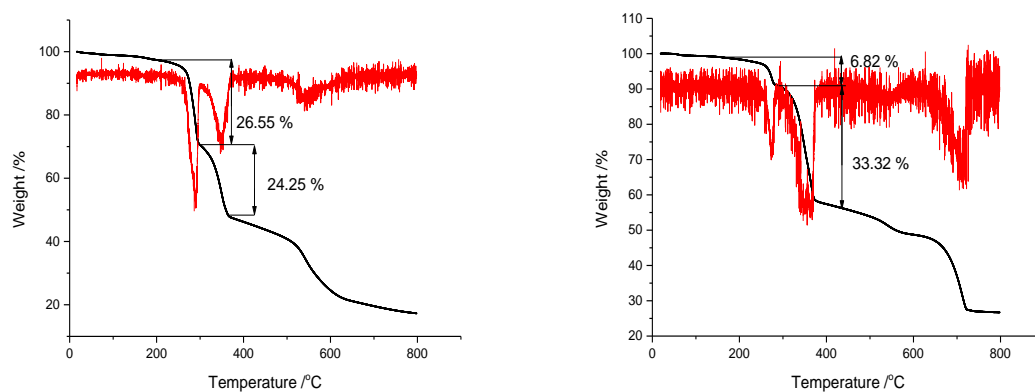
Figure 5.32: Thermogravimetric analysis data of the bulk sample containing $[Co(SO_4)(dab)]$ (left) and the crystal-picked sample of $[Co(SO_4)(dab)]$ (right) heated under N_2 (black) and the corresponding derivative (DTG) curve (red).

5.6 Conclusions

The formation of sulfate materials in this work, while difficult to handle manually, produced some interesting structures and properties, such as the magnetism present in **(14)** and **(15)**. Using a glove bag filled with N_2 for post-reaction washing and drying enabled structural characterisation to be carried out on samples that showed an extreme sensitivity to air or moisture. The use of different organic amines during synthesis is important to maximise the potential possibilities that solvothermal synthesis can form. In general, the longer the chain length of the amine molecules, the more difficult to handle they became. Tepa for example, was viscous and hardened after the reaction compared to deta which was easier to handle both before and after the reaction. The increase in viscosity made it difficult to stir and at the end of the reaction it made it even harder to remove the product from the Teflon liner.

Compound **(14)** is a discrete cobalt complex that magnetic data suggest contain Co(II), with charge balance achieved through protonation of the non-coordinated ethylamine "arm" of deta. IR data confirm the presence of amine-related bends and stretches. TGA reveals the materials undergoes a one-step decomposition at 320 ˚C, through complete loss of the organic

216

component. The diffuse reflectance measurements indicated a band gap of 4.5(2) eV of the material.

Compound **(15)**, is the only material in this work to contain an aromatic amine. The structure consists of infinite 1-D chains between which there are free 4,4'-bipy molecules located between parallel sets of coordinated 4,4'-bipy molecules within the chains through π-π interactions. While various 4,4'-bipy transition-metal containing chains have been produced previously [187, 303], this is the first to be produced with two monodentate sulfate ions and two coordinated water molecules as ligands. A band gap of 3.8(3) eV was observed and a detailed thermal breakdown of the structure can be seen through the TGA (section 5.3.1.2). The Uv/vis diffuse reflectance spectrum of **(15)** also displayed transitions arising from aromatic rings and its comparison to the chain based structure of [Co(H_2O)$_4$(4,4'-bipy)] [303] which share similar structural motif but different ligands on its Co(II) centres.

The magnetic data for compounds **(14)** and **(15)** showed that they both contain Co(II) and exhibit antiferromagnetic interactions between moments. The magnetic interactions were relatively weak with low negative theta values obtained from the Curie-Weiss expression which was applied to the inverse χ plots. Compound **(14)** also displayed spontaneous magnetism in the form of ferromagnetic behaviour at low temperatures. There is a presence of a hysteresis loop and a saturation level was calculated to be below what is expected of a true ferromagnet. The data collected from **(15)** was too noisy/weak due to such a small sample to provide further insight.

The synthesis of compound **(16)** was the most problematic, the longer chain of the tepa molecule made the amine difficult to handle. The crystals were brittle and encased in a highly viscous liquid, which could not be identified. The structure solution is the result of a poor crystal whilst being overly sensitive to moisture. Attempts to move a crystal into a capillary were not successful due to the crystals brittle nature. The structure itself contained an interesting Co-SO$_4$-Co chain with penta-coordinate "halos" of tepa.

Other sulfate chain based structures were produced: compounds **(17)** and **(18)** contain dap and deta respectively which form different structural motifs. Structure of **(17)** produces a simple straight chain motif while **(18)** contains a square-wave function looking chain with both monodentate and bidentate sulfate ligands. The presence of the deta molecules in **(18)** was accounted for by thermal degradation when using dab as a reagent. The synthesis of **(17)** produced two phases, but due to their similar shape and colouration, analysis and

217

characterisation produced conflicting data. As with **(16)**, compound **(18)** was moisture sensitive, this sample could not be handled outside of an N_2 atmosphere which meant that characterisation outside of single-crystal X-ray diffraction could not take place. The binding of the SO_4^{2-} ligand was discussed in section 5.3.4.2, and based on study [308] it was proposed that the bidentate ligand variant is seen when the metal involved is a strong Lewis acid. The literature study however is based on rare earth metals, not transition metals, and no research has been conducted thus far into transition metals. This is due to the appearance of bidentate ligands being uncommon.

One 3-D structure was produced, compound **(19)**, which contain cobalt-sulfate layers that are linked together by 1,4-diaminobutane. The production of **(19)** could not be optimised to produce enough crystals of sufficient size and when picking crystals out, the other phases began to react with the moisture in the air and stick to the handpicked crystals, thus producing a contaminated TGA plot (see section 5.3.1.2).

All sulfate structures displayed acceptor-donor interactions between protonated atoms, supporting the presence of hydrogen bonding. Additionally, all structures, apart from **(15)**, displayed distorted cobalt geometries. This was due to the rigidity of the chain-based amine reagents such as deta or tepa and even the sulfate ion when acting as a bidentate ligand. All structures displayed these distortions which were comparable to the literature for cobalt [168, 294, 295] or manganese [197, 304] metal centres.

Chapter 6: Synthesis and Characterisation of Miscellaneous Materials

6.1 Introduction

Throughout the research work undertaken (Chapters 3-5), a few additional materials were discovered which do not match the criteria required of them to be included in those chapters. This chapter therefore contains the synthesis and characterisation of [Fe(tren)][Sb$_2$S$_4$] **(20)** and [Co(tren)]$_2$[μ-Ge$_2$S$_6$] **(21)**, both with [M(tren)]$^{2+}$ counterions. In addition, [Fe(en)$_3$][FeSe$_2$] **(22)** is described from preliminary work on iron-selenide materials.

6.2 An Iron-Antimony Sulfide Analogue of [Mn(tren)]Sb$_2$S$_4$

6.2.1 [Fe(tren)][Sb$_2$S$_4$] (20)
6.2.1.1 Synthesis

Compound [Fe(tren)][Sb$_2$S$_4$] **(20)** was prepared under solvothermal conditions from a mixture of Sb$_2$S$_3$ (38 mg, 0.25 mmol), FeS (22 mg 0.25 mmol) and tris(2-aminoethyl)amine (tren) (0.9 ml). The reagent mixture was stirred for 10 minutes in a 23 ml Teflon-lined stainless-steel autoclave before being stirred, sealed and heated to 453 K for 5 days. The ramp rate for both heating and cooling was at 1 K min^{-1}. The resulting product was then filtered and washed with ethanol, water and acetone. Two different compounds formed in this reaction; one crystallised as dark orange/red blocks and had the formula [Fe(tren)][Sb$_2$S$_4$] **(20)**, whilst the other crystallised as deep-orange blocks corresponding to the known structure [Fe(tren)][Sb$_4$S$_7$] [309]. The two phases were determined to be present using both single-crystal and powder X-ray diffraction techniques. Powder X-ray diffraction analysis of the brown coloured-bulk sample confirmed the presence of [Fe(tren)][Sb$_2$S$_4$] **(20)** (Figure 6.1), [Fe(tren)][Sb$_4$S$_7$] [309], and elemental Sb. It proved impossible to separate these phases and so only analysis of the crystal structure and powder diffraction pattern can be reported.
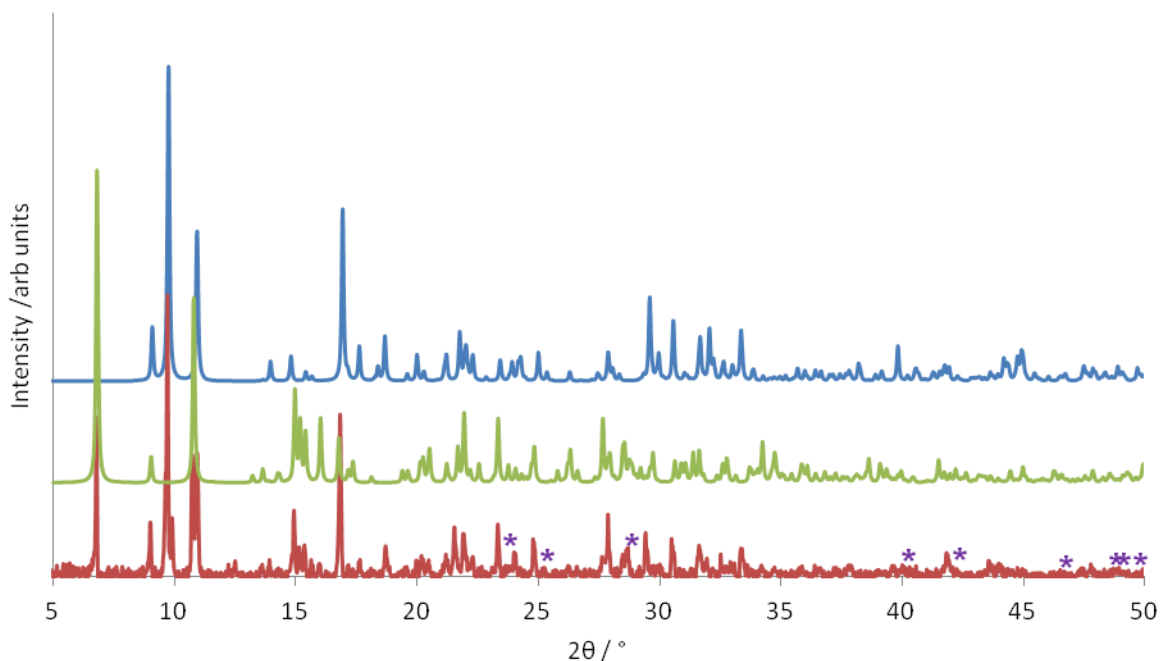
Figure 6.1: X-ray diffraction pattern of the bulk, as-synthesised product (red) which contained crystals of [Fe(tren)][Sb$_2$S$_4$] (**20**). The simulated pattern calculated from single-crystal X-ray data for (**20**) is shown above (blue) alongside the calculated pattern of [Fe(tren)][Sb$_4$S$_7$] [309] (green). Peaks in the bulk sample annotated with asterisks correspond Sb (purple).

Single-crystal X-ray diffraction experiments were conducted on an Oxford Diffraction Gemini S Ultra X-ray diffractometer fitted with an Oxford Cryosystems Cryostream cooling device. The collection was at 150 K using a monochromated CuKα radiation source (λ = 1.54184 Å). The structure was solved using SIR92 [227] and refined with the CRYSTALS suite of programs [230]. The refinement was conducted on *F* and a Chebyshev polynomial weighting scheme was applied. Hydrogen atoms on the amine ligands were placed geometrically with a U[equiv] value 1.2 times the U[equiv] of the carbon to which they are attached. Crystallographic details are summarised in Table 6.1 and atomic coordinates of all non-hydrogen atoms can be found in Table A4.1.

Table 6.1: Crystallographic data for structure [Fe(tren)][Sb$_2$S$_4$] **(20).**

Chemical formula	[Fe(tren)][Sb$_2$S$_4$]
Formula mass	573.85
Crystal Habit	Block
Crystal system	Monoclinic
Symmetry space group	$P2_1/n$
Temp /K	150
a /Å	9.5722(4)
b /Å	8.8292(4)
c /Å	19.5904(7)
β /°	98.077(4)
V /Å³	1639.27(6)
Z	4
μ /mm^{-1}	37.608
Total reflections ($I > 3\sigma(I)$)	2699
R factor	0.0341
wR factor	0.0397
Goodness of fit ref	1.0061

The structure of [Fe(tren)][Sb$_2$S$_4$] **(20)**, is related to that of [Mn(tren)]Sb$_2$S$_4$ [310] (*C*2/*c*, a = 23.4380(12), b = 8.8525(7), c = 19.1565(10) Å, β = 122.788(5) °) which contains the same chain motif, but the packing of the layers is dissimilar. The structure of **(20)** is in the space group $P2_1/n$ whilst the Mn analogue is in *C*2/*c*. It was not possible to solve the structure for the iron compound in the space group *C*2/c. Curiously, the literature reaction took 33 days to form crystals of [Mn(tren)]Sb$_2$S$_4$ whereas compound **(20)** formed, albeit at a higher temperature, within just 5 days.

6.2.1.2 Structure Description and Analysis

The structure of **(20)** (Figure 6.2) is built up of edge sharing Sb(2)S$_4{}^{5-}$ units forming an Sb$_2$S$_6$ ring. This ring then shares 2 corner sulfur atoms with 2 Sb(1)S$_3{}^{3-}$ trigonal pyramid units, in which two sulfur atoms, S(3) and S(2) bonds to an octahedral [Fe(tren)]$^{2+}$ complex. The Sb(1)S$_3{}^{3-}$ bonds its remaining sulfur atom to the Sb$_2$S$_6$ ring either, generating an infinite chain motif (Figure 6.3a).
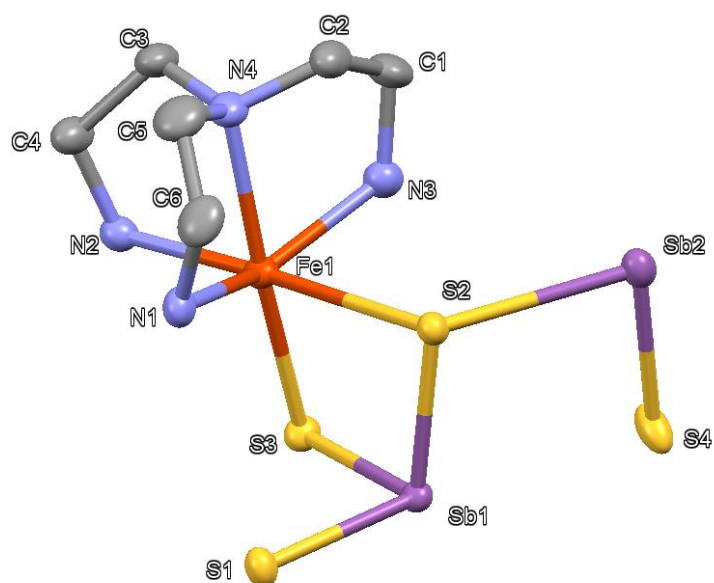
Figure 6.2: Asymmetric unit of [Fe(tren)][Sb$_2$S$_4$] (20) displaying thermal ellipsoids of each atom at 50 % probability. Key: Orange: Fe atoms, purple: Sb atoms, yellow: S atoms, light blue: N atoms, grey: C atoms. Hydrogen atoms are omitted for clarity.

Bond-valence calculations suggest that Sb(1) and Sb(2) are both in a +3 oxidation state (3.02 and 3.17 v.u, respectively) and that Fe(1) is in a +2 oxidation state (2.24 v.u.). The Sb(2)S$_4^{5-}$ units contain 2 long (2.8347(11) and 2.6225(12) Å) and 2 short bond lengths (2.4348(10) and 2.3998(12) Å), which is a common geometry among SbS$_4^{5-}$ moieties [18, 149, 311]. Antimony-sulfur bonds can range up to 3.8 Å [312] when van der Waals' radii are taken into consideration and typically bond lengths under 3 Å are taken as evidence that a bond is present (as discussed in Chapter 1). The iron complex bonds through two sulfur atoms to connect to the framework where one bond Fe(1)-S(3) 2.4218(11) Å, is shorter than the other Fe(1)-S(2) 2.8670(12) Å. Compared to the analogue [Mn(tren)]Sb$_2$S$_4$ [310], the inclusion of iron has led to an increase of the longest [M]-S bond (M = Mn in [310], Fe in (20)) by 0.08 Å in length and a reduction in 0.05 Å in the other. This leads to a 3° increase in the Sb(1)-S(3)-Fe(1) angle as the complex now needs to lean further away from the chain. The bonding of transition-metal complexes to two sulfur atoms in an antimony-sulfide structure is quite rare and has only been observed a few times, for example, in the 2-D structure [M(tren)][Sb$_2$S$_4$] (M=Co and Ni) [313]. The angles present in the equatorial plane of the complexes in (20) do not suggest a solely trigonal bipyramidal geometry due to the 145.02(15) ° angle present

between N(1)-Fe(1)-N(3), allowing some room for the Fe(1)-S(2) bond. Selected bond lengths and angles can be seen in Tables 6.2 and 6.3 respectively.

The packing of the structure relies on stacking the chains down [010] (Figure 6.3). Each row down [100] are all the same orientation (Figure 6.4a) so that when together the complexes do not clash (Figure 6.4b). The neighbouring row is parallel but staggered to fill in the space between sets of complexes seen in Figure 3b with their own complexes.

Table 6.2: A selection of bond lengths and bond-valence sums in [Fe(tren)][Sb$_2$S$_4$] **(20).**

Symmetry operations: a = -x+2, -y+2, -z+1; b = -x+2, -y+1, -z+1

	Length /Å	vij		Length /Å	vij
Sb(1)-S(1)	2.5042(11)	0.86	Sb(2)-S(4)[a]	2.6225(12)	0.63
Sb(1)-S(2)	2.4064(10)	1.13	Sb(2)-S(1)[b]	2.4348(10)	1.04
Sb(1)-S(3)	2.4376(10)	1.03	Sb(2)-S(2)	2.8347(11)	0.35
			Sb(2)-S(4)	2.3998(12)	1.15
∑vij		**3.02**			**3.17**
Fe(1)-S(2)	2.8670(12)	0.15			
Fe(1)-S(3)	2.4218(11)	0.49			
Fe(1)-N(1)	2.177(4)	0.42			
Fe(1)-N(2)	2.166(4)	0.44			
Fe(1)-N(3)	2.178(4)	0.42			
Fe(1)-N(34)	2.291(4)	0.31			
∑vij		**2.24**			

Table 6.3: A selection of bond angles in [Fe(tren)][Sb$_2$S$_4$] **(20).**

Symmetry operations: a= -x+2, -y+2, -z+1; b= -x+2, -y+1, -z+1

	Angle / °		Angle / °		Angle / °
S(1)-Sb(1)-S(2)	100.75(4)	S(2)-Fe(1)-N(1)	79.62(10)	S(3)-Fe(1)-N(4)	172.79(12)
S(1)-Sb(1)-S(3)	89.40(3)	S(3)-Fe(1)-N(1)	109.13(11)	N(1)-Fe(1)-N(4)	77.96(15)
S(2)-Sb(1)-S(3)	94.01(3)	S(2)-Fe(1)-N(2)	172.72(11)	N(2)-Fe(1)-N(4)	79.08(14)
S(4)[a]-Sb(2)-S(1)[a]	88.61(4)	S(3)-Fe(1)-N(2)	98.88(10)	N(3)-Fe(1)-N(4)	77.33(15)
S(4)[a]-Sb(2)-S(2)	175.50(4)	N(1)-Fe(1)-N(2)	93.10(15)	Sb(1)-S(1)-Sb(2)[b]	105.52(4)
S(1)[b]-Sb(2)-S(2)	91.59(3)	S(2)-Fe(1)-N(3)	80.33(10)	Sb(2)-S(2)-Sb(1)	103.08(4)
S(4)[a]-Sb(2)-S(4)	88.05(4)	S(3)-Fe(1)-N(3)	96.75(11)	Sb(2)-S(2)-Fe(1)	120.90(4)
S(1)[b]-Sb(2)-S(4)	100.31(4)	N(1)-Fe(1)-N(3)	145.02(15)	Sb(1)-S(2)-Fe(1)	84.56(3)
S(2)-Sb(2)-S(4)	87.49(3)	N(2)-Fe(1)-N(3)	106.02(15)	Fe(1)-S(3)-Sb(1)	94.35(4)
S(2)-Fe(1)-S(3)	83.67(4)	S(2)-Fe(1)-N(4)	99.20(10)	Sb(2)[a]-S(4)-Sb(2)	91.95(4)
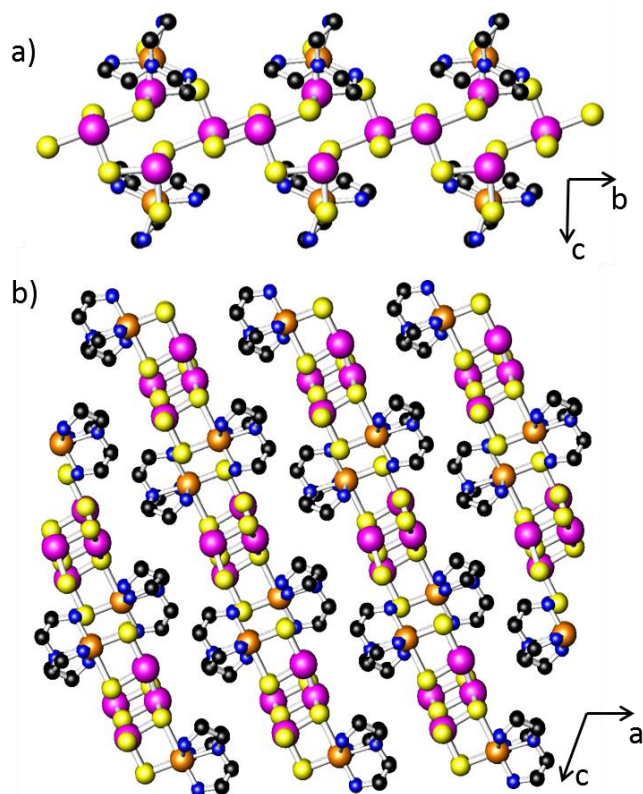
Figure 6.3: a) A single chain of (20) viewed down [100] and b) containing the stacked repeated rows down [010]. Key: Orange: Fe atoms, pink: Sb atoms, yellow: S atoms, blue: N atoms, black: C atoms. Hydrogen atoms are omitted for clarity.
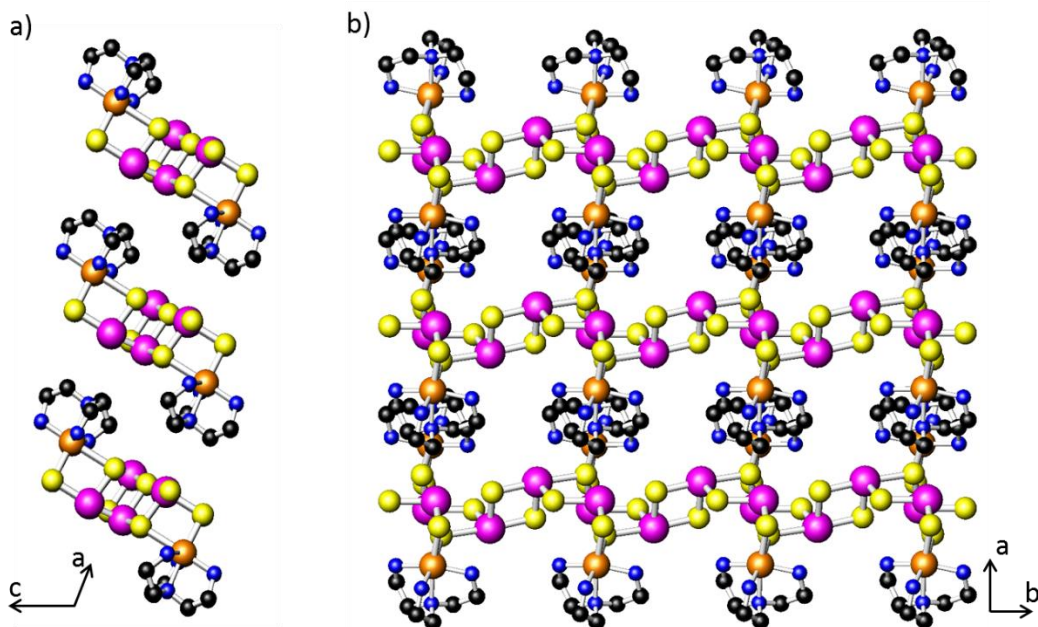
Figure 6.4: a) A row of chains of (20) viewed down [010] and b) the same 3 viewed down [001]. Key: Orange: Fe atoms, pink: Sb atoms, yellow: S atoms, blue: N atoms, black: C atoms. Hydrogen atoms are omitted for clarity.

The difference in structure packing between (20) and that of [Mn(tren)]Sb$_2$S$_4$ [310], is best observed when viewing multiple chains along a row in each structure. In the Mn analogue, every other chain in a row is rotated while each row in (20) have chains align precisely.
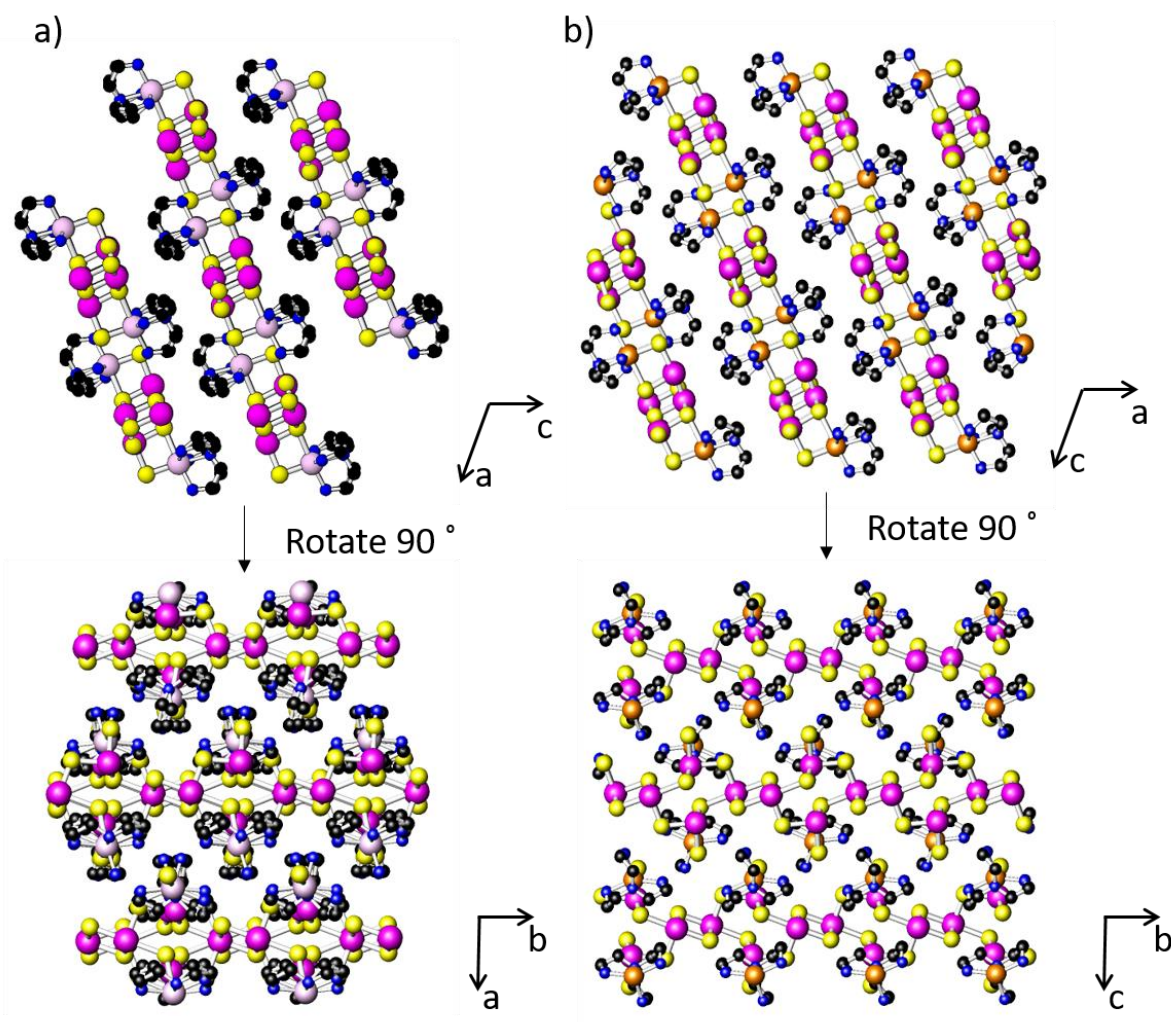
Figure 6.5: The difference when rotating packed structures horizontally by 90 degrees of a) [Mn(tren)]Sb$_2$S$_4$ [310] and b) [Fe(tren)][Sb$_2$S$_4$] (20). Key: Orange: Fe atoms, light pink: Mn atoms, pink: Sb atoms, yellow: S atoms, blue: N atoms, black: C atoms. Hydrogen atoms are omitted for clarity.

Donor-acceptor distances from opposing chains can be seen in Table 6.4, N…S interactions support the presence of hydrogen bonding within (20) to stabilise the crystal structure. In addition, weaker interactions are present between C(4)…S(4). Within the same chains, two additional interactions occur between N(3)…S(2) and N(1)…S(2) at 3.298(4) Å and 3.274(4) Å, respectively. This is another factor in the octahedral/trigonal bipyramidal geometry

discussion, the hydrogen bonding interaction would promote trigonal bipyramidal geometry, but the repulsive forces of the S atom against the two N atoms forces a heavy distortion of the Fe geometry and promotes the use of an additional bond producing a distorted pseudo-octahedral geometry, as seen with the pendant containing layered-structure of $[M(tren)][Sb_2S_4]$ (M=Co and Ni) [313]. It is also the only other compounds with the $[M(tren)][Sb_2S_4]$ formula but not structurally similar.

Table 6.4: Bond lengths found in (**20**) between acceptor and donor atoms containing hydrogen bonding.

	Length /Å		Length /Å
N(3)…S(3)	3.393(4)	N(2)…S(3)	3.506(5)
C(4)…S(4)	3.619(4)	N(1)…S(3)	3.514(4)
N(2)…S(1)	3.455(4)		

6.3 A Germanium Sulfide $[Ge_2S_6]^{4-}$ Anion

6.3.1 $[Co(tren)]_2[\mu-Ge_2S_6]$ (21)
6.3.1.1 Synthesis

Compound $[Co(tren)]_2[\mu-Ge_2S_6]$ (**21**) was prepared under solvothermal conditions from a mixture of GeO_2 (120 mg, 1.15 mmol), CoS (34 mg 0.57 mmol) S (96 mg, 3 mmol), tris(2-aminoethyl)amine (tren) (3.2 ml) and water (2 ml). The reagent mixture was stirred for 10 minutes in a 23 ml Teflon-lined stainless-steel autoclave before being stirred, sealed and heated to 433 K for 8 days. The ramp rate for both heating and cooling was at 1 K min^{-1}. The resulting product was then filtered and washed with ethanol, water and acetone. Single crystals of (**21**) in the form of purple plates were produced along with a black powder. Powder X-ray diffraction analysis (Figure 6.6) confirms the presence of (**21**) as well as Co_9S_8 and Co_3S_4.

The small crystals produced in this reaction made it very difficult to remove them manually from the bulk sample, optimisation reactions were attempted by changing reagent ratios to produce larger crystals, but they were unsuccessful. Combustion analysis of hand-picked

crystals gave; C 15.84 %, H 3.73 %, N 11.92 %, does not compare that well with the crystallographically determined formula $[Co(tren)]_2[\mu\text{-}Ge_2S_6]$ (C 19.38 %, H 4.30 %, N 15.07 %) suggesting that picking out such small crystals may have resulted in powder from other inorganic phases contaminating the sample, reducing the observed organic values. The C/N ratio of the measured value fits the crystallographically determined values supporting this proposition.
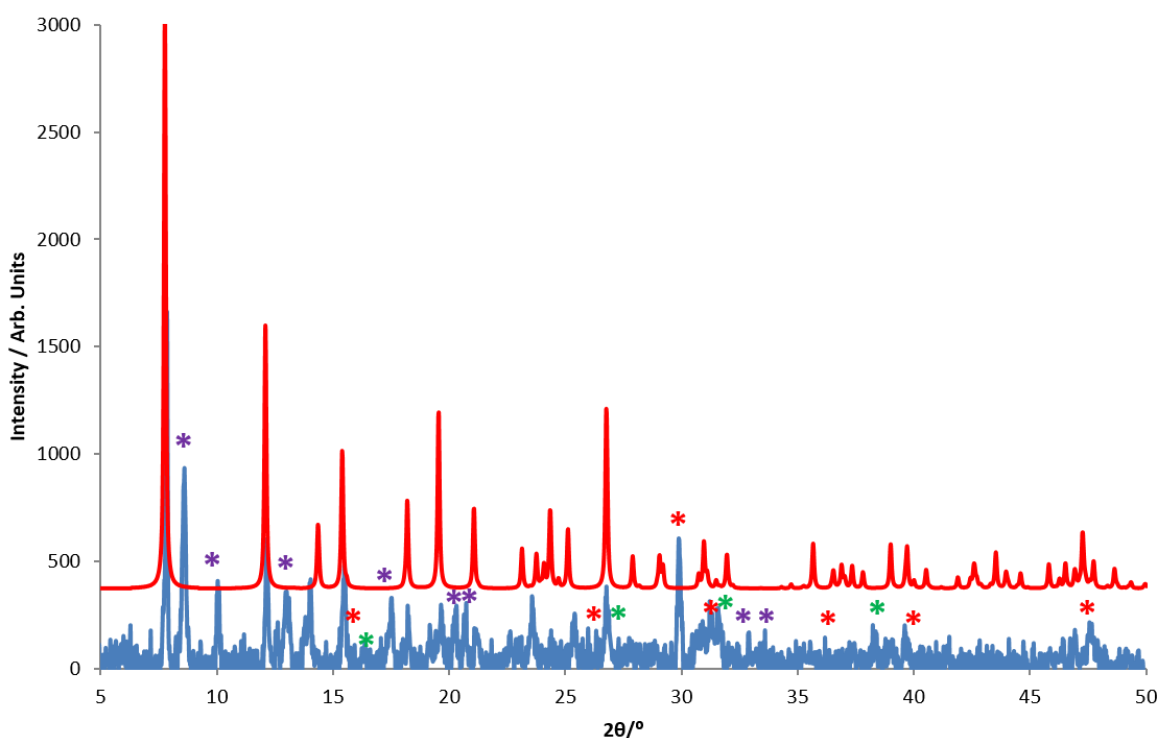
Figure 6.6: X-ray diffraction pattern of the bulk, as-synthesised product (blue) which contained crystals of $[Co(tren)]_2[\mu\text{-}Ge_2S_6]$ **(21)**. The simulated pattern calculated from single-crystal X-ray data for **(21)** is shown above (red). Peaks in the bulk sample annotated with asterisks correspond to Co_9S_8 (red), Co_3S_4 (green) and an unidentified material (purple).

Single-crystal X-ray diffraction experiments were conducted at 150 K using graphite monochromated MoK$_\alpha$ (λ = 0.71073 Å) radiation. The structure was solved using SIR92 [227] and the model refined using the CRYSTALS suite of programs [230]. The model was refined in F and a Chebychev polynomial weighting scheme was applied. Some disorder was found for C atoms C(1), C(2) and C(4) of the tren molecule, which are located near *x, -y, z* symmetry sites. Therefore, each atom was modelled with 0.5 occupancy and appear split. Moving the C atoms onto the mirror plane itself results in long elongated ellipsoids. Hydrogen atoms on the amine ligands were placed geometrically with a U[equiv] value 1.2

times the U[equiv] of the carbon to which they are attached. Crystallographic details are summarised in Table 6.5 and atomic coordinates of all non-hydrogen atoms can be found in Table A4.2.

Table 6.5: Crystallographic data for compound $[Co(tren)]_2[\mu\text{-}Ge_2S_6]$ **(21).**

Chemical formula	$[Co(tren)]_2[\mu\text{-}Ge_2S_6]$
Formula mass	742.89
Crystal Habit	Purple plate
Crystal system	monoclinic
Symmetry space group	*C*2/*m*
Temp /K	150
a /Å	12.7815(7)
b /Å	9.0732(9)
c /Å	11.7769(5)
β /°	105.395(5)
V /Å³	1316.75(6)
Z	2
μ /mm^{-1}	3.993
Total reflections ($I > 3\sigma(I)$)	1610
R factor	0.0407
w*R* factor	0.0347
Goodness of fit ref	1.1668

6.3.1.1 Structure Description and Analysis

The structure is built from two GeS_4^{4-} tetrahedra sharing a common edge to form a $[Ge_2S_6]^{4-}$ unit which then bridges two trans positioned $Co[(tren)]^{2+}$ complexes (Figure 6.7). The complexes are of a 5-coordinate trigonal bipyramidal geometry using all four nitrogen sites on the tren molecule and a shared sulfur atom from the $[Ge_2S_6]^{4-}$ unit. An analogue of this structural unit was observed in $[Mn(tren)]_2[\mu\text{-}Ge_2S_6]$ [104] but was solved in *P-1* and contained the same trans positioned complexes.

228
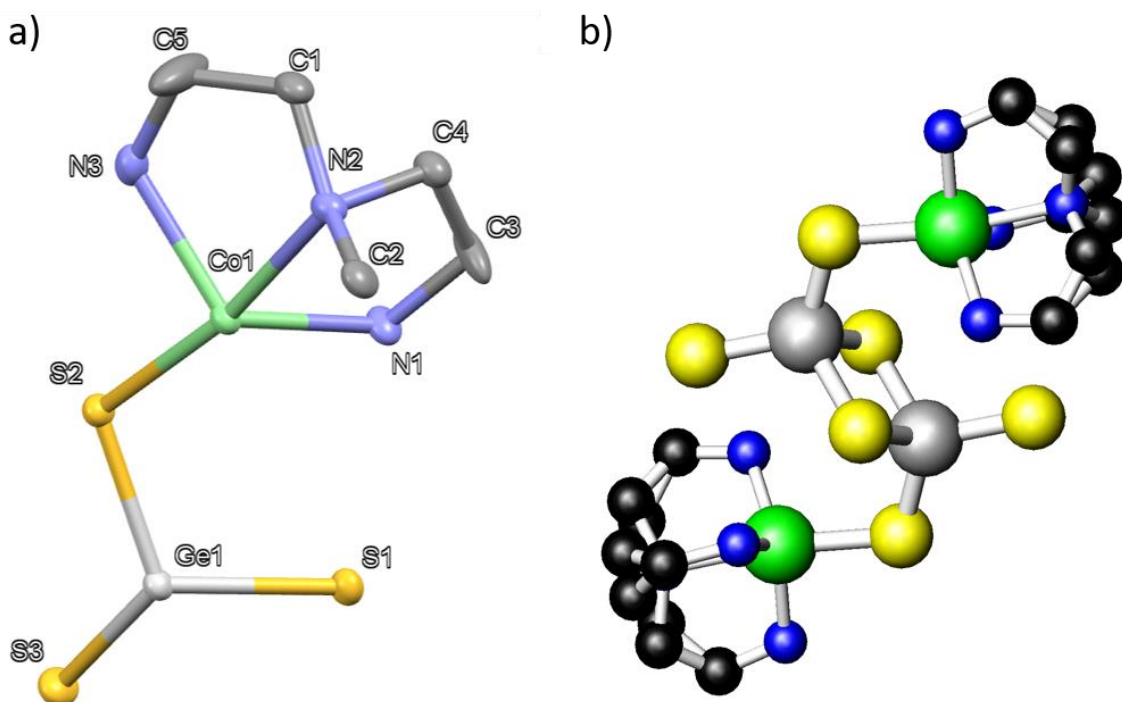
Figure 6.7: a) the asymmetric unit displaying thermal ellipsoids at 50 % probability and b) a single discrete unit of [Co(tren)]$_2$[μ-Ge$_2$S$_6$] **(21)** using a ball and stick model. Key: Green: Co atoms, light grey: Ge atoms, yellow: S atoms, blue: N atoms, dark grey/black: C atoms. Hydrogen atoms are omitted for clarity.

The bond-valence sums of the metal centres in **(21)** suggest +4 oxidation state (4.01 v.u.) for germanium and +2 (2.28 v.u.) for cobalt. This results in a charge of zero overall for [Co(tren)]$_2$[Ge$_2$S$_6$]. The complex-ligand bond lengths (Table 6.6) are comparable to those of [Co(tren)]$_2$[Sn$_2$S$_6$] [314] with the longest bond length between the sulfur atom and transition metal. Co-N bonds in the equatorial plane are between $(2.077(3) \leq d/\text{Å} \leq 2.112(4))$ Å and the longer axial bond of 2.260(4) Å. The complex is distorted due to the rigid tren molecule. The N-Co-N biting angles are between $(78.53(15) \leq \alpha/° \leq 79.64(9))$ (Table 6.7) instead of the ideal 90 ° this geometry would prefer. The Ge-S bond lengths are similar to those reported in chapter 4 and in the literature, for example [(Co(tepa)]$_2$[(μ-Ge$_2$S$_6$)] (tepa = tetraethylenepentamine) [315] and [Y$_2$(tepa)$_2$(μ-OH)$_2$(μ-Ge$_2$S$_6$)](tepa)$_{0.5}$.H$_2$O [103]. Specifically, Terminal sulfur S(1)-Ge(1) and bridging Ge(1)-S(1), Ge(1)-S(1)* bond distances are 2.1371(12) Å and 2.2856(9)-2.2856(9) Å are comparable to the analogue [Mn(tren)]$_2$[μ-Ge$_2$S$_6$], with 2.141(1) Å and 2.286(1)–2.293(1) Å for the same terminal and bridging sulfur bonds, respectively.

The Ge_2S_6 unit has only been reported a few times with $[(Co(tepa)]_2[(\mu\text{-}Ge_2S_6)]$ [315] being the first. Since then, many variations of the formula $[TM(ligand)][M_2S_6]$ (TM = Co, Fe, Ni, Mn, M = Ge, Sn) have been reported, including compounds containing Ge_2S_6 units with either discrete complexes [316, 317] or bridging complexes as seen in compound (**21**) [318, 319].

Table 6.6: A selection of bond lengths in $[Co(tren)]_2[Ge_2S_6]$ (**21**).

Symmetry operations: a = -x+1, -y+1, -z+1; b= x, -y+1, z

	Length /Å	vij		Length /Å	vij
Ge(1)-S(1)[a]	2.2856(9)	0.84	Co(1)-N(1)[b]	2.077(3)	0.53
Ge(1)-S(1)	2.2856(9)	0.84	Co(1)-S(2)	2.3758(11)	0.43
Ge(1)-S(2)	2.1896(11)	1.09	Co(1)-N(1)	2.077(3)	0.53
Ge(1)-S(3)	2.1371(12)	1.25	Co(1)-N(2)	2.260(4)	0.32
			Co(1)-N(3)	2.112(4)	0.48
∑vij		**4.01**			**2.28**

Table 6.7: A selection of bond angles in $[Co(tren)]_2[Ge_2S_6]$ (**21**).

Symmetry operations: a = -x+1, -y+1, -z+1; b = x, -y+1, z

	Angle / ˚		Angle / ˚		Angle / ˚
S(1)[a]-Ge(1)-S(1)	92.70(4)	N(1)[b]-Co(1)-S(2)	105.03(7)	N(1)[b]-Co(1)-N(3)	119.43(9)
S(1)[a]-Ge(1)-S(2)	111.09(2)	N(1)[b]-Co(1)-N(1)	110.91(16)	S(2)-Co(1)-N(3)	92.74(11)
S(1)-Ge(1)-S(2)	111.09(2)	S(2)-Co(1)-N(1)	105.03(7)	N(1)-Co(1)-N(3)	119.43(9)
S(1)[a]-Ge(1)-S(3)	111.61(3)	N(1)[b]-Co(1)-N(2)	79.64(9)	N(2)-Co(1)-N(3)	78.53(15)
S(1)-Ge(1)-S(3)	111.61(3)	S(2)-Co(1)-N(2)	171.27(11)	Ge(1)[a]-S(10)- Ge(1)	87.30(4)
S(2)-Ge(1)-S(3)	116.33(5)	N(1)-Co(1)-N(2)	79.64(9)	Co(1)-S(2)-Ge(1)	108.77(5)

The crystal packing of the discrete units can be viewed in Figure 6. Layers of staggered rows form down [100] (Figure 6.8a) which then stack on top of each other (Figure 6.8b). Due to the trans positioning of the complexes, the rows do not need to be staggered and can fit on top of each other without clashing, so one unit sits directly atop another down [001].

Interactions between hydrogen donors and acceptors are present between N(1)…S(2) and N(3)…S(1) atoms at 3.434 Å and 3.540 Å respectively. These interactions are longer than in previous structures from previous chapters suggesting a weak hydrogen bonding network.
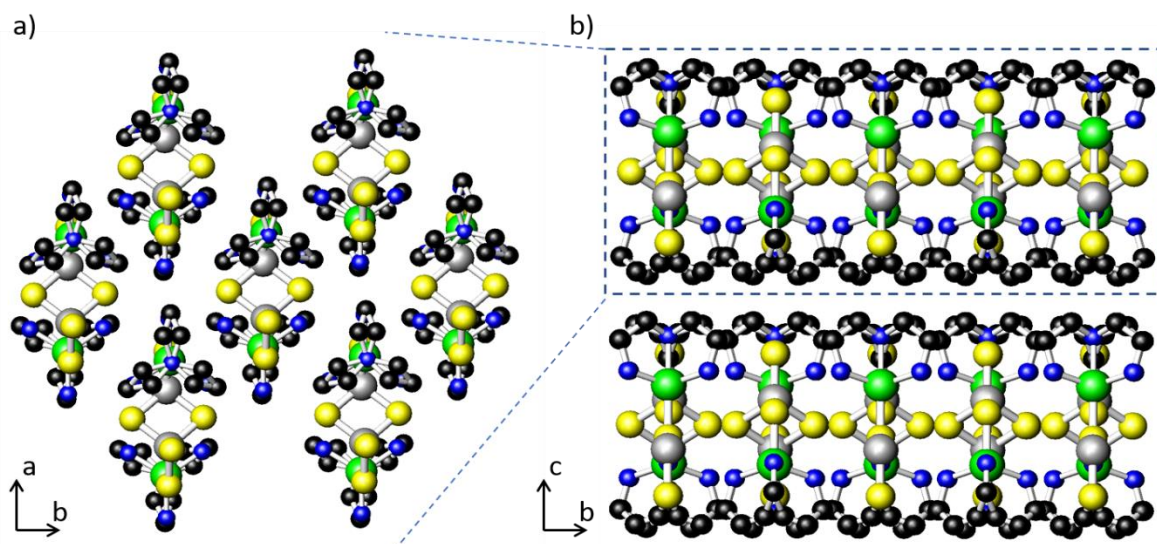
Figure 6.8: a) A layer of discrete clusters $[Co(tren)]_2[Ge_2S_6]$ **(21)** in staggered rows viewed down [001] and b) two layers of clusters stacked on top of each other viewed down [100]. Key: Green: Co atoms, light grey: Ge atoms, yellow: S atoms, blue: N atoms, black: C atoms. Hydrogen atoms are omitted for clarity.

6.4 Iron Selenides

This project was conducted over the course of 3-4 months. Considerable effort was put into this project and the solvothermal reactions attempted are listed in Appendix A4.4. Unfortunately, apart from $[Fe(tren)][FeSe_2]_2$, which has been reported previously [42], only one new phase, $[Fe(en)_3][FeSe_2]$, was prepared. This section describes the structure of this material. Due to the difficulties of synthesis it was not able to produce the material again.

Iron-selenide materials [320] have been studied over the past decade for their superconducting properties [39]. Various forms of iron-selenides, for example nano material production [321] or doped FeSe materials [322, 323, 324, 325] have recently been prepared to observe the effects of particle size or levels of impurity on superconductivity. More specifically, it is possible to prepare $[FeSe_2]$-based chains of edge-sharing tetrahedra using high-temperature solid-state synthesis [326], but this produces toxic H_2Se gas. Recently, it was discovered that the $[FeSe_2]$ chains can also be prepared in a safer environment using solvothermal synthesis, producing chain-based units, such as $Fe_3Se_4(en)_2$ [41], $[Fe(deta)_2][FeSe_2]_2$ and $[Fe(tren)][FeSe_2]_2$ [42]. These chain-based structures exhibit magnetic properties that can be controlled by choice of amine used to form it. For example, shortening Fe···Fe distances and complex-Fe-Se chain distances by switching from deta to tren changes the nearest neighbour

magnetic interactions from ferromagnetic to antiferromagnetic. Being able to tune the magnetic properties of superconductors makes this a valuable field of study. To find new materials using Fe, reactions in the literature have relied on the mineraliser, NH_4Cl, to increase the yield and to make iron more soluble.

6.4.1 [Fe(en)₃][FeSe₂] (22)

6.4.1.1 Synthesis

Compound $[Fe(en)_3][FeSe_2]$ **(22)** was prepared under solvothermal conditions from a mixture of Fe (42 mg, 0.75 mmol), Se (79 mg, 0.10 mmol) and tetraethylenepentamine (tepa) (5 ml). The reagent mixture was stirred for 10 minutes in a 23 ml Teflon-lined stainless-steel autoclave before being stirred and heated to 433 K for 5 days. The ramp rate for both heating and cooling was at 1 K min^{-1}. The resulting product was then filtered and washed with ethanol, water and acetone. A few single crystals of **(22)** in the form of black blocks were observed along with black/dark red powder. Powder X-ray diffraction analysis (Figure 6.9) was conducted on the bulk sample of **(22)** but it does not contain the peaks associated with the pattern generated from single-crystal X-ray data. This suggests that this is a very minor product as the bulk sample contained mainly the starting reagent Se, a side-product of Fe_3O_4 and an unknown phase.
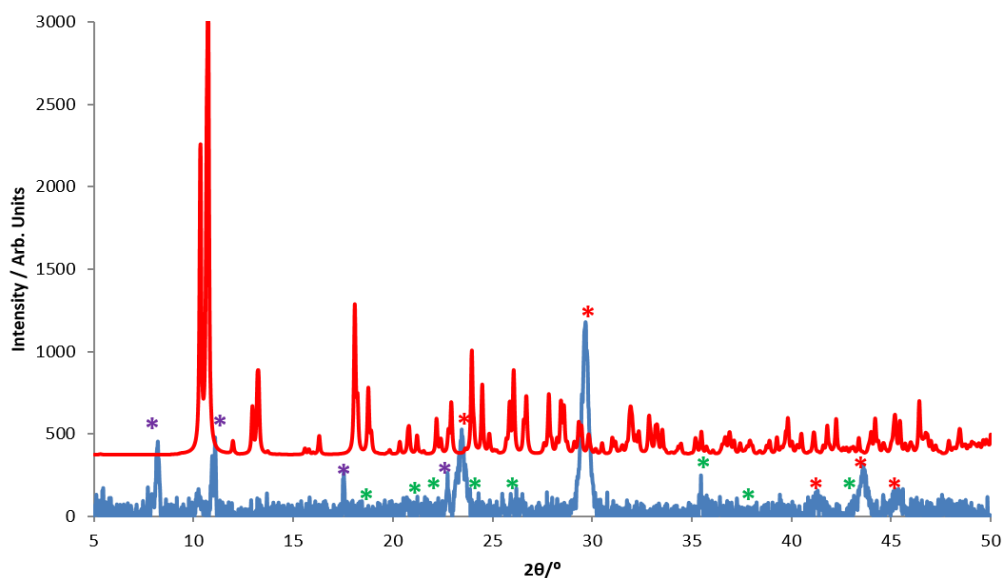
Figure 6.9: X-ray diffraction pattern of the bulk, as-synthesised product (blue) which contained crystals of $[Fe(en)_3][FeSe_2]$ **(22)**. The simulated pattern calculated from single-crystal X-ray data for **(22)** is shown above (red). Peaks in the bulk sample annotated with asterisks correspond to Se (red), side-product Fe_3O_4 (green) and an unidentified material (purple).

232

Single-crystal X-ray diffraction experiments were conducted at 150 K using graphite monochromated MoK$_\alpha$ (λ = 0.71073 Å) radiation. The structure was solved using SUPERFLIP [228] and the model refined using the CRYSTALS suite of programs [230]. The model was refined against F and a Chebychev polynomial weighting scheme was applied. All carbon and nitrogen atoms were refined isotropically due to disorder, U_{ij} restraints were used across all atoms in the organic molecule but it did not improve the thermal parameters. Attempting to solve this structure in space groups of higher symmetry have not succeeded. Hydrogen atoms on the amine ligands were placed geometrically with a U[equiv] value 1.2 times the U[equiv] of the carbon to which they are attached. The asymmetric unit can be found in Figure 6.10, crystallographic details are summarised in Table 6.8 and atomic coordinates of all non-hydrogen atoms can be found in Table A4.3.

Table 6.8: Crystallographic data for [Fe(en)$_3$][FeSe$_2$] **(22).**

Chemical formula	[Fe(en)$_3$][FeSe$_2$]
Formula mass	663.70
Crystal Habit	Black block
Crystal system	monoclinic
Symmetry space group	$P2_1$
Temp /K	150
a /Å	9.7444(7)
b /Å	11.3733(10)
c /Å	16.6290(19)
β /°	92.417(8)
V /Å³	1841.3(2)
Z	2
μ /mm^{-1}	10.234
Total reflections ($I > 3\sigma(I)$)	3302
R factor	0.0581
wR factor	0.0544
Goodness of fit ref	1.1141
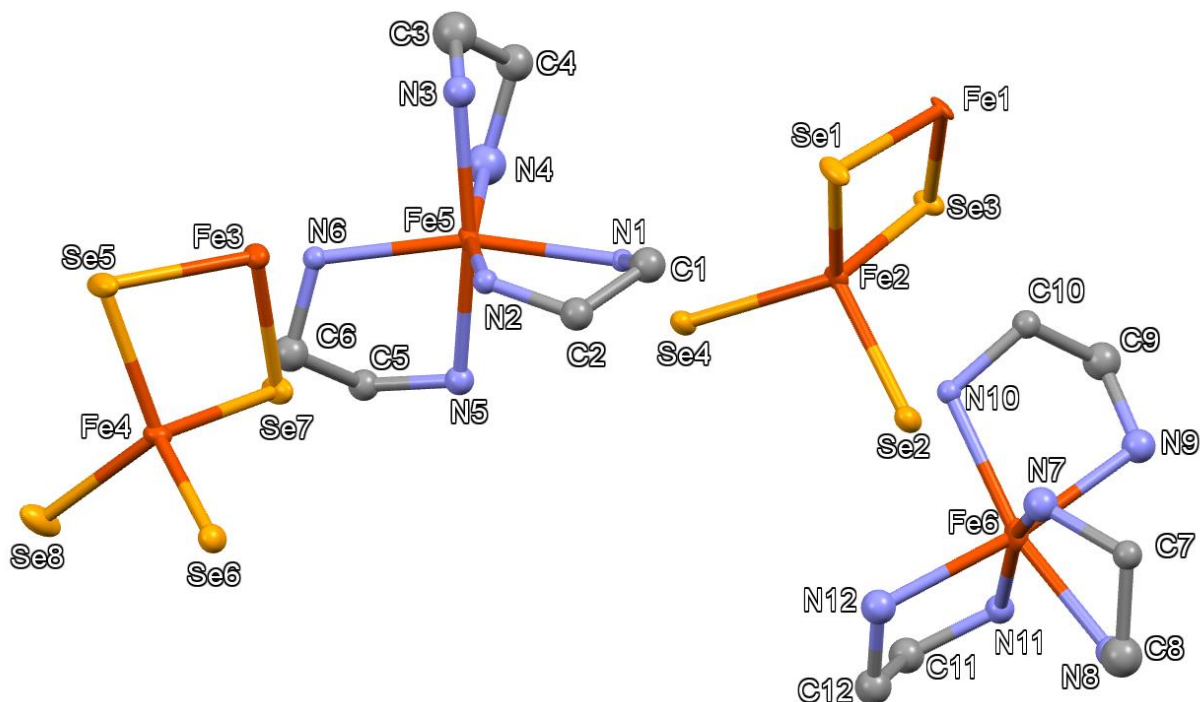
Figure 6.10: Asymmetric unit of [Fe(en)₃][FeSe₂] **(22)** displaying thermal ellipsoids at 50 % probability and spheres. Key: Orange: Fe atoms, dark yellow: Se atoms, blue: N atoms, grey: C atoms. Hydrogen atoms are omitted for clarity.

6.3.1.2 Structure Description and Analysis

The inorganic component present in **(22)** contains edge sharing $FeSe_4^{5-}$ tetrahedra linked to form infinite $[FeSe_2]^{2-}$ chains. Surrounding the chains are pseudo-octahedral $[Fe(en)_3]^{2+}$ complexes. Metal centres within the crystal structure of **(22)** were calculated to have a bond-valence sum of +3 for Fe atoms within the inorganic chains and +2 for Fe atoms within the complexes (Table 6.9). The resulting opposing charges balance and produce a neutral charge. Bond lengths (Table 6.9) within the complex are typical for N-Fe interactions, observed between ($2.188(16) \leq d/\text{Å} \leq 2.28(2)$) which compares well to two of the other known FeSe chain-based structures $[Fe(deta)_2][FeSe_2]_2$ and $[Fe(tren)][FeSe_2]_2$ [42] containing 2.20-2.24 Å and 2.16-2.28 Å respectively for N-Fe bonds. The internal biting angles of each ligand (Table 6.10) N-Fe-N are between ($77.6(6) \leq \alpha\ /° \leq 79.9(7)$) due to their rigidity which results in a slightly distorted octahedral geometry. The Fe-Se bond lengths within the chains also compare well with the literature; values of ($2.334(4) \leq d/\text{Å} \leq 2.412(4)$) are observed in **(22)** and values of ($2.33 \leq d/\text{Å} \leq 2.41$) are observed in the literature [42].

Table 6.9: A selection of bond lengths and bond valence sums in [Fe(en)$_3$][FeSe$_2$] (22).

Symmetry operations: a = -x+1, y+1/2, -z+1; b = -x+2, y+1/2, -z

	length /Å	vij		length /Å	vij		length /Å	vij
Se(1)-Fe(1)	2.347(4)	0.83	Se(1)-Fe(2)	2.383(4)	0.76	Se(5)-Fe(3)	2.388(4)	0.75
Se(2)-Fe(1)[a]	2.354(4)	0.82	Se(2)-Fe(2)	2.356(4)	0.81	Se(6)-Fe(3)[b]	2.374(4)	0.78
Se(3)-Fe(1)	2.406(4)	0.71	Se(3)-Fe(2)	2.385(4)	0.75	Se(7)-Fe(3)	2.376(4)	0.77
Se(4)-Fe(1)[a]	2.390(4)	0.74	Se(4)-Fe(2)	2.383(4)	0.75	Se(8)-Fe(3)[b]	2.374(4)	0.78
∑vij		**3.11**			**3.08**			**3.07**
Se(5)-Fe(4)	2.386(4)	0.75	N(1)-Fe(5)	2.188(16)	0.41	N(7)-Fe(6)	2.228(17)	0.37
Se(6)-Fe(4)	2.412(4)	0.70	N(2)-Fe(5)	2.238(15)	0.36	N(8)-Fe(6)	2.210(18)	0.39
Se(7)-Fe(4)	2.374(4)	0.78	N(3)-Fe(5)	2.223(19)	0.37	N(9)-Fe(6)	2.28(2)	0.32
Se(8)-Fe(4)	2.334(4)	0.86	N(4)-Fe(5)	2.22(2)	0.38	N(10)-Fe(6)	2.255(17)	0.34
			N(5)-Fe(5)	2.273(18)	0.33	N(11)-Fe(6)	2.218(17)	0.38
			N(6)-Fe(5)	2.214(16)	0.38	N(12)-Fe(6)	2.232(19)	0.37
∑vij		**3.09**			**2.23**			**2.17**

Table 6.10: A selection of bond angles in [Fe(en)$_3$][FeSe$_2$] (22).

Symmetry operations: a = -x+1, y+1/2, -z+1; b = -x+2, y+1/2, -z; c = -x+1, y-1/2, -z+1

	Angle / °		Angle / °		Angle / °
N(1)-Fe(5)-N(2)	78.2(6)	N(1)-Fe(5)-N(6)	165.4(6)	Fe(3)[b]-Se(6)-Fe(4)	74.76(12)
N(1)-Fe(5)-N(3)	99.7(6)	N(2)-Fe(5)-N(6)	95.9(6)	Fe(3)-Se(7)-Fe(4)	75.19(10)
N(2)-Fe(5)-N(3)	87.4(6)	N(3)-Fe(5)-N(6)	93.4(6)	Fe(3)[b]-Se(8)-Fe(4)	76.21(13)
N(1)-Fe(5)-N(4)	91.7(7)	N(4)-Fe(5)-N(6)	97.2(7)	Se(3)-Fe(1)-Se(4)[c]	115.60(15)
N(2)-Fe(5)-N(4)	162.2(8)	N(5)-Fe(5)-N(6)	79.2(6)	Se(3)-Fe(1)-Se(2)[c]	110.30(14)
N(3)-Fe(5)-N(4)	79.8(7)	Fe(1)-Se(1)-Fe(2)	74.19(13)	Se(4)[c]-Fe(1)-Se(2)[c]	104.37(15)
N(1)-Fe(5)-N(5)	89.0(6)	Fe(1)[a]-Se(2)-Fe(2)	75.45(13)	Se(3)-Fe(1)-Se(1)	106.10(15)
N(2)-Fe(5)-N(5)	103.2(6)	Fe(1)-Se(3)-Fe(2)	73.10(12)	Se(4)[c]-Fe(1)-Se(1)	110.39(14)
N(3)-Fe(5)-N(5)	167.6(6)	Fe(1)[a]-Se(4)-Fe(2)	74.28(13)	Se(2)[c]-Fe(1)-Se(1)	110.09(15)
N(4)-Fe(5)-N(5)	91.1(7)	Fe(3)-Se(5)-Fe(4)	74.74(10)		

The crystal packing of the chains in **(22)** can be seen in Figure 6.10. Infinite [FeSe$_2$] chains align down [010] and line up in rows (Figure 6.11a), each row alternates between one of the two crystallographically distinct chains (Figure 6.11b). Between the rows are pairs of staggered complexes separating the chains. Donor-acceptor interactions between Se…N have been observed between $(3.52(2) \leq d/\text{Å} \leq 3.87(2))$ supporting the presence of hydrogen bonding interactions. Additionally, weaker Se…C interactions have also been observed between $(3.62(2) \leq d/\text{Å} \leq 3.91(2))$.
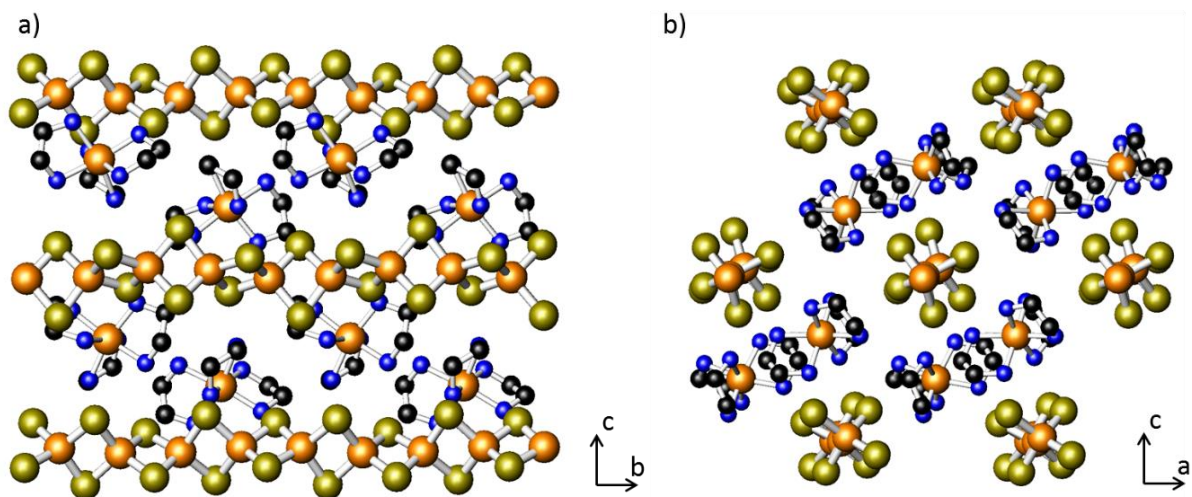
Figure 6.11: a) Three rows of chains in the structure of **(22)** viewed down [100] and b) three rows of chains viewed down [010]. Key: Orange: Fe atoms, dark yellow: Se atoms, blue: N atoms, black: C atoms. Hydrogen atoms are omitted for clarity.

6.4.1 The Reactions of Iron Selenide

As previously mentioned, the iron-selenide project did not progress as well as planned. If it was more successful, the project would have demonstrated that solvothermally producing superconducting materials from iron selenides to be a cost-effective synthesis route.

Reactions described in [42] (which produced the chain based structures of $FeSe_2(deta)_2$ and $FeSe_2(tren)$) used a mineraliser NH_3Cl to help elemental iron dissolve into solution during the solvothermal reactions. While this helped for those reactions in the literature, many which were conducted in a comparable manner using different amines did not produce any chain-based structures at all, or any FeSe framework materials. All reactions that were conducted under this project can be viewed in Table A4.4, the products from each reaction were inspected manually and any crystals (if present) were tested via single-crystal X-ray diffraction, most bulk powder were analysed through powder X-ray diffraction. Fe, Se, Fe_3O_4 and $FeSe_2$ were very common phases from the reactions conducted. Incorporation of water as a secondary mineraliser or substitute was often employed but this too did not work. Without mineraliser, it was less likely that iron would be soluble enough to produce new materials. Similar problems have also been observed in the formation of Sn_4As_3 [327]. Interestingly, the only reaction that produced a new compound was reaction JL0284 which formed $[Fe(en)_3][FeSe_2]$ **(22)**, this reaction did not use mineraliser at all. When attempting to

reproduce this structure, repeat experiments failed and optimising the reaction using varying amounts of mineraliser, varying stoichiometry and water did not produce more favourable results. Due to the unsuccessful attempts reproducing **(22)** and all other attempts at trying to produce other new materials, this project was deemed too time-consuming for little reward.

6.5 Conclusions

This chapter describes a collection of structures that were produced during the course of the PhD project. The structure of [Fe(tren)][Sb$_2$S$_4$] **(20)** displays a chain-based structure with pendants that was previously produced on using different transition metal, Fe. Unfortunately, it could not be produced without another similarly coloured crystal being present, rendering crystal picking impossible. Compound **(21)** was produced from investigating the oxothiogermanate structures of Chapter 4. While many crystals were produced, they were too small to accurately remove without the removal of some powder from the bulk sample. Attempts at producing larger crystals were not successful. Lastly, Compound **(22)** was the only structure obtained from the iron-selenide side-project. If this project was to be re-visited later, more time should be focused on reagent ratios and mineraliser type, for example, perhaps the use of NaCl or KCl as a substitution. As there have been no publications with respect to solvothermally producing chain based or framework iron-selenide structures since 2015 [42], it could be an indication that producing them solvothermally still contains a challenge to overcome.

Chapter 7: Conclusion

7.1 Overview

The work described in this thesis demonstrates that solvothermal synthesis is a powerful tool to prepare new materials (sulfates and sulfides) that may also generate new areas of research (oxothiogermanate materials).

Chapter 3 describes the results of efforts to synthesise indium containing sulfides, including $(H_{1.3}tren)[In_{2.67}Sb_{1.33}S_8]\cdot tren$ (**1**) (tren = tris(2-aminoethyl)amine), the details of which have appeared in a published paper [250]. A 3-D indium-antimony T2 supertetrahedral based framework, where the unit-cell volume can reduce in size when immersed in water, through the removal of unprotonated tren molecules and their replacement with water molecules. While the attempts to ion-exchange the protonated tren molecules with alkali-metal ions did not provide evidence for cations ions entering the framework, they showed an uptake of water molecules and the reduction in the amount of organic component. The framework in both cases, immersion in salt solution and water alone, reduced by ~9% in unit-cell volume.

Other Sb-In materials produced include two layered 2-D structural analogues $[Co(tren)(H_3tren)][In_4SbS_{10}]\cdot 3H_2O$ (**2**) and $[Co(tren)(H_3tren)][In_3Sb_2S_9]\cdot H_2O$ (**3**) and a new chain motif within $[Co(tren)]_2[Sb_2In_2S_8]$ (**4**). Varying the reaction ratios resulted in two variants of the layered structural motif with one of the atoms in the T2 supertetrahedra being replaced with an antimony atom in a crystallographically ordered manner, changing the distance between layers drastically. The chain motif of (**4**) contains a unique sequence of varying sized ring systems in a 2-3-4-3-2 arrangement, with pendant complexes attached to terminal sulfur positions. A 3-D indium sulfide $(Hdap)_6[In_{10}S_{18}]$ (**5**) was successfully synthesised using a different amine to those reported previously in the literature. Unfortunately, there were problems optimising the reactions to form compounds (**2**)-(**5**) arising from the large array of parameters in solvothermal synthesis. Reactions to form crystals of (**2**) and (**3**) demonstrated this difficulty.

A number of oxothiogermanate materials were synthesised (Chapter 4) and structurally characterised. All Ge-O-S structural motifs produced in this work are summarised in Figure 7.1. The presence of the Ge_4O_6 core has been observed in only two other applications, either having vertex positions terminated with tellurium [271] or with tungsten complexes at the vertex positions [272, 273].

Four variants of the $[Ge_4O_6S_4]^{4-}$ cluster (built from $[GeO_3S]^{4-}$ primary building units) were discovered (**6-9**) and are considered to be the basic unit of the oxothiogermanates produced in this work. Further experimentation produced two other clusters by increasing the sulfur concentration, $[Ge_4O_4S_6]^{4-}$ (**10**) and $[Ge_4O_2S_8]^{4-}$ (**11**), where primary units included $[Ge_2O_2S_2]^{4-}$, $[GeOS_3]^{4-}$ and $[GeS_4]^{4-}$. This is the first time sulfur has been bonded to the terminal positions of the Ge_4O_6 core, which is then further manipulated to produce (**10**) and (**11**) through anion exchange with sulfur.

(10)

$[Ge_4O_4S_6]^{4-}$

(11)

$[Ge_4O_2S_8]^{4-}$

(6-9)

$[Ge_4O_6S_4]^{4-}$

Ge_4O_6
core

(12)

$[Ge_9O_{14}S_8]^{8-}$

(13)

$[Co(tren)]_2[Ge_5O_9(OH)_2S_2]$
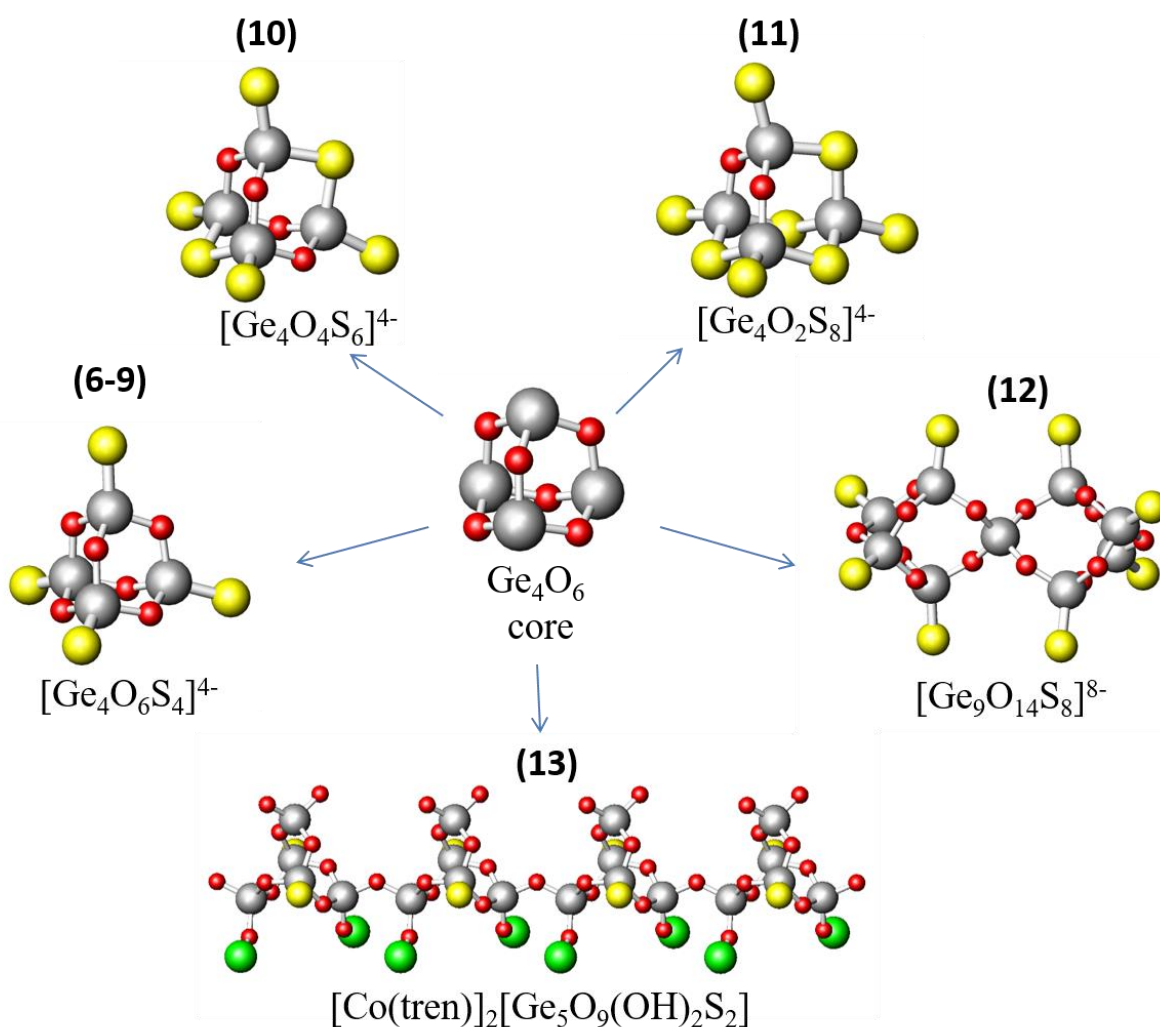
Figure 7.1: Overview of the inorganic oxothiogermanate materials produced. Key: grey: Ge atoms, red: O atoms, yellow: S atoms, green: Co atoms. Organic component of the complex omitted for clarity in (**13**).

The work reported here provide further insight into combining oxide and sulfide anions to produce materials that have the stability of an oxide but contain the reduced band gap typically found in sulfides. The thermal and optical data recorded during this work showed

that, on increasing the number of sulfur atoms within the cluster, thermal stability decreases but so too does the band gap (discussed in more depth in section 4.4).

The structure of $[Co(deta)_2]_4[Ge_9O_{14}S_8]$ (**12**) (deta = diethylenetriamine) contains the first 'fused' T2 supertetrahedral system: a large inorganic unit two $[Ge_4O_6S_4]^{4-}$ units (seen in compounds (**6-9**)) are connected through a GeO_2 molecule. Additionally, the structure of $[Co(tren)]_2[Ge_5O_9(OH)_2S_2]$ (**13**) represents the first example of a material containing an oxothiogermanate chain, suggesting that $[Ge_4O_6S_4]^{4-}$ units can be manipulated into structures containing other dimensionalities, instead of only forming discrete clusters.

With further research, more oxothiogermanate structures could be produced containing higher dimensionalities, as evidenced by the chain structure of (**13**).

Transition-metal sulfate materials produced in the work described in Chapter 5 reveal a wide range of structural motifs and different structural dimensionalities. Many of the compounds produced were difficult to handle due to moisture/air sensitivity and had to be stored under an inert atmosphere. Some compounds were particularly sensitive which placed constraints on the characterization that could be carried out for such materials.

Compound $[Co(Hdeta)_2(SO_4)_2]$ (**14**) is a discrete octahedral complex that exhibits a relatively high band gap of 4.5(2) eV, whereas the compound $(H_24,4'-bipy)[Co(H_2O)_2(4,4'-Bipy)(SO_4)_2]\cdot H_2O$ (**15**) exhibits a smaller band gap at 3.8(3) eV; this is attributed to its chain-like structure with weak aromatic π stacking between chains. The magnetic properties of both compounds were determined and shown to be antiferromagnetic materials with weak ferromagnetic contributions.

Other 1-D chains were also produced, $[Mn(tepa)(SO_4)]$ (**16**) (tepa = tetraethylenepentamine), $[CoSO_4(dap)]$ (**17**) (dap = 1,2-diaminopropane) and $[Co(SO_4)(deta)]$ (**18**), but detailed characterisation of these compounds could not be carried out due to moisture/air sensitivity issues described above. Compound, (**16**) contains an unusual seven co-ordinate Mn metal centre with tepa ligands bonding to each centre forming a 'halo'. While (**17**) contains a straight cobalt sulfate chain using dap ligands and (**18**) contains a chain with a square-wave function looking motif containing both monodentate and bidentate sulfate ligands. These compounds deteriorated too quickly to be able to remove crystals manually from the bulk sample for analysis.

One 3-D framework sulfate was also produced. The structure of $[Co(SO_4)(dab)]$ (**19**) contains a cobalt sulfate layer linked to other layers through putrescine (dab) molecules. While compound (**19**) was in fact stable, the bulk powder it resided in was not. It deteriorated in air due to moisture and stuck to the crystals during their extraction from the bulk material, rendering further characterisation impossible.

Of the additional materials prepared and described in Chapter 6, the structure of $[Fe(tren)][Sb_2S_4]$ (**20**) is analogous to that of the crystals reported in [310], where crystals of (**20**) contain a different transition metal complex and space group. $[Co(tren)]_2[Ge_2S_6]$ (**21**) exhibits a dimeric Ge_2S_6 unit that has not been reported previously with tren complex pendants. $[Fe(en)_3][FeSe_2]$ (**22**) was the only iron selenide that was produced out of ~70 reactions, all with varying parameters e.g. reagents, times and temperatures. This material adopts a new structure and follows on from previously reported compounds $Fe_3Se_4(en)_2$ [41], $[Fe(deta)_2][FeSe_2]_2$ and $[Fe(tren)][FeSe_2]_2$ [42] by containing discrete $[Fe(en)_3]^{2+}$ clusters instead of complexes that bridge between chains. Unfortunately, it could not be reproduced and so characterisation beyond single-crystal X-ray analysis could not take place.

7.2 Future Work

The work described in this thesis has contributed to already established classes of compound such as main-group sulfides and sulfates but has also generated a new class of compound, oxothiogermanates, which have not been reported previously. The sulfate materials appeared to be much easier to produce experimentally (due to ease of preparation and quantity of new crystals discovered in a short time-frame) but were more difficult to isolate as many showed a high level of sensitivity to moisture/air.

The work reported here suggests a number of areas where future efforts could be focussed.

- New oxothiogermanate materials could be investigated. So far, only discrete building blocks and a 1-D chain structure have been produced. It may be possible to produce other types of inorganic clusters/primary building units which could assemble into structures of higher dimensionality. Further research may also highlight structures that produce smaller band gaps similar to those found in oxothio structures reported previously in the form of $(N_2H_2)_2Mn_3Sb_4S_8(\mu_3\text{-OH})_2$ [27].

- The sulfate work has highlighted changes that could be implemented to improve future results. Firstly, the use of Schlenk lines for filtering samples instead of a glove bag, enabling easier manipulation, less nitrogen or argon use and increased sample longevity. Secondly, for a mixed phase sample to be separated (crystal picking), a tailor-made glove bag for microscope work would likely be required. While crude and liable to increasing the difficulty of manipulating the single crystals, this may be the only way to handle these sensitive materials in an inert atmosphere.

- Further investigation into FeSe based materials should be carried out with a more comprehensive study of mineraliser/Fe ratios.

Appendix 1 (A1) – Chapter 3 Supplementary information

Table A1.1: Crystallographic data for (H$_{1.33}$tren)[In$_{2.67}$Sb$_{1.33}$S$_8$]·tren.

Fractional Coordinates, Occupancy and Isotropic Thermal Parameters / Å^2

Atom	x	y	z	U_{equiv}	Occupancy
In(1)	0.90968(6)	0.62082(6)	0.67954(5)	0.0663	0.6675
Sb(1)	0.90968(6)	0.62082(6)	0.67954(5)	0.0663	0.3325
S(1)	0.7767(3)	0.5220(3)	0.7453(2)	0.0834	1.0000
S(2)	1	1/2	0.6060(3)	0.0951	1.0000
S(3)	0.7947(3)	3/4	5/8	0.0937	1.0000

Anisotropic Thermal Parameters / Å^2

	$U(11)$	$U(22)$	$U(33)$	$U(23)$	$U(13)$	$U(12)$
In(1)	0.0488(4)	0.0586(4)	0.0916(6)	-0.0009(4)	-0.0140(4)	0.0047(3)
Sb(1)	0.0488(4)	0.0586(4)	0.0916(6)	-0.0009(4)	-0.0140(4)	0.0047(3)
S(1)	0.0621(18)	0.0716(19)	0.116(3)	0.0113(19)	-0.0099(18)	0.0027(13)
S(2)	0.100(4)	0.108(4)	0.073(3)	0	0	0.011(4)
S(3)	0.047(2)	0.098(4)	0.141(5)	0.071(4)	0	0

	Bond distance /Å
M – S(1)	2.412(4)
M – S(1)′	2.451(4)
M – S(2)	2.382(3)
M – S(3)	2.427(3)

	Bond Angle /°
S(2) – M – S(1)	115.20(9)
S(1) – M – S(1)′	110.908(7)
S(1)′ – M – S(2)	108.35(11)
S(1) – M – S(3)	104.83(11)
S(1)′ – M – S(3)	99.22(11)
S(2) – M – S(3)	117.03(4)
M – S(1) – M′	104.36(13)
M – S(2) – M	106.2(4)
M – S(3) – M	106.52(16)
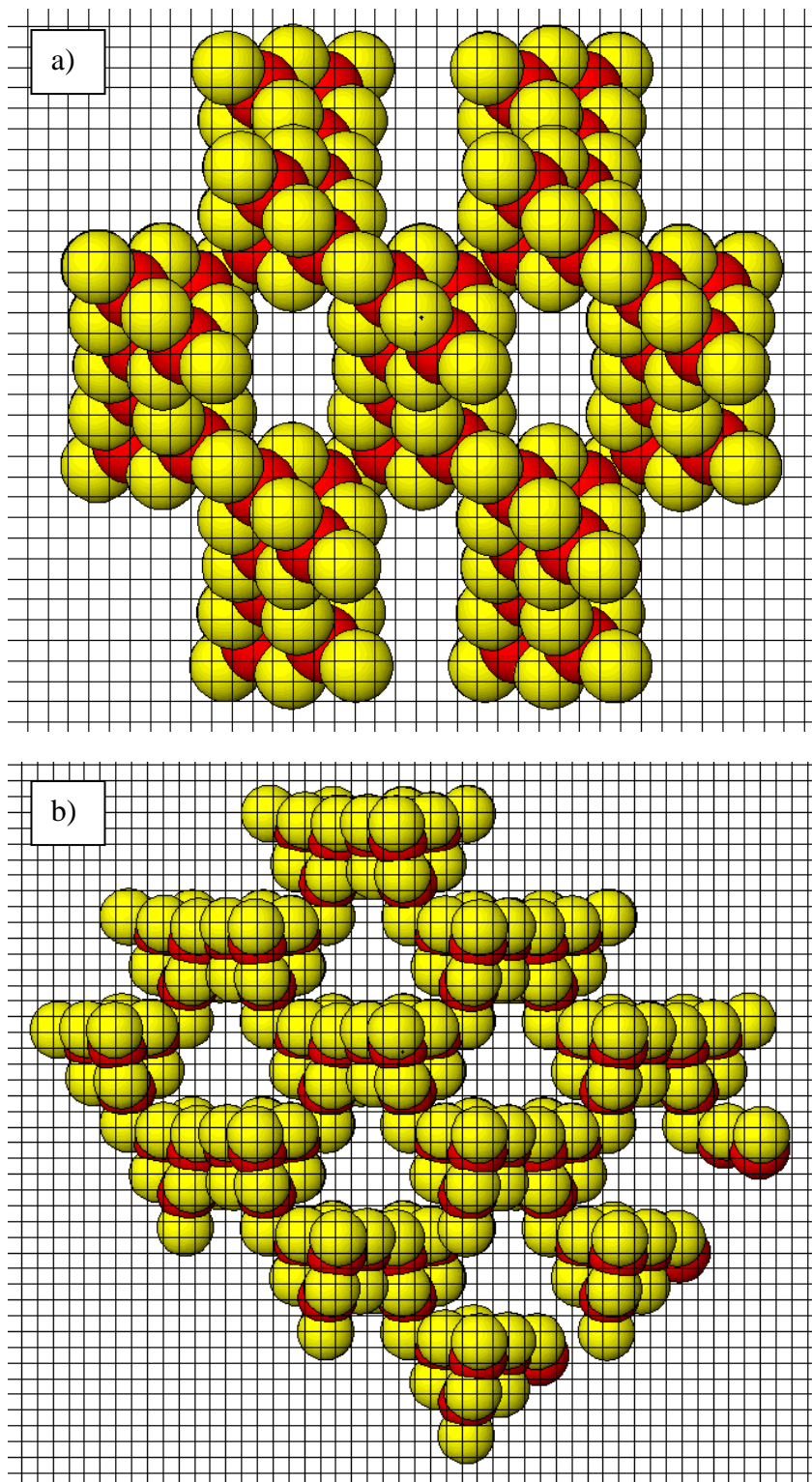
Figure A1.1: Structure of framework $(H_{1.33}tren)[In_{2.67}Sb_{1.33}S_8]\cdot tren$ drawn on a 1 Å × 1 Å grid using van der Waals' radii: a) view along [100] b) view parallel [111]. Key: red spheres: M, yellow spheres: S.
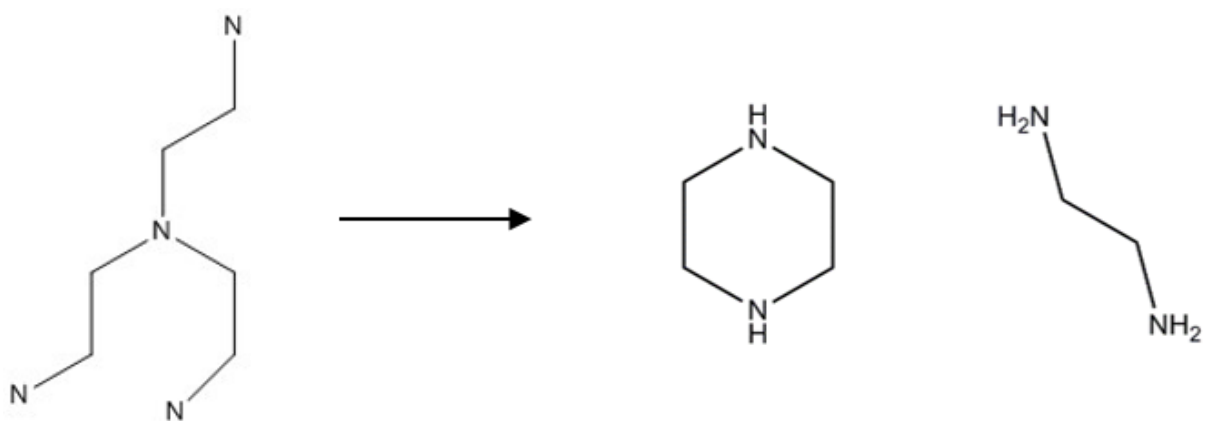
Figure A1.2: Schematic representation of the thermal breakdown of tren to piperazine and ethylenediamine
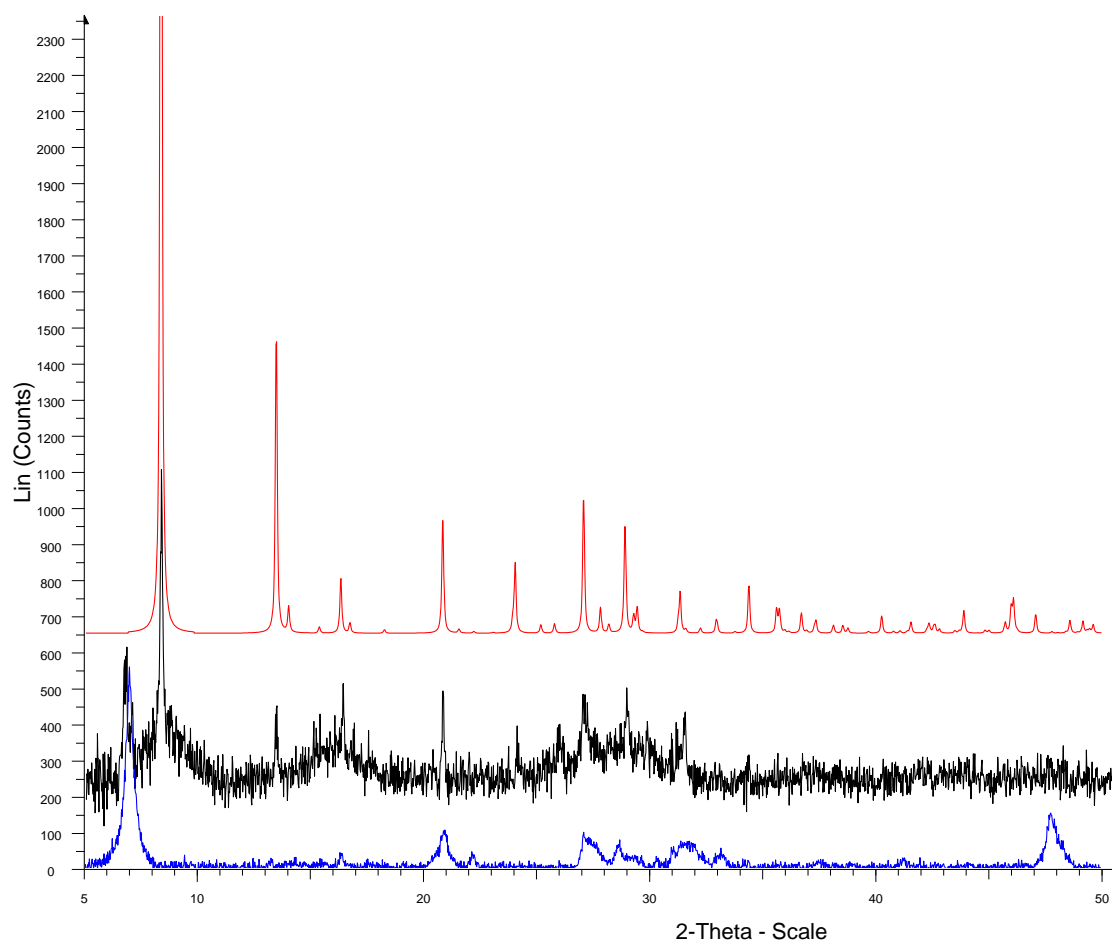
Figure A1.3: PXRD patterns after heating in TGA under nitrogen at 673 K (blue), and at 519 K (black) compared with the simulated pattern for $(H_{1.33}tren)[In_{2.67}Sb_{1.33}S_8]\cdot tren$ (red) (calculated from single-crystal data).

(Figure A1.4) Soaking Experiments: Thermogravimetric analyses of crystals of (H$_{1.33}$tren)[In$_{2.67}$Sb$_{1.33}$S$_8$]·tren after soaking in alkali-metal halide solutions and water

0.1M K$^+$ for 3 hours
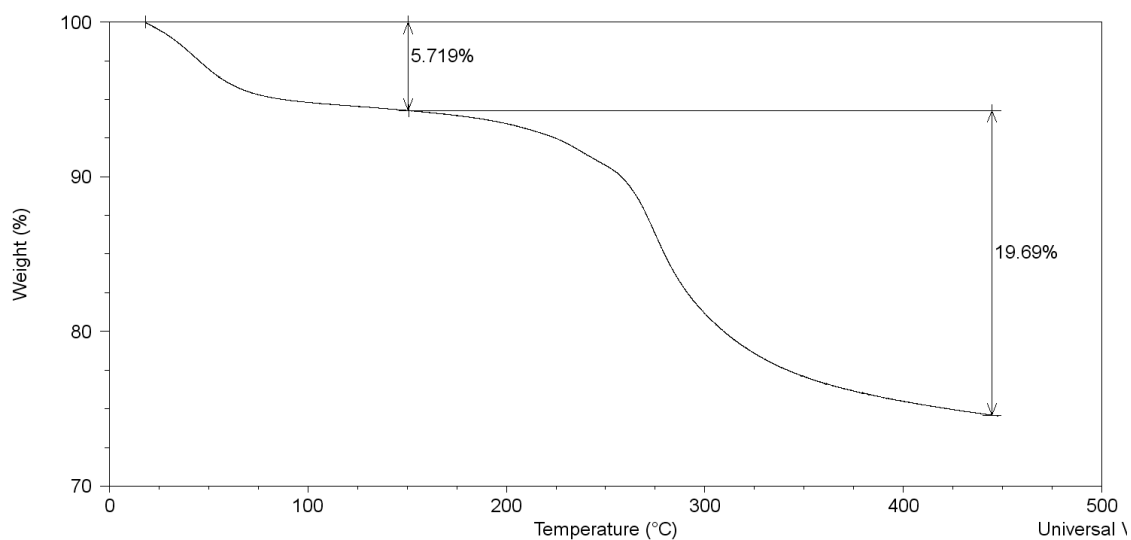
2M K$^+$ for 3 hours
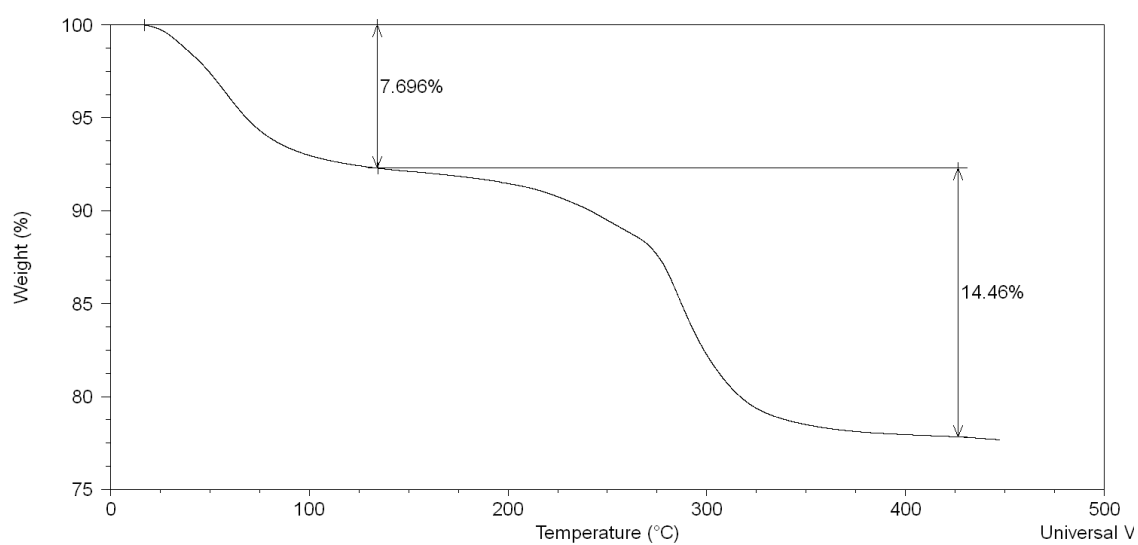
2M K$^+$ for 3 hours followed by another 3 hour reimmersion
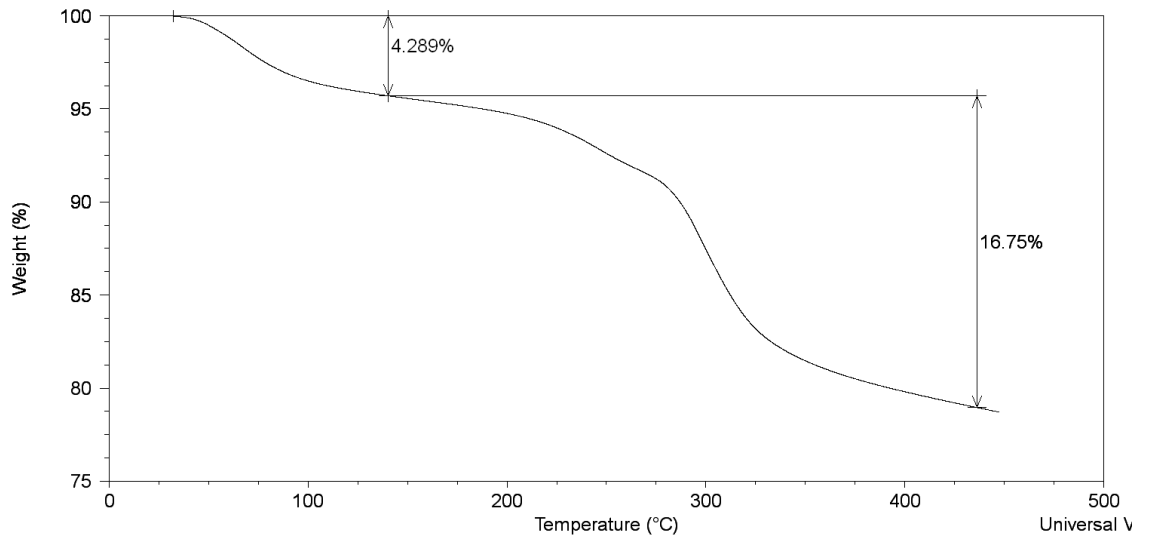
3M K$^+$ for 3 hours
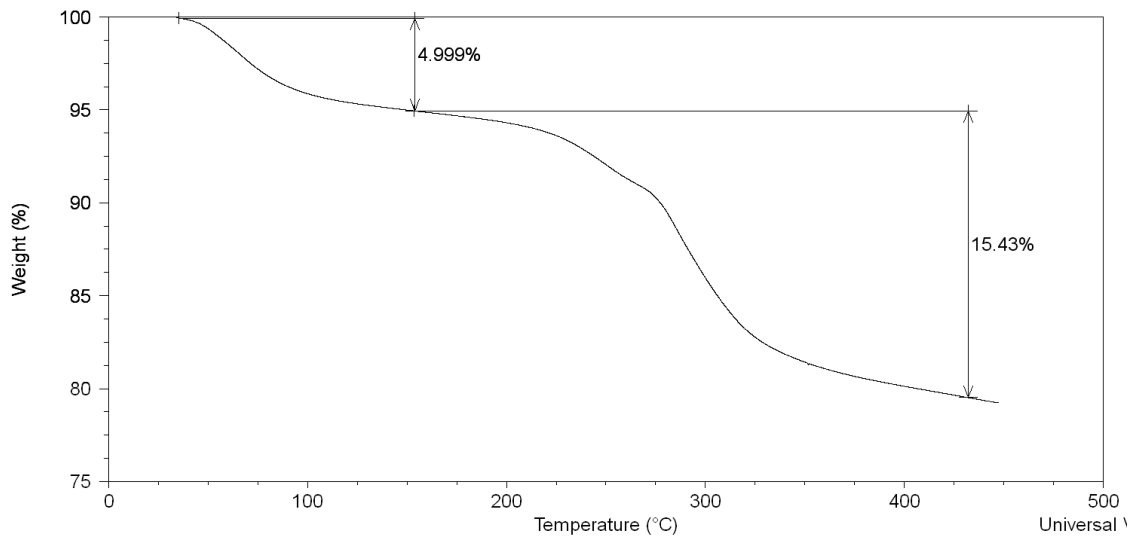
3M K⁺ for 5 days

0.1M Li⁺ for 3 hours

248
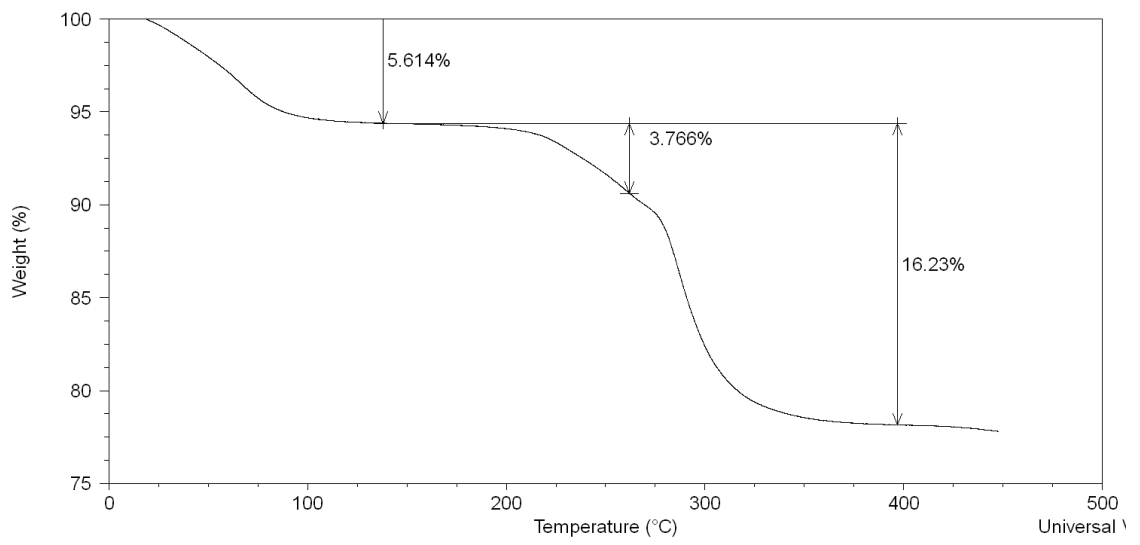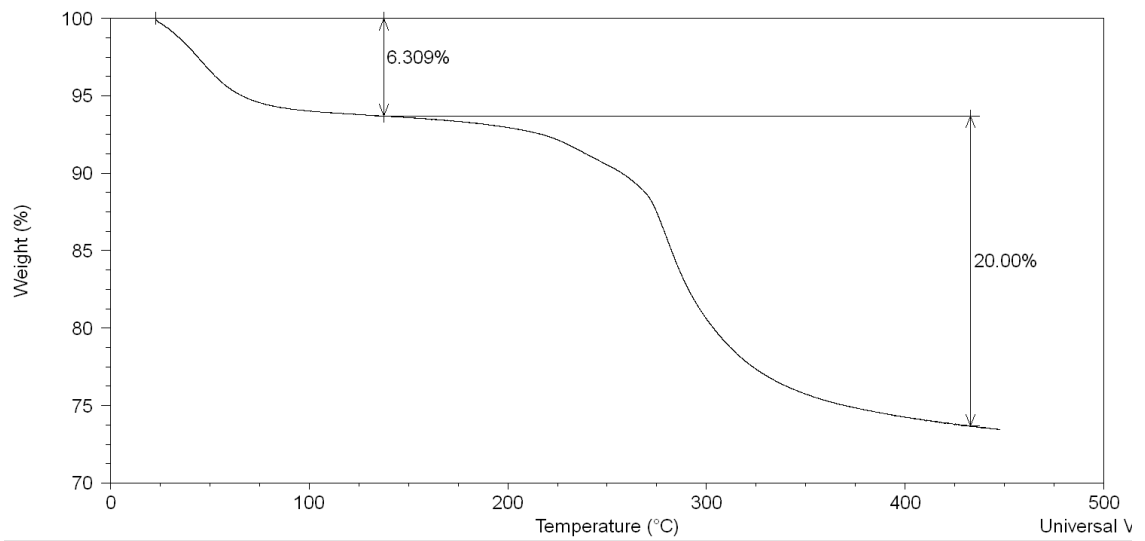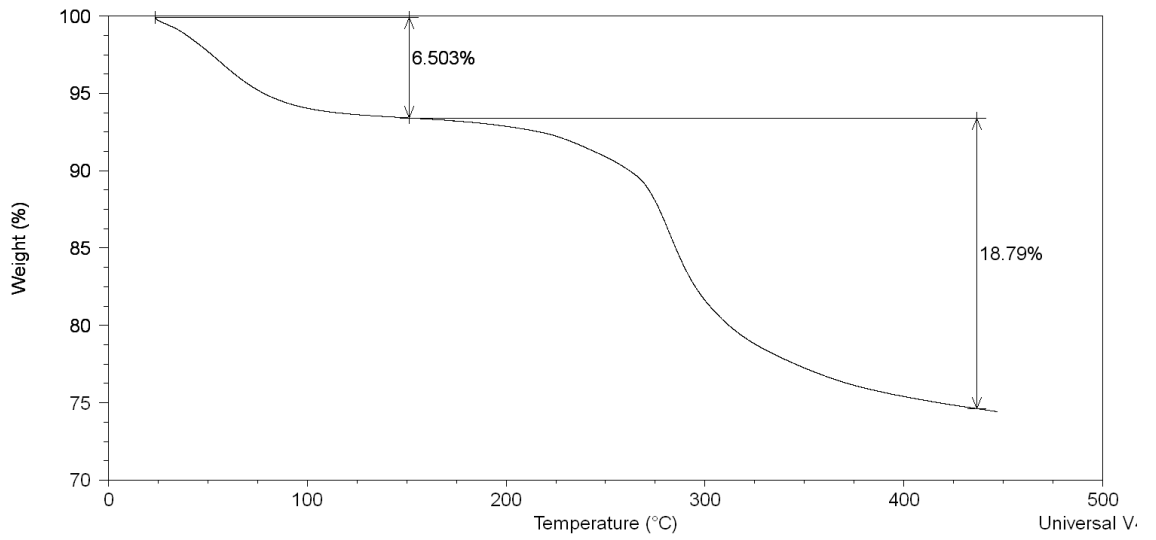
2M Li$^+$ for 3 hours

2M for 3 hours followed by another 3 hour reimmersion
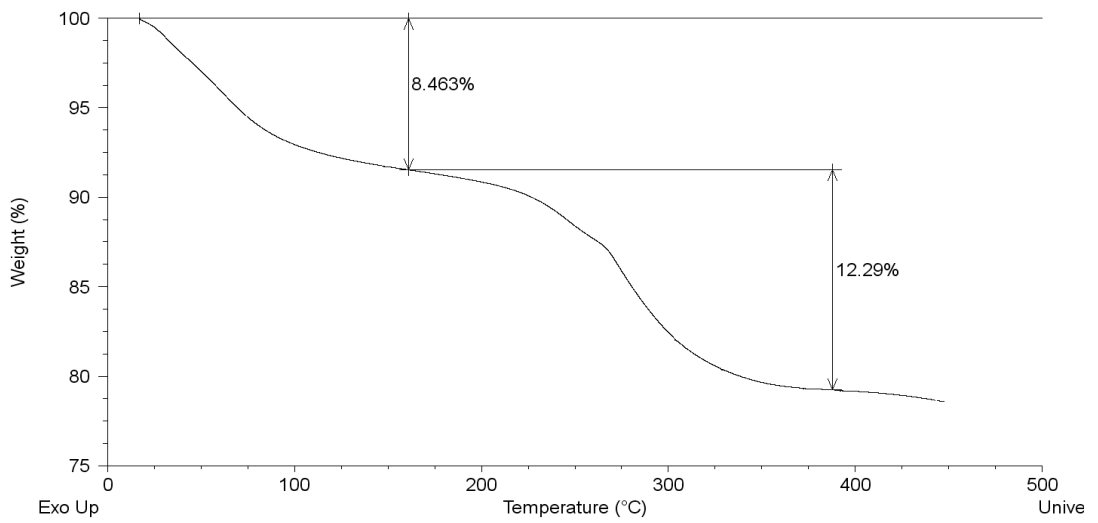
3M Li$^+$ for 3 hours

3M Li⁺ for 5 days

3M Li$^+$ for 5 days

Weight (%) vs Temperature (°C)

8.772%

16.61%

Exo Up   Un
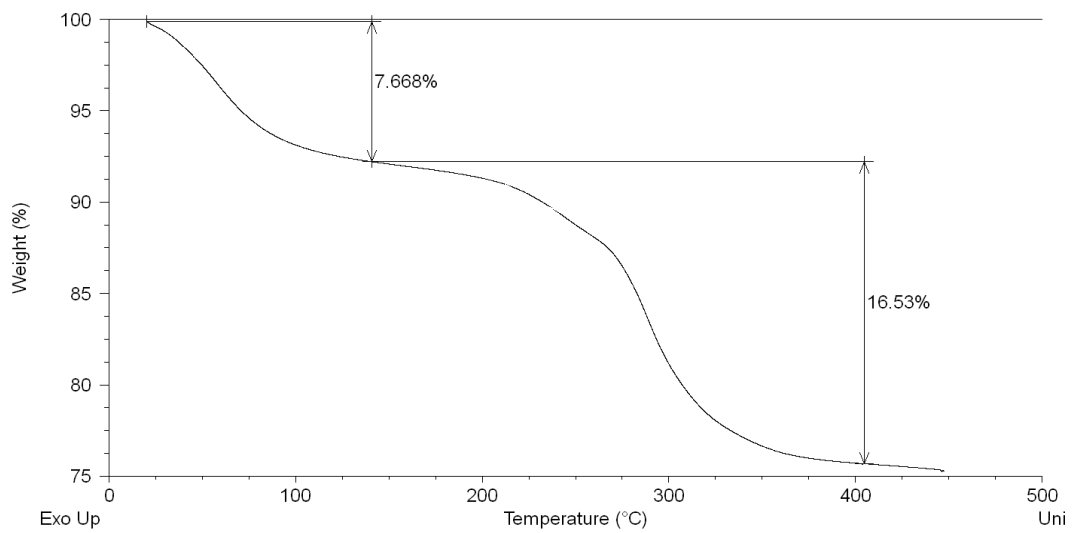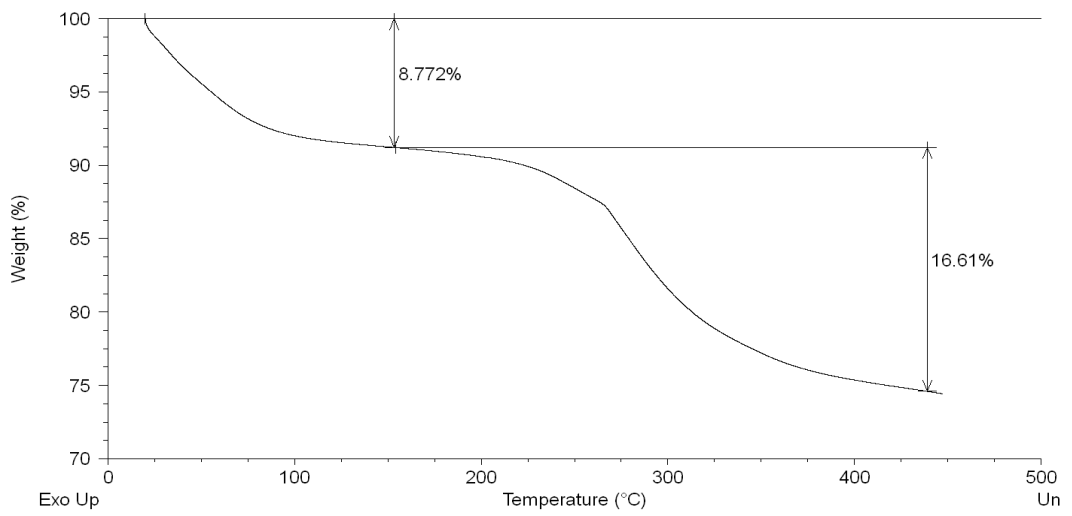
Water only at 343 K for 3 h

Water only at 343 K for 3 h

Weight (%) vs Temperature (°C)

7.396%

19.71%

Universal V4.5A TA Instruments

250
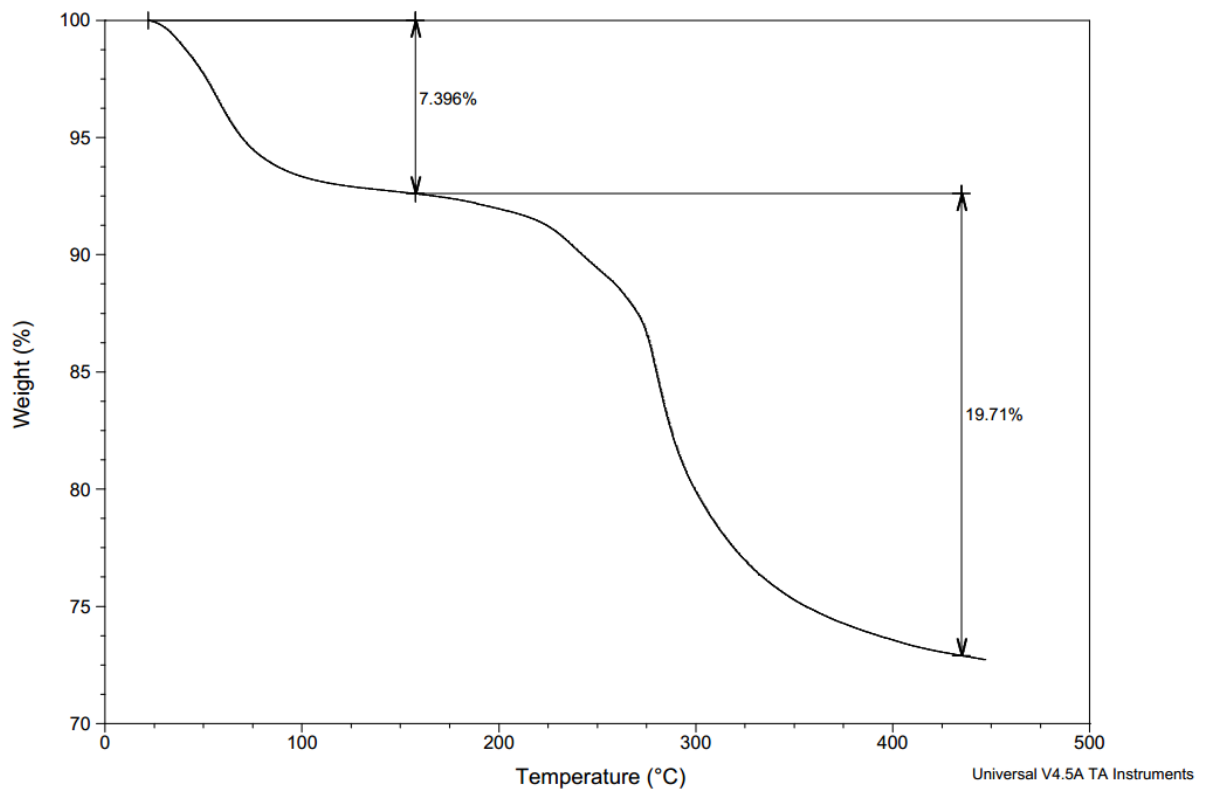
Water only at room temperature for 3 h
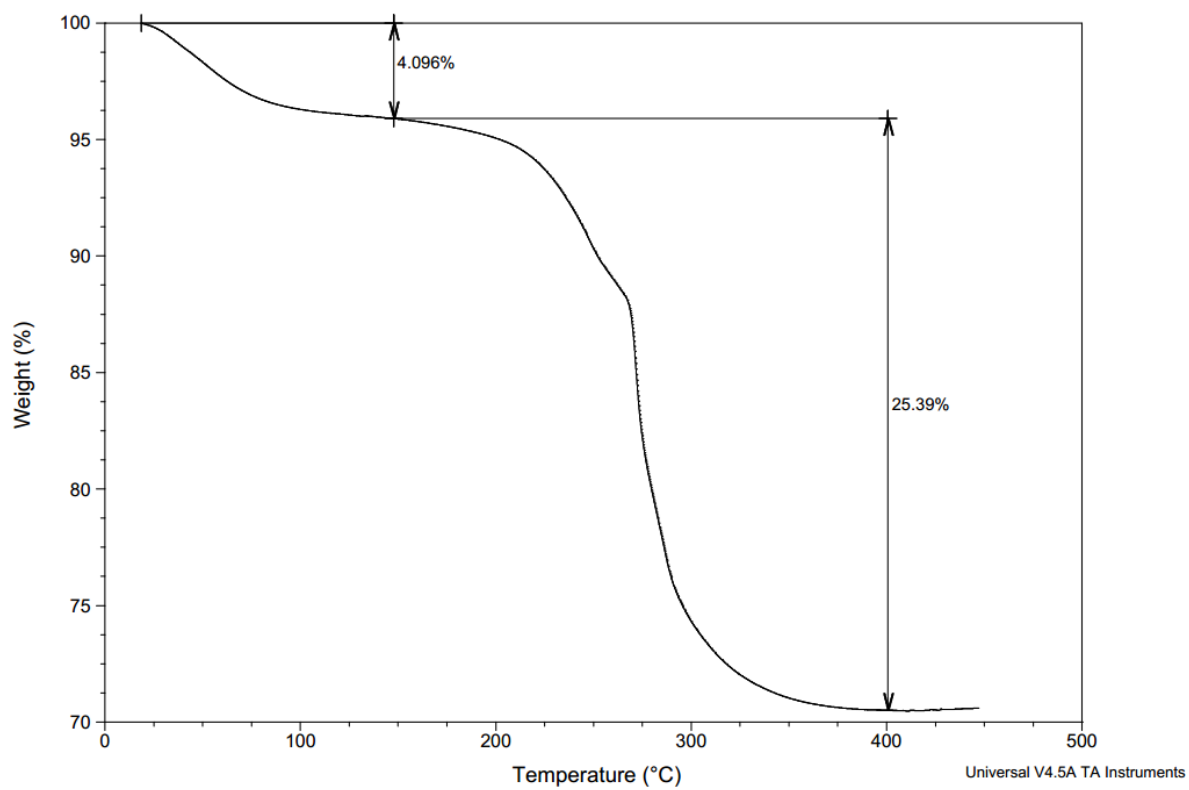
Figure A1.4: TGA data for crystals soaked in KCl, LiCl and water.

Table A1.2: Summary of CHN and TGA analyses CHN and TGA analyses for the solid products resulting from the immersion of $(H_{1.33}tren)[In_{2.67}Sb_{1.33}S_8]\cdot tren$ in water, lithium chloride and potassium chloride solutions of different concentrations and for different soaking times.

Concentration of LiCl soln at 343 K / soaking time	0[†]	0.1M – 3h	2M – 3 h	3M – 3 h	3M – 5 days
CHN Analysis					
C /%	13.98	9.93	7.66	7.41	7.00
H /%	3.98	3.72	2.51	2.40	2.38
N /%	10.37	5.86	5.58	5.44	5.00
Total (C + H + N) /%	28.33	19.51	15.75	15.25	14.38
TGA					
x from TGA[§]		3.45	3.51	4.07	4.72
y from TGA[§]		0.66	0.76	0.93	0.91
% Organic removed		30.7	34.89	42.7	42.45

Concentration of KCl soln at 343 K /soaking time	0[†]	0.1 M – 3 h	2M – 3 h	3M - 3 h	3M - 5 days
CHN Analysis					
C /%	13.98	8.33	7.59	7.04	8.71
H /%	3.98	2.55	2.55	2.26	2.59
N /%	10.37	6.11	5.65	5.39	6.73
Total (C + H + N) /%	28.33	16.99	16.79	14.69	18.03
TGA					
x from TGA[§]		3.00	3.98	2.52	2.96
y from TGA[§]		0.70	1.09	1.05	0.85
% Organic removed		31.84	50.00	46.33	43.76

Water only	0[†]	3 h – room temp	3 h – 343 K
CHN Analysis			
C /%	13.98	11.23	7.73
H /%	3.98	3.17	2.42
N /%	10.37	8.56	5.98
Total (C + H + N) /%	28.33	22.96	16.13
TGA			
x from TGA[§]		2.34	3.96
y from TGA[§]		0.29	0.67
% Organic removed		12.02	31.70

[†] Formula is $(H_{1.33}tren)[In_{2.67}Sb_{1.33}S_8]\cdot tren$

[§] Formula is $(H_{1.33}tren)[In_{2.67}Sb_{1.33}S_8]\cdot(tren)_{1-y}(H_2O)_x$

Table A1.3: Crystallographic data for crystal soaked for 3h in 0.1 M KCl solution

Crystal Habit	Orange block
Crystal system	Tetragonal
Space group	$I\text{-}4\ 2\ d$
Temp /K	150
a /Å	12.3435(16)
c /Å	18.638(4)
V /Å³	2839.8(8)
Z	4
Wavelength /Å	0.71073
Total reflections ($I > 3\sigma(I)$)	310
R_{int}	0.0874
$R(F)$	0.0769 (after SQUEEZE)
$wR(F)$	0.0797

Table A1.4: Reaction outcomes for attempts of producing structures (**2**) and (**3**)

Sample ID	Target structure	Reagents used	Days	Temp °C	Structure in PXRD?	Crystals?
JL0313	3	Sb_2S_3 0.0670g, $InCl_3$ 0.0812g, CoS 0.0344g, S 0.0250g, tren 3.2ml, water 2ml	8	160	y	n
JL0318	3	Sb_2S_3 0.0675g, $InCl_3$ 0.0818g, CoS 0.0347g, S 0.0257g, tren 3ml, water 2ml	8	160	y	n
JL0428	3	Sb_2S_3 0.0677g, $InCl_3$ 0.0782g, CoS 0.0357g, S 0.0265g, tren 3.2ml, water 2ml	8	160	y	n
JL0429	3	Sb_2S_3 0.0677g, $InCl_3$ 0.0806g, CoS 0.0334g, S 0.0257g, tren 3.2ml, water 1ml	8	160	y	one or two
JL0430	3	Sb_2S_3 0.0690g, $InCl_3$ 0.1210g, CoS 0.0340g, S 0.0267g, tren 3.2ml, water 2ml	8	160	structure 2	one or two
JL0432	3	Sb 0.0464g, $InCl_3$ 0.1225g, CoS 0.0333g, S 0.0963g, tren 0.11ml, water 0.5ml	8	160	structure 2	one or two
JL0433	3	Sb 0.0461g, $InCl_3$ 0.1216g, CoS 0.0358g, S 0.0961g, tren 0.11ml	8	160	n	n
JL0539	3	Sb_2S_3 0.0675g, $InCl_3$ 0.0810g, CoS 0.0354g, S 0.0260g, tren 3.2ml, water 2ml	8	160	n/a*	one or two
JL0608	2	Sb 0.0455g, $InCl_3$ 0.1240g, CoS 0.0345g, S 0.0103g, tren 3.2ml, water 2ml	8	160	y	one or two
JL0609	2	Sb 0.0916g, $InCl_3$ 0.2391g, CoS 0.0678g, S 0.0183g, tren 3.2ml, water 2ml	8	160	n	n
JL0643	2	Sb 0.0448g, $InCl_3$ 0.1195g, CoS 0.0347g, S 0.0971g, tren 3.2ml, water 2ml	8	160	y	one or two
JL0644	3	Sb_2S_3 0.0684g, $InCl_3$ 0.0794g, CoS 0.0334g, S 0.0260g, tren 3.2ml, water 2ml	8	160	n/a*	one or two**
JL0645	2	Sb 0.0547g, In_2O_3 0.0806g, CoS 0.0338g, S 0.0961g, tren 3.2ml, water 2ml	8	160	n	one or two
JL0672	2	Sb 0.0451g, $InCl_3$ 0.1250g, CoS 0.0344g, S 0.0958g, tren 3.2ml, water 2ml	8	160	y	one or two**
JL0673	3	Sb_2S_3 0.0665g, $InCl_3$ 0.0815g, CoS 0.0335g, S 0.0259g, tren 3.2ml, water 1ml	8	160	n	one or two
JL0674	2	Sb 0.0544g, In_2O_3 0.0806g, CoS 0.0350g, S 0.0963g, tren 3.2ml, water 2ml	8	160	n	one or two
JL0675	3	Sb_2S_3 0.0669g, In_2O_3 0.1002g, CoS 0.0339g, S 0.0250g, tren 3.2ml, water 2ml	8	160	n	n
JL0676	3	Sb 0.0255g, In_2O_3 0.1010g, CoS 0.0350g, S 0.0321g, tren 3.2ml, water 2ml	8	160	n	one or two
JL0677	2	Sb 0.0451g, In_2O_3 0.1020g, CoS 0.0336g, S 0.0960g, tren 3.2ml, water 2ml	8	160	y	one or two**
JL0678	3	Sb 0.0244g, In_2O_3 0.0826g, CoS 0.0353g, S 0.0308g, tren 3.2ml, water 2ml	8	160	n	one or two**
JL0679	3	Sb 0.0486g, In_2O_3 0.1642g, CoS 0.0678g, S 0.0634g, tren 3.2ml, water 2ml	8	160	n	n
JL0680	3	Sb 0.0235g, In_2O_3 00843g, CoS 0.0344g, S 0.0399g, tren 3.2ml, water 2ml	8	160	y	one or two

*Powder X-ray diffraction (PXRD) unaccounted for

**Single-crystal x-ray of crystals were too disordered to confirm presence

Ramp rate was 1°C min^{-1} for all experiments

Table A1.5 Fractional coordinates and isotropic temperature factors (in Å^2) of the non-hydrogen atoms in [Co(tren$_2$)][In$_4$SbS$_{10}$].3H$_2$O **(2)**

Atom	x	y	z	U_{equiv}	Occupancy
Sb(1)	0.27423(6)	0.253891(18)	0.28403(6)	0.0194	1
Sb(2)	-0.27137(6)	0.473625(19)	-0.13466(6)	0.021	1
In(1)	0.53977(6)	0.264691(19)	-0.30784(6)	0.0186	1
In(2)	0.42364(6)	0.259196(19)	-0.00142(6)	0.0182	1
In(3)	0.60256(8)	0.19442(2)	-0.08792(8)	0.0294	1
In(4)	0.83866(6)	0.262695(19)	0.09746(6)	0.019	1
In(5)	-0.00384(7)	0.47143(2)	-0.31416(6)	0.0216	1
In(6)	-0.09638(6)	0.461687(19)	-0.71738(6)	0.0173	1
In(7)	0.31339(6)	0.466608(19)	-0.42279(6)	0.0192	1
In(8)	0.06216(8)	0.53375(2)	-0.51513(8)	0.0287	1
Co(1)	0.41682(13)	0.49981(3)	0.19890(13)	0.0187	1
Co(2)	0.94658(14)	0.22640(3)	0.62036(14)	0.0212	1
S(1)	0.4786(2)	0.28613(6)	-0.5522(2)	0.0222	1
S(2)	0.2179(2)	0.27550(5)	0.0498(2)	0.0206	1
S(3)	0.3442(2)	0.28145(5)	-0.2467(2)	0.019	1
S(4)	0.4028(3)	0.20584(6)	-0.0260(3)	0.0277	1
S(5)	0.5441(3)	0.21161(6)	-0.3341(3)	0.0284	1
S(6)	0.8566(3)	0.20908(6)	0.0961(3)	0.0306	1
S(7)	0.6605(2)	0.28093(5)	0.1805(2)	0.0212	1
S(8)	1.0779(2)	0.27975(6)	0.3088(3)	0.0259	1
S(9)	0.7811(2)	0.28743(5)	-0.1355(2)	0.0205	1
S(10)	0.6057(7)	0.14033(9)	-0.1103(8)	0.0806	1
S(11)	-0.0374(2)	0.45356(5)	-0.1020(2)	0.0212	1
S(12)	-0.1749(2)	0.44445(5)	-0.5378(2)	0.0204	1
S(13)	-0.2914(2)	0.44118(6)	-0.9567(2)	0.0226	1
S(14)	0.1522(2)	0.44181(5)	-0.6589(2)	0.0182	1
S(15)	0.2518(2)	0.45218(6)	-0.2299(2)	0.0227	1
S(16)	0.5662(3)	0.44678(6)	-0.3585(3)	0.0284	1
S(17)	0.3204(3)	0.51961(6)	-0.4515(3)	0.028	1
S(18)	-0.1247(3)	0.51454(6)	-0.7560(3)	0.0257	1
S(19)	-0.0168(3)	0.52471(6)	-0.3290(3)	0.031	1
S(20)	0.0598(8)	0.58747(9)	-0.5515(7)	0.0864	1
O(1)	0.8590(8)	0.89040(18)	0.1793(9)	0.0353	1
O(2)	0.2058(11)	0.8770(2)	0.0333(10)	0.0406	1
O(3)	0.6632(11)	0.8398(2)	0.4270(11)	0.045	1
N(1)	0.9752(14)	0.2101(2)	0.8189(13)	0.047	1
N(2)	0.9264(11)	0.1784(2)	0.5715(10)	0.028	1

N(3)	1.1245(11)	0.2215(2)	0.5708(13)	0.0372	1
N(4)	0.7350(12)	0.2266(2)	0.4428(13)	0.0524	1
N(5)	0.9788(8)	0.26945(17)	0.6891(9)	0.0234	1
N(6)	0.9097(8)	0.34777(16)	0.5488(8)	0.0178	1
N(7)	0.8185(9)	0.3909(2)	0.7023(9)	0.0285	1
N(8)	1.1172(10)	0.3853(2)	0.5101(10)	0.032	1
N(9)	0.5909(10)	0.5145(2)	0.3942(12)	0.0349	1
N(10)	0.3967(10)	0.5479(2)	0.1533(10)	0.0301	1
N(11)	0.4662(11)	0.5008(2)	0.0269(11)	0.0318	1
N(12)	0.1989(11)	0.50594(19)	0.1601(10)	0.028	1
N(13)	0.4417(8)	0.45586(16)	0.2580(8)	0.0175	1
N(14)	0.3723(9)	0.37727(18)	0.1210(9)	0.023	1
N(15)	0.5736(9)	0.3369(2)	-0.0512(9)	0.0261	1
N(16)	0.0590(11)	0.3495(2)	0.0379(13)	0.0384	1
C(1)	0.9720(18)	0.1787(3)	0.8233(16)	0.0454	1
C(2)	0.917(4)	0.1646(4)	0.6900(19)	0.1202	1
C(3)	1.1357(16)	0.1926(3)	0.5197(16)	0.0421	1
C(4)	1.058(2)	0.1705(4)	0.565(3)	0.0906	1
C(5)	0.6800(16)	0.1978(3)	0.3860(14)	0.048	1
C(6)	0.791(2)	0.1748(3)	0.434(2)	0.091	1
C(7)	0.9091(10)	0.2928(2)	0.5769(9)	0.0193	1
C(8)	0.9708(9)	0.32266(19)	0.6496(10)	0.0171	1
C(9)	0.7521(10)	0.3543(2)	0.5054(12)	0.0272	1
C(10)	0.7243(11)	0.3643(2)	0.6289(12)	0.0274	1
C(11)	0.9333(11)	0.3451(2)	0.4169(10)	0.0257	1
C(12)	0.9716(11)	0.3742(2)	0.3828(12)	0.0297	1
C(13)	0.5886(15)	0.5464(3)	0.4114(19)	0.0504	1
C(14)	0.5311(14)	0.5615(3)	0.2696(13)	0.0376	1
C(15)	0.4755(13)	0.5314(2)	-0.0252(12)	0.0306	1
C(16)	0.3778(14)	0.5514(2)	0.0043(15)	0.0359	1
C(17)	0.1388(13)	0.5351(3)	0.0990(13)	0.0338	1
C(18)	0.2622(15)	0.5578(3)	0.1679(17)	0.0418	1
C(19)	0.3895(9)	0.43278(19)	0.1450(9)	0.0163	1
C(20)	0.4142(10)	0.4025(2)	0.2221(9)	0.0194	1
C(21)	0.4982(10)	0.3693(2)	0.0900(10)	0.0207	1
C(22)	0.4447(10)	0.3511(2)	-0.0477(12)	0.027	1
C(23)	0.3410(10)	0.3515(2)	0.1922(12)	0.0268	1
C(24)	0.1847(14)	0.3537(2)	0.1831(14)	0.0353	1

Table A1.6 Fractional coordinates and isotropic temperature factors (in $\mathring{A}^2$) of the non-hydrogen atoms in [Co(tren$_2$)][In$_3$Sb$_2$S$_9$].H$_2$O (**3**)

Atom	x	y	z	U_{equiv}	Occupancy
Sb(1)	0.34699(15)	-0.10369(15)	0.26006(9)	0.0498	1
Sb(2)	0.0459(3)	0.4677(3)	0.40659(13)	0.1046	1
In(1)	0.09109(15)	0.32091(15)	0.22410(8)	0.0452	1
In(2)	0.19816(15)	0.61585(15)	0.23985(8)	0.0446	1
In(3)	-0.21246(16)	0.71491(17)	0.24158(10)	0.0543	1
Co(1)	-0.3119(3)	0.2171(3)	0.31736(13)	0.0403	1
S(1)	0.1428(6)	0.0848(6)	0.1808(3)	0.0539	1
S(2)	0.0894(9)	0.2590(8)	0.3528(4)	0.0701	1
S(3)	0.2269(8)	0.5522(8)	0.3686(3)	0.0673	1
S(4)	0.2820(5)	0.3892(5)	0.1832(3)	0.0446	1
S(5)	0.3995(6)	0.6791(6)	0.2055(4)	0.0615	1
S(6)	-0.0480(6)	0.8190(6)	0.1954(3)	0.053	1
S(7)	-0.2093(9)	0.6698(10)	0.3686(4)	0.081	1
S(8)	-0.1616(6)	0.5084(6)	0.1776(3)	0.0531	1
S(9)	-0.4562(6)	0.9364(6)	0.2020(4)	0.0548	1
O(1)	-0.791(9)	0.304(7)	0.022(3)	0.2772	1
N(1)	-0.339(2)	0.413(2)	0.3507(13)	0.0666	1
N(2)	-0.298(2)	0.147(2)	0.4321(8)	0.0443	1
N(3)	-0.098(2)	0.038(2)	0.3203(9)	0.0541	1
N(4)	-0.489(2)	0.169(2)	0.3275(8)	0.053	1
N(5)	-0.350(2)	0.309(2)	0.2114(10)	0.058	1
N(6)	-0.281(5)	0.235(4)	0.0264(19)	0.1128	1
N(7)	-0.036(5)	0.381(6)	-0.0541(19)	0.1107	0.5
N(8)	-0.546(10)	0.214(12)	-0.052(2)	0.2821	1
C(1)	-0.371(3)	0.412(3)	0.4278(14)	0.0631	1
C(2)	-0.273(4)	0.253(3)	0.4681(11)	0.0696	1
C(3)	-0.168(4)	-0.011(3)	0.4423(13)	0.0762	1
C(4)	-0.034(3)	-0.025(3)	0.3958(13)	0.0641	1
C(5)	-0.438(4)	0.141(4)	0.4513(12)	0.0788	1
C(6)	-0.485(3)	0.083(3)	0.3966(13)	0.0629	1
C(7)	-0.288(3)	0.216(3)	0.1578(9)	0.0563	1
C(8)	-0.340(3)	0.313(3)	0.0852(10)	0.0743	1
C(9)	-0.315(7)	0.117(5)	0.017(4)	0.3036	1
C(10)	-0.138(6)	0.217(8)	-0.002(3)	0.2878	1
C(11)	-0.090(9)	0.332(7)	0.011(3)	0.9176	0.5
C(12)	-0.485(6)	0.168(13)	0.019(3)	0.9864	1

Table A1.7 Fractional coordinates and isotropic temperature factors (in Å^2) of the non-hydrogen atoms in [Co(tren)]$_2$[Sb$_2$In$_2$S$_8$] **(4)**

Atom	x	y	z	U_{equiv}	Occupancy
Sb(1)	0.34772(4)	0.19837(3)	0.50199(3)	0.0194	1
Sb(2)	0.22478(4)	-0.35018(3)	0.78900(3)	0.0215	1
In(1)	0.30835(4)	-0.08515(3)	0.65038(3)	0.0171	1
In(2)	0.12033(4)	-0.06967(3)	0.91654(3)	0.0186	1
Co(1)	-0.16784(8)	-0.31118(7)	0.88121(7)	0.0221	1
Co(2)	-0.03698(8)	0.31059(7)	0.54669(6)	0.0205	1
S(1)	0.31632(15)	0.03064(12)	0.47144(11)	0.0214	1
S(2)	0.51436(15)	-0.25487(13)	0.66007(12)	0.0251	1
S(3)	0.25714(16)	0.02912(14)	0.77934(12)	0.0252	1
S(4)	0.19511(16)	-0.28704(13)	0.95057(12)	0.0246	1
S(5)	0.11863(14)	-0.16211(13)	0.68409(12)	0.0223	1
S(6)	0.04675(15)	-0.42711(13)	0.80857(12)	0.0246	1
S(7)	-0.12576(15)	0.01903(14)	0.92044(12)	0.0255	1
S(8)	0.15188(16)	0.34281(14)	0.43386(15)	0.031	1
N(1)	-0.3737(5)	-0.2192(5)	0.9622(4)	0.0228	1
N(2)	-0.2839(6)	-0.4074(5)	0.8702(5)	0.0317	1
N(3)	-0.1191(5)	-0.3180(5)	1.0219(4)	0.0268	1
N(4)	-0.2114(6)	-0.1490(5)	0.7811(4)	0.0299	1
N(5)	-0.2408(6)	0.3179(5)	0.6451(5)	0.0329	1
N(6)	-0.0418(5)	0.1507(5)	0.5455(4)	0.0238	1
N(7)	-0.1672(6)	0.4538(5)	0.4573(5)	0.0283	1
N(8)	0.0066(8)	0.3036(6)	0.6920(5)	0.0393	1
C(1)	-0.3554(6)	-0.0791(5)	0.7991(5)	0.0271	1
C(4)	-0.3644(8)	-0.2424(6)	1.0741(5)	0.0335	1
C(6)	-0.4749(6)	-0.2621(6)	0.9449(6)	0.0291	1
C(5)	-0.4118(7)	-0.3884(6)	0.9416(6)	0.0324	1
C(2)	-0.4047(7)	-0.0949(6)	0.9131(5)	0.0288	1
C(3)	-0.2275(8)	-0.2445(6)	1.0878(5)	0.0326	1
C(8)	-0.2702(7)	0.2193(6)	0.6345(6)	0.0364	1
C(7)	-0.1426(7)	0.1158(5)	0.6278(6)	0.0278	1
C(10)	-0.3384(7)	0.4302(6)	0.6056(7)	0.0413	1
C(9)	-0.3110(7)	0.4616(7)	0.4895(7)	0.0383	1
C(12)	-0.2260(11)	0.3077(7)	0.7563(6)	0.0485	1
C(11)	-0.1208(11)	0.3580(6)	0.7582(6)	0.044	1

Table A1.8 Fractional coordinates and isotropic temperature factors (in Å^2) of the non-hydrogen atoms in $(Hdap)_6[In_{10}S_{18}]$ **(5)**

Atom	x	y	z	U_{equiv}	Occupancy
In(1)	0.14917(5)	0.92111(5)	0.41042(3)	0.0359	1
In(2)	0.09895(5)	0.78695(4)	0.49477(3)	0.0312	1
In(3)	0.24774(5)	0.75125(5)	0.40934(3)	0.0325	1
In(4)	0.27611(5)	0.89044(5)	0.50070(3)	0.031	1
In(5)	0.06003(5)	0.65192(5)	0.57912(3)	0.0397	1
In(6)	0.20169(4)	0.61030(4)	0.49747(3)	0.0299	1
In(7)	0.22925(5)	0.74978(5)	0.59004(3)	0.037	1
In(8)	0.34563(5)	0.58248(5)	0.41662(3)	0.0375	1
In(9)	0.37796(5)	0.71274(5)	0.50600(3)	0.0333	1
In(10)	0.39884(6)	0.84882(5)	0.59319(3)	0.0419	1
S(1)	0.05458(19)	0.87401(19)	0.45097(14)	0.0441	1
S(2)	0.23255(19)	0.97665(18)	0.45529(13)	0.039	1
S(3)	0.2042(2)	0.8378(2)	0.36452(13)	0.0458	1
S(4)	0.00787(18)	0.73868(18)	0.53527(13)	0.0412	1
S(5)	0.18300(17)	0.83928(16)	0.54308(11)	0.0295	1
S(6)	0.15403(17)	0.69874(16)	0.45065(11)	0.0301	1
S(7)	0.3570(2)	0.9403(2)	0.54781(13)	0.0484	1
S(8)	0.33276(17)	0.80133(16)	0.45803(11)	0.0305	1
S(9)	0.2988(2)	0.6650(2)	0.36751(13)	0.0525	1
S(10)	-0.0261(3)	0.5853(2)	0.61327(16)	0.0578	1
S(11)	0.1363(2)	0.7033(2)	0.63020(13)	0.0512	1
S(12)	0.11113(19)	0.56140(18)	0.53722(14)	0.0439	1
S(13)	0.3109(3)	0.7975(2)	0.63745(12)	0.0531	1
S(14)	0.28559(18)	0.65949(17)	0.54745(11)	0.0319	1
S(15)	0.25559(18)	0.52435(18)	0.45570(13)	0.0382	1
S(16)	0.4595(2)	0.7623(2)	0.55313(14)	0.0484	1
S(17)	0.43188(18)	0.6273(2)	0.46462(16)	0.0522	1
S(18)	0.4154(2)	0.5018(2)	0.37979(15)	0.0544	1

Appendix 2 (A2) – Chapter 4 Supplementary Information

Table A2.1 Fractional coordinates and isotropic temperature factors (in Å^2) of the non-hydrogen atoms in [Co(tren)$_2$]$_2$[Ge$_4$S$_4$O$_6$] **(6)**

Atom	x	y	z	U_{equiv}	Occupancy
Ge(1)	0.52290(3)	0.85359(3)	0.83722(3)	0.0117	1
Ge(2)	0.72548(3)	0.70548(3)	0.83566(3)	0.0116	1
Ge(3)	0.59645(3)	0.74664(3)	0.67624(3)	0.0122	1
Ge(4)	0.73764(3)	0.93438(3)	0.68937(3)	0.0124	1
Co(1)	0.16636(5)	0.84446(5)	0.69756(4)	0.0147	1
Co(2)	0.65452(5)	0.31186(4)	0.78936(4)	0.0144	1
S(1)	0.38295(9)	0.89712(10)	0.92155(7)	0.0201	1
S(2)	0.81099(9)	0.58791(9)	0.92002(8)	0.0194	1
S(3)	0.54023(10)	0.67861(9)	0.58427(8)	0.0199	1
S(4)	0.84107(10)	1.07365(9)	0.61308(8)	0.0201	1
O(2)	0.6064(3)	0.7555(2)	0.89900(19)	0.0156	1
O(6)	0.6733(2)	0.6565(2)	0.7534(2)	0.0151	1
O(1)	0.4885(2)	0.7922(3)	0.7549(2)	0.0165	1
O(4)	0.6866(2)	0.8658(2)	0.6189(2)	0.0138	1
O(5)	0.8047(2)	0.8301(2)	0.7645(2)	0.0146	1
O(3)	0.6179(2)	0.9658(2)	0.7645(2)	0.0141	1
N(1)	0.1521(4)	1.3044(3)	0.5427(3)	0.0293	1
N(2)	0.0275(3)	0.8524(3)	0.8110(3)	0.0182	1
N(3)	0.1992(3)	1.0149(3)	0.6971(3)	0.0166	1
N(4)	0.3227(3)	0.8898(3)	0.5901(3)	0.0245	1
N(5)	0.0503(3)	0.8782(3)	0.6077(3)	0.0182	1
N(6)	0.1368(3)	0.6756(3)	0.6915(2)	0.0155	1
N(7)	0.2467(3)	0.7502(3)	0.8069(3)	0.0184	1
N(8)	0.3046(4)	0.5279(3)	0.5263(3)	0.0271	1
N(9)	0.6021(3)	0.3872(3)	0.9012(3)	0.0207	1
N(10)	0.4761(3)	0.3210(3)	0.7954(3)	0.0156	1
N(11)	0.2300(4)	0.1438(4)	0.9712(3)	0.0317	1
N(12)	0.8352(3)	0.3054(3)	0.8064(3)	0.0166	1
N(13)	0.7259(3)	0.4642(3)	0.6872(3)	0.0202	1
N(14)	0.9728(4)	0.3239(4)	0.9968(3)	0.037	1
N(15)	0.6674(3)	0.1402(3)	0.8536(2)	0.0144	1
N(16)	0.6478(3)	0.2641(3)	0.6604(2)	0.0153	1
C(1)	0.4577(4)	0.3221(4)	0.7031(3)	0.0218	1
C(2)	0.0269(4)	0.9646(4)	0.8192(3)	0.0207	1
C(3)	0.1455(4)	1.0133(3)	0.7922(3)	0.0155	1

Atom	x	y	z	U	Occupancy
C(4)	0.3254(4)	1.0200(4)	0.6814(4)	0.0241	1
C(5)	0.3750(4)	0.9917(4)	0.5937(3)	0.0252	1
C(6)	0.1594(4)	1.1030(4)	0.6251(3)	0.02	1
C(7)	0.1901(4)	1.2225(4)	0.6159(3)	0.0241	1
C(8)	0.0058(4)	0.7752(4)	0.5987(3)	0.0208	1
C(9)	0.0233(4)	0.6789(4)	0.6770(3)	0.0241	1
C(10)	0.1445(4)	0.6032(3)	0.7849(3)	0.0154	1
C(11)	0.2479(4)	0.6327(4)	0.8121(3)	0.0204	1
C(12)	0.2184(4)	0.6520(3)	0.6145(3)	0.0182	1
C(13)	0.2084(5)	0.5392(4)	0.5989(3)	0.0284	1
C(14)	0.4908(4)	0.4344(4)	0.8988(3)	0.0245	1
C(15)	0.4533(4)	0.4280(3)	0.8145(4)	0.0224	1
C(16)	0.4108(4)	0.2294(3)	0.8719(3)	0.0189	1
C(17)	0.2847(4)	0.2397(4)	0.8959(3)	0.0236	1
C(18)	0.8980(4)	0.3985(4)	0.7311(3)	0.0203	1
C(19)	0.8393(4)	0.4396(3)	0.6510(3)	0.0171	1
C(20)	0.8496(4)	0.3054(4)	0.8989(3)	0.0198	1
C(21)	0.9680(4)	0.2903(5)	0.9148(4)	0.0285	1
C(22)	0.8655(3)	0.1999(3)	0.7890(3)	0.0133	1
C(23)	0.7846(4)	0.1087(4)	0.8549(3)	0.0191	1
C(24)	0.5309(4)	0.2374(4)	0.6663(3)	0.0165	1

Table A2.2 Fractional coordinates and isotropic temperature factors (in $\mathring{A}^2$) of the non-hydrogen atoms in $[(Co(tren))_2\mu\text{-tren}][Ge_4S_4O_6].2H_2O$ **(7)**

Atom	x	y	z	U_{equiv}	Occupancy
Ge(1)	0.78363(12)	0.77691(10)	0.16231(9)	0.0509	1
Ge(2)	0.52134(11)	0.74878(8)	0.29249(8)	0.0383	1
Ge(3)	0.69164(11)	0.83500(9)	0.36903(9)	0.0389	1
Ge(4)	0.64309(12)	0.98660(8)	0.17883(8)	0.0397	1
Co(1)	0.1946(3)	0.86117(14)	0.18461(14)	0.0817	1
Co(2)	0.59412(14)	0.35447(17)	0.29145(14)	0.0527	1
S(1)	0.9167(4)	0.7065(3)	0.0689(3)	0.0835	1
S(2)	0.3716(3)	0.6430(3)	0.3409(2)	0.0581	1
S(3)	0.7301(3)	0.8363(2)	0.4968(2)	0.0474	1
S(4)	0.6219(3)	1.1527(2)	0.1004(2)	0.0551	1
O(2)	0.6449(8)	0.7031(6)	0.2079(6)	0.0495	1
O(6)	0.5636(7)	0.7522(6)	0.3966(5)	0.0362	1
O(1)	0.8005(7)	0.7812(6)	0.2774(6)	0.051	1

O(4)	0.6729(7)	0.9712(6)	0.2929(6)	0.0454	1
O(5)	0.5167(7)	0.8925(5)	0.2222(5)	0.0373	1
O(3)	0.7571(7)	0.9198(6)	0.1054(6)	0.0472	1
O(7)	0.9545(9)	0.6450(11)	0.3516(8)	0.0933	1
O(8)	0.7071(16)	0.6185(13)	0.0473(12)	0.0499	0.5
O(9)	0.552(2)	0.6582(16)	0.0605(17)	0.0748	0.5
N(1)	0.1494(10)	1.0217(8)	0.2276(8)	0.057	1
N(2)	0.1398(18)	0.7991(10)	0.3429(10)	0.1086	1
N(3)	0.3514(12)	0.9505(13)	0.1095(9)	0.0843	1
N(4)	0.0924(12)	0.9156(11)	0.1022(9)	0.0744	1
N(6)	0.2208(7)	0.4515(6)	0.2218(6)	0.0395	1
N(8)	0.5659(11)	0.1839(13)	0.3624(16)	0.1093	1
N(9)	0.7622(8)	0.3184(7)	0.3140(7)	0.0371	1
N(11)	0.5782(8)	0.4395(7)	0.3949(6)	0.0363	1
N(50)	0.196(3)	0.688(3)	0.209(2)	0.1045	0.35
N(51)	0.2703(13)	0.7125(12)	0.1470(10)	0.0505	0.65
N(100)	0.6947(11)	0.3712(15)	0.1503(11)	0.03	0.5
N(101)	0.7231(14)	0.4385(16)	0.1345(12)	0.0432	0.5
N(120)	0.4296(16)	0.3767(15)	0.2837(12)	0.0447	0.6
N(121)	0.460(2)	0.436(2)	0.236(3)	0.0605	0.4
C(1)	0.0868(14)	0.9908(11)	0.3374(10)	0.066	1
C(2)	0.1252(18)	0.8869(12)	0.3939(10)	0.0836	1
C(3)	0.2626(15)	1.0820(13)	0.1955(13)	0.0778	1
C(4)	0.3375(15)	1.0673(17)	0.0974(13)	0.0812	1
C(5)	0.0788(16)	1.0824(13)	0.1657(12)	0.0934	1
C(6)	0.0156(13)	0.9903(11)	0.1390(12)	0.0706	1
C(7)	0.1913(12)	0.6477(9)	0.1270(11)	0.0664	1
C(10)	0.0859(10)	0.3808(9)	0.4013(7)	0.0475	1
C(11)	0.6409(18)	0.1451(12)	0.4183(15)	0.0999	1
C(12)	0.7622(12)	0.1939(9)	0.3515(10)	0.0525	1
C(13)	0.8565(10)	0.3698(10)	0.2132(9)	0.0483	1
C(14)	0.8191(10)	0.3639(16)	0.1279(10)	0.0819	1
C(15)	0.7643(11)	0.3702(9)	0.3930(9)	0.0467	1
C(16)	0.6926(12)	0.4728(9)	0.3878(9)	0.0468	1
C(17)	0.4160(10)	0.3679(9)	0.1904(9)	0.0492	1
C(80)	0.2883(11)	0.3544(11)	0.2147(15)	0.0604	0.6
C(81)	0.3215(15)	0.415(2)	0.1509(15)	0.0581	0.4
C(90)	0.0992(10)	0.4271(14)	0.2907(8)	0.0342	0.6
C(91)	0.151(2)	0.3531(13)	0.3030(11)	0.052	0.4
C(180)	0.1521(19)	0.5251(11)	0.169(2)	0.0515	0.4
C(181)	0.224(2)	0.5314(10)	0.1244(10)	0.0404	0.6
N(70)	0.1208(14)	0.4675(13)	0.4366(11)	0.0432	0.6

Atom	X	y	z	U_{equiv}	Occupancy
N(71)	0.1634(18)	0.413(2)	0.444(2)	0.0512	0.4

Table A2.3 Fractional coordinates and isotropic temperature factors (in Å^2) of the non-hydrogen atoms in [Co(deta)$_2$]$_2$[Ge$_4$O$_6$S$_4$].H$_2$O (**8**)

Atom	X	y	z	U_{equiv}	Occupancy
Ge(1)	0.65403(3)	0.87282(4)	0.33323(7)	0.0281	1
Ge(2)	0.59820(4)	0.91387(4)	0.25731(7)	0.0303	1
Ge(3)	0.59957(3)	0.83648(3)	0.24386(7)	0.0261	1
Ge(4)	0.65423(3)	0.87867(3)	0.16811(7)	0.0259	1
Ge(5)	0.62344(4)	0.65409(4)	0.58272(7)	0.0297	1
Ge(6)	0.62810(4)	0.65429(4)	0.41720(7)	0.0276	1
Ge(7)	0.58643(4)	0.59986(3)	0.49437(7)	0.0268	1
Ge(8)	0.66414(4)	0.59855(4)	0.50541(8)	0.0339	1
Co(1)	0.72396(5)	0.62066(5)	0.25002(8)	0.0227	1
Co(2)	0.62942(5)	0.77580(5)	0.50221(8)	0.0222	1
Co(3)	0.61915(5)	0.47638(5)	0.50002(9)	0.0277	1
Co(4)	0.52325(5)	0.63095(5)	0.24754(9)	0.0269	1
S(1)	0.68654(9)	0.86967(10)	0.42180(19)	0.0369	1
S(2)	0.56556(12)	0.95499(10)	0.2673(2)	0.046	1
S(3)	0.56810(10)	0.79416(9)	0.2347(2)	0.0395	1
S(4)	0.68649(9)	0.88159(11)	0.07965(19)	0.0406	1
S(5)	0.62046(11)	0.68571(10)	0.6722(2)	0.0415	1
S(6)	0.62975(11)	0.68639(10)	0.3279(2)	0.0426	1
S(7)	0.54340(10)	0.56901(11)	0.4864(3)	0.0452	1
S(8)	0.70581(12)	0.56672(14)	0.5145(3)	0.0574	1
O(2)	0.6261(3)	0.9080(2)	0.3345(6)	0.0324	1
O(6)	0.5763(3)	0.8760(3)	0.2519(5)	0.0332	1
O(1)	0.6258(2)	0.8375(2)	0.3205(6)	0.0261	1
O(4)	0.6278(2)	0.8431(2)	0.1682(6)	0.03	1
O(5)	0.6252(2)	0.9138(2)	0.1805(4)	0.0176	1
O(3)	0.6767(2)	0.8770(3)	0.2508(4)	0.0225	1
O(7)	0.6275(3)	0.6761(3)	0.4967(5)	0.0339	1
O(8)	0.5926(2)	0.6279(2)	0.4185(5)	0.021	1
O(9)	0.5871(3)	0.6264(3)	0.5694(6)	0.0352	1
O(10)	0.6255(3)	0.5755(2)	0.4988(4)	0.0243	1
O(11)	0.6633(2)	0.6256(3)	0.4274(7)	0.037	1
O(12)	0.6583(3)	0.6266(3)	0.5788(5)	0.0321	1
N(1)	0.6884(3)	0.5862(3)	0.2917(5)	0.0313	1
N(2)	0.7574(4)	0.5792(4)	0.2746(8)	0.052	1

N(3)	0.7320(3)	0.6032(3)	0.1452(6)	0.0376	1
N(4)	0.7319(3)	0.6427(3)	0.3550(7)	0.0385	1
N(5)	0.7573(3)	0.6645(4)	0.2259(8)	0.0467	1
N(6)	0.6877(3)	0.6555(3)	0.2114(6)	0.0319	1
N(7)	0.6646(4)	0.8117(3)	0.5411(7)	0.0429	1
N(8)	0.6705(4)	0.7434(4)	0.5229(9)	0.0496	1
N(9)	0.6473(4)	0.7692(3)	0.3931(7)	0.045	1
N(10)	0.6075(3)	0.7683(3)	0.6090(7)	0.041	1
N(11)	0.5860(4)	0.7428(3)	0.4777(8)	0.0485	1
N(12)	0.5955(4)	0.8128(3)	0.4634(7)	0.047	1
N(13)	0.5837(5)	0.4380(4)	0.5399(9)	0.0671	1
N(14)	0.5768(5)	0.4900(4)	0.4319(12)	0.0737	1
N(15)	0.6444(5)	0.5055(6)	0.4098(10)	0.0813	1
N(16)	0.6530(4)	0.4354(3)	0.4710(8)	0.0472	1
N(17)	0.6652(7)	0.4909(6)	0.5591(16)	0.1056	1
N(18)	0.6018(4)	0.5080(4)	0.5892(9)	0.0608	1
N(19)	0.5654(4)	0.5988(4)	0.2786(9)	0.0605	1
N(20)	0.5115(4)	0.5852(5)	0.1881(9)	0.0638	1
N(21)	0.4926(4)	0.6481(5)	0.1588(8)	0.0581	1
N(22)	0.5607(4)	0.6678(5)	0.2092(9)	0.0643	1
N(23)	0.5104(4)	0.6722(4)	0.3126(7)	0.0545	1
N(24)	0.4946(5)	0.6065(6)	0.3392(9)	0.0758	1
C(1)	0.7036(5)	0.5550(6)	0.3091(12)	0.0668	1
C(2)	0.7386(5)	0.5575(4)	0.3296(9)	0.0494	1
C(3)	0.7663(5)	0.5626(5)	0.2063(10)	0.0536	1
C(4)	0.7388(6)	0.5660(6)	0.1517(12)	0.0686	1
C(5)	0.7382(4)	0.6768(4)	0.3456(9)	0.0371	1
C(6)	0.7653(4)	0.6837(4)	0.2915(9)	0.0432	1
C(7)	0.7402(4)	0.6814(5)	0.1661(9)	0.0488	1
C(8)	0.7022(4)	0.6884(4)	0.1891(10)	0.0491	1
C(9)	0.6953(7)	0.7966(6)	0.5567(12)	0.0725	1
C(10)	0.6919(4)	0.7594(7)	0.5797(10)	0.0673	1
C(11)	0.6871(5)	0.7340(4)	0.4589(10)	0.0499	1
C(12)	0.6840(5)	0.7611(5)	0.3965(11)	0.0618	1
C(13)	0.5726(3)	0.7611(3)	0.5989(6)	0.0271	1
C(14)	0.5662(4)	0.7345(4)	0.5415(9)	0.0426	1
C(15)	0.5694(6)	0.7598(4)	0.4229(10)	0.0593	1
C(16)	0.5624(5)	0.7972(4)	0.4423(11)	0.0531	1
C(17)	0.5479(5)	0.4535(9)	0.5362(15)	0.1053	1
C(18)	0.5484(7)	0.4645(7)	0.4541(19)	0.1026	1
C(19)	0.5876(7)	0.4931(6)	0.3680(12)	0.0733	1
C(20)	0.6165(7)	0.5179(5)	0.3624(9)	0.071	1

264

C(21)	0.6871(6)	0.4485(7)	0.4739(16)	0.0835	1
C(22)	0.6904(7)	0.4644(7)	0.5462(19)	0.0922	1
C(23)	0.6564(7)	0.4949(6)	0.6323(9)	0.0692	1
C(24)	0.6291(8)	0.5186(5)	0.6356(10)	0.0855	1
C(25)	0.5527(8)	0.5650(7)	0.2760(17)	0.0986	1
C(26)	0.5383(8)	0.5603(6)	0.202(2)	0.107	1
C(27)	0.5064(5)	0.5926(7)	0.1119(11)	0.0669	1
C(28)	0.4820(6)	0.6222(7)	0.1136(10)	0.0737	1
C(29)	0.5479(9)	0.7019(6)	0.2199(14)	0.102	1
C(30)	0.5333(7)	0.7007(6)	0.2973(13)	0.0789	1
C(31)	0.5082(5)	0.6619(7)	0.3873(12)	0.0728	1
C(32)	0.4829(5)	0.6324(6)	0.3871(9)	0.0569	1

Table A2.4 Fractional coordinates and isotropic temperature factors (in Å^2) of the non-hydrogen atoms in $[Co(deta)_2]_2[Ge_4O_6S_4].H_2O$ **(9)**

Atom	x	y	z	U_{equiv}	Occupancy
Ge(1)	0.92708(3)	0.57112(3)	0.60338(4)	0.0125	1
Ge(2)	1.10438(3)	0.53798(3)	0.51033(4)	0.0142	1
Ge(3)	0.95405(3)	0.38101(3)	0.52380(4)	0.0131	1
Ge(4)	0.90860(3)	0.56368(3)	0.44048(4)	0.0129	1
Co(1)	1.28031(4)	0.21769(4)	0.50701(4)	0.0151	1
Co(2)	0.69090(4)	0.81153(4)	0.51686(4)	0.0116	1
S(2)	1.24922(8)	0.56450(9)	0.49862(7)	0.0224	1
S(1)	0.86890(8)	0.63620(8)	0.69345(6)	0.0192	1
S(3)	0.92954(9)	0.23508(7)	0.52925(7)	0.0195	1
S(4)	0.82618(8)	0.61808(8)	0.35737(6)	0.0173	1
O(2)	1.0516(2)	0.5859(2)	0.58959(15)	0.0153	1
O(6)	1.0766(2)	0.4148(2)	0.51416(18)	0.0162	1
O(1)	0.9127(2)	0.4454(2)	0.59850(16)	0.0164	1
O(4)	0.8995(2)	0.4378(2)	0.44921(16)	0.016	1
O(5)	1.0332(2)	0.5845(2)	0.43938(15)	0.0144	1
O(3)	0.8733(2)	0.6120(2)	0.52375(18)	0.0155	1
O(7)	0.7857(4)	0.7642(5)	0.2175(3)	0.0769	1
N(1)	1.3864(3)	0.1348(3)	0.5584(2)	0.0238	1
N(2)	1.2472(3)	0.0779(3)	0.4633(2)	0.0226	1
N(3)	1.1602(3)	0.1821(3)	0.5711(2)	0.0274	1
N(4)	1.1979(3)	0.2818(3)	0.4230(2)	0.0227	1
N(5)	1.3941(3)	0.2804(3)	0.4392(2)	0.0238	1
N(6)	1.3140(4)	0.3417(3)	0.5665(2)	0.0301	1

N(7)	0.6681(3)	0.7520(3)	0.6204(2)	0.0188	1
N(8)	0.6624(3)	0.6627(3)	0.4889(2)	0.0197	1
N(9)	0.5476(3)	0.8235(3)	0.4802(2)	0.0167	1
N(10)	0.6956(3)	0.9528(3)	0.5612(2)	0.0172	1
N(11)	0.8433(3)	0.8248(3)	0.5375(2)	0.0168	1
N(12)	0.7435(3)	0.8400(3)	0.4116(2)	0.0176	1
C(1)	1.4068(3)	0.0536(3)	0.5123(2)	0.0258	1
C(2)	1.3158(4)	0.0075(3)	0.4904(3)	0.0271	1
C(3)	1.1495(4)	0.0561(4)	0.4836(3)	0.03	1
C(4)	1.1338(4)	0.0830(4)	0.5610(3)	0.032	1
C(5)	1.2557(4)	0.3430(3)	0.3786(2)	0.0228	1
C(6)	1.3522(4)	0.3008(3)	0.3691(2)	0.0267	1
C(7)	1.4310(4)	0.3669(4)	0.4742(3)	0.032	1
C(8)	1.4119(5)	0.3671(4)	0.5534(3)	0.0386	1
C(9)	0.6054(4)	0.6692(4)	0.6119(3)	0.0253	1
C(10)	0.6427(4)	0.6075(3)	0.5536(3)	0.0242	1
C(11)	0.5853(4)	0.6647(4)	0.4361(3)	0.0255	1
C(12)	0.5082(3)	0.7314(4)	0.4578(2)	0.0234	1
C(13)	0.7931(4)	0.9810(3)	0.5801(3)	0.0244	1
C(14)	0.8532(3)	0.8950(4)	0.5936(2)	0.0209	1
C(15)	0.8948(3)	0.8457(4)	0.4718(3)	0.0222	1
C(16)	0.8313(3)	0.8929(3)	0.4166(3)	0.0194	1
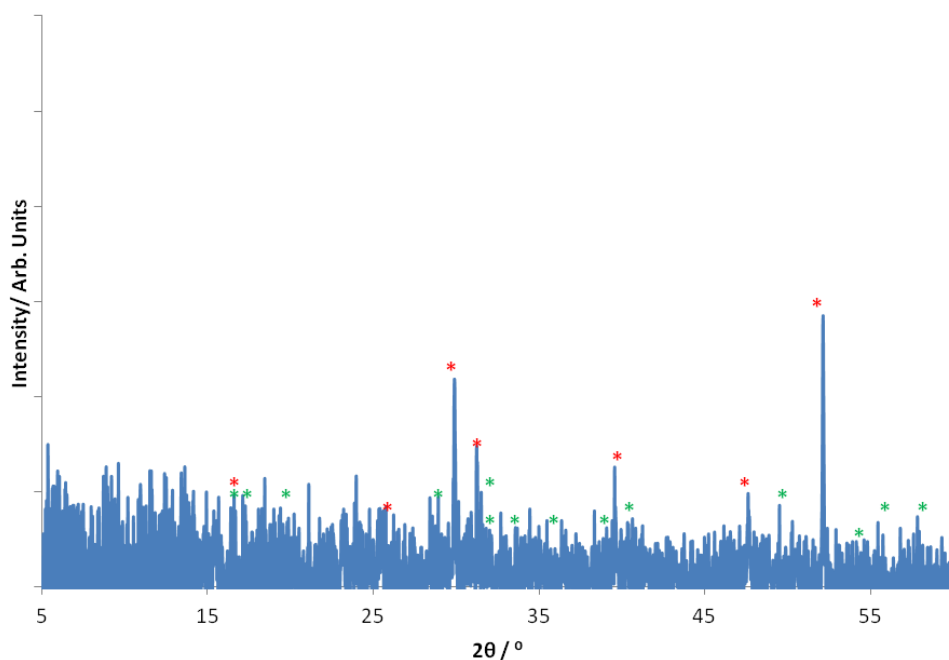
Figure A2.1: Powder X-ray diffraction pattern of $[Co(deta)_2]_2[Ge_4O_6S_4].H_2O$ **(8)** after the TGA experiment. Peaks in the pattern are annotated with asterisks and correspond to Co_9S_8 (red) and GeS_2 (green). Signal/noise ratio is poor due to lack of sample post TGA.

Table A2.5 Fractional coordinates and isotropic temperature factors (in Å^2) of the non-hydrogen atoms in $[Co(deta)_2]_2$ $[Ge_4O_4S_6]$ **(10)**

Atom	x	y	z	U_{equiv}	Occupancy
Ge(1)	0.94751(6)	0.20469(5)	0.65902(5)	0.0259	1
Ge(2)	1.09892(6)	0.33957(6)	0.70389(6)	0.032	1
S(1)	1	0.1115(2)	0.75	0.0343	1
S(2)	0.88803(15)	0.14783(13)	0.55448(14)	0.0325	1
S(3)	1.2151(2)	0.39655(16)	0.65358(17)	0.0508	1
S(4)	1	0.4326(3)	0.75	0.0713	1
Co(1)	0.70801(7)	0.37894(6)	0.51679(8)	0.0326	1
O(1)	1.0431(4)	0.2696(4)	0.6296(4)	0.0328	1
O(2)	0.8713(4)	0.2727(3)	0.7115(3)	0.0265	1
N(1)	0.7047(6)	0.3954(6)	0.3831(7)	0.0558	1
N(2)	0.8465(5)	0.3462(5)	0.4841(5)	0.0416	1
N(3)	0.7798(6)	0.4941(6)	0.5430(8)	0.0739	1
N(4)	0.6858(5)	0.3544(6)	0.6487(5)	0.0455	1
N(5)	0.6699(6)	0.2514(5)	0.5098(5)	0.042	1
N(6)	0.5782(5)	0.4338(4)	0.5342(6)	0.0387	1
C(1)	0.7899(9)	0.3730(8)	0.3448(8)	0.0693	1
C(2)	0.8475(10)	0.3220(14)	0.3957(9)	0.0997	1
C(3)	0.8703(7)	0.4750(8)	0.5612(6)	0.051	1
C(4)	0.9082(7)	0.4106(7)	0.5097(13)	0.0847	1
C(5)	0.6132(6)	0.2308(6)	0.5827(7)	0.0446	1
C(6)	0.6561(7)	0.2669(9)	0.6588(7)	0.0609	1
C(7)	0.6196(8)	0.4163(9)	0.6777(7)	0.064	1
C(8)	0.5419(7)	0.4223(7)	0.6177(7)	0.0497	1
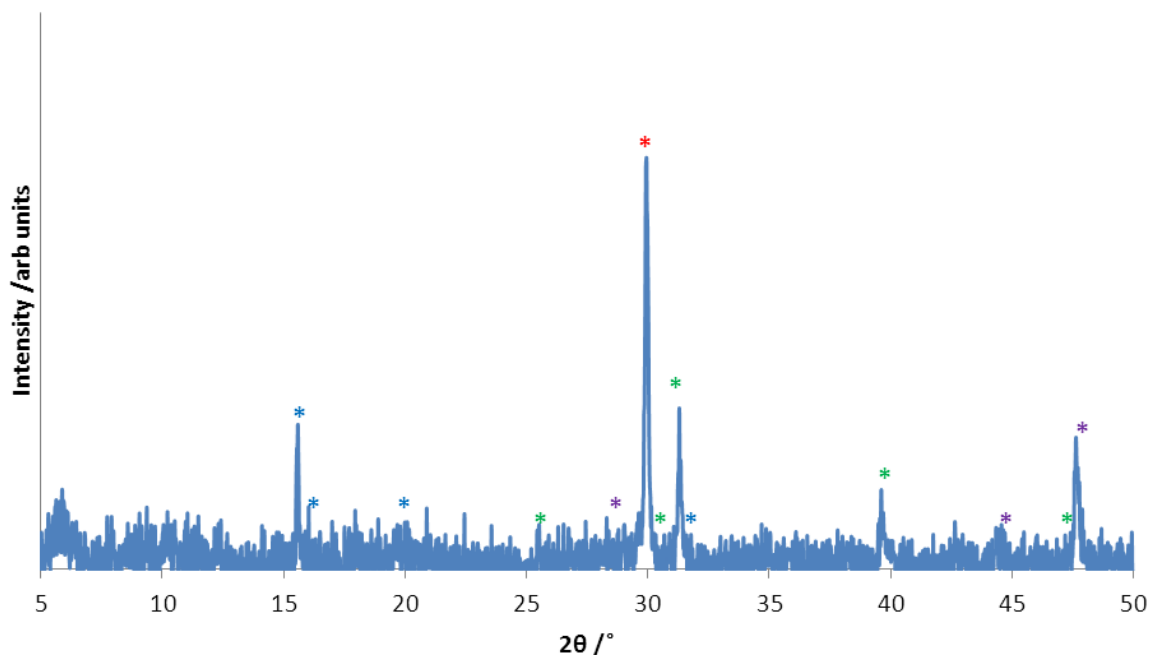
Figure A2.2: Powder X-ray diffraction pattern of [Co(deta)$_2$]$_2$ [Ge$_4$O$_4$S$_6$] **(10)** after the TGA experiment. Peaks in the pattern are annotated with asterisks and correspond to Co$_4$S$_3$ (red), Co$_9$S$_8$ (green), CoS (purple) and GeS$_2$ (blue)

Table A2.6 Fractional coordinates and isotropic temperature factors (in Å^2) of the non-hydrogen atoms in [Co(dap)$_3$)]$_2$[Ge$_4$O$_2$S$_8$] **(11)**

Atom	x	y	z	U_{equiv}	Occupancy
Ge(1)	0.44433(3)	0.54202(5)	0.24016(3)	0.0277	1
Ge(2)	0.50714(4)	0.79769(6)	0.32514(4)	0.0418	1
Ge(3)	0.59420(4)	0.63534(7)	0.21202(4)	0.0418	1
Ge(4)	0.44301(4)	0.78102(6)	0.15307(4)	0.0436	1
Co(1)	0.18601(5)	0.62843(9)	0.10978(5)	0.0408	1
Co(2)	0.60005(5)	0.16381(8)	0.16275(5)	0.0401	1
S(1)	0.38877(9)	0.37742(14)	0.23254(10)	0.0396	1
S(2)	0.44882(9)	0.63156(17)	0.34050(9)	0.0421	1
S(3)	0.61461(9)	0.74737(16)	0.30768(12)	0.0498	1
S(4)	0.68674(11)	0.5565(3)	0.18878(17)	0.0807	1
S(5)	0.54418(14)	0.7395(2)	0.12528(17)	0.0769	1
S(6)	0.45001(15)	0.9001(2)	0.23793(14)	0.072	1
S(7)	0.37772(19)	0.8636(3)	0.06960(18)	0.1058	1
S(8)	0.51204(15)	0.9138(2)	0.41069(13)	0.0748	1
O(1)	0.5317(2)	0.5238(4)	0.2250(2)	0.0338	1
O(2)	0.4044(2)	0.6452(4)	0.1761(2)	0.0327	1

Atom	x	y	z	U_{equiv}	Occupancy
N(1)	0.0848(3)	0.7041(6)	0.1174(4)	0.0546	1
N(2)	0.1812(6)	0.7762(9)	0.0378(6)	0.0972	1
N(3)	0.1908(9)	0.5145(11)	0.1977(8)	0.1431	1
N(4)	0.1415(4)	0.4963(8)	0.0371(5)	0.086	1
N(5)	0.2811(4)	0.5544(10)	0.0829(4)	0.0876	1
N(6)	0.2385(5)	0.7504(14)	0.1840(6)	0.1176	1
N(7)	0.7114(5)	0.1683(10)	0.1651(5)	0.0841	1
N(8)	0.6101(5)	0.0151(8)	0.0947(5)	0.077	1
N(9)	0.6025(5)	0.2943(8)	0.2407(5)	0.0809	1
N(10)	0.5780(6)	0.3009(9)	0.0859(6)	0.1068	1
N(11)	0.4851(4)	0.1599(7)	0.1412(4)	0.0667	1
N(12)	0.6076(5)	0.0474(8)	0.2507(5)	0.0818	1
C(14)	0.6072(12)	0.1155(13)	0.3094(7)	0.1375	1
C(13)	0.7012(11)	-0.115(2)	0.0585(11)	0.159	1
C(19)	0.5945(7)	0.3132(19)	0.3652(8)	0.129	1
C(8)	0.2606(7)	0.7025(11)	0.2481(8)	0.1016	1
C(5)	0.1982(8)	0.4158(19)	0.0213(12)	0.1792	1
C(10)	0.2386(10)	0.585(4)	0.3320(8)	0.2968	1
C(1)	0.0670(6)	0.7978(10)	0.0647(5)	0.0713	1
C(2)	0.1279(7)	0.8627(10)	0.0534(6)	0.0758	1
C(4)	0.2164(8)	0.6067(9)	0.2609(5)	0.0861	1
C(3)	0.1125(10)	0.9631(13)	0.0009(7)	0.1169	1
C(11)	0.7267(6)	0.0853(15)	0.1099(7)	0.0932	1
C(12)	0.6836(5)	-0.0198(11)	0.1054(6)	0.0755	1
C(17)	0.5037(5)	0.3243(9)	0.0687(6)	0.0725	1
C(18)	0.4632(5)	0.2126(10)	0.0732(6)	0.0761	1
C(7)	0.2635(8)	0.477(3)	0.0249(14)	0.2339	1
C(15)	0.6054(16)	0.2415(14)	0.3061(6)	0.1942	1
C(21)	0.3887(11)	0.232(2)	0.0554(10)	0.0811	0.5
C(9)	0.2414(18)	0.566(5)	-0.059(3)	0.2098	0.5
C(16)	0.470(2)	0.408(3)	0.023(2)	0.1766	0.5
C(6)	0.200(6)	0.309(5)	0.042(3)	0.3791	0.5

Table A2.6 Fractional coordinates and isotropic temperature factors (in $Å^2$) of the non-hydrogen atoms in [Co(deta)$_2$]$_4$[Ge$_9$O$_{14}$S$_8$] **(12)**

Atom	x	y	z	U_{equiv}	Occupancy
Ge(1)	0.84057(9)	0.57893(5)	0.64203(4)	0.0161	1
Ge(2)	0.96344(8)	0.65430(4)	0.68155(4)	0.0146	1
Ge(3)	1.125	0.625	0.625	0.0182	1
Co(1)	0.99823(12)	0.51653(6)	0.77119(5)	0.0184	1

Atom	x	y	z	U_{equiv}	Occupancy
S(1)	0.7710(2)	0.52636(13)	0.66686(11)	0.0287	1
S(2)	0.9746(2)	0.67108(11)	0.74374(10)	0.0217	1
O(1)	0.7800(8)	0.625	0.625	0.0165	1
O(2)	0.9236(5)	0.6007(3)	0.6739(3)	0.0178	1
O(3)	0.8937(6)	0.5610(3)	0.5970(2)	0.0222	1
O(4)	1.0628(6)	0.6592(3)	0.6549(3)	0.0256	1
N(1)	1.0134(6)	0.4602(3)	0.7344(3)	0.0167	1
N(2)	1.0493(7)	0.5447(4)	0.7159(4)	0.0243	1
N(3)	0.9487(8)	0.4664(4)	0.8133(3)	0.0253	1
N(4)	0.8581(7)	0.5287(4)	0.7588(3)	0.0254	1
N(5)	0.9783(7)	0.5747(4)	0.8056(3)	0.0267	1
N(6)	1.1228(7)	0.5200(3)	0.8030(3)	0.0197	1
C(1)	1.0137	0.4723	0.6925	0.0335	1
C(2)	1.0742	0.5104	0.6877	0.0332	1
C(3)	0.9474	0.4282	0.7477	0.0395	1
C(4)	0.9543	0.4242	0.794	0.0395	1
C(5)	0.8353	0.5714	0.7746	0.0347	1
C(6)	0.8852	0.5788	0.8144	0.0296	1
C(7)	1.035	0.5735	0.8402	0.0272	1
C(8)	1.1255	0.561	0.8274	0.0251	1

Table A2.6 Fractional coordinates and isotropic temperature factors (in Å^2) of the non-hydrogen atoms in $[Co(tren)]_2[Ge_5O_{11}S_2]$ **(13)**

Atom	x	y	z	U_{equiv}	Occupancy
Ge(1)	0.59320(10)	0.9990(2)	-0.11809(16)	0.0145	1
Ge(2)	0.58609(9)	1.2915(2)	0.10534(16)	0.0158	1
Ge(3)	0.67287(9)	1.0370(3)	0.06718(17)	0.0171	1
Ge(4)	0.51349(10)	0.9768(3)	-0.00735(17)	0.0173	1
Ge(5)	0.60033(9)	0.7233(2)	0.11257(16)	0.0163	1
Co(1)	0.49607(12)	1.3448(4)	0.1989(2)	0.0197	1
Co(2)	0.69294(13)	0.6695(4)	0.2885(2)	0.0204	1
S(1)	0.75362(18)	1.0465(7)	0.1125(3)	0.0255	1
S(2)	0.43286(19)	0.9707(7)	-0.0383(3)	0.0258	1
O(1)	0.5605(5)	1.1537(18)	-0.1958(9)	0.0263	1
O(2)	0.6262(5)	0.8343(16)	-0.1602(8)	0.023	1
O(3)	0.6419(5)	1.1128(16)	-0.0419(9)	0.0229	1
O(4)	0.5442(5)	0.8952(17)	-0.0862(9)	0.0294	1
O(5)	0.5402(5)	1.1964(19)	0.0166(9)	0.0256	1
O(6)	0.5416(5)	0.837(2)	0.0875(9)	0.0287	1
O(7)	0.6467(5)	0.8196(18)	0.0687(8)	0.0213	1

O(8)	0.6457(4)	1.1798(18)	0.1331(10)	0.0286	1
O(9)	0.5655(5)	1.2956(19)	0.1981(9)	0.0303	1
O(10)	0.5919(5)	0.5078(15)	0.0629(9)	0.0222	1
O(11)	0.6218(4)	0.7146(16)	0.2254(9)	0.0236	1
N(1)	0.5099(6)	1.4818(19)	0.3172(11)	0.023	1
N(2)	0.4667(6)	1.075(3)	0.1896(12)	0.0322	1
N(3)	0.4688(7)	1.4962(19)	0.0797(12)	0.0271	1
N(4)	0.4158(6)	1.404(2)	0.1989(12)	0.0297	1
N(5)	0.7207(7)	0.942(2)	0.3085(11)	0.03	1
N(6)	0.6807(7)	0.519(2)	0.3936(10)	0.0231	1
N(7)	0.7173(6)	0.532(2)	0.1911(10)	0.0212	1
N(8)	0.7734(6)	0.610(2)	0.3612(11)	0.028	1
C(1)	0.4654(7)	1.584(4)	0.3268(14)	0.0394	1
C(2)	0.4171(9)	1.471(3)	0.2884(17)	0.0372	1
C(3)	0.4195(8)	1.069(3)	0.2177(13)	0.0292	1
C(4)	0.3863(8)	1.226(3)	0.1803(16)	0.0348	1
C(5)	0.4128(9)	1.507(2)	0.0526(16)	0.0341	1
C(6)	0.3957(8)	1.543(3)	0.1324(16)	0.0348	1
C(7)	0.7693(8)	0.943(3)	0.3818(12)	0.0272	1
C(8)	0.8021(7)	0.792(3)	0.3685(18)	0.039	1
C(9)	0.7300(9)	0.419(3)	0.4422(13)	0.0321	1
C(10)	0.7764(9)	0.548(3)	0.4472(15)	0.0321	1
C(11)	0.7741(7)	0.528(3)	0.2132(15)	0.0322	1
C(12)	0.7947(7)	0.487(2)	0.3101(16)	0.0304	1

Cut bonds

Replace S with O,
New O bonds to Co,
Cut O1-Ge1,
Protonation of Oxygen

Fused T2 unit of **(12)**

Repeating unit of **(13)**
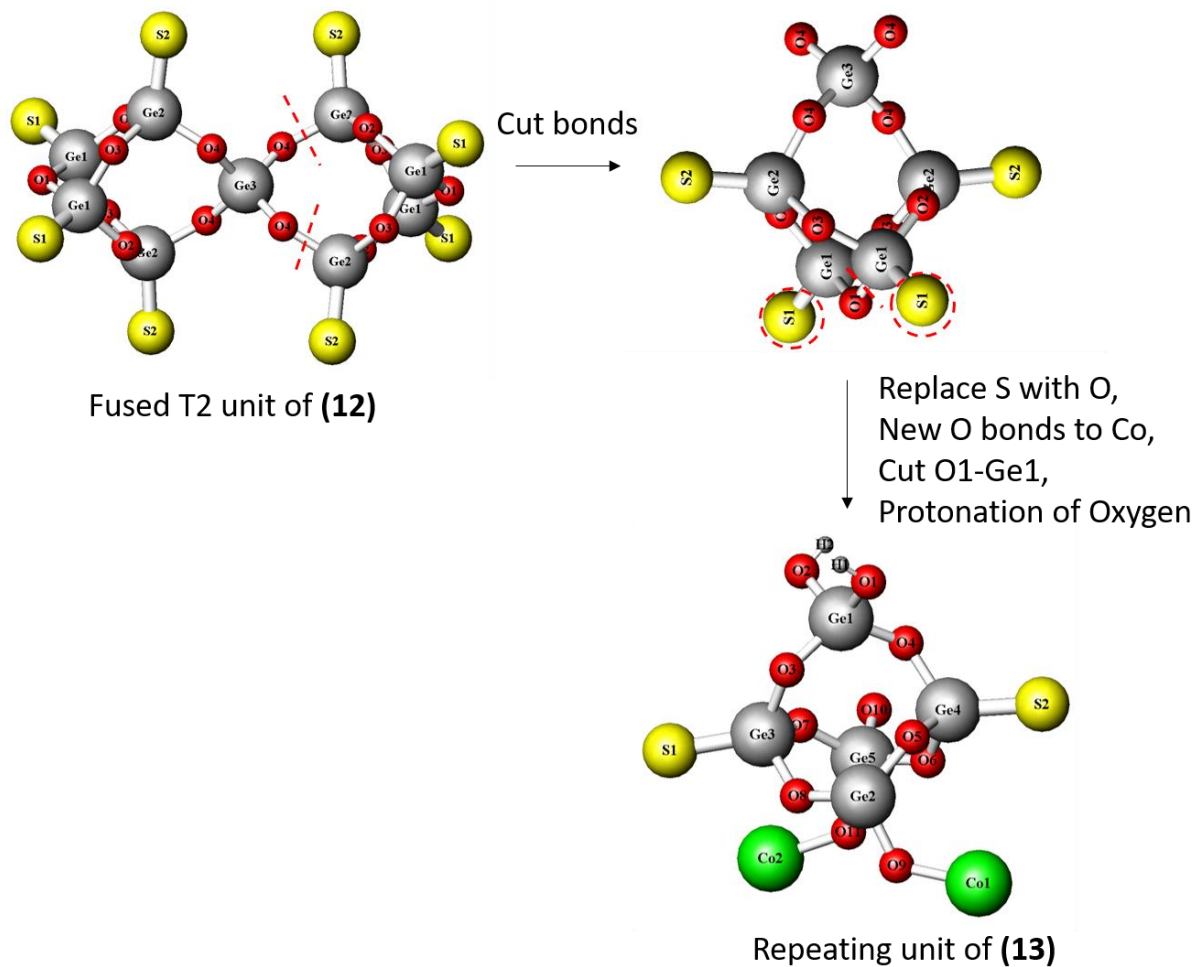
Figure A2.3: A schematic showing a proposed transformation from structure **(12)** to **(13).** Key: Ge, grey spheres; O, red spheres; S, yellow spheres; Co, green spheres.
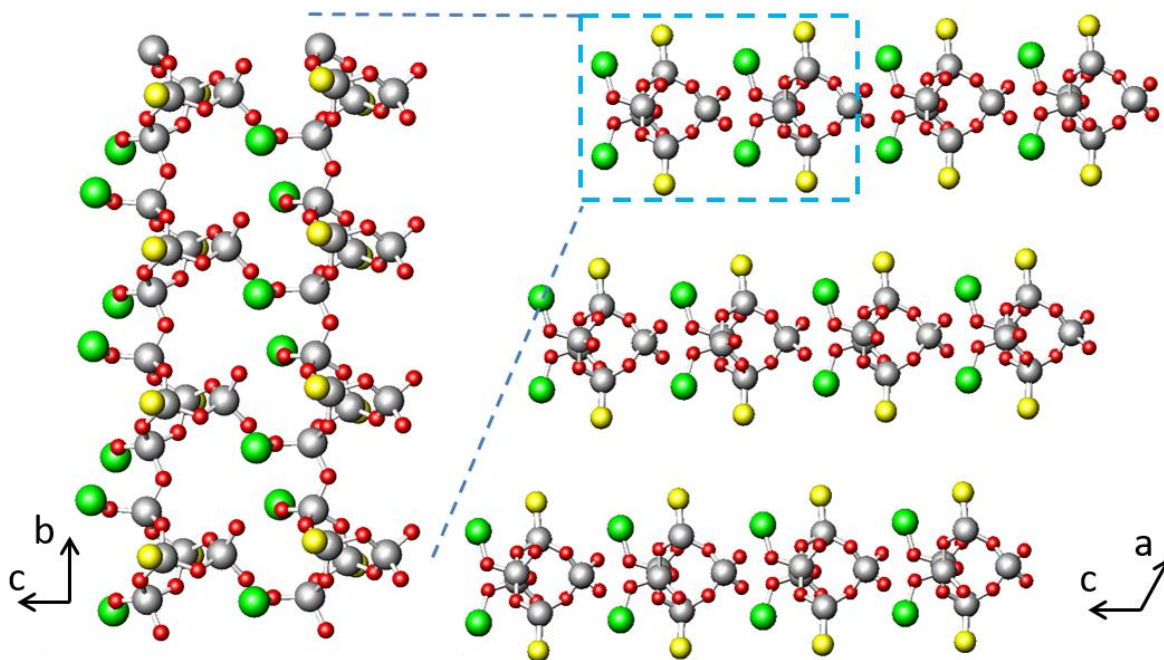
Figure A2.4: (left) Two chains of [Co(tren)]$_2$[Ge$_5$O$_{11}$S$_2$] (**13**) found in the [010] direction, but viewed along [100] and (right) displays multiple rows and columns of chains in a fully packed crystal structure down [100]. Key: grey Ge, red O, yellow S, green Co. Hydrogen, carbon and nitrogen omitted for clarity.

Appendix 3 (A3) – Chapter 5 Supplementary Information

Table A3.1 Fractional coordinates and isotropic temperature factors (in Å^2) of the non-hydrogen atoms in $[Co(Hdeta)_2(SO_4)_2]$ **(14)**

Atom	x	y	z	Uequiv	Occupancy
Co(1)	1	½	1	0.0092	1
O(1)	0.79202(13)	0.40446(10)	0.87042(10)	0.0125	1
S(1)	0.72934(4)	0.44512(3)	0.73008(3)	0.0104	1
O(4)	0.86690(14)	0.43312(12)	0.65139(11)	0.0189	1
O(3)	0.59032(13)	0.36084(10)	0.67416(11)	0.0154	1
O(2)	0.67185(14)	0.57938(10)	0.73271(12)	0.0173	1
N(1)	0.91182(15)	0.68841(11)	0.94078(12)	0.0124	1
C(1)	0.8236(2)	0.74045(14)	1.04620(15)	0.0179	1
C(2)	0.72625(18)	0.63383(14)	1.10019(15)	0.0161	1
N(2)	0.84236(14)	0.52917(11)	1.14866(12)	0.0105	1
C(3)	0.75876(18)	0.41981(13)	1.20230(13)	0.0128	1
C(4)	0.73747(17)	0.44347(13)	1.34654(14)	0.0126	1
N(3)	0.63546(15)	0.34093(12)	1.39631(12)	0.0124	1

Table A3.2 Fractional coordinates and isotropic temperature factors (in Å^2) of the non-hydrogen atoms in $(H_24,4'-bipy)[Co(H_2O)_2(4,4'-bipy)(SO_4)_2].H_2O$ **(15)**

Atom	x	y	z	Uequiv	Occupancy
Co(1)	1	0	½	0.0086	1
Co(2)	1	0	1	0.0107	1
S(1)	1.16134(6)	0.16700(5)	0.62748(4)	0.0112	1
S(2)	0.85637(6)	-0.19959(5)	0.88813(4)	0.0124	1
O(1)	0.85369(19)	-0.10528(15)	0.60465(12)	0.0128	1
O(2)	1.08414(19)	0.05837(16)	0.61521(12)	0.0143	1
O(3)	1.1715(2)	0.26155(16)	0.53795(13)	0.0165	1
O(4)	1.31738(18)	0.09438(18)	0.64123(14)	0.0181	1
O(5)	1.0732(2)	0.24733(19)	0.71832(14)	0.0215	1
O(6)	1.1465(2)	0.08603(18)	0.88547(13)	0.016	1
O(7)	0.9239(2)	-0.07981(17)	0.88919(12)	0.0149	1
O(8)	0.7559(2)	-0.16064(19)	0.81560(14)	0.0222	1
O(9)	0.7658(3)	-0.2191(2)	0.98933(14)	0.028	1
O(10)	0.9744(2)	-0.32843(19)	0.85718(17)	0.0284	1
O(11)	0.9394(2)	0.5424(2)	0.68962(17)	0.0287	1
N(1)	0.8114(2)	0.19380(18)	0.50992(14)	0.0119	1

N(2)	0.8147(2)	0.19459(18)	0.99692(14)	0.0135	1
N(3)	0.6376(2)	0.1105(2)	0.78927(15)	0.0161	1
N(4)	0.3733(2)	0.8382(2)	0.70989(15)	0.0173	1
C(1)	0.6664(3)	0.1850(2)	0.52323(16)	0.0129	1
C(2)	0.5426(3)	0.3007(2)	0.52072(16)	0.0124	1
C(3)	0.5646(2)	0.4361(2)	0.50270(15)	0.0102	1
C(4)	0.7142(3)	0.4460(2)	0.48933(18)	0.0133	1
C(5)	0.8323(2)	0.3240(2)	0.49343(17)	0.012	1
C(6)	0.8363(3)	0.3239(2)	0.97768(18)	0.0159	1
C(7)	0.7168(3)	0.4470(2)	0.97753(18)	0.0162	1
C(8)	0.5654(2)	0.4364(2)	0.99987(16)	0.0118	1
C(9)	0.5436(3)	0.3011(2)	1.01996(17)	0.0136	1
C(10)	0.6681(3)	0.1845(2)	1.01816(17)	0.0145	1
C(11)	0.4876(3)	0.1680(2)	0.79677(18)	0.0171	1
C(12)	0.4309(3)	0.3114(2)	0.78306(17)	0.0162	1
C(13)	0.5306(2)	0.3973(2)	0.76103(16)	0.0125	1
C(14)	0.6878(2)	0.3323(2)	0.75263(16)	0.0148	1
C(15)	0.7373(3)	0.1887(2)	0.76677(17)	0.0157	1
C(16)	0.4756(2)	0.5516(2)	0.74485(15)	0.0127	1
C(17)	0.3185(2)	0.6209(2)	0.76237(17)	0.0158	1
C(18)	0.2706(3)	0.7634(2)	0.74461(18)	0.019	1
C(19)	0.5241(3)	0.7781(2)	0.69435(18)	0.0181	1
C(20)	0.5787(3)	0.6353(2)	0.71011(17)	0.0159	1

Table A3.3 Fractional coordinates and isotropic temperature factors (in Å^2) of the non-hydrogen atoms in [Mn(tepa)(SO4)] (**16**)

Atom	x	y	z	Uequiv	Occupancy	Isotropy
Mn(1)	-0.6172(8)	0	½	0.0309	1	Uani
Mn(2)	-0.5796(5)	0	0.1698(2)	0.0263	1	Uani
Mn(3)	-0.4800(6)	½	0.3345(2)	0.0247	1	Uani
Mn(4)	-0.5193(6)	½	0	0.0126	1	Uani
S(1)	-0.5723(10)	0	0.3347(4)	0.0439	1	Uani
S(2)	-0.5938(8)	0	0	0.0114	1	Uani
S(3)	-0.5064(8)	½	½	0.0083	1	Uani
S(4)	-0.4988(14)	0.49	0.1674(7)	0.0578	1	Uani
O(1)	-0.644(2)	0	0.3905(14)	0.050(8)	1	Uiso
O(2)	-0.6277(18)	0	0.2720(11)	0.033(5)	1	Uiso
O(3)	-0.5305(14)	0	0.0593(9)	0.015(4)	1	Uiso
O(4)	-0.690(2)	0.0422(19)	0	0.052(7)	1	Uiso
O(5)	-0.5023(14)	-0.0726(11)	0.3387(7)	0.035(4)	1	Uiso

O(6)	-0.4379(17)	0.5	0.4415(11)	0.026(5)	1	Uiso
O(7)	-0.5595(18)	0.4167(17)	½	0.029(5)	1	Uiso
O(8)	-0.513(5)	0.4858	0.226(4)	0.20(3)	1	Uiso
O(9)	-0.441(2)	0.4068(19)	0.1653(12)	0.087(8)	1	Uiso
O(10)	-0.529(6)	½	0.110(4)	0.24(4)	1	Uiso
N(11)	-0.5256(19)	0.1381(18)	0.1880(13)	0.053(7)	1	Uiso
N(14)	-0.398(3)	0.025(2)	0.1698(14)	0.084(11)	1	Uiso
N(15)	-0.7031(19)	0.1063(18)	0.1435(12)	0.055(7)	1	Uiso
N(20)	-0.744(2)	-0.102(2)	½	0.035(7)	1	Uiso
N(23)	-0.530(3)	-0.119(3)	0.5099	0.049(10)	1	Uiso
N(25)	-0.449(8)	0	½	0.12(3)	1	Uiso
N(34)	-0.3457(18)	0.4154(17)	0.3121(11)	0.046(6)	1	Uiso
N(37)	-0.541(2)	0.355(2)	0.3539(15)	0.070(8)	1	Uiso
N(40)	-0.671(5)	½	0.348(3)	0.12(2)	1	Uiso
N(42)	-0.379(3)	0.577(3)	-0.0124	0.056(13)	1	Uiso
N(45)	-0.609(5)	0.626(4)	0	0.12(2)	1	Uiso
N(47)	-0.716(7)	½	0	0.11(3)	1	Uiso
C(12)	-0.419(2)	0.1473(16)	0.1718(11)	0.030(5)	1	Uiso
C(13)	-0.341(3)	-0.064(3)	0.1930(17)	0.077(11)	1	Uiso
C(16)	-0.713(2)	0.1642(18)	0.1673(13)	0.039(6)	1	Uiso
C(17)	-0.615(4)	0.199(3)	0.168(2)	0.085(13)	1	Uiso
C(21)	-0.701(4)	-0.180(4)	½	0.072(15)	1	Uiso
C(22)	-0.592(4)	-0.188(4)	½	0.057(12)	1	Uiso
C(24)	-0.427(3)	-0.122(3)	½	0.044(9)	1	Uiso
C(35)	-0.338(5)	0.320(4)	0.325(3)	0.15(2)	1	Uiso
C(36)	-0.450(5)	0.291(4)	0.332(2)	0.12(2)	1	Uiso
C(38)	-0.635(2)	0.3295(17)	0.3353(12)	0.039(6)	1	Uiso
C(39)	-0.699(3)	0.397(3)	0.3511(17)	0.065(9)	1	Uiso
C(43)	-0.430(3)	0.686(3)	0	0.037(8)	1	Uiso
C(44)	-0.536(3)	0.698(3)	0	0.047(9)	1	Uiso
C(46)	-0.717(4)	0.619(3)	0	0.057(12)	1	Uiso
C(20)	-0.387(5)	0.043(4)	½	0.086(18)	1	Uiso

Table A3.4 Fractional coordinates and isotropic temperature factors (in Å^2) of the non-hydrogen atoms in [CoSO$_4$(dap)$_2$] (**17**)

Atom	x	y	z	Uequiv	Occupancy
Co(1)	½	0.72825(5)	0.60897(4)	0.0216	1
O(1)	½	0.6713(3)	0.4456(2)	0.0254	1
S(1)	½	0.76901(9)	0.35813(8)	0.0244	1
O(2)	½	0.6892(3)	0.2636(2)	0.0271	1

O(3)	0.43734(15)	0.8547(2)	0.36272(18)	0.0363	1
N(2)	0.42079(15)	0.5845(3)	0.6396(2)	0.0275	1
C(1)	0.3549(2)	0.6406(4)	0.6058(3)	0.0397	1
C(2)	0.3537(2)	0.7920(4)	0.6312(3)	0.0396	1
N(1)	0.41396(16)	0.8556(2)	0.58366(19)	0.0272	1
C(4)	0.2939(7)	0.5697(13)	0.6611(11)	0.0692	0.45
C(3)	0.2873(4)	0.8569(10)	0.5999(8)	0.058	0.55

Table A3.5 Fractional coordinates and isotropic temperature factors (in Å^2) of the non-hydrogen atoms in [Co(SO$_4$)(deta)] **(18)**

Atom	x	y	z	Uequiv	Occupancy
Co(1)	0.35459(3)	0.86989(3)	¾	0.0134	1
S(1)	0.00752(6)	0.83935(4)	¾	0.0144	1
O(1)	0.11607(13)	0.86982(11)	0.64469(9)	0.0202	1
O(2)	-0.14509(18)	0.92516(14)	¾	0.019	1
O(3)	-0.0442(2)	0.70128(15)	¾	0.0254	1
N(1)	0.3470(2)	0.65593(18)	¾	0.0217	1
N(2)	0.51908(16)	0.83803(12)	0.60500(11)	0.0189	1
C(1)	0.4227(3)	0.60970(15)	0.63798(15)	0.0284	1
C(2)	0.5673(2)	0.69672(17)	0.59822(14)	0.027	1

Table A3.6 Fractional coordinates and isotropic temperature factors (in Å^2) of the non-hydrogen atoms in [Co(SO$_4$)(dab)] **(19)**

Atom	X	y	z	Uequiv	Occupancy
Co(1)	0.70594(6)	0.82624(11)	¾	0.0079	1
O(2)	0.83171(18)	0.5315(4)	0.68454(10)	0.0176	1
S(1)	0.89650(9)	0.40150(16)	¾	0.0126	1
O(3)	0.8789(3)	0.0945(5)	¾	0.0162	1
O(1)	1.0444(3)	0.4618(5)	¾	0.0173	1
N(1)	0.6288(2)	1.0490(4)	0.65947(12)	0.0165	1
C(1)	0.5913(3)	0.8966(6)	0.59138(15)	0.0199	1
C(2)	0.5254(3)	1.0824(6)	0.53321(15)	0.0218	1

Appendix 4 (A4) – Chapter 6 Supplementary Information

Table A4.1 Fractional coordinates and isotropic temperature factors (in $\mathring{A}^2$) of the non-hydrogen atoms in [Fe(tren)][Sb_2S_4] **(20)**

Atom	x	y	z	U_{equiv}	Occupancy
Sb(1)	1.03147(2)	0.52100(3)	0.392821(12)	0.0179	1
Sb(2)	0.86807(3)	0.85532(3)	0.504573(14)	0.0237	1
Fe(1)	0.66931(7)	0.50039(8)	0.31984(3)	0.0204	1
S(1)	1.03321(11)	0.23843(12)	0.38197(5)	0.0224	1
S(2)	0.83025(10)	0.55662(12)	0.45218(5)	0.0196	1
S(3)	0.89376(10)	0.53717(12)	0.27853(5)	0.0213	1
S(4)	1.07752(14)	0.86827(13)	0.45036(6)	0.0311	1
N(1)	0.6656(4)	0.2764(5)	0.36600(19)	0.0254	1
N(2)	0.5454(4)	0.4286(5)	0.22426(18)	0.0238	1
N(3)	0.6209(4)	0.7392(5)	0.3316(2)	0.0276	1
N(4)	0.4480(4)	0.4929(5)	0.3515(2)	0.0272	1
C(1)	0.4894(5)	0.7701(7)	0.3602(3)	0.0395	1
C(2)	0.4410(5)	0.6276(7)	0.3943(3)	0.0353	1
C(3)	0.3492(5)	0.4996(7)	0.2859(3)	0.0346	1
C(4)	0.3974(5)	0.3965(7)	0.2318(2)	0.0324	1
C(5)	0.4307(6)	0.3516(7)	0.3889(3)	0.0416	1
C(6)	0.5692(6)	0.2824(7)	0.4193(3)	0.0365	1

Table A4.2 Fractional coordinates and isotropic temperature factors (in $\mathring{A}^2$) of the non-hydrogen atoms in [Co(tren)]$_2$[μ-Ge_2S_6] **(21)**

Atom	x	y	z	U_{equiv}	Occupancy
Ge(1)	0.38835(4)	½	0.40226(4)	0.0148	1
Co(1)	0.26849(5)	½	0.65699(5)	0.0149	1
S(1)	½	0.68227(12)	½	0.0177	1
S(2)	0.23336(9)	½	0.44851(9)	0.0169	1
S(3)	0.37947(10)	½	0.21848(9)	0.0252	1
N(1)	0.3600(2)	0.6885(3)	0.7121(2)	0.0209	1
N(2)	0.2742(3)	½	0.8504(3)	0.018	1
N(3)	0.1017(3)	½	0.6500(3)	0.0205	1
C(1)	0.1656(5)	0.5432(7)	0.8607(5)	0.0223	0.5
C(2)	0.3588(6)	0.3937(8)	0.9086(5)	0.0212	0.5
C(3)	0.3736(4)	0.7285(5)	0.8359(3)	0.0371	1

Atom	x	y	z			Occupancy
C(4)	0.3020(6)	0.6542(8)	0.8948(5)	0.021		0.5
C(5)	0.0789(5)	½	0.7640(5)	0.0548		1

Table A4.3 Fractional coordinates and isotropic temperature factors (in Å^2) of the non-hydrogen atoms in [Fe(en)$_3$][FeSe$_2$] **(22)**

Atom	x	y	z	U_{equiv}	Occupancy
Se(1)	0.6319(2)	0.4612(2)	0.42303(13)	0.0142	1
Se(2)	0.5798(2)	0.6761(2)	0.59854(12)	0.0134	1
Se(3)	0.3178(2)	0.4259(2)	0.54854(12)	0.0132	1
Se(4)	0.3494(2)	0.7153(2)	0.41434(12)	0.0128	1
Se(5)	1.0027(2)	1.0692(3)	-0.12316(11)	0.0171	1
Se(6)	1.1764(2)	1.2710(2)	0.05289(13)	0.0148	1
Se(7)	0.8485(2)	1.0634(3)	0.07564(11)	0.0169	1
Se(8)	0.8344(2)	1.3568(2)	-0.04165(17)	0.0241	1
Fe(1)	0.5048(3)	0.3208(3)	0.4917(2)	0.0094	1
Fe(2)	0.4662(2)	0.5694(3)	0.49409(15)	0.0108	1
Fe(3)	0.9589(3)	0.9373(3)	-0.01546(17)	0.0127	1
Fe(4)	0.9683(3)	1.1918(3)	-0.00937(18)	0.012	1
Fe(5)	0.5765(3)	0.7716(3)	0.18634(17)	0.0126	1
Fe(6)	1.0023(3)	0.7372(3)	0.67907(18)	0.0151	1
N(1)	0.6464(15)	0.6953(15)	0.3017(9)	0.009(3)	1
N(2)	0.8016(16)	0.8107(15)	0.1885(10)	0.011(4)	1
N(3)	0.6190(17)	0.6217(16)	0.1053(10)	0.018(4)	1
N(4)	0.3776(19)	0.677(2)	0.1889(12)	0.030(5)	1
N(5)	0.4885(16)	0.9260(16)	0.2540(9)	0.015(4)	1
N(6)	0.5199(15)	0.8914(15)	0.0853(9)	0.010(4)	1
N(7)	1.2202(17)	0.6941(18)	0.6561(11)	0.021(4)	1
N(8)	1.1075(17)	0.8021(16)	0.7908(11)	0.017(4)	1
N(9)	0.9506(16)	0.562(2)	0.7373(9)	0.020(4)	1
N(10)	0.9298(16)	0.6279(15)	0.5724(10)	0.010(4)	1
N(11)	0.8163(16)	0.8231(16)	0.7243(10)	0.015(4)	1
N(12)	0.9993(18)	0.9044(17)	0.6087(11)	0.021(4)	1
C(1)	0.799(2)	0.687(2)	0.3038(13)	0.022(5)	1
C(2)	0.861(2)	0.787(2)	0.2647(13)	0.019(5)	1
C(3)	0.490(2)	0.560(3)	0.0915(13)	0.033(5)	1
C(4)	0.404(2)	0.550(2)	0.1611(13)	0.024(5)	1
C(5)	0.406(2)	0.9916(19)	0.1946(12)	0.017(5)	1
C(6)	0.485(2)	1.008(2)	0.1145(13)	0.023(5)	1
C(7)	1.299(2)	0.693(2)	0.7344(12)	0.015(4)	1
C(8)	1.259(2)	0.804(2)	0.7815(15)	0.030(6)	1
C(9)	0.870(2)	0.494(2)	0.6811(14)	0.025(5)	1
C(10)	0.926(2)	0.5053(19)	0.6002(12)	0.014(5)	1
C(11)	0.789(2)	0.933(2)	0.6787(12)	0.022(5)	1
C(12)	0.923(2)	0.991(2)	0.6509(13)	0.023(5)	1

Table A4.4 All reactions that were conducted within the iron selenide project

ID	Reagents	Temp /°C	days	content present*
JL0262	Fe 0.0420g, Se 0.0794g, phen 0.09g, methylamine 9ml	160	5	n/a
JL0263	Fe 0.0418g, Se 0.0783g, bipy 0.0775, methylamine 5ml	160	5	Fe, FeSe$_2$
JL0264	Fe 0.0433g, Se 0.0776g, 2,2-dithiopyridine 0.109g, methylamine 5ml	160	5	Fe, FeSe$_2$
JL0265	Fe 0.0420g, Se 0.0790g, phen 0.090g, ethylamine 5ml	160	5	Fe, FeSe$_2$
JL0266	Fe 0.0428g, Se 0.0800g, bipy 0.0767g, ethylamine5ml	160	5	Fe, FeSe$_2$
JL0267	Fe 0.0426g, Se 0.0797g, 2,2-dithiopyridine 0.1090g, ethylamine 5ml	160	5	FeSe$_2$
JL0268	Fe 0.0418g, Se 0.0789g, CoS 0.0268g, ethylamine 5ml	160	5	Fe, FeSe$_2$
JL0280	Fe 0.0416g, Se 0.0793g, tren 9ml	160	5	Fe, Se, Fe$_2$O$_3$, Fe$_3$O$_4$
JL0281	Fe 0.0281g, Se 0.0798g, tren 9ml	160	5	SiO$_2$, Fe, SeO$_5$, Fe$_3$O$_4$
JL0282	Fe 0.0410g, Se 0.0789, en 5ml, NH4Cl 0.0248g	160	5	amorphous
JL0283	Fe 0.0274g, Se 0.0790g, tren 9ml, NH4Cl 0.0220g	160	5	amorphous
JL0284	Fe 0.0417g, Se 0.0788, en 5ml	160	5	[Fe(en)$_3$][FeSe$_2$] Se, Fe$_3$O$_4$ and unknown phase
JL0285	Fe 0.0285g, Se 0.0789g, en 5ml	160	5	Se and unknown phase
JL0286	Fe 0.0416g, Se 0.0786g, tren 9ml, NH4Cl 0.0271g	160	5	Fe$_2$O(SeO$_3$)s, Fe
JL0287	Fe 0.0279g, Se 0.0787g, en 5ml, NH4Cl 0.0245g	160	5	n/a
JL0288	Fe 0.0415g, Se 0.0784g, phen 0.0328g, H2O 9ml	160	5	n/a
JL0289	Fe 0.0273g, Se 0.0789g, phen 0.0330g, H2O 9ml	160	5	n/a
JL0290	Fe 0.0423g, Se 0.0775g, Sb 0.0400g, tren 9ml, NH4Cl 0.0240g	160	5	n/a
JL0291	Fe 0.0411g, Se 0.0789g, Bipy 0.0292g, H2O 9ml	160	5	FeSe$_2$, Fe$_3$O$_4$
JL0292	Fe 0.0279g, Se 0.0799g, Bipy 0.0292g, H2O 9ml	160	5	FeSe$_2$
JL0293	Fe 0.0414g, Se 0.0287g, 2,2-dithiopyridine 0.0395g, H2O 9ml	160	5	n/a
JL0294	Fe 0.0279g, Se 0.0778g, 2,2-dithiopyridine 0.0404g, H2O 9ml	160	5	Se, FeSe$_2$
JL0295	Fe 0.0277g, Se 0.0792g, 2,2-dithiopyridine 0.0403g, H2O 9ml, NH4Cl 0.0250g	160	5	Se, FeSe$_2$, Fe$_3$O$_4$
JL0296	Fe 0.0279g, Se 0.0785g, Bipy 0.0294g, H2O 9ml, NH4Cl 0.211g	160	5	Se, FeSe$_2$, Fe$_3$O$_5$
JL0297	Fe 0.0416g, Se 0.0778g, methylamine 5ml, NH4Cl 0.2132g	160	5	FeSe$_2$, Fe$_3$O$_4$
JL0298	Fe 0.0277g, Se 0.0791g, methylamine 5ml, NH4Cl 0.2129g	160	5	FeSe$_2$, Fe
JL0299	Fe 0.0415g, Se0.0786g, ethylamine 5ml, NH4Cl 0.2230g	160	5	FeSe$_2$, Fe$_3$O$_4$, Fe
JL0300	Fe 0.0283g, Se 0.0799g, ethylamine 5ml, NH4Cl 0.2114g	160	5	FeSe$_2$
JL0301	Fe 0.0501g, Se 0.0904g, 2,6, dimethylmorpholine 2ml, H2O 3ml, NH4Cl 0.1185g	160	5	FeSe$_2$, FeSe, Fe$_{2.89}$O$_4$, Fe$_3$Se$_4$
JL0302	Fe 0.0420g, Se 0.0779g, tren 9ml, NH4Cl 0.0212g	200	5	[Fe(tren)][FeSe$_2$]$_2$, FeSe$_2$
JL0303	Fe 0.0270g, Se 0.0779g, tren 9ml, NH4Cl 0.2160g	200	5	[Fe(tren)][FeSe$_2$]$_2$,

				$FeSe_3$
JL0304	Fe 0.0407g, Se 0.0784g, diazo 0.0237g, NH4Cl 0.0237g, H2O 7ml	200	5	SEe, $FeSe_2$, $Fe_{2.95}O_4$
JL0305	Fe 0.0289g, Se 0.0797g, 1,4 diazo 0.0205, NH4Cl 0.2147g, H2O 7ml	200	5	$FeSe_2$, Se, $Fe_{2.939}O_4$
JL0306	Fe 0.0408g, Se 0.0785g, 3,3 diaminodipropylamine 4ml, NH4Cl 0.2160g, H2O 3ml	200	5	$FeSe_2$, $FeS_{2.95}$, Fe_3Se_2, Fe_5Se_4
JL0307	Fe 0.0273g, Se 0.0786g, 3,3 diaminodipropylamine 4ml, NH4Cl 0.2100g, H2O 3ml	200	5	FeSe, Fe_3Se_4
JL0308	Fe 0.0424g, Se 0.0794g, 2,6 diaminopyridine 0.0209g, NH4Cl 0.215g, H2O 7ml	200	5	Fe, $FeSe_2$
JL0309	Fe 0.0278g, Se, 0.0779g 2,6 diaminopyridine 0.0194g, NH4Cl 0.2193g, H2O 7ml	200	5	$FeSe_2$, $Fe_{2.962}O_4$
JL0310	Fe 0.0405g, Se 0.0793g, imidiazole 0.0135g, NH4Cl 0.2140, H2O 7ml	200	5	$FeSe_2$, $Fe_{2.878}O_4$, Fe_3Se_4
JL0311	Fe 0.0290g, Se 0.0791g, imidiazole 0.272, NH4Cl 0.2017g, H2O 7ml	200	5	$FeSe_2$, Fe_3O_4
JL0312	Fe 0.0270g, Se 0.0776g, phen 0.0330g, H2O 9ml	200	5	$FeSe_2$,
JL0319	Fe 0.0420g, Se 0.0785g, imidiazole 0.0133g, H2O 7ml	160	8	$FeSe_2$, Se, FeSe, Fe_3Se_4, Fe
JL0320	Fe 0.0423g, Se 0.0780g, 2,6 diaminopyridine 0.0215g, H2O 7ml	160	8	FeSe, $FeSe_2$, $Fe_{2.959}O_4$
JL0321	Fe 0.0420g, Se 0.0798g, 3,3 diaminodipropylamine 4ml, H2O 3ml	160	8	amorphous with unknown phase
JL0322	Fe 0.0408g, Se 0.0789g, 1,5 -diazabicyclo[3.4.0]non05-ene0.0206g, H2O 7ml	160	8	amorphous with unknown phase
JL0323	Fe 0.0421g, Se 0.0781g, Bipy 0.0292g, H2O 9ml	200	6	n/a
JL0324	Fe 0.0283g, Se 0.0784g, Bipy 0.0288g, H2O 9ml	200	6	n/a
JL0325	Fe 0.0415g, Se 0.0784g, Bipy 0.0290g, H2O 9ml, NH4Cl 0.2220g	200	6	n/a
JL0326	Fe 0.0405g, Se 0.0775g, 2,6, dimethylmorpholine 2ml, H2O 5ml	200	6	n/a
JL0327	Fe 0.0415g, Se 0.1004g, 2,6 diaminopyridine 0.0409g, NH4Cl 0.2180g, H2O 7ml	200	6	n/a
JL0328	Fe 0.0413g, Se 0.0785g, phen 0.0318g, NH4Cl 0.2100g, H2O 9ml	200	6	n/a
JL0335	Fe 0.0426g, Se 0.0772g, Bipy 0.02963g, ethylamine 3ml, ethanol 1ml	200	5	$FeSe_2$, Fe
JL0336	Fe 0.0418g, Se 0.0785g, Bipy 0.0600g, ethylamine 3ml, ethanol 1ml	200	5	$FeSe_2$, Fe
JL0337	Fe 0.4040g, Se0.0770g, imidiazole 0.0250g, NH4Cl 0.2140g, ethylamine 6ml	200	5	$FeSe_2$, Fe_3Se_4, $Fe_{2.95}O_4$
JL0338	Fe 0.0416g, Se 0.0783g, 3,3 diaminodipropylamine 3ml, NH4CL 0.214g, H2O 1ml	200	5	$FeSe_2$, $Fe_{2.95}O_4$, FeSe
JL0340	Fe(oAc)2 0.0069g, Se 0.0043g, Bipy 0.0041g, NH4Cl 0.0202g, H2O 9ml	200	5	$FeSe_2$
JL0341	Fe(oAc)2 0.0315g, Se 0.0185g, Bipy 0.0200g, NH4Cl 0.1004g, H2O 9ml	200	5	FeSe3
JL0342	Fe(oAc)2 0.0317g, Se 0.0189g, imidiazole 0.0202g, NH4cl 0.1012g, H2O 9ml	200	5	Se, $FeSe_2$, Fe_2O_3
JL0343	Fe(oAc)2 0.0632g, Se 0.0378g, phen 0.0384g, NH4cl 0.2010g, H2O 9ml	200	5	Se, $FeSe_2$, Fe_2O_3
JL0344	Fe(oAc)2 0.0312g, Se 0.0191g, imidiazole 0.0204g, NH4cl 0.1010g, en 5ml, H2O 4ml	200	5	$FeSe_2$

JL0345	Fe(oAc)2 0.2005g, Se 0.1185g, en 5ml, NH4cl 0.300g, H2O 2ml	200	5	n/a
JL0346	Fe(oAc)2 0.0316g, Se 0.0189g, 2,6 diaminopyridine 0.015g, NH4cl 0.1015g, H2O 9ml	200	5	$FeSe_2$ and unknown phase
JL0347	Fe(oAc)2 0.2031g, Se 0.1205g, Co(oAc) 0.1902g, en 5ml, H2O 2ml	200	5	$Fe_{2.95}O_4$, CoSe2
JL0348	Fe(oAc)20.2005g, Se 0.1206g, Co(oAc) 0.1907g, en 5ml, H2O 2ml	200	5	$Fe_{2.96}O_4$, $Co_{6.85}Se_8$, $CoSe_2$
JL0349	Fe(oAc)2 0.0324g, Se 0.1680g, 2,6 diaminopyridine 0.0137g, ethylamine 5ml, NH4cl 0.1030g, H2O 4ml	200	5	$FeSe_2$, Fe_2O_3, $Fe_{2.938}O_4$
JL0350	Fe(oAc)2 0.02128g, Se 0.0188g, phen 0.0423g, NH4cl 0.1015g, en 5ml	200	5	Se, $FeSe_2$ and unknown phase
JL0359	Fe(oAc)2 0.0210g, Se 0.0182g, putricine 2ml, H2O 3ml	200	5	$FeSe_2$
JL0360	Fe(oAc)2 0.0216g, Se 0.0175g, TETA 2ml, H2O 3ml	200	5	$FeSe_2$
JL0361	Fe(oAc)2 0.0310g, Se 0.0195g, putricine 6ml, H2O 3ml, NH4Cl 0.1000g	200	5	$Fe_{2.95}O_4$, $FeSe_2$
JL0371	Fe(oAc)2 0.1746g, Se 0.0774g, DETA 5ml	200	5	n/a
JL0372	Fe(oAc)2 0.1743g, Se 0.0790g, TETA 5ml	200	5	n/a
JL0455	Fe 0.0420g, Se 0.0770g, TETA 5ml	170	8	n/a
JL0456	Fe(oAc)2 0.1991g, Se 0.1208g, 1-2 diaminopropane 5ml, NH4Cl 0.3000g	170	8	unknown phase

*PXRD measurements were used to determine presence of materials.

Key: Phen = phenanthroline, en = ethylamine, TETA = triethylenetetramine, DETA = diethylenetriamine, bipy = 4,4'-bypyradine

References

[1] S. Wang, Y. Peng, *Chem. Eng. J*., 2010, **156**, 11-24

[2] S. Babel, T.-A. Kurniawan, *J. Hazard. Mater*., 2003, **97**, 219-243

[3] A. Hedstorm, *J. Environ. Eng. ASCE*, 2001, **127**, 219-243

[4] G. A. Ozin, A. Kuperman, A. Stein, *Angew. Chem. Int. Ed. Engl*., 1989, **28**, 359–376

[5] J. Weitkamp, *Solid State Ionics*, 2000, **131**, 175-188

[6] A. Dyer, D. Keir, *Zeolites*, 1984, **4**, 215-217

[7] Ch. Baerlocher, L.B. McCusker, Database of Zeolite Structures, http://www.iza-structure.org/databases/, (accessed 01/03/2017)

[8] M. E. Davis, R. F. Lobo, *Chem. Mater.*, 1992, **4**, 756-768

[9] R. E. Morris, S. J. Weigel, *Chem. Soc. Rev.*, 1997, **26**, 309-317

[10] R. M. Barrer, *J. Chem. Soc.*, 1948, 127-132

[11] R. M. Milton, *US-Pat. 2882434,* 1959

[12] N.F. Zheng, X.H. Bu, B.Wang, P.Y. Feng, *Science*., 2002, **298**, 2366-2369

[13] A. K. Cheetham, G. Férey, T. Loiseau, *Angew. Chem. Int. Ed.*, 1999, **38**, 3268-3292

[14] J. B. Parise, Y. Ko, *Chem. Mater.*, 1992, **4**, 1446-1450

[15] A. V. Powell, *International Journal of Nanotechnology*, 2011, **8**, 783-794

[16] R. J. E. Lees, PhD thesis, Heriot-Watt University, 2007

[17] A. V. Powell and R. Mackay, *J. Solid State Chem*. 2011, **184**, 3144-3149

[18] R. J. E. Lees, A. V. Powell, A. M. Chippindale, *J. Phys. Chem. Solids*, 2008, **69**, 1000-1006

[19] P. E. Lippens, J. OlivierFourcade, J. C. Jumas, A. Gheorghiu, S. Dupont, C. Senemaud, *Physical Review B*, 1997, **56**, 13054-13065

[20] F. Q. Huang, J. A. Ibers, *J. Solid State Chem.*, 2005, **178**, 212-217

[21] K.-Y. Wang, M.-L. Feng, J.-R. Li, X.-Y. Huang, *J. Mater. Chem., A,* 2013, **1,** 1709-1715

[22] A. Taguchi, F. Schöth, *Micropor Mesopor Mat.,* 2005*,* **77**, 1-45

[23] B. J. Riley, J. D. Vienna, D. M. Strachen, J. S. McCloy, J. L. Jerden Jr, *J. Nucl Mater*., 2016, **470**, 307-326

[24] M. J. Manos, M. G. Kanatzidis, *Chem. Sci.*, 2016, **7**, 4804-4824

[25] H. Ahari, C. L. Bowes, T. Jiang, A. Lough, G. A. Ozin, R. L. Bedard, S. Petrv, D. Young.*, adv. Mater.* 1995, **7**, 375-378

[26] N. Zheng, X. Bu, H. Vu, P. Feng, *Angew. Chem. Int. Ed.,* 2005, **44**, 5299-5303

[27] J. Gao, Q. Tay, P.-Z. Li, W.-W. Xiong, Y. Zhao, Z. Chen, Q. Zhang, *Chem. Asian J.,* 2014, **9**, 131-134

[28] X.-M. Zhang, D. Sarma, Y.-Q. Wu, L. Wang, Z.-X. Ning, F.-Q. Zhang, M. G. Kanatzidis, *J. Am. Chem. Soc.* 2016, **138**, 5543-5546

[29] A. K. Cheetham, G. Férey, T. Loiseau, *Angew. Chem. Int. Ed.*, 1999, **38**, 3268-3292

[30] A. Choudhury, J. Krishnamoorthy, C. N. R. Rao, *Chem. Commun.*, 2001, 2610-2611

[31] J. N. Behera, K. V. Gopalkrishnan, C. N. R. Rao, *Inorg. Chem.* 2004, **43**, 2636-2642

[32] C. N. R. Rao,E. V. Sampathkkumaran, R. Nagarajan, G. Paul, J. N. Behera, A. Choudhury, *Chem. Mater.* 2004, **16**, 1441-1446

[33] B. Yotnoi, A. Rujiwatra, M. L. P. Reddy, D. Sarma, S. Natarajan, *Cryst. Growth Des.*, 2011, **11**, 1347–1356

[34] L. Yan, Q. Yue, Q.-X. Jia, G. Lemercier, E.-Q. Gao, *Cryst. Growth Des*. 2009, **9**, 2984-2987

[35] K. Binnemans, *Chem. Rev*. 2009, **109**, 4283-4374

[36] J. G Bednorz, K. A. Muller, *Z. Phys. B. Con. Mat.*, 1986, **B64**, 189

[37] K. Takada, H. Sakurai, E. Takayama-Muromachi, F. Izumi, R. A. Dilanian, T. Sasaki, *Nature,* 2003, **422**, 53-55

[38] Y. Kamihara, T. Watanabe, M. Hirano, H. Hosono, *J. Am. Chem. Soc.*, 2008, **130**, 3296

[39] S. Kashara, T. Watashige, T. Hanaguri, Y. Kohsaka, T. Yamashita, Y. Shimoyama, Y. Mizukami, R. Endo, H. Ikeda, K. Aoyama, T. Terashima, S. Uji, T. Wolf, H. von Lohneysen, T. Shibauchi, Y. Matsuda, *P. Natl. Acad. Sci. USA.*, 2014, **111**, 16309-1313

[40] J. Guo, S. Jin, G. Wang, S. Wang, K. Zhu, T. Zhou, M. He, X. Chen, *Phys, Rev. B,* 2010, **82**, 180520

[41] C. Pak, S. Kamali, J. Pham, K. Lee, J. T. Greenfield, K. Kovnir, *J. Am. Chem. Soc.*, 2013, **135**, 19111-19114

[42] J. T. Greenfield, C. Pak, S. Kamali, K. Lee, K. Kovnir, *Chem. Commun.*, 2015, **51**, 5355-5358

[43] A. Kaltzoglou, P. Vaqueiro, T. Barbier, E. Guilmeau, A. V. Powell, *J. Electron Mater.*, 2014, **43**, 2029-2034

[44] J. R. Sootsman, D. Y. Chung, M. G. Kanatzidis, *Angew. Chem. Int. Edit*., 2009, **48**, 8616–8639

[45] K. Feng, W. Yin, Z. Lin, J. Yao, Y. Wu, *Inorg. Chem.*, 2013, **52**, 11503-11508

[46] J. He, X. Zhang, P. Gau, Y. Cheng, C. Zheng, F. Huang, *RSC Adv*., 2016, **6**, 76789

[47] J. Wang, K. Lee, K. Kovnir, *Inorg. Chem. Front.,* 2016, **3**, 306-312

[48] F. Lopez-Vergara, A. Galdamez, V. Manriquez, G. Gonzalez, *Solid State Sci*. 2015, **49**, 54-60

[49] S. K. Kim, A. Mao, S. Sen, S. Kim, *Chem. Mater.*, 2014, **26**, 5695–5699

[50] L. Isaenko, A. Yelisseyev, S. Lobanov, A. Titov, V. Petrov, J. J. Zondy, P. Krinitsin, A. Merkulov, V. Vedenyapin, J. Smirnova, *Cryst. Res. Technol*., 2003, **38**, 379–387

[51] Ch. Raju, M. Falmbigl, P. Rogl, X. Yan, E. Bauer, J. Horky, M. Zehetbauer, R. C. Mallik, *AIP Advances*, 2013, **3**, 32106

[52] Z. K. Heiba, N. G. Imam, M. B. Mohamed, *Mat. Sci. Semicon. Proc*., 2015, **39**, 39-44

[53] K. J. Tiwari, D.S. P. Kuwat, R. C. Mallik, P. Malar, *J. Electron. Mater*., 2017, **46**, 30-39

[54] J.-L. Adam, L. Calvez, J. Troles, V. Nazabal, *Int. J. Appl. Glass Sci*., 2015, **6**, 287-294

[55] A. Hayashi, S. Hama, H. Morimoto, M. Tatsumisago, T. Minami, *J. Am. Ceram. Soc.,* 2001, **84**, 477–479

[56] A. E. Zaghi, M. Buffiere, G. Brammertz, M. Batuk, N. Lenaers, B. Kniknie, J. Hadermann, M. Meuris, J. Poortmans, J. Vleugels, *Adv. Powder, Technol*., 2014, **25**, 1254-1261

[57] J. P. Tiwari, K. Shahi, *Solid State Ionics*, 2005, **176**, 1271-1280

[58] D. Kim, K. Park, S. Lee, B. Yoo, *Mater. Chem. Phys*. 2016, **179**, 10-16

[59] G. V. Govindaraju, G. P. Wheeler, D. Lee, K.-S. Choi, *Chem. Mater.*, 2017, **29**, 355-370

[60] T.A. Gessert, S. Asher, S. Johnston, M. Young, P. Dippo, C. Corwine, *Thin Solid Films*, 2007, **15**, 6103

[61] B. Spath, J. Fritsche, F. Sauberlich, A. Klein, W. Jaegermann, *Thin Solid Films*, 2005, **480**, 204.

[62] N. Amina, K. Sopianb, M. Konagai, *Sol. Energy Mater. Sol. Cells*, 2007, **91**, 1202-1208

[63] C. H. Chang, H. Jung, Y. Rheem, K.-H. Lee, D.-C. Lim, Y. Jeong, J.-H. Lim, N. V. Myung, *Nanoscale*, 2013, **5**, 1616

[64] Q. Qiu, *Nanotechnology*, 2015, **9**, 3-16.

[65] H. Wang, S. Zhuo, Y. Liang, X. Han, B. Zhang, *Angew. Chem. Int. Ed*. 2016, **55**, 9055-9059

[66] P. K. Singh, U. Singh, B. Bhattacharya, H.-W. Rhee, *J. Renew. Sustain. Ener*. 2014, **6**, 013125

[67] A. C. Sutorik, M. G. Kanatzidis, *Chem. Mater.* 1997, **9***,* 387-398

[68] A. S. Ionkin, B. M. Fish, W. J. Marshal, R. H., Senigo, *Sol. Energ. Mat. Sol. C.*, 2012, **104**, 23-31

[69] P. Durichen, O. Krause, W. Bensch, *Chem. Mater.* 1998, **10**, 2127-2134

[70] H. Li, C. D. Malliakas, J. A. Peters, Z. Liu, J. Im, H. Jin, C. D. Morris, L.-D. Zhao, B. W. Wessels, A. J. Freeman, M. G. Kanatzidis, *Chem. Mater.* 2013, **25**, 2089−2099

[71] S. Santner, J. Heine, S. Dehnen, *Angew. Chem. Int. Ed.* 2016, **55**, 876 –893

[72] G. Zhang, P. Li, J. Ding, Y. Liu, W.-W. Xiong, L. Nie, T. Wu, Y. Zhao, A. L. Y. Tok, Q. Zhang, *Inorg. Chem.* 2014, **53**, 10248−10256

[73] Y. Lin, W. Massa, S. Dehnen, *Chem. Eur. J.* 2012, **18**, 13427-13434

[74] C. Li, H. Li, L. Han, C. Li, S. Zhang, *Mater Lett*, 2011, **65**, 2537-2540

[75] A. M. Guloy, R. Ramlau, Z. Tang, W. Schnelle, M. Baitinger, Y. Grin, *Nature,* 2006, **443**, 320-323

[76] E. R. Cooper, C. D. Andrews, P. S. Wheatley, P. B. Webb, P. Wormald, R. E. Morris, *Nature* 2004, **430**, 1012–1016

[77] Z. Lin, D. S. Wragg, J. E. Warren, R. E. Morris, *J. Am. Chem. Soc.* 2007, **129**, 10334-10335

[78] R. E. Morris, *Chem. Commun.*, 2009, 2990-2998

[79] E. R. Parnham and R. E. Morris, *Chem. Mater.*, 2006, **18**, 4882–4887

[80] B. Krebs, D. Voelker, K. Stiller, *Inorg. Chim. Acta*, 1982, **65**, L101-L102

[81] C. L. Cahill, J. B. Parise, *J. Chem. Soc. Dalton Trans.*, 2000, 1475-1482

[82] Z. X. Lei, Q. –Y. Zhu, X. Zhang, W. Luo, W. Q. Mu, J. Dai, *Inorg Chem.* 2010, **49**, 4385-4387

[83] T. Wu, X. Bu, P. Liao, L. Wang, S. -T. Zheng, R. Ma, P. Feng, J. *Am. Chem. Soc.*, 2012, **134**, 3619–3622

[84] L. Pauling, *J. Am. Chem. Soc.*, 1929, **51**, 1010–1026

[85] X.-W. Zhao, L.-W. Qian, H.-C. Su, C.-J. Mo, C.-J. Que, Q.-Y. Zhu, J. Dai, *Cryst. Growth Des.*, 2015, **15**, 5749–5753

[86] J. Zhou, Y. Zhang, M.-H. Zhang, Z.-X. Lei, J. Dai, *Z. Naturforsch.*, 2009, **64b**, 504-508

[87] P. Vaqueiro, *J. Solid State Chem.*, 2006, **179**, 302-307

[88] J. Zhou, G.-Q. Bian, Y. Zhang, Q.-Y. Zhu, C.-Y. Li, J. Dai, *Inorg. Chem.*, 2007, **46**, 6347–6352

[89] J. Zhou, L. An, X. Liu, H. Zou, F. Hu, C. Liu**,** *Chem. Commun.***,** 2012, **48**, 2537-2539

[90] X. Zhang, W. Luo, Y.-P. Zhang, J.-B. Jiang, Q.-Y. Zhu, J. Dai, *Inorg. Chem.*, 2011, **50**, 6972-6978

[91] C. L. Cahill, B. Gugliotta, J. B. Parise, *Chem. Commun.*, 1998, 1715-1716

[92] B. Eisenmann, A. Hofmann, *Z. für Kristallogr.*, 1991, **195**, 318-319

[93] D. Pitzschke, C. Näther, W. Bensch, *Solid State Sci.,* 2002, **4,** 1167-1171

[94] W. Su, X. Huang, J. Li, H. Fu, *J. Am. Chem. Soc.*, 2002, **124**, 12944-12945

[95] C. L. Cahill, Y. Ko, J. B. Parise, *Chem. Mater.* 1998, **10**, 19-21

[96] H. Li, A. Laine, M. O'Keeffe, O. M. Yaghi, *Science*, 1999, **283**, 1145-1147

[97] H. Li, M. Eddaoudi, A. Laine, M. O'Keefe, O. M. Yaghi, *J. Am. Chem. Soc.*, 1999, **121**, 6096-6097

[98] X. Bu, N. Zheng, Y. Li, P. Feng, *J. Am. Chem. Soc.*, 2002, **124**, 12646–12647

[99] L. Wang, T. Wu, F. Zuo, X. Zhao, X. Bu, J. Wu, P. Feng, *J. Am. Chem. Soc.*, 2010, **132**, 3283–3285

[100] C. Wang, X. Bu, N. Zheng, P. Feng, *Angew. Chem.,* 2002, **114**, 2039-2041

[101] M. Melullis, M. K. Brandmayer, S. Dehnen, *Z. Anorg. Allg. Chem.*, 2006, **632**, 64-72

[102] J. Wang, C. Näther, J. Djamil, W. Bensch, *Z. Anorg. Allg. Chem.*, 2012, **638**, 1452-1456

[103] X. Liu, F. Hu, J. Zhou, L. An, D. Liang, J. Lin, *CrystEngComm.*, 2012, **14**, 3464-3468

[104] G.-N. Liu, G.-C. Guo, M.-S. Wang, L.-Z. Cai, J. S. Huang, *J. Mol. Struct.*, 2010, **983**, 104-111

[105] J.-J. Liang, J. Zhao, W.-W. Tang, Y. Zhang, D.-X. Jia, *Inorg. Chem. Commun.*, 2011, **14**, 1023-1026

[106] F. Zhang, X. Liu, J. Zhou, X. Hong, J. He, *Monatsh Chem.*, 2011, **142**, 763-768

[107] O. M. Yaghi, Z. Sun, D. A. Richardson, T. L. Groy, *J. Am. Chem. Soc.*, 1994, **116**, 807-808

[108] M.-S. Wang, W.-T. Chen, L.-Z. Cai, G.-W. Zhou, G.-C. Guo, J.-S. Huang, *J. Clust. Sci.*, 2003, **14**, 495-504

[109] X. Liu, J. Zhou, J. He, Z.-W. Huang, *Z. Naturforsch.*, 2011, **66b**, 659-663

[110] W.-Q. Mu, Q.-Y. Zhu, L-S. You, X. Zhang, W. Luo, G.-Q. Bian, J. Dai, *Inorg. Chem.*, 2012, **51**, 1330-1335

[111] S. A. Polling, C. R. Nelson, J. T. Sutherland, S.W. Martin *J. Phys. Chem. B,* 2003, **107**, 5413-5418

[112] K. O. Klepp, M. Zeitlinger, *Z. Kristallogr.*, 2000, **215**, 7-8

[113] D. M. Nellis, Y. Ko, K. Tan, S. Koch, J. B. Parise, *J. Chem. Soc., Chem. Commun.*, 1995, 541-542

[114] C.-Y. Yue, Z.-D. Yuan, L.-G. Zhang, Y.-B. Wang, G.-D. Liu, L.-K. Gong, X.-W. Lei, *J. Solid State Chem.*, 2013, **206**, 129-133

[115] Q. C. Zhang, G. Armatas, M. G. Kanatzidis, *Inorg. Chem.*, 2009, **48**, 8665-8667

[116] B. Eisenmann, J. Hansa, *Z. Kristallogr.*, 1993, **205**, 325-326

[117] B. Eisenmann, J. Hansa, *Z. Kristallogr.*, 1993, **206**, 101-102

[118] S. Dhingra, R. C. Haushalter, *Polyhedron,* 1994, **13**, 2775-2780

[119] O. Achak, J. Y. Pivan, M. Maunaye, M. Louer, D. Louer, *J. Solid State Chem.*, 1996, **121**, 473-478

[120] T. Van Almsick, W. S. Sheldrick, *Acta Crystallogr.,* 2005. **E61**, m2348-m2350

[121] M. J. MacLachlan, S. Petrov, R. L. Bedard, I. Manners, G. A. Ozin, *Angew. Chem. Int. Ed. Engl.*, 1998, **37**, 2075-2079

[122] H. O. Stephan, M. G. Kanatzidis, *Inorg. Chem.*, 1997, **36**, 6050-6057

[123] D.-X. Jia, Y. Zhang, J. Dai, Q.-Y. Zhu, X.-M. Gu, *J. Solid State Chem.*, 2004, **177**, 2477-2483

[124] R. Stähler, B.-D. Mosel, H. Eckert, W. Bensch, *Angew. Chem. Int. Ed.*, 2002, **41**, 4487-4489

[125] I. D. Brown, D. Altermatt, *Acta Crystallogr.*, 1985, B**41**, 244-247

[126] N. E. Brese, M. O'Keeffe, *Acta Crystallogr.*, 1991, B**47**, 192-197

[127] M. Schur, H. Rijnberk, C. Näther, W. Bensch, *Polyhedron*, 1998, **18**, 101-107

[128] M. Schur, W. Bensch. *Acta Crystallogr.*, 2000, C**56**, 1107-1108

[129] P. Bayliss, W. Nowacki, *Z. Kristallogr.*, 1972, **135**, 308-315

[130] P. Vaqueiro, A. M. Chippindale, A. V. Powell, *Polyhedron*, 2003, **22**, 2839-2845

[131] M. Schaefer, L. Engelke, W. Bensch, *Z. Anorg. Allg. Chem.*, 2003, **629**, 1912-1918

[132] R. Stahler, W. Bensch, *J. Chem. Soc., Dalton Trans.*, 2001, 2518-2522

[133] A. V. Powell, R. Paniagua, P. Vaqueiro, A. M. Chippindale, *Chem. Mater.*, 2002, **14**, 1220-1224

[134] L. Engelke, W. Bensch, *Acta Crystallogr.*, 2003, E**59**, m378-m380

[135] X. Wang, A. J. Jacobson, F. Liebau, *J. Solid State Chem.*, 1998, **140**, 387-395

[136] R. Kiebach, F. Studt, C. Näther, W. Bensch, *Eur. J. Inorg. Chem.*, 2004, 2553–2556

[137] W. Bensch, M. Schur, A. Gruhl, C. Näther, I. Jeb*, Z. Naturforsch.*, 1999, **54B**, 1524-1528

[138] P. Vaqueiro, D. P. Darlow, A. V. Powell, A. M. Chippindale, *Solid State Ionics*, 2004, **172**, 601-605

[139] V. Spetzler, R. Kiebach, C. Näther, W. Bensch, *Z. Anorg. Allg. Chem.*, 2004, **630**, 2398-2404

[140] W. Bensch, M. Schur, *Z. Naturforsch.*, 1997, **52B**, 405-409

[141] J. B. Parise, Y. Ko, *Chem. Mater.*, 1992, **4**, 1446-1450

[142] C.-Y. Yue, X.-W. Lei, Y.-X. Ma, N. Sheng, Y.-D. Yang, G.-D. Liu, X.-R. Zhai, *Crystal Growth & Design*, 2014, **14**, 101-109

[143] W. Bensch, C. Näther, R. Stähler, *Chem. Commun.*, 2001, 477-478

[144] W. Wang, F. Liebau, *J. Solid State Chem.*, 1994, **111**, 385-389

[145] R. Stahler, C. Näther, W. Bensch, *J. Solid State Chem.*, 2003, **174**, 264-275

[146] A. V. Powell, D. Boissière, A. M. Chippindale, *Chem. Mater.*, 2000, **12**, 182-187

[147] A. Puls, M. Schaefer, C. Näther, W. Bensch, A. V. Powell, S. Boissière, A. M. Chippindale, *J. Solid State Chem.*, 2005, **178**, 1171-1181

[148] W. Bensch, M. Schur, *Eur. J. Solid State Inorg. Chem.*, 1997, **34**, 457-466

[149] P. Vaqueiro, A. M. Chippindale, A. V. Powell, *Inorg. Chem.*, 2004, **43**, 7963-7965

[150] K. Z. Du, M. L. Feng, L. H. Li, B. Hu, Z. J. Ma, P. Wang, J. R. Li, Y. L. Wang, G. D. Zou, X. Y. Huang, *Inorg. Chem.*, 2012, **51**, 3926-3928

[151] A. V. Powell, R. J. Lees, A. M. Chippindale, *Inorg. Chem.*, 2006, **45**, 4261-4267

[152] X. Liu, *Inorg. Chem. Commun.*, 2011, **14**, 437-439

[153] J. Zhou, X. Yin, F. Zhang, *Inorg. Chem.*, 2010, **49**, 9671-9676

[154] M.-L. Feng, P.-X. Li, K.-Z. Du, X.-Y. Huang, *Eur. J. Inorg. Chem.*, 2011, 3881–3885

[155] M. L. Feng, W. W. Xiong, D. Ye, J. R. Li, X. Y. Huang, *Chem. Asian J.*, 2010, **5**, 1817-1823

[156] M.-L. Feng, C.-L. Hu, K.-Y.Wang, C.-F. Du, X.-Y. Huang, *CrystEngComm.*, 2013, **15**, 5007–5011

[157] J. Zhou, L. An, X. Liu, L. Huang, X. Huang, *Dalton Trans*, 2011, **40**, 11419-11424

[158] B. Zhang, M. L. Feng, H. H. Cui, C.-F. Du, X.-H. Qi, N.-N. Shen, X.-Y. Huang, *Inorg. Chem.*, 2015, **54**, 8474–8481

[159] K. Y. Wang, B. Zhang, X.-H. Qi, N.-N. Shen, C.-F. Du, Z.-F. Wu, M.-L. Feng, X.-Y. Huang, *Cryst. Growth Des.*, 2015, **15**, 29-38

[160] N. Ding, M. G. Kanatzidis, *Chem. Mater.*, 2007, **19**, 3867–3869

[161] K.-Y. Wang, M.L. Feng, D.-N. Kong, S. J. Liang, L. Wu, X.-Y. Huang, *CrystEngComm.*, 2012, **14**, 90-94

[162] M.-L. Feng, D.-N. Kong, Z.-L. Xie, X.-Y. Huang, *Angew. Chem. Int. Ed.,* 2008, **47**, 8623-8626

[163] J. Zhou, L. An, *CrystEngComm.*, 2011, **13**, 5924-5928

[164] J. Zhou, L. An, F. Zhang, *Inorg. Chem.*, 2011, **50**, 415-417

[165] T. Guerfel, A. Jouin, *Journal De La Societe Chemique De Tunisie*, 2000, **4**, 723-735

[166] S. P. Petrosyants, A. B. Ilyukhin, A. Yu. Sukhorukov, *Koordinatsionnaya Khimiya*, 2005, **31**, 576-582

[167] B. Singh, R. Srivastava, K. K. Narang, V. P. Singh, *Syn. React. Inorg. Met.*, 1999, **29**, 1867-1881

[168] H.-L. Zhu, Y.-J. Pan, X.-J. Wang, K.-B.-Yu, *J. Chem. Crystallogr.,* 2004, **34**, 199-202

[169] S. Yano, M. Doi, M. Kato, I. Okura, T. Nagano, Y. Yamamoto, T. Tanase, *Inorg. Chim. Acta.,* 1996, **246**, 1-3

[170] F. Setifi, J. M. Knaust, Z. Setifi, R. Touzani, *Acta Crystallogr.*, 2016, **E72**, 470-476

[171] M. I. Khan, S. Cevik, R. J. Doedens, *Inorg. Chim. Acta*, 1999, **292**, 112-116

[172] M. M. Ibrahim, A.-M. M. Ramadan, G. A. M. Mersal, S. A. El-Shazly, *J. Mol. Struct.*, 2011, **998**, 1-10

[173] G. Paul, A. Choudhury, C. N. R. Rao, *J. Chem. Soc., Dalton Trans.*, 2002, 3859-3867

[174] H.-Y. Guo, Z.-H. Li, X.-Y. Li, C.-Y. Zhang, R.-J. Wang, *Chin. J. Chem.*, 2003, **21**, 466-470

[175] J. N. Behera, C. N. R. Rao, *Angew. Chem. Int. Ed.*, 2005, **631**, 3030-3036

[176] F. C. Hawthorne, S. V. Krivovichev, P. C. Burns, *Rev. Mineral. Geochem.*, 2003, **40**, 1-112

[177] X. Hu, J. Guo, C. Liu, H. Zen, Y. Wang, W. Du, *Inorg. Chim. Acta*, 2009, **362**, 3421-3426

[178] G. Paul, A. Choudhury, R. Natarajan, C. N. R. Rao, *Inorg. Chem.*, 2003, **42**, 2004-2013

[179] X. C. Sun, G. P. Zhou, X. F. Zheng, Y. Xu, *Acta Crystallogr.*, 2007, **E63**, m1388

[180] Y. Fu, Z. Xu, J. Ren, H. Wu, R. Yuan, *Inorg. Chem.*, 2006, **45**, 8452-8458

[181] G. Paul, A. Choudhury, C. N. R. Rao, *Chem. Mater.*, 2003, **15**, 1174-1180

[182] D. Shi, S. li, J. Zhao, W. Niu, S. Shang, Y. Li, P. Ma, L. Chen, *Inorg. Chem. Commun.*, 2012, **20**, 277-281

[183] L. Ma, D. Liu, Y. Xing, X. Liu, G. Li, *Z. Anorg. Allg. Chem.*, 2010, **636**, 2681-2685

[184] Y. Ren, M. An, M. Zhang, J. Wang, L. Gao, F. Fu, *Russ. J. Coord. Chem.*, 2015, **41**, 255-260

[185] G.-W. Ge, Z.-Y. Qi, Y.-R. Miao, H.-B. Du, X.-Z. You, *CrystEngComm.*, 2013,**15**, 435-438

[186] C.-L. Zhou, S.-M. Wang, S.-N. Liu, T.-T. Yu, R.-Y. Li, H. Xu, Z.-Y. Liu, H. Sun, J. J. Cheng, J.-P. Li, H.-W. Hou, J.-B. Chang, *J. Mol. Struct.*, 2016, **1118**, 139-146

[187] J. Lu, C. Yu, T. Niu, T. Pliwala, G. Crisci, F. Somosa, A. J. Jacobson, *Inorg. Chem.*, 1998, **37**, 4637-4640

[188] L. F. Jones, C. A. Kilner, M. A. Halcrow, *New J. Chem.*, 2007, **31**, 1530-1534

[189] F.-N. Shi, A. R. Silva, J. Rocha, *J. Solid State Chem.*, 2011, **8**, 2196-2203

[190] M. Cavellec, D. Riou, G. Fèrey, *J. Solid State Chem.*, 1994, **112**, 441-447

[191] J. N. Behera, C. N. R. Rao, *Inorg. Chem.*, 2006, **45**, 9475–9479

[192] J. Kanamori, *Phys. Chem. Solids*, 1959, **10**, 87-98

[193] G. Paul, A. Choudhury, E. V. Sampathakumaran, C. N. R. Rao, *Angew. Chem. Int. Ed.*, 2002, **41**, 1224

[194] Y. Fu, Z. Xu, J. Ren, J. Yang, *Cryst. Growth Des.*, 2007, **7**, 1198–1204

[195] W. Xu, J.-L. Lin, *Z. Naturforsch.* 2013, **68b**, 877–884

[196] J. N. Behera, K. V. Gopalkrishnan, C. N. R. Rao, *Inorg. Chem.*, 2004, **43**, 2636–2642

[197] Z. Weng, Z. Chen, F. Liang, *Inorg. Chem.*, 2009, **48**, 8703–8708

[198] F. C. Hawthrone, S. V. Krivovichev, P. C. Burns, *Rev. Miner. Geochem.* 2000, **40**, 55

[199] A. V. Powell, P. Leyva-Bailen, P. Vaqueiro, R. D. Sanchez, *Chem. Mater.*, 2009, **21**, 4102–4104

[200] J. Lin, D.-W. Guo, Y.-Q. Tian, *Cryst. Growth Des.*, 2008, **8**, 4571–4575

[201] S. Lauchan, T. J. Prior, S. Meansiri, A. Rujiwatra, *J. Inorg. Organomet. P.*, 2008, **18**, 352-357

[202] S. Biswas, Y.-Y. Liu, M. Tonigold, M. Weil, D. Volkmer, *Eur. J. Inorg. Chem.*, 2014, 5362–5369

[203] M. B. Salah, S. Vilminot, G. André, M. Richard-Plouet, F. Bourée-Vigneron, T. Mhiri, M. Kurmoo, *Chem. Eur. J.*, 2004, **10**, 2048-2057

[204] S. Vilminot, M. Richard-Plouet, G. André, D. Swierczynski, F. Bourée-Vigneron, M. Kurmoo, *Inorg. Chem.*, 2003, **42**, 6859–6867

[205] Y. Fan, G. H. Li, L. Yang, Z. M. Zhang, Y. Chen, T. Y. Song, S. H. Feng, *Eur. J. Inorg. Chem.*, 2005, 3359-3364

[206] Z.-J. Feng, Z.-W. Yan, T.-H. Li, F. Li, *J. Inorg. Organomet. P.*, 2016, **26**, 711-716

[207] N. Lah, I. K. Cigić, I. Leban, *Inorg. Chem. Commun.*, 2003, **6**, 1441-1444

[208] N. Chen, M.-X. Li, P. Yang, X. He, M. Shao, S.-R. Zhu, *Cryst. Growth Des.*, 2013, **13**, 2650–2660

[209] C. Liu, Y. Yin, X. Shi, D. Zhang, M. Hu, *Inorg. Chem. Commun.*, 2007, **10**, 37-39

[210] J. Heine, K. Müller-Buschbaum, *Chem. Soc. Rev.*, 2013, **42**, 9232

[211] Y. P. Yuan, R. Y. Wang, D. Y. Kong, J. G. Mao, A. Clearfield, *J. Solid State Chem.*, 2005, **178**, 2030

[212] Y.-G. Sun, W.-H. G. Xiong, M.-Y. Guo, F. Ding, S.-J. Wang, L.-X. You, B.-Y. Ren, Z.-H. Xu, E.-J. Gao, *Polyhedron*, 2014, **83**, 68-76

[213] Y. Guo, Z. Shi, J. Yu, J. Wang, Y. Liu, N. Bai, W. Pang, *Chem. Mater.*, 2001, **13**, 203–207

[214] L. Wang, H. Ding, T. Hou, L. Zhu, Z. Shi, S. Feng, *J. Solid State Chem.*, 2006, **179**, 2584-2588

[215] N. Takako, I. Takuji, A. Chie, H. Yasuhisa, K. Yoshimichi, H. Takaaki, *Cryst. Growth Des.*, 2012, **12**, 1752–1761

[216] R. J. E. Lees, A. V. Powell, A. M. Chippindale, *Polyhedron*, 2005, **24**, 1941-1948

[217] X.-L. Sun, Q.-Y. Zhu, W.-Q. Mu, L.-W. Qian, L. Yu, J. Wu, G.-Q. Bian, J. Dai, *Dalton Trans.*, 2014, **43**, 12582–12589

[218] X.-L. Sun, Q.-Y. Zhu, L.-W. Qian, L. Yu, Z.-G. Ren, G.-Q. Bian, J. Dai, *Inorg. Chem. Commun.*, 2014, **46**, 130-133

[219] G.-N. Liu, J.-D. Lin, Z.-N. Xu, Z.-F. Liu, G.-C. Guo J.-S. Huang, *Cryst. Growth Des.*, 2011, **11**, 3318–3322

[220] K. K. Rangan, M. G. Kanatzidis, *Inorg. Chim. Acta.*, 2004, **357**, 4036–4044

[221] W. L. Bragg, The Diffraction of Short Electromagnetic Waves by a Crystal, Proceedings of the Cambridge Philosophical Society, 1913, **17**, 43-57

[222] P. W. Atkins, *The Elements of Physical Chemistry*, Oxford University Press, 1992, ch. 10, 407-413

[223] L. E. Smart and E. A. Moore, *Solid State Chemistry an Introduction*, CRC Press, 2012, ch. 2, 79-86

[224] *DIFFRAC.PDFMAINT*, (2008) Bruker

[225] *DIFFRAC.EVA*, (2008) Bruker

[226] A. J. Blake, W. Clegg, J. M. Cole, J. S. O. Evans, P. Main, S. Parsons and D. J. Watkin, *Crystal Structure Analysis Principles and Practice*, second edn., Oxford University Press, 2009

[227] A. Altomare, G. Cascarano, C. Giacovazzo, A. Guagliardi, *J. Appl. Crystallogr.*, 1993, **26**, 343-350

[228] L. Palatinus, G. Chapuis, *J. Appl. Crystallogr.*, 2007, **40**, 786-790

[229] Agilent (2014). *CrysAlis PRO*. Agilent Technologies Ltd, Yarnton, Oxfordshire, England

[230] P. W. Betteridge, J. R. Carruthers, R. I. Cooper, K. Prout, D. J. Watkin, *J. Appl. Crystallogr.*, 2003, **36**, 1487

[231] J. R. Carruthers, D. J. Watkin, *Acta Crystallogr.,* 1979, A**35**, 698-699

[232] C. F. Macrae, I. J. Bruno, J. A. Chisholm, P. R. Edgington, P. McCabe, E. Pidcock, L. Rodriguez-Monge, R. Taylor, J. van de Streek, P. A. Wood, *J. Appl. Crystallogr.*, 2008, **41**, 466-470

[233] *ATOMS*, (1989) Shape Software, 521 Hidden Valley Road, Kingsport, TN 37663 USA

[234] F. H. Allen, O. Johnson, G. P. Shields, B. R. Smith, M. Towler, *J. Appl. Cryst.,* 2004, **37**, 335-338

[235] S. P. Tandon, J. P. Gupta*, Phys. Stat. Sol.*, 1070, **38**, 363-369

[236] P. E. Lippens, J. OlivierFourcade, J. C. Jumas, A. Gheorghiu, S. Dupont, C. Senemaud, *Physical Review B*, 1997, **56**, 13054-13065

[237] F. Q. Huang, J. A. Ibers, *J. Solid State Chem.*, 2005, **178**, 212-217

[238] G. Kortűm, W. Braun, G. Herzog, *Angew. Chem. Internat. Ed.* 1963, **2**, 7

[239] A. C. Reimschuessel, *J. Chem. Educ.,* 1972, **49**, No 8, / A413

[240] A. C. Reimschuessel, *J. Chem. Educ.,* 1972, **49**, No 9, / A449

[241] C. E. Housecroft and E. C. Constable, *Chemistry*, Pearson Education Limited, Edinburgh, 3rd edn, 2006, ch. 14, 401-425

[242] C. A. Fyfe and R. E. Wasylishen, *Solid State Chemistry Techniques*, ed. A. K. Cheetham and P. Day, 1990, ch. 6, 190-230

[243] F. A. Cotton, G. Wilkinson and P. L. Gaus, *Inorganic Chemistry*, John Wiley and sons, 3rd ed, 1995, 85

[244] A. R. West, *Solid State Chemistry and Its Applications*, Second edition, 2014, 449

[245] L. E. Smart and E. A. Moore, *Solid State Chemistry an Introduction*, CRC Press, 4th ed, 2012, ch. 8, 341-350

[246] M. Elfresh, Fundamentals of Magnetism and Magnetic Measurements Featuring Quantum Design's Magnetic Property Measurement System, Quantum design, 1994, 1-34

[247] A. D. Baker and R. Engel, *Organic Chemistry*, West Publishing Company, St Paul, 1992, ch 4, 97-98

[248] Z. Su, X. Li, Y. Lan, G. Jin, J. Xie, C. Zheng, J. Jin, S. Li, *Mater Lett.*, 2008, **62**, 2802-2805

[249] C. Wang, Y. Li, X. Bu, N. Zheng, P. Zivkovic, C. -S. Yang, P. Feng, *J. Am. Chem. Soc.*, 2001, **123**, 11506-11507

[250] J. D. Lampkin, A. V. Powell, A. M. Chippindale, *J. Solid State Chem.*, 2016, **243**, 44-49

[251] P. V. D. Sluis, A. L. Spek, *Acta Crystallogr.*, 1990, **A46**, 194–201

[252] B. D. A. Levin, M. J. Zachman, J. G. Werner, U. Wiesner, L. F. Kourkoutis, D. A. Muller *Microsc. Microanal.*, 2014, **20**, 446–447

[253] Stein, S.E. IR and Mass Spectra. *NIST Chemistry WebBook*; P.J. Linstrom, W.G. Mallard Eds. NIST Standard Reference Database Number 69; National Institute of Standards and Technology: Gaithsburg, MD, (December) 2017, Tris(2-aminoethyl)amine

[254] W. M. Hutchinson, A. R. Collett, C. L. Lazzell, *J. Am. Chem. Soc.*, 1945, **67**, 1966–1968

[255] S. Satapathi, *Inorg. Chem. Commun.*, 2015, **56**, 89–101

[256] H. Kleinke, *Chem. Soc. Rev.*, 2000, **29**, 411-418

[257] K. W. Klinkhammer, P. Pykkö, *Inorg. Chem.*, 1995, **34**, 4134-4138

[258] H. Bürger, R. Eujen, G. Becker, O. Mundt, M. Westerhausen, C. Witthauer, *J. Mol. Struct.*, 1983, **98**, 265-276

[259] R. Kiebach, C. Näther, W. Bensch, *Z. Nat.*, 2004, **56B**, 1314-1319

[260] S. Alvarez, *Chem. Rev.*, 2015, **115**, 13447-13483

[261] L. M. Brines, J. Shearer, J. K. Fender, D. Schweitzer, S. C. Shoner, D. Barnhart, W. Kaminsky, S. Lovell, J. A. Kovacs, *Inorg. Chem.*, 1998, **37**, 5721–5726

[262] J. Zhou, X. Liu, L. T. An, F. L. Hu, Y. H. Kan, R. Li, Z. M. Shen, *DaltonTrans.*, 2013, **42**, 1735-1742

[263] Z. Wang, H. Zhang, C. Wang, *Inorg. Chem.* 2009, **48**, 8180–8185

[264] P. Vaqueiro, M. L. Romero, *J. Phys. Chem. Solids*, 2007, **68**, 1239-1243

[265] O. Slupecki, I. D. Brown, *Acta Crystallogr.*, 1982, **B38**, 1078-1079

[266] B. Krebs, D. Voelker, K. Stiller, *Inorg. Chem. Acta*, 1982, **65**, 101-102

[267] P. Vaqueiro, M. L. Romero Perez, *Chem. Commun.*, 2007, 3282–3284

[268] K. Tsamourtzi, J. H. Song, T. Bakas, A. J. Freeman, P. N. Trikalitis, M. G. Kanatzidis, *Inorg. Chem.*, 2008, **47**, 11920-11929

[269] W. Schiwy, B. Krebs, *Angew. Chem.*, 1975, **87**, 451

[270] N. Zheng, X. Bu, P. Feng, *J. Am. Chem. Soc.*, 2003, 125, 1138.

[271] T. van Almsick, A. Kromm, W. S. Sheldrick, *Z. Anorg. Allg. Chem.*, 2005, **631**, 19-20

[272] P. Kitschke, L. Mertens, T. Ruffer, H. Lang, A. A. Auer, M. Mehring., *Eur. J. Inorg. Chem.,* **2015**, 4996–5002

[273] G. Renner, G. Huttner, P. Rutsch, *Z. Naturforsch. B,* **2001**, *56*, 1328–1339

[274] J. C. M. Rivas, L. Brammer, *Acta Crystallogr.,* 1998, **C54**, 757-760

[275] Y. Yoshikawa, B. *Chem. Soc. Jpn.*, 1976, **49**, 159-162

[276] M. Di Vaira, P. L. Orioli, *Inorg. Chem.*, 1967, **6**, 955-957

[277] C. E. Housecroft, A. G. Sharpe, *Inorganic Chemistry*, Pearson, England, 3rd edition, 2008, ch 21, 663-665

[278] J. Zhou, W.-H. Fang, C. Rong, G.-Y. Yang, *Chem. Eur. J.*, 2010, **16**, 4852–4863

[279] Stein, S.E. IR and Mass Spectra. *NIST Chemistry WebBook*; P.J. Linstrom*, W.G. Mallard Eds. NIST Standard Reference Database Number 69; National Institute of Standards and Technology: Gaithsburg, MD, (December) 2017, Diethylenetriamine

[280] J. Lichte, C. Näther, W. Bensch., *CrystEngComm.*, 2014, **16**, 5551-5559

[281] J.-F. Chen, Q.-Y. Jin, Y.-L. Pan, Y. Zhang, D.-X. Jia, *Z. Anorg. Allg. Chem.,* 2010, **636**, 230–235

[282] R. Stahler, W. Bensch, *Eur. J. Inorg. Chem.,* 2001, **12**, 3073-3078

[283] R. Kiebach, W. Bensch, R.-D. Hoffmann, R. Pottgen, *Z. Anorg. Allg. Chem.*, 2003, **629**, 532-538

[284] G.-N. Liu, J.-D. Lin, Z.-N. Xu, Z.-F. Liu, G.-C. Guo, J.-S. Huang, *Cryst. Growth Des.*, 2011, **11**, 3318–3322

[285] M. B. Salah, S. Vilminot, G. Andre, F. Bouree-Vigneron, M. Richard-Plouet, T. Mhiri, M. Kurmoo, *Chem. Mater.,* 2005, **17***, 2612-2621

[286] M. B. Salah, S. Vilminot, G. Andre, M. Richard-Plouet, T. Mhiri, S. Takagi, M. Kurmoo, *J. Am. Chem. Soc.*, 2006, **128**, 7972-7981

[287] J. Moriyama, H. Nishiguchi, T. Ishihara, Y. Takita, *Ind. Eng. Chem. Res.*, 2002, **41**, 32-36

[288] J. Reedijk, *Inorg. Chim. Acta*, 1992, **198-200**, 873-881

[289] S.-Y. Wan, Y.-Z. Li, T.-A. Okamura, J. Fian, W.-Y. Sun, N. Ueyama, Eur. *J. Inorg. Chem*. 2003, 3783

[290] C. N. R. Rao, J. N. Behera, M. Dan, *Chem. Soc. Rev.*, 2006, **35**, 375-387

[291] S. R. Marri, J. Kumar, K. Panyarat, S. Horike, J. N. Behera, *Dalton Trans*., 2016, **45**, 17792-17797

[292] K. L. Marshall, Q. L. Wang, H. S. I. Sullivan, M. T. Weller, *Dalton Trans.,* 2016, **45**, 8854-8861

[293] N. Singh, G. Anantharaman, *CrystEngComm.*, 2014, **16**, 6203-6212

[294] L. Rodriguez, E. Labisdal, A. Souse-Pendrares, J. Garcia-Vazquez, J. Romero, M. L. Duran, J. A. Real, A. Sousa, *Inorg. Chem*., 2006, **45**, 7903-7914

[295] W. Rekik, H. Naili, T. Mhiri, T. Bataille, *Mater. Res. Bull*., 2008, **43**, 2709-2718

[296] R. S. Raveendra, P. A. Prashanth, B. M. Nagabhushana, *Journal of Advanced Chemical Sciences*, 2016, **2**, 334–336

[297] J. Zhou, W.-H. Fang, C. Rong, G.-Y. Yang, *Chem. Eur. J*., 2010, **16**, 4852 – 4863

[298] K. Nakamoto, *Infrared and Raman Spectra of Inorganic and Coordination Compounds: Part A: Theory and Applications in Inorganic Chemistry*, Sixth Edition, 2009, **1**, 84-85

[299] C. Papatriantafyllopoulou, E. Manessi-Zoupa, A. Escuer, S. P. Perlepes, *Inorg. Chem. Acta,* 2009, **362**, 634-650

[300] J. G. Malecki, M. Balanda, T. Gron, R. Kruszynski, *Struct. Chem*., 2012, **23**, 1219-1232

[301] Y. L. Page, *J. Appl. Cryst*., 1987, **20**, 264-269

[302] Z.-X. Lian, J. Cai, C.-H. Chen, *Polyhedron*, 2007, **26**, 2647-2654

[303] T. J. Prior, B. Yotnoi, A. Rujiwatra, *Polyhedron*, 2011, **30**, 259-268

[304] S. Chaabouni, S. Kamoun, A. Daoud, T. Jouini, *Acta Cryst*., 1996, **C52**, 505-506

[305] P. Leyva-Bailen, PhD Thesis, Heriot-Watt University, 2009

[306] L. Nie, W.-W. Xiong, P. Li, J. Han, G. Zhang, S. Yin, Y. Zhao, R. Xu, Q. Zhang, *J. Solid State Chem*., 2014, **220**, 118-123

[307] C. V. Blerk, G. J. Kruger, *J. Chem. Crystallogr*., 2008, **38**, 175

[308] R. E. Wilson*, Inorg. Chem*., 2012, **51**, 8942−8947

[309] M. Schaefer, R. Stahler, W.-R. Kiebach, C. Näther, W. Bensch, *Z. Anorg. Allg. Chem.,* 2004, **630**, 1816-1822

[310] M. Schaefer, D. Kurowski, A. Pfitzner, C. Näther, Z. Rejai, K. Moller, N. Ziegler, W. Bensch, *Inorg. Chem.,* 2006, **45**, 3726-3731

[311] N. Herzberg, C. Näther, W. Bensch, *Z. Krist-Cryst. Mater*., 2012, **227**, 552-556

[312] A. Bondi, *J. Phys. Chem.*, 1964, **68**, 441-451

[313] R. Stahler, W. Bensch, *Eur. J. Inorg. Chem.*, 2001, 3073-3078

[314] M. Behrens, S. Scherb, C. Näther, W. Bensch, *Z. Anorg. Allg. Chem.,* 2003, **629**, 1367–1373

[315] J.-F. Chen, Q.-Y. Jin, Y.-L. Pan, Y. Zhang, D.-X. Jia, *Z. Anorg. Allg. Chem.,* 2010, **636**, 230–235

[316] D. X. Jia, J. Dai, Q. Y. Zhu, Y. Zhang, X. M. Gu, *Polyhedron*, 2004, **23**, 937–942

[317] D. X. Jia, J. Dai, Q. Y. Zhu, L. H. Cao, H. H. Lin, *J. Solid State Chem.,* 2005, **178**, 874–881

[318] M. Behrens, S. Scherb, C. Näther, W. Bensch, *Z. Anorg. Allg. Chem.,* 2003, **629**, 1367–1373

[319] N. Pienack, S. Lehmann, H. Lühmann, M. El-Madani, C. Näther, W. Bensch, *Z. Anorg. Allg. Chem.,* 2008, **634**, 2323–2329

[320] A. J. Williams, T. M. Mcqueen, R. J. Cava, *Solid State Commun.,* 2009, **149**, 1507-1509

[321] L. Chen, X. Yang, X. Fu, C. Wang, C. Liang, M. Wu, *Eur. J. Inorg. Chem.,* 2011, 2098–2102

[322] J. Ge, S. Cao, S. Shen, S. Yaun, B. Kang, J. Zhang, *Cryogenics*, 2011, **51**, 253-256

[323] Sudesh, S. Rani, G. D. Varma, *Physica C*, 2013, **485**, 137-144

[324] A. Ciechan, M. J. Winiarski, M. Samsel-Czekala, *Intermetallics*, 2013, **41**, 44-50

[325] K. W. Leh, T.-W. Huang, Y.-L. Huang, T.-K. Chen, F.-C. Hsu, P. M. Wu, Y.-C. Lee, Y.-Y. Chu, C.-L. Chen, J.-Y. Luo, D.-C. Yan, M.-K. Wu, *EPL*, 2008, **84**, 37002

[326] W. Bronger, A. Kyas, P. Müller, *J. Solid State Chem.*, 1987, **70**, 262-270

[327] K. Kovnir, Y. V. Kolen'ko, A. I. Baranov, I. S. Neira, A. V. Sobolev, M. Yoshimura, I. A. Presniakov, A. V. Shevelkov, *J. Solid State Chem.,* 2009, **182**, 630-639